University of Niš
Faculty of Mechanical Engineering

ADEKO
Association for Design, Elements and Constructions

irmes 2025
Vrnjačka Banja

11th INTERNATIONAL SCIENTIFIC CONFERENCE IRMES 2025

PROCEEDINGS

Research and Development of Mechanical Elements and Systems

19. – 21. June 2025
Department of Mechanical Constructions, Development and Engineering

DB RAZVITAK
Sve na jednom mestu!

Publisher

Faculty of Mechanical Engineering Niš
Prof. dr Goran Janevski, Dean

Editors
Prof. dr Dragan Milčić
Prof. dr Aleksandar Miltenović
Prof. dr Milan Banić
Doc. dr Miodrag Milčić

Technical preparation
Ass. Damjan Rangelov
Ass. Marko Perić

Cover design
Ass. Damjan Rangelov

Number of copies
120

Printing

Grafika Galeb, Niš

Ministry of Science, Technological Development and Innovation of the Republic of Serbia has participated in printing costs of the Proceedings of the 11th International Scientific Conference – IRMES 2025 Research and Development of Mechanical Elements and Systems

All the publications in these Proceedings have the authorship, whereas the authors of the papers carry entire responsibility for originality and content.

PREFACE

Modern product development is no longer just an engineering process – it is a strategic activity that connects technology, the market, design, user experience, and sustainability. Market success depends on the ability to develop innovative solutions quickly, efficiently, and intelligently, using the latest technologies. For this reason, product development must be at the core of educational programs, research centers, and industrial strategies. Today's technological trends – including artificial intelligence, additive manufacturing methods, digitalization, and environmentally sustainable industry – open up a broad range of new perspectives and opportunities for the advancement of this dynamic profession.

The 11th International Scientific Conference – IRMES 2025 – Research and Development of Mechanical Elements and Systems is organized by the Chair of Mechanical Constructions, Development, and Engineering at the Faculty of Mechanical Engineering, University of Niš, and the Association for Design, Elements and Constructions – ADEKO. With a tradition of over three decades, IRMES remains committed to its mission – to bring together researchers, engineers, industry representatives, and students with the aim of enhancing knowledge and its application in industry.

At the previous ten IRMES conferences (the first held in 1995), around one thousand papers were presented, with participation from over one thousand individuals from across the globe. This long-standing and successful tradition forms a solid foundation for organizing this and future IRMES conferences.

All submitted papers for IRMES 2025 underwent international peer review, and 37 papers met the high standards required for publication in the Conference Proceedings. The accepted papers are categorized into four thematic areas of the conference: Mechanical Elements and Systems, Product Development Process, Advanced Technologies in Mechanical Engineering and Mechanical Engineering Education.

We are especially pleased that a significant number of participants from abroad have registered for IRMES 2025. In total, 119 authors from 11 countries are participating. During the two plenary sessions, lectures will be delivered by distinguished professors:

- Prof. Dr.-Ing. Dr. h.c. Bernd-Robert Höhn, Technical University of Munich, School of Engineering and Design
- Prof. Dr. Dražan Kozak, University of Slavonski Brod, Faculty of Mechanical Engineering
- Prof. Dr. Damjan Klobčar, University of Ljubljana, Faculty of Mechanical Engineering
- Prof. Dr. Tomaž Vuherer, University of Maribor, Faculty of Mechanical Engineering
- Prof. Dr. Jasmin Kaljun, University of Maribor, Faculty of Mechanical Engineering
- Prof. Dr. Lorenzo Maccioni, Free University of Bozen-Bolzano, Faculty of Engineering
- Prof. Dr. Franco Concli, Free University of Bozen-Bolzano, Faculty of Engineering
- Prof. Dr. Vladimir Milovanović, University of Kragujevac, Faculty of Engineering
- Prof. Dr. Milan Banić, University of Niš, Faculty of Mechanical Engineering

In today's rapidly changing world, influenced by global economic, environmental, and social factors, it is essential that all of us involved in mechanical engineering in various capacities remain aware of our responsibility. In this context, engineering ethics, quality of work, and lifelong learning play a vital role. Although scientific research is fundamental to economic progress, the education of new generations of mechanical engineers is equally important.

As part of the conference, a Panel Session will be held under the title: The Future of Mechanical Engineering Education: Mechanical Engineering in the Era of Artificial Intelligence.

We are confident that the work at IRMES 2025 will be fruitful and that each of you will leave the conference with new ideas, knowledge, and contacts that will support your further professional development. This is an opportunity not only to learn from one another but also to jointly build the foundation for future research projects and industrial innovations.

Moreover, we hope that in the coming days, we will have the opportunity to get to know each other better, discuss common challenges, and establish new forms of collaboration. In this sense, we emphasize that all your suggestions and proposals are more than welcome and will be carefully considered by the Organizing and Scientific Committees with the aim of improving future conferences.

IRMES 2025 will be further enriched by additional events to support the effective exchange of knowledge and experiences, as well as to ensure a pleasant stay in Vrnjačka Banja in June 2025.

We would like to thank all authors, committee members, reviewers, and others who contributed to the organization and relevance of this conference. Without their support, the organization and realization of IRMES would not have reached the level that its importance and reputation deserve. Special appreciation goes to the Ministry of Science, Technological Development and Innovation and to our general sponsor DB-RAZVITAK d.o.o. Veternik, whose support was crucial.

We wish all participants a successful IRMES 2025 and a pleasant stay in Vrnjačka Banja.

Niš, June 12th, 2025

President of the Scientific Committee

PhD Dragan Milčić,
Full professor

President of the Organizing Committee

PhD Miodrag Milčić,
Associate Professor

University of Niš

11th International Scientific Conference

IRMES 2025

Research and Development of Mechanical Elements and Systems

Faculty of Mechanical Engineering

Organizers

University of Niš, Faculty of Mechanical Engineering
Department of Mechanical Constructions, Development, and Engineering
and
ADEKO – Association for Design, Elements and Construction

Scientific Committee

Prof. dr Dragan Milčić, President
Prof. dr Milan Banić, Aleksandar Miltenović, Vice Presidents

Daniela Alic (ROU)
Ivana Atanasovska (SRB)
Mirko Blagojević (SRB)
Marian Borzan (ROU)
Mehmet Bozca (TR)
István Budai (HU)
Marco Ceccarelli (IT)
Maja Čavić (SRB)
Erwin-Christian Lovasz (ROU)
Remzo Dedić (BIH)
Eleonora Desnica (SRB)
Lubomir Dimitrov (BG)
Mircea-Viorel Dragoi (ROU)
Zorica Đorđević (SRB)
Dragan Đurđanović (USA)
Aleksija Đurić (BIH)
Srečko Glodež (SVN)
Jana Gulanova (SK)
Fuad Hadžikadunić (BIH)
Safet Isić (BIH)
Lozica Ivanović (SRB)
Goran Janevski (SRB)
Janko Jovanović (MNE)
Nenad Kolarević (SRB)
Snežana Ćirić Kostić (SRB)
Nenad Kostić (SRB)
Janez Kramberger (SVN)
Vladislav Krstić (SRB)
Tatjana Lazović (SRB)
Stanislaw Legutko (PL)
Nikhil Londhe (IN/USA)
Aleksandar Marinković (SRB)
Dragan Marinković (DE)
Jelena Stefanović Marinović (SRB)
Nenad Marjanović (SRB)
Biljana Marković (BIH)
Miloš Matejić (SRB)
Athanassios Mihailidis (GRC)
Miroslav Mijajlović (SRB)
Miodrag Milčić (SRB)
Marko Miloš (SRB)
Ljubica Milović (SRB)
Ile Mirčeski (MK)
Žarko Mišković (SRB)
Radivoje Mitrović (SRB)
Dejan Momčilović (SRB)
Tamás Mankovits (HU)
Nenad Petrović (SRB)
Milan Rackov (SRB)
Nebojša Rašović (BIH)
Božidar Rosić (SRB)
Ivan Samardžić (HRV)
József Sárosi (HU)
Miloš Simonović (SRB)
Vasilis Spitas (GRC)
Zoran Stamenić (SRB)
Dušan Stamenković (SRB)
Blaža Stojanović (SRB)
Milan Tica (BIH)
Radoslav Tomović (MNE)
Sanjin Troha (HRV)
Adisa Vučina (BIH)
Krešimir Vučković (HRV)

Organizing Committee

Doc. dr Miodrag Milčić, President
Prof. dr Miroslav Mijajlović
Prof. dr Jelena Stefanović–Marinović
Damjan Rangelov
Marko Perić
Nataša Zdravković

Honorary Committee

Prof. dr Vojislav Miltenović
Prof. dr Radoš Bulatović
Prof. dr Vlastimir Đokić
Prof. dr Siniša Kuzmanović
Prof. dr Milosav Ognjanović, emeritus
Prof. dr Vilmos Simon
Prof. dr Slobodan Tanasijević
Prof. dr Miroslav Vereš
Prof. dr Aleksandar Vulić

Program Committee

Prof. dr Radivoje Mitrović, emeritus, President, University of Belgrade, Serbia
Prof. dr Žarko Mišković, Secretary, University of Belgrade, Serbia
Prof. dr Dragan Milčić, University of Niš, Serbia
Prof. dr Nenad Marjanović, University of Kragujevac, Serbia
Prof. dr Milan Rackov, University of Novi Sad, Serbia
Prof. dr Radoslav Tomović, University of Montenegro, Montenegro
Prof. dr Milan Tica, University of Banja Luka, Republic of Srpska
Prof. dr Biljana Marković, University of East Sarajevo, Republic of Srpska
Prof. dr Adisa Vučina, University of Mostar, Bosnia and Herzegovina

Reviewers

Prof. dr Dragan Milčić, University of Niš, Serbia
Prof. dr Milan Banić, University of Niš, Serbia
Doc. dr Marko Mančić, University of Niš, Serbia
Prof. dr Biljana Marković, University of East Sarajevo, Republic of Srpska
Doc. dr Miloš Matejić, University of Kragujevac, Serbia
Prof. dr Miroslav Mijajlović, University of Niš, Serbia
Doc. dr Miodrag Milčić, University of Niš, Serbia
Prof. dr Aleksandar Miltenović, University of Niš, Serbia
Prof. dr Žarko Mišković, University of Belgrade, Serbia
Doc dr. Vukašin Pavlović, University of Niš, Serbia
Prof. dr Milan Rackov, University of Novi Sad, Serbia
Prof. dr Miloš Simonović, University of Niš, Serbia
Prof. dr Dušan Stamenković, University of Niš, Serbia
Prof. dr Jelena Stefanović–Marinović, University of Niš, Serbia
Prof. dr Milan Tica, University of Banja Luka, Republic of Srpska

Patron

Ministry of Science, Technological Development and Innovation of Republic of Serbia

Cofinanciers

DB RAZVITAK

CONTENTS

Plenary Lecture A

P.A.1 RESEARCH AT FZG I
Bernd-Robert HÖHN

P.A.2 FROM CONCEPT TO CREATION: LEVERAGING ARTIFICIAL INTELLIGENCE IN MECHANICAL DESIGN AND IDEATION III
Jasmin KALJUN, Andrej CUPAR, Klavdija KOPŠE KALJUN

P.A.3 OPEN-SOURCE CFD FOR LUBRICATED COMPONENTS: MODELING AERATION, CAVITATION, AND NON-NEWTONIAN EFFECTS WITH COMPUTATIONAL EFFICIENCY XIII
Lorenzo MACCIONI, Franco CONCLI

P.A.4 AgAR: A MULTIPURPOSE ROBOTIC PLATFORM FOR THE DIGITAL TRANSFORMATION OF AGRICULTURE XXIII
Milan BANIĆ, Lazar STOJANOVIĆ, Marko PERIĆ, Damjan RANGELOV, Vukašin PAVLOVIĆ, Aleksandar MILTENOVIĆ, Miloš SIMONOVIĆ

Plenary Lecture B

P.B.1 EXPERIMENTAL AND NUMERICAL INVESTIGATION OF HSS WELDED JOINTS FRACTURE BEHAVIOR XXXIII
Dražan KOZAK, Damir TOMERLIN, Ivan SAMARDŽIĆ, Pejo KONJATIĆ, Nenad GUBELJAK

P.B.2 ENHANCING THE MECHANICAL PROPERTIES OF DIRECTED ENERGY DEPOSITION ARC (DED-Arc) VIA PROCESSING INNOVATIONS XXXV
Damjan KLOBČAR, Uroš TRDAN, Mirza IMŠIROVIĆ, Drago BRAČUN, Mohammad REZA GHAVI, Tomaž VUHERER, Marek POLANSKI, Aleksija ĐURIĆ, Matija BUŠIĆ, Miodrag MILČIĆ

P.B.3 STRAIN AND STRESS/FORCE-CONTROLLED FATIGUE TESTING OF METALLIC MATERIALS, POST-PROCESSING OF EXPERIMENTALLY OBTAINED RESULTS AND APPLICATION IN FEA XLIX
Vladimir MILOVANOVIĆ

Mechanical Elements and Systems

1.1. THE INFLUENCE OF CRYOGENIC TREATMENT ON THE HARDNESS OF ROLLING BEARNINGS' BALLS 1
Jovana ANTIĆ, Žarko MIŠKOVIĆ, Danilo PEJČIĆ, Martin DIX, Alexander PIERER, Jürgen HEIDRICH, Matthias DEMMLER

1.2. ANALYSIS OF THE INFLUENCE OF WAVINESS AND AXIAL LOAD ON THE DYNAMIC BEHAVIOR OF BALL BEARINGS 5
Ivan KNEŽEVIĆ, Milan RACKOV, Aleksandar ŽIVKOVIĆ, Mirjana BOJANIĆ ŠEJAT, Željko KANOVIĆ

1.3. ANALYSIS OF NATURAL FREQUENCIES OF A HYBRID ALUMINUM/COMPOSITE SHAFT 13
Zorica ĐORĐEVIĆ, Sonja KOSTIĆ, Danijela NIKOLIĆ, Saša JOVANOVIĆ

1.4. METHODOLOGY FOR CALCULATING SURFACE PRESSURE ON THE CONTACT SURFACES OF CONICAL CLAMPING RINGS 17
Goran MIHAJLOVIĆ, Marina KARIĆ, Jelena ERIĆ OBUĆINA, Zvonko PETROVIĆ

1.5. DATA DRIVEN PREDICTION OF SHEAR STRENGTH OF COMPOSITE SLIDER JOINTS 23
Miloš MILOVANČEVIĆ, Srđan STOJIČIĆ, Mirjana MILJANOVIĆ, Nikola SIMONOVIĆ, Dragana TRNAVAC

1.6. DEVELOPMENT AND THERMAL ASSESSMENT OF A HIGH-POWER GEARBOX 27
Vojkan NOJNER, Dragan MILČIĆ, Milan BANIĆ

1.7. OPPORTUNITIES FOR THE APPLICATION OF A PLANETARY GEARBOX AS A REVERSING UNIT 33
Sanjin TROHA, Jelena STEFANOVIĆ MARINOVIĆ, Željko VRCAN, Kristina MARKOVIĆ, Marko PERIĆ
1.8. MECHANICAL PROPERTIES OF BONDED JOINTS MADE OF SLM ADDITIVE MANUFACTURED ADHERENDS 39
Natalija MRATINKOVIĆ, Miodrag MILČIĆ, Nataša ZDRAVKOVIĆ, Dragan MILČIĆ, Marko PERIĆ
1.9. GEAR MATERIAL SELECTION BY USING MCDM SOLVER 45
Dušan PETKOVIĆ, Miloš MADIĆ

Product Development Process

2.1 TOWARDS SMART ENGINEERING PRODUCTS 51
Radivoje MITROVIĆ, Zarko MISKOVIĆ, Vidosav D. MAJSTOROVIĆ
2.2. SELECTING OF SOLUTIONS IN DEVELOPING THE BOBCAT E62 EXCAVATOR CONTROL HANDLE 65
Biljana MARKOVIĆ, Vidak ČAJEVIĆ, Aleksija ĐURIĆ, Srđan SAMARDZIĆ
2.3. APPLICATION OF FIXTURES PRODUCED WITH FDM TECHNOLOGY IN THE ADHESIVE BONDING OF PARTS IN THE RAILROAD INDUSTRY 71
Srđan SAMARDŽIĆ, Damjan KLOBČAR, Aleksija ĐURIĆ, Biljana MARKOVIĆ
2.4 ANALYSIS OF PROGRESS IN THE DEVELOPMENT OF HYDRAULIC ACTUATOR-BASED ABOVE-KNEE PROSTHESIS AND FUTURE GUIDELINES 75
Aleksandar TOMOVIĆ, Remzo DEDIĆ, Adisa VUČINA, Nebojša RAŠOVIĆ, Radoslav TOMOVIĆ, Milanko DAMJANOVIĆ
2.5. DEVELOPMENT OF THE CRNOJEVIC PRINTING MACHINE REPLICA 79
Radoslav TOMOVIĆ, Aleksandar TOMOVIĆ
2.6. ASSESSING ACHIEVED SAVINGS USING OPTIMIZED TRUSSES WITH CARDINALITY CONSTRAINTS 83
Nenad KOSTIĆ, Nenad PETROVIĆ, Vesna MARJANOVIĆ, Nenad MARJANOVIĆ
2.7. MEASUREMENT OF THE KINEMATIC CHARACTERISTICS OF ZIPLINE PASSENGERS 89
Tanasije JOJIĆ, Jovan VLADIĆ, Radomir ĐOKIĆ, Nikola ILANKOVIĆ, Mirko KATONA

Advanced Technologies in Mechanical Engineering

3.1. NUMERICAL ANALYSIS OF FOUR TYPES OF ARC STAR SHAPED AUXETIC STRUCTURES 95
Vladimir SINĐELIĆ, Snežana ĆIRIĆ-KOSTIĆ, Aleksandar NIKOLIĆ, Nebojša BOGOJEVIĆ
3.2. COMPARISON OF CONVENTIONAL AND IMACHINING STRATEGIES USING THE SOLIDCAM SOFTWARE 101
Eleonora DESNICA, Ivan PALINKAŠ, Dejan LANDUP, Mića ĐURĐEV, Borivoj NOVAKOVIĆ, Luka ĐORĐEVIĆ
3.3. CAVITATION EROSION PARAMETERS OF LASER SINTERED MS1 STEEL TESTED ACCORDING TO ASTM G32 STANDARD 107
Pavle LJUBOJEVIĆ, Tatjana LAZOVIĆ, Marina DOJČINOVIĆ
3.4. VAT PHOTOPOLYMERIZATION RISK ASSESSMENT USING THE KINNEY METHOD 113
Danilo PEJČIĆ, Žarko MIŠKOVIĆ, Jovana ANTIĆ, Radivoje MITROVIĆ, Lubos MAGDOLEN, Tomas MILESICH, Jan DANKO
3.5. APPLICATIONS AND ANALYSIS OF NANOSTRUCTURED ADHESIVES: A REVIEW 119
Aleksija ĐURIĆ, Biljana MARKOVIĆ, Srđan SAMARDŽIĆ, Dragan MILČIĆ, Damjan KLOBČAR, Miodrag MILČIĆ
3.6. EXPERIMENT PREPARATION FOR LASER-CUT SPUR GEARS EFFICIENCY TESTING 123
Anđela PEROVIĆ, Mirko BLAGOJECIĆ, Miloš MATEJIĆ, Lozica IVANOVIĆ, Ivan MILETIĆ

3.7. ANALYSIS NETWORK INFRASTRUCTURE IMPACT ON INFORMATION – COMMUNICATION TECHNOLOGY (ICT) DEVELOPMENT 129
Miloš MILOVANČEVIĆ, Srđan STOJIČIĆ, Mirjana MILJANOVIĆ, Nikola SIMONOVIĆ, Dragana TRNAVAC
3.8. OPTIMIZATION OF PREDICTIVE MODELS FOR THE THERMAL BEHAVIOR OF LEADING AND THREADED SPINDLES AND THEIR CORRESPONDING ROLLING BEARINGS USING AI AND BIG DATA 133
Vladislav KRSTIĆ, Dragan MILČIĆ, Miodrag MILČIĆ
3.9. EFFICIENCY OPTIMIZATION OF A WORM GEAR TRANSMISSION USING THE CCD METHOD AND ANOVA 139
Sandra GAJEVIĆ, Aleksandar SKULIĆ, Anđela ŽIVKOVIĆ, Slavica MILADINOVIĆ, Stefan ČUKIĆ, Milan BUKVIĆ, Blaža STOJANOVIĆ
3.10. EXPERIMENTAL AND NUMERICAL ANALYSIS OF SINGLE LAP ALUMINIUM JOINTS BONDED WITH DIFFERENT EPOXY ADHESIVES 147
Nataša ZDRAVKOVIĆ, Milan BANIĆ, Damjan KLOBČAR, Miodrag MILČIĆ, Szabolcs FISCHER
3.11. FINITE ELEMENT ANALYSIS OF THREE-STAGE PLANETARY GEAR TRAIN FOR ROAD VEHICLE WINCH 151
Marko PERIĆ, Aleksandar MILTENOVIĆ, Jelena STEFANOVIĆ-MARINOVIĆ, Damjan RANGELOV, Lazar STOJANOVIĆ, Saša PAVLOVIĆ, Daniela ALIC
3.12. AN EXPERIMENTAL STUDY ON LAYER ADHESION IN FDM 3D PRINTING: COMPARING CONVENTIONAL AND BRICK-LAYER DEPOSITION PATTERNS 155
Damjan RANGELOV, Lazar STOJANOVIĆ, Aleksandar MILTENOVIĆ, Jovan ARANĐELOVIĆ, Marko PERIĆ
3.13. PREDICTION OF TRIBOLOGICAL PROPERTIES OF ALUMINUM WELDED BY FRICTION STIR WELDING (FSW), A REVIEW 159
Amir ALSAMMARRAIE, Abdul SALAM Y. OBAID

Mechanical engineering education

4.1. COMPETENCIES FOR MECHANICAL ENGINEERS IN MACHINE DESIGN AND PRODUCT DEVELOPMENT 167
Milan BANIĆ, Aleksandar MILTENOVIĆ, Dragan MILČIĆ

Index of authors

Plenary Lecture A

11th International Scientific Conference
IRMES 2025
Research and Development of
Mechanical Elements and Systems
June 19 – 21, 2025; Vrnjačka Banja, Serbia

Abstract only

DOI: not assigned

RESEARCH AT FZG

Bernd-Robert HÖHN[1]

[1]Technical University of Munich, School of Engineering and Design, Munich, Germany, 80333; bernd-robert.hoehn@tum.de;

Abstract: *The first part will show the activity of FZG in the topic transmission systems. The pictures 3- 22 will show the running Project "opt4E". it is the follower of the project 1 and 2, where a new driveline for electric cars with al lot of partners from industry and universities have produced a prototype for electric cars. The focus of the two projects in the past was the increasing speed of electric engines. In the first project the income speed of the electric engine was roughly 20000min^{-1}. It has be shown that a highspeed electric engine will become a reduced weight of the engine. Therefore, the next step was an increasing input speed of about 50000min^{-1}. The result was very simple: power is the multiplication of torque and speed. As higher the speed as lower is the torque. And torque is the factor, which influences the dimension/size of the engine. Nevertheless, high speeds are problematic for dynamic of the driveline.*
The third part of the project is now running. A further increase of speed is not more in the focus, because difficulties from the dynamic problems arise more and more. It can be shown, that the influence of e-motor (type), transmission and inverter show a big relation between the components. Therefore, a multicriterial optimization should solve the problems, which are shown in the second project. This new method will optimize the design of E-Motor, inverter and transmission to optimize the energy-consumption.
The second part is the summary of a project, which is financed from the DFG (Deutsche Forschungs Gemeinschaft, Kosseleck-program) in first part of my retirement. The principal idea is that lubricants in transmission have two tasks: first to produce a film between the two surfaces, and second to transfer the energy-losses (heat) away from the contact. In normal gears 10% is necessary for lubrication and 90% for transport the heat. With better gears (higher efficiency, lower sliding in the contact) and better lubricants (lower friction coefficient) we need lower amount of lubricant in the contact for the heat-transport. This should be possible with lubricants inside of the material. The pictures show the result: sometimes it works, sometime not. A typical result of research. Till now it is not recommended for real application for engineers. The result show at the end of the project that the production of the surface (grinding for low roughness) is the main key for solving the problem. It can be shown in the last pictures.
The third part show the influence of low-loss-gear in the example of a wolfrom-transmission. Low-loss-gears are characterized with small contact ratio of $\varepsilon\alpha \geq 1$ (1,1) and the pitchpoint C in the middle of the line of contact. With this type of involute gears the sliding in the surface contact can be minimized, the efficiency can be improved. The wolfrom-transmission are wellknown, but the engineers have in mind: low number of parts for high ratio (advantage), but worse efficiency (disadvantage). The worse efficiency is coming from the blind power of the plus transmission (one part of the wolfrom-transmission). This responsible gear-mesh can be optimized, with low losses and increasing efficiency. Therefore, the shown wolfrom-transmission without carrier is the solution for better efficiency and lower backlash. The application of this type for high ratio can be in the robotic-, medicine- and food-industry.

Keywords: *driveline, sinter material with inside lubricants, low-loss-gears; wolfrom-transmission.*

11th International Scientific Conference
IRMES 2025
Research and Development of
Mechanical Elements and Systems
June19 – 21, 2025;Vrnjačka Banja, Serbia

Original scientific paper DOI: 10.46793/IRMES25.plA2K

FROM CONCEPT TO CREATION: LEVERAGING ARTIFICIAL INTELLIGENCE IN MECHANICAL DESIGN AND IDEATION

Jasmin KALJUN[1]
Andrej CUPAR[2]
Klavdija KOPŠE KALJUN[3]

[1]University of Maribor, Faculty of Mechanical Engineering, Maribor, Slovenia, 2000; jasmin.kaljun@um.si;
ORCID iD: 0000-0003-3473-7839
[2]University of Maribor, Faculty of Mechanical Engineering, Maribor, Slovenia, 2000; andrej.cupar@um.si
[3]Celje School Centre, Celje, Slovenia, 3000; klavdija.kaljun@sc-celje.si

Abstract:*This paper explores the integration of artificial intelligence (AI) into mechanical design workflows, with a focus on improving ideation, creativity and iterative development. Traditional design processes, limited by sequential workflows, time-consuming iterations and reliance on intuition, are increasingly unable to cope with the complexity and pace of modern product development. To overcome these limitations, an AI-driven design framework is proposed that consists of four interconnected components: generative design algorithms, surrogate modelling and performance prediction, data-driven decision support, and a human-AI interaction layer. The framework is validated through two case studies: the generative design of an ergonomic armrest optimised for additive manufacturing and biomechanical performance, and an educational study investigating the impact of AI-assisted sketching (Vizcom) on student creativity in sustainable product design. The results show that iteration was accelerated, design diversity improved, and user engagement increased. In addition to presenting the technical results, the paper builds on the author's previous research on intelligent ergonomic and aesthetic guidance systems and provides a long-term perspective on the development of AI-powered design tools. The discussion emphasises the need for human-centred AI, robust data infrastructures and ethical accountability. The paper concludes with an outlook on future directions in adaptive AI learning, training and responsible implementation in technical practise.*

Keywords: *AI-driven design; generative design; design iteration; human-AI collaboration; ergonomic optimization*

1. INTRODUCTION

The integration of artificial intelligence (AI) into mechanical engineering is transforming how products are conceived, developed, and brought to market. Traditional mechanical design has long relied on human intuition, iterative development, and experience-based decision-making to create functional and market-relevant products. However, as product complexity increases and development cycles shorten, conventional design processes face growing limitations in terms of efficiency, flexibility, and innovation potential [1].

Historically, mechanical design has been defined by a sequential and human-centred workflow. Designers sketch concepts, engineers translate ideas into technical models, and simulation or prototyping validates assumptions. This model, while methodical, often restricts creative exploration due to time constraints, risk aversion, and the cognitive load associated with evaluating multiple alternatives [2, 3]. Furthermore, the fragmented nature of design data across various digital tools and platforms creates additional inefficiencies and limits the reuse of knowledge [4].

Artificial intelligence introduces the potential to augment, restructure, and optimize these workflows. Tools powered by AI,such as generative design algorithms, neural networks, and reinforcement learning agents, can autonomously generate, simulate, and evaluate thousands of design alternatives in parallel. This capacity allows for significantly broader design space exploration while reducing the manual labour required in early-stage ideation [5, 6].

AI not only addresses the technical constraints of traditional design methods but also opens opportunities for deeper human-machine collaboration (Fig.1). Designers are increasingly supported by intelligent assistants that provide predictive insights, accelerate creative visualization, and recommend optimized configurations based on defined objectives and constraints

[7]. Yet, these benefits are coupled with challenges, including over-reliance on algorithms, interpretability concerns, and the need for ethical oversight in automated decision-making [8].

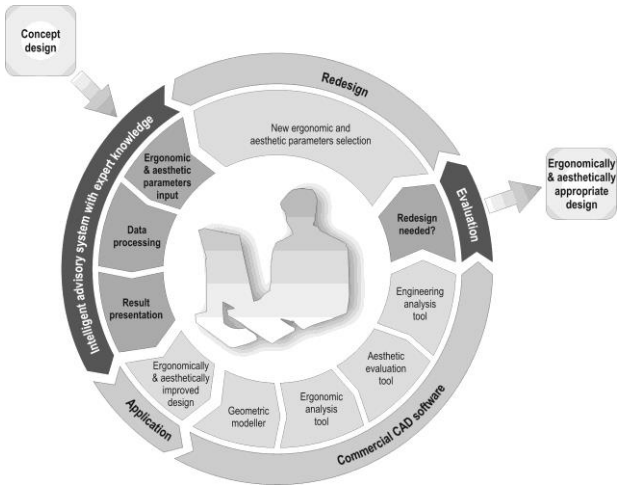

Fig.1. Design cycle using intelligent advisory system

This paper explores the evolving relationship between AI and mechanical design by examining critical limitations of conventional workflows and presenting a human-centred AI design framework. Through two detailed case studies, the paper demonstrates how AI-enhanced methods can increase creativity, improve performance, and streamline design iteration. The discussion highlights not only the advantages of AI integration but also the risks and responsibilities associated with this paradigm shift.

1.1. Development of AI-Driven Ergonomic and Aesthetic Advisory Frameworks

The integration of artificial intelligence in product design has been an active field of research for over a decade. The authors of this paper have contributed to this area, particularly through the development and validation of intelligent advisory systems for ergonomic and aesthetic optimization in mechanical product design. These research efforts have primarily focused on enhancing decision-making in the early conceptual phase, where critical ergonomic and aesthetic decisions are made and where the designer's knowledge base often shows the greatest variance in quality and completeness.

In response to the limitations of existing ergonomic Computer-Aided Design (CAD) tools, which typically offer only passive analysis capabilities, the authors developed an intelligent decision support system Oscar (Fig.2). This system was designed to actively advise designers on ergonomic and aesthetic design strategies, using a structured knowledge base and rule-based inference engine to emulate expert reasoning. The Oscar system is described in depth across several peer-reviewed publications [9–11].

The primary motivation for Oscar was the recognition that designers, especially those early in their careers or operating within small and medium-sized enterprises (SMEs), often lack access to ergonomic experts and structured design guidelines. While conventional ergonomic tools such as RAMSIS, SAFEWORK, or ErgoSHAPE allow simulation-based assessment of postural comfort or anthropometric fit, they do not offer prescriptive advice or actionable design feedback. Oscar bridges this gap by incorporating knowledge from human factors engineering, industrial design, and cognitive ergonomics into a reasoning framework capable of proposing concrete design actions.

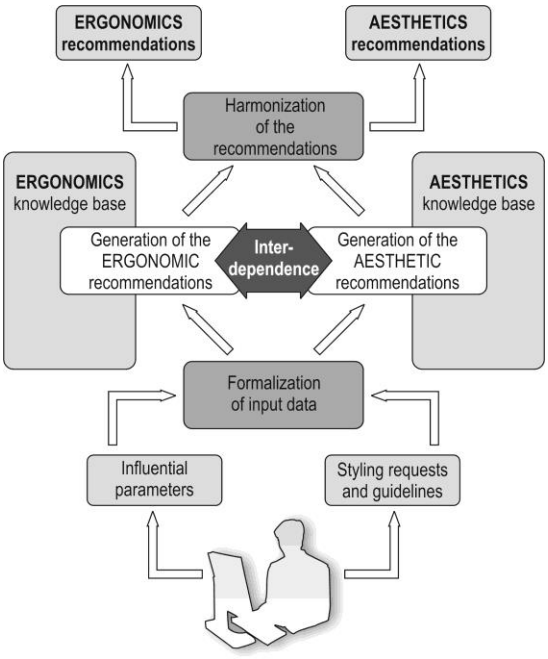

Fig.2. The architecture of the proposed intelligent system.

The system architecture is based on modular expert subsystems for ergonomics and aesthetics. The ergonomic module emphasizes handle design, grip comfort, and neutral joint alignment, while the aesthetic module incorporates compositional harmony, semantic intent, and material expressiveness. These modules can function independently or synergistically, depending on the design phase and user requirements. The underlying logic relies on IF–THEN production rules that encode validated ergonomic and aesthetic guidelines into executable reasoning structures [11].

One of the most advanced features of the system is its ability to harmonize potentially conflicting ergonomic and aesthetic goals. For instance, while optimal grip thickness may enhance comfort and reduce tissue compression, it may conflict with minimalistic visual goals. Oscar's inference engine can negotiate such trade-offs by assigning confidence values to competing recommendations and suggesting balanced solutions. This capability has been validated through use cases including the redesign of hand tool grips and pneumatic hammer handles [10].

In earlier work, Oscar was applied to ergonomic analysis and redesign of hand tools manipulated with upper extremities – one of the most critical domains due to high exposure to repetitive strain and force exertion. The research formalized ergonomic design knowledge into a multi-level framework. At the general level, it guided form and posture recommendations. At the intermediate

level, it advised on anthropometric and biomechanical alignment. At the detailed level, it generated recommendations (Fig.3) for material selection, pressure distribution, and surface contouring based on user profiles and tool function.

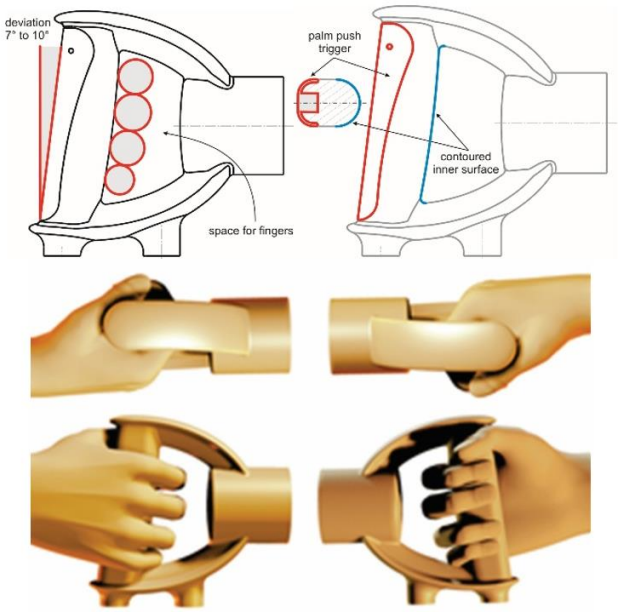

Fig.3. Recommendations generated by Oscar intelligent advisory system

These principles were extended in later work to include aesthetic and semantic dimensions of product perception. Kaljun [12] emphasized that the visual and tactile congruence of products-how well they "feel" as they "look"-is critical for achieving high user satisfaction. Oscar's aesthetic module thus incorporated not only stylistic trends but also user expectation modelling, semantic signalling (e.g., aggressive or soft forms), and material-based impression consistency. This extension was particularly impactful for product categories such as consumer electronics and hand-operated tools, where visual identity significantly affects purchasing decisions.

An important outcome of this research has been the methodological formalization of aesthetic ergonomics – an emerging field that addresses how visual and tactile product characteristics affect perceived comfort, usability, and emotional response. The author's work contributes an actionable model for integrating anthropometry, user emotion, and semantic intent into early-phase design decisions, grounded in AI-based logic reasoning and supported by validated data structures.

The research efforts also underscore the role of intelligent systems as democratizing tools. By encoding expert knowledge into reusable and interactive formats, Oscar reduces dependency on high-level individual expertise and promotes evidence-based design practices accessible to a broader range of practitioners. This approach aligns with broader goals of AI in engineering – to not only accelerate workflows but to ensure quality, safety, and user-centred outcomes across varying levels of designer expertise.

2. CHALLENGES IN TRADITIONAL MECHANICAL DESIGN

Despite decades of methodological and technological advancement, traditional mechanical design processes continue to encounter persistent bottlenecks that limit their responsiveness, innovation capacity, and scalability. These challenges are most evident in the early phases of product development, where ideation, concept generation, and iterative refinement intersect with cognitive, temporal, and organizational constraints [1]. This section identifies four critical limitations: time-consuming iterations, limited exploration of design alternatives, reliance on human intuition, and fragmented design knowledge.

2.1. Time-Consuming Iterations

Iteration is fundamental to engineering design, enabling progressive refinement through repeated modelling, simulation, and evaluation. However, in traditional workflows, each iteration demands significant time and manual effort, especially when changes to one component cascade across dependent subsystems [13]. Even minor design modifications may require complete regeneration of CAD models, re-execution of simulations, and labour-intensive documentation updates. According to Wynn and Eckert [1], such iterative dependencies significantly prolong development cycles and inflate project costs, particularly in complex systems.

Iteration is further hampered by a lack of automation across design environments. Disconnected modelling and simulation tools force engineers to repeat routine operations manually. This inefficiency is exacerbated in multidisciplinary projects, where coordination between teams often introduces additional delays and communication barriers [14].

2.2. Limited Exploration of Design Alternatives

Designers often face trade-offs between thoroughness and practicality. Time and resource constraints typically force early convergence on familiar solutions, limiting exploration of novel configurations that may offer better performance or user value. Traditional CAD environments do not inherently support rapid generation or comparison of large sets of alternatives, making it difficult to move beyond incremental improvements.

Research in design optimization has shown that manual methods tend to focus on local optima, shaped by the designer's prior experience and available heuristics [15]. As a result, truly innovative or non-intuitive solutions are frequently overlooked. Moreover, the lack of integrated optimization frameworks within most engineering workflows limits the ability to evaluate complex trade-offs, such as structural strength versus manufacturability or material usage versus aesthetics, in a rigorous and scalable way.

2.3. Dependence on Human Intuition

Intuition plays a crucial role in design ideation and decision-making, especially in ill-defined or exploratory tasks. However, reliance on intuition introduces

subjectivity and inconsistency. Designers bring different experiences, cognitive biases, and aesthetic preferences, which can result in divergent design outcomes even under similar conditions [16]. Moreover, intuitive reasoning is often undocumented, making it difficult to transfer knowledge, justify decisions, or ensure repeatability across teams or generations.

While tacit knowledge is invaluable, it is not always reliable in complex systems or novel application domains. Anchoring bias, fixation on precedent solutions, and confirmation bias can all distort design judgments. These cognitive limitations underscore the need for data-supported methodologies that complement intuition without eliminating it [17].

2.4. Data and Knowledge Fragmentation

Modern product development relies on vast quantities of geometric, functional, and performance-related data. However, this data is often fragmented across heterogeneous platforms (e.g., CAD, CAE, PLM systems), which are rarely interoperable. The result is a design ecosystem where valuable knowledge like past project insights, simulation results, user feedback, is poorly connected, inconsistently formatted, and difficult to reuse.

This fragmentation not only impairs collaboration but also limits the ability of engineers to learn from historical data or benchmark current designs against past solutions. In many organizations, informal communication channels and individual memory remain the primary mechanisms of knowledge transfer. Without structured data curation and automated insight extraction, design teams face an avoidable loss of efficiency and innovation potential[4].

3. AI-DRIVEN DESIGN FRAMEWORK

The limitations of traditional mechanical design workflows have catalysed interest in AI-assisted systems capable of accelerating ideation, expanding solution spaces, and augmenting engineering judgment. The AI-driven design framework proposed in this section (Fig.4) integrates state-of-the-art computational tools into each phase of the mechanical design process-shifting from sequential to parallelized, data-informed development. By embedding AI into the conceptual, generative, and evaluative stages of design, the framework enables a more intelligent, scalable, and collaborative engineering methodology.

3.1. Architecture of the Framework

At its core, the AI-driven design framework is structured around four interrelated components:

- Generative Design Algorithms, which automate the creation of design variants based on defined performance constraints.
- Surrogate Modelling and Performance Prediction, which allow for rapid, approximate evaluation of design alternatives without full simulation cycles.
- Data-Driven Decision Support, which leverages design repositories, performance databases, and user preferences to guide concept selection.
- Human-AI Interaction Layer, which ensures transparency, control, and interpretability of AI-generated suggestions.

This modular architecture facilitates flexible integration with existing CAD/CAE environments and supports iterative refinement through continuous learning and feedback loops.

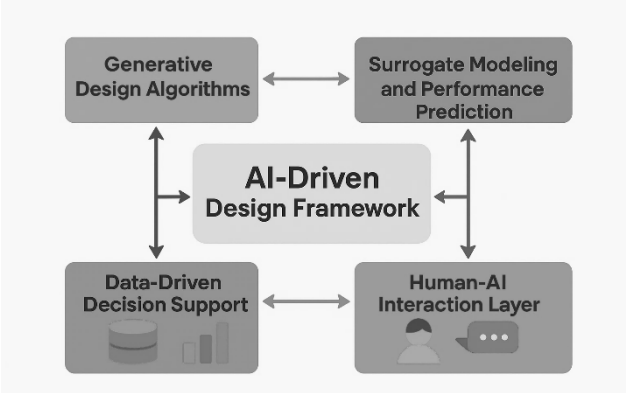

Fig.4. AI-driven design framework

3.2. Generative Design and Concept Exploration

Generative design enables the automated synthesis of thousands of concept variants based on objectives such as material minimization, structural strength, or thermal conductivity. Algorithms such as topology optimization, evolutionary strategies, or generative adversarial networks (GANs) can generate complex, non-intuitive geometries that would be difficult to discover manually [18].

The output of these systems is not a single “optimal” design but a spectrum of viable solutions, each representing a unique trade-off. This diversity fosters early-stage innovation by encouraging designers to consider unconventional configurations that meet performance criteria while supporting manufacturability and user experience.

3.3. Surrogate Modelling and Deep Learning

High-fidelity simulations such as finite element analysis (FEA) are computationally intensive and often prohibit real-time iteration. Surrogate models, typically based on machine learning techniques such as Gaussian processes or deep neural networks, provide a solution by approximating simulation outputs with high accuracy and low latency [19]. These models are trained on historical simulation data and enable near-instantaneous predictions of stress distribution, deformation, or energy efficiency for new designs.

In addition, autoencoders and convolutional neural networks (CNNs) are used to translate 2D sketches into 3D geometry, enabling AI to bridge the gap between concept drawing and CAD modelling. This capacity supports rapid design evolution directly from visual ideation inputs.

3.4. Data-Driven Optimization and Retrieval

Large-scale design repositories, both institutional and public, can be mined using AI for precedent-based learning, component matching, and trend detection. This

approach enables designers to leverage prior knowledge, identify successful patterns, and avoid reinventing existing solutions [20]. Optimization algorithms can then refine selected designs by adjusting parameters to meet competing goals under multi-objective constraints.
By incorporating user feedback, performance outcomes, and lifecycle data, the AI system evolves over time, improving its recommendations and adapting to domain-specific requirements.

3.5. Human-AI Collaboration Layer

The integration of AI into mechanical design must remain grounded in human-centred principles. Transparency in algorithmic reasoning, user control over generated outputs, and interpretability of results are essential to foster trust and ensure that final decisions remain with the human designer [7].
This collaboration is not hierarchical but synergistic: AI enhances speed and scale, while humans provide context, ethical reasoning, and creative interpretation. Interactive interfaces allow users to adjust constraints, guide generative logic, and refine outputs in a co-creative workflow.

4. HUMAN-AI COLLABORATION

Artificial intelligence in mechanical design is not intended to replace the human designer, but to augment cognitive and creative capabilities. Human-AI collaboration defines a new interaction model in which designers and machines co-create, learn from each other, and share responsibility across the design process. This paradigm shift requires not only technological innovation but also careful attention to human-centred principles such as interpretability, trust, empowerment, and ethical alignment [7].

4.1. Principles of Human-Centred AI in Design

Effective collaboration between designers and AI systems depends on the careful orchestration of roles and responsibilities. While AI can automate low-level tasks, such as parametric variation or simulation-based screening, it lacks the contextual understanding and ethical reasoning required for higher-level design decisions [17]. Human-centred AI frameworks emphasize transparency, user empowerment, and context sensitivity to ensure alignment between machine outputs and human objectives [8].
Transparency refers to the ability of users to understand how an AI system reaches its conclusions. Design decisions must be explainable, particularly when safety, compliance, or user well-being is at stake. Empowerment ensures that users retain control over AI-generated outputs, with options to accept, reject, or modify proposals. Context awareness allows AI systems to adapt their suggestions based on user expertise, design phase, and specific domain constraints [21].

4.2. Creativity and Intuition in Human-AI Teams

While AI can rapidly generate and evaluate thousands of designs, the ability to synthesize abstract goals, cultural values, and user needs remains a uniquely human capability. Designers apply aesthetic judgment, ergonomic reasoning, and contextual framing-qualities that are difficult to encode algorithmically. The most productive collaborations occur when AI is used to expand the design space while humans curate and guide the selection process.
Lockhart [17] argues that genuine creativity arises not from computational novelty but from human interpretation and narrative construction. For example, an AI may produce structurally optimal but aesthetically undesirable geometries. It is the designer who interprets these results, modifies them for usability, and aligns them with user expectations. This reinforces the need for interaction models that allow real-time dialogue between designer and machine.

4.3. Interaction Strategies and Tool Design

The nature of human-AI collaboration depends strongly on the user interface and workflow integration. Ethnographic studies by Ma et al. [21] show that design professionals engage with AI tools in multiple ways: some use AI for exploratory co-creation, while others treat it as a decision-support utility. These strategies depend on factors such as trust, familiarity with the system, and task complexity.
AI tools designed for collaborative ideationsuch as Vizcom or Autodesk Generative Design, enable users to adjust constraints, visualize alternatives, and modify inputs dynamically. They support fluid transitions between divergent and convergent thinking, allowing iterative refinement across concept phases. Key usability features include visual traceability, editable parameter spaces, and real-time feedback [7].
To foster adoption, these tools must be intuitive and accessible to users with diverse technical backgrounds. This includes clear documentation, visual guidance, and seamless integration with existing CAD/CAE environments.

4.4. Building Trust and Accountability

For AI tools to be effective collaborators, users must develop calibrated trust-relying on AI when appropriate but maintaining scepticism in ambiguous or high-stakes situations. Over-reliance can lead to design errors, while under-trust limits the benefits of automation. Calibrated trust arises from system reliability, transparency, and continuous user feedback [8].
Accountability remains a human responsibility, regardless of AI involvement. Final design decisions, especially in regulated industries such as aerospace or medical devices, must be traceable to human judgment. Ethical frameworks like Ethics by Design advocate for transparent audit trails, validation procedures, and clearly defined roles for AI and human agents [22].
In conclusion, human-AI collaboration in mechanical design requires more than technical integration-it demands careful attention to interface design, human values, and creative agency. When implemented thoughtfully, AI becomes a powerful ally, enhancing not only productivity but also the quality, inclusiveness, and

innovation potential of design outcomes. The following case studies demonstrate these principles in practice.

5. CASE STUDIES

To demonstrate the real-world applicability of AI-enhanced design, two complementary case studies are presented. The first explores the generative design of an ergonomic armrest developed through collaboration between academic and industrial partners. The second evaluates the use of AI-assisted sketching in an educational context, focusing on creativity and user satisfaction.

5.1. Generative Design of a Lightweight Ergonomic Armrest

This case study illustrates the use of generative tools, biomechanical simulation, and additive manufacturing in developing a forearm-support device intended for desktop ergonomics. The project was executed by the lead author in collaboration with Addiflex d.o.o. (Slovenia).
The process began with a critical analysis of two commercial products - Cherry and ErgoFlow - which revealed ergonomic and aesthetic limitations (Fig.5).

Fig.5. Reference armrests Cherry (a) and ErgoFlow (b) used for benchmarking.

Ideation was conducted via sketching, and the most promising form was selected based on comfort and aesthetic criteria (Fig.6).

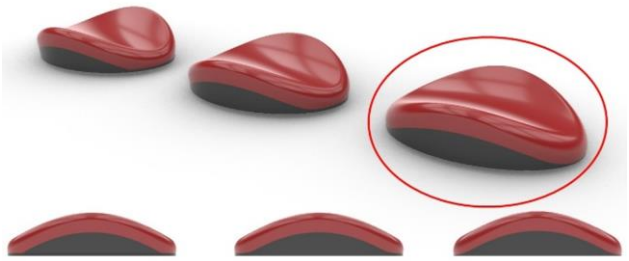

Fig.6. Selected concept sketch featuring dual-curvature geometry.

Initial models were generated using Rhinoceros 3D and Grasshopper, allowing exploration of variants. Vizcom was used to accelerate concept refinement and visualization. A sinusoidal surface contour was added to improve contact comfort and visual flow.
The contact pad was then optimized in nTop using a generative approach, informed by pressure maps from finite element simulations of forearm contact.
The final version (Fig.7) featured a graded structure with dense outer cells for stability and softer inner geometry for comfort.

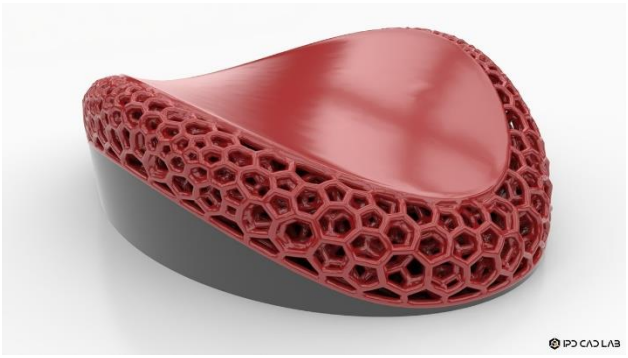

Fig.7. Final contact pad with recessed smooth overlay revealing inner lattice.

Additive manufacturing was used for prototyping with SLA technology. The design reduced weight by 34% compared to the original solid model, while improving pressure distribution and aesthetic uniqueness.

5.2. Enhancing Design Creativity Through Vizcom: A Student Study

The second case study[23] involved a classroom-based experiment with 22 mechanical and product design students who were tasked with developing a sustainable charcoal barbecue grill (Fig.8). Participants were divided into two groups: one using traditional sketching and the other using Vizcom for AI-assisted ideation.

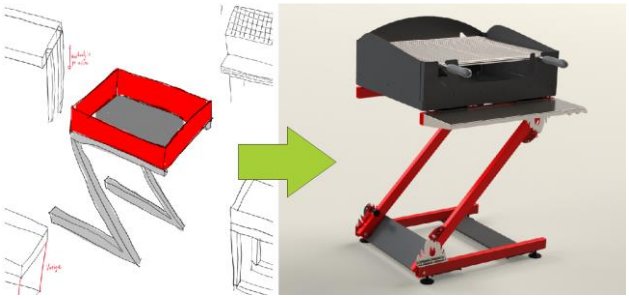

Fig.8. Sample AI-assisted concept generated using Vizcom.

Quantitative results showed a shift from divergent to iterative behaviour: AI-supported students generated fewer initial sketches but significantly more redesigns, reflecting enhanced concept refinement (Fig.9).

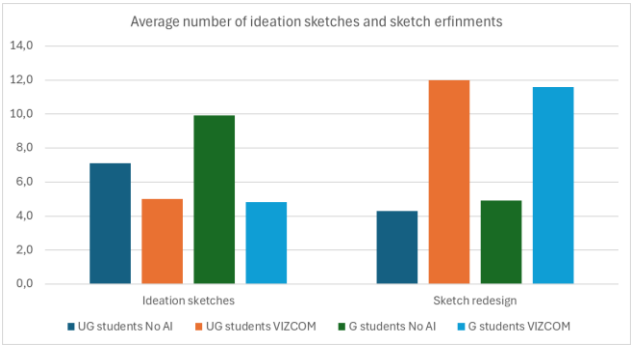

Fig.9. Average number of ideation sketches and sketch redesigns

Teacher assessments confirmed higher design quality among AI-assisted groups, especially in visualization and creativity (Fig.10).

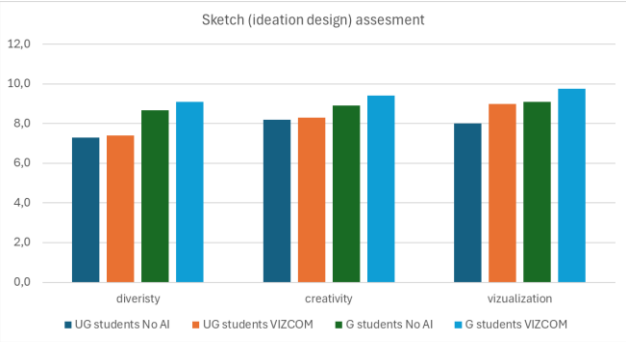

Fig.10. Influence on diversity, creativity and visualization

Student feedback also indicated reduced cognitive load and higher engagement during the Vizcom-supported sessions (Fig.11).

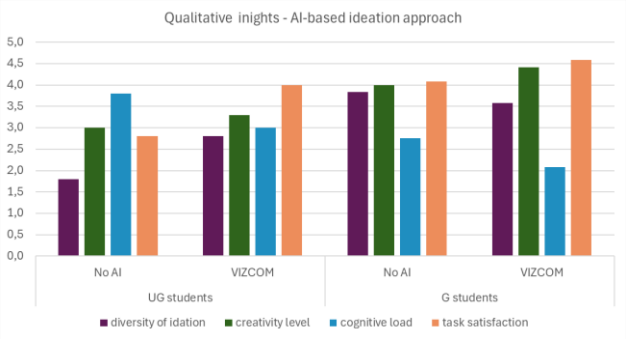

Fig.11. Participant experiences

This case underscores the potential of generative AI tools to act as creativity amplifiers when embedded within design education. Students retained control over decision-making while benefiting from faster iterations and higher visual quality.

6. DISCUSSION

The integration of artificial intelligence into mechanical design processes is not merely a technological enhancement, but a paradigmatic shift that redefines how design problems are explored, validated, and communicated. The two case studies presented in this paper, one focused on the generative development of an ergonomic armrest and the other on educational use of AI-assisted ideation tools, illustrate the tangible and strategic benefits of incorporating AI into both professional and academic contexts. The discussion synthesizes these insights through four key themes:

- acceleration of iteration,
- amplification of creativity,
- transformation of design roles, and
- the systemic challenges introduced by AI-enhanced workflows.

6.1. Acceleration and Deepening of Iterative Design

In both case studies, AI enabled faster, more iterative development cycles by automating redundant tasks and reducing cognitive effort. In the armrest project, the use of generative design and biomechanically informed cellular structures facilitated exploration of complex geometries that would have been infeasible using manual methods. Each iteration-from sketch to simulation to final print-was accelerated through data-driven optimization tools and generative modelling platforms.

Similarly, in the Vizcom-supported educational experiment, students produced more refined and diverse redesigns despite generating fewer initial sketches. This pattern suggests that AI systems encourage deeper exploration within each concept branch rather than superficial divergence. It also highlights a shift from linear to recursive ideation cycles, where students continuously evaluate and adapt evolving alternatives.

This finding aligns with prior research emphasizing the value of rapid, low-barrier iterations in fostering innovation [1]. AI tools reduce the friction traditionally associated with re-modelling or performance evaluation, thereby allowing designers to test hypotheses more frequently and confidently.

6.2. Creativity as Co-Construction

The case studies further indicate that AI does not stifle creativity, actually,when used thoughtfully, it amplifies it. In the ergonomic design example, AI tools generated highly unconventional geometries that the designer could interpret, modify, and refine. In the student study, AI-assisted concepts were rated significantly higher in creativity, visualization, and user satisfaction by both instructors and participants.

Rather than displacing creative effort, AI redistributed it. Designers spent less time drafting and more time on aesthetic judgment, scenario evaluation, and user-centered reasoning. This shift supports the idea of co-constructed creativity, where human designers supply intention, context, and critique, while AI offers computational diversity and optimization [11].

Such synergy reinforces the need to frame AI tools not as generative engines alone, but as reflective partners in design, a shift that calls for new pedagogical approaches and user interface standards.

6.3. Evolving Role of the Designer

AI systems have begun to reshape the very role of the mechanical designer. The human agent increasingly assumes the roles of curator, orchestrator, and evaluator rather than sole creator. In the armrest project, for instance, while the structure was generated through algorithmic optimization, the form, material, and manufacturing pathway were determined by the human designer based on ergonomic, aesthetic, and practical considerations.

This expanded role demands a hybrid skillset: designers must be proficient not only in mechanical principles and aesthetics but also in AI tool logic, constraint definition, and critical interpretation of machine-generated outputs.

In educational settings, this has implications for curricula, which must now integrate AI literacy, ethical reflection, and data interpretation alongside classical design theory.

6.4. Data, Feedback, and Knowledge Integration

The efficacy of AI tools is fundamentally dependent on data quality. In the armrest case, the successful implementation of a biomechanically optimized cellular structure relied on high-fidelity simulations and well-structured design constraints. In the student experiment, the usefulness of Vizcom's outputs depended heavily on the clarity of the prompt and quality of sketch input (Fig.12).

Without robust, interoperable, and semantically enriched datasets, AI tools are prone to generating unusable, unsafe, or irrelevant alternatives. Moreover, current industrial design environments often lack adequate data integration between CAD, CAE, and PLM systems, leading to isolated data silos that diminish the value of machine learning-driven insights.

Feedback mechanisms are also essential. AI tools must continuously learn from user preferences, selections, and outcomes. Closing this loop requires platforms that track decisions, accept explicit feedback, and adapt over time to organizational or domain-specific goals. This dynamic co-evolution is a defining characteristic of truly intelligent design systems.

Fig.12. Usefulness of Vizcom's outputs

6.5. Risks and Ethical Considerations

The benefits of AI-enhanced design must be balanced against its risks. Over-reliance on AI systems, especially those with low interpretability, can result in inappropriate design decisions, reduced user agency, and erosion of fundamental design skills [17]. In regulated industries such as medical devices or aerospace, blind acceptance of AI-generated outputs could result in safety-critical errors or non-compliance.

The armrest project demonstrated the need for human validation of simulation results, manufacturing feasibility, and user comfort, none of which can be reliably inferred by current AI models. Likewise, student feedback in the Vizcom experiment underscored the importance of preserving individual creativity and critical thinking, even as tools automate parts of the workflow.

Ethical design frameworks such as Ethics by Design [8] must guide the deployment of AI in engineering, ensuring that final accountability remains with human agents and that systems are transparent, auditable, and bias-aware.

7. CONCLUSION

This paper has examined the transformative role of artificial intelligence in mechanical design, with a focus on how AI tools reshape ideation, optimization, and collaboration. By analyzing the limitations of traditional design processes and introducing a structured AI-driven framework, we have outlined a path toward more intelligent, responsive, and creative product development workflows.

The two case studies presented, the ergonomic redesign of a lightweight armrest and an educational experiment using AI-assisted sketching, demonstrate that AI can be successfully integrated into both industrial and pedagogical contexts. In both examples, AI enhanced design iteration, expanded the range of explored alternatives, and elevated overall design quality. At the same time, human designers retained their central role as decision-makers, interpreters, and ethical agents.

These results reinforce the concept that AI should not replace human creativity but instead augment it. AI excels in computational exploration, optimization, and pattern recognition; humans contribute context awareness, aesthetic judgment, and value-based reasoning. Together, they form a hybrid design team capable of addressing challenges that neither could solve alone.

However, the adoption of AI in design is not without challenges. Effective use depends on access to high-quality, structured data, careful definition of constraints, and thoughtful integration of human-centred principles. Over-reliance on AI tools may lead to diminished critical thinking or ethical oversight if not managed properly. Moreover, the success of human-AI collaboration is contingent on the transparency, interpretability, and adaptability of the tools involved.

Future directions for research and practice include the development of adaptive learning systems that evolve with user input, the creation of standardized ontologies for design knowledge, and the integration of real-time simulation with generative AI. Educational institutions must also prepare future engineers to work fluently with AIthrough interdisciplinary curricula that bridge design, data science, and ethics.

In conclusion, artificial intelligence presents a powerful opportunity to reimagine the mechanical design process, not as a replacement for human ingenuity, but as a force multiplier that amplifies what designers do best: create meaningful, efficient, and innovative solutions. By aligning technical capabilities with human values, the field can move confidently toward a new era of augmented design intelligence.

ACKNOWLEDGMENT

The authors acknowledge the financial support from the Slovenian Research and Innovation Agency (Research Core Funding No. P2-0063).

REFERENCES

[1] Wynn, D.C., Eckert, C.M.: Perspectives on iteration in design and development. *Res Eng Des*, 28 (2), pp. 153–184, 2017

[2] Young, M.T.: Intuition and Ineffability: Tacit Knowledge and Engineering Design. *Philosophy of Engineering and Technology*, 31, pp. 53–67, 2018

[3] Sheng, I.L.S.: Improving Product Ideation Among Engineering Undergraduates Using TRIZ and Design Thinking. *2023 IEEE 12th International Conference on Engineering Education, ICEED 2023*, pp. 41–43, 9798350307429, 2023

[4] Wang, Q. et al.: Conceptual Design Method for Mechanical Products Based on Historical 3D Model Design Knowledge. *Mechanisms and Machine Science*, 155 MMS, pp. 377–396, 978-981-97-0922-9, 2024

[5] Saadi, J.I., Yang, M.C.: Generative Design: Reframing the Role of the Designer in Early-Stage Design Process. *Journal of Mechanical Design*, 145 (4), 2023

[6] Yoo, S. et al.: Integrating Deep Learning into CAD/CAE System: Generative Design and Evaluation of 3D Conceptual Wheel. *Structural and Multidisciplinary Optimization*, 64 (4), pp. 2725–2747, 2020

[7] Song, B. et al.: Human-AI collaboration by design. *Proceedings of the Design Society*, 4, pp. 2247–2256, 2024

[8] Brey, P., Dainow, B.: Ethics by design for artificial intelligence. *AI and Ethics 2023 4:4*, 4 (4), pp. 1265–1277, 0123456789, 2023

[9] Kaljun, J., Dolšak, B.: Ergonomic design knowledge built in the intelligent decision support system. *Int J Ind Ergon*, 42 (1), pp. 162–171, 2012

[10] Kaljun, J., Dolšak, B.: Improving products' ergonomic value using intelligent decision support system. *StrojniskiVestnik/Journal of Mechanical Engineering*, 58 (4), pp. 271–280, 2012

[11] Kaljun, J. et al.: Intelligent support used for providing a pleasant user experience. *2014 37th International Convention on Information and Communication Technology, Electronics and Microelectronics, MIPRO 2014 - Proceedings*, pp. 1083–1087, 9789532330816, 2014

[12] Kaljun, J. et al.: Aesthetics as parameter of intelligent design support. *DS 70: Proceedings of DESIGN 2012, the 12th International Design Conference, Dubrovnik, Croatia*, pp. 1293–1300, 2012

[13] Bremer, F. et al.: Analyzing iterations in mechanical design processes - A method for data acquisition in meso-level studies. *Procedia CIRP*, 100, pp. 756–761, 2021

[14] Dugan, K.E., Daly, S.R.: Investigation of Mechanical Engineering Students' Perceptions of Design Process Models. *Proceedings of the ASME Design Engineering Technical Conference*, 9780791886267, 2022

[15] Gerschütz, B. et al.: Digital Engineering Methods in Practical Use during Mechatronic Design Processes. *Designs 2023, Vol. 7, Page 93*, 7 (4), pp. 93, 2023

[16] Young, M.T.: Intuition and Ineffability: Tacit Knowledge and Engineering Design. *Philosophy of Engineering and Technology*, 31, pp. 53–67, 2018

[17] Lockhart, E.N.S.: Creativity in the age of AI: the human condition and the limits of machine generation. *J Cult Cogn Sci*, 2024

[18] Koul, P.: A Review of Generative Design Using Machine Learning for Additive Manufacturing. *Advances in Mechanical and Materials Engineering*, 41, pp. 145–159, 2024

[19] Shi, L. et al.: Deep Learning-Based Multifidelity Surrogate Modeling for High-Dimensional Reliability Prediction. *ASCE-ASME Journal of Risk and Uncertainty in Engineering Systems, Part B: Mechanical Engineering*, 10 (3), 2024

[20] Abdeen, H. et al.: Multi-objective optimization in rule-based design space exploration. *ASE 2014 - Proceedings of the 29th ACM/IEEE International Conference on Automated Software Engineering*, pp. 289–300 9781450330138, 2014

[21] Figoli, F.A. et al.: AI in the design process: training the human-ai collaboration. *DS 117: Proceedings of the 24th International Conference on Engineering and Product Design Education (E&PDE 2022), London South Bank University in London, UK. 8th - 9th September 2022*, 978-1-912254-16-3, 2022

[22] Ethics By Design and Ethics of Use Approaches for Artificial Intelligence. 2021

[23] Kaljun, K.K., Kaljun, J.: Enhancing Creativity in Sustainable Product Design: The Impact of Generative AI Tools at the Conceptual Stage. *47th ICT and Electronics Convention, MIPRO 2024 - Proceedings*, pp. 451–456, 9798350382495, 2024

11th International Scientific Conference
IRMES 2025
Research and Development of
Mechanical Elements and Systems
June 19 – 21, 2025; Vrnjačka Banja, Serbia

Original scientific paper DOI: 10.46793/IRMES25.plA3M

OPEN-SOURCE CFD FOR LUBRICATED COMPONENTS: MODELING AERATION, CAVITATION, AND NON-NEWTONIAN EFFECTS WITH COMPUTATIONAL EFFICIENCY

Lorenzo MACCIONI[1]
Franco CONCLI[2]

[1]Free University of Bozen-Bolzano, Bolzano, Italy, 39100; lorenzo.maccioni@unibz.it;
[2]Free University of Bozen-Bolzano, Bolzano, Italy, 39100; franco.concli@unibz.it; ORCID iD: 0000-0002-1237-5542

Abstract: *In recent years, energy efficiency has become a key priority across multiple industrial domains. Within the automotive sector, in particular, there is increasing pressure to design drivetrains that balance economic viability with environmental sustainability and operational reliability. Accurately forecasting both the efficiency and lubrication behavior of gearboxes continues to pose a significant engineering challenge. Existing analytical models, largely grounded in empirical correlations and dimensional analysis, typically offer precise predictions only within limited operating conditions. A robust, physics-based methodology capable of reliably simulating lubricant flow patterns and quantifying power losses in geared systems would represent a major step forward. With the rapid advancements in computational technologies, Computational Fluid Dynamics (CFD) has emerged as a powerful resource for investigating lubrication processes and drivetrain efficiency. However, its widespread industrial adoption has been constrained by the high computational demand of such simulations. The introduction of a more efficient mesh-handling framework, combined with the creation of advanced solvers that can address complex phenomena—such as cavitation, aeration, oil mist generation, and non-standard lubrication regimes (e.g., involving non-Newtonian fluids)—has significantly broadened CFD's practical applicability. Compared to methods from a decade ago, computational time has been reduced by up to 97%, allowing even highly intricate systems to be analyzed within minutes. This paper presents a variety of application cases across different gear geometries, demonstrating the flexibility of the proposed method. Real-world scenarios, including a multi-stage industrial gearbox and a planetary gearbox, are discussed in detail. The developed approach not only proves computationally efficient but also deepens the comprehension of the underlying physical mechanisms, offering theoretical insights into experimental results that were previously difficult to interpret.*

Keywords: *Lubrication; Tribology; Gearbox; Rolling Element Bearing; OpenFOAM®*

1. INTRODUCTION

Over the past decades, energy efficiency has emerged as a critical objective across numerous industries, from construction to automotive manufacturing. Among the most common mechanical components are gears and power transmission systems, whose performance efficiency plays a significant role in achieving large-scale energy savings on a global scale.

The energy losses encountered within gearboxes stem from multiple mechanisms. These losses are typically classified based on the specific mechanical components involved and whether they vary with the applied load. While empirical and analytical models are generally adequate for estimating load-dependent losses, such as those caused by friction under torque, predicting load-independent losses—particularly those resulting from lubricant-gear interactions—remains a significant challenge using traditional methods. In this context, the integration of advanced numerical tools during the early stages of design can meaningfully support the development of more efficient systems.

Computer-based methods, particularly those grounded in Computational Fluid Dynamics (CFD), offer a promising solution to the complex task of quantifying load-independent losses. CFD not only provides insight into the fluid dynamics of lubrication but also facilitates the evaluation of lubricant distribution and reliability across the entire system. Nonetheless, its application to gear systems is complicated by the dynamic geometry of the simulation domain, which evolves during gear engagement due to the movement of the air-lubricant mixture. This variation significantly increases the complexity of mesh management.

A variety of CFD approaches have been proposed in the literature, differing in both computational cost and prediction accuracy. Building upon previous research, the

present study applies CFD using an innovative Global Remeshing Approach (GRA) developed by the authors [1], along with its enhanced version incorporating mesh clustering, known as GRAMC, introduced by Mastrone et al. [2–4]. This enhanced methodology allows for precise simulations to be completed within reduced timeframes.

Developed within the open-source platform OpenFOAM®, the GRA^{MC} framework includes user-friendly interfaces and pre-processing tools, enabling its adaptation to diverse gear types [5–7] and gearbox architectures [3,8–12]. Its modularity and ease of use make it accessible even for designers without extensive CFD experience.

In addition to efficient mesh management, the framework includes a suite of custom solvers tailored to represent a range of lubrication conditions and fluid behaviors. These encompass solvers for immiscible, incompressible, isothermal fluids used in oil-bath lubrication; models accounting for cavitation [13], aeration [13–15], and oil mist (aerosol) formation typical in jet lubrication systems; as well as solvers capable of handling non-Newtonian fluids like grease [16].

Following an outline of the GRA^{MC} approach and the key solver implementations, several application examples are discussed. In many of these, simulation results are compared directly with laboratory test data, demonstrating a strong correlation in terms of both power losses and lubricant flow patterns.

Furthermore, the simulations help clarify the root causes of various loss mechanisms—including churning, windage, pocketing/squeezing, cavitation, aeration, and oil suspension—offering a theoretical foundation for understanding experimental data that previously lacked clear explanation. This deeper understanding enables engineers to formulate more effective loss mitigation strategies tailored to specific gearbox designs.

Eventually, the paper evaluates the computational efficiency of the proposed approach relative to conventional commercial software solutions, highlighting the notable reduction in processing time achieved using GRA^{MC}.

2. POWER LOSSES IN GEARBOXES

Power dissipation within a gearbox originates from several mechanical components. These losses can be grouped according to their source: gears (denoted by subscript $|_G$), bearings ($|_B$), seals ($|_S$), and additional elements such as clutches and synchronizers ($|_X$). Gear and bearing losses are further divided into load-dependent and load-independent categories (denoted $|_0$). Load-dependent losses are directly linked to the torque transmitted through the system and typically arise from mechanical friction or, in lubricated systems, from the shear forces acting within the oil film between contacting surfaces. Conversely, load-independent losses are caused by the interaction between the lubricant and mechanical components, regardless of load [17]. This paper concentrates on the load-independent losses associated with gears, which can be further categorized into three main types: churning losses ($PLG_{0,C}$), windage losses ($PLG_{0,W}$), and pocketing or squeezing losses ($PLG_{0,S}$). Churning involves multiphase flow interactions, whereas windage occurs in a single-phase (usually air) context. Windage becomes particularly significant in high-speed gearboxes or systems using grease lubrication or oil jets, where the primary resistance is due to air flow. Squeezing losses occur when the volume between meshing teeth rapidly changes, generating axial lubricant flows and resulting in viscous energy dissipation—though generally to a lesser extent than churning or windage.

Bearings also exhibit load-independent losses. However, due to their relatively simple and consistent geometries, these losses can often be adequately estimated using standard equations provided by manufacturers [18]. In contrast, gear losses are highly sensitive to the specific configuration and geometry of both the gear set and housing. As such, purely analytical or empirical models frequently fall short, making advanced numerical approaches essential for accurate evaluation.

3. CFD APPLICATION TO LUBRICATION OF GEARBOXES

3.1. Theoretical background

As previously discussed, accurately quantifying the load-independent power losses in gear systems requires a deep understanding of lubricant behavior under real operating conditions—an inherently fluid dynamic problem. Due to the intricate geometries involved—formed by the motion of gears, shafts, and bearings—an analytical approach is generally impractical. The geometry of the gearbox housing, which can vary significantly across designs, also plays a crucial role in shaping lubricant flow and, consequently, energy losses. Furthermore, the volume within the gearbox changes dynamically during operation, being alternately filled with oil, air, or a mixture of both. Given this complexity, numerical techniques such as CFD become essential for obtaining meaningful and accurate predictions.

As noted in [12], particle-based models may be useful for visualizing lubricant behavior qualitatively, but when it comes to calculating power losses with numerical precision, the Finite Volume (FV) method is preferred. This approach involves dividing the computational domain into a mesh of discrete cells and solving the governing conservation equations for mass and momentum within each one.

To resolve the fluid behavior within these discretized cells, most CFD simulations adopt numerical schemes based on the PIMPLE algorithm—a hybrid of the PISO and SIMPLE methods. The SIMPLE (Semi-Implicit Method for Pressure-Linked Equations) scheme is traditionally used for steady-state problems and does not account for temporal evolution. In contrast, the PISO (Pressure-Implicit with Splitting of Operators) algorithm is suited for transient simulations but necessitates significantly smaller time steps to maintain accuracy, thus increasing computational load. PIMPLE strategically combines these methods: it begins iterations in SIMPLE mode and switches to PISO only in the final steps, striking a balance between stability, accuracy, and efficiency.

Before delving deeper, it is important to distinguish between two primary types of multiphase flows: separated and dispersed. In separated flows, different phases maintain a continuous, clearly defined interface throughout the domain—such as the oil surface in bath lubrication. Dispersed flows, on the other hand, involve isolated pockets or particles of one phase scattered within another, such as oil droplets suspended in air or vice versa (as illustrated in Figure 1).

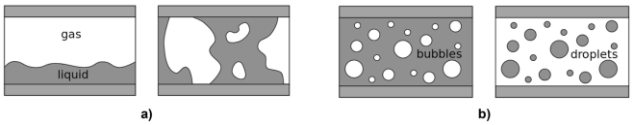

Fig.1. a) Separated vs. b) Dispersed flows.

A typical example of separated flow is oil-bath lubrication, where the free surface of the lubricant is distinct and easily observable. In contrast, dispersed flows occur in situations involving fine air bubbles trapped within the lubricant (commonly referred to as foaming or aeration) or when the lubricant itself is atomized into droplets, as seen in oil jet or spray lubrication systems.

When dealing with separated phases, it is standard practice to employ interface-tracking techniques—most notably the VOF method [19]—to accurately reconstruct the shape and position of the free surface between phases.

For both single-phase simulations, such as those modeling windage, and for separated-phase conditions like churning, the CFD framework typically solves one continuity equation and one momentum conservation equation to describe the flow field.

$$\frac{\partial \rho}{\partial t} + \nabla \cdot \left(\rho \vec{U}\right) = 0$$

$$\frac{\partial \rho \vec{U}}{\partial t} + \nabla \cdot \left(\rho \vec{U}\right) = -\nabla p + \nabla \cdot \left(\mu \nabla \vec{U}\right) + S_U$$

$$\frac{d\gamma}{dt} + \vec{U} \cdot \nabla \gamma = 0$$

Where:

ρ is the density, U is the velocity vector, μ is the viscosity, and S_U represents the external forces.

For applications involving multiple phases, an additional scalar quantity, known as the volume fraction (γ), is introduced to indicate the share of the phases in each cell. γ is calculated for each cell through an additional balance equation.

After the calculation of γ, the properties of the fluid mixture in the cell are computed with an average weight (γ) from those of the different phases.

$$\phi = \phi_g \cdot \gamma + \phi_l \cdot (1 - \gamma)$$

Where:

ϕ represents a generic property to be calculated, such as density or viscosity.

Subscript |g refers to the gas phase, while subscript |l denotes the liquid phase.

Phenomena like cavitation can be incorporated into simulations by introducing a source term in the mass conservation equation to represent the phase transition rate [20–22]. Similarly, aeration effects can be modeled by adding an appropriate source term to the continuity equation [15].

Although this approach is well-suited for modeling churning flows—where large, well-defined phase interfaces exist—it becomes ineffective for dispersed flow regimes. The core limitation arises from the resolution constraints of the computational mesh. Capturing small-scale features such as individual oil droplets or entrained air bubbles requires an extremely fine mesh, often on the order of micrometers. However, achieving such resolution across a domain of even modest size (e.g., a volume comparable to a dice) is computationally impractical with current hardware capabilities. As a result, interface-tracking methods are generally not feasible for industrial-scale simulations involving complex lubrication modes beyond basic splashing or churning, where mesh sizes typically remain in the millimeter range.

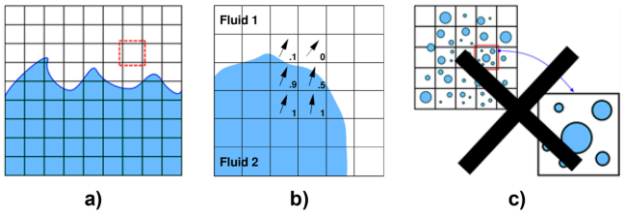

Fig.2. VOF: a) Interface tracking; b) the velocity field is shared by the phases; c) features smaller than the grid-scale could not be captured.

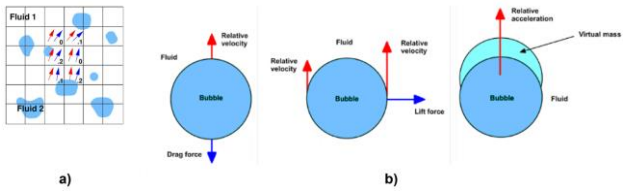

Fig.3. Euler-Euler: a) each phase has its own velocity field; b) closure model for drag, lift and virtual mass.

For scenarios involving dispersed phases, a more suitable modeling strategy is the Euler–Euler approach [23]. In this framework, both phases are treated as continuous media, each governed by its own set of Eulerian conservation equations. The phases are assumed to interpenetrate one another, and their behaviors are described using averaged forms of the mass and momentum conservation equations. Each phase has its own velocity field, represented by a distinct velocity vector. However, this averaging process introduces additional terms in the momentum equations, necessitating the inclusion of closure models to account for the unresolved interactions between phases.

The most widely used averaging techniques include temporal, volumetric, and ensemble averaging. These methods operate over control volumes that are larger than the characteristic size of the dispersed features—such as oil droplets—thus alleviating the computational burden.

However, this comes at the cost of losing detailed information at smaller scales. To compensate, sub-models are incorporated, particularly to account for the drag force exerted by the continuous phase (e.g., air in oil suspensions) on the dispersed phase (lubricant).
The drag force itself results from both surface shear stresses and pressure gradients across the droplet's surface. It is commonly expressed using the following formulation:

$$\vec{F}_{I,k}^{D} = \frac{1}{2}\rho_N C_{D,k} A \vec{u}_r \vec{u}_r$$

where $CD_{D,k}$ is the drag coefficient—typically derived from empirical correlations [24]— A is the surface area, and u_r is the relative velocity between phases. In cases where the lubricant is dispersed in the form of spherical droplets, the surface area can be estimated based on the droplet diameter $d_{b,k}$.
This drag force is then included in the momentum equation for the dispersed phase. In the Euler–Euler model, separate conservation equations are solved for each phase, with the subscript $|_N$ denoting the primary (continuous) phase and $|_k$ representing the k-th dispersed phase.

$$\frac{\partial \gamma_N \bar{\rho}_N}{\partial t} + \nabla \cdot \left(\gamma_N \bar{\rho}_N \hat{\vec{u}}_N\right) = 0$$

$$\frac{\partial \gamma_k \bar{\rho}_k}{\partial t} + \nabla \cdot \left(\gamma_k \bar{\rho}_k \hat{\vec{u}}_k\right) = 0$$

$$\frac{\partial \gamma_N \bar{\rho}_N \hat{\vec{u}}_N}{\partial t} + \nabla \cdot \left(\gamma_N \bar{\rho}_N \hat{\vec{u}}_N \hat{\vec{u}}_N\right) = \nabla \cdot \left(\gamma_N \bar{\rho}_N \left(\nabla \hat{\vec{u}}_N + \nabla \hat{\vec{u}}_N^T\right)\right) - \nabla \cdot \left(\gamma_N \mu_N \frac{1}{3} \nabla \hat{\vec{u}}_N \vec{I}\right) - \gamma_N \nabla p + \gamma_N \bar{\rho}_N \vec{g} + \sum_{k=1}^{N-1} \frac{3}{4} \bar{\rho}_N \gamma_N \frac{C_{D,k}}{d_{b,k}} |\hat{\vec{u}}_k - \hat{\vec{u}}_N| (\hat{\vec{u}}_k - \hat{\vec{u}}_N)$$

$$\frac{\partial \gamma_k \bar{\rho}_k \hat{\vec{u}}_k}{\partial t} + \nabla \cdot \left(\gamma_k \bar{\rho}_k \hat{\vec{u}}_k \hat{\vec{u}}_k\right) = \nabla \cdot \left(\gamma_k \bar{\rho}_k \left(\nabla \hat{\vec{u}}_k + \nabla \hat{\vec{u}}_k^T\right)\right) - \nabla \cdot \left(\gamma_k \mu_k \frac{1}{3} \nabla \hat{\vec{u}}_k \vec{I}\right) - \gamma_k \nabla p + \gamma_k \bar{\rho}_k \vec{g} - \gamma_k \nabla p + \gamma_k \bar{\rho}_k \vec{g} - \frac{3}{4} \bar{\rho}_N \gamma_k \frac{C_{D,k}}{d_{b,k}} |\hat{\vec{u}}_k - \hat{\vec{u}}_N| (\hat{\vec{u}}_k - \hat{\vec{u}}_N)$$

3.2. Mesh Handling

The continuous geometric changes occurring within a gearbox during operation—particularly those caused by the gear meshing cycles—create a major challenge for accurately simulating internal fluid dynamics. These changes require the computational mesh to be frequently updated to adapt to the evolving topology. Notably, the variation in volume where the gear teeth engage often leads to significant distortion of mesh elements, which in turn compromises numerical stability and accuracy.
Standard strategies employed in commercial simulation software are generally not well-suited to such demanding applications. A commonly used technique is mesh smoothing, which involves replacing or adjusting elements that no longer meet predefined quality criteria. However, as illustrated in Figure 4a, this method is often insufficient for gear simulations. While mesh smoothing can accommodate large-scale geometric variations, it tends to generate very small elements in critical regions. This necessitates a reduction in time step size, thereby increasing the overall computational cost and limiting simulation efficiency [25, 26].

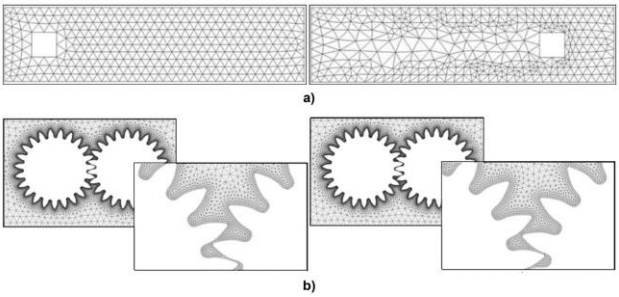

Fig.4. 2 subsequent meshes: a) LRA: the grids differ significantly in terms of element size; b) GRA: the grids are comparable.

To address the challenges posed by dynamic mesh deformation, the authors introduced an innovative strategy based on full mesh replacement after a set number of iterations. This method, known as the Global Remeshing Approach (GRA), facilitates systematic regeneration of the computational grid according to predefined topological criteria. Compared to conventional methods that only substitute degraded elements within unpredictable geometries, GRA ensures a more uniform mesh quality and consistent element sizing (Figure 4b). To maintain solution continuity, results are interpolated from the old mesh to the newly generated one. By preserving a consistent average element size throughout the simulation, the method allows for a constant time step, significantly enhancing numerical stability. Further insights and examples—such as its application to back-to-back test rigs—are detailed in [22].
Nonetheless, as noted in [2, 27, 28], the original GRA method has certain limitations, particularly in cases where generating a 2D mesh and extruding it to 3D is not practical. To overcome this constraint, a partitioning-based enhancement was developed and combined with the GRA strategy. This advancement removes previous limitations, making the approach compatible with a broader range of gearbox configurations—including planetary systems—through the use of arbitrary mesh interfaces [29]. Additionally, the integration of a mesh clustering mechanism, referred to as GRA^{MC} [30], further improves computational efficiency by enabling recursive grid refinement and reuse.

4. EXAMPLES OF APPLICATIONS AND VALIDATION

4.1. Full-immersion lubrication of a back-to-back test rig: Windage and cavitation

The first application of the proposed methodology involves a simple back-to-back test rig with a 1:1 gear ratio. This configuration is well-documented in the literature, with available experimental data on power losses. Otto et al. [31] conducted tests across a range of rotational speeds—corresponding to tangential velocities from 0 to 38 m/s—using oil bath lubrication at both 50% and 100% fill levels, and under varying pressure conditions (ambient and 6 bar).
In partially filled conditions, the power loss trend is largely linear. However, for the fully flooded case,

noticeable discrepancies emerge between the two pressurization levels. These differences are attributed to pressure variations: overpressures develop on the front flanks due to forward movement, while suction effects generate negative pressures on the rear flanks—both contributing to energy dissipation. Since the lubricant can be considered incompressible, these variations in experimental results are not easily explained (Figure 5). Otto et al. suggest that the most plausible cause is the presence of entrapped air bubbles within the oil reservoir.

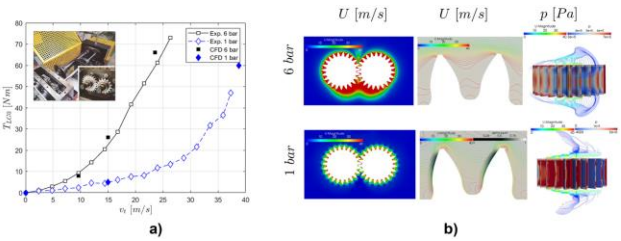

Fig.5. Application of an incompressible multiphase solver with interface tracking to a back-to- back test rig: pressurized condition (windage) vs. ambient pressure (cavitation). Resistant torque; b) velocity and pressure fields [22].

To investigate this hypothesis, CFD simulations were carried out using a multiphase VOF solver suitable for separated-phase flows. This solver accounts for critical phenomena such as aeration and cavitation. The numerical outcomes not only aligned closely with the experimental measurements but also revealed the physical mechanisms responsible for the observed power losses.

At higher pressure (6 bar), pressure distributions on the gear flanks appeared symmetrical, with characteristic peaks at the tip of the teeth—indicative of windage effects. Flow pathlines showed that the lubricant, after being ejected axially, re-entered adjacent gear spaces, establishing circulation over a broad region. In contrast, at ambient pressure (1 bar), the system approached the vaporization threshold (P_{vap} = 2,340 Pa). Beyond this point, the lubricant began transitioning from liquid to vapor, capping further pressure reduction. This phase change limited the suction effect on the rear flanks, as confirmed by the streamline analysis, where the expelled fluid did not return between the teeth. Interestingly, this suppression of suction corresponded to a reduction in power losses.

These CFD results provided a detailed understanding of the pressure and velocity distributions across the domain (Figure 5) and highlighted how different loss mechanisms dominate under varying conditions. This case study effectively demonstrates the versatility and diagnostic power of the numerical approach, showing its capability not only to replicate experimental findings but also to offer new insights into the fluid dynamics that drive gearbox losses.

4.2. Grease lubrication of a back-to-back test rig: Channeling and circulation

Maintaining the same back-to-back test rig geometry, but with gears configured to a 3:2 ratio, we now refer to the experimental study conducted by Stemplinger et al. [32]. Their investigation examined grease-lubricated conditions at three different fill levels—40%, 50%, and 80% of the gearbox volume—while operating the pinion at 3,500 rpm. Unlike traditional oil bath lubrication, their results revealed a distinct trend: power losses initially increased with higher grease quantities but then plateaued as the fill level continued to rise (Figure 6a). This behavior reflects a fundamentally different lubrication mechanism associated with grease compared to liquid oils.

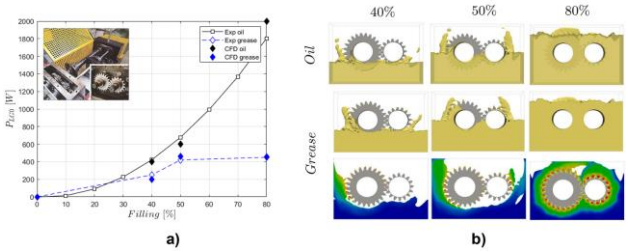

Fig.6. Application of an incompressible multiphase solver with interface tracking to a back-to- back test rig: oil (churning) vs. grease (channeling and circulation) lubrication. a) Power losses; b) lubricant distribution [16].

The CFD simulations performed by the author provided a comprehensive explanation for this experimental observation, revealing the presence of a threshold lubricant volume that dictates a shift in lubrication behavior. When the grease fill level is relatively low (around 40–50%), a phenomenon known as channeling occurs. In this regime, the lubricant is displaced toward the lateral areas of the gearbox, creating a void between the gear teeth and the main grease mass. As a result, the grease fails to re-enter the meshing zone. In contrast, at higher fill levels (such as 80%), circulation is established: the grease saturates the gear teeth completely and continuously flows through the engagement region.

Figure 6b illustrates this distinction. Under channeling conditions, power losses correlate with the extent of tooth immersion in the lubricant, which increases proportionally with grease volume. However, once circulation is achieved, further additions of grease do not significantly affect the losses, as the dissipation depends primarily on the velocity gradient between the gear teeth and the moving lubricant.

While this case focuses on a conventional back-to-back test rig, grease lubrication is also commonly employed in large rolling bearings. In such systems, the relatively small grease volume compared to the bearing's total internal space often leads to similar channeling behavior [33]. Therefore, integrating the advanced meshing strategies described in Section 4.4 [34,35] with the CFD solver used in this study offers a powerful tool for simulating and analyzing grease-lubricated rolling bearings.

4.3. Oil-jet lubrication of a back-to-back test rig: Oil suspension/aerosol

The third case study again involves a back-to-back test rig, this time with a 26:17 gear ratio, as examined by Dindar et al. [36]. In their setup, lubrication was delivered

via a nozzle with a diameter of 0.71 mm, supplying oil at a rate of 1 liter per minute. This produced a high-speed jet of 14.4 m/s. The combination of the high jet velocity, limited oil quantity, and elevated gear rotational speed favored the atomization of the lubricant, resulting in the formation of a fine aerosol comprised of oil droplets. Similar observations have been reported by Kunz et al. [37], who emphasized that power loss behavior is heavily influenced by the concentration of suspended oil droplets.

To replicate Dindar et al.'s test conditions, numerical simulations were performed using two approaches: a traditional compressible multiphase solver with interface tracking, and a compressible Euler–Euler solver incorporating a drag model. The former was expected to underperform in this context, given that the minimum mesh size achievable with standard hardware (approximately 0.1 mm) was orders of magnitude larger than the average droplet diameter, which is typically around 1 μm [37].

As anticipated, the interface tracking solver struggled with mass conservation of the dispersed oil phase and substantially underestimated power losses. By contrast, the Euler–Euler model accurately captured key aspects of the flow: the penetration of the oil jet into the gear contact zone, the axial and tangential expulsion of lubricant, and the accumulation of oil at the bottom of the housing, where it formed a thin lubricating film. Figure 7 illustrates the velocity fields of both the continuous (air) and dispersed (oil) phases along symmetry planes. Centrifugal forces cause the air to flow radially outward, as shown in prior studies [22]. The oil droplets, represented as a dispersed cloud subject to drag forces computed using Schiller's model [38], followed paths governed by the interplay between airflow transport, gravity, and interphase drag.

After the gears engage, oil retained on the flanks is either flung off or drips down to the housing base, forming a cone-shaped spray. The cone's angle narrows with increasing rotational speed. Additionally, a fine oil mist persists around the gear teeth, significantly contributing to power losses beyond those caused by air windage alone.

Figure 7a presents the power loss results across a range of speeds: the solid line reflects the experimental data reported by Dindar et al. [36], the dashed line corresponds to the Euler–Euler simulation, and the dotted line shows results from the interface tracking solver. The figure clearly highlights the superior predictive accuracy of the Euler–Euler model under these lubrication conditions.

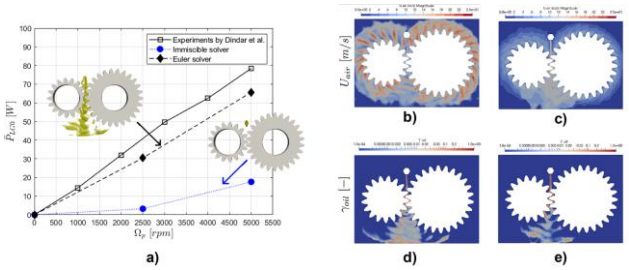

Fig.7. a) power losses; b) velocity field continuous phase (air) Ωp = 2,500 rpm; velocity field dispersed phase (lubricant) Ωp = 2,500 rpm; d) Volume fraction dispersed phase (lubricant) Ωp = 2,500 rpm; e) Volume fraction dispersed phase (lubricant) Ωp = 5,000 rpm.

4.4. Oil-bath lubrication of a rolling bearing: Churning and aeration

As previously mentioned, the two solvers discussed earlier are applicable not only to gears but also to bearings, which are integral components of any geared system. A representative case involves a vertically oriented tapered roller bearing fully immersed in lubricant. Due to its conical geometry, such a bearing naturally induces a pumping effect that promotes axial lubricant circulation [39]. At elevated rotational speeds, turbulent flow conditions can cause air entrapment within the lubricant reservoir, leading to a phenomenon known as *aeration*. Once aeration occurs, air bubbles become trapped in the lubricant, significantly altering its physical behavior.

The literature categorizes aeration into three main forms [40]: (1) entrained air, which consists of suspended bubbles; (2) foam, which forms when air rises to the surface and creates thin liquid films driven by surface tension; and (3) dissolved air, typically present in pressurized systems and invisible to the naked eye. The overall degree of aeration depends on the dynamic balance between air incorporation and release. These phenomena can substantially influence lubrication performance by modifying the characteristics of the lubricant mixture, thereby affecting its effectiveness—especially in forming high-pressure lubricant (HPL) films. This behavior was experimentally observed by the authors through high-speed camera (HSC) recordings and particle image velocimetry (PIV) measurements conducted on a 32312-A tapered roller bearing fitted with a transparent sapphire cage [13, 41–43]. These techniques enabled detailed assessment of the tangential velocity field between the cage and the outer race. To replicate the experimental conditions numerically, simulations were carried out using both a conventional incompressible Volume of Fluid (VOF) solver and a newly developed solver specifically designed to model aeration. As shown in Figure 8b, at lower tangential speeds (vt < 1 m/s), both solvers produced results in close agreement with the experimental data.

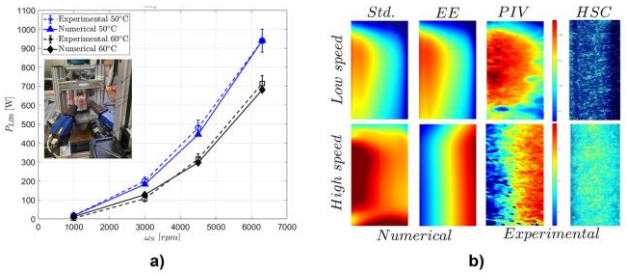

Fig.8. a) Power losses [44] and b) tangential velocity fields in a 32312-A bearing [42].

However, when the rotational speed increases to vt = 5 m/s, the predictions from the two numerical models begin to diverge significantly. The conventional incompressible solver yields a velocity field that closely resembles the one at lower speeds, differing only by a scaling factor. In contrast, the aeration-capable solver predicts a mirrored flow pattern. When compared to experimental observations, the results from the aeration model align

much more closely, validating its ability to capture the underlying physical mechanisms. The observed reversal in the velocity field at higher speeds is attributed to the presence of entrained air bubbles—a hypothesis strongly supported by high-speed camera (HSC) footage, which reveals both air bubbles and fluorescent seeding particles used in the PIV measurements.

Further validation was carried out at MEGT [44], where the same 32312-A bearing was tested under various thermal conditions. Figure 8a shows the comparison between measured and simulated power losses across different operating temperatures. In each case, the predictions from the developed CFD solvers remained within the range of experimental uncertainty, confirming their robustness and accuracy.

Although this particular application of the aeration solver focuses on rolling bearings, similar aeration phenomena have been documented in other mechanical components, such as gear systems and Gerotor pumps [45]. As demonstrated in prior work by the authors [14], the proposed numerical framework is readily adaptable to these systems, offering a valuable tool for analyzing aeration-driven effects across a wide range of machine elements.

4.5. Industrial application: Multistage parallel axis gearbox

While the earlier case studies primarily served to validate the accuracy of the proposed numerical approach, the following example demonstrates its practical relevance for day-to-day engineering applications. The focus here is a two-stage parallel-axis gearbox, developed by DANA [3], which operates under oil-bath lubrication conditions.

As illustrated in Figure 9a, the comparison between experimental measurements and simulation results for dimensionless power loss as a function of operating temperature shows excellent agreement. Across all test cases, the error remains below 20%—a notable achievement given the complexity of the system and the simplifying assumption of a uniform temperature throughout the gearbox. Beyond confirming the overall predictive accuracy of the model, the numerical analysis also provides detailed insights into the distribution of different power loss mechanisms. For instance, Figure 9b illustrates how the load-independent losses are apportioned among the four gears, and how this distribution varies with rotational speed. In this configuration, Gear 4 emerges as the dominant contributor to losses. This is attributed to its large size and mounting position, which ensures that it is consistently, at least partially, immersed in the oil sump.

Figure 9c further breaks down the losses among various components, including gears, bearings, and seals. In the unloaded condition examined here, bearing-related losses are minimal compared to those from the gears. However, this distribution is configuration-dependent, underscoring the importance of having simulation tools capable of quantifying component-specific losses prior to prototyping.

Eventually, Figure 9d highlights the relationship between inertial losses—linked to lubricant density—and viscous losses—associated with oil viscosity. This breakdown is critical for optimizing gearbox lubrication. For example, the figure reveals that Gear 4, which remains partially submerged, incurs losses predominantly through splashing effects (inertial), whereas the other gears, which are only slightly wetted by the oil, experience power losses primarily due to viscous effects (windage).

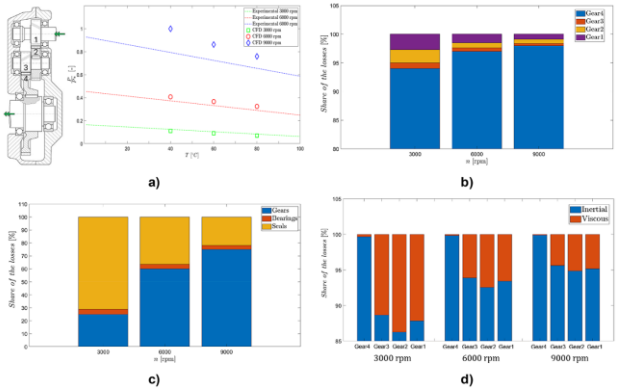

Fig.9. a) Power losses and share of the losses among b) the different gears, c) the mechanical components and d) between viscous and inertial contributions [3].

4.6. Industrial application: Planetary gearbox

Planetary gear systems possess unique kinematic properties that enable high reduction ratios and exceptional power density. However, the combined rotational and translational motion of the planet gears generates intense oil splashing, complicating lubrication management and resulting in notable load-independent power losses. These dynamics also present substantial challenges from a simulation standpoint. Nevertheless, the current CFD framework—leveraging the GRA^{MC} methodology—has demonstrated its ability to accurately simulate the behavior of planetary gear architectures [46].

Figure 10b depicts the emergence of Taylor–Couette flow between the planet carrier and the gearbox housing, a phenomenon well documented in the literature and experimentally observed using a transparent housing setup [48]. The CFD model successfully reproduced this flow pattern. As shown in Figure 10c, experimental results confirm that increasing rotational speed intensifies oil entrainment by the planet carrier. This leads to pronounced churning in the left portion of the gearbox (highlighted by a red dashed rectangle) and oil ejection on the right (blue dashed dot rectangle)—both effects are well captured by the simulation model [47].

Additionally, the simulations revealed the presence of squeezing effects at the interface between the planets and the ring gear. These effects, previously documented by Boni et al. [49], occur as the gear teeth mesh and the inter-tooth volume fluctuates. During engagement, the gap between the teeth narrows, creating a localized overpressure that drives axial lubricant flow. Once the minimum volume is reached and the gap opens again, a corresponding pressure drop occurs. Notably, the resulting pressure fluctuations remain well above the threshold for cavitation, as they do not fall below ambient pressure (1 bar). It is important to clarify that the pressure

gradients predicted by this model refer to macro-scale fluid behavior and do not reflect localized pressures at the actual tooth contact surfaces.

Finally, Figure 10a illustrates the model's ability to accurately predict power losses across varying rotational speeds and temperatures (θ), even for such a complex gearbox configuration. This validates the CFD methodology as a powerful tool for analyzing and optimizing planetary transmission systems.

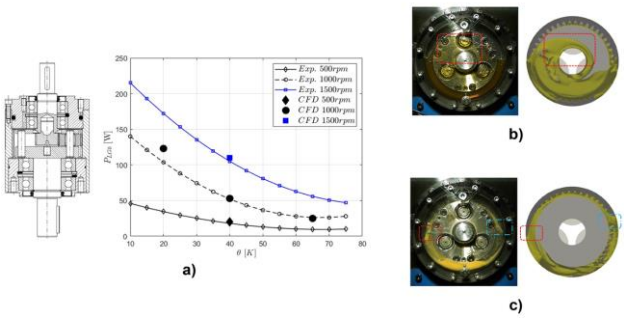

Fig.10. a) Power losses [8]; b,c) oil distribution: experimental vs. CFD [47]

5. COMPUTATIONAL EFFORT

Although the feasibility of simulating complex lubrication phenomena and handling intricate mesh topologies has been demonstrated, it is equally important to assess the computational cost associated with such analyses. To provide a meaningful comparison, we refer to a well-established benchmark in the literature [50]. In that study, Gorla et al. simulated a back-to-back test rig using commercial software that employed mesh smoothing and localized remeshing algorithms. Executed on hardware with a computing power of 38 GFLOPs (billion floating-point operations per second), their simulations required approximately 2,466 minutes—roughly 41 hours.

In contrast, the same test rig was simulated using the Global Remeshing Approach (GRA), which completed the task in just 172 minutes (under 3 hours). Further improvements were achieved by implementing the GRA^{MC} strategy, which reduced computation time to only 75 minutes.

While these comparisons are based on a relatively simple system, they highlight the dramatic improvements in computational efficiency enabled by advanced mesh handling. With access to more powerful hardware, even the simulation of highly complex gearboxes becomes feasible within practical timeframes. For example, the oil-bath-lubricated planetary gearbox discussed in Section 4.6 required around 400 hours to simulate using conventional local remeshing techniques, but only 20 hours when utilizing GRA^{MC} [47]. Similarly, the multi-stage gearbox examined in Section 4.5 was completed in 23 hours on a 48 GFLOPs system.

6. CONCLUSIONS

With the increasing emphasis on energy efficiency and reliability in gearbox design, CFD has become an essential tool for evaluating load-independent power losses—areas where analytical or empirical models often fall short—and for analyzing lubricant flow behavior within transmission components.

Standard methodologies used in commercial CFD software frequently encounter difficulties in accurately capturing real-world gearbox dynamics, largely due to limitations in mesh handling strategies that significantly affect computational efficiency. To overcome these challenges, the author proposes an open-source solution based on finite volume solvers, incorporating global remeshing and mesh clustering techniques tailored for complex fluid dynamic simulations.

This approach has been validated through a range of initial applications on experimental test setups, such as back-to-back rigs, while accounting for often-overlooked physical effects, including cavitation, aeration, aerosol formation, and grease-specific phenomena like channeling and circulation. The results not only confirm the method's reliability in predicting power losses and flow patterns but also provide new insights into the fundamental physical processes, offering valuable input for performance-driven design refinement.

Following the refinement of the global remeshing technique, the methodology has been successfully extended to challenging configurations, including planetary gear systems and industrial multi-stage gearboxes. These applications highlight the tool's capability to deliver accurate and timely results, making it a practical asset for design engineers focused on improving gearbox performance from the earliest development phases.

Future efforts will concentrate on enhancing user accessibility and interface usability, with the aim of integrating the tool more seamlessly into standard design office workflows.

REFERENCES

[1] Concli, F., Della Torre, A., Gorla, C., Montenegro, G. A New Integrated Approach for the Prediction of the Load Independent Power Losses of Gears: Development of a Mesh-Handling Algorithm to Reduce the CFD Simulation Time. Advances in Tribology 2016, 2016, doi:10.1155/2016/2957151.

[2] Mastrone, M.N., Concli, F. Application of the GRAMCmesh-Handling Strategy for the Simulation of Dip and Injection Lubrication in Gearboxes. International Journal of Computational Methods and Experimental Measurements 2022, 10, 303–313, doi:10.2495/CMEM-V10-N4-303-313.

[3] Mastrone, M.N., Concli, F. A Multi Domain Modeling Approach for the CFD Simulation of Multi-Stage Gearboxes. Energies (Basel) 2022, 15, doi:10.3390/en15030837.

[4] Mastrone, M.N., Concli, F. Development of a Mesh Clustering Algorithm Aimed at Reducing the Computational Effort of Gearboxes' CFD Simulations. In Proceedings of the WIT Transactions on Engineering Sciences; 2021; Vol. 131, pp. 59–69.

[5] Concli, F., Maccioni, L., Gorla, C. Lubrication of Gearboxes: CFD Analysis of a Cycloidal Gear Set. In Proceedings of the WIT Transactions on Engineering Sciences; 2019; Vol. 123, pp. 101–112.

[6] Fraccaroli, L., Pagliari, L., Concli, F. A Combined Analytical-Numerical Approach to Evaluate the Efficiency of Cycloidal Speed Reducers. Lecture Notes in Networks and Systems 2023, 745 LNNS, 590–599, doi:10.1007/978-3-031-38274-1_49.

[7] Concli, F., Maccioni, L., Gorla, C. Development of a Computational Fluid Dynamics Simulation Tool for Lubrication Studies on Cycloidal Gear Sets. International Journal of Computational Methods and Experimental Measurements 2020, 8, 220–232, doi:10.2495/CMEM-V8-N3-220-232.

[8] Concli, F., Gorla, C. Computational and Experimental Analysis of the Churning Power Losses in an Industrial Planetary Speed Reducer. In Proceedings of the WIT Transactions on Engineering Sciences; 2012; Vol. 74, pp. 287–298.

[9] Concli, F., Gorla, C. Numerical Modeling of the Churning Power Losses of Gears: An Innovative 3D Computational Tool Suitable for Planetary Gearbox Simulation. VDI Berichte 2017, 2017, 800–811.

[10] Concli, F., Mastrone, M.N. Latest Advancements in the Lubrication Simulations of Geared Systems: A Technology Ready for Industrial Applications. VDI Berichte 2023, 2023, 499–518, doi:10.51202/9783181024225-499.

[11] Concli, F., Mastrone, M.N. Latest Advancements in the Lubricant Simulations of Geared Systems: A Technology Ready for Industrial Applications [Neuste Fortschritte Bei Der Schmierstoffsimulation von Getriebesystemen: Eine Industrietaugliche Technologie]. Forschung im Ingenieurwesen/Engineering Research 2023, 87, 1181–1191, doi:10.1007/s10010-023-00698-z.

[12] Maccioni, L., Concli, F. Computational Fluid Dynamics Applied to Lubricated Mechanical Components: Review of the Approaches to Simulate Gears, Bearings, and Pumps. Applied Sciences (Switzerland) 2020, 10, 1–29, doi:10.3390/app10248810.

[13] Maccioni, L., Chernoray, V.G., Mastrone, M.N., Bohnert, C., Concli, F. Study of the Impact of Aeration on the Lubricant Behavior in a Tapered Roller Bearing: Innovative Numerical Modelling and Validation via Particle Image Velocimetry. Tribol Int 2022, 165, doi:10.1016/j.triboint.2021.107301.

[14] Mastrone, M.N., Concli, F. Numerical Modeling of Fluid's Aeration: Analysis of the Power Losses and Lubricant Distribution in Gearboxes. Journal of Applied and Computational Mechanics 2023, 9, 83–94, doi:10.22055/jacm.2022.40666.3625.

[15] Mastrone, M.N., Concli, F. Simulation of Fluid's Aeration: Implementation of a Numerical Model in an Open Source Environment. In Proceedings of the WIT Transactions on Engineering Sciences; 2021; Vol. 132, pp. 27–36.

[16] Mastrone, M.N., Concli, F. CFD Simulation of Grease Lubrication: Analysis of the Power Losses and Lubricant Flows inside a Back-to-Back Test Rig Gearbox. J Nonnewton Fluid Mech 2021, 297, doi:10.1016/j.jnnfm.2021.104652.

[17] Niemann, G., Winter, H. Maschinenelemente—Band 2: Getriebe Allgemein,Zahnradgetriebe—Grundlagen, Stirnradgetriebe—2.Auflage; Berlin, Germany, 2003; ISBN 9783540773405.

[18] Concli, F., Schaefer, T.C., Bohnert, C. Innovative Meshing Strategies for Bearing Lubrication Simulations. Lubricants 2020, 8, doi:10.3390/lubricants8040046.

[19] Hirt, C.W., Nichols, B.D. Volume of Fluid (VOF) Method for the Dynamics of Free Boundaries. J Comput Phys 1981, 39, 201–225.

[20] Concli, F. Pressure Distribution in Small Hydrodynamic Journal Bearings Considering Cavitation: A Numerical Approach Based on the Open-Source CFD Code OpenFOAM®. Lubrication Science 2016, 28, 329–347, doi:10.1002/ls.1334.

[21] Kunz, R.F., Boger, D.A., Stinebring, D.R., Chyczewski, T.S., Lindau, J.W., Gibeling, H.J., Venkateswaran, S., Govindan, T.R. A Preconditioned Navier-Stokes Method for Two-Phase Flows with Application to Cavitation Prediction. Comput Fluids 2000, 29, 849–875, doi:10.1016/S0045-7930(99)00039-0.

[22] Concli, F., Gorla, C. Numerical Modeling of the Power Losses in Geared Transmissions: Windage, Churning and Cavitation Simulations with a New Integrated Approach That Drastically Reduces the Computational Effort. Tribol Int 2016, 103, 58–68, doi:10.1016/j.triboint.2016.06.046.

[23] Rusche, H. Computational Fluid Dynamics of Dispersed Two-Phase Flows at High Phase Fractions, 2002.

[24] Simonnet, M., Gentric, C., Olmos, E., Midoux, N. CFD Simulation of the Flow Field in a Bubble Column Reactor: Importance of the Drag Force Formulation to Describe Regime Transitions. Chemical Engineering and Processing: Process Intensification 2008, 47, 1726–1737.

[25] Hwang, C.J., Wu, S.J. Global and Local Remeshing Algorithms for Compressible Flows. J Comput Phys 1992, 102, 98–113, doi:10.1016/S0021-9991(05)80009-9.

[26] Concli, F., Gorla, C., Torre, A.D., Montenegro, G. Windage Power Losses of Ordinary Gears: Different CFD Approaches Aimed to the Reduction of the Computational Effort. Lubricants 2014, 2, 162–176, doi:10.3390/lubricants2040162.

[27] Mastrone, M.N., Concli, F. Development of a Mesh Clustering Algorithm Aimed at Reducing the Computational Effort of Gearboxes' CFD Simulations. In Proceedings of the WIT Transactions on Engineering Sciences; 2021; Vol. 131, pp. 59–69.

[28] Mastrone, M.N., Concli, F. CFD Simulations of Gearboxes: Implementation of a Mesh Clustering Algorithm for Efficient Simulations of Complex System's Architectures. International Journal of Mechanical and Materials Engineering 2021, 16, doi:10.1186/s40712-021-00134-6.

[29] Concli, F., Gorla, C. Numerical Modeling of the Churning Power Losses in Planetary Gearboxes: An Innovative Partitioning-Based Meshing Methodology for the Application of a Computational Effort Reduction Strategy to Complex Gearbox

Configurations. Lubrication Science 2017, 29, 455–474, doi:10.1002/ls.1380.

[30] Mastrone, M.N., Concli, F. Application of the GRAMCmesh-Handling Strategy for the Simulation of Dip and Injection Lubrication in Gearboxes. International Journal of Computational Methods and Experimental Measurements 2022, 10, 303–313, doi:10.2495/CMEM-V10-N4-303-313.

[31] Höhn, B.-R., Michaelis, K., Otto, H.-P. Influence on No-Load Gear Losses. Ecotrib 2011 Conference Proceedings 2011, 2, 639–644.

[32] Stemplinger, J.-P., Stahl, K., Höhn, B.-R., Tobie, T., Michaelis, K. Analysis of Lubrication Supply of Gears Lubricated with Greases NLGI 1 and 2 and the Effects on Load-Carrying Capacity and Efficiency. NLGI Spokesman 2014, 78, 18–22.

[33] KR, S.C., Lugt, P.M. The Process of Churning in a Grease Lubricated Rolling Bearing: Channeling and Clearing. Tribol Int 2021, 153, 106661.

[34] Wingertszahn, P., Koch, O., Maccioni, L., Concli, F., Sauer, B. Predicting Friction of Tapered Roller Bearings with Detailed Multi-Body Simulation Models. Lubricants 2023, 11, doi:10.3390/lubricants11090369.

[35] Maccioni, L., Concli, F. Estimation of Hydraulic Power Losses in a Double-Row Tapered Roller Bearing via Computational Fluid Dynamics. Lecture Notes in Networks and Systems 2023, 745 LNNS, 655–666, doi:10.1007/978-3-031-38274-1_55.

[36] Dindar, A., Chaudhury, K., Hong, I., Kahraman, A., Wink, C. An Experimental Methodology to Determine Components of Power Losses of a Gearbox. J Tribol 2021, 143, doi:10.1115/1.4049940.

[37] Kunz, R.F., Hill, M.J., Schmehl, K.J., McIntyre, S.M. Computational Studies of the Roles of Shrouds and Multiphase Flow in High Speed Gear Windage Loss. In Proceedings of the Annual Forum Proceedings – AHS International; 2012; Vol. 3, pp. 1953 – 1963.

[38] Schiller, L. A Drag Coefficient Correlation. Zeit. Ver. Deutsch. Ing. 1933, 77, 318–320.

[39] Liebrecht, J., Si, X., Sauer, B., Schwarze, H. Investigation of Drag and Churning Losses on Tapered Roller Bearings. Strojniški vestnik-Journal of Mechanical Engineering 2015, 61, 399–408.

[40] Nemoto, S., Kawata, K., Kuribayashi, T., Akiyama, K., Kawai, H., Murakawa, H. A Study of Engine Oil Aeration. JSAE review 1997, 18, 271–276.

[41] Maccioni, L., Concli, F. Flows in Oil-Bath Lubricated Tapered Roller Bearings: CFD Simulations Validated via PIV. VDI Berichte 2023, 2023, 247–266, doi:10.51202/9783181024157-247.

[42] Maccioni, L., Chernoray, V.G., Concli, F. Fluxes in a Full-Flooded Lubricated Tapered Roller Bearing: Particle Image Velocimetry Measurements and Computational Fluid Dynamics Simulations. Tribol Int 2023, 188, doi:10.1016/j.triboint.2023.108824.

[43] Maccioni, L., Chernoray, V.G., Bohnert, C., Concli, F. Particle Image Velocimetry Measurements inside a Tapered Roller Bearing with an Outer Ring Made of Sapphire: Design and Operation of an Innovative Test Rig. Tribol Int 2022, 165, doi:10.1016/j.triboint.2021.107313.

[44] Maccioni, L., Rüth, L., Koch, O., Concli, F. Load-Independent Power Losses of Fully Flooded Lubricated Tapered Roller Bearings: Numerical and Experimental Investigation of the Effect of Operating Temperature and Housing Wall Distances. Tribology Transactions 2023, 66, 1078–1094, doi:10.1080/10402004.2023.2254957.

[45] Changenet, C., Leprince, G., Ville, F., Velex, P. A Note on Flow Regimes and Churning Loss Modeling. J. Mech. Des 133 2011, 1–5.

[46] Concli, F., Gorla, C. Influence of Lubricant Temperature, Lubricant Level and Rotational Speed on the Churning Power Loss in an Industrial Planetary Speed Reducer: Computational and Experimental Study. International Journal of Computational Methods and Experimental Measurements 2013, 1, 353–366, doi:10.2495/CMEM-V1-N4-353-366.

[47] Mastrone, M.N., Hildebrand, L., Paschold, C., Lohner, T., Stahl, K., Concli, F. Numerical and Experimental Analysis of the Oil Flow in a Planetary Gearbox. Applied Sciences (Switzerland) 2023, 13, doi:10.3390/app13021014.

[48] de Gevigney, J.D., Changenet, C., Ville, F., Velex, P., Becquerelle, S. Experimental Investigation on No-Load Dependent Power Losses in a Planetary Gear Set. In Proceedings of the International Gear Conference; 2013; Vol. 2, pp. 1101–1112.

[49] Boni, J.-B., Neurouth, A., Changenet, C., Ville, F. Experimental Investigations on Churning Power Losses Generated in a Planetary Gear Set. Journal of Advanced Mechanical Design, Systems, and Manufacturing 2017, 11, JAMDSM0079–JAMDSM0079.

[50] Gorla, C., Concli, F., Stahl, K., Höhn, B.-R., Michaelis, K., Schultheiß, H., Stemplinger, J.-P. Hydraulic Losses of a Gearbox: CFD Analysis and Experiments. Tribol Int 2013, 66, 337–344, doi:10.1016/j.triboint.2013.06.005.

11th International Scientific Conference
IRMES 2025
Research and Development of
Mechanical Elements and Systems
June 19 – 21, 2025; Vrnjačka Banja, Serbia

Original scientific paper DOI: 10.46793/IRMES25.plA4B

AgAR: A MULTIPURPOSE ROBOTIC PLATFORM FOR THE DIGITAL TRANSFORMATION OF AGRICULTURE

Milan BANIĆ[1]
Lazar STOJANOVIĆ[2]
Marko PERIĆ[3]
Damjan RANGELOV[4]
Vukašin PAVLOVIĆ[5]
Aleksandar MILTENOVIĆ[6]
Miloš SIMONOVIĆ[7]

[1]Faculty of Mechanical Engineering, University of Niš, Niš, Serbia, 18104; milan.banic@masfak.ni.ac.rs; ORCID iD: 0000-0001-8684-042X
[2]Coming Computer Engineering, Belgrade, Serbia, 11000; lazar.stojanovic@coming.rs; 0000-0001-5120-8889
[3]Faculty of Mechanical Engineering, University of Niš, Niš, Serbia, 18104; marko.peric@masfak.ni.ac.rs; ORCID iD: 0000-0001-9350-0351
[4]Faculty of Mechanical Engineering, University of Niš, Niš, Serbia, 18104; damjan.rangelov@masfak.ni.ac.rs; ORCID iD: 0000-0003-3071-893X
[5]Faculty of Mechanical Engineering, University of Niš, Niš, Serbia, 18104; vukasin.pavlovic@masfak.ni.ac.rs; ORCID iD: 0000-0002-5090-9277
[6]Faculty of Mechanical Engineering, University of Niš, Niš, Serbia, 18104; aleksandar.miltenovic@masfak.ni.ac.rs; ORCID iD: 0000-0002-1453-2548
[7]Faculty of Mechanical Engineering, University of Niš, Niš, Serbia, 18104; milos.simonovic@masfak.ni.ac.rs; ORCID iD: 0000-0003-1364-7746

Abstract: *The paper presents the design and engineering rationale behind AgAR, a multipurpose robotic platform developed to address the evolving needs of digital agriculture. The AgAR platform represents a significant advancement in unmanned ground vehicles (UGVs) by integrating a hybrid active-passive suspension system that ensures dynamic leveling and adaptable chassis geometry, enabling safe operation on complex terrains including steep inclines up to 30°. The paper first provides a comprehensive review of state-of-the-art UGVs in agriculture, analyzing mobility strategies, suspension concepts, powertrain options, and implement integration. Building on these insights, the AgAR platform is introduced with a focus on mechanical design, emphasizing modularity, high torque electric drivetrains, standardized agricultural implement compatibility, and fast battery swapping to enable long operational autonomy. AgAR's structural components were optimized using a digital twin approach to reduce weight while maintaining strength, thereby increasing efficiency and reducing soil compaction. Comparative analysis demonstrates that AgAR uniquely combines terrain adaptability, multi-task versatility, and system level robustness. These attributes position AgAR as a scalable, cost-effective solution suitable for a wide range of agricultural operations, from precision monitoring to heavy implement deployment. The paper concludes by identifying future design trends in agricultural UGVs informed by the AgAR development process.*

Keywords: *Unmanned Ground Vehicle (UGV); Agriculture robot; Mechanical design; Hybrid suspension; Design advantages.*

1. INTRODUCTION

Unmanned Ground Vehicles (UGVs) are becoming increasingly important in agriculture, where they promise to automate labour intensive tasks, enhance productivity, and reduce operational costs. Unlike conventional tractors or machinery, UGVs can be designed without accommodating a human operator, enabling new form factors optimized for specific tasks and terrains. However, agricultural environments present significant challenges: unstructured terrains, variable soil conditions, crop obstacles, and the need for long duty cycles demand careful mechanical design. Modern agricultural UGVs must balance mobility in rough and sloped fields, stability, payload capacity, and recently energy efficiency as their electrification is underway. Achieving a low vehicle mass while maintaining structural strength is

particularly important for off-road robots to improve manoeuvrability and autonomy [1].

This paper presents a comprehensive review of the state of the art in agricultural UGV design over the past decade, highlighting key technologies, mechanical strategies, and structural features in modern platforms. The AgAR (Agriculture Autonomous Robot) platform, a new UGV developed as a universal solution for indoor/outdoor farming tasks, is than introduced and its mechanical design is than detailed. Finally, AgAR is than compared in respect to design features to existing platforms, emphasizing its unique advantages.

2. STATE OF THE ART UGV DESIGNS FOR AGRICULTURE

2.1. Locomotion and Chassis Architectures in Modern Agricultural Robots

Agricultural UGVs have adopted a variety of mobility architectures, primarily wheeled platforms (4-wheel and 6-wheel designs commonly), and occasionally tracked or hybrid systems, to meet the demands of different crops and terrain. Four-wheeled UGVs with either skid-steering or Ackermann steering dominate many designs due to mechanical simplicity and efficient on road mobility. For example, the commercial Naïo Orio robot is a 4-wheel electric platform for weeding row crops, using steerable wheels to accurately follow crop rows [2]. Orio weighs around 1500 kg (depends on existence of additional batteries), has a maximal speed of 5.5 km/h [3], and runs from 3 to 7 hours on batteries, demonstrating the viability of electric drives for whole day field operations with a battery swap technology. Recently, tracked agricultural robots also appeared, particularly for specialty crops on soft soil or steep slopes like the EU funded VineRobot and VineScout projects for vineyard monitoring, trading speed for increased traction on inclines and loose soil [4], or providing a high power tractor replacement as AgXEED 3A [5]. In general, wheels are preferred for energy efficiency on moderate terrain, while tracks or high traction wheels are chosen for extreme conditions like deep mud or very steep grades [2].

Another architectural consideration is whether the chassis is articulated. Some UGVs use articulated frames or multi module designs to improve manoeuvrability or load distribution. The AgroIntelli Robotti, for instance, consists of two modules with four wheels in total (each module with a diesel engine) and a central linkage that holds standard farm implements. This semi articulated configuration allows Robotti to carry heavy attachments (up to ~750 kg on a Category 3 point hitch) while spreading weight over a longer wheelbase [6]. Its diesel engines (total 106 kW) and optional PTO drive enable towing or powering implements, and it can run up to 80 hours on a single fuel tank. The trade-off is a heavier and more complex platform which compacts the soil and is quite costly, suited to larger farms. Smaller robots like Ecorobotix's solar rover and FarmDroid take the opposite approach: extremely lightweight platforms with low speed electric drivetrains and even solar panels for energy supply, which is ideal for tasks like seeding or weeding in flat fields. Such platforms are not capable of handling large attachments or rough terrain. Between these extremes, many research UGVs weight a few hundred kilograms, use electric motors (often one per wheel), and aim for a modular tool carrier design: a flat or open chassis to which different tools (sprayers, cameras, manipulators, etc.) can be mounted [2]. This modularity is key to modern designs, as it allows a single robot base to perform multiple tasks, improving cost effectiveness. But almost all the commercial solutions of tool carriers rely on usage of custom specialized tools specific to platform manufacturers. This again hampers the ability of smaller/mid-sized farms to adopt robotic solutions for agriculture.

2.2. Suspension and Stability

Navigating uneven realistic farmland requires careful attention to suspension design and centre of gravity management for UGVs. Past literature classifies UGV suspension strategies into four categories: rigid, passive, active, and hybrid [2]. In a rigid suspension, wheels are directly fixed to the chassis, transfering any ground unevenness directly to the chassis. Robots with rigid chassis are simpler and suitable for relatively flat, even terrain at low speeds. Examples include early platforms like AgTracker [7] and Fendt's small Xaver seeding robots [8], but also newer designs as VitiBOT BAKUS [9]. Rigid designs are prone to wheel lift-off or loss of traction on uneven terrain, limiting their mobility, path planning and repeatability, slope handling and speed.

Passive suspensions add suspension elements or articulation joints that allow the wheels to move relative to the chassis, suppressing out terrain irregularities without active control. A simple example is Wageningen's weeding robot [10] or University of Illinois' TerraSentia robot [11]. Passive suspension improves movement stability and traction but cannot actively correct large tilt angles. Some designs use partially passive approaches like adjustable dampers like variable stiffness shock absorbers, providing limited control over the stiffness and damping of passive elements.

Active suspension involves actuators, either electric, hydraulic, or pneumatic, to actively adjust the wheel height or chassis orientation, guided by sensors and control algorithms [2]. Such approach is more complex, but it can significantly enhance stability on uneven terrain by keeping the chassis in level or by preferable load distribution. In agriculture, active suspension has been less common, and it is usually combined with passive suspension, thus forming the hybrid suspension. Such systems are still not released on the market, but a lot of research effort is directed into researching new hybrid suspension concepts such as Agri.Q [12]. Agri.Q is an eight wheeled rover with wheels arranged in four rocker arm pairs, with electric linear actuators that actively control the robotic platform. This Agri.Q hybrid approach, which combines the articulation and electric actuators, enables movement over unstructured terrains without above noted penalties associated with rigid and passive suspension concepts. Both active and hybrid concepts require robust control and using of tilt and IMU sensors, as well as wheel odometry, to react in real time to

disturbances caused by terrain. The benefit is greatly improved stability which is a traditional problem of agricultural machines. Furthermore, hybrid suspension has some passive shock absorption to supress the high frequency vibrations, thus lowering the load of the actuators and their speed requirements.

Overall, the trend in the last decade is toward increased attention to stability control. A review by Fernandes et al. stresses that stability is crucial for ag robots since the lack of a human driver means the robot must handle unpredictable terrain on its own [2]. Thus, the modern UGVs must include at least basic stability monitoring, even if they do not have active or hybrid suspension. The new generation of autonomous tractors retrofits have automated stability cutoff systems rather than active levelling.

2.3. Powertrains

Powering an agricultural UGV is achieved via internal combustion engines or via battery powered electric motors. Trends in electric vehicles related to electrification also reflected in shift toward electric drivetrains in UGVs, but at a lower pace. Although electric motors offer finer control for automation and lower noise/emissions for farming only few commercial solutions took the electrification approach, primary in . small and medium UGVs. Notible examples are robots manufactured by Naïo (Ted, Oz, Jo, Orio) [3] or Bonirob by Bosch [13], equipped with a 15 kW electric drive and a battery supported by an onboard gasoline generator.

Hybrid systems are becoming popular in larger robots to ensure full day operation while still providing electric actuation. Fully battery powered robots are common in smaller robots with multiple research prototypes typically achieving from 2 to 10 hours per charge. Some new designs incorporate fast battery swap systems or even solar charging. For large autonomous tractors, diesel remains common due to high power demands. The AgroIntelli Robotti has twin Kubota diesel engines, driving hydrostatic transmissions with an optional PTO. The recently introduced Monarch MK-V electric tractor provides 40 hp continuous (70 hp peak) with a large battery for up to 14 hours autonomy, but its weight is over 2300 kg due to battery. Higher power machines would have even greater weight which prevents their application in realistic environment due to soil compaction. Thus, researchers are exploring compromises like smaller robots working in fleets or hybrids for peak loads. As a summary, the last decade has proven the viability of battery electric UGVs for many agricultural tasks, especially when combined with innovations in energy management like swappable batteries, onboard generators, or solar augmentation. The choice of powertrain in current platforms is usually tied to scale and purpose: small robots (under ~500 kg) tend to be electric, while larger which carry implements use diesel or hybrid to deliver the required power.

2.4. Payload and Implement Integration

Agricultural robots can be divided into two categories: task specific vs. multipurpose designs. Task specific robots integrate custom tool or payload as part of the design. As a for example, a robot designed solely to weed will have fixed weeders and cannot easily be reconfigured for other jobs. On the other hand, multipurpose platforms aim to accept various attachments, like a small tractor or tool carrier. The past ten years have seen a quite modest push towards multipurpose robots to increase number of functions and justify investment cost. Many modern UGVs feature mounting interfaces or hitches but mostly require specialized implements like for instance Slopehelper [15]. Some small robots use a simple flatbed or mounting rails on which implements or sensor masts can be attached, but such approach demands implement adaptation. This means a farmer in most cases could not mount standard implements on the robot without custom adaptation. Only few advanced solutions like AgXEED adopt standard tractor attachment points.

The inclusion of implement interfaces comes with mechanical demands: the robot must handle significant loads and forces from implements. It needs sufficient drawbar pull and hitch lift capacity to, say, pull a small plough or carry a tank of fertilizer.

3. MECHANICAL DESIGN OF THE AgAR PLATFORM

The AgAR robotic platform has been engineered as a modular system composed of multiple mechanical subassemblies that collectively support its versatility and adaptability in agricultural operations. The platform consists of several main mechanical subassemblies, as shown in Figure 1:

1. the main body frame (chassis) with its protective shell,
2. the wheel-leg modules each containing a wheel with drive motor and a suspended actuated leg,
3. the drivetrain and power subassembly, including motors, gears and battery,
4. safety elements which stop the robot in case of emergency,
5. optional 3-point hitch subassembly with counterweight which enables the connection of implements,
6. optional PTO drivetrain motor, gearbox and battery,
7. additional protective shell for the PTO electronics and battery,
8. environment perception, localisation and communication sensor housing.

Additionally, sensor integration is built into the design to monitor and control mechanical functions. As clear from the description, the design incorporates the base robot platform and an optional PTO and a 3-point hitch subsystem which enables usage of standard tractor implements. This approach enables the modularity as PTO and 3-point hitch can be removed to accommodate robotic or some custom-made functional attachment which can be used for harvesting, crop monitoring, … The noted design choice was made to enable the robot platform to be used in as many as possible agricultural operation to increase effectiveness and decrease investment costs related to agriculture robotization. The field operations with robotic attachments increase days in

operation during the regular farming season with an ultimate goal to automate all agricultural operations.

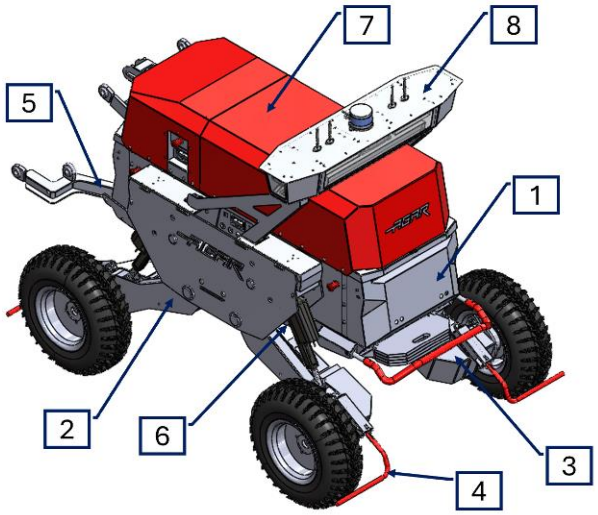

Fig.1. 3D model of the AgAR robotic platform

The main body of AgAR is essentially the backbone to which all other modules attach. It was designed to be both strong and lightweight, using a combination of standard aluminium profiles and custom fabricated steel parts. The base frame uses extruded aluminium beams in a rectangular arrangement, providing a modular structure that is easy to assemble and modify. Aluminium offers a good strength-to-weight ratio and inherent corrosion resistance, important for outdoor use and exposure to fertilizers or moisture. To further reinforce the frame and mount external panels, aluminium sheet metal housings are attached, which also serve as the outer shell. The outer panels protect internal components from environmental damage and provide mounting for some of the sensors and lights. Bolted connections are used extensively, which allow disassembly for maintenance or upgrades. In summary, AgAR's body structure reflects a modular and optimized design – modular for flexibility and material optimizations for weight reduction. Front robot profile is equipped with a safety bumper with a 10 cm travel, which stops the robot if the collision with objects occur in the traveling path of the main body.

Each of the four wheel modules on AgAR is essentially a small powered leg. It comprises: a wheel with skid steer off-road tire, a gearmotor, a leg linkage with an electric linear actuator for height adjustment, and mounting interfaces with dampened adjustable shock absorber to attach the electric actuator to the chassis. Multiple wheel diameters (480 to 735 mm) and widths (175 to 300 mm) can be mounted to adjust robot speed and traction force, as well as to influence the soil pressure. The drive motor for each wheel is a 1.5 kW brushless DC motor coupled to a planetary gear transmission (40:1 ratio). The planetary gear provides a high reduction, converting the motor's high-speed low-torque output into high torque at the wheel. The electric motors are equipped with electromagnetic brakes which engage in case of emergency stop, making the emergency stopping distance smaller than 10 cm. Furthermore, the wheel hubs are equipped with 203 mm disk brake which supplements the motor electric braking when necessary, especially on the slopes. The mechanical brakes are actuated by electric linear actuators attached to the lower part of the chassis. The powered leg also houses a safety bumper, as shown in Figure 2, which stops the robot in case of collision with the objects on the wheel path.

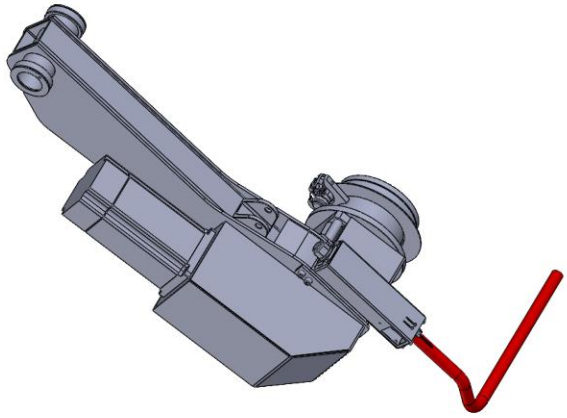

Fig.2. 3D model of the AgAR drive train

Furthermore, the wheels can be repositioned laterally with extenders. This effectively allows adjusting track width from a maximum to a narrower stance.

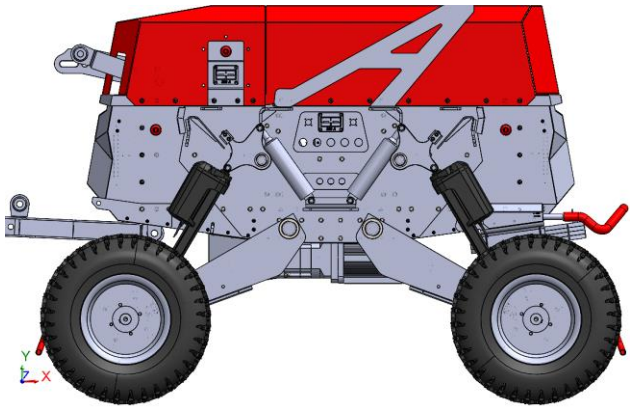

Fig.3. Hybrid suspension system

The wheel modules attach to the chassis as shown in Figure 3, via vertical pivot pins, effectively acting as swing arms that can raise or lower. The leg actuator on each module is a heavy-duty electric linear actuator which can extend or retract to change the wheel's vertical position relative to the body. The actuator is connected via amplification mechanism with air damped adjustable shock absorber connected with chassis with a pin. This is the core of the dynamic leveling system. The actuators are coordinated to keep the platform level or to adjust height on command. They must support the robot's weight and any payload; thus, they were specified with a high load rating (each supporting 11 kN when static). During driving, shocks are encountered (e.g., hitting a bump), as well as small terrain unevenness, which are suspended by damped shock absorbers, keeping the platform level, effectively making it an active-passive hybrid suspension, as shown on Figure 4.

Fig.4. AgAR hybrid suspension system in action

Fig.5. AgAR in lowest and uppermost configuration

Practically, the levelling system in AgAR also doubles as a height adjustment feature. The operator can command the robot to raise or lower uniformly when needed, for example, to lift the chassis for lifting the implement from the ground, clearing high obstacles or to align an attached robotic arm to a higher fruit tree branch. In this mode, as shown in Figure 5, all four actuators move in unison to change height while keeping level. AgAR can achieve a working reach height of over 3.5 m with an attached robot arm. When lowered, it can be just a bit above ground to perform tasks like strawberry picking or going under low-hanging canopy. This versatility is a direct outcome of the dynamic leg design.

The drivetrain is completed by the power electronics: each motor is controlled by a dedicated motor driver (with closed-loop current and speed control). A central computer (running ROS2, Robot Operating System) issues velocity commands to each wheel motor and position commands to each leg actuator based on sensor inputs. The motors use Hall sensors for speed/position feedback, enabling precise skid-steer manoeuvres and odometry for navigation. The leg actuators also have position feedback via Hall sensors to allow accurate height control. This arrangement essentially makes each corner of the robot an independent suspension unit that can be computer controlled.

The battery pack is housed in the main body and powers all motors and controllers. AgAR's primary battery is a lithium-phosphate pack providing 11 kWh of energy, which is sufficient for 8 - 12 hours of typical use. The battery module design includes a swap mechanism as the battery pack can be removed from the front of the robot by removing the front panel and pulling out a drawer, as shown in Figure 6. This design was chosen to minimize downtime as depleted battery can be changed in up to 3 minutes. For extended operations, the design envisions using multiple battery packs in rotation by charging one battery while the robot runs on another. AgAR also supports an auxiliary top-mounted battery, as the body top platform has mounting rails where an extra 27 kWh battery can be added for tasks that need more energy, effectively extending the operational time to more than 24h during for instance monitoring applications. The upper battery serve also as an energy storage for the PTO motor. This flexibility again ties into the AgAR multi-purpose nature.

Fig.6. AgAR battery swap

In terms of performance, the drivetrain provides a maximum robot speed of ~6 km/h when on flat terrain. The control system limits acceleration and deceleration to prevent instability, especially when carrying heavy loads. The skid-steer can rotate the robot about its centre (in-place turning radius 0°), which was tested on concrete and

soil. Pivoting in place on high friction surfaces produces the highest motor currents i.e. motor torque (and thus mechanical stress), so the software avoids aggressive pivots on asphalt, for instance, to extend mechanical life.
Furthermore, the drive control system monitors motor currents and can limit torque to protect the drivetrain.
The PTO drivetrain is attached to the bottom of the robot body, as shown in Figure 7, and it is powered by the auxiliary battery. The PTO drivetrain consist of the BLDC motor connected to the planetary gearbox, providing almost 200 Nm with a 48V 10 kW motor. The PTO shaft is shielded according to ISO 5673-2 standard.

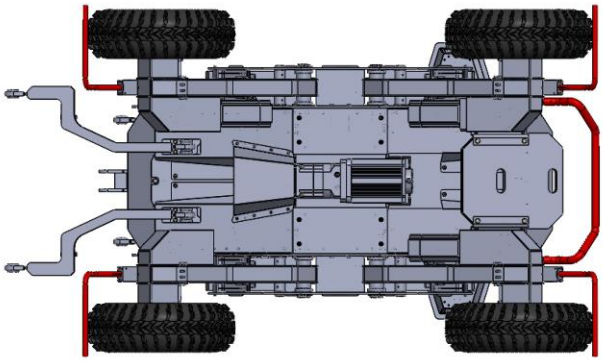

Fig.7. AgAR PTO drivetrain

The AgAR platform can be also equipped with a 3-point Category I hitch according to ISO 11001-1:2016 standard, as shown on Figure 8. Such configuration enables the robot to use all the Category I tractor implements. Furthermore, the hitch can be modified to drawing hook enabling the towing of trailers or implements such as towed sprayers and atomizers or ballers. As the robotic platform is agnostic to moving direction, the hitch system can be used to position implements in front of the robot. Such configuration is supported by design of the sensor bridge, which can be easily positioned on the other robot side. Furthermore, the sensor bridge can be rotated by a hinge system which enables quick dismantling of the auxiliary battery cover to enable its swap.

Fig.8. AgAR 3-point hitch subsystem and a sensor bridge

Fig.8. Emergency stop when bumper is activated

Besides sensors which detect possible obstacles and generate 3D map of the robot surroundings, AgAR is equipped with a low-level safety system which almost instantly stops the robot when the bumpers are activated, as shown in Figure 8. The same effect is achieved when the safety stop buttons are activated. In both cases, the power to the driving motos is instantly stopped and electromagnetic and mechanical brakes are activated.
The complete design of structural components was tested in virtual environment with finite element analysis, based on operation data provided by the robot digital twin. The complete procedure for robot structural analysis and topology optimisation performed for structural components lightweighting with digital twin data is described in a separate publication by authors [16].

4. DESIGN ADVANTAGES OF AgAR VS. CONTEMPORARY PLATFORMS

AgAR was conceived to address several gaps observed in existing UGVs. A comparison of key specifications is given in Table 1.

Fig.9. AgAR on a 40° slope with levelling system activated

Table 1. Comparison of AgAR with selected agricultural UGVs. Key: AWD – All-wheel drive; PTO – Power Take-Off; Levelling indicates if active chassis leveling is present; runtime assumes one refuel or full battery charge.

Platform	Drive & Power	Weight (kg)	Payload / Hitch	Terrain & Slope	Notable Features
AgAR (Coming, 2024)	4×4 electric (4×1.5 kW motors); Battery 8 - 12 h, swap in 3 min	~900	600 kg payload; Cat-I 3-pt hitch	Active leveling, 30° max slope	Dynamic height adjustment (0.7 m); standard Category I implement; Multi-robotic attachment support; Autonomous & teleopation modes
Robotti (AgroIntelli, 2018)	4×4 diesel (2×25 kW engines); 60 - 80 h per refuel	~1500	1500 kg implement; Cat-II hitch, optional PTO	Rigid chassis; 15° max slope	High endurance; Full tractor implements; RTK-GPS navigation; No active suspension
Dino (Naïo, 2017)	4×4 electric (hub motors); Battery 8 - 10 h	~600	Approx. 100 kg tool load (weeding tools)	Passive suspension, flat fields (vegtable rows)	Autonomous weeding robot; Vision guided row following; Task-specific (cultivator)
Agri.Q (Polito, 2020)	8×8 electric (hub motors); Battery ~6 h	~800	200 kg sensors & arm (no hitch)	Hybrid suspension, active leveling (rocker-arms)	

Fig.10. AgAR performing various applications with existing implements

Terrain Adaptability: Most UGVs introduced to market in last ten years had either no suspension or passive suspension, limiting them to relatively even terrain or requiring very slow operation on rough ground. AgAR's four point hybrid dynamic levelling system actively keeps the platform level on inclines, enabling safe operation on very steep terrains, which was tested up to 40° even in sand as shown in Figure 9. This is a major advantage in

hilly vineyards or terraced fields, where previously only tracked vehicles or human operated machines could go.

Multipurpose attachment support: Unlike robots dedicated to a single task, AgAR is designed as a universal platform. It provides standardized mounting for agricultural implements, specifically supporting Category I 3-point hitch attachments and multiple power outputs. This means farmers can use existing small tractor tools (for plowing, seeding, mowing, spraying, etc.) with the robot as shown in Figure 6.

Competing robots often lack this; e.g., Dino carries only its built-in weeder tools and cannot accept a standard hitch implement. Robotti and a few others do support attachments (very often custom ones), but AgAR brings this capability to a fully electric, smaller footprint platform. Additionally, AgAR includes multiple high power electrical outputs to drive attachments (or an onboard inverter for tools) and can accommodate an auxiliary battery or even a robotic arm on its top deck as shown in Figure 11.

The design philosophy is akin to a "master of none, but jack of all trades". This universality addresses the economic challenge of robots in agriculture by spreading cost over many uses.

Adjustable Geometry: AgAR features variable ground clearance and track width through its leg mechanisms. The chassis height can change by nearly 0.9 m, which is used both for leveling and for task-specific adjustment. As already noted, the robot can lower itself for stability or to interact with low crops, or raise itself to increase clearance (e.g., straddling taller crops or lining up a manipulator with tree branches). As the wheels can be repositioned laterally, the change of running width along with different tires provides enhanced flexibility. Such flexibility is rare as most robots have a fixed width, or at best a manual adjustment. AgAR's ability to quickly reconfigure width means it can operate in different crop row layouts.

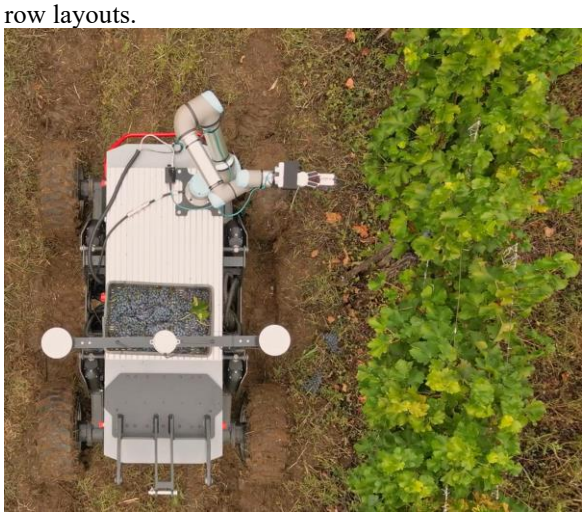

Fig.11. AgAR platform equipped with a robotic system for grape harvesting

High Torque Drivetrain in a Compact Package: With four 1.5 kW motors, AgAR's raw power (6 kW continuous) is lower than large diesel robots, but it is geared for torque. Each wheel drive uses a high transmission ration planetary reduction, providing high torque at the wheels for pulling heavy loads at low speed. The combination of high-torque drive and chassis leveling allows AgAR to pull implements or trailers on slopes that would stall or destabilize other electric robots of similar size. While its top speed is modest, this is sufficient for almost all agricultural operations. Many conventional tractors or UGVs would also operate around 5 - 8 km/h for such tasks, so AgAR's speed is on par. By concentrating on torque and traction, the design ensures it can utilize its multi-attachment capability effectively. AgAR's wheels are all driven and can skid-steer by counterrotating sides, giving it zero radius turning like a skid steer loader. This is advantageous in tight farm layouts. However, skid-steering imposes high loads on the soil as well as the chassis and motors due to friction.

Safety and Reliability Features: Modern UGVs must also integrate safety for working near humans and crops. AgAR includes multiple safety measures: emergency stop buttons at its corners and mechanical bumpers to stop the robot and absorb collisions. These bumpers and guards protect both the robot and bystanders, and the exterior panels cover all moving parts (wheels, actuators) to prevent entanglement. Many state-of-art robots similarly have LiDAR-based obstacle detection and emergency stop protocols; AgAR follows suit with a 360° sensor suite for obstacle avoidance based on fusion of data from stereo cameras and LiDAR. What is notable is that even with a highly articulated design all electromechanical components are sealed within either the movable leg frames or the main body. This protects sensitive parts from dust, moisture, and impact, as well as contributing to a sleek form Not all research robots achieve this level of robustness.

5. CONCLUSION

In this paper, the survey of the recent advancements in unmanned ground vehicle design for agriculture was performed and it was examined how the AgAR platform builds upon and surpasses the state of the art. Over the past decade, agricultural UGVs are evolving from task specific prototypes into robust, general purpose machines. Key technologies identified include modular chassis allowing multiple attachments, the shift to electric drivetrains for precision control and sustainability, and increasingly sophisticated suspension mechanisms to handle unstructured farm terrain. However, most designs until now faced trade-offs between versatility, terrain capability, and complexity.

AgAR represents a convergence of solutions to these challenges: it is a fully electric, universal farming robot that does not sacrifice stability on rough terrain. By integrating a four point hybrid leveling system, AgAR addresses the critical issue of stability that many UGVs struggle with. Its ability to maintain orientation on slopes up to 30° and adjust clearance on the fly is a clear advancement over typical rigid or passively-sprung platforms. The comparative analysis showed that AgAR uniquely offers a single platform to perform diverse tasks by utilizing standard tractor implements as well adaptable chassis to accommodate multiple robotic attachments. In mechanical terms, it achieves high strength and load capacity at a moderate weight through careful structural

design and topology optimization via digital twin-driven redesign without compromising durability. This approach of data informed iterative design is likely to become standard in agricultural robotics as it allows optimization for both performance and efficiency.

AgAR's development also highlights the importance of interdisciplinary design: the mechanical, electronic, and software systems were conceived together to meet the demands of autonomous field operation. For instance, the mechanical design anticipates sensor integration and includes fail safes like bumper systems and emergency stops required for safe autonomous work. The result is a platform that is not only capable in a technical sense but also practically deployable on farms – it is user-friendly, maintainable, and scalable.

Moving forward, the mechanical design strategies seen in AgAR and its peers suggest several trends. One can expect that future UGVs increasingly incorporate adaptive geometries for example like variable track width or active suspension as standard, especially for applications in heterogeneous terrains like orchards, vineyards, and hilly farmlands. The emphasis on lightweighting through advanced materials and optimization will continue, as robots must balance strength with the need to minimize soil compaction and maximize energy efficiency. AgAR's use of both aluminium alloys and high-strength steel, and the iterative removal of excess material, exemplifies how achieving the right weight balance is a new design focus beyond traditional tractor engineering.

ACKNOWLEDGMENT

The AGAR development was partially financed by the Innovation Fund in Serbia from the Pre-Accession Funds of the European Union and the budget of the Republic of Serbia from the Ministry of Science, Technological Development and Innovation of the Republic of Serbia and supported by the StarTech support program implemented by NALED and funded by Philip Morris International.

REFERENCES

[1] Banić, M., Simonović, M., Stojanović, L., Rangelov, D., Miltenović, A. and Perić, M., 2022. Digital twin based lightweighting of robot unmanned ground vehicles. Facta Universitatis, Series: Automatic Control and Robotics, 1(3), pp.187-199.

[2] Fernandes, H.R., Polania, E.C.M., Garcia, A.P., Mendonza, O.B. and Albiero, D., 2020. Agricultural unmanned ground vehicles: A review from the stability point of view. *Revista Ciência Agronômica*, *51*(spe), p.e20207761.

[3] https://www.naio-technologies.com, accessed on 24.05.2005

[4] Diago, M.P., Rovira-Mas, F., Blasco, J., Saiz-Rubio, V., Faenzi, E., Evain, S., Labails, S., Stoll, M., Scheidweiler, M., Millot, C. and Campos-Gómez, E., 2015. Vinerobot: On-the-go vineyard monitoring with non-invasive sensors. In *19th International Meeting of Viticulture GiESCO*. Editions GiESCO (Group of International Experts of vitivinicultural Systems for Co-Operation).

[5] https://www.agxeed.com/our-solutions/3a, accessed on 24.05.2025

[6] https://agrointelli.com/robotti, accessed on 24.05.2025

[7] Grift, T.E., 2007. Robotics in crop production. *Encyclopedia of Agricultural, Food and Biological Engineering*, pp.1-3.

[8] https://directdriller.com/xaver-robot-system-for-planting-and-accurate-documentation, accessed on 24.05.2025

[9] https://vitibot.fr, accessed on 24.05.2025

[10] Bakker, T., 2009. An Autonomous Robot for Weed Control–Design, Navigation and Control PhD Thesis. *Wageningen University. Department of Agricultural Engineering*.

[11] McGuire, M., Soman, C., Diers, B. and Chowdhary, G., 2021. High Throughput Soybean Pod-Counting with In-Field Robotic Data Collection and Machine-Vision Based Data Analysis. *arXiv preprint arXiv:2105.10568*.

[12] Quaglia, G., Visconte, C., Carbonari, L., Botta, A. and Cavallone, P., 2020. Agri.q: a sustainable rover for precision agriculture. In *Solar Energy Conversion in Communities: Proceedings of the Conference for Sustainable Energy (CSE) 2020* (pp. 81-91). Springer International Publishing.

[13] Biber, P., Weiss, U., Dorna, M. and Albert, A., 2012, October. Navigation system of the autonomous agricultural robot Bonirob. In *Workshop on Agricultural Robotics: Enabling Safe, Efficient, and Affordable Robots for Food Production (Collocated with IROS 2012), Vilamoura, Portugal*.

[14] https://www.monarchtractor.com/mk-v-electric-tractor, accessed on 27.05.2025

[15] https://slopehelper.com, accessed on 27.05.2025

[16] Banić, M., Simonović, M., Stojanović, L., Rangelov, D., Miltenović, A. and Perić, M., 2022. Digital twin based lightweighting of robot unmanned ground vehicles. *Facta Universitatis, Series: Automatic Control and Robotics*, *1*(3), pp.187-199.

[17] ISO 5673-2:2005, Agricultural tractors and machinery - Power take-off drive shafts and power-input connection, Part 2: Specification for use of PTO drive shafts, and position and clearance of PTO drive line and PIC for various attachments. ISO, 2005.

[18] ISO 11001:2016, Agricultural wheeled tractors - Three-point hitch couplers. ISO, 2016.

Plenary Lecture B

11th International Scientific Conference
IRMES 2025
Research and Development of
Mechanical Elements and Systems
June 19 – 21, 2025; Vrnjačka Banja, Serbia

Abstract only DOI: not assigned

EXPERIMENTAL AND NUMERICAL INVESTIGATION OF HSS WELDED JOINTS FRACTURE BEHAVIOR

Dražan KOZAK[1]
Damir TOMERLIN[2]
Nenad GUBELJAK[3]
Ivan SAMARDŽIĆ[4]
Pejo KONJATIĆ[5]

[1]University of Slavonski Brod, Mechanical Engineering Faculty in Slavonski Brod, Trg I. B. Mažuranić 2, Slavonski Brod, Croatia, 35000; dkozak@unisb.hr; ORCID iD: 0000-0001-6542-0688
[2]University of Slavonski Brod, Mechanical Engineering Faculty in Slavonski Brod, Trg I. B. Mažuranić 2, Slavonski Brod, 35000; dtomerlin@unisb.hr; ORCID iD: 0000-0002-3461-4954
[3]University of Maribor, Faculty of Mechanical Engineering, Smetanova 17, Maribor, Slovenia, 2000; nenad.gubeljak@um.si; ORCID iD: 0000-0002-3276-8431
[4]University of Slavonski Brod, Mechanical Engineering Faculty in Slavonski Brod, Trg I. B. Mažuranić 2, Slavonski Brod, Croatia, 35000; isamardzic@unisb.hr
[5]University of Slavonski Brod, Mechanical Engineering Faculty in Slavonski Brod, Trg I. B. Mažuranić 2, Slavonski Brod, Croatia, 35000; pkonjatic@unisb.hr; ORCID iD: 0000-0002-1516-3027

Abstract: *Fusion welded joints are significantly heterogeneous structures, which can principally be divided into the base material (BM), weld metal (WM) and heat affected zone (HAZ) regions. The microstructural heterogeneity of the welded joints material regions affects their mechanical properties, which can vary significantly throughout the individual weld zones. The fracture behavior of welded joints consequently depends on the mechanical properties of the material zone in which the crack is located. The paper investigates S690QL1 grade high strength steel (HSS), and welded joint manufactured with slightly overmatching filler metal. In order to gain deeper insights into welded joint fracture behavior, the investigation is oriented in two directions: experimental testing and numerical analysis. The experimental investigation determines the tensile stress-strain material properties of individual material regions. Fracture mechanical testing is done on single edge notch bend (SENB) specimens, with pre-initiated cracks in material regions of interest. The fracture toughness using the characteristic parameters is determined. The numerical investigation, on the other hand, relies on Ductile Damage material model, for prediction of the fracture behavior of metallic materials, through the initiation and evolution of damage. Such a model generally relies on curves obtained from tensile tests of individual material regions within the observed heterogeneous structure. In this paper, the methodology for modeling the material heterogeneity of welded joints in HSS is presented, while the fracture behavior of SENB specimens from HSS steel is simulated based on experimental inputs.*

Keywords: *welded joints; heterogeneity; fracture behavior; SENB; numerical analysis.*

11th International Scientific Conference
IRMES 2025
Research and Development of
Mechanical Elements and Systems
June19 – 21, 2025;Vrnjačka Banja, Serbia

Original scientific paper DOI: 10.46793/IRMES25.plB2K

ENHANCING THE MECHANICAL PROPERTIES OFDIRECTED ENERGY DEPOSITION ARC (DED-Arc) VIA PROCESSING INNOVATIONS

Damjan KLOBČAR[1]
Uroš TRDAN[1]
Mirza IMŠIROVIĆ[1]
Drago BRAČUN[1]
Mohammad REZA GHAVI[2]
Tomaž VUHERER[3]
Marek POLANSKI[4]
Aleksija ĐURIĆ[5]
Matija BUŠIĆ[6]
Miodrag MILČIĆ[7]

[1]Faculty of Mechanical Engineering, University of Ljubljana, Aškerčeva cesta 12, 1000, Ljubljana, Slovenija, damjan.klobcar@fs.uni-lj.si, ORCID: 0000-0002-6130-0328;
uros.trdan@fs.uni-lj.si, ORCID iD: 0000-0002-0688-2919;mirza.imsirovic@fs.uni-lj.si,ORCID: 0009-0004-3350-4536;
drago.bračun@fs.uni-lj.si, ORCID iD: 0000-0002-0107-9983;
[2]Rudolfovo – Science and Technology Centre Novo mesto, Slovenia, mohammad.reza.ghavi@rudolfovo.eu, ORCID iD: 0009-0007-0926-9806;
[3]Faculty of Mechanical Engineering, University of Maribor, Smetanova 17, 2000 Maribor, tomaz.vuherer@um.si, ORCID iD: 0000-0002-1866-8266;
[4]Faculty of Advanced Technologies and Chemistry, Military University of Technology, ul. gen. Sylwestra Kaliskiego 200-908 Warsaw, Poland, marek.polanski@wat.edu.pl, ORCID iD: 0000-0003-0163-514X;
[5]University of East Sarajevo, Faculty of Mechanical Engineering Vuka Karadžića 30, East Sarajevo, RS, Bosnia and Herzegovina, aleksija.djuric@ues.rs.ba, ORCID iD: 0000-0002-0251-6364;
[6]University Nord - University Center Varaždin, Department of Mechanical Engineering, J. Križanića 31b, 42000 Varaždin, Croatia, mbusic@unin.hr, ORCID iD: 0000-0003-4027-3479;
[7]Faculty of Mechanical Engineering, University of Niš, Aleksandra Medvedeva 14, 18000 Niš, Republic of Serbia, miodrag.milcic@masfak.ni.ac.rs, ORCID iD: 0000-0002-1089-8390;

Abstract: *Directed Energy Deposition (DED) processes offer the advantage of producing larger parts with higher deposition rates compared to Powder Bed Fusion (PBF) additive manufacturing (AM). However, DED typically results in simpler geometries and lower resolution. When using Wire and Arc-based DED, even larger components can be manufactured at an accelerated rate, but the higher heat input may lead to undesirable microstructures, adversely affecting mechanical properties.*
To ensure defect-free depositions, precise process control is essential, including optimizing deposition paths, regulating inter-layer temperature, and maintaining a consistent nozzle-to-layer distance. One effective approach to improving material integrity is the application of in-situ vibrations during deposition. This technique helps reduce porosity and grain size while also enhancing surface waviness and mitigating residual stress buildup. Further refinement of material properties can be achieved through appropriate thermo-mechanical processing, leading to mechanical characteristics comparable to conventionally produced steel. This paper explores the impact of in-situ vibrations and heat treatment through case studies, analysing their effects on surface waviness, residual stress distribution, porosity, microstructure, grain size, mechanical properties, and fracture toughness. The findings demonstrate the significant benefits of these process enhancements in improving the mechanical performance of DED-fabricated components.

Keywords: *Directed Energy Deposition (DED); Wire and Arc Additive Manufacturing (WAAM); in-situ vibrations; heat treatment; porosity reduction; residual stress; grain refinement; surface waviness; mechanical properties; fracture toughness; Computed Tomography (CT) Scan.*

1. INTRODUCTION

Additive Manufacturing (AM), often referred to as 3D printing, is a technology enabling the layer-by-layer construction of objects from digital designs [1]. Among the various AM processes, Direct Energy Deposition (DED) techniques are recognized for their efficiency, particularly in manufacturing large-scale components. Direct Energy Deposition-Arc (DED-Arc), also widely known as Wire Arc Additive Manufacturing (WAAM), represents a significant advancement in metal AM by leveraging mature welding technologies. This process utilizes an electric arc as the heat source to melt a metallic wire feedstock, which is then deposited layer upon layer using a computer numerical control (CNC) or robotic manipulator. Common arc-based welding processes like Gas Metal Arc Welding (GMAW), Gas Tungsten Arc Welding (GTAW), Plasma Arc Welding (PAW) or high deposition processes as Tandem GMAW form the basis of many DED-Arc systems [2].

Compared to powder-based AM processes such as Powder Bed Fusion (PBF) and powder-fed DED-Laser Beam (DED-LB), which are often limited by small build chamber sizes and thin layer thicknesses (typically 3–30 μm), DED-Arc offers substantial advantages in terms of build size and deposition rate. DED-Arc can deposit material with layer thicknesses closer to 3 mm, leading to significantly faster build times – up to 100 times faster deposition rates than PBF [3]. This capability makes WAAM highly suitable for manufacturing medium-to-large complex parts, reducing material wastage and lead time while enabling customized designs. Other benefits include lower capital costs compared to some other metal AM techniques, efficient material utilization (reducing waste), and potential environmental advantages. DED-Arc also facilitates the production of complex geometries and near net shape parts, potentially eliminating the need for extensive tooling and re-fixturing. Specialties of the WAAM process include in-situ alloying and the production of functionally graded materials (FGMs) [4], [5].

Despite these compelling advantages, the DED-Arc process presents inherent challenges largely stemming from the high energy input and complex thermal cycles involved in melting and depositing metal wire at high rates. The localized heat input and subsequent cooling affect the deposited material's microstructure and can introduce defects and residual stresses. This can result in significant variations in material properties and dimensional inaccuracies. Consequently, extensive post-processing is often required to achieve the desired metallurgical characteristics, mechanical properties, and dimensional tolerances. The development of standardized procedures for DED AM is still underway, highlighting the complexities in ensuring consistent quality and performance [6].

This review will delve into the critical challenges faced by DED-Arc technology and explore the state-of-the-art research and solutions being developed to overcome these limitations, with a focus on in-situ processing with thermal management, process control, process simulations, defect mitigation, path planning, and post-processing strategies.

2. CHALLENGES IN DIRECT ENERGY DEPOSITION-ARC

A primary challenge in DED-Arc originates from the high heat input associated with arc welding processes, material physical properties and the resulting complex thermal cycling during the layer-by-layer deposition process [7]. Each deposited layer is subjected to repeated heating and cooling from subsequent layers, leading to significant thermal gradients and distortions, which are related to physical and mechanical properties of material used [8]. This thermal environment has several detrimental consequences such as a) Residual Stresses and Distortion, b) Microstructural Non-homogeneity, c) Deposition defects, d) Surface Quality, d) Path Planning Limitations and e) Process Control.

The non-uniform heating and cooling inherent in DED-Arc generate significant residual stresses within the manufactured part. These stresses can lead to substantial distortion of the component, affecting dimensional accuracy and potentially requiring significant post-build straightening or stress relief treatments. Issues like the deformations and lifting of the base plate from the bench are observed in WAAM, which in extreme situations leads also to braking of the deposit from the base plate if later is firmly fixed. One solution for this is production of symmetrical parts with sequential deposition or simultaneous deposition [9].

The repeated thermal cycles and high cooling rates influence the solidification process and solid-state phase transformations [10]. This often results in a non-uniform microstructure throughout the deposited part, characterized by features like coarse columnar grains, and elongated grains especially in the as-deposited state. In addition, non-metallic inclusions, intermetallic phases and segregations occurs. Non-metallic inclusions and intermetallic phases often arise in AM primarily due to the distinct thermal cycles involving rapid heating and cooling rates. These conditions lead to non-equilibrium solidification and significant elemental segregation, where alloying elements concentrate in interdendritic areas. This localized chemical enrichment promotes the formation of secondary phases and intermetallic compounds, such as Laves phases in some nickel alloys or specific carbides and iron phases in steels depending on their composition [11]. The inherent chemical composition of the wire feedstock is also a determining factor in which phases are thermodynamically possible and likely to form under these conditions. The resulting as-built microstructure is typically inhomogeneous with these segregated regions and phases. Materials like maraging steel exhibit very long crystal grains and microsegregations oriented in the heat sink direction in the as-built state. This lack of microstructural homogeneity, including the presence of transitional layers or undesirable secondary phases, can compromise the mechanical properties and performance consistency of the material. Consequently, post-processing heat treatments are often applied to dissolve detrimental phases, homogenize the microstructure, and

promote desirable precipitate formation [10], [12]. If material microstructure cannot be repaired by a heat treatment a mechanical treatment such rolling, hammering or some sort of shot-peening is used to get more uniform microstructure.

The DED-Arc process is susceptible to various defects that can impair the integrity and performance of the manufactured part. Critical defects include porosity, lack of fusion, and cracking [13]. Porosity can result from issues like gas entrapment from shielding gas or moisture/hydrocarbon residue on the wire feedstock. A high purity material should be used together with careful storage and handling to avoid porosities. Lack of fusion can occur if insufficient heat input prevents proper melting between layers or tracks. Cracks, particularly solidification or liquation cracks, can form due to thermal stresses or unfavourable solidification microstructures and segregations [13]. Achieving high quality DED-Arc process parameters and control is essential to avoid these defects.

The nature of the arc welding process and the relatively large layer thickness in DED-Arc often lead to increased surface roughness and surface waviness compared to powder-based techniques. Temperature is a key factor in surface waviness, as excessive heat input, thermal gradients from rapid cooling, and interlayer temperature control influence molten metal spreading, solidification, and bead geometry, impacting waviness. Surface tension gradients, which drive Marangoni flow, can smooth the surface [14]. Material physical properties, including thermal expansion and surface energy characteristics influenced by composition and volatile elements, also affect wetting behaviour and shrinkage that contribute to the final surface profile. This typically necessitates extensive machining or other surface finishing operations as part of post-processing. Irregular grain geometry due to excessive heat input also contributes to the machining process and obtained surface roughness [15].

Traditional path planning methods for DED-Arc are often limited to 2.5 degrees of freedom (DOF), which can be inefficient and may require support structures for complex geometries. While 5-DOF path planning exists, its industrial implementation is still limited. The chosen deposition pattern can significantly impact mechanical effects, defect occurrence during the deposition, deposition shape and distortion due to of residual stresses [16].

Ensuring consistent and repeatable deposition quality, dimensional accuracy, and material properties requires precise control over numerous process parameters, including welding current, voltage, deposition speed, wire feed speed, shielding gas flow, and interpass temperature/time. Achieving robust and adaptive process control remains a challenge. FEM simulations can provide a valuable information for process control to meet the desired part shape, by optimizing deposition paths based on non-uniform temperature distribution of the layer. Simulations can additionally predict time of pauses between the depositions and manufacturing time, residual stresses and distortion [17].

These challenges collectively pose key knowledge gaps to the widespread adoption of DED-Arc, particularly for high-performance applications where material integrity and dimensional accuracy are paramount.

3. STATE-OF-THE-ART RESEARCH AND SOLUTIONS

Significant research efforts are underway to address the challenges inherent in DED-Arc, focusing on improving in-situ: thermal management, enhancing process control, vibration assisted deposition to improve microstructure, mitigating defects, optimizing deposition strategies, and refining post-processing techniques.

3.1. Thermal management

Strategies to better manage the thermal environment are crucial for controlling microstructure and minimizing residual stress and distortion. Approaches include a) deposition with lower heat input, b) preheating, interlayer cooling and active cooling, and c) Advanced Simulation and Modelling (Figure 1) [18].

The Cold Metal Transfer (CMT) process, a modified version of GMAW-based WAAM, allows for lower heat input, which can reduce distortion, minimize the heat-affected zone (HAZ), and potentially decrease porosity. Heat input can also be minimized by using GTAW or PTA deposition, but deposition rate usually decreases and new challenges regarding off-centre wire deposition arise [19].

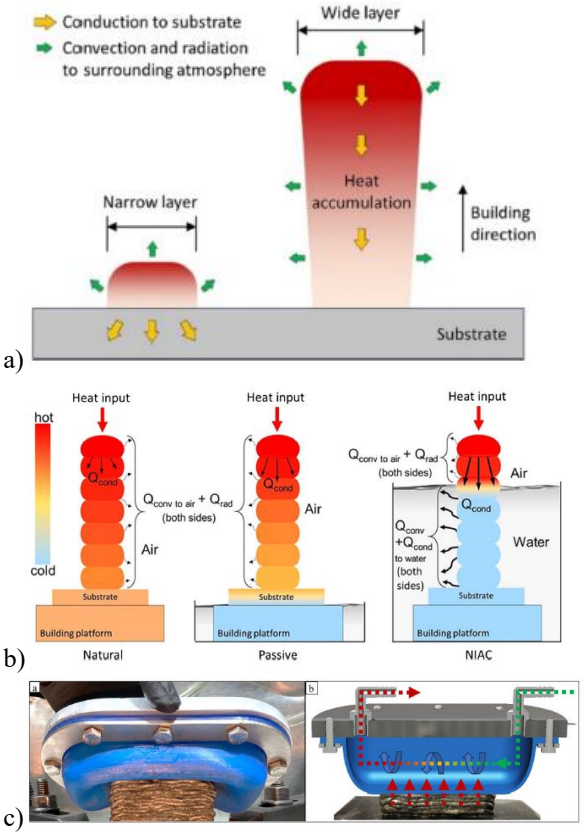

Figure 1: Schematic illustration a) of width variation along the hight of a wall in DED-Arc without proper thermal management, and b) and c) different thermal management approaches [18].

Advanced thermal management techniques are crucial for controlling the heat flow during the build process and ensuring part quality and integrity [18]. Preheating the substrate helps to reduce thermal gradients between the base material and deposited layers, thereby minimizing residual stresses and the risk of cracking, particularly in high-strength alloys; this is typically achieved using electrical resistance heaters, induction heaters, or gas torches. Equally important is the control of interpass temperature, which involves pausing between layers, utilizing active cooling systems like fans or air jets, and monitoring temperatures through thermocouples or infrared sensors to prevent microstructural degradation. Active cooling systems, such as air or water-based cooling, and even cryogenic cooling with liquid nitrogen, are employed to dissipate heat rapidly and manage thermal gradients, especially in builds involving thermally conductive materials. Additionally, heat sink integration, either through high-conductivity inserts or by leveraging the build plate, assists in drawing heat away from critical regions [6]. Maintaining interpass temperatures above transformation thresholds—such as above the martensite start temperature or at levels like 250 °C depending on the welding parameters—is essential for achieving strong metallurgical bonding. Innovative in-situ cooling methods, like conformal conductive upper cooling, are under exploration to provide precise thermal regulation, potentially enabling as-deposited parts to achieve properties comparable to post-processed materials. While other approaches such as thermoelectric heat sinks and bypass arcs offer additional heat extraction mechanisms, they may introduce drawbacks like porosity or reduced upper-layer efficiency. Techniques like air jet impingement further exemplify the expanding toolkit for effective thermal management in DED-Arc AM, underscoring the potential for achieving high-performance, near-net-shape metal parts directly from the build process [6].

3.2. Vibration assisted deposition

In situ vibration techniques, including base plate vibration (Figure 2), wire vibration, and arc pulsing, have demonstrated significant potential in refining microstructures, reducing porosity, and enhancing mechanical properties of fabricated components [20]. Base plate vibration introduces mechanical energy that disrupts dendritic growth during solidification, leading to grain refinement and improved mechanical strength. For instance, applying in situ vibration during the deposition of low-carbon steel reduced the average grain size from 9.8 µm to 7.1 µm in fine-grain zones and from 10.6 µm to 7.4 µm in coarse-grain zones, resulting in a 10% increase in ultimate tensile strength and a 13.8% increase in yield strength [20]. Applying vibrations during DED-Arc deposition of AlMg5 leaded to a notable 25% reduction in grain size and reduced microstructural anisotropy. Vibrations also contribute to material homogenization, decreasing segregation and refining precipitate dispersion. Furthermore, gas porosity is substantially reduced, decreasing from 1.5 ± 0.04% in as-built parts to 0.34 ± 0.07% in vibration-assisted deposition. Base plate vibrations also improved the deposition shape and surface quality improve by reducing surface waviness, while residual stress anisotropy decreased by 60% and tensile strength anisotropy is effectively eliminated. A slight increase in average hardness was also observed, due to grain refinement and solid solution strengthening [21]. Wire vibration, particularly through ultrasonic assistance, has been effective in disrupting columnar grain structures and promoting equiaxed grain formation. This technique enhances melt pool dynamics, leading to a more uniform microstructure and improved mechanical properties. In the fabrication of 2319 Al-Cu alloy, the integration of ultrasonic vibration with ZrO_2 particle addition resulted in a 13.8% increase in tensile strength and a 92.4% improvement in elongation, attributed to the uniform distribution of fine grains and precipitates [22]. Arc pulsing, involving the modulation of current and voltage during deposition, influences the thermal profile and solidification behavior of the molten pool. Adjusting pulse frequency and current has been shown to reduce porosity and refine grains in aluminum alloys. For example, in the deposition of AlSi5 alloy, increasing the pulse frequency to 50 Hz improved density and refined grains, leading to enhanced tensile strength [23]. Moreover, in the wire-arc DED of 7075 aluminum alloy, optimizing wire feeding rates and employing pulsed arc modes significantly reduced porosity by up to 95.8% and improved mechanical properties, achieving an ultimate tensile strength of 527.80 MPa and elongation of 7.57% after heat treatment [24]. These findings underscore the efficacy of in situ vibration techniques in DED-Arc processes. By tailoring vibration methods, whether through base plate oscillation, ultrasonic wire agitation, or arc pulsing, manufacturers can achieve refined microstructures, reduced porosity, and enhanced mechanical performance in additively manufactured metal components.

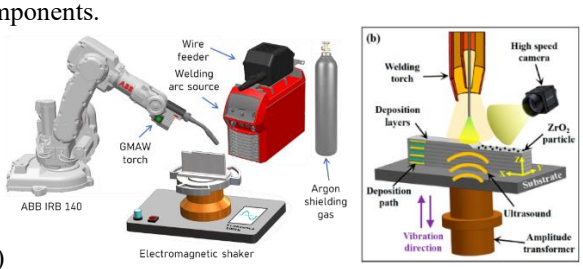

a)

Figure 2: Schematic illustration vibrations-assisted DED-Arc process a) lower [21] *and b) ultrasonic frequency* [22].

3.3. Advanced process control

Process control is a critical aspect of DED-Arc essential for mitigating challenges such as high heat input and heat accumulation, which lead to issues like geometric inaccuracies, distortion, residual stress, and non-uniform microstructure and mechanical properties [25]. Effective process control aims to achieve precise, efficient weld quality, reduce human errors, and execute complex tasks with high accuracy and repeatability. Research focuses on various strategies to enhance part quality, geometric accuracy, and mechanical properties by managing these thermal effects. These strategies often involve the

development of both feedforward methods, which use process planning techniques to compensate for accumulated errors, and feedback methods, which utilize closed-loop control to improve building accuracy (Figure 3). Feedback control systems are commonly used to dynamically adjust welding parameters based on real-time sensor feedback signals. Control approaches range from maintaining constant parameters and optimizing travel speed or other parameters to implementing feedback loops for layer height or geometry control, adaptive process control, and dynamic in-process path replanning based on detected deviations [26]. Process control actions can be classified into various levels based on complexity and hierarchy, involving stages like sensor input, workpiece detection, path planning, trajectory generation, motion control, welding process control, feedback control, and error handling. The system can adapt parameters and make real-time adjustments to achieve the desired weld quality while effectively managing errors and faults by executing these steps [27], [28].

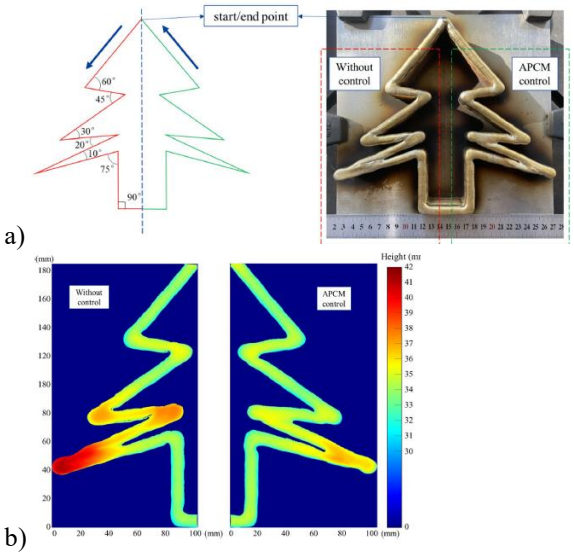

Figure 3: a) The component after depositing 15 layers and b) surface contour height without and with process control.

Sensor technologies play a crucial role in DED-Arc control systems, enabling real-time monitoring of welding parameters and ensuring optimal process control [27]. Sensors help improve weld accuracy and quality and ensure they meet desired specifications. Various types of sensors are utilized in welding robots, emphasizing their contribution to enhancing weld quality and overall system performance. Common monitoring techniques include the analysis of arc current, vision systems for tracking bead and melt pool geometry or layer height, temperature measurement using sensors like pyrometers or IR cameras, force sensors, arc sensors for process stability monitoring, current sensors for monitoring welding current, and distance or position sensors for CTWD or layer height measurement [29]. These sensors provide feedback data, such as joint positions, weld quality, and temperature, which are compared with desired values to generate error signals used by control algorithms. The controller then generates signals to actuators to adjust welding parameters like torch position and wire feed rate. Sensors are critical in DED-Arc and multi-pass welding processes by providing real-time feedback, enabling the robot to adjust its movements, welding parameters, and heat input. Seam tracking in robotic welding, weld cladding and DED-Arcmainly relies on sensors to monitor and adjust the position of the welding torch precisely. Recent advancements include the use of novel sensors like the coherent range-resolved interferometry (RRI) sensor for capturing layer and wall shape information, which has been used in closed-loop layer-by-layer processes for wall height compensation [30]. Despite their importance, challenges such as sensor calibration, signal noise, and environmental interference have been identified, indicating the need for further research. Integrating various control components, including sensors, actuators, and control algorithms, into a coherent system remains a primary challenge. Effective control methods, often combining different approaches, are required to balance competing quality factors and achieve robust and precise DED-Arc manufacturing [26].

3.4. Process simulation

Process simulation is a vital tool in DED-Arc primarily utilizing Finite Element Modeling (FEM). It is essential for understanding and predicting the complex thermal and mechanical behaviour inherent to the process (Figure 4) [17]. These simulations are employed to predict crucial outcomes like thermal cycles, distortion, residual stress distribution, and microstructure evolution. Simulation can also aid in predicting defects such as porosity. Studies highlight that accurate prediction, particularly of distortion and residual stress, is significantly improved when using physically derived instantaneous arc power and heat source parameters, with validation often involving comparing simulated thermal cycles to experimental measurements. Simulation results are instrumental in developing effective process control strategies, optimizing parameters, pause times and path planning, and predicting part quality and manufacturing time. Furthermore, process simulation efficiently reduces the need for extensive experimental pre-processing tests for optimization, contributing to more sustainable manufacturing and supporting the realization of smart manufacturing frameworks in DED-Arc [31]. The virtualization of DED-Arc is recognized as a future research challenge. It enables process validation that is more sustainable as it avoids material waste and significant energy consumption compared to physical testing. Simulation can also help visualize complex results, aiding user understanding of effects like distortions and informing decisions on aspects such as fixture placement. Specific applications include simulating thermal behaviour for path planning considerations and FEM analysis of residual stress in components like repair welds or thin-wall structures. Methods have been developed within FEM to mitigate thermal gradients and accurately prescribe heat transfer boundary conditions [17].

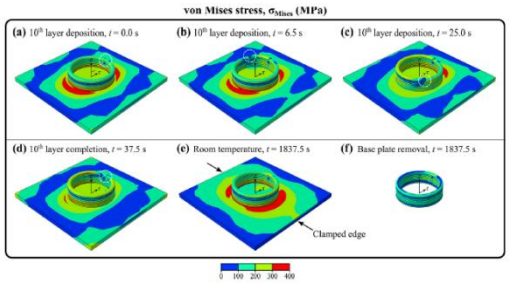

Figure 4: Computed von Mises stress field history [17].

3.5. Path planning

Path planning is an important data pre-processing step in DED-Arc, transforming a CAD model into the deposition trajectory used by the printer head or heating source. It is a key step in production planning and is essential for controlling material deposition and heat distribution. Path planning directly influences part quality, impacting geometric accuracy, distortion, residual stresses, and the occurrence of defects like voids or insufficient material filling [25]. A core challenge lies in dealing with intricate geometries such as thin walls, internal bottlenecks, wide internal areas, and overhangs, as the specificities of arc deposition can render traditional static path strategies unreliable across various topologies [14]. Furthermore, arc starts and stops within a path can induce transient phenomena that affect deposition accuracy.

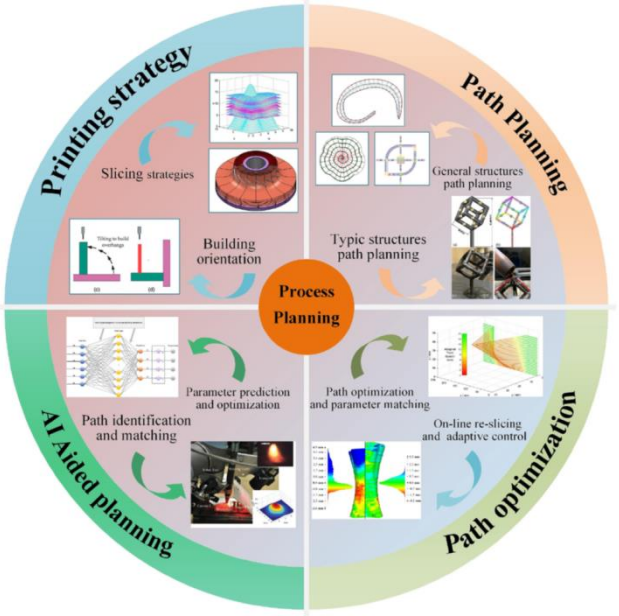

Figure 5: Schematic illustration of process planning [32].

To address these challenges, a variety of path planning strategies have been developed, including basic raster, zigzag, contour, spiral, continuous, and hybrid paths. Geometric-oriented strategies focus on the features of the part; for example, the Medial Axis Transformation (MAT) algorithm has been proposed to solve filling gap issues in contour-based planning and is particularly applied to thin-walled structures, sometimes allowing for continuous alteration of deposition width [34]. Modular or feature-based approaches segment 3D models or layers into distinct regions like thin walls, contours, bottlenecks, or large internal areas, enabling the application of tailored deposition strategies such as offset contours, zigzag patterns, or oscillatory paths [35]. These methods leverage techniques like image-based processing of binary images to map regions and generate paths (Figure 5). Adaptive slicing and multi-directional deposition are employed to manage complex geometries and overhangs by dynamically adjusting layer heights or building directions, often after decomposing complex parts into simpler geometries [36]. Continuous path strategies, such as helical-based methods, are used to minimize disruptive arc stops, potentially leading to more uniform layers. Path planning is also explored for specific features like strut structures, sharp corners, or deposition on non-planar surfaces, with weaving trajectories sometimes employed, including adapting weaving amplitude for varying thickness (Figure 6). The introduction of new paths, such as the 3D weaving path, is being investigated to improve wetting behaviour and reduce surface micro-waviness. This path promotes metal spreading and reduces the contact angle, leading to improved surface smoothness. Experimental results suggest that the 3D weavingpath can significantly reduce surface waviness compared to conventional paths [14]. Combining different deposition strategies, such as depositing an initial outline before filling the interior, has shown potential for better surface finishes. Studies are also analysing how parameters like the overlap angle between passes influence the texture of the deposited part [37].

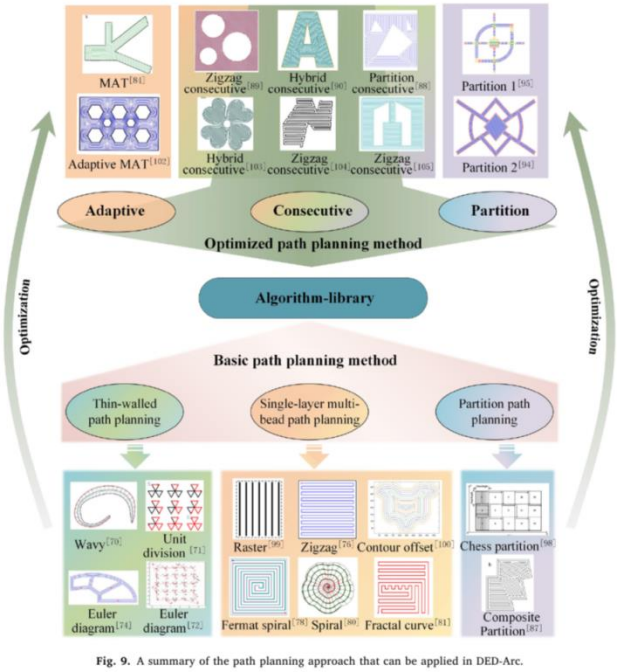

Figure 6: A summary of path planning approaches that can be used in DED-Arc [32].

Path planning is linked with process parameters such as travel speed and heat input, which are matched to the generated paths. It is considered a form of intrinsic thermal management because the chosen deposition strategy directly influences the temperature evolution and cooling rates of the layers by defining the heat input distribution. Advanced approaches integrate process

parameter planning directly into the path strategy based on prior knowledge. Dynamic path planning further combines path planning with process control by using online monitoring (e.g., of layer height variation) to trigger in-process adjustments like re-slicing if necessary [25]. Tools like process simulation are instrumental in validating path plans by predicting thermal behaviour and distortion. Extended Reality (XR) can potentially aid in visualizing complex path plans, assisting in collision avoidance and testing robot trajectories before physical deposition. Furthermore, identifying manufacturing restraints, such as minimum wall thickness or overhang limitations, through experimental case studies using specific path plans can inform subsequent design and path planning decisions [38]. Despite significant research, accurately mapping complex regions and generating truly optimal paths remains a challenge, and current methods are often limited in their degrees of freedom, highlighting the need for continued work, particularly on non-planar path planning.

3.6. Post processing

While research aims to minimize the need for post-processing, it remains a vital step for achieving the required material properties and mitigating defects [2], [7].

Post-deposition heat treatments, such as solution annealing and aging, are essential for many alloys, including maraging steel and Inconel 625, to obtain uniform, fine-grained microstructures and achieve mechanical properties comparable to conventionally manufactured materials. Specific heat treatment protocols have been developed for maraging steel deposited by DED-Arc to achieve tensile strength and hardness comparable to forged material. For Inconel 625 fabricated by WAAM-CMT, heat treatment at specific temperatures (e.g., 1100 °C) followed by water quenching has shown the best overall performance [9]. Heat treatment can also improve corrosion resistance.

Applying mechanical deformation, such as rolling, hammering or shot-peening, between deposited layers (Figure 7) is an effective technique to refine the coarse columnar grains characteristic of the as-deposited state and significantly reduce residual tensile stresses. This can lead to improved mechanical properties [19].

Other techniques like Hot Isostatic Pressing (HIPing) and hot rolling are also employed to reduce porosity, mitigate defects, and improve mechanical properties. HIPing is mentioned in the context of Inconel 718 to reduce surface-connected defects [1].

Research continues to expand the range of materials processable by DED-Arc and explore novel structures. A wide variety of materials are being investigated, including various steels (stainless, maraging, mild), titanium alloys (Ti-6Al-4V), aluminum alloys, nickel alloys (Inconel 718, Inconel 625), Co-Cr, and tungsten [19]. The potential for manufacturing radial bimetallic structures with enhanced properties through in-situ mechanical interweaving has been demonstrated, showing improved compressive strength.

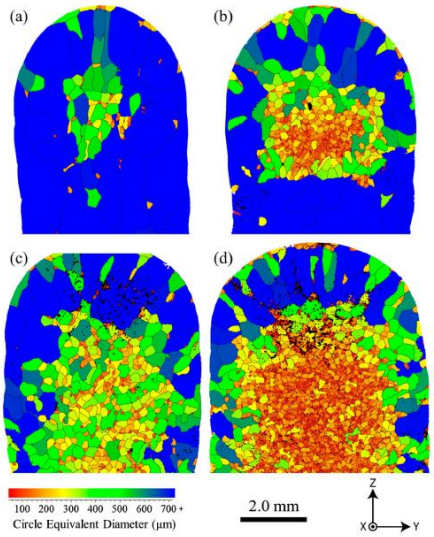

Figure 7: EBSD map of the effect of rolling on beta grain size: a) and b) to second last layer only and c) and d) to each layer (50 and 75 kN) [8].

4. CASE STUDIES

The following chapter shows a three case studies dealing with a) in-process height control for improving geometry precision,b) in-situ vibration assisted DED-Arc deposition and c) post-processing heat treatment to improve microstructure and mechanical properties.

4.1. In-process height control for improving geometry precision

The inherent variability in layer height can lead to geometric inaccuracies, affecting the quality of the final product. To mitigate this, the research integrated combined in-process path replanning with real-time layer height control. By adjusting deposition parameters based on continuous feedback, the method aims to maintain consistent layer heights, thereby enhancing the precision and reliability of WAAM processes.

The developed system integrates toolpath planning, real-time monitoring, and adaptive control to ensure consistent layer height. Initially, the user sets process parameters (layer height, travel speed, wire feed rate, and interpass temperature) via a GUI. A slicer algorithm generates toolpaths layer-by-layer. During deposition, arc current is monitored continuously. Since arc current is influenced by electrical resistance, which depends on the wire stickout (distance between contact tip and workpiece), variations in layer height are detected through changes in current (Figure 8). After each layer, the arc stops and cooling is monitored using an IR sensor until the surface reaches the defined interpass temperature. The substrate is then lowered, and the next layer begins. For the first three layers, height increments remain fixed to stabilize current data. From the fourth layer onward, arc current serves as feedback for adaptive height control. If the actual part deviates from the CAD model beyond a threshold, the system re-slices and replans toolpaths accordingly.

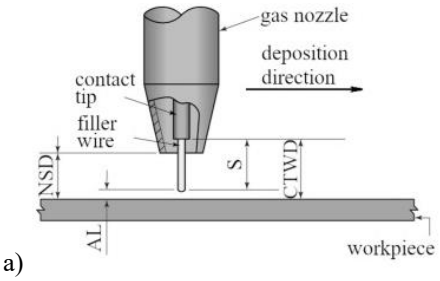

Figure 8: Working principle for determining height distance from gas nozzle to contact surface.

To ensure consistent layer height in DED-Arc, a layer height control algorithm was developed and tested based on working principle of filler wire distance as shown in Figure 9a. Figure 9b shows a torch Z position when building walls with constant Z_{incr} and with layer height controller based on exponential moving average (EMA) of arc current.Due to the changes of wall thickness, which is caused byheat dissipation to the substrate or to the air, the average layer heightis changing. At the bottom of the part the average layer high was constant, but at higher levels the average height became lower. This was the reason for lower height of the sample test piece shown on the figure 10b.

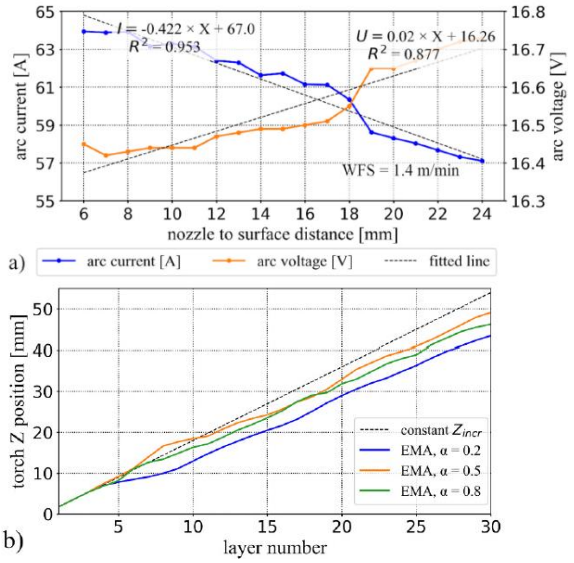

Figure 9: a) An average arc current and voltage as a function of CTWD with the WFS of 1.4 m/min. b) Torch Z position when building walls with constant Z_{incr} and with layer height controller based on exponential moving average (EMA) of arc current.

The re-slicecontroller was addedto the EMA controller.After deposition with the same process parameters, the finished parts have variation in the final height Figs 10 and 11.It ranged from 148.33 mm for the part built using EMA layer height controller to 159.86 mm for part built using EMA controller combined with the re-slice controller, while the CAD model was 160 mm tall (Figure 10.).

Figure 10: As deposited shell parts: a) constant height increment Zincr, b) EMA layer height controller and c) EMA layer height controller combined with the re-slice controller.

Figure 11 illustrates that the combined control strategy results in fewer zones with material excess or deficiency. However, some localized deviations still occur, particularly in the form of small blobs in the middle and upper regions of the build. These are attributed to irregularities during arc ignition and termination, which cause transient instability in material deposition. Despite these minor imperfections, the overall part geometry is much closer to the CAD model, confirming the effectiveness of the re-slice control in enhancing dimensional fidelity during DED-Arcfabrication.

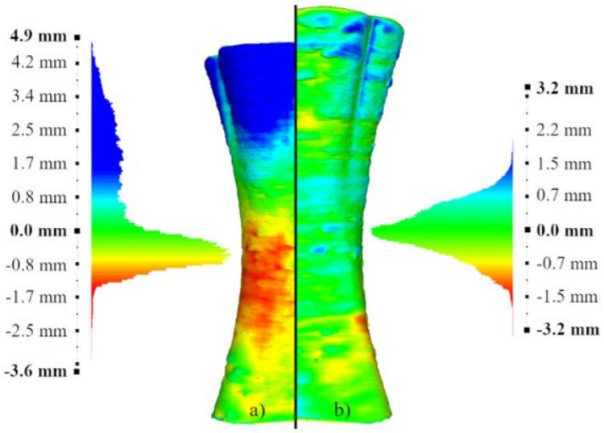

Figure 11: Laser scanning for determining geometry of case study sample: a) As built sample, b) with added height control and reslicing algorithm.

4.2. In-situ vibration assisted DED-Arc

In recent years, innovative mid-processing techniques like interlayer rolling and ultrasonic vibrations have emerged as transformative solutions to improve material properties and manufacturing efficiency. Among this, vibration assisted deposition emerged as promising solution to address challenges such as residual stresses, gas porosity, and surface quality. The figure 2a illustrates the scheme of vibration-assisted DED-Arc, highlighting its potential to enhance microstructural homogeneity and energy-efficient fabrication processes.

The system consists of traditional DED-Arc equipment, the 6-axis robot with mounted GMAW torch. The robot projects the desired trajectory of the desired 3D shape. In our case, ER5356 was used as filler material, hence the argon shielding gas was used. The electromagnetic shaker

was used to induce vibrations onto the substrate and consequently onto the molten pool via deposition.

4.2.1. Geometry improvement

In Figure 12.a, the deposited layer of as-build (AB) sample shows significant waviness, as indicated by the red dashed lines. This waviness suggests inconsistent melt pool dynamics, resulting in uneven layer deposition.
Figure 12.b illustrates the effect of vibration assistance (VA). The melt pool exhibits a partial collapse, shown by the orange arrows, indicating more dynamic melt pool behavior. The vibrations help break up the surface tension of the melt pool, leading to better flow and redistribution of material. This agitation flattens the deposited layer, reducing surface waviness compared to the AB sample, resulting in a smoother, more consistent deposition.
Table 1contains the waviness measurements and building efficiency factors for the AB and VA samples in the DED-Arc process. The AB sample exhibits higher maximum waviness (+420 µm and +370 µm) compared to the VA sample (+160 µm), indicating more distinct transitions between deposited layers due to inadequate melt pool stabilization. The reduced waviness in the VA sample, with a minimum of -90 µm, reflects smoother layer transitions attributed to vibration-assisted melt pool agitation, which enhances material flow.

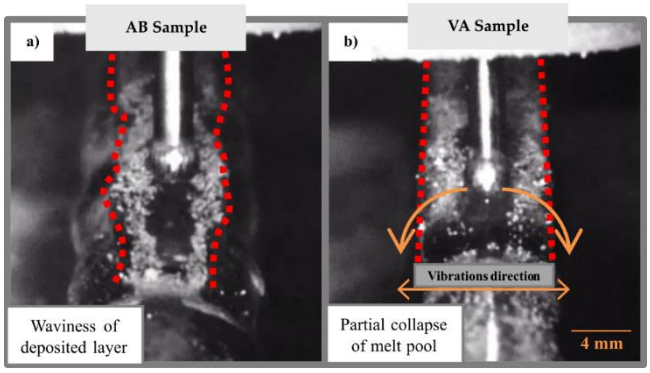

Figure 12: Meltpoolgeometry: a) AB and, b) VA sample.

Table 1: Waviness measurements and building efficiency results.

Sample	Profile	Max Waviness (µm)	Min Waviness (µm)	RMS Waviness (µm)	Building efficiency (%)
AB Sample	W_1	+420	-430	420	78.5
AB Sample	W_2	+370	-430	370	
VA Sample	W_1	+160	-90	160	92.25
VA Sample	W_2	+150	-120	150	

Consequently, the building efficiency improves significantly from 78.5% for the AB sample to 92.25% for the VA sample, demonstrating the effectiveness of vibrations in promoting superior surface quality and operational efficiency in additive manufacturing processes.

4.2.2. Gas porosity reduction

In the AB sample porosity decreases as the interpass temperature increases from the bottom to the top of manufactured product. At the bottom significant porosity and larger merged pores are visible, indicating poor degassing at low temperatures, due to high cooling rate. As the interpass temperature increases toward the middle and top, the porosity reduces slightly, but remains substantial, with large pores still present due to insufficient melt pool agitation and gas entrapment during deposition (Figure 13).
In contrast, the VA sample shows a significant reduction in porosity at all cross-sectional levels. Vibration-assisted deposition promotes better melt pool agitation, enhancing degassing and preventing pore formation. The combination of vibrations and increased temperature promotes more efficient gas escapefrom the meltpool, leading to a more homogenous and less porous structure throughout the part.The comparison clearly highlights the benefits of vibration assistance, where the continuous agitation of the melt pool, combined with rising interpass temperatures, effectively enhances degassing, reduces porosity, and leads to improved material quality.

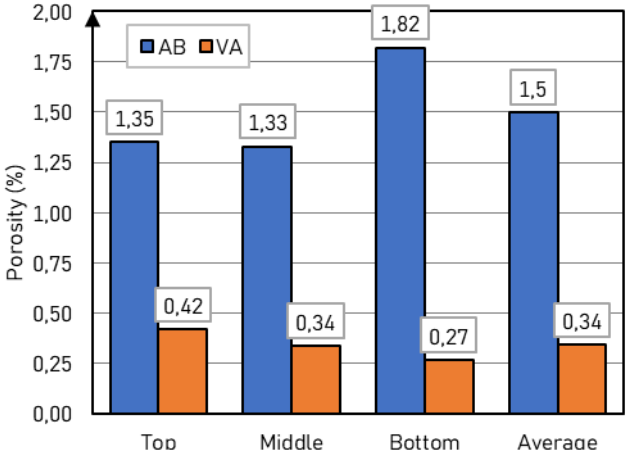

Figure 13: Gas porosity in different area of manufactured samples.

Table 2 shows detailed geometry properties of gas porosity particles.

Table 2: Detailed geometry of gas porosity particles.

Sample Type	Location	Temperature (°C)	Porosity (%)	Average Pore Area (µm²)
AB Sample	Bottom	45	1.82	2771.8 ± 4410.2
	Middle	135	1.33	1937.0 ± 2820.0
	Top	185	1.35	1931.7 ± 2560.7
VA Sample	Bottom	50	0.42	1292.7 ± 2554.3
	Middle	130	0.34	833.66 ± 1359.8
	Top	170	0.27	856.9 ± 1082.0

4.2.3. Tensile testing results

Figure 14a presents the stress-strain curves for AB and VA specimens, measured along the x and z directions. The black and yellow curves represent AB samples, while the green and blue curves show VA samples. A notable improvement in tensile strength is observed for VA samples in the z-direction, with a 12.1% increase compared to the AB sample (268 MPa vs. 239 MPa). This indicates that the VA samples exhibit a more isotropic mechanical state, with only a 0.4% difference between the x and z directions, whereas the AB samples show a larger 7.9% difference in UTS between these directions.

Figure 14b summarizes the average ultimate tensile strength (UTS) and elongation at break for both AB and VA samples. The VA samples show higher UTS at 267 ± 1 MPa, compared to 248.5 ± 9.5 MPa for AB samples. Additionally, the VA samples exhibit greater ductility, with an elongation at break of 32.5 ± 1.5%, versus 28 ± 6% for AB samples. The improved mechanical properties in VA samples are attributed to a 25% reduction in grain size, decreased gas porosity, and a significant relaxation of residual stress in the z-direction due to in-situ vibrations, which contributes to their more uniform and isotropic behavior.

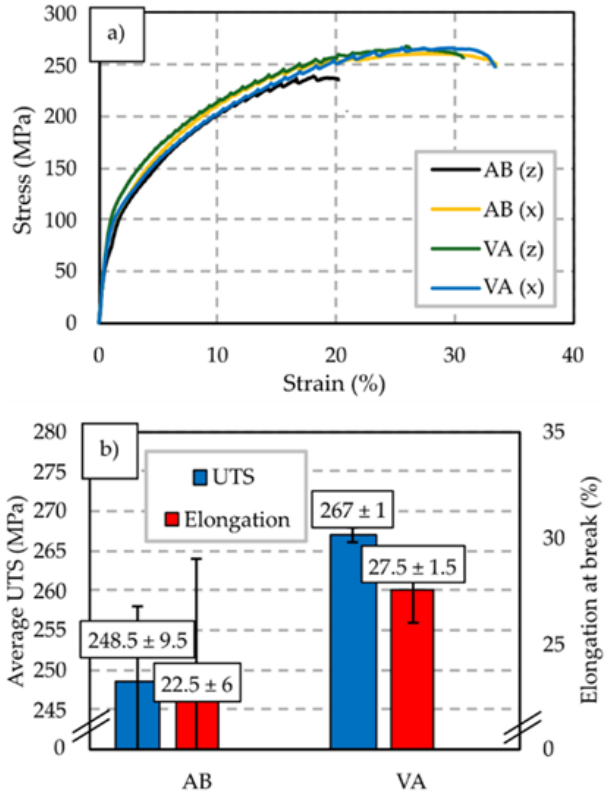

Figure 14: a) Stress - strain curves for AB and VA samples in different directions, b) average values for UTS and elongation.

4.3. Post-processing heat treatment for improving mechanical properties of 15-5 PH stainless steel

15-5 PH stainless steel is a precipitation-hardened martensitic alloy known for its high strength and corrosion resistance, making it suitable for aerospace and structural applications. DED-Arc offers a cost-effective method for producing complex geometries of this alloy. However, the as-deposited material often exhibits suboptimal mechanical properties due to rapid cooling rates and thermal gradients inherent. Tailoring post-deposition heat treatments is essential to enhance its performance. The study showsthe effects of solution annealing followed by aging on the microstructure and mechanical properties of DED-Arc 15-5 PH stainless steel. Solution annealing at 1050 °C for 1 hour ensures the dissolution of solute elements into the matrix, while subsequent aging at various temperatures promotes the formation of fine precipitates, primarily copper-rich phases, which are responsible for the alloy's strengthening. This two-step heat treatment process is crucial for optimizing the material's hardness and tensile strength.

4.3.1. Heat treatment

Precipitation hardening involved three key steps: solution annealing, quenching, and aging. Typically, solution annealing for this type of steel is performed at 1038 °C for 1 hour. However, due to the unique microstructure resulting from DED-Arc, tailored heat treatment parameters are necessary. To determine the optimal conditions for DED-Arc-produced samples, solution annealing was conducted at three temperatures1040 °C, 1105 °C, and 1170 °C and three durations 0.5 hours, 1.5 hours, and 2.5 hours. After each heat treatment, samples were rapidly quenched in water to 20 °C. The ideal solution annealing parameters were identified through optical microscopy (OM), scanning electron microscopy (SEM), and hardness testing, with an emphasis on achieving microstructural homogenization in the shortest time and lowest temperature possible. Following this, aging was doneon samples treated with the optimal solution annealing settings. Aging was done at three temperatures 400 °C, 500 °C, and 600 °C for 1 hour, 2.5 hours, and 6 hours respectively, with samples cooled in air down to 20 °C afterwards.

4.3.2. Microstructure

Figure 15presents micrographs of DED-Arc-produced 15-5 PH stainless steel showing a defect-free macrostructure with large columnar grains angled at 45° to the build direction, a result of directional heat flow during solidification. The as-deposited microstructure mainly consists of lath martensite alongside a secondary lathy delta ferrite phase, enriched in chromium and silicon but depleted in nickel. This delta ferrite phase negatively impacts impact toughness and anisotropy, making its reduction through solution annealing essential. Optimal homogenization was achieved at 1105 °C for 1.5 hours, producing an equiaxed grain structure while avoiding undesirable grain growth seen at higher temperatures.

SEM analysis revealed two microstructural inclusions: spherical Fe-Mn-Cr-Si metal oxide particles originating from oxidation during DED-Arc, which have limited detrimental effects due to their small size and shape, and fine niobium carbonitride (NbC) precipitates that inhibit austenite grain growth, broadening the heat treatment window for achieving an optimal microstructure.

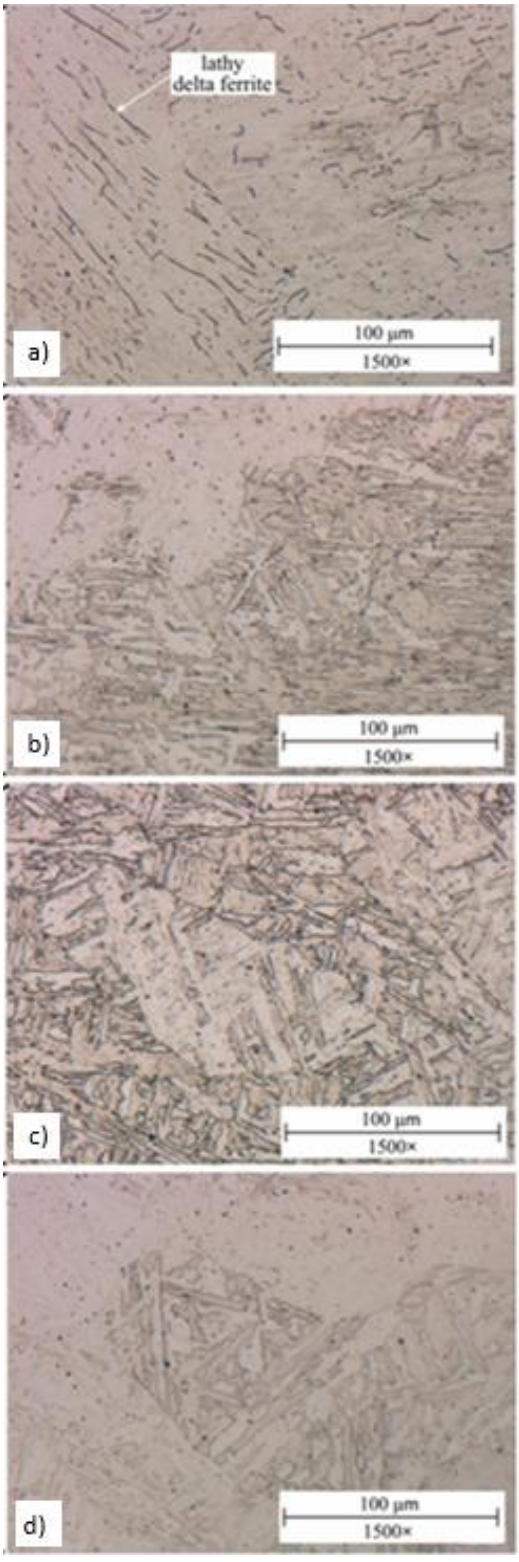

Figure 15: a) AD condition, b) S1 0.5 h 1040 °C, c) S5, 1.5 h 1105 °C, d) S9 2.5 h 1170 °C

4.3.3. Hardness

Vickers hardness (HV10) was measured in the Z–Y plane for as-deposited (AD), solution annealed (S), and solution annealed plus aged (S+A) samples. The AD condition exhibited an average hardness of 352 HV10 (±9). After solution annealing, hardness decreased even at the lowest temperature/time (0.5h; 1040 °C) due to the dissolution of secondary phases formed during the DED-Arcprocess. Increasing the temperature or time of solution annealing did not significantly affect hardness, indicating that microstructure and hardness must both guide heat treatment optimization.

Table 3: Hardness measurements with HV10.

#	S1	S2	S3	S4	S5	S6	S7	S8	S9
Temp.	1040 °C			1105 °C			1170 °C		
Time [h]	0.5	1.5	2.5	0.5	1.5	2.5	0.5	1.5	2.5
HV	326	325	316	326	326	319	337	332	339
±	8	8	11	7	9	10	9	9	9

Aging significantly increased hardness, with peak hardness (450 HV10) achieved after 1 hour at 500 °C, comparable to conventionally produced 15-5 PH steel (~455 HV). Aging at 400 °C for 6 hours showed an increase but did not reach peak hardness. Prolonged aging beyond peak conditions led to reduced hardness due to precipitate coarsening (over-aging). Despite similar hardness values at some points, microstructural differences impact tensile and toughness properties.

4.3.4. Tensile strength

Figure 16 presents stress–strain curves for as-deposited (AD), under-aged (S+A1), peak-aged (S+A4), and over-aged (S+A9) conditions of 15-5 PH steel. The AD sample has an ultimate tensile strength (R_m) of 1085 MPa, yield strength ($R_{p0.2}$) of 585 MPa, elongation of 19.6%, and reduction in area of 59%. Under-aging (S+A1) increases yield strength significantly to 885 MPa, with a slight R_m increase to 1105 MPa, and improves ductility (elongation 23.1%). Peak-aging (S+A4, 500 °C, 1h) achieves the highest strengths ($R_{p0.2}$ =1260 MPa, R_m= 1370 MPa) but the shortest elongation (9.2%) and high RA (52.8%), coinciding with peak hardness. Over-aging (S+A9, 600 °C, 6h) causes a marked strength drop ($R_{p0.2}$=875 MPa, R_m=1002 MPa) but restores ductility (elongation 20.9%) due to copper precipitate coarsening and reverted austenite formation. These aging effects balance strength and ductility through microstructural changes.

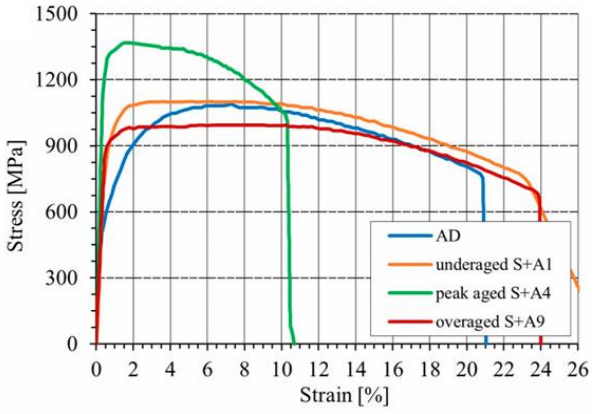

Figure 16: Stress-strain graphs for specimen in different states.

4.3.5. Impact toughness

Figure 17 presents impact toughness results for as-deposited (AD), under-aged (S+A1), peak-aged (S+A4), and over-aged (S+A9) 15-5 PH steel. The AD condition shows an average impact toughness of 56 J/cm², with energy for crack initiation (Ei) around 27.6 J, energy for crack propagation (Ep) 17.2 J, and ductile fracture fraction (DF) 87%. Under-aging at 400 °C for 1 hour (S+A1) slightly improves toughness to 61 J/cm². However, aging for 6 hours at 400 °C (S+A3) results in the lowest toughness (11 J/cm²), caused by a sharp reduction in crack initiation energy (Ei ~8–10 J) at peak-aged condition (S+A4). This leads to embrittlement and a significant drop in impact toughness. As aging continues at 500 °C and especially at 600 °C, impact toughness gradually recovers, with the highest value (77 J/cm²) observed after 6 hours at 600 °C (S+A9). This recovery is mainly driven by increased energy for crack propagation (Ep).

SEM and macrographs reveal ductile transgranular fracture with deep dimples in AD and under-aged specimens, characterized by prominent shear lips. Peak-aged specimens show a predominance of quasi-cleavage fracture and shallow dimples, indicating embrittlement under high loading rates. Over-aged samples regain ductility, exhibiting pronounced shear lips and crack arrest areas signaling the transition to ductile crack growth.

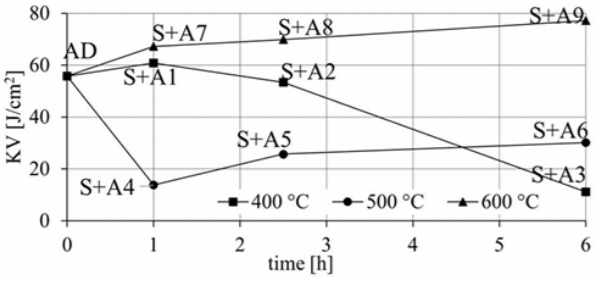

Figure 17: Impact toughness results for specimens in different states.

5. CONCLUSION

DED-Arc stands out as a highly productive metal additive manufacturing technology, offering compelling advantages in terms of build size, deposition rate, cost-effectiveness, and material efficiency, making it particularly well-suited for large-scale components. However, the intrinsic high heat input of the arc welding process poses significant challenges, leading to issues such as complex thermal cycling, microstructural non-uniformity, substantial residual stresses and distortion, and the prevalence of defects like porosity, lack of fusion, and cracking. These challenges often necessitate considerable post-processing to achieve the required material properties and dimensional accuracy.

The state-of-the-art research is actively tackling these limitations through a multi-faceted approach. Significant progress is being made in thermal management via techniques like lower heat input processes and the development of advanced in-situ cooling strategies aimed at controlling microstructural evolution and reducing the reliance on post-process heat treatments. Advancements in path planning and deposition strategies, such as the innovative 3D weaving path, are demonstrating the potential to improve surface quality and reduce defects. Furthermore, more accurate simulation models are being developed to better predict and control the thermal and mechanical behavior of the deposited material. While post-processing remains critical, techniques like heat treatment and interlayer rolling are being optimized to enhance the mechanical properties and refine the microstructure of DED-Arc parts, achieving properties comparable to conventionally manufactured materials. The exploration of new materials and novel structural designs, such as bimetallic components, continues to expand the application potential of DED-Arc.

Despite the notable progress, challenges related to consistently achieving microstructural homogeneity, minimizing residual stresses and distortion without extensive post-processing, and ensuring robust process control for a wider range of complex geometries and advanced alloys still require further investigation and development. The continued focus on integrating sophisticated control systems, enhancing thermal management strategies, and developing advanced deposition techniques will be crucial for the wider adoption and qualification of DED-Arc for demanding industrial applications. The ongoing research indicates a strong trajectory towards overcoming these challenges and unlocking the full potential of DED-Arc as a key enabler for high-speed, large-scale metal additive manufacturing.

ACKNOWLEDGMENT

The research of the authors was partially funded by the Slovenian Research and Innovation Agency (ARIS) under grant number P2-0270, and bilateral project Weave N2-0328, and by ARIS and the European Union Next Generation EU through DIGITOP project. This work was also partly supported by the Slovenian Research Agency, under grant number BI-BA/24-25-034. The paper was also partly supported by EU ERASMUS+ Strategic

Partnership Key Action 2, number:2024-1-RO01-KA220-HED-000244949 (SMARTIE) and 2023-1-RO01-KA220-HED-000158031 (ANGIE).

REFERENCES

[1] A. Biserova-Tahchieva, M. V. Biezma-Moraleda, N. Llorca-Isern, J. Gonzalez-Lavin, and P. Linhardt, "Additive Manufacturing Processes in Selected Corrosion Resistant Materials: A State of Knowledge Review," *Materials (Basel).*, vol. 16, no. 5, 2023, doi: 10.3390/ma16051893.

[2] D. Klobčar *et al.*, "A Review of Recent Advances and Future Trends in Wire Arc Additive Manufacturing," vol. 163, pp. 21–37, 2025, doi: 10.4028/p-Gq1x0e.

[3] V. V. Popov *et al.*, "Powder bed fusion additive manufacturing using critical raw materials: A review," *Materials (Basel).*, vol. 14, no. 4, pp. 1–37, 2021, doi: 10.3390/ma14040909.

[4] C. Shen, Z. Pan, D. Cuiuri, J. Roberts, and H. Li, "Fabrication of Fe-FeAl Functionally Graded Material Using the Wire-Arc Additive Manufacturing Process," *Metall. Mater. Trans. B Process Metall. Mater. Process. Sci.*, vol. 47, no. 1, pp. 763–772, 2016, doi: 10.1007/s11663-015-0509-5.

[5] L. Squires, E. Roberts, and A. Bandyopadhyay, "Radial bimetallic structures via wire arc directed energy deposition-based additive manufacturing," *Nat. Commun.*, vol. 14, no. 1, 2023, doi: 10.1038/s41467-023-39230-w.

[6] T. Lehmann *et al.*, "Large-scale metal additive manufacturing: a holistic review of the state of the art and challenges," *Int. Mater. Rev.*, vol. 67, no. 4, pp. 410–459, 2022, doi: 10.1080/09506608.2021.1971427.

[7] L. Squires, V. K. Champagne, and A. Bandyopadhyay, "In Situ microstructure control during electric-arc- directed energy deposition," *Virtual Phys. Prototyp.*, vol. 20, no. 1, pp. 1–19, 2025, doi: 10.1080/17452759.2025.2499929.

[8] K. S. Derekar, "A review of wire arc additive manufacturing and advances in wire arc additive manufacturing of aluminium," *Mater. Sci. Technol. (United Kingdom)*, vol. 34, no. 8, pp. 895–916, 2018, doi: 10.1080/02670836.2018.1455012.

[9] H. Sharma *et al.*, "Influence of post heat treatment on metallurgical, mechanical, and corrosion analysis of wire arc additive manufactured inconel 625," *J. Mater. Res. Technol.*, vol. 27, no. November, pp. 5910–5923, 2023, doi: 10.1016/j.jmrt.2023.11.074.

[10] U. Ziesing, J. Lentz, A. Röttger, W. Theisen, and S. Weber, "Processing of a Martensitic Tool Steel by Wire-Arc Additive Manufacturing," *Materials (Basel).*, vol. 15, no. 21, 2022, doi: 10.3390/ma15217408.

[11] M. Godec *et al.*, "Hybrid additive manufacturing of Inconel 718 for future space applications," *Mater. Charact.*, vol. 172, 2021, doi: 10.1016/j.matchar.2020.110842.

[12] M. Lindi, "Journal of Advanced Joining Processes Heat treatment optimisation of 18 % Ni maraging steel produced by DED-ARC for enhancing mechanical properties ˇ ˇ," vol. 11, no. May, 2025, doi: 10.1016/j.jajp.2025.100312.

[13] T. Özel, H. Shokri, and R. Loizeau, "A Review on Wire-Fed Directed Energy Deposition Based Metal Additive Manufacturing," *J. Manuf. Mater. Process.*, vol. 7, no. 1, 2023, doi: 10.3390/jmmp7010045.

[14] C. K. Kim *et al.*, "3D weaving path optimization for enhanced surface quality in wire arc-based directed energy deposition," *J. Mater. Process. Technol.*, vol. 340, no. April, p. 118838, 2025, doi: 10.1016/j.jmatprotec.2025.118838.

[15] O. C. Ozaner, D. Klobčar, and A. Sharma, "Machining Strategy Determination for Single- and Multi-Material Wire and Arc Additive Manufactured Thin-Walled Parts," *Materials (Basel).*, vol. 16, no. 5, 2023, doi: 10.3390/ma16052055.

[16] M. Köhler, A. Sarmast, J. Schubnell, and K. Dilger, "Influence of energy input and interpass temperature on the mechanical properties of DED-arc manufactured 316L stainless steel," *Weld. World*, p. Submitted, 2024, doi: 10.1007/s40194-025-02066-7.

[17] D. Kovšca, B. Starman, D. Klobčar, M. Halilovič, and N. Mole, "Towards an automated framework for the finite element computational modelling of directed energy deposition," *Finite Elem. Anal. Des.*, vol. 221, 2023, doi: 10.1016/j.finel.2023.103949.

[18] R. P. Reis and L. J. da Silva, *Thermal management approaches for arc additive manufacturing: a comprehensive review over a decade of developments and applications*. Springer London, 2025. doi: 10.1007/s00170-024-14791-2.

[19] B. O. Omiyale, T. O. Olugbade, T. E. Abioye, and P. K. Farayibi, "Wire arc additive manufacturing of aluminium alloys for aerospace and automotive applications: a review," *Mater. Sci. Technol. (United Kingdom)*, vol. 38, no. 7, pp. 391–408, 2022, doi: 10.1080/02670836.2022.2045549.

[20] C. Ma *et al.*, "Investigation of In Situ Vibration During Wire and Arc Additive Manufacturing," vol. 10, no. 3, pp. 524–535, 2023, doi: 10.1089/3dp.2021.0053.

[21] M. Imširović, U. Trdan, D. Klobčar, D. Bračun, A. Nagode, and L. Berthe, "Mitigating defects in directed energy deposited aluminium 5356 alloy through in-situ workpiece vibration," *J. Mater. Res. Technol.*, vol. 33, no. August, pp. 1581–1599, 2024, doi: 10.1016/j.jmrt.2024.09.179.

[22] F. Lyu, L. Wang, J. Wang, Y. Zhang, J. Zhang, and X. Zhan, "Integrated control mechanism of ultrasound and ZrO 2 particles on differential microstructures for the wire arc additive manufacturing," vol. 18, no. 1, pp. 1–23, 2023.

[23] R. Porosity, A. Arc, and P. Frequency, "Reducing Porosity and Refining Grains for Arc Additive Manufacturing Aluminum Alloy by Adjusting Arc Pulse Frequency and Current," 2018, doi: 10.3390/ma11081344.

[24] Y. Wang, D. Wu, J. Chen, H. Komen, M. Chen, and H. Su, "Pore suppression and performance improvement mechanisms in wire-arc directed energy deposition of 7075 alloy," *Virtual Phys. Prototyp.*, vol. 20, no. 1, pp. 1–24, 2025, doi:

10.1080/17452759.2025.2464953.
[25] M. A. Chipanski *et al.*, "DED-IM: A Novel Method for Mapping and Path Planning in Wire Arc Directed Energy Deposition," *IEEE Trans. Autom. Sci. Eng.*, vol. 22, pp. 13286–13297, 2025, doi: 10.1109/TASE.2025.3553309.
[26] S. C. A. Costello, C. R. Cunningham, F. Xu, A. Shokrani, V. Dhokia, and S. T. Newman, "The state-of-the-art of wire arc directed energy deposition (WA-DED) as an additive manufacturing process for large metallic component manufacture," *Int. J. Comput. Integr. Manuf.*, vol. 36, no. 3, pp. 469–510, 2023, doi: 10.1080/0951192X.2022.2162597.
[27] J. T. Kahnamouei and M. Moallem, "Advancements in control systems and integration of artificial intelligence in welding robots: A review," *Ocean Eng.*, vol. 312, no. P3, p. 119294, 2024, doi: 10.1016/j.oceaneng.2024.119294.
[28] T. F. Lam, Y. Xiong, A. G. Dharmawan, S. Foong, and G. S. Soh, "Adaptive process control implementation of wire arc additive manufacturing for thin-walled components with overhang features," *Int. J. Adv. Manuf. Technol.*, vol. 108, no. 4, pp. 1061–1071, 2020, doi: 10.1007/s00170-019-04737-4.
[29] A. Ščetinec, D. Klobčar, and D. Bračun, "In-process path replanning and online layer height control through deposition arc current for gas metal arc based additive manufacturing," *J. Manuf. Process.*, vol. 64, no. March, pp. 1169–1179, 2021, doi: 10.1016/j.jmapro.2021.02.038.
[30] J. Qin *et al.*, "Automated Interlayer Wall Height Compensation for Wire Based Directed Energy Deposition Additive Manufacturing," *Sensors*, vol. 23, no. 20, 2023, doi: 10.3390/s23208498.
[31] P. Nagaraj, S. K. Gurunathan, and M. Amirthalingam, "Physically derived instantaneous modelling of complex current-voltage waveform-controlled arc-wire DED process—residual stress and distortion analysis," *Int. J. Adv. Manuf. Technol.*, pp. 687–708, 2025, doi: 10.1007/s00170-025-15547-2.
[32] T. Zhao *et al.*, "A comprehensive review of process planning and trajectory optimization in arc-based directed energy deposition," *J. Manuf. Process.*, vol. 119, no. February, pp. 235–254, 2024, doi: 10.1016/j.jmapro.2024.03.093.
[33] Isaac Chang Yuyuan Zhao, Ed., *Advances in Powder Metallurgy, Properties, Processing and Applications*, 1st Editio. Woodhead Publishing, 2013.
[34] T. A. Rodrigues, V. Duarte, R. M. Miranda, T. G. Santos, and J. P. Oliveira, "Current status and perspectives on wire and arc additive manufacturing (WAAM)," *Materials (Basel).*, vol. 12, no. 7, 2019, doi: 10.3390/ma12071121.
[35] T. Zhao, Z. Yan, Y. Zhao, Y. Jia, and S. Chen, "Path planning in additive manufacturing with multi-robot collaboration based on structural primitive partitioning," *Adv. Eng. Softw.*, vol. 197, no. August, p. 103754, 2024, doi: 10.1016/j.advengsoft.2024.103754.
[36] T. Wang *et al.*, "Robot-assisted additive manufacturing for aerospace applications: recent trends and its future possibilities," *Int. J. Comput. Integr. Manuf.*, vol. 00, no. 00, pp. 1–41, 2025, doi: 10.1080/0951192X.2025.2478007.
[37] K. Kelly, A. Thien, D. K. Saleeby, and D. C. Saldana, "A novel approach to path planning related to the intersections of aluminum WAAM," *Int. J. Adv. Manuf. Technol.*, pp. 2579–2593, 2025, doi: 10.1007/s00170-025-15285-5.
[38] H. Lund, S. Penttilä, and T. Skriko, "Extended reality implementation possibilities in direct energy deposition-arc," *Front. Sustain.*, vol. 5, no. June, 2024, doi: 10.3389/frsus.2024.1408604.

11th International Scientific Conference
IRMES 2025
Research and Development of
Mechanical Elements and Systems
June 19 – 21, 2025; Vrnjačka Banja, Serbia

Original scientific paper DOI: 10.46793/IRMES25.plB3M

STRAIN AND STRESS/FORCE-CONTROLLED FATIGUE TESTING OF METALLIC MATERIALS, POST-PROCESSING OF EXPERIMENTALLY OBTAINED RESULTS AND APPLICATION IN FEA

Vladimir MILOVANOVIĆ[1]

[1]Faculty of Engineering University of Kragujevac, Kragujevac, Serbia, 34000; vladicka@kg.ac.rs;
ORCID iD: 0000-0003-3071-4728

Abstract: *Fatigue of metals is a very complex phenomenon, which is still not fully understood and is also the topic of much active research. Fatigue testing is a method used to evaluate how a material behaves under repeated stress and cyclic loading. The aim of this paper is to show strain and stress/force-controlled testing of metallic materials using developed procedures according to relevant standards. The paper has presented a very useful developed software application for the determination of fatigue properties of metallic materials, whereas the user is enabled to display the corresponding fatigue properties of the tested material as well as the corresponding ε-N or S-N curves. The obtained fatigue properties of the tested materials can be used with great success in numerical calculations, especially FEA, to estimate the endurance limit and fatigue life of various types of metallic structures.*

Keywords: *structural fatigue tests; fatigue life; S–N fatigue curves; ε–N fatigue curves.*

1. INTRODUCTION

There is no exact data, but many books and scientific articles have suggested that 50% to 90% of all mechanical failures are fatigue failures. Fatigue is the appearance of a gradual destruction of materials under periodic variable load. Fatigue tests measure the resistance of materials to damage, losing strength, and failure under the repeated application of load [1]. There are many experimental methods for fatigue testing. Experimental methods for fatigue testing are very expensive and time-consuming.

Despite the development of new alloys and composite materials, steels are still the most widely utilized materials in mechanical and civil engineering. Steels still represent the most used group of mechanical materials for constructing bridges, buildings, ships, cars, rail vehicles, railways, and etc. Steel structural elements and constructions are frequently subjected to varying loads over their service (fatigue) lives [2], [3].

In this paper, the cyclic deformation behaviour and fatigue life of metallic materials under strain and stress/force-controlled fatigue testing studied experimentally.

Another idea of this paper is to develop a software solution for post-processing of experimentally obtained fatigue properties of metallic materials in accordance with the appropriate standard for statistical analysis and application fatigue properties in Finite element Analysis (FEA) for prediction of fatigue life of different steel structures.

2. FATIGUE BEHAVIOR ASSESSMENT

The fatigue approaches may be divided into three classes (approaches): fatigue tests and stress-life (*S–N*) approach, cyclic deformation and the strain-life (*ε–N*) approach and linear elastic fracture mechanics-based approach (LEFM) [1].

Stress-life (*S–N*) approaches are most useful at high cycle fatigue, where the applied stresses are elastic, and no plastic strain occurs anywhere other than at the tips of fatigue cracks. At low number of cycles, scatter in the fatigue data makes these methods increasingly less reliable. *S–N* approach is a global approach that relates the stress range (e.g. nominal, structural or geometric) applied to the component with the fatigue life [4]. The *S–N* approach is the basis of many standards for assessing the fatigue life, such as the Eurocode 3, part 1-9 [5]. For most stress-life calculations, the math is relatively easy, since there is only one stress component. In strain life calculations, the math is more difficult, as the elastic and plastic components of the strain must be dealt with separately.

Strain life (*ε–N*) approach and linear elastic fracture mechanics approach (LEFM) belong to local approach and it can be used for low cycle and high-cycle fatigue. The local approaches, recognizing the localized nature of the fatigue damage, propose the correlation of a local damage parameter (e.g. strain, energy) with the number of cycles required to initiate a macroscopic crack. LEFM approach represents an alternative approach to fatigue, based on the fatigue crack propagation phenomena [6],

[7]. This approach is based on crack propagation laws, with Paris' law [8] and residual life computation of a structural component with an initial crack.

2.1. Basic equations

Mathematical model used to describe fatigue behavior of material under cyclic strain-controlled tests to obtained cyclic stress-strain (σ-ε) curve is given by Ramberg–Osgood approach presented by equations (1) and (2):

$$\varepsilon_a = \frac{\Delta\varepsilon}{2} = \varepsilon_{a,e} + \varepsilon_{a,p} = \frac{\Delta\varepsilon_e}{2} + \frac{\Delta\varepsilon_p}{2} \quad (1)$$

$$\varepsilon_a = \frac{\Delta\sigma}{2E} + \left(\frac{\Delta\sigma}{2K'}\right)^{\frac{1}{n'}} = \frac{\sigma_a}{E} + \left(\frac{\sigma_a}{K'}\right)^{\frac{1}{n'}} \quad (2)$$

The total strain-life (ε-N_f curve) is therefore expressed as the sum of elastic Basquin's and plastic Manson-Coffin's part by equations (1) and (2):

$$\varepsilon_a = \varepsilon_{a,e} + \varepsilon_{a,p} = \frac{\Delta\varepsilon_e}{2} + \frac{\Delta\varepsilon_p}{2} = \frac{\sigma_f'}{E}\left(2N_f\right)^b + \varepsilon_f'\left(2N_f\right)^c \quad (3)$$

In equations (1-3) ε_a, $\varepsilon_{a,e}$, $\varepsilon_{a,p}$ are, respectively, the total, elastic and plastic strain amplitude; K', n' are, respectively, cyclic strain coefficient and cyclic strain hardening exponent; σ_f', b, are, respectively, fatigue strength coefficient and fatigue strength exponent; ε_f', c are, respectively, fatigue ductility coefficient and fatigue ductility exponent; $2N_f$ is the number of reversals to failure; σ_a is true stress amplitude; E is the Young's modulus.

All constants in equations (1-3) will be determined from fatigue tests of smooth specimens under strain-controlled conditions for Strain life (ε–N) approach.

For Stress-life (S–N) approach results relating directly a global definition of stress range (stress amplitude) to the total number of reversals to failure. Often, Basquin's part of equation (3) is adopted for representing the Wöhler curve as a straight line in a double logarithmic plot.

2.2. Fatigue Analysis Using the Experimental Method

This section describes a complete fatigue characterization of metallic materials, carried out according to the internal procedures of the Centre for engineering software and dynamic testing at Faculty of Engineering University of Kragujevac, based on the ASTM E468-90 [9], ASTM E466-96 [10] and ASTM E606-92 [11] standards.

Before fatigue testing it is necessary to determine monotonic mechanical properties (minimum yield stresses, minimum tensile strength and Young's modulus) in accordance to the standards EN ISO 6892-1 [12] and ASTM E8M-01 [13].

All tests (the uniaxial tensile tests and fatigue tests) were performed using a SHIMADZU type EHF EV101K3-070-0A servo-hydraulic testing machine (Shimadzu Corporation, Tokyo, Japan) with a force of ±100 kN and a stroke of ±100 mm.

Uniaxial tensile tests must be performed on representative flat specimens for each metallic material, with the same thickness in all cross-sections to investigate the static strength properties. Uniaxial tensile tests perform at room temperature with a constant stroke control rate without a change in the speed of testing. One of the investigated specimens at the end of the uniaxial tensile test is presented in Figure 1a. An MFA25 extensometer with a gauge length of 50 mm was used to determine the Young's modulus (Figure 1b).

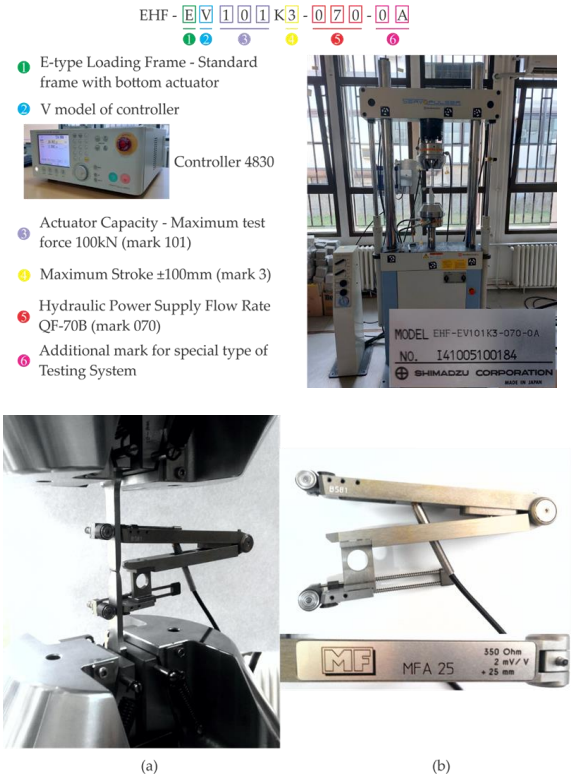

Fig.1. Testing equipment: (a) SHIMADZU servo-hydraulic machine, (b) MFA25 extensometer

All specimens utilized to determine the fatigue properties were prepared according to the standard E468-90 [9]. The technical drawing and real shape of one of the investigated specimens for fatigue testing, before testing, is shown in Figure 2. All nominal dimensions of the specimen shown in Figure 2 are in millimetres (mm). All specimens were finely polished to minimize surface roughness effects. The mean roughness level achieved on the surface of the gauge length of the specimens was in the range of 1–5 μm.

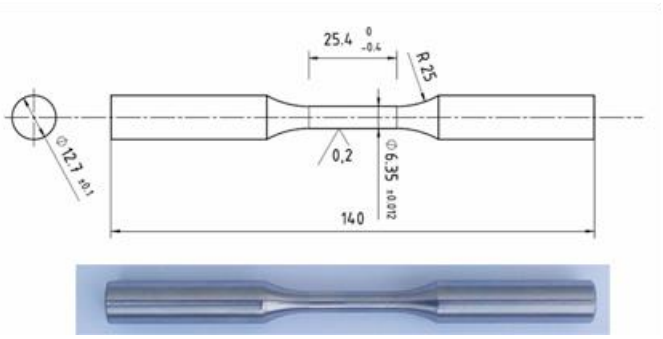

Fig.2. Technical drawing of fatigue testing specimen and real specimen (unit: mm)

One series for any uniaxial fatigue test consists of a minimum of 15 specimens. The specimens are exposed to

high cycle fatigue under force/stress-controlled, fully reversed (tensile-compression) testing conditions The stress levels used to control the fatigue tests must be chosen from the previously performed monotonic uniaxial tensile test.

For strain-controlled fatigue tests, for investigating low-cycle fatigue, and for controlling testing conditions SHIMADZU DYNASTRAIN TCK-1-LH dynamic extensometer with *a* ±1 mm working range (Figure 3.) is necessary.

The uniaxial tension-compression test planning (stress or strain-controlled fatigue tests) is minimum five levels, three repetitions per level with a range of stress or strain amplitude. The test frequency in the characterization is in the range of 3–10 Hz (low cycle fatigue) and 10-15 Hz (high cycle fatigue). The crack initiation criterion (failure criterion) was quick stiffness loss (load amplitude loss of about 10%).

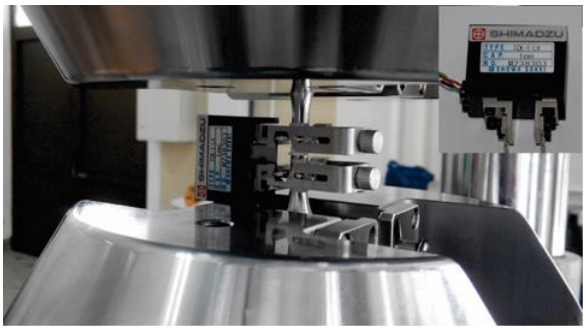

Fig.3. SHIMADZU DYNASTRAIN TCK-1-LH dynamic extensometer

After the fatigue testing of all specimens in the series, all testing results must be presented in accordance with ASTM: E468-90 [9] (Figure 4.).

According to the experimental data shown in a proper manner and statistical analysis (linear model Y= A + BX, log-normal fatigue life distribution with constant variance along the entire interval of X used in testing) in accordance with standard ASTM E739-91 [14], the fatigue properties would be determined.

Specimen No	Δσ [MPa]	F_{min} [kN]	F_{max} [kN]	ΔF [kN]	R	A [mm^2]	Number of cycles	Place of the failure
S-N approach for highcycle fatigue								

Specimen No	ε_a [%]	ε_{min} [%]	ε_{max} [%]	σ_a [MPa]	E [MPa]	l [mm]	Number of cycles	Place of the failure
ε-N approach for lowcycle fatigue								

Fig.4. Table for presentation of Fatigue Test Results for Metallic Materials in accordance to [14]

Experimentally obtained uniaxial tension–compression strain controlled mechanical properties of S355J2+N steel grade strain–life curve (log–log representation), have been determined and shown in Figure 5 [15].

Cyclic stress-strain curve from uniaxial tension–compression strain-controlled fatigue tests and graphical method for obtaining cyclic yield strength are shown in Figure 6 [15].

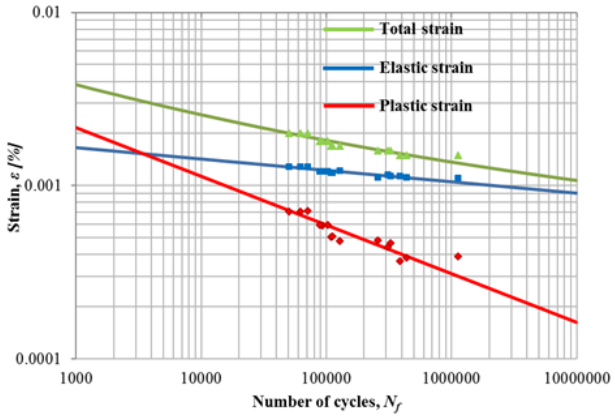

Fig.5. Strain–life curve from uniaxial tension–compression strain-controlled fatigue test of S355J2+N steel grade [15]

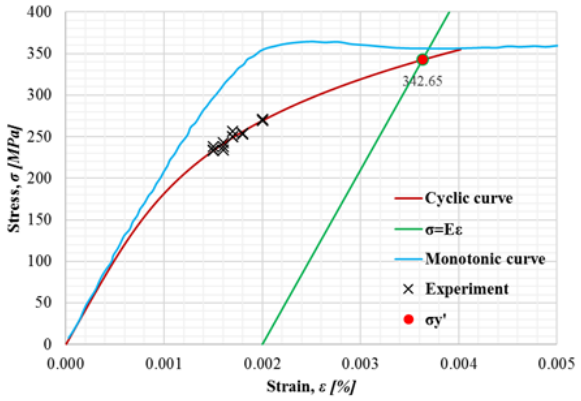

Fig.6. Cyclic stress-strain curve from uniaxial tension–compression strain-controlled fatigue test of S355J2+N steel grade [15]

Based on uniaxial tension–compression stress-controlled experiments, the *S–N* curves (semi-log representation) for S355J2+N, S690QL, and X37CrMoV5-1 steel grades were determined and are shown in Figure 7 [16].

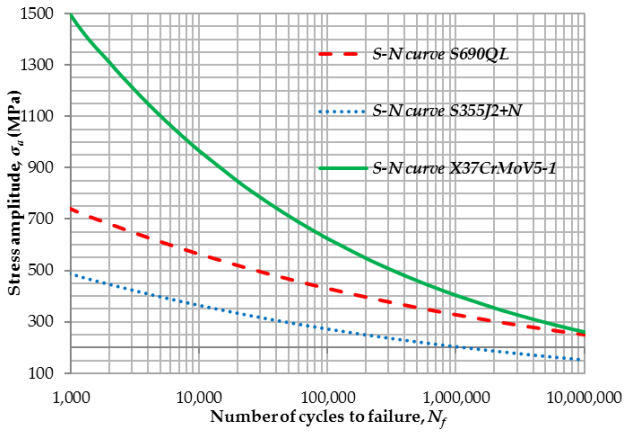

Fig.7. Combined diagram of semi-log S-N curves for S355J2+N, S690QL, and X37CrMoV5-1 steel grades [16]

3. DEVELOPMENT OF AN SOFTWARE APPLICATION

As noted in the previous chapter for each series of fatigue test specimens (strain or stress/force controlled) it is necessary to do statistical analysis according to algorithm and procedure for determination fatigue properties [14]. Because we never have the same number of test specimens in a series, this task is not easy and takes a lot of time.

The main idea is to develop a software solution for post-processing of experimentally obtained fatigue properties of metallic materials [17] in accordance with the appropriate standard for statistical analysis ASTM E739-91 [14], using the Python programming language with appropriate libraries.

3.1. The concept of a software application

The software application for post-processing of experimentally obtained fatigue properties was developed in the Python 3.10.7 programming language [18]. Beside to the standard libraries, additional libraries (NumPy, pandas, matplotlib, tkinter) were used for working with data, drawing graphics, creating a graphical user interface, and Visual Studio Code software [19].

The idea of a general algorithm program for post-processing of experimentally obtained fatigue properties is as follows:

- All obtained results of the experimental tests are collected in an Excel file performed in accordance to ASTM E468-90 standard [9].
- Starting the application is done by running the *.exe file.
- Step 1 is choosing the type of analysis low cycle fatigue or high cycle fatigue.
- Step 2 is to select the appropriate Excel document. For low cycle fatigue, the table contains the following data: modulus of elasticity E, number of the sample, and their values of total strain amplitude ε_a, stress amplitude σ_a and number cycles to failure N. For high cycle fatigue, the table contains the number of samples, stress amplitude σa and and number cycles to failure N.
- Step 3 is the display of the obtained fatigue properties. For low cycle fatigue: fatigue strength coefficient σ_f', fatigue strength exponent b, fatigue ductility coefficient ε_f', fatigue ductility exponent c. For high cycle fatigue: fatigue strength coefficient σ_f', fatigue strength exponent b, Slope of fatigue strength curve m.
- Step 4 is plotting of corresponding ε-N and S-N curves in semi-log or log-log representation with all results of the experimental tests.

3.2. Visualization of a software application

Starting the program (*.exe file) opens the window shown in Figure 8., in which it is necessary to select the type of fatigue properties.

By selecting one type of fatigue assessment, a new file selection window opens. Selecting a file opens a new window, which offers the option to start a program for post-processing the data of the loaded file, prepared in accordance with ASTM E468-90 [9]. By loading the data from the selected file, the calculation procedure of the appropriate fatigue properties of the material is started in accordance with ASTM standard: E739-91 [14]. Results of obtained fatigue properties are shown in Figure 9.

Fig.8. Main window of software application

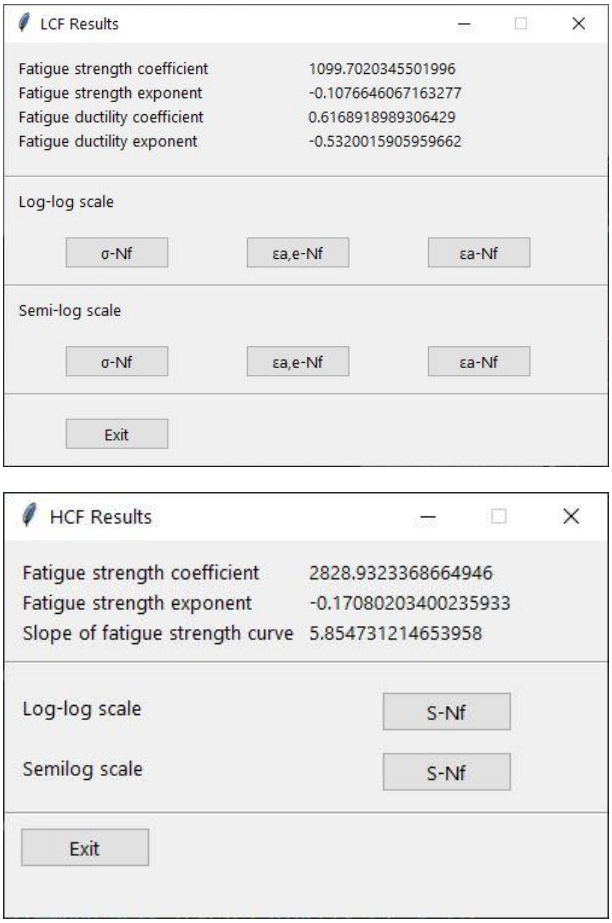

Fig.9. Obtained fatigue properties, window with results

On windows shown in Figure 9 user is enabled to plot different types of ε-N curves and S-N curves. ε-N and S-N curves can be represented in semi-log or log-log form with all results of the experimental tests.

Figure 10. present ε-N curves in log-log representation as results of using the developed software application for the determination of low-cycle fatigue properties of tested metallic material.

Figure 11. present S-N curve in semi-log representation as results of using the developed software application for the determination of high-cycle fatigue properties of tested metallic material.

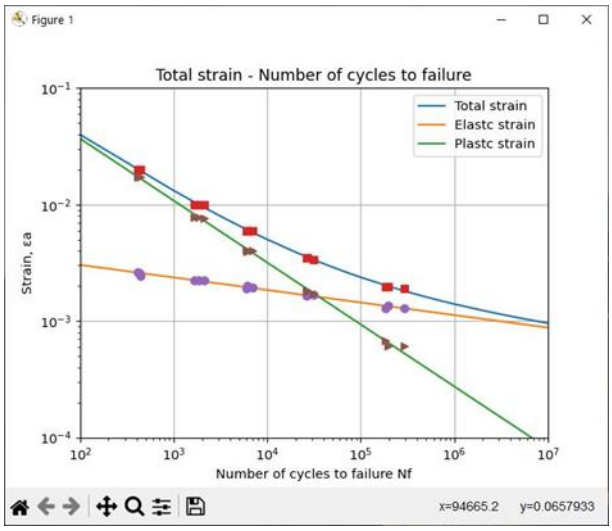

Fig.10. ε-N curves

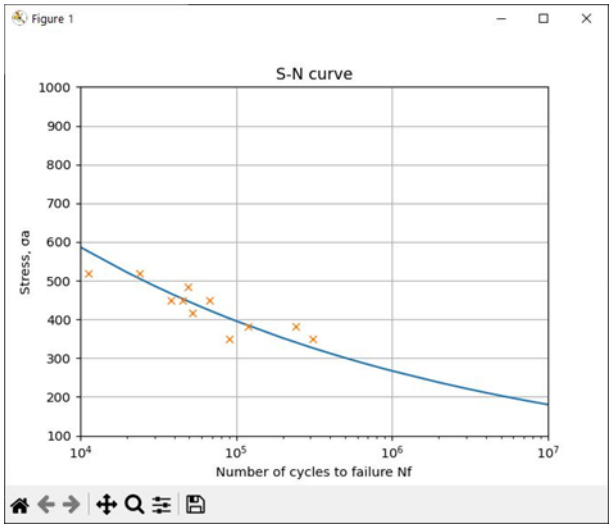

Fig.11. S-N curve

4. APPLICATION IN FINITE ELEMENT ANALYSIS

4.1. Low cycle fatigue application

This example investigates how shape optimisation affects the ultimate fatigue strength of a mechanical part. The mechanical part chosen for this investigation is an axle guard of running gear elements of the Hccrrs 2x2 axle car-carrying wagon.

Material properties were determined experimentally and the necessary numerical calculations were performed by using the finite element method. The observed axle guard is exposed to low cycle fatigue. ε–N curves and material properties of the S355J2+N steel grade are obtained by combining theoretical formulae and a mathematical function. According to the obtained experimental and numerical results the number of cycles until failure for both shapes of axle guards is obtained.

According to the scheme of the model loading presented in [20], the strength of the axle guards and analysis of rigidity was done for both shapes of the axle guards when the maximum lateral force is applied to the axle guard. Elastoplastic analysis for both shapes of the axle guards in the case of lateral displacement of 22 mm were done.

The aim of the elastoplastic analysis of the axle guard is the determination of the plastic strain field. Number of cycles before damage can be determined based on the maximum value of the plastic strain.

The plastic strain fields calculated by using the elastoplastic analysis for the old and the new optimized shape of the axle guard are shown in Figure 12 and Figure 13, respectively.

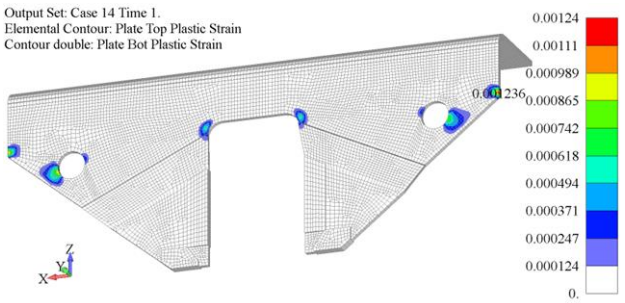

Fig.12. Plastic strain field –old shape of axle guard

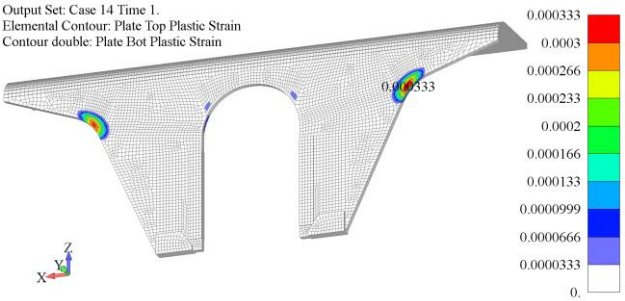

Fig.13. Plastic strain field –new optimized shape of axle guard

The maximum values of the plastic deformation of both shapes of the axle guards are shown in Figure 12 and Figure 13. The results of the elastoplastic analysis are required for the determination of the axle guard's fatigue strength, which is expressed with the number of cycles to failure. This means that the maximum value of the plastic deformation determines the number of cycles that the wagon structure part can withstand.

The strain–life curve, determined experimentally for the S355J2+N steel grade, is shown in Figure 14.

According to the results obtained by the FEM calculation, the maximum value of the plastic deformation of the old shape of the axle guard is 0.00124 (Figure 12), while the maximum value of the plastic deformation of the new optimized shape of the axle guard is 0.000333 (Figure 13).

According to the values of the plastic deformation obtained for both shapes of the axle guards and the fatigue material properties of S355J2+N, the number of cycles to failure is determined. For the old shape of the axle guard the obtained fatigue life reaches 10673 cycles, while the obtained fatigue life of the new optimized shape of axle guard reaches 287937 cycles (Figure 14).

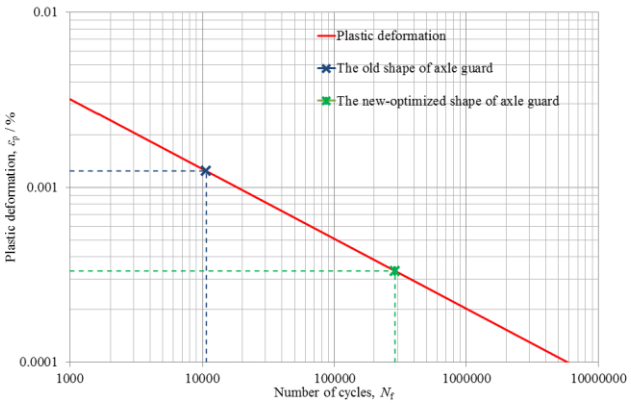

Fig.14. Plastic strain-life curve of S355J2+N material obtained by calculation of old and new optimized shape of axle guard [20]

The example presents the ε–N approach or a fatigue analysis based on strain, which assumes that the critical areas of material behaviour depend on the strain. The methodology presented in this section contains an experimental definition of fatigue parameters, shape optimization, a definition of the numerical model, numerical calculation of strength according to standards and estimation of fatigue strength by using experimental and numerical results.

4.2. High cycle fatigue application

This example presents a methodology used to identify causes of cracking nearby the welded joint on the underframe of wagon type Sgmns for the transportation of containers and swap bodies, exposed to high cycle fatigue [21].

Eighty percent of all wagons, which were used in transport, have failure or initial crack. After visual inspection of the wagons type Sgmns, cracks and failure were observed on the bottom side of underframe, on the side of the parking brake, Figure 15.

According to this fact, it was necessary to determine the reason for the appearance of the crack growth on the wagon bottom side of underframe. The observed cracks appear on the welded joint or near the welded joint of two plates which close rolled steel profile of bottom side of underframe, Figure 16.

Fatigue load case is specified by TSI standard [22], Clause 4.2.2.3.3 and British Standard (BS EN 12663:2000) [23], Clause 4.6, 5.2, Table 16.

Limit values for static test to verify fatigue strength, are determined for minimum number of two million constant amplitude cycles, using Eurocode 3, part 1.9 [24] as well as TSI standard [22], Annex N. Limit values for static test to verify fatigue strength for different Detail category (Constructional detail of parent material or welded joint) are shown in Table 1.

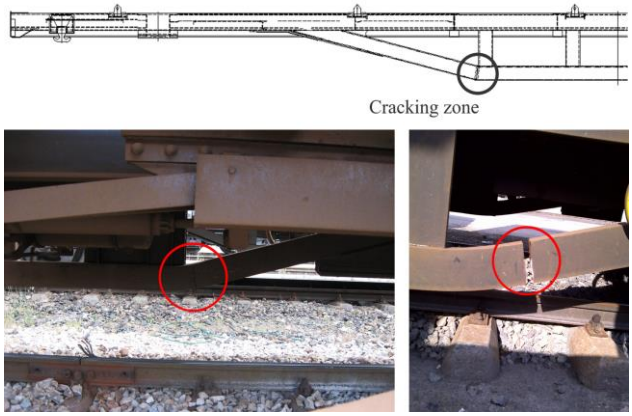

Fig.15. Crack at the bottom side of underframe

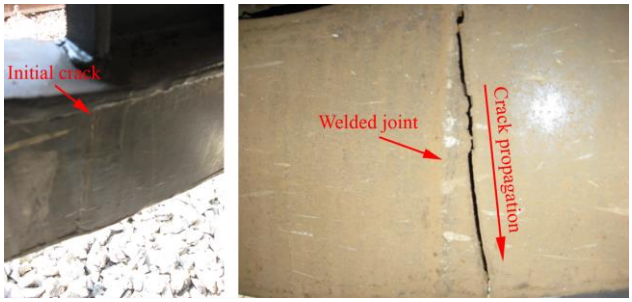

Fig.16. Initial crack and crack propagation nearby welded joint

Table 1. Limit stress values for static test to verify fatigue strength in steel S355J2+N [21]

Detail category	Permissible maximum fatigue stress [MPa]	Limit stress for safe life [MPa]	
		Low consequence (γ_{Mf}=1.15)	High consequence (γ_{Mf}=1.35)
160	347	301	257
100	217	188	160
90	195	170	144
80	173	151	128
71	154	134	114
63	136	119	101
56	121	106	90
50	108	94	80

The fatigue load used in design is in range of ±30% of vertical static load. The Von Mises equivalent stress field is shown in Figure 17. Maximal value of the equivalent stress is 291.6 MPa. The aim of this analysis was to identify cause of cracking in the bottom part of underframe, shown in Figure 15. In Figure 18, Von Mises equivalent stress field at the place of observed cracks is shown. Stress levels used in the legend in Figures 17 and 18 are defined according to Table 1.

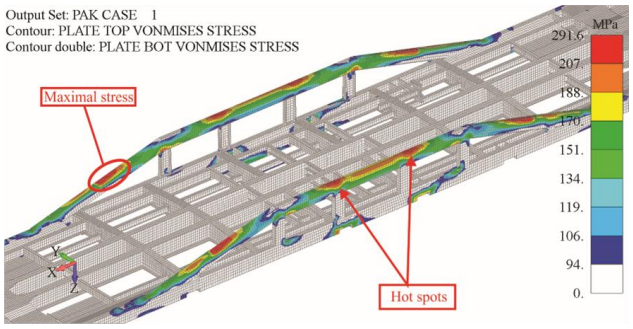

Fig.17. Crack at the bottom side of underframe

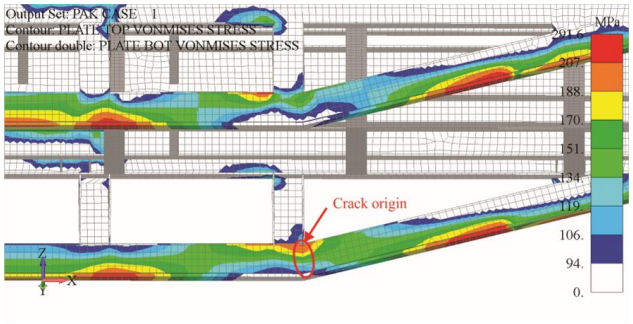

Fig.18. Initial crack and crack propagation nearby welded joint

A review of types of welds in accordance with the Eurocode-3, Section 1.9 [24] and based on the documentation on the technology of welding, observed type of welded joint belongs into the category 71 type of welds. This type of weld is given in the Eurocode-3, Section 1.9 [24] in Table 8.3, constructional detail 13 (butt welds made from one side only).

According to Table 1 for detail category 71 of transverse butt, the welds limit stress for safe life is 134 MPa. According to calculation results at the place of weld, Figure 18, stress is 194 MPa, which is higher than permissible maximum fatigue stress in Table 1. In Table 1 are shown the values of permissible stress for static fatigue testing of welded joints in accordance with Eurocode 3 Part 1.9, Figure 7.1 and Table 3.1 [24].

Maximum value of calculated stress and significant loaded zones are shown in Figure 17. All of these hot spots are in the parent material. The values of calculated stresses in these hot spots are below the limit stress for safe life in parent material (detailed category 160) according to Eurocode 3: Part 1.9 [24], Table 1.

On the basis of these facts, it can be concluded that the cracks on wagon type Sgmns are caused by service (fatigue) load.

The example presents the *S–N* approach or a fatigue analysis based on stress for high cycle fatigue strength assessment of wagon type Sgmns, at a maximal vertical load. This analysis determines that cracks are caused by fatigue in the zone of welded joint (place which connect two closing plates).

5. CONCLUSION

This paper has presented procedures for strain and stress/force-controlled fatigue testing of metallic materials. Procedures are carried out according to the internal procedures of the Centre for engineering software and dynamic testing at Faculty of Engineering University of Kragujevac, based on the relevant standards.

Using prescribed procedures, it is possible to obtain fatigue properties of tested metallic materials, both those that describe the behaviour of materials under high-cycle fatigue and those under low-cycle fatigue.

Experimental tests results have provided the basis for recommendation to use in fatigue life calculations the material cyclic properties determined in controlled conditions which are dominant during operation of structure components.

Developed software application presents useful tool for the determination of fatigue properties of metallic materials in accordance with relevant standard. As a result, the user is enabled to display the corresponding fatigue properties of the tested material as well as the corresponding *ε-N* or *S-N* curves.

For two representative examples, one for low-cycle fatigue and another for high-cycle fatigue, it is shown that the application of this methodology for fatigue assessment of different types of metallic structures.

The developed methodology based on the application of theoretical, experimental and numerical, techniques of fatigue mechanics has proven to be a powerful tool for the assessment of the fatigue life of structures exposed to fatigue loads to estimate the endurance limit and fatigue life.

ACKNOWLEDGMENT

This research was supported by the Science Fund of the Republic of Serbia, #GRANT No 7475, Prediction of damage evolution in engineering structures – PROMINENT.

REFERENCES

[1] Stephens, R., Fatemi, A., Stephens, R., Fuchs, H., *Metal Fatigue in Engineering*, John Wiley & Sons Inc., New York, ISBN 978-0-471-51059-8, 2001.

[2] Schutz, W., A History of Fatigue, *Engineering Fracture Mechanics*, Vol. 54, No. 2, pp. 263-300, ISSN 0013-7944, 1996.

[3] Schijve, J., Fatigue of Structures and Materials in the 20th Century and the State of the Art, *International Journal of Fatigue*, Vol. 25, pp. 679-702, ISSN 1879-3452, 2003.

[4] Hobbacher, A., The New IIW Recommendations for Fatigue assessment of Welded Joints and Components - A Comprehensive Code Recently

Updated, *International Journal of Fatigue*, Vol. 31, pp. 50-58, ISSN 1879-3452, 2009.
[5] European standard. Eurocode 3: design of steel structures – Part 1.9: Fatigue. pr EN 1993-1-9, 2003.
[6] Baik, B., Yamada, K., Ishikawa, T., Fatigue crack propagation analysis for welded joint subjected to bending, *International Journal of Fatigue*, Vol. 33, pp. 746-758, ISSN 1879-3452, 2011.
[7] Taylor, D., Hoey, D., High cycle fatigue of welded joints: The TCD experience, *International Journal of Fatigue*, Vol. 31, pp. 20-27, ISSN 1879-3452, 2009.
[8] Paris, P. C., Erdogan, F. A., A Critical Analysis of Crack Propagation Laws, *Journal of Basic Engineering*, Vol. D85, pp. 528-534, ISSN 0021-9223, 1963.
[9] ASTM: E486-90 Standard Practice for Presentation of Constant Amplitude Fatigue Test Results for Metalic Materials, 2004.
[10] ASTM E466-96 Standard Practice for Conducting Force Controlled Constant Amplitude Axial Fatigue Tests of Metallic Materials, 2004.
[11] ASTM: E606-92 Standard Practice for Strain-Controlled Fatigue Testing, 1998.
[12] EN ISO 6892-1:2011; Metallic Materials—Tensile Testing—Part 1: Method of Test at Room Temperature, 2011.
[13] ASTM: E8M-01; Standard Test. Method for Tension Testing of Metalic Material, 2002.
[14] ASTM: E739-91; Standard Practice for Statistical Analysis of Linear or Linearised Stress-Life (S–N) and Strain-Life ("-N) Fatigue Data, 2004.
[15] Milovanović, V., Dišić, A., Jovanović, N., Jovičić, G., Živković, M., Experimental study of deformation behaviour and fatigue life of S355J2+N steel grade under cyclic loading, *Proceedings of The 6th International Congress of Serbian Society of Mechanics*, 19-21 June, Mountain Tara, Serbia, pp. S2e:1-8, ISBN 978-86-909973-6-7, 2017.
[16] Milovanović, V., Arsić, D., Milutinović, M., Živković, M. Topalović, M., A Comparison Study of Fatigue Behavior of 355J2+N, S690QL and X37CrMoV5-1 Steel, *Metals*, Vol.12, No.7, pp. 1199, ISSN 2075-4701, 2022.
[17] Milovanović, V., Gicić, M., Živković, M., Živković, J., Dunić, V., Development of a software application for post processing experimentally obtained fatigue properties of metallic materials, *Proceedings of 39th Danubia-Adria Symposium on Advances in Experimental Mechanics*, 26-29 September, Siófok, Hungary, pp. 1-2, ISBN 978-963-421-927-9, 2023.
[18] Python, https://docs.python.org/, Accessed October, 2022.
[19] Visual Studio Code, https://code.visualstudio.com/, Accessed October, 2022.
[20] Milovanović, V., Živković, M., Jovičić, G., Živković, J., Kozak, D., The influence of wagon structure part on ultimate fatigue strength, *TRANSACTIONS OF FAMENA*, Vol.39, No.4, pp. 23-35, ISSN 1333-1124, 2015.
[21] Milovanović, V., Dunić, V., Rakić, D., Živković, M., Identification causes of cracking on the underframe of wagon for containers transportation - Fatigue strength assessment of wagon welded joints, *Engineering Failure Analysis*, Vol.31, No.-, pp. 118-131, ISSN 1350-6307, 2013.
[22] TSI standard. Commission decision of 28 July 2006 concerning the technical specification of interoperability relating to the subsystem rolling stock G - freight wagons of the trans-European conventional rail system (notified under document number C (2006) 3345); 2006.
[23] EN 12663-2:2010 - Railway applications – Structural requirements of railway vehicle bodies, European Standard, 2010.
[24] EN 1993-1-9: 2005 - Eurocode 3: Design of steel structures - Part 1.9: Fatigue, 2005.

Mechanical Elements and Systems

11th International Scientific Conference
IRMES 2025
Research and Development of
Mechanical Elements and Systems
June 19 – 21, 2025; Vrnjačka Banja, Serbia

Original scientific paper DOI: 10.46793/IRMES25.001A

THE INFLUENCE OF CRYOGENIC TREATMENT ON THE HARDNESS OF ROLLING BEARINGS' BALLS

Jovana ANTIĆ[1]
Žarko MIŠKOVIĆ[2]
Danilo PEJČIĆ[3]
Martin DIX[4]
Alexander PIERER[5]
Jürgen HEIDRICH[6]
Matthias DEMMLER[7]

[1]Faculty of Mechanical Engineering, University of Belgrade, Belgrade, Serbia, 11000; jrantic@mas.bg.ac.rs; ORCID iD: 0009-0002-6452-0294
[2]Faculty of Mechanical Engineering, University of Belgrade, Belgrade, Serbia, 11000; zmiskovic@mas.bg.ac.rs; ORCID iD: 0000-0002-8320-7191
[3]Faculty of Mechanical Engineering, University of Belgrade, Belgrade, Serbia, 11000; dpejcic@mas.bg.ac.rs; ORCID iD: 0009-0007-1661-2924
[4]Institute for Machine Tools and Production Processes, Chemnitz University of Technology, Reichenhainer Str. 70, Chemnitz, Germany, 09126; Fraunhofer Institute for Machine Tools and Forming Technology IWU, Reichenhainer Straße 88, Chemnitz, Germany, 09126; martin.dix@iwu.fraunhofer.de; ORCID iD: 0000-0002-2344-1656
[5]Fraunhofer Institute for Machine Tools and Forming Technology IWU, Reichenhainer Straße 88, Chemnitz, Germany, 09126; alexander.pierer@iwu.fraunhofer.de; ORCID iD: 0000-0003-1881-8989
[6]Fraunhofer Institute for Machine Tools and Forming Technology IWU, Reichenhainer Straße 88, Chemnitz, Germany, 09126; juergen.heidrich@iwu.fraunhofer.de
[7]Fraunhofer Institute for Machine Tools and Forming Technology IWU, Reichenhainer Straße 88, Chemnitz, Germany, 09126; matthias.demmler@iwu.fraunhofer.de

Abstract: *This study examines the effects of Deep Cryogenic Treatment (DCT) applied after conventional quenching (Q) and tempering (T) on the hardness of rolling bearing balls—a geometric shape that has been significantly less studied compared to other sample forms, such as plates or cylindrical specimens. The primary objective is to determine whether DCT, when applied to commercially available rolling bearing balls (supplied by the manufacturer after completing Q and T), negatively impacts their performance or enhances it. The bearing balls analyzed in this study were from bearing types 6306, 6308, and 6310, manufactured from 100Cr6/AISI 52100 steel. The DCT process involved a controlled cooling rate of 1.5°C per minute, a soaking temperature of -160°C, and a soaking duration of 24 hours. Experimental results revealed that the hardness of the bearing balls remained largely unchanged, with a percentage variation of less than 1% across all tested bearings. Although previous studies on the same bearing material have suggested that DCT can improve hardness, our findings indicate that this effect may not be as significant when DCT is applied to bearing balls after quenching and tempering under the specific conditions of this study. Future research will explore the influence of DCT on additional factors such as dimensional stability, surface roughness, and residual stress to gain a more comprehensive understanding of its overall impact on bearing performance.*

Keywords: *Deep Cryogenic Treatment; Rolling bearings; Ball bearings; 100Cr6 material; Hardness*

1. INTRODUCTION

Ball bearings are essential components in a wide variety of mechanical systems, where they serve to reduce rotational friction while supporting both radial and axial loads. Their pivotal role in ensuring smooth operation and optimal performance across numerous applications underscores the importance of their reliability and longevity. As such, considerable efforts are consistently directed towards improving ball bearing performance, with a focus on enhancing the material properties of their components, which must withstand significant mechanical and thermal stresses during operation.

The research presented in this paper is part of a broader study aimed at assessing whether applying Deep Cryogenic Treatment (DCT) to commercially available bearing assemblies, including their rolling elements, can

enhance their operational characteristics - specifically service life, wear resistance, and overall strength.

DCT usually involves gradually cooling the material to extremely low temperatures, well below 0°C, maintaining this temperature for a specified period (soaking time), and then gradually reheating the material to room temperature. As there are no universally defined parameters for DCT, determining optimal conditions requires comprehensive research and comparison of results.

In this research, bearing balls were selected for treatment due to their distinct cooling behavior. Unlike bearing rings, which undergo a more uniform cooling process, bearing balls experience pronounced temperature differences between their surface and core. This unique characteristic makes them especially valuable for investigating the effects of DCT. The temperature gradients within the balls can influence residual stresses and microstructural changes, ultimately affecting the distribution of hardness across the material.

The sequence of thermal treatments, such as quenching (Q), DCT, and tempering (T), is not universally standardized and often varies depending on the application. In this study, however, the bearing balls were acquired from the manufacturer after having already undergone quenching and tempering, requiring DCT to be applied as a subsequent step (Q-T-DCT) – presented at the Figure 1.

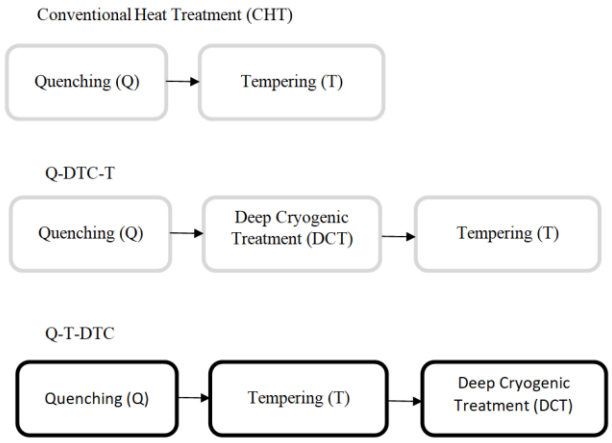

Fig.1. Schematic representation of different heat Treatment Sequences

2. LITERATURE REVIEW

Based on the literature reviewed, it is widely acknowledged that the increase in hardness observed with DCT is primarily attributed to the extremely low temperatures, which facilitate the transformation of a larger proportion of austenite into martensite— a phase known for its higher hardness—compared to results achieved through Conventional Heat Treatment (CHT).

While numerous studies have focused on the impact of DCT on tool steels and high-speed steels, there has also been growing interest in its application to bearing steels. These studies examine how DCT affects the mechanical properties of bearing materials by exploring various cryogenic treatment parameters, sample shapes, thermal treatment sequences, and bearing steel types.

In one study [1], a cylindrical sample of AISI 52100 bearing steel (18 mm in diameter, 10 mm in height) was analyzed. The analysis of retained austenite revealed that after CHT, 14% of austenite remained, while only 3% was present after DCT. As a result of this transformation from austenite to martensite, hardness increased by 15%. The DCT process was carried out at -180°C with a soaking time of 24 hours.

Another study focused on 100Cr6 bearing steel, using samples of 6 mm diameter and 6 mm height, which were subjected to DCT at -185°C for 24 hours. The results indicated an 18% increase in hardness. The cryogenic treatment was effective in reducing retained austenite and promoting the precipitation of fine secondary carbides, which strengthened the material through dispersion hardening. Additionally, the smaller grain size of martensite compared to austenite further contributed to the hardness improvement [2].

In a separate study [3], samples measuring 10 mm in diameter and 10 mm in height underwent a treatment sequence involving quenching, tempering, DCT, and a second tempering step. Four key metallurgical factors were identified to explain the observed changes in material properties: the transformation of retained austenite to martensite, the formation of eta-carbides, the precipitation of ultrafine carbides, and the development of a more homogeneous microstructure. As a result, hardness increased by 10% compared to conventional heat treatment.

Research has also extended to other bearing materials, such as AISI 400C. In one study [4], bearing steel samples with a square cross-section (10x10 cm) underwent two types of cryogenic treatments: Shallow Cryogenic Treatment (SCT) at -80°C for 5 hours and DCT at -196°C for 24 hours. The findings revealed a 4% increase in hardness after SCT and a 7% increase after DCT, highlighting the significant impact of cryogenic treatment on the material's hardness properties.

The effects of cryogenic treatment have also been investigated for EN 31 bearing steel. In study [5], both SCT and DCT were applied to samples, showing a 13% increase in hardness for SCT and a 14% increase for DCT when compared to CHT.

While many studies report a hardness increase following DCT, there are cases where no improvement was observed. For example, a study [6] investigated various cryogenic treatment sequences on tool steels AISI D2 and Vanadis 4E, including Q-T, Q-DCT, Q-DCT-T, and Q-T-DCT. The Q-T-DCT sequence, which mirrors the approach used in this study, resulted in a 3% decrease in hardness compared to conventional Q-T treatment. Despite the reduction in hardness, other material properties, such as cyclic hardening potential, showed improvement, indicating the complex and varied effects of cryogenic treatment on different steel grades. While much of the research on DCT and bearing materials has been conducted on plate or cylinder shaped specimens, there is limited research on how actual bearing components respond to such treatments. This study seeks

to address this gap by applying DCT to bearing balls and analyzing the resultant changes in their hardness.

3. BEARING BALLS TEST SAMPLES

The test samples in this experiment consisted of bearing balls (rolling elements) from bearing types 6306, 6308, and 6310, commonly used in conveyor idlers. The average diameters of the balls were approximately 12.303 mm, 15.081 mm, and 19.052 mm, respectively. These balls were made from 100Cr6 steel (SAE/AISI 52100), a material classified as "ball and roller bearing steel" according to the SRPS EN ISO 683-17:2023 standard [7]. The chemical composition of the material is presented in Table 1.

Table 1. Material specification of 100Cr6 steel

Chemical composition (%):	C	Si	Mn	Cr	other
	1.00	0.25	0.35	1.50	-

The bearing balls were obtained from the manufacturer after undergoing conventional quenching and tempering processes. As a result, the cryogenic treatment was applied following these two steps, rather than between quenching and tempering, which is the conventional procedure.

Fig.2. Ball Bearing Samples: 6306, 6308, and 6310 Types

4. DEEP CRYOGENIC TREATMENT (DCT) PARAMETERS

In this study, the Deep Cryogenic Treatment (DCT) process was conducted under precisely controlled conditions to assess its effect on the hardness of bearing balls. The temperature was gradually reduced at a rate of 1.5°C per minute until it reached -160°C, where the bearing balls were held for a soaking period of 24 hours. Afterward, the temperature was slowly increased back to room temperature (20°C) at the same rate of 1.5°C per minute. These gradual cooling and warming rates were used to minimize thermal stresses and avoid microstructural damage.

Figure 3 illustrates the temperature profile during the DCT process, highlighting the cooling, soaking, and warming stages.

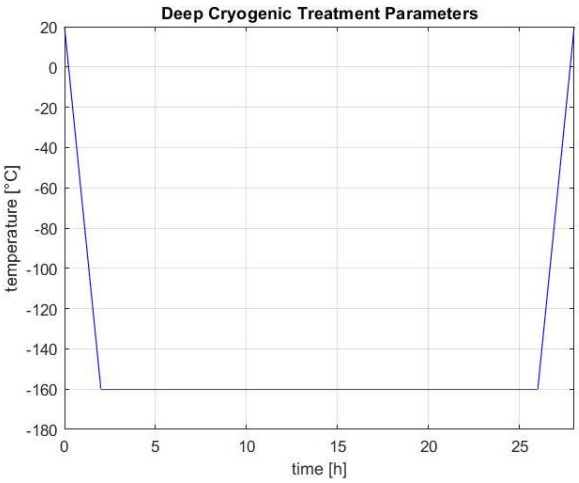

Fig.3. DCT Temperature-Time Profile

5. HARDNESS MEASUREMENTS

The hardness of the bearing balls was measured using the Zwick Roell ZHU 2.5 Universal Hardness Testing Machine, which is capable of high-precision testing using various methods, including Rockwell, Vickers, and Brinell. For this study, the Rockwell C hardness test (HRC) was utilized, following the SRPS EN ISO 6508-1:2017 standard [8]. Figure 4 illustrates the Zwick Roell ZHU 2.5 machine, which was used for hardness testing in this research, located in the accredited LIMES laboratory (Laboratory for Testing of Machine Elements and Systems) at the Faculty of Mechanical Engineering, University of Belgrade. According to [9], the hardness of bearing balls must be within the range of 58 to 66 HRC (Rockwell Hardness).

Fig.4. Universal Hardness Testing Machine Zwick Roell ZHU 2.5

6. EXPERIMENTAL RESULTS

The hardness measurements of the bearing balls, both before and after Deep Cryogenic Treatment (DCT), are shown in Table 2. For the 6306 bearing ball, the hardness increased slightly from 64,4 HRC to 64,9 HRC, resulting in a difference of 0,5 HRC and a percentage increase of 0,78%. In contrast, the 6308 bearing ball experienced a decrease in hardness from 64,4 HRC to 64,1 HRC, reflecting a change of -0,3 HRC and a percentage change of -0,47%. Similarly, the 6310 bearing ball showed a reduction in hardness from 65,5 HRC to 65,3 HRC, indicating a difference of -0,2 HRC and a percentage change of -0,31%.

For all bearing ball types, the percentage change in hardness after DCT was below 1%, indicating that the observed variations are minimal and not significant under the conditions of this study.

Table 2. Hardness values of bearing balls before and after Deep Cryogenic Treatment

	Before DCT [HRC]	After DCT [HRC]	Difference [HRC]	Percentage change [%]
6306	64,4	64,9	0,5	0,78
6308	64,4	64,1	-0,3	-0,47
6310	65,5	65,3	-0,2	-0,31

7. CONCLUSIONS

The primary aim of this research was to assess the potential for increasing or decreasing the hardness of commercially available bearing balls, which are delivered in a quenched and tempered state. To achieve this, Deep Cryogenic Treatment (DCT) was applied following these initial processes. The DCT was carried out with a cooling rate of 1.5°C per minute, a soaking temperature of -160°C, and a soaking duration of 24 hours. The results showed only minimal changes in the hardness of all three treated bearing ball types, with percentage variations staying below 1%. This outcome differs from the expectations set by previous studies on the same material (100Cr6 / AISI 52100), which typically observed an increase in hardness after DCT. This discrepancy can be explained by the fact that previous research applied DCT between quenching and tempering, while in this study, DCT was applied after both of these treatments. It is also important to note that the decrease in the hardness of the bearing ball material is not significant enough to negatively affect their wear resistance or service life.

Although no significant improvement in hardness was observed, this does not suggest that DCT lacked beneficial effects on the bearing ball's material properties. Other mechanical and microstructural characteristics may have been positively influenced, which requires further examination. Future research will focus on these aspects to provide a more comprehensive understanding of how DCT affects bearing performance.

As noted in [10], future studies will also investigate the impact of DCT on additional parameters such as dimensional stability, surface roughness, and residual stress, with the goal of offering deeper insights into the effects of DCT on bearing performance.

ACKNOWLEDGMENT

The results presented in this paper are the results of the cooperation between the Faculty of Mechanical Engineering at the University of Belgrade (Belgrade, Serbia) and Fraunhofer Institute (Chemnitz, Germany) within study supported by the Ministry of Science, Technological Development, and Innovation of the Republic of Serbia under Contract No. 451-03-137/2025-03/200105, dated February 4, 2025.

REFERENCES

[1] Shunmuga Priyan, M., Siva, R.: Residual Stress and Wear Studies of Deep Cryogenically Treated SAE 52100 Bearing steel. *Journal of Mechanical Engineering,* Vol. 16, No. 3, pp. 91-104, ISSN 1823-5514, 2019

[2] Siva, R. S., Jaswin, M. A., & Lal, D. M.: Enhancing the Wear Resistance of 100Cr6 Bearing Steel Using Cryogenic Treatment. *Tribology Transactions,* Vol.55, No.3, pp. 387-393, ISSN 1547-397X, 2012

[3] Kara, F., Cicek, A., Demir, H.: Effect of Deep Cryogenic Treatment on Microstructure, Mechanical Properties, and Residual Stress of AISI 52100 Bearing Steel. *Engineered Science*, Vol. 26, 2023

[4] Idayan, A., Gnanavelbabu, A., Rajkumar, K.: Influence of Deep Cryogenic Treatment on the Mechanical Properties of AISI 440C Bearing Steel. *Procedia Engineering,* Vol. 97, pp. 1683-1691, ISSN 1877-7058, 2014

[5] Harisha, S., Benselyb, A., Mohan Lalb, D., Rajaduraic, A., Lenkeyd, B.: Microstructural study of cryogenically treated En 31 bearing steel. *Journal of Materials Processing Technology*, Vol. 209, No.7, pp. 3351-3357, ISSN 0924-0136, 2008

[6] Blinn, B., Winter, S., Weber, M., Demmler, M., Kräusel, V., Beck, T.: Analyzing the influence of a deep cryogenic treatment on the mechanical properties of blanking tools by using the short-time method PhyBaLCHT. *Materials Science and Engineering:A*, Vol. 824, ISSN 0921-5093, 2021

[7] SRPS EN ISO 683-17:2023, Heat-treated steels, alloy steels and free-cutting steels - Part 17: Ball and roller bearing steels

[8] SRPS EN ISO 6508-1:2017, Metallic materials - Rockwell hardness test - Part 1: Test method

[9] Rulebook on Technical and Other Requirements for Roller Bearings, Official Gazette of the Republic of Serbia, No. 98/2016 and 66/2018

[10] Mišković, Ž., Antić, J., Pierer, A., Heidrich, J., Mitrović, R.: Deep cryogenic treatment of rolling bearings - initial experimental results, *Proceedings of International Conference of Experimental and Numerical Investigations and New Technologies – CNN TECH 2022,* 5-8 July 2022, Zlatibor, Serbia, pp. 23, ISBN: 978-86-6060-120-1, 2022

11th International Scientific Conference
IRMES 2025
Research and Development of
Mechanical Elements and Systems
June 19 – 21, 2025; Vrnjačka Banja, Serbia

Original scientific paper DOI: 10.46793/IRMES25.005K

ANALYSIS OF THE INFLUENCE OF WAVINESS AND AXIAL LOAD ON THE DYNAMIC BEHAVIOR OF BALL BEARINGS

Ivan KNEŽEVIĆ[1]
Milan RACKOV[2]
Aleksandar ŽIVKOVIĆ[3]
Mirjana BOJANIĆ ŠEJAT[4]
Željko KANOVIĆ[5]

[1]PhD Ivan Knežević, Novi Sad, Serbia, 21000; ivanknezevic@uns.ac.rs; ORCID iD: 0000-0002-6573-756X
[2]PhD Milan Rackov, Novi Sad, Serbia, 21000; racmil@uns.ac.rs; ORCID iD: 0000-0003-4956-5849
[3]PhD Aleksandar Živković, Novi Sad, Serbia, 21000; acoz@uns.ac.rs; ORCID iD: 0000-0003-2274-4927
[4]PhD Mirjana Bojanić Šejat, Novi Sad, Serbia, 21000; bojanicm@uns.ac.rs; ORCID iD: 0000-0003-1963-0195
[5]PhD Željko Kanović, Novi Sad, Serbia, 21000; kanovic@uns.ac.rs

Abstract: Deep groove ball bearings are one of the most commonly used shaft support. Beside material quality, internal geometry of bearing raceways has the key role in bearing quality. One of the most common ways to inspect bearing quality is measuring of the vibration level. Paper presents analysis of the influence of waviness of the raceways on the vibrations. Axial load were investigated as influential factor. Experimental data were analyzed, and neural network was trained to analyze dynamic behaviour of ball bearing. Prediction of neural network is used for determination of correlation between analyzed factors and vibration level in three frequency bands.

Keywords: *waviness; axial load; ball bearing; neural network, analysis.*

1. INTRODUCTION

Deep groove ball bearings are used in various machine systems, from the simplest applications to those operating in demanding operating conditions. The final stage of the deep groove ball bearing manufacturing process requires quality control. One of the quality control processes that is carried out is the measurement of vibrations generated by the bearing and checking the size of the internal radial clearance of the bearing for classification.

In addition to the quality of the material, the internal geometry of the bearing raceways plays a key role in the quality of the bearings. One of the most common ways to check the quality of bearings is to measure the vibration level. The paper presents an analysis of the influence of wavy raceways on vibrations.

A mathematical model for determining the nonlinear dynamic behavior of ball bearings that takes into account the waviness and the number of rolling elements is proposed by Harsha and Kankar [1]. The analysis is performed on a rigid rotor supported by ball bearings, and the contact between the rolling elements and the raceways is represented by a nonlinear spring. The spring stiffness is determined using Hertz's contact theory and the stability of the rigid rotor is analyzed. The nonlinear differential equations are solved iteratively using the Newmark-β technique with the Newton-Raphson method. The results indicate that the number of rolling elements participating in the load transfer and the number of waves are. Theoretical and experimental studies of the influence of the waviness of the raceways on the vibrations generated by the bearing are presented by Shah and Patel [2]. The dynamic model takes into account the mass of the shaft, rings, and housing. They conclude that there is a correlation between the theoretical and experimental results and that large vibration amplitudes occur when the number of waves is equal to the number of rolling elements. on the rolling element is a significant parameter that affects the dynamic behavior of the system. Experimental research on the influence of rolling surface waviness on vibration amplitudes in frequency ranges defined by the standard was carried out by Adamczak and Zmarzli [3]. The analysis of the results shows that increasing the waviness of the outer and inner raceways affects the increase in vibration amplitudes in all ranges. Liu and Shao [4] investigate the influence of the number of waves, the maximum wave amplitude and the uneven distribution of waviness on the vibrations of a rolling bearing. The dynamic model takes into account the change in the bearing structure and the change in stiffness at the lubricated contact point affected by waviness. The presented model gives more accurate results than others available in the literature. Yang and Jeong [5] present an analytical model to investigate the vibrations caused by ball bearing waviness in a system supported by two or more bearings. The model takes into account the centrifugal force and gyroscopic moment of the ball, and the waviness is described by sinusoidal functions. They

show that the gyroscopic moment and centrifugal force of the ball, along with waviness, affect the fundamental frequencies and harmonics at which the vibration amplitude occurs. Mathematical model for predicting vibration response proposed by Choudhury and Tandon, where they consider the distribution of defects on the raceways as waviness, in a radially loaded bearing [6]. Akturk [7] investigates the influence of the waviness of the racewasy of a ball bearing on vibrations in the radial and axial directions. The developed model simulates the waviness of the raceways of the outer and inner rings, as well as of the rolling elements. The result of the simulations is a spectrum of vibrations in the time and frequency domains. The results show that the waviness of the racewasy of the outer ring occurs at the amplitudes at the frequency of the passing of the rolling bodies and its harmonics.

2. MATERIALS AND METHODS

In this paper, deep groove ball bearing of the designation 6006 were analyzed. The set consisted of 30 bearings that were divided into five groups according to the size of the radial clearance. In addition to the size of the radial clearance, the characteristics of the bearings internal geometry were analyzed, that is, the geometric characteristics of the raceways of the inner and outer rings of each bearing in the sample. Geometric deviations were measured using the Taylor-Hobson Form Talysurf 112/1849 device as shown in Figure 1.The statistical features of the geometric deviations and internal radial clearance are presented in Table 1.

They are internal radial clearance (G_r), raceway radius ratio (R_i/R_e), surface roughness of the raceway of the outer ring (R_{ae}), raceway waviness of the outer ring ($W_{te\ max}$), deviation from the circularity of the raceway of the outer ring (W_{te}) surface roughness of the raceway of the inner ring (R_{ai}), raceway waviness of the inner ring ($W_{ti\ max}$), and deviation from the circularity of the raceway of the inner ring (W_{ti}).

Fig.1. Taylor–Hobson Form Talysurf 112/18

The geometric deviation parameters of the raceways for the inner and outer rings are independent. Production process of inner and outer rings gives independent surface characteristics of all rings. Mounting process of ball bearings normally do not consider geometric surface characteristics. One way to consider differences is introducing the equivalent parameters of geometric surface characteristics.

The equivalent amplitude of raceway waviness (*Wt max ekv*) is calculated as:

$$W_{t\max\ ekv} = \frac{W_{te\max} \cdot W_{ti\max}}{W_{te\max} + W_{ti\max}} \tag{1}$$

Table 2 shows the main statistical characteristics of equivalent bearing parameter.

Table 1. Main statistical characteristics of analyzed bearing parameters

Bearing Characteristics	Minimum Value x_{min}	Maximum Value x_{max}	Mean Value $\bar{x}$	Standard Deviation s
G_r, [µm]	6	51	24.03	14.54
R_i/R_e	0.95	0.98	0.96	0.01
R_{ae}, [µm]	0.07	0.28	0.13	0.04
R_{ai}, [µm]	0.07	0.56	0.26	0.1
$W_{te\ max}$, [µm]	0.1	1.97	0.8	0.32
$W_{ti\ max}$, [µm]	0.25	0.66	0.39	0.13
W_{te}, [µm]	1.5	17.82	5.01	2.86
W_{ti}, [µm]	0.4	2.63	0.92	0.41

Table 2. Statistical characteristic of equivalent bearing parameter

Bearing Characteristic	Minimum Value x_{min}	Maximum Value x_{max}	Mean Value $\bar{x}$	Standard Deviation s
$W_{te\ max\ ekv}$	0.16	0.47	0.25	0.06

Beside measurement of geometrical characteristics of ball bearing rings, vibration velocity amplitudes are measured. The measurement of vibration velocity amplitudes was carried out using a device for measuring and analyzing bearing vibrations. Figure 2 shows the experimental device consisting of a test table on which there is a

spindle mounted with hydrodynamic bearings, a pneumatic cylinder for axial loading of the bearing, a drive motor and a control cabinet (control unit). The bearing is placed over the inner ring on the measuring mandrel, which is connected to the spindle by means of a cone and a threaded connection. During the measurement, the spindle rotates at a constant number of revolutions (n = 1800 RPM) with a permissible deviation of +1% and -2%, according to ISO 15242-1. The outer ring is stationary and loaded with an axial load via a pneumatic cylinder, as standard ISO 15242-21 recommends. The basic element in the vibration measurement chain is the electrodynamics pickup (Figure 3) that generates a voltage at its output, and whose amplitude and frequency is proportional to the velocity of the vibrations generated by the ball bearing. The electrodynamic pickup is connected to a computer by a USB cable, which controls the measurement process and stores the measured signals. The measurement takes 5 seconds from the moment the bearing reaches a constant rotation velocity. Since the amplitude of the signal obtained by the electrodynamic pickup used is small, the signal is amplified by an amplifier for digital processing and display.

Fig.2. Experimental device for measuring

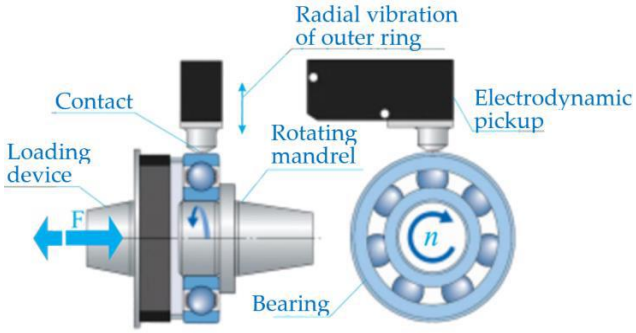

Fig.3. Schematic view of the vibrations measuring principle using the electrodynamic pickup.

A block diagram illustrating the measurement and control system for the vibration testing of ball bearings is shown in Figure 4. The elements responsible for analogue signal processing are the amplifier and the bandwidth filter. The amplifier has the task of amplifying the signal level from the electrodynamic velocity sensor to a level suitable for digital processing and display. An amplifier with a gain of 1500 was used, providing sufficient signal amplitude for digital processing. The frequency band of the signal that is of interest for vibration testing of ball bearings is from 50 Hz to 10 kHz. The filter functions to limit the spectrum of the signal received from the amplifier to the mentioned band. The designed filter introduces a relatively small attenuation of wave oscillations in one or more frequency bands and a relatively large attenuation for oscillations of other frequencies (below 50 Hz and above 10 kHz) according to the ISO 15242-1 standard. The bandwidth of the filter is also defined based on the mentioned standard. Signal digitization is performed using the NI DAQ USB-6009 measurement acquisition system. The sampling frequency is 48 kHz, while the resolution of the internal A/D converter is 13 bits. In this way, the quality preparation of the signal obtained using the electrodynamic velocity sensor and its digitization for further computer processing is ensured.

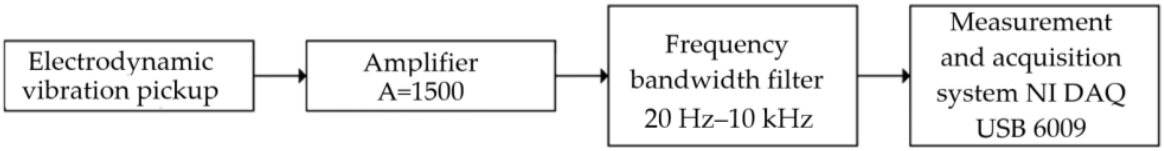

Fig.4. Block diagram of the measurement and control system

The signal recorded in the time domain is transformed into the frequency domain for further analysis using fast Fourier transformation. The standard requires the analysis of vibrations in three characteristic frequency bands, namely, low frequencies (50 ÷ 300 Hz), medium frequencies (300 ÷ 1800 Hz), and high frequencies (1800 ÷ 10,000 Hz).

2.1. Analysis of Measured Data

The measurements of the geometric characteristics of the bearing raceway and the amplitude of the vibration velocity were analyzed to find mutual dependencies. The analysis was performed by calculating the coefficients of linear correlation between the characteristic parameters of the bearing and the amplitude of the vibration velocity in the frequency bands. In this analysis, the input parameters were the geometric characteristics of the bearing raceway, and the output velocities of vibrations in characteristic bands. The analyzed cases were those when the geometric characteristics of the bearing raceway were observed for each ring separately and when equivalent parameters were used. Figure 5 shows the values of the linear correlation coefficient of the characteristic bearing parameters where the technological parameters are observed for the outer and inner ring separately according to the characteristic frequency bands. The linear correlation coefficients of the bearing parameters for the low-frequency band are shown in Figure 5a. The highest correlation coefficient was found for the deviation from circularity of the outer ring,

followed by waviness and surface roughness of the outer ring. The next most important influencing parameter was the surface roughness of the inner ring, followed by the ratio of the radius of the raceway, the radial clearance, the deviation from the circularity and the waviness of the inner ring.

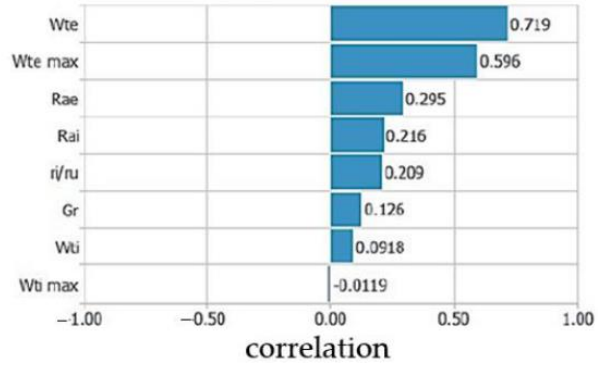

Fig.5a. Linear correlation coefficients of bearing parameters and low- frequency band

Figure 5b shows the linear correlation coefficients of the bearing parameters for the medium-frequency band. The surface roughness of the outer ring has the highest influence, followed by the deviation from the circularity of the outer ring, the ratio of the radius of the raceway, the waviness of the outer ring, the radial clearance, and further parameters of the inner ring of the bearing. The correlation coefficients are lower compared with the correlation coefficients in the low-frequency band. The linear correlation coefficients of the bearing parameters for the high-frequency band are shown in Figure 5c. The values of the coefficients are significantly lower compared with the low and medium frequency bands. The surface roughness of the inner ring, the deviation from the circularity of the outer ring and the radial clearance have the highest influence. Parameters with low influence are the surface roughness of the outer ring, the ratio of the radius of the raceway, the waviness of both rings and the deviation from the circularity of the inner ring.

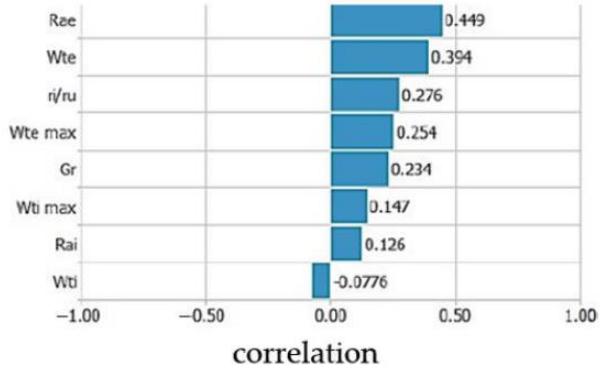

Fig.5b. Linear correlation coefficients of bearing parameters and medium- frequency band

The linear correlation coefficients of the bearing parameters for the high-frequency band are shown in Figure 5c. The values of the coefficients are significantly lower compared with the low and medium frequency

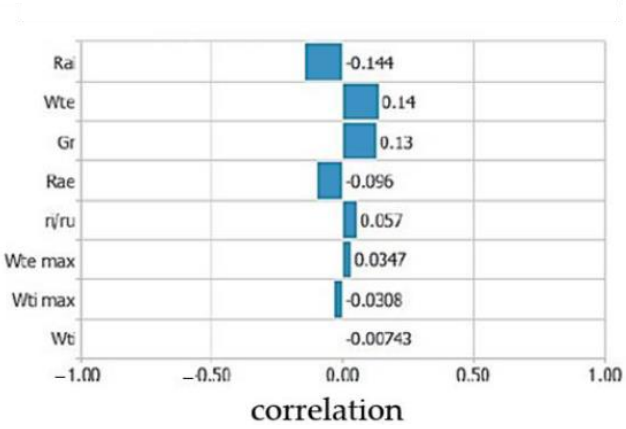

Fig.5c. Linear correlation coefficients of bearing parameters and high- frequency band

bands. The surface roughness of the inner ring, the deviation from the circularity of the outer ring and the radial clearance have the highest influence. Parameters with low influence are the surface roughness of the outer ring, the ratio of the radius of the raceway, the waviness of both rings and the deviation from the circularity of the inner ring.

Figure 6 shows the linear correlation coefficients of the characteristic bearing parameters and equivalent technological parameters in the three frequency bands. Figure 6a shows the linear correlation coefficients of the bearing parameters for the low-frequency band. The highest correlation coefficient was observed for the equivalent surface roughness, followed by the ratio of the radius of the raceways. Equivalent waviness and equivalent deviation from roundness were the next two influencing parameters. Radial clearance had the least influence in the low-frequency band.

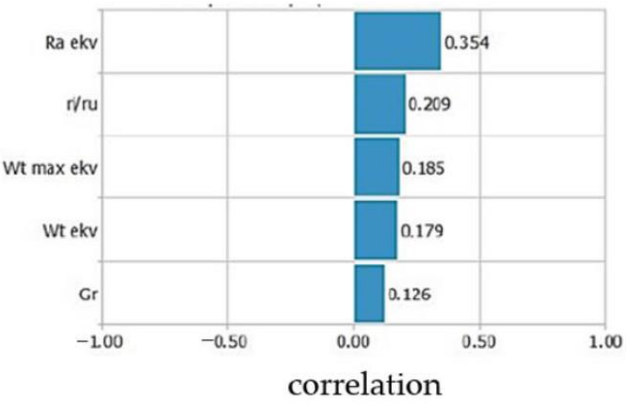

Fig.6a. Linear correlation coefficients of bearing parameters and frequency bands (equivalent technological parameters) in low-frequency band

Figure 6b shows the linear correlation coefficients of the bearing parameters for the medium-frequency band. The equivalent surface roughness has the highest influence, followed by the ratio of the radius of the raceways and the radial clearance. The less influential parameters were equivalent waviness and deviation from circularity.

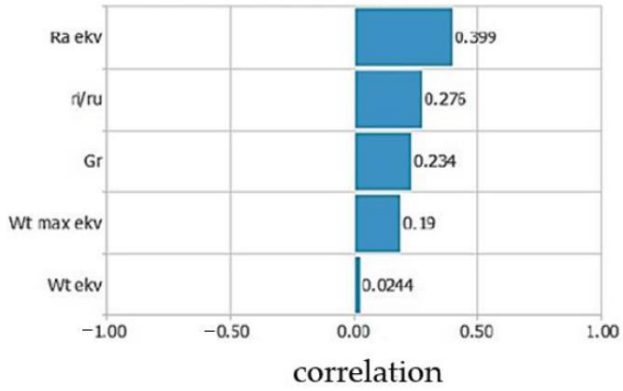

Fig.6b. Linear correlation coefficients of bearing parameters and frequency bands (equivalent technological parameters) in medium-frequency band

The linear correlation coefficients of the bearing parameters for the high-frequency band are shown in Figure 6c. The values of the coefficients were also significantly lower compared with those for the low and medium-frequency bands.

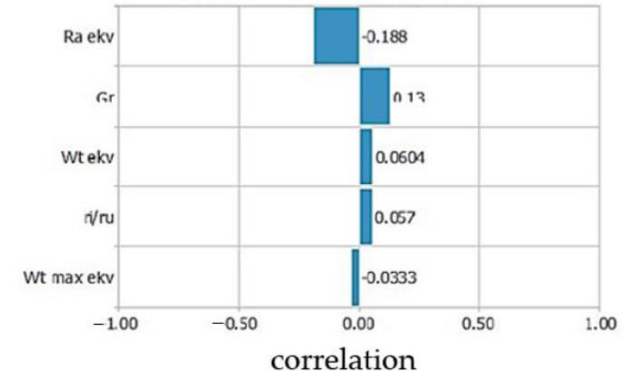

Fig.6c. Linear correlation coefficients of bearing parameters and frequency bands (equivalent technological parameters) in high-frequency band

The equivalent surface roughness had the highest influence, which affects the reduction of the vibration velocity amplitudes. Radial clearance was the next most important influencing parameter. The parameters with lower influence were the equivalent deviation from circularity, the ratio of the radius of the raceways and equivalent waviness.

2.2. Application of the Neural Network

Artificial neural networks are used in this paper to investigate the influence of the surface waviness of the raceways and the clearance in the bearing on the vibration velocity amplitudes. The paper applies a multilayer perceptron (MLP), where a feedforward signal and a learning algorithm with error backpropagation are used. The neural network has one hidden layer with d inputs, k neurons in the hidden layer, and one output, and the total ratio of inputs to outputs in this case is a function of $f : \mathbf{R}^d \to \mathbf{R}$ which maps the input vector $x \in \mathbf{R}^d$ into a scalar output using the following equation [8]:

$$x \to f_{v,} w(x) := \sum_{i=1}^{k} v_l \phi\left(\left(w_l, x\right)\right) \tag{2}$$

Vectors $w_l \in \mathbf{R}^d$ contain weighting coefficients between the inputs and *l*-th hidden node, and $v_l \in \mathbf{R}^d$ is the weight coefficient of the *l*-th hidden node and the output. Finally, $\phi : \mathbf{R} \to \mathbf{R}^d$ denotes the activation function applied to each hidden node.

2.3. Organization of Data Set

The results of the experimental research are divided into groups of I/O parameters for the application of the artificial neural network. The input parameters are the geometric characteristics of the bearing and external load, and the output results are the vibration measurements of the bearing as shown in Figure 7. Figure 8 shows the I/O parameters when the technological parameters of the bearing are considered as equivalent.

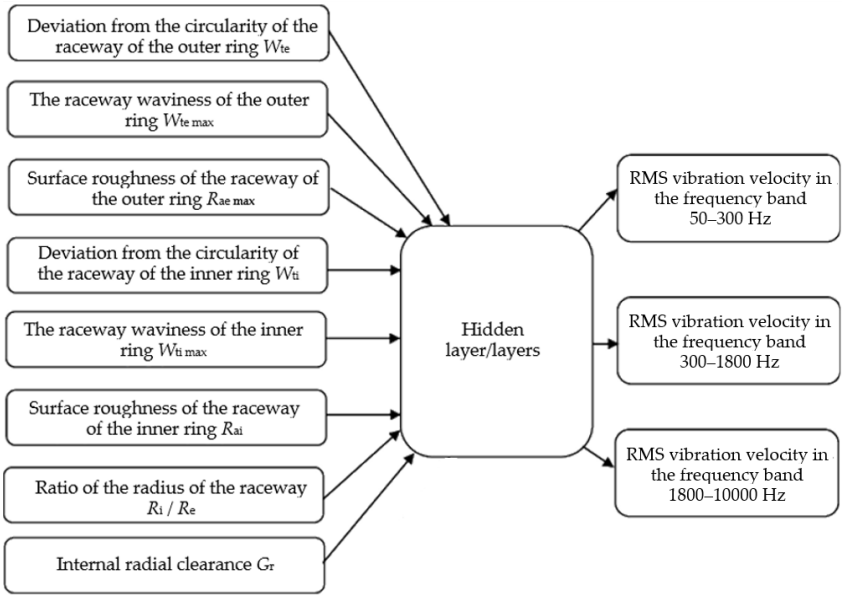

Fig.7. Structure of I/O parameters of the artificial neural network

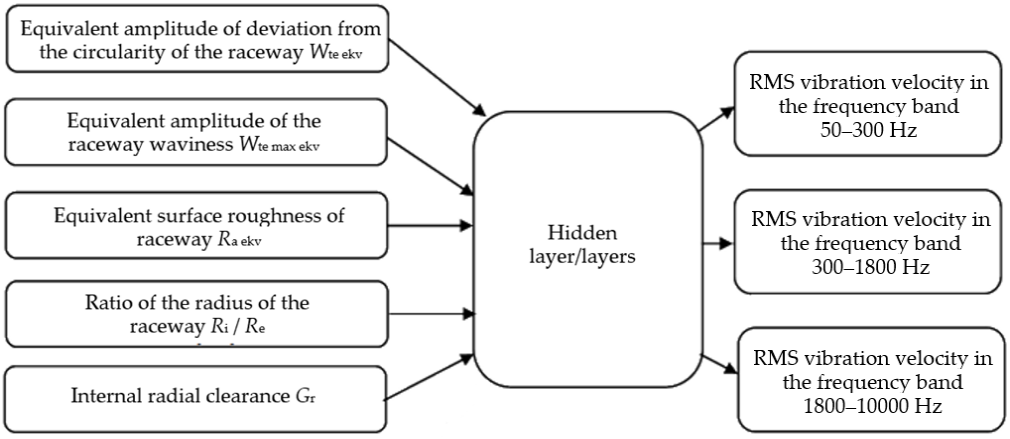

Fig.8. Structure of I/O parameters of the artificial neural network; input parameters are considered together (equivalent technological parameters)

Output data is pre-processed by linear scaling in the interval from 0.5 to 0.8 according to equation:

$$x_{skal} = \bar{x}_{\min} + \frac{x - x_{\min}}{x_{\max} - x_{\min}} \cdot \left(\bar{x}_{\max} - \bar{x}_{\min} \right) \quad (3)$$

The training was conducted with three different training algorithms: Levenberg–Marquardt (LM), Bayesian Regularization (BR), and Scaled Conjugate Gradient (SCG). The training process of the artificial neural networks was carried out for each training configuration, which includes the training algorithm, the number of hidden layers, and the number of neurons in the hidden layer. A special training algorithm was created to enable automation of the training process. An algorithm was written to enable the training process to be repeated *n* times for a certain configuration. Every configuration has 28 neural networks.

2.4. Selection of Artificial Neural Network Models

One set consists of 28 networks that are tested on two previously separated bearings. The adopted result is the mean value of the predicted vibration velocity amplitude in all three bands for all 28 networks. The separate average values of the prediction fault for all three bands, and the cumulative values of the Pearson's correlation coefficient and the coefficient of determination are calculated for all 10 sets. Based on the calculated parameters, the sets are evaluated, and the set with the smallest fault and the highest values of Pearson's correlation coefficient and coefficient of determination is adopted. After calculating the parameters for evaluating the prediction quality of the artificial neural network, the model with the best prediction was selected. The model with the lowest prediction fault had one hidden layer with 11 neurons, and the scaled conjugate gradient (SCG) training algorithm was then applied. With this model, the technological parameters of the bearing were observed separately. The average prediction fault of the selected model was 8.1% in each frequency band. The adopted model was further used for the purpose of predicting the quality class of a new ball bearing and analyzing the influence of the surface roughness of the raceway and the internal radial clearance on the bearing vibrations. The best performing model, where technological parameters were considered together (equivalent), had 3 hidden layers with 15 neurons in each layer, used a Levenberg–Marquardt training algorithm and achieved a prediction fault of 8.9%.

3. RESULTS AND DISCUSSION

Figure 9 shows the mutual influence of the axial load and the amplitude of the waviness of the outer ring on the RMS value of the amplitude of the vibration velocity. In the area of low frequencies, the waviness of the outer ring does not have a significant effect on the change in the amplitude of the vibration velocity. An increase in the amplitude of the waviness of the raceway in the area of medium frequencies causes an increase in the vibration velocity, with the minimum occurring when the amplitude of the waviness is between 0.8 and 1.2 μm. In the area of high frequencies, under the effect of axial load of higher intensity, there is an increase in the amplitude of the vibration velocity with an increase in the amplitude of the waviness. When the axial load is minimal, the vibration velocity amplitudes are the highest at the minimum waviness amplitude and with the increase of the waviness amplitude above 1 μm, the vibration velocity amplitudes decrease.

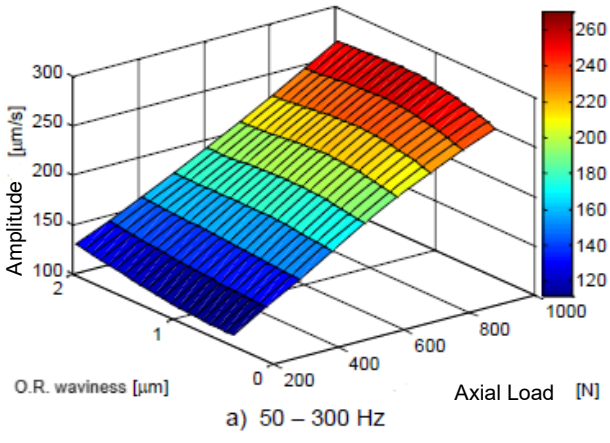

a) 50 – 300 Hz

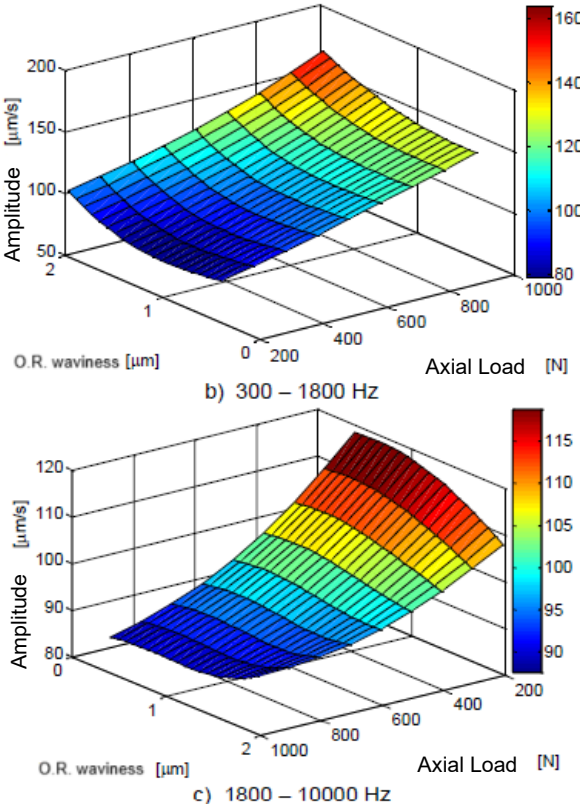

Fig.9. Mutual influence of axial load and amplitude of waviness of the outer ring on the RMS value of the amplitude of the vibration velocity

In the low frequency range, the change in the amplitude of the inner ring waviness has no significant effect on the amplitudes of the vibration velocity, regardless of the intensity of the axial load. In the area of medium and high frequency bands, the amplitudes of the vibration velocity increase slightly with the increase in the amplitude of the waviness of the raceway of the inner ring.

The amplitude of the equivalent waviness has no significant effect on the amplitude of the vibration velocity in the area of low frequencies, Figure 11. In the area of medium and high frequencies, the growth of the amplitude of the equivalent waviness affects the increase of the vibration velocity. When the amplitude is equivalent waviness less than or equal to 0.25 μm, minimum vibration velocity amplitudes are achieved. When the waviness amplitude is greater than 0.25 μm, there is a significant increase in the vibration velocity in both bands. From the point of view of the minimum amplitudes of the vibration velocity, it can be recommended that the amplitude of the equivalent waviness should not exceed 0.3 μm.

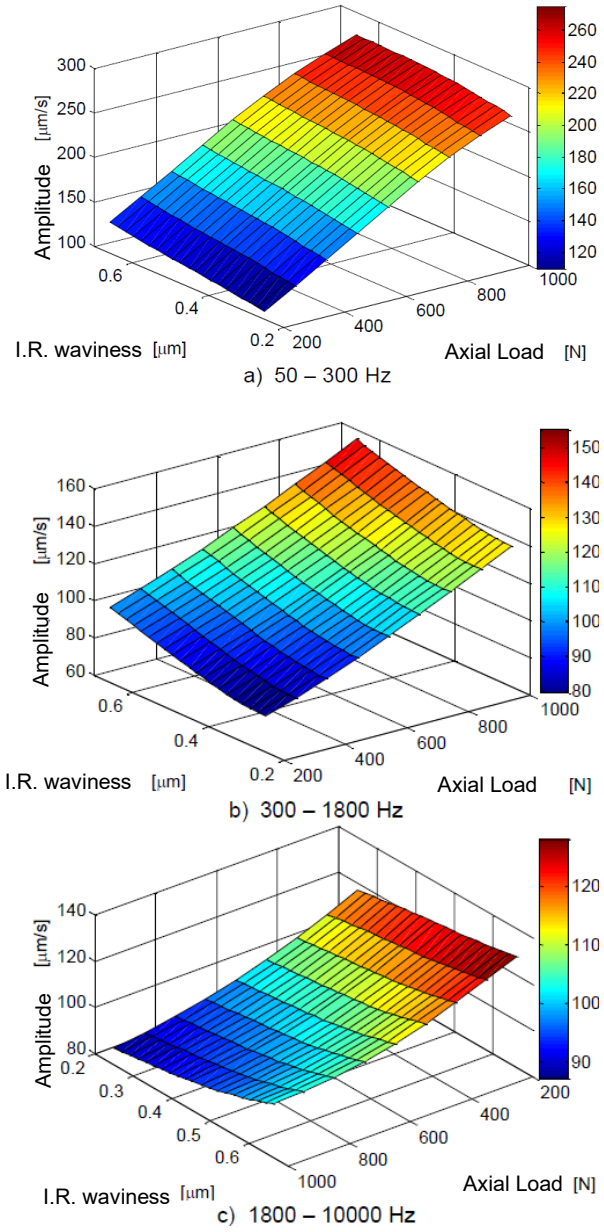

Fig.10. The mutual effect of axial load and the amplitude of the waviness of the inner ring on the RMS value of the amplitude of the vibration velocity

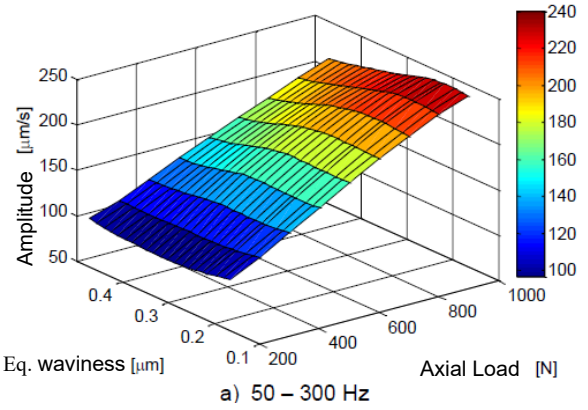

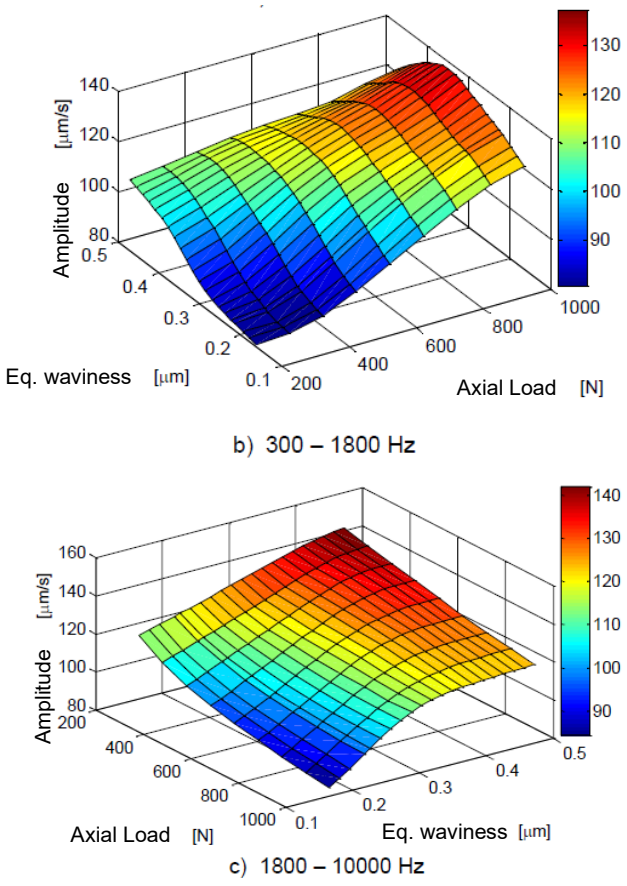

Fig.11. Mutual influence of axial load and amplitude of equivalent waviness on RMS value of amplitude of vibration velocity

4. CONCLUSION

Within the results, the impact of the axial load and the size of the waviness of the raceways of the inner and outer ring on the amplitudes of the vibrations generated by the bearing is shown. In addition, a parameter was introduced that describes the joint influence of the waviness of both rings on the amplitudes of vibration velocity in the frequency ranges. On the basis of the above, it can be concluded that the amplitude of the axial load has an almost linear and most significant influence in the low frequency band. The waviness amplitude of the outer ring has the least influence in the low frequency band, but there is a trend of increasing vibration amplitudes with increasing waviness amplitude. The results indicate that the impact is most significant in the area of high frequency band. The described trends also apply to the waviness of the inner ring. The joint influence expressed by means of the equivalent waviness indicates the most significant influence on the vibration amplitudes in the midle-frequency range.

The directions of further research in this area will be directed towards processing the influence of other technological parameters on vibration velocity. In addition, an attempt will be made to apply new models with Deep Learning neural networks that will allow for more detailed research and processing of the connection between the influential parameters and the amplitude of the vibration velocity in characteristic frequency bands.

ACKNOWLEDGMENT

This research has been supported by the Ministry of Science, Technological Development and Innovation (Contract No. 451-03-137/2025-03/200156) and the Faculty of Technical Sciences, University of Novi Sad through project “Scientific and Artistic Research Work of Researchers in Teaching and Associate Positions at the Faculty of Technical Sciences, University of Novi Sad 2025” (No. 01-50/295).

REFERENCES

[1] Harsha S, Kankar PJIJoMS. Stability analysis of a rotor bearing system due to surface waviness and number of balls. 2004;46:1057-81.

[2] Shah DS, Patel VJM. Theoretical and experimental vibration studies of lubricated deep groove ball bearings having surface waviness on its races. 2018;129:405-23

[3] Adamczak S, Zmarzły PJBotPAoSTS. Influence of raceway waviness on the level of vibration in rolling-element bearings. 2017;65:541-51

[4] Liu J, Shao YJJoV, Control. Vibration modelling of nonuniform surface waviness in a lubricated roller bearing. 2017;23:1115-32

[5] Jang G, Jeong S-WJJos, vibration. Vibration analysis of a rotating system due to the effect of ball bearing waviness. 2004;269:709-26

[6] Choudhury A, Tandon N. A theoretical model to predict vibration response of rolling bearings to distributed defects under radial load. 1998

[7] Aktürk NJJot. The effect of waviness on vibrations associated with ball bearings 1999;121:667-77

[8] Soltanolkotabi, M.; Javanmard, A.; Lee, J.D. Theoretical insights into the optimization landscape of over-parameterized shallow neural networks. IEEE Trans. Inf. Theory 2018, 65, 742–769

11th International Scientific Conference
IRMES 2025
Research and Development of
Mechanical Elements and Systems
June 19 – 21, 2025; Vrnjačka Banja, Serbia

Original scientific paper DOI: 10.46793/IRMES25.013DJ

ANALYSIS OF NATURAL FREQUENCIES OF A HYBRID ALUMINUM/COMPOSITE SHAFT

Zorica ĐORĐEVIĆ[1]
Sonja KOSTIĆ[2]
Danijela NIKOLIĆ[3]
Saša JOVANOVIĆ[4]

[1]Faculty of Engineering, University of Kragujevac, Kragujevac, Serbia, 34000; zoricadj@kg.ac.rs;
ORCID ID: 0000-0003-0194-4698
[2] Academy of Professional Studies Šumadija, Department in Kragujevac, Kragujevac, Serbia, 34000;
skostic@asss.edu.rs; ORCID ID: 0000-0002-6120-6139
[3] Faculty of Engineering, University of Kragujevac, Kragujevac, Serbia, 34000; danijelan@kg.ac.rs;
ORCID ID: 0000-0003-3267-3974
[4] Faculty of Engineering, University of Kragujevac, Kragujevac, Serbia, 34000; dviks@kg.ac.rs;
ORCID ID: 0000-0001-5916-2483

Abstract: *The study analyzes the influence of material type, shaft wall thickness, and fiber orientation angle on the natural frequencies of a hybrid aluminum/composite driveshaft for a Nissan vehicle. The composite layers were made of carbon, glass, and aramid fibers combined with epoxy resin. The analysis was conducted using the Finite Element Method (FEM) within the FEMAP 2021.2 software package. The results showed that reducing the shaft wall thickness leads to an increase in the natural frequency values. It was also concluded that hybrid shafts combining aluminum and carbon fiber/epoxy composites exhibit the highest natural frequencies, while increasing the fiber orientation angle in the layers reduces the natural frequency values for all analyzed material types.*

Keywords: *aluminum/composite driveshaft; carbon fibers; glass fibers; aramid fibers; natural frequencies.*

1. INTRODUCTION

The role of an automobile driveshaft is to transmit power, i.e., torque, from the engine to the differential gears and further to the vehicle's wheels. A specific characteristic of these shafts is the transmission of torque at varying angles between transmission components.

To achieve satisfactory natural frequency values, steel driveshafts are most commonly manufactured as two-piece assemblies connected by joints. Synchronization between shaft joints is achieved using universal (Cardan) joints, which allow angular misalignment by enabling rotation around two axes.

In order to ensure effective power transmission, a driveshaft must meet three basic requirements:

- the ability to operate at high rotational speeds, i.e., to achieve high natural frequencies,
- sufficient load-carrying capacity, i.e., the ability to transmit the required torque,
- adequate torsional flexibility.

Metal driveshafts have certain limitations, primarily due to their high mass and the inability to reach high critical speeds, i.e., rotational speeds. To reduce their weight, such shafts are typically manufactured as hollow; however, it is necessary to account for the allowable values of torsional deformation.

Given the growing emphasis on environmental protection, there is a strong motivation to reduce vehicle weight by decreasing the mass of individual components, including the driveshaft. This would directly contribute to reduced fuel consumption and lower emissions of harmful gases, thereby improving overall quality of life.

One effective approach to weight reduction is the use of composite materials—such as carbon, glass, or aramid fibers combined with suitable resins—in driveshaft manufacturing. Composite materials exhibit high specific strength (R_m/ρ) and specific modulus (E/ρ). These material properties allow the shafts to transmit the required torque, reach appropriate rotational speeds, resist corrosion and fatigue, reduce noise and vibration, and achieve a long service life, among other benefits.

In the study [1], the authors analyzed the influence of the number of layers and fiber orientation in the layers of a composite driveshaft, taking into account specific design and reliability constraints. Among other findings, it was concluded that a drive shaft made of carbon fiber reinforced plastic (CFRP) has a 30% lower mass compared to an equivalent metal shaft, while maintaining satisfactory reliability.

Study [2] focuses on the dynamic behavior of carbon/epoxy and boron/epoxy composite shafts with a mounted disk. The influence of the disk position along the shaft, as well as the fiber orientation angle in the composite, on the critical speed and natural frequencies of the shaft was analyzed.
In study [3], the authors investigated the effect of the length-to-mean-diameter ratio of carbon/epoxy, glass/epoxy, and boron/epoxy shafts on the natural frequency values. Additionally, the influence of fiber orientation angle on this characteristic was considered.
The main objective of study [4] was to explore the feasibility of manufacturing driveshafts from more environmentally friendly materials. In addition to different materials (natural fibers, synthetic fibers, and hybrid natural/synthetic fibers combined with epoxy resin), the effects of fiber orientation and laminate stacking sequence on stress levels and natural frequencies were also examined.
In study [5], the authors investigated whether natural fibers can adequately replace synthetic fibers in driveshaft manufacturing. They analyzed both solid and hollow shafts made of kenaf fibers, as well as hybrid shafts combining glass and kenaf fibers. It was concluded that hybrid shafts exhibit significantly better performance characteristics, and that, when using composite materials, it is crucial to align the reinforcing fibers in the direction of the applied load.
In study [6], the authors explored the potential of replacing conventional steel driveshafts with composite shafts made from basalt/epoxy, carbon/epoxy, and carbon nanotube (CNT) reinforced carbon/epoxy composites. The results indicated that the use of composite materials can lead to weight savings of up to 90%, while achieving safety factors up to 50% higher.

2. CHARACTERISTICS OF THE COMPOSITE DRIVESHAFT

Testing has shown that switching from a steel to a composite driveshaft results in an approximate 5% increase in wheel power due to reduced mass. Composite fibers (such as carbon, glass, etc.) help reduce vibrations, thereby minimizing power losses. Specifically, the composite driveshaft absorbs part of the impact loading, which reduces the load on the entire drivetrain and enables a more uniform stress distribution, positively affecting the service life of the entire system.
The analyzed driveshaft corresponds to a 2004 Nissan 350Z vehicle (Figure 1).

Fig.1. Nissan 350Z driveshaft [7]

The aim of the study was to analyze the natural frequency values of hybrid driveshafts made by combining aluminum with carbon, glass, and aramid fibers in epoxy resin. Specifically, eight composite layers, each 0.12 mm thick, were applied around the aluminum tube using the mentioned materials. The study analyzed the influence of fiber type, fiber orientation angles in the layers, and the wall thickness of the hollow driveshaft on the natural frequency values, i.e., the critical speed of the driveshaft.
The characteristics of the analyzed driveshaft materials are presented in Table 1.

Table 1. Material Properties of the Driveshaft

Material	Elasticity modulus E_1, MPa	Elasticity modulus E_2, MPa	Density ρ, kg/m^3
Aluminum	72000	72000	2695
USN 150 carbon /epoxy	131600	8200	1550
UGN 150 glass/epoxy	43300	14700	2100
UKN 100 aramid/epoxy	81800	5100	1380

The length of the analyzed driveshaft is 1500 mm, and the mean diameter is 78 mm.

3. ANALYSIS OF THE DRIVESHAFT'S NATURAL FREQUENCIES

The natural frequency of the driveshaft is the frequency at which the shaft naturally vibrates or oscillates under the influence of an applied load, i.e., it represents the structure's response to dynamic excitation. The values of the natural frequencies depend on the shaft's geometric dimensions, mass, and material.
Natural frequencies are an important parameter in the analysis and design of all mechanical systems. Knowing the natural frequency values can prevent the occurrence of unwanted vibrations that lead to material fatigue, structural damage, and reduced service life.
The analysis of the natural frequencies was performed using the Finite Element Method (FEM) in the FEMAP 2021.2 software. The model of the analyzed driveshaft, along with the generated finite element mesh, is shown in Figure 2.

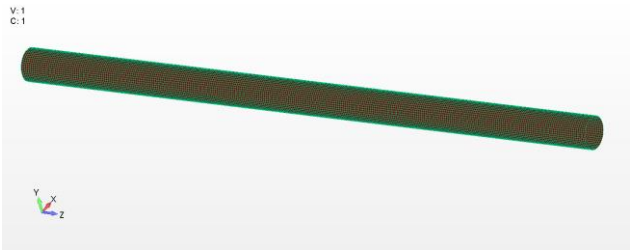

Fig.2. Driveshaft finite element model

The influence of the material type (aluminum, Al/USN 150 carbon/epoxy, Al/UGN 150 glass/epoxy, and Al/UKN 100 aramid/epoxy), wall thickness of the shaft with a ring cross-section (1.5 mm, 2 mm, 2.5 mm, and 3 mm), and the fiber orientation angle in the laminate layers (0°, ±15°, ±30°, ±45°) on the natural frequency values of the driveshaft was analyzed. The obtained natural frequency values for a fiber orientation angle of 0° in all laminate layers are shown in the form of a diagram in Figure 3.

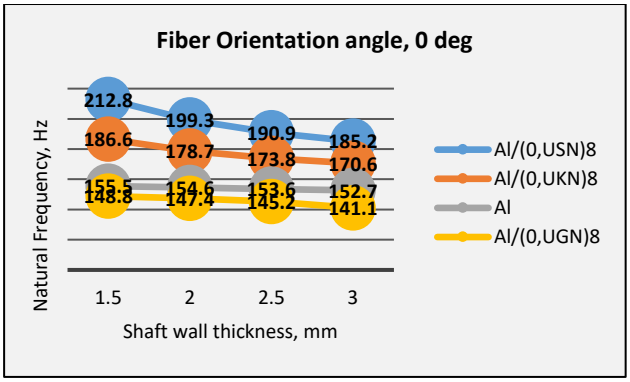

Fig.3. Natural frequencies of the driveshaft at a fiber orientation angle of 0°

Analysis of Figure 3 shows that the best performance is exhibited by the hybrid driveshaft composed of aluminum and carbon fiber/epoxy composite (Al/[0,$_{USN}$]$_8$). Slightly lower performance is observed when carbon fibers are replaced with aramid fibers (Al/[0,$_{UKN}$]$_8$), while the combination of aluminum and glass fiber/epoxy composite (Al/[0,$_{UGN}$]$_8$) yields the lowest performance. Regarding the shaft wall thickness, it is observed that an increase in thickness leads to a decrease in the natural frequency values. This effect is particularly pronounced in the case of carbon and aramid fibers. Specifically, for carbon fibers, increasing the wall thickness from 1.5 mm to 3 mm results in a reduction of natural frequencies by approximately 13%, while for aramid fibers the reduction is about 9%. The influence of wall thickness is less significant in the case of glass fibers, with a decrease of around 5%. For the pure aluminum shaft, the wall thickness of the aluminum tube has a minimal effect, where increasing the thickness from 1.5 mm to 3 mm leads to a reduction in natural frequencies of only about 2%.

The relationship between the natural frequencies and the wall thickness of the driveshaft for the same materials, but with a fiber orientation of ±15° in the laminate layers, is shown in Figure 4.

It can be concluded that, similar to the case with 0° fiber orientation, the best results are achieved with the Al/[±15,$_{USN}$]$_4$ material configuration. However, the natural frequency values are lower compared to the previous orientation (0°). The same trend is observed for the other materials as well.

For this fiber orientation as well, the lowest natural frequency values are obtained with the aluminum/glass fiber/epoxy composite material (Al/[±15,$_{UGN}$]$_4$). As in the case of 0° fiber orientation, the natural frequency values for this material are lower than those of the pure aluminum driveshaft.

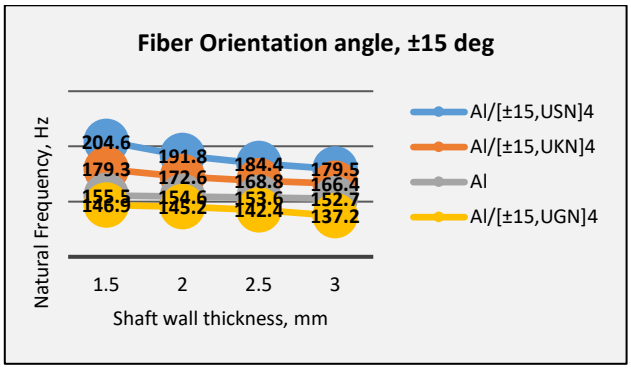

Fig.4. Natural frequencies of the driveshaft at a fiber orientation angle of ±15°

The same analysis was carried out for the case of fiber orientation angles of ±30° (Figure 5), as well as for fiber orientation angles of ±45° (Figure 6).

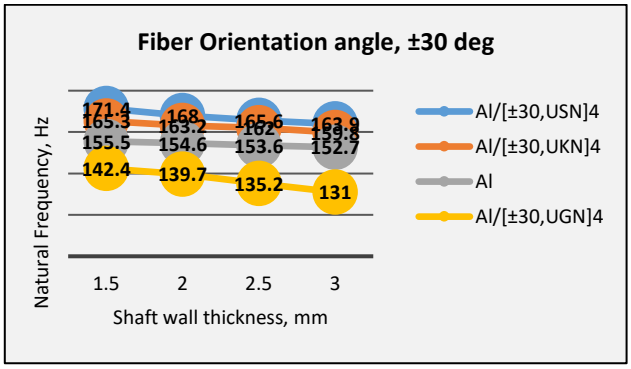

Fig.5. Natural frequencies of the driveshaft at a fiber orientation angle of ±30°

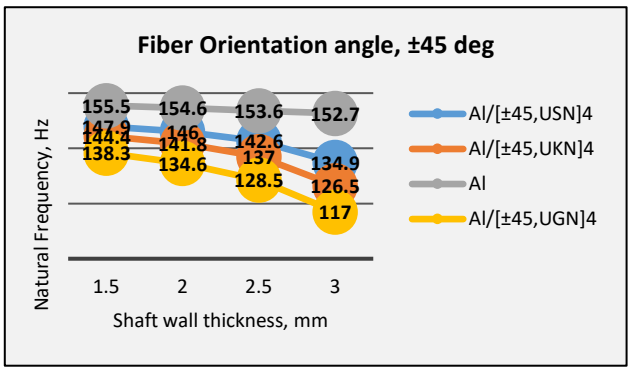

Fig.6. Natural frequencies of the driveshaft at a fiber orientation angle of ±45°

By analyzing the natural frequency values shown in Figures 3, 4, 5, and 6, it can be concluded that for fiber orientation angles of 0°, ±15°, and ±30°, the best results are achieved with the aluminum/carbon fiber/epoxy composite material (Al/USN), followed by the aluminum/aramid fiber/epoxy composite (Al/UKN), while the aluminum/glass fiber/epoxy composite (Al/UGN) shows the lowest natural frequency values. It can also be concluded that increasing the fiber orientation angle leads to a decrease in the natural frequency values, and this trend holds for all materials used. In the case of ±45° fiber

orientation, the natural frequencies of all hybrid driveshafts are lower than those of the pure aluminum shaft.
The significant influence of fiber orientation on the natural frequencies is evident in the case of the highest-performing composite material (carbon fiber/epoxy), where increasing the fiber orientation angle from 0° to ±45° results in a reduction of the driveshaft's natural frequency values by approximately 27%.
It can also be concluded that the wall thickness of the driveshaft has a significant influence on the values of natural frequencies. For all materials and all fiber orientation angles, an increase in wall thickness results in a decrease in natural frequency values.
It is well known that the mass of the shaft, i.e., the ratio E/ρ, has a major impact on natural frequency values. Given that the carbon fiber/epoxy composite has the highest value of this ratio, it is clear why the highest natural frequencies are achieved with this material. On the other hand, the glass fiber/epoxy composite is characterized by the lowest E/ρ ratio among all the analyzed materials, which explains its correspondingly lower natural frequency values.
The natural frequency in the first mode of vibration f_i and the circular (angular) frequency ω_i are related by the following expression:

$$f_i = \frac{\omega_i}{2\pi}, Hz \tag{1}$$

so that the critical rotational speeds can be easily determined using the following expression:

$$f_i = 60 \cdot n_i, \min^{-1} \tag{2}$$

where *fi*, Hz are the values of the natural frequencies.
It is evident that the highest critical rotational speeds are achieved using carbon fiber/epoxy composites, followed by the aramid fiber/epoxy combination, while the glass fiber/epoxy combination results in the lowest critical speeds.

4. CONCLUSION

The rapid advancement of technology requires the use of new composite materials that improve product performance, reduce weight, and offer significant flexibility in terms of design and shaping. By reducing the mass of an automotive composite driveshaft, the energy required to start the vehicle—as well as fuel consumption—is significantly decreased. From an environmental standpoint, this is highly important, as it also leads to reduced pollution.
In this study, the natural frequencies of hybrid driveshafts for the Nissan 350Z were analyzed. These shafts were manufactured by combining aluminum with carbon (Al/CF), glass (Al/GF), and aramid (Al/AF) fibers in conjunction with epoxy resin. The analysis was performed using the finite element method (FEM), and the following conclusions were drawn:

- The material of the shaft significantly affects the natural frequencies. The highest values are achieved using the Al/USN material, while the combination of aluminum with glass fibers (Al/UGN) gives the poorest results,
- Increasing the wall thickness of the hollow shaft reduces the natural frequency values for all shaft materials,
- The fiber orientation angle in the composite layers has a significant impact on the natural frequencies. The smaller the fiber orientation angle, the higher the natural frequencies. An increase in the fiber orientation angle from 0° to ±45° can lead to a reduction in the natural frequency values by nearly 30%,
- The mass of the shaft greatly influences the natural frequencies, which is why the best results are achieved with the combination of aluminum and carbon fibers.

To prevent resonance, i.e., the coincidence of the actual and critical rotational speed, for metallic shafts, it is necessary to make some geometric changes to the shaft or change the material. This study has shown that, in the case of composite materials, this can be achieved only by changing the fiber orientation angle in the laminate layers.

REFERENCES

[1] Zhang, H., Li, S., Wu, Y., Zhi, P., Wang, W., Wang, Z.: A Multiscale Reliability-Based Design Optimization Method for Carbon-Fiber-Reinforced Composite Drive Shafts. *CMES - Computer Modeling in Engineering and Sciences,* Vol. 140, No. 2, pp. 1975-1996, 2024
[2] Kaneria, A.J., Patel, V.N.: Mathematical modelling and dynamic analysis of composite hollow shaft. *Materialstoday: PROCEEDINGS*, Vol. 80, No. 1, pp. 264-271, 2023
[3] Udatha, P., Sekhar, A.S., Velmurugan, R.: Eigen value analysis of composite hollow shafts using modified EMBT formulation considering the shear deformation along the thickness direction. *Defence Technology*, Vol. 28, pp. 1-12, 2023
[4] Bisheh, H.: Design and analysis of hybrid natural / synthetic fibre - reinforced composite automotive drive shafts. *Structures*, Vol. 61, 2024
[5] Zakaria, N.A., Ishak, M.R., Mustapha, F., Yidri, N.: Tensile properties of a hybrid kenaf-glass fibre composite shaft. *Materialstoday: PROCEEDINGS*, Vol. 74, No. 3, pp. 492-498, 2023
[6] Searle, J., Meng, M., Summerscales, J.: FEA modelling and environmental assessment of a thin- walled composite drive shaft. *Thin-Walled Structures*, Vol. 180, 2022
[7] https://www.ebay.com/b/Genuine-OEM-Driveshafts-Parts-for-Nissan-350Z/262250/bn_33044463, Accessed on: 2025-05-07

11th International Scientific Conference
IRMES 2025
Research and Development of
Mechanical Elements and Systems
June 19 – 21, 2025; Vrnjačka Banja, Serbia

Original scientific paper DOI: 10.46793/IRMES25.017M

METHODOLOGY FOR CALCULATING SURFACE PRESSURE ON THE CONTACT SURFACES OF CONICAL CLAMPING RINGS

Goran MIHAJLOVIĆ[1]
Marina KARIĆ[2]
Jelena ERIĆ OBUĆINA[3]
Zvonko PETROVIĆ[4]

[1] Academy of Applied Studies Šumadija, Trstenik, Serbia, 37240; goran.vtms@gmail.com; 0000-0002-6362-8415
[2] Academy of Applied Studies Šumadija, Trstenik, Serbia, 37240; karicmarina@gmail.com; 0009-0002-0248-0514
[3] Academy of Applied Studies Šumadija, Trstenik, Serbia, 37240; jericobucina@gmail.com; 0009-0000-6782-7625
[4] Academy of Applied Studies Šumadija, Trstenik, Serbia, 37240; zpetrovic@asss.edu.rs; 0009-0007-3765-7259

Abstract: *During the operation of various tribomechanical systems, their constituent elements perform the intended working function under greater or lesser working load, moving at a certain relative speed in relation to the contact surfaces of the elements with which they are in contact. Then, a specific stress arises in the contact zone, which in tribology is known as surface-contact stress. It further causes working stresses that manifest themselves in the form of surface pressure that is equal on the contacting surfaces of both solid bodies (because the force of action is equal to the force of reaction). For those materials for which it is possible to find the value of their modulus of elasticity in the appropriate tables and catalogs, the Hertz surface pressure is calculated (most common machine materials), while for materials for which there are no measured values of the modulus of elasticity, the Stribek surface pressure is calculated using empirical formulas (these are all soft materials).*
As a consequence of this condition, various types of surface damage occur on the contact surfaces of the bonded elements. In practice, they manifest themselves in the behavior of the outer and inner boundary layers on the surfaces of solid bodies, as well as in the occurrence of larger or smaller plastic deformations if the surface pressure exceeds permissible values. Therefore, tribology is often defined as the science and technology of the processes of material mass dissipation of solid bodies that are in direct contact.
In this paper, using a two-factor selection experimental design, an analysis of the significance of the influence of the following experimental factors was performed: axial wedging force (F_a) and static friction coefficient (μ) on the value of the surface pressure (p) at the contact of conical clamping rings. Surface pressure is considered one of the most important parameters on which the load capacity of a conical clamping joint directly depends.
The entire experiment was carried out in the Hydraulics and Pneumatics Laboratory of the Academy of Applied Studies Šumadija - Department in Trstenik, during testing of the load-bearing capacity of the shaft-gear mechanical connection of the hydraulic unit of a building machine.

Keywords: *tribology; surface pressure; conical rings.*

1. INTRODUCTION

By analogy with volume stresses that can cause permanent plastic deformations or static and dynamic fractures on machine parts, excessive surface stresses can also lead to various types of surface destruction on their contact surfaces. Which specific type of surface destruction will manifest itself in practice will depend on the type of contact (on the surface, on a line, or at a point), the geometry of the contact surface (flat, convex, concave), as well as on the relative mobility of the parts in contact (Fig. 1), [1].

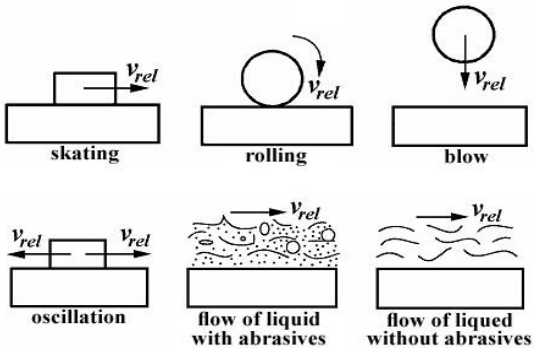

Fig.1. Different types of relative motion between the elements of the tribomechanical system

What both volume and surface stresses have in common is that they have an identical mechanism of action, so they can be represented by the following general block diagram (Fig. 2):

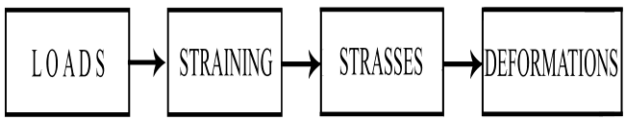

Fig.2. Mechanism of action of volume and surface stresses

Contact stresses occur during the mutual contact (touch) of the surfaces of solid bodies, which basically represent thin layers of material whose physical, chemical and mechanical properties are significantly different from the properties of the basic mass of material of solid bodies. The following statements can be applied to surface stresses (tribological phenomena and processes in the contact zone of two solid bodies):

• the load of the contact zone always represents the *normal force* F_n which is perpendicular to the pressed contact surface (in the case of flat contact surfaces), or is perpendicular to the plane on which the pressed contact surface is projected (in the case of curved contact surfaces);

• stress is external superficial, ie. it is the so-called *contact stress*;

• during operation, stresses manifest themselves in the form of *surface pressure*, which, due to the law of action and reaction, is always equal on the contact surfaces of both solid bodies;

• deformations due to contact stresses occur first in the boundary layers, and sometimes they can even reach the base mass of the material. They depend on the relative mobility of the contact surfaces: when the contact surfaces slide, surface damage manifests itself in the form of *wear*; *pitting* occurs when rolling; upon impact *crushing and pulverization* of the surface layer; when oscillating it is *vibration-fretting wear*; when a liquid containing an abrasive flows over the surface of a solid body, *erosive wear* occurs; when a liquid that does not contain an abrasive flows over the surface of a solid body, *cavitation wear* occurs. A special case is surface destruction at relative rest of the contact surfaces (v_{rel}=0), when *crushing and lateral spilling of the surface layers* of solid elements of the tribomechanical system can occur.

The special case (v_{rel}= 0) is often encountered in real operating conditions, when there must be no relative movement (slippage) of parts that are in immediate contact. The problem that is treated in this paper is directly related to this.

In technical practice, we encounter a special type of machine joints almost every day, consisting of shafts and various rotating elements mounted on them (gears, sprockets, belts, various wheels, couplings, etc.). At the same time, it is necessary that the shaft and all rotating parts located on it form a single and harmonious rotating unit, that is, that in each specific case two basic conditions must be met:

• exact position, i.e. centering of the rotating element in relation to the shaft;

• reliability (slip-free operation) in transmitting power (that is, its components of torque T and angular velocity ω) from the shaft to the hub of the rotating element or vice versa, depending on whether the specific rotating element transmits or receives power.

The mentioned joints can be realized in practice in several characteristic ways (with wedges without inclination or with an inclination, grooved joints, profiled-polygonal joints, friction joints, etc.). Each of the mentioned above compounds has its advantages and disadvantages. In this paper, one special type of friction joints, the so-called conical clamping joints, which are achieved by axial tightening using threaded elements, i.e. axial wedging between the shaft sub-hub and the rotating element hub.

Conical clamping joints (Fig. 3), [2], have the good feature that they do not require any grooves, notches, rests, etc. on the shaft, as a result of which there will be no harmful stress concentration. This significantly increases the dynamic durability of the shaft, especially with alternating load (rotation in both directions). The connection solution with direct contact (case "A") is structurally the simplest, but it has the disadvantage that it requires very high accuracy when making the conical contact surfaces of both parts.

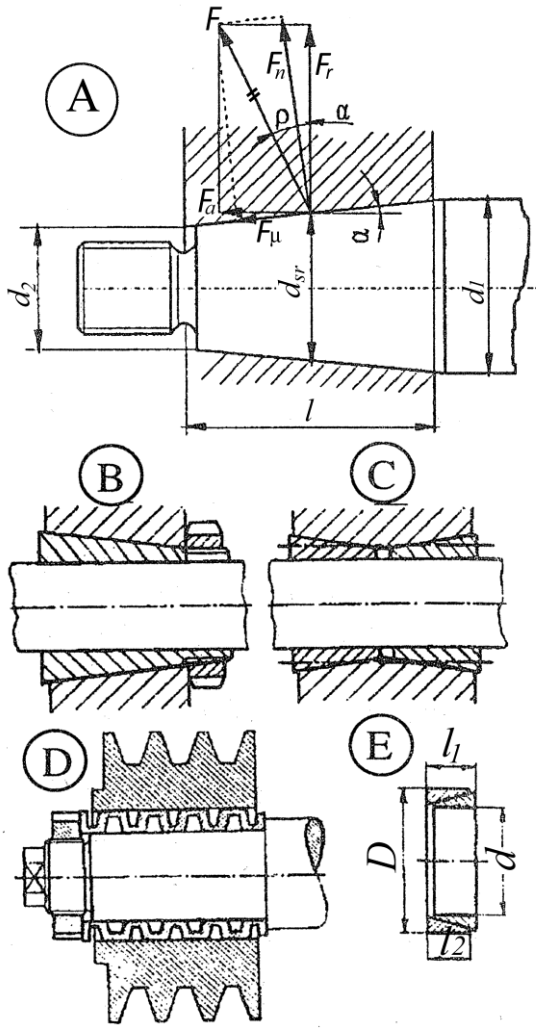

Fig.3. Conical clamping joints with direct contact (case "A") and with indirect contact (cases "B", "C", "D", "E") between the shaft and the hub of the rotating element

Therefore, in practice, conical clamping joints with intermediate contact between the shaft and rotating elements are used much more often, where the role of an intermediary (intermediate element) can be played by: an elastic split conical sleeve with a cut thread at one end for tightening the nut (case "B"); elastic split cone bushing with both sides wedged, which is tightened with screws (case "C"); elastic wavy sleeve (case "D"); a pair of special conical clamping rings (case "E"); etc.

2. ANALYSIS OF FORCES ON A CONE CLAMPING JOINT

The analysis of the forces on the conical clamping joint is shown in Fig. 3 only for case "A", with a note that it is exactly the same for all other cases ("B" to "E"). For easier analysis, it is considered that all forces always act on the middle diameter of the cone ($d_{sr}=(d_1+d_2)/2$). By tightening the nut (not shown in the picture) the hub is pulled on the shaft, i.e. axial wedging is carried out, as a result of this process a frictional force (F_μ) occurs at the contact of the conical surfaces. This frictional force must at all times be greater than the tangential (circumferential) force (F_t) that is transmitted from the shaft to the hub (or vice versa) through the joint, because otherwise there would be slippage between the shaft and the hub:

$$F_\mu \geq F_t \tag{1}$$

$$F_\mu = \mu \cdot F_n \tag{2}$$

$$T = F_t \cdot \frac{d_{sr}}{2} \Rightarrow F_t = \frac{2T}{d_{sr}} \tag{3}$$

Substituting (2) and (3) into (1) gives:

$$\mu \cdot F_n \geq \frac{2T}{d_{sr}} \quad /:\mu$$

$$F_n \geq \frac{2T}{d_{sr} \cdot \mu} \text{ (theoretical formula)}$$

$$F_n \geq \frac{2T}{d_{sr} \cdot \mu} \cdot C_A \cdot S_\mu \text{ (practical formula)} \tag{4}$$

With Fig. 3, case "A", the following vectorial dependencies and trigonometric dependencies are also observed:

$$\vec{F} = \vec{F}_n + \vec{F}_\mu = \vec{F}_r + \vec{F}_a \tag{5}$$

$$\cos\rho = \frac{F_n}{F} \Rightarrow F_n = F \cdot \cos\rho \tag{6}$$

$$\sin(\alpha+\rho) = \frac{F_a}{F} \Rightarrow F = \frac{F_a}{\sin(\alpha+\rho)} \tag{7}$$

Changing (7) to (6) gives:

$$F_n = \frac{F_a}{\sin(\alpha+\rho)} \cos\rho = \frac{F_a \cdot \cos\rho}{\sin\alpha \cdot \cos\rho + \cos\alpha \cdot \sin\rho}$$

When the last equation is divided by /:$cos\rho$ it is obtained:

$$F_n = \frac{F_a}{\sin\alpha + \cos\alpha \cdot tg\rho} \quad [tg\rho=\mu]$$

$$F_n = \frac{F_a}{\sin\alpha + \mu \cdot \cos\alpha} \tag{8}$$

In the mentioned formulas (1) to (8), certain quantities have the following meaning::

F_n - normal force on the mutual contact of the conical surfaces of the shaft and rotating element hubs;
μ - static friction coefficient (slip resistance) on mentioned touch;
T - torque transmitted by the conical clamping joint;
C_A - factor of working conditions ie. character of work change loads;
S_μ= 1,25 ... 1,5 - the degree of safety against slipping hubs per shaft;
F_r - radial component of the total (oblique) force F;
F_a - axial component of the total (oblique) force F;
ρ - angle of friction of unsmooth touch;
α - semiangle of cone (2α - the angle of cone).

Based on the previous analysis, it is possible to conclude the following: in order for the conical clamping joint to be able to transmit a certain torque (T), it is necessary that there is a sufficiently large normal force (F_n) at the contact between the conical surfaces of the shaft and the hub so that slippage does not occur. However, on the other hand, the force intensity (F_n) is limited by the maximum allowable surface pressure (p) on the contact surfaces, where plastic deformation must not occur [2]:

$$p \approx \frac{F_n}{A} \approx \frac{F_n}{d_{sr} \cdot \pi \cdot l} \leq p_{doz} \tag{9}$$

A - contact surface (in developed form) between shaft and hub;
l - contact length between shaft and hub;
p_{doz} - the maximum allowable surface pressure of the weaker material in contact (either the shaft or the hub).

3. PROBLEM OF RESEARCH

As already pointed out in the introductory part, in practice conical clamping joints with intermediate contact between the shaft and the rotating element hub are used much more often, and the most suitable solutions of this type include joints with special conical rings (Fig. 3, case "E").

The rings are tightened using a nut with a certain axial force, i.e. tightening force (F_a=F_p), as a result of which the rings slide relative to each other on their conical surfaces, on which a normal force (F_n) is generated. According to (8), this force depends on three factors (F_a, μ, α). However, as these rings are produced as standard machine elements of precisely prescribed shape and dimensions, the cone angle of the rings is invariable [3], i.e. $\alpha \approx 17° = \text{const}$. Therefore, the normal force is a function of only two quantities (only two independent variables), so it will be:

$$F_n = f(F_a; \mu) \tag{10}$$

From (9) it follows that $p = f(F_n)$, which is why it will also be:

$$p = f(F_a; \mu) \tag{11}$$

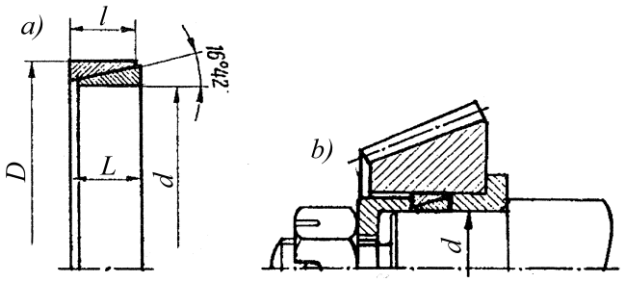

Fig.4. The appearance of conical clamping rings (a) and the construction of the joint (b)

In this way, observing the dependencies (10) and (11), the problem of our research could be expressed as follows: experimentally, the value of the minimum necessary normal force (F_{ninin}) at the contact of the rings should be determined, with which it is possible to transfer a certain torque (T), that is, the value of the minimum surface pressure (p_{min}) that corresponds to the mentioned force should be determined.

We will set the following RESEARCH HYPOTHESES, whose accuracy will be accepted or rejected, [4], [5]:

H1: Axial force (F_a) and friction coefficient (μ) are significant quantities, i.e. the normal force (F_n), that is, the surface pressure (p), in a statistical sense really depends on these two quantities.

H2: Statistically significant is also the mutual effect of the quantities (F_a) and (μ), i.e. the intensity with which the force (F_a) affects the observed characteristics (F_n) and (p) of the conical clamping joint significantly depends on the intensity of the friction coefficient (μ) and vice versa.

4. MEASURING EQUIPMENT, EXPERIMENT PLAN AND METHODOLOGY OF CALCULATING SURFACE PRESSURE

The measurement of the normal force (F_n), i.e. the surface pressure (p) at the contact of the rings, was carried out in workshop conditions according to the schematic view given in Fig. 5. The picture shows a separate shaft (II) of a hydraulic unit, whose interchangeable gears (2) and (3) are connected to the mentioned shaft by means of conical clamping rings. In that way the rings enable quick and easy mounting and dismounting of the gears.

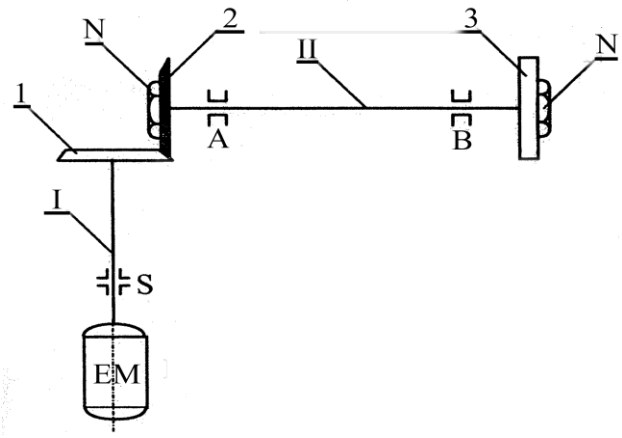

Fig.5. Hydraulic unit shaft with conical clamping rings for connection with interchangeable gears

♦ Data: P_{em}=5,5kW; n_{em}=960min^{-1}; z_1=24; z_2=36; $i_{1\text{-}2}$=z_2/z_1=36/24=1,5;

$$T_1 = \frac{30 \cdot P_1}{\pi \cdot n_1} = \frac{30 \cdot 5500}{\pi \cdot 960} = 54{,}7Nm \tag{12}$$

$$T_2 = T_1 \cdot i_{1-2} \cdot \eta_{1-2} = 54{,}7 \cdot 1{,}5 \cdot 0{,}96 \approx 80Nm \tag{13}$$

d_{v2}=d_{v3}=40mm – diameters of subheads of shaft II.

♦ Measurements of conical clamping rings, [3]:

d=40mm - the inside diameter of the inner ring;

D=45mm - the outside diameter of the outer ring;

d_{sr}=$(d+D)/2$=(40+45)/2=42,5mm - mean cone diameter;

l=5,2mm - the contact length between the rings.

The required minimum value of the surface pressure at the contact of the rings is obtained indirectly [6], by means of the tightening torque of the nut (T_p) which is read out on the scale of the torque wrench (Fig. 6).

Fig.6. Torque wrench with scale for measuring nut tightening torque (T_p)

This moment is read out at the moment when the shaft (II), which has been stationary until then, starts to rotate slightly [7], which corresponds to the limit case of friction (F_μ=F_t=$\mu \cdot F_{nmin}$). Then the read out value (T_p) on the torque wrench is inserted into the formulas for calculating the tightening force (F_p) known from the theory of screw connections, where the calculated value (F_p) in the observed example corresponds to the axial wedging force (F_a). In the next step, based on (8) and (9), the required quantities (F_n) and (p) are calculated. This methodology would correspond to the following general measurement and calculation scheme:

$$T_p \rightarrow (F_p = F_a) \rightarrow F_n \rightarrow p \tag{14}$$

The scheme (14) applied to individual factor levels in our experiment leads to the plan of the experiment shown in Table 1 and Table 2 (at T_2= 80Nm=const, C_A=1-smooth work without impact, n=2-number of repetitions of experiments at the same factor level), [8].

Table 1. Two-factor experimental design (general model)

Factor B	Factor A	
	Level "a_1"	Level "a_2"
Level "b_1"	Y_{111} Y_{112}	Y_{211} Y_{212}
Level "b_2"	Y_{121} Y_{122}	Y_{221} Y_{222}

Table 2. Measured values of surface pressure p_{ijq} [MPa]

Friction coefficient μ	Axial force F_a	
	F_{a1} (S_μ=1)	F_{a2} (S_μ=1,5)
"Dry" friction μ_1=0,15	p_{111}=37,6 p_{112}=38,7	p_{211}=56,4 p_{212}=58,05
"wet" friction μ_2=0,10	p_{121}=55,15 p_{122}=58,83	p_{221}=82,73 p_{222}=88,25

*Note: In the indicated marking system, the first number in the index indicates the column in Tables 1 and 2, the second number the row in the Tables, and the third number the ordinal number of repetitions of the experiment [8] at a certain factorial level of the coefficients μ_1, μ_2.

- Measured results on the levels a_1, b_1 (S_μ=1- borderline case of wedging; μ_1=0,15 -"dry" friction):
  T_{p111}=46Nm → F_{p111}=11,39kN → F_{n111}=26,13kN → p_{111}=37,6MPa
  T_{p112}=48Nm → F_{p112}=11,88kN → F_{n112}=26,87kN → p_{112}=38,7MPa
- Measured results on the levels a_1, b_2 (S_μ=1- borderline case of wedging; μ_1=0,10 -"wet" friction):
  T_{p121}=60Nm → F_{p121}=14,86kN → F_{n121}=38,29kN → p_{121}=55,15MPa
  T_{p122}=64Nm → F_{p122}=15,85kN → F_{n122}=40,84kN → p_{122}=58,83MPa
- Measured results on the levels a_2, b_1 (S_μ=1,5 - usual degree of safety against slipping; μ_1=0,15 -"dry" friction):
  T_{p211}=69Nm → F_{p211}=17,09kN → F_{n211}=39,2kN → p_{211}=56,4MPa
  T_{p212}=72Nm → F_{p212}=17,83kN → F_{n212}=40,3kN → p_{212}=58,05MPa
- Measured results on the levels a_2, b_2 (S_μ=1,5 – usual degree of safety against slipping; μ_1=0,10 -"wet" friction):
  T_{p221}=90Nm → F_{p221}=22,28kN → F_{n221}=57,43kN → p_{221}=82,73MPa
  T_{p222}=96Nm → F_{p222}=23,77kN → F_{n222}=61,26kN → p_{222}=88,25MPa

In order to verify the hypotheses *H1* and *H2*, a statistical procedure known as *dispersion analysis* was applied. The complete dispersion analysis is shown in Table 3.

Table 3. Dispersion analysis of the measured values of surface pressure p_{ijq}

Source of dispersion	Number of degrees of freedom	Sums of squares	Dispersion relations	Calculation "F" value	Tabular "F" value	"F"-test	Significance assessment
A	f_A=1	S_A=1131,69	S_A^2=1131,69	F_{rA}=188,85	F_{tA}=7,71	F_{rA}>F_{tA}	significant
B	f_B=1	S_B=1109,44	S_B^2=1109,44	F_{rB}=185,14	F_{tB}=7,71	F_{rB}>F_{tB}	significant
AB	f_{AB}=1	S_{AB}=92,36	S_{AB}^2=92,36	F_{rAB}=15,41	F_{tAB}=7,71	F_{rAB}>F_{tAB}	significant
Experiment error	f_{GE}=4	S_{GE}=23,97	S_{GE}^2=5,9925	---	---	---	---
Total sum	f_0=7	S_0=2309,52	S_0^2=329,93	---	---	---	---

*Note: Tabular "F" values of F_{tA}, F_{tB}, F_{tAB} in the table 3 according to [8].

5. CONCLUSION

Complete research of studied problem is based on the exposed measuring equipment, the plan of the experiment and the exposed methodology of calculations. Based also on the statistical procedure known as dispersion analysis and Fisher's "F"-test for testing the significance of the influence of experimental factors on the research object [9], the following conclusions can be drawn:

- Both experimental factors (F_a) and (μ) are significant, because in statistical terms they significantly affect the object of research, ie. to the surface pressure (p) at the contact of the conical clamping rings. Thus, hypothesis *H1* is fully confirmed with a probability of correctness of the statement of P=95%, i.e. with a certain risk coefficient of α_r=5%.
- The effect of the mutual interaction of factors (F_a) and (μ) is also statistically significant, i.e. the intensity of the influence of one factor on the quantities (F_n) and (p) significantly depends on the intensity of the other factor (and vice versa). Thus, the hypothesis *H2* is completely proven, also with the probability of correctness of the statement P=95%, i.e. with a certain risk coefficient of α_r=5%.
- Based on Table 2, it can be concluded that in each concrete case the necessary condition given by relation (9) is fulfilled, because:

$$p_{ijq} \leq p_{doz} \tag{15}$$

where is:

p_{doz} - allowed surface pressure at the contact of the conical rings surfaces;

$p_{doz} = R_e/3 = 0.33R_e = 0.33\cdot(300 \dots 350) = (100 \dots 115)MPa$;

$R_e = (300 \dots 350)MPa$ - yield strength of the material of conical rings.

This practically means the following: in real operating conditions, during the implementation of conical clamping joints, with wedging forces ($F_a = F_p$) and with friction coefficients (μ) whose values are equal to those from our experiment (for the case of $S_\mu = 1.5$ because it is considered the optimal value), the allowed surface pressure will not be exceeded, and therefore no plastic deformations will occur on the contact surfaces of the conical clamping rings.

REFERENCES

[1] Mihajlović, G.: *Tribologija,* Visoka tehnička mašinska škola strukovnih studija, Trstenik, ISBN 86-83803-15-5, 2014.

[2] Miltenović, V.: *Mašinski elementi-oblici, proračun, primena*, Univerzitet u Nišu-Mašinski fakultet, Niš, ISBN 86-80587-12-5, 2006.

[3] Miltenović, V.: *Mašinski elementi-tablice i dijagrami,* Univerzitet u Nišu-Mašinski fakultet, Niš, ISBN 86-80587-12-5, 2006.

[4] Mihajlović, G., Tadić, B.: Vibroplatform modeling with allowance for tribological aspects*, Journal of Friction and Wear*, Vol. 38, No. 3, pp. 184-189, ISSN 1068-3666, Allertion Press, Inc., SCI-M23, 2017.

[5] Laurentie, J., Traore, P, Dascalescu, L.: Discrete element modeling of triboelectric charging of insulating materials in vibrated granular beds*, Journal Electrostat,* Vol. 71, No. 6, pp. 951-957, , 2013.

[6] Myshkin, N.K., Grigoriev, A.: Roughness and Texture Concepts in Tribology*, Tribology in Industry*, Vol. 35, No. 2, pp. 97-103, 2013.

[7] Olsson, M.: *Analysis of Structures Subjected to Moving Loads,* Lund Institute of Technology, Lund, Sweden, 1986.

[8] Stankov, J.: *Osnove merne tehnike-metode planiranja eksperimen*ta*,* Univerzitet u Novom Sadu-FTN, Novi Sad, 1982.

[9] Petrović, R., Mihajlović, G., Đuričić, Lj.: Experimental research and analysis of working and constructive parameters of hydro pumps with constant pressure and variable flow*, The third international workshop on aircraft system technologies*, march 31÷april 1, Hamburg, Germany, pp105÷112, ISBN 978-3-8322-8071-0, 2011.

11th International Scientific Conference
IRMES 2025
Research and Development of
Mechanical Elements and Systems
June 19 – 21, 2025; Vrnjačka Banja, Serbia

Original scientific paper DOI: 10.46793/IRMES25.023M

DATA DRIVEN PREDICTION OF SHEAR STRENGTH OF COMPOSITE SLIDER JOINTS

Miloš MILOVANČEVIĆ[1]
Srđan STOJIČIĆ[2]
Mirjana MILJANOVIĆ[3]
Nikola SIMONOVIĆ[4]
Dragana TRNAVAC[5]

[1]University of Niš, Faculty of Mechanical Engineering, 18000, Serbia;
milos.milovancevic@masfak.ni.ac.rs; ORCID iD: 0000-0002-7891-1010
[2]University of Niš, Faculty of Mechanical Engineering, 18000, Serbia;
srdjan.stojicic@masfak.ni.ac.rs; ORCID iD: 0000-0002-6743-2196
[3]University of East Sarajevo, Faculty of Production and Management Trebinje; ORCID iD: 0000-0002-7394-8703
[4]University MB, Faculty of Business and Law, 11000 Belgrade, Serbia;
[5]University MB, Faculty of Business and Law, 11000 Belgrade, Serbia; ORCID iD: 0000-0003-1571-4500

Abstract: *The primary objective of the research was to investigate the impact that multi-walled carbon nanotubes, aging temperature, aging period, and thickness of interfacial intermetallic compounds had on the ability to forecast the shear strength of composite solder junctions. It was determined that an adaptive neuro fuzzy inference system (ANFIS), which is a form of soft computing methodology that is ideal for nonlinear data samples, was the most appropriate method to apply in order to examine the shear strength of composite solder joints. After loading the data samples into the ANFIS toolbox inside the MATLAB program, the findings that corresponded to those samples were noticed. According to the findings, the thickness of interfacial intermetallic compounds has the most significant influence on the ability to estimate the shear strength of composite solder junctions. Based on the effect that the inputs had on the outputs that were provided, the findings demonstrated a high level of predictive consistency.*

Keywords: *composite solder; shear strength; carbon nanotube; ANFIS.*

1. INTRODUCTION

Utilization of lead-based solder alloys for electronics packaging could have impact for reduction of hazardous on the environment. Therefore there are many environmental friendly lead-free solder alloys have been developed and improved in regard to thermal properties and mechanical behavior. These lead-free solder alloys have high strength, high melting temperature and good wettability. Despite of these advantageous there is fragility of interfacial intermetallic compounds layer which growth overtime which reduce mechanical performance and hence wider applications. Therefore there is need to add some reinforcement in order to improve the mechanical performance of the lead-free solder alloys. One of the most popular reinforcement is carbon nanotubes.

The effect of temperature and strain rate on the tensile properties of Sn–3.8Ag–0.7Cu (SAC387) alloy as well as SAC387 alloy reinforced with two different weight percentages (wt.%) of SWCNT was investigated in article [1] where was found that addition of 0.05 wt.% SWCNT to SAC387 alloy results in an increase in yield and ultimate tensile strengths without affecting the total elongation at all temperatures and strain rates studied, although the increase in strength values at 75 °C was marginal. A composite solder was prepared in article [2] by adding different amount Ni modified multi-walled carbon nanotubes (MWCNTs) into the Sn-3.0Ag-0.5Cu (SAC305) solder where it was suggested that the fracture mode of the solder joints changed from mix fracture mode to ductile fracture mode as the amount of Ni-CNTs increased. Nano material addition into the solder plays a significant role in the solder material in order to improve the joint reliability [3]. An analysis of the role played by the addition of carbon nanotubes (CNTs) to the solder matrix of conventional Sn-5Sb lead-free solder was performed in article [4] where the shear strength assessment revealed that the composite solder joints gave a superior shear strength property, especially the Sn-5Sb-0.01CNT solder joint sample. Microstructure and mechanical properties including tensile strength as well as creep resistance of Ni-Coated Carbon Nanotube reinforced Sn–Ag–Cu solders were investigated in study [5] where was found the increase in strengthening effect of solder joints can be attributed to the consumption of Ni by interface reaction during soldering. The influence of

multi-walled carbon nanotube (MWCNT) concentration on the thermo-mechanical reliability properties of carbon nanotube (CNT)-filled solderable anisotropic conductive adhesives (SACAs) containing low-melting-point-alloy (LMPA) fillers was investigated in article [6]. The melting temperatures of the composite solders were found to be unchanged with the carbon nanotube additions [7]. Microstructural studies determined that rapid solidification refined brittle and elongated intermetallic compounds (IMCs) into small particles with an average diameter of a few hundred nanometers [8]. With increasing the carbon nanotube (CNT) concentration in an electrodeposition solution to 10 g/l, the shear energy of the Sn–CNT composite bumps increased more than 50%, indicating that the mechanical reliability of the solder joints can be substantially improved by using a composite solder reinforced with CNTs [9].

Artificial neural networks represent one of the most popular approach for modeling and simulation of different systems and processes. These is because since the artificial neural networks have parallel architectures for solving of difficult and highly nonlinear problems. Therefore the main aim of the study is to apply artificial neural network merged with fuzzy logic controller for analyzing of mechanical performances of lead-free solder alloys. The effects of multi-walled carbon nanotubes, aging temperature, aging time, thickness of interfacial intermetallic compounds on prediction of shear strength of composite solder joints have been investigation. Adaptive neuro fuzzy inference system (ANFIS) [10] is used as a type of artificial neural network which is suitable for nonlinear data samples.

2. METHODOLOGY

2.1. Experimental procedure

The schematic flowchart of the experimental procedure for production of single-lap composite solder joint is shown in Fig. 1. Composite lead-free solder systems were developed in the first step. Multi-walled carbon nanotubes were used as reinforcement in the next step. In the next step the homogeneous dispersion is ensured through drying of the composite solder by cylindrical die system.

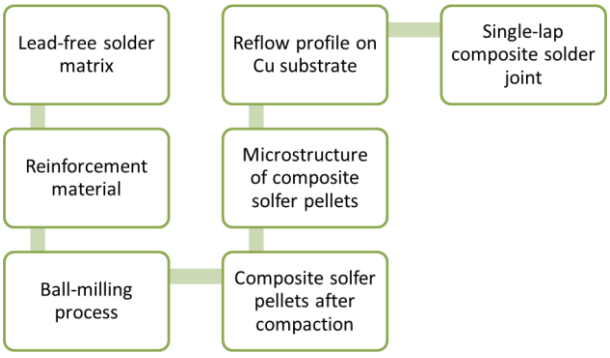

Fig. 1: Schematic flowchart of the production of single-lap composite solder joint

Table 1 shows input and output parameters used in the study. The input parameters are, content of multi-walled carbon nanotubes, aging temperature, aging time, thickness of interfacial intermetallic compounds, while output is shear strength of the composite solder joints.

Table 1. Input parameters [11]

Input 1	Input 2	Input 3	Input 4	Output
Content of multi-walled carbon nanotubes (%)	Aging temperature (°C)	Aging time (h)	Thickness of interfacial intermetallic compounds (μm)	Shear strength (MPa)
0	0	0	3.04	18.74
0.01	0	0	2.65	24.15
0.05	0	0	2.6	19.81
0.1	0	0	2.76	20.35
0	120	500	4.65	17.86
0.01	120	500	4.22	22.9
0.05	120	500	3.75	18.3
0.1	120	500	4.25	17.4
0	120	1000	5.21	17.05
0.01	120	1000	4.87	21.7
0.05	120	1000	4.68	18
0.1	120	1000	4.96	16.8
0	120	1500	5.64	16.7
0.01	120	1500	5.26	21.1
0.05	120	1500	5.1	17.2
0.1	120	1500	5.29	16.5
0	150	500	6.11	16.8
0.01	150	500	5.47	20.8
0.05	150	500	5.05	17.9
0.1	150	500	5.67	15.6
0	150	1000	7.95	15.4
0.01	150	1000	7.14	19.6
0.05	150	1000	6.41	16.4
0.1	150	1000	7.25	14.7
0	150	1500	9.7	13.8
0.01	150	1500	8.49	17.5
0.05	150	1500	7.86	15.6
0.1	150	1500	8.9	13.2
0	170	500	7.69	15.94
0.01	170	500	7.05	20.2
0.05	170	500	6.73	17.49
0.1	170	500	7.41	15.32
0	170	1000	11.67	14.49
0.01	170	1000	9.75	18.71
0.05	170	1000	9.03	15.72
0.1	170	1000	9.9	13.3
0	170	1500	14.06	11.51
0.01	170	1500	13.02	15.24
0.05	170	1500	11.99	13.93
0.1	170	1500	12.42	11.77

2.2. ANFIS methodology

ANFIS network has five layers as it shown in Fig. 2. The main core of the ANFIS network is fuzzy inference system. Layer 1 receives the inputs and convert them in the fuzzy value by membership functions. In this study bell shaped membership function is used since the function has the highest capability for the regression of the nonlinear data.

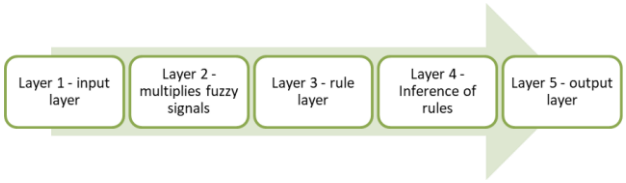

Fig. 2. ANFIS layers

Bell-shaped membership functios is defined as follows:

$$\mu(x) = bell(x; a_i, b_i, c_i) = \frac{1}{1 + \left[\left(\frac{x - c_i}{a_i}\right)^2\right]^{b_i}} \quad (1)$$

where $\{a_i, b_i, c_i\}$ is the parameters set and x is input.

Second layer multiplies the fuzzy signals from the first layer and provides the firing strength of as rule. The third layer is the rule layers where all signals from the second layer are normalized. The fourht layer provides the inference of rules and all signals are converted in crisp values. The final layers sumarized the all signals and provied the output crisp value.

3. RESULTS

3.1. Accuracy indicies

Performances of the proposed models are presented as root means square error (RMSE) as follows:

$$RMSE = \sqrt{\frac{\sum_{i=1}^{n} (P_i - O_i)^2}{n}} \quad (2)$$

where P_i and O_i are known as the experimental and forecast values, respectively, and n is the total number of dataset.

3.2. Feature selection

ANFIS methodology was used for feature selection of the prediction of shear strength of the composite solder joints. The feature selection is important as preprocessing of the input parameters in order to remove unnecessary inputs. Data samples are divided in two groups for analyzing purpose. 50% data is used for training and remaining 50% is used for checking purpose of the ANFIS network. ANFIS network is trained based on input and output pairs in Table 1.

According to results in Fig 3, thickness of interfacial intermetallic compounds (input 4) has the strongest impact on prediction of shear strength of the composite solder joints. Input 1 or content of multi-walled carbon nanotubes has the lowest impact on the prediction of shear strength of the composite solder joints. Table 2 shows numerical values of the effects of single parameter on the shear strength of the composite solder joints.

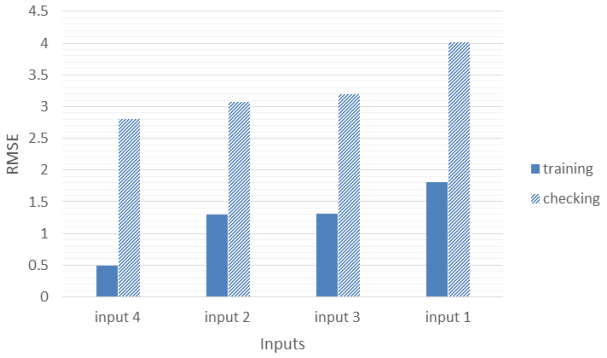

Fig. 3: Effects of single parameter on the shear strength of the composite solder joints

Table 2. Effects of single parameter on the shear strength of the composite solder joints

input 1 --> training=1.8111, checking=4.0174
input 2 --> training=1.2911, checking=3.0798
input 3 --> training=1.3177, checking=3.1926
input 4 --> training=0.4881, checking=2.8068

According to results in Fig. 4, combination of aging temperature and thickness of interfacial intermetallic compounds (input 2 and input 4) has the strongest impact on prediction of shear strength of the composite solder joints. Combination of input 1 and input 2 or content of multi-walled carbon nanotubes and aging temperature has the lowest impact on the prediction of shear strength of the composite solder joints. Table 3 shows numerical values of the effects of two parameters on the shear strength of the composite solder joints.

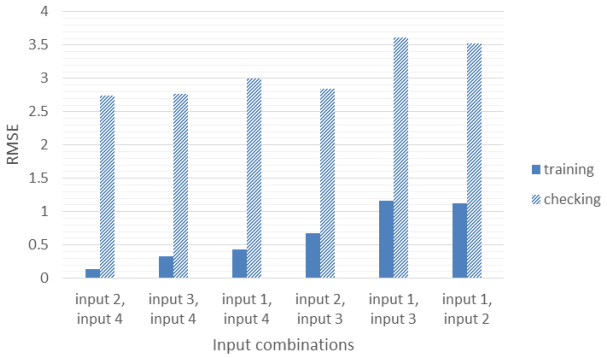

Fig. 4. Effects of two parameters on the shear strength of the composite solder joints

Table 3. Effects of two parameters on the shear strength of the composite solder joints

input 1, input 2 --> training=1.1209, checking=3.5228
input 1, input 3 --> training=1.1654, checking=3.6120
input 1, input 4 --> training=0.4334, checking=2.9930
input 2, input 3 --> training=0.6755, checking=2.8421
input 2, input 4 --> training=0.1364, checking=2.7426
input 3, input 4 --> training=0.3287, checking=2.7692

4. CONCLUSION

This study analyzed the effect of multi-walled carbon nanotubes, aging temperature, aging time, and the thickness of interfacial intermetallic compounds on predicting the shear strength of composite solder joints using the adaptive neuro-fuzzy inference system (ANFIS). The investigation focused on understanding the relative importance and interplay of these variables in determining the shear strength of the joints, a critical factor for the performance and reliability of composite solder materials. The findings provided valuable insights into the predictive power and consistency of the ANFIS model, particularly concerning the influence of the input variables on the output.

The analysis revealed that the thickness of interfacial intermetallic compounds had the strongest impact on predicting the shear strength of composite solder joints. This input variable emerged as the most significant determinant, underscoring its crucial role in influencing the mechanical performance of the solder joints. The formation and growth of intermetallic compounds at the interface are known to directly affect joint strength by altering the microstructure and bonding characteristics, making this parameter a key focus for optimizing solder joint performance.

In contrast, the content of multi-walled carbon nanotubes was found to have the least impact on the prediction of shear strength. While these nanotubes are often incorporated to enhance the mechanical and thermal properties of composite materials, their relatively lower influence in this context highlights the complex interactions between nanomaterials and other factors, such as aging and intermetallic compound formation. This finding suggests that the role of nanotubes may be more pronounced in other performance metrics or under specific conditions not explored in this study.

The combination of aging temperature and the thickness of interfacial intermetallic compounds demonstrated the strongest combined effect on the prediction of shear strength. This synergistic relationship underscores the importance of considering the interplay between these factors, as aging temperature directly influences the growth kinetics of intermetallic compounds, thereby amplifying their impact on joint strength. The findings suggest that optimizing aging temperature in conjunction with managing interfacial thickness could yield significant improvements in the mechanical properties of composite solder joints.

Overall, the results showcased the high predictive consistency of the ANFIS model, effectively capturing the complex relationships between input variables and the resulting shear strength. The model's ability to provide reliable predictions based on the influence of these inputs highlights its potential as a valuable tool for designing and optimizing composite solder materials. By leveraging the insights gained from this analysis, researchers and engineers can better understand the critical factors affecting solder joint performance and develop more effective strategies for enhancing the reliability and durability of electronic assemblies. This study also emphasizes the importance of adopting advanced modeling approaches, like ANFIS, to address the challenges posed by the multifactorial nature of composite material systems.

REFERENCES

[1] Niranjani, V. L., Rao, B. C., Singh, V., & Kamat, S. V. (2011). Influence of temperature and strain rate on tensile properties of single walled carbon nanotubes reinforced Sn–Ag–Cu lead free solder alloy composites. *Materials Science and Engineering: A*, *529*, 257-264.

[2] Wang, H., Hu, X., & Jiang, X. (2020). Effects of Ni modified MWCNTs on the microstructural evolution and shear strength of Sn-3.0 Ag-0.5 Cu composite solder joints. *Materials Characterization*, 110287.

[3] Mayappan, R., Hassan, A. A., Ab Ghani, N. A., Yahya, I., & Andas, J. (2016). Improvement in intermetallic thickness and joint strength in carbon nanotube composite Sn-3.5 Ag Lead-free Solder. *Materials Today: Proceedings*, *3*(6), 1338-1344.

[4] Dele-Afolabi, T. T., Hanim, M. A., Norkhairunnisa, M., Yusoff, H. M., & Suraya, M. T. (2015). Investigating the effect of isothermal aging on the morphology and shear strength of Sn-5Sb solder reinforced with carbon nanotubes. *Journal of Alloys and Compounds*, *649*, 368-374.

[5] Yang, Z., Zhou, W., & Wu, P. (2014). Effects of Ni-coated carbon nanotubes addition on the microstructure and mechanical properties of Sn–Ag–Cu solder alloys. *Materials Science and Engineering: A*, *590*, 295-300.

[6] Yim, B. S., Shin, Y. E., & Kim, J. M. (2018). Influence of multi-walled carbon nanotube (MWCNT) concentration on the thermo-mechanical reliability properties of solderable anisotropic conductive adhesives (SACAs). *Microelectronics Reliability*, *91*, 201-212.

[7] Nai, S. M. L., Wei, J., & Gupta, M. (2006). Improving the performance of lead-free solder reinforced with multi-walled carbon nanotubes. *Materials Science and Engineering: A*, *423*(1-2), 166-169.

[8] Mehrabi, K., Khodabakhshi, F., Zareh, E., Shahbazkhan, A., & Simchi, A. (2016). Effect of alumina nanoparticles on the microstructure and mechanical durability of meltspun lead-free solders based on tin alloys. *Journal of Alloys and Compounds*, *688*, 143-155.

[9] Choi, E. K., Lee, K. Y., & Oh, T. S. (2008). Fabrication of multiwalled carbon nanotubes-reinforced Sn nanocomposites for lead-free solder by an electrodeposition process. *Journal of Physics and Chemistry of Solids*, *69*(5-6), 1403-1406.

[10] Jang, J.-S.R, ANFIS: Adaptive-Network-based Fuzzy Inference Systems, IEEE Trans. On Systems, Man, and Cybernetics (1993), Vol.23, 665-685.

11th International Scientific Conference
IRMES 2025
Research and Development of
Mechanical Elements and Systems
Junen19 – 21, 2025; Vrnjačka Banja, Serbia

Original scientific paper
DOI: 10.46793/IRMES25.027N

DEVELOPMENT AND THERMAL ASSESSMENT OF A HIGH-POWER GEARBOX

Vojkan NOJNER[1]
Dragan MILČIĆ[2]
Milan BANIĆ[3]

[1]Goša Fom, Equipment and Machines Factory, 11420 Smederevska Palanka, Serbia, RS; v.nojner@gosafom.info;
ORCID iD: 0009-0003-1634-4481
[2]Faculty of Mechanical Engineering, University of Niš, 18000 Nis, Serbia, RS; dragan.milcic@masfak.ni.ac.rs;
ORCID iD: 0000-0002-3936-7462
[3]Faculty of Mechanical Engineering, University of Niš, 18000 Nis, Serbia, RS; milan.banic@masfak.ni.ac.rs;
ORCID iD: 0000-0001-8684-042X

Abstract: *This paper presents the development of a high-power gearbox used for belt conveyor drives in open-pit mining. The gearbox is designed for continuous operation at high speeds, which leads to the generation of a large amount of heat. The main cause of overheating is the heat generated inside the gearbox due to friction in the bearings, friction in the seals, and above all, friction between the tooth flanks during meshing. The thermal stability of the gearbox was predicted using the finite element method (FEM). Validation of the FEA thermal analysis results was carried out through power transmission testing on a proof stand, by measuring various parameters such as temperatures, vibrations, and noise of the gearbox and housing, for both unloaded and partially loaded conditions.*

Keywords: *high-power gearboxes; heat calculation; thermal analysis of gearbox; testing of gearbox*

1. INTRODUCTION

Gear units are intended for transmission of power and torque from drives to working machines. High power gearboxes are used for belt conveyor drives in coal open pits mines for the transfer of material from the excavator to the spreader.

They are designed for continuous operation at high speed - transmit a lot of power, so unavoidable power losses generates significant amount of heat, which is absorbed by oil and housing. Depending on working conditions cooling of gearbox casing is done by passive or active convection. When natural airflow is insufficient, then forced ventilation is applied (using a fan). On the basis of conducted thermal analysis of gearbox housing is determined required fan capacity.

A deep understanding of the interplay of machine elements in geared transmissions is fundamental for an optimal design. Except for selected space applications [2], a oil is present in a gearbox. The interaction of rotating machine elements with fluid causes a fluid flow connected with no-load power loss. According to ISO/TR 14179-2, the gear-based no-load gearbox power loss includes power losses due to churning, squeezing, impulse, and ventilation effects.

In the past decade, research in the field of thermal analysis of high specific power gearboxes has significantly advanced, focusing on heat transfer optimization, loss reduction, and increased reliability under heavy load conditions.

With the rise in gearbox mechanical power, the thermal power limit is increasingly becoming a constraining factor. To achieve a balanced system, additional cooling of the gearbox is required. A common solution involves the use of a fan mounted on the high-speed input shaft.

The optimal design of this solution is the subject of ongoing research. Due to the complexity of the gearbox's thermal balance, analytical calculation methods are too inaccurate for precise evaluation of changes in the cooling system. In studies [1, 7] a numerical approach was applied to determine the optimal cooling concept involving a fan and an air guide.

Power losses in gearboxes result in frictional heating. Sufficient heat transfer from the gearbox to the environment is required for reliable operation. The heat dissipation from gears is linked to their interaction with fluids in the gearbox. Recent research has demonstrated the use of Computational Fluid Dynamics (CFD) to predict the gearbox fluid flow and no-load losses in an isothermal manner. Study [3] focuses on a numerical analysis of heat dissipation in a dry-lubricated gearbox under atmospheric conditions.

Testing on proof stand is the final phase of the process of production any gearbox. This is especially applies to high-power gear units, which are of special construction

and have significant heat losses, and such as a prototype, is required to be tested first in factory conditions [4,5].
The paper presents the development of a high-power gearbox intended for driving belt conveyors in open-pit mines, with a particular emphasis on thermal stability. In order to ensure reliable operation, a thermal FEA (Finite Element Analysis) of the gearbox housing was carried out to optimize its shape. The design validation was performed through testing of the gearbox on a test bench.

2. HIGH-POWER GEARBOXES

For the belt conveyor drives with high capacity used powerful bevel-helical gearboxes with flanged output shaft. Housing is considerably enlarged and completely ribbed. The fan is on the input shaft with deflection hood that follows the contour of the housing.
Depending on the transmission ratio (usually in the range i=14...18) are applied two or three transmission stages. Three-stage gearboxes are more used, because they have a larger surface of the housing (and better thermal capacity), increasing the possibility of combining, and avoid high partial transmission ratios, as well as smaller size of spur gear to the output stage.
For transfer the nominal power of 1000 kW (power EM) the company GOŠA FOM [9] has developed two basic types of three stage gearbox, with application factor K_A=1,8 and 2, and the transmission ratio i=17,267 and i=17,198. The gear units are specially designed and manufactured according to specific customer requirements (see Table 1). We used a long-standing experience in producing gear unit for belts on different machines on surface mining, such as excavators, conveyors and spreaders.

Table 1. Three-stage gearboxes with power 1000 kW

Type	Ratio i	Application factor K_A	Max. Housing temperature t °C	Housing surface A m^2
1	17,267	1,8	90	34,7
2	17,198	2,0	85	44,6

For dimensioning gear unit with high load capacity it is necessary to make a calculation of toothed parts and bearings to the criteria of customer requirements (application factor $K_{A\min}$= 1,8 at safety factors of toothing for contact and bending stress S_H=1,2 and S_F=1,4, and operating bearing lifetime min. 50.000h). Nominal working input speed of gearbox is 1000 (range 600-1200) rpm.
Based on gearing and bearing calculations and thermal stability of the housing is made workshop documentation to produce of toothed parts and housing. Spiral bevel gear pair is made in HPG-quality by the Klingelnberg Cyclo-Paloid system. Gearing of helical gears is ground, with tooth profile correction and flank modification (so-called "barreling"). Premium materials are used (case-hardened steels), as well as finishing tooth flanks to all gearings.
The overview of typical gearbox dimensions is given in the Figure 1.
During operation of gearbox which continuously ("24/7") transmit high power, in all bearings and in each engaged gearing pair generated some power losses, which are converted into heat, so that the oil and the inside of gearbox are heated, and the outer surface of the housing is transferred to the environment. These losses in a three-stage bevel-helical gear unit amounts to about 4% of the rated power (about 1% in the spiral bevel gear pair and around 1,5% for helical gears set; losses in the bearings is about 0,1% per bearing). Regarding the high-power gearboxes these losses of a few percent is converted into a considerable amount of heat (precisely about 40 kW), that must be, over the outer surface of the housing, is transferred to the environment.

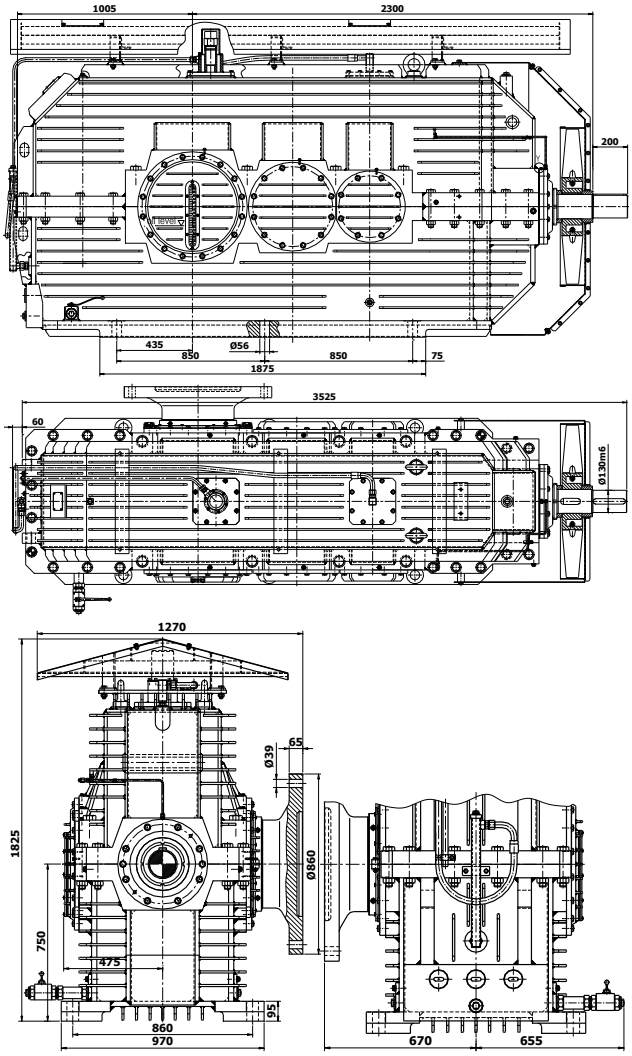

Fig.1. Typical Gearbox Dimensions Overview

Natural cooling of gear unit is improved by increasing the outer surface of the housing with ribbing and elongation in free area behind the output shaft. Display of enlarged and ribbed gearbox housing with main measures for factor K_A=1,8, is shown in Figure 2.
With such housing temperature in the interior of the gearbox in the exploitation during the summer is about 120 °C.
When natural convection is not sufficient, apply to forced cooling (used to fan on input shaft), which must increase the speed of air flow around the gearbox, which must increase the speed of air flow around the housing, thus causing faster heat transfer from the inner to the outer

housing surface, and so contribute to cooling the interior of the gear unit.

Enlarged housing of three-stage gearbox (using the fan) has a sufficient surface for the thermal stability of the gear unit below 80 (max.90) ºC. To gearbox in operation with mineral oil had a working temperature below 85 °C, in all weather conditions, it should calculate the thermal behavior of the housing, i.e. conduct an analysis of the different airflow speeds around the casing.

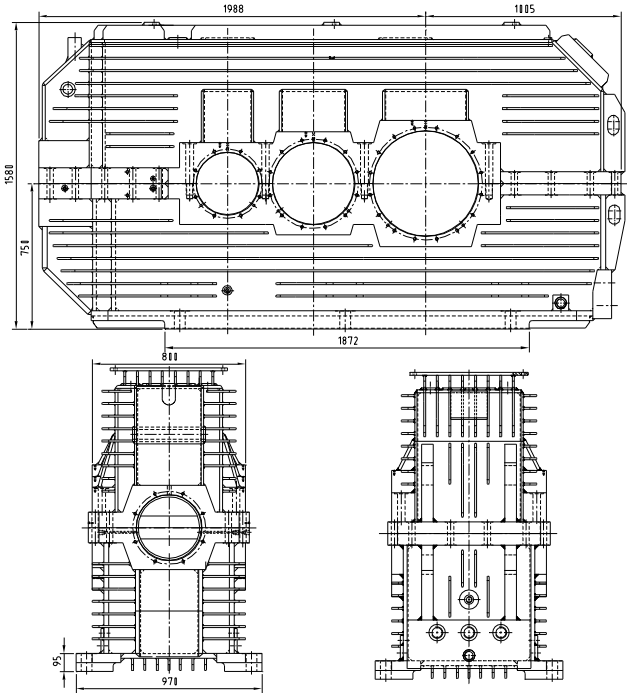

Fig.2. Enlarged and ribbed gearbox housing

3. HEAT CALCULATION AND THERMAL ANALYSIS

Due to the power losses that are converted into heat, when designing is very important to implement thermal analysis of gearbox or housing.

For thermal analysis of gearbox, and thermal stability of the housing is used basic calculation, according to the literature, as well as thermal analysis of casing is performed using finite element method (FEM). The basic heat calculation is used to obtain basic data on the required surface for housing sizing and thermal analysis is used to check the temperature condition of the outer and inner surfaces of the housing and the choice of fan capacity.

3.1. Heat calculation

For heat calculation using the following basic equations [8]:

$$P_v = P_N \cdot (1-\eta) \cdot \frac{ED}{100} \quad (1)$$

$$\Delta t = \frac{P_v \cdot 10^3}{\alpha_k \cdot A_G} \quad (2)$$

$$t = t_u + \Delta t \quad (3)$$

where:

-Loss of rating: P_v = 39 kW

-Rating power: P_N = 1000 kW

-Periodic rating: ED = 100%

-Gearbox efficiency: η = 0,99·0,985·0,985=0,961

-Temperature difference: Δt = 51,1 K

-Heat transfer coeff. (fan no/yes): α_k =22 / 35 W/(m²·K)

-Gearbox surface: A_G = 34,7 m² (acc. to Fig. 1)

-Housing surface: A_H = 30,4 m² (acc. to Fig. 2)

-Ambient temperature: t_u = max.40°C

-Inside temperature: t = 80 (max. 90) °C

Using equations (1) to (3) with a modification of parameters t, α_k and A_G, the below typical cases are obtained the following results for the required developed outer housing surface A_G, as well as the temperature inside the housing t:

1. Done: t=90 ºC, α_k=22 W/m²/K. Result: A_G=35,5 m².
2. Done: t=90 ºC, α_k=35 W/m²/K. Result: A_G=22,3 m².
3. Done: t=80 ºC, α_k=35 W/m²/K. Result: A_G=27,9 m².
4. Done: A_H= 30,4 m², α_k=22 W/m²/K. Result: t=98,3 ºC.
5. Done: A_G= 34,7 m², α_k=35 W/m²/K. Result: t=72,1 ºC.

According to the literature [8], the convection factor without a fan is 20-22 W/(m²·K), and with fan is 30-40 W/(m²·K) (for the calculation taken mean empirical value of 35 W/(m²·K)). The temperature inside the gearbox is highly dependent on the ambient temperature. As authoritative, for calculation takes the maximum ambient temperature in summer of 40 °C.

For the lubrication of gearbox used high-quality industrial gear oil, ISO viscosity grade 320 acc. to DIN 51517-3, e.g. 6 EP acc. to AGMA grade – CLP gear oils (kinematic viscosity 320 mm²/s at 40 °C, with a tolerance of ±10%). Mineral gearbox oil is with additives (corrosion protection, oxidation and foam resistance, extreme pressure (EP), anti wear (AW), VI improver).

To use synthetic oil obtained lower values by about 10-15 °C. However, these oils are very expensive (5-8 times the mineral) and in practice are applied in up to 20-25% of cases.

The external surface of the extended housing is increased up to 35% in relation to a basic surface, by elongation in the free space behind the output shaft, as well as the fins on all sides of the housing. Ribs must be set in the direction of airflow, thus in the longitudinal direction and horizontally. It should be noted that for the smaller gear units, where the fan is not in use, the ribs are placed vertically and transversely.

To reduce the temperature inside the casing at the final installation on site, above the gear unit sets roof. Gearbox can be painted with a special paint that repels sunlight. These additional passive protection measures can reduce the temperature inside the gearbox housing by 5-8 °C.

3.2. Thermal analysis of housing

The distribution of temperature in the worm gear transmission using FEM is done with the ANSYS Workbench software. The analysis is defined as a thermal analysis in the time domain that is used in the ANSYS module for transient thermal analysis. For generating the finite element mesh the elements of a higher order or

SOLID 226 are used. The mesh is generated with 236298 nodes which form 45824 elements.
Figures 3 and 4 shows 3D model of gearbox and simulation model of the gearbox housing with a generated finite element mesh.

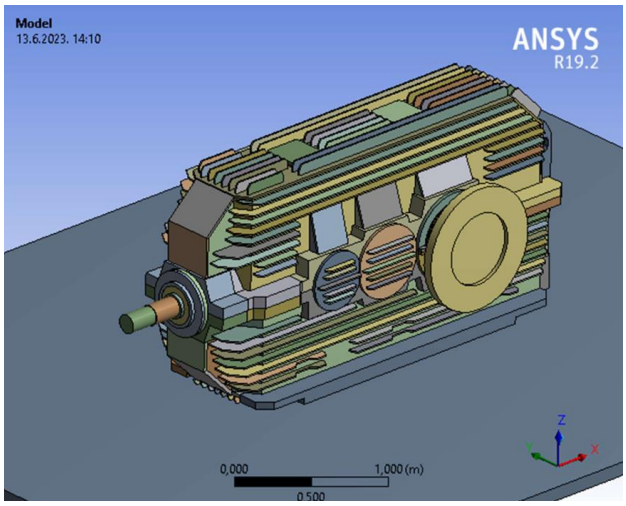

Fig.3. 3D-simulation model of gearbox

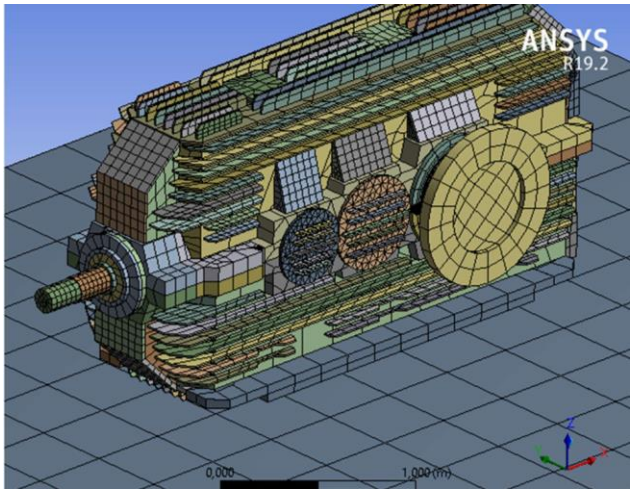

Fig.4. Generated finite element mesh of the gearbox

Based on analytically determined power losses in the gear pairs, bearings, and seals (Fig. 5), a simulation was applied to determine the temperature distribution of the gearbox housing (Fig. 6).

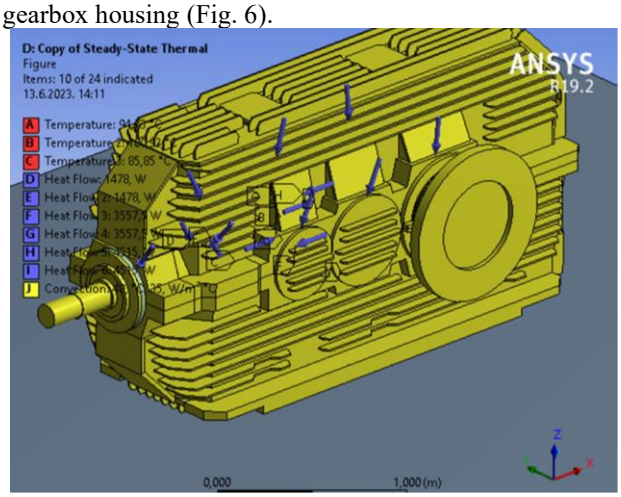

Fig. 5. Thermal load of the gearbox

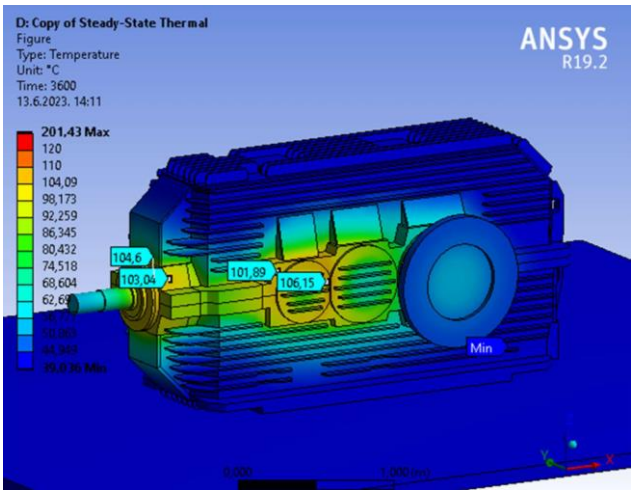

Fig.6. Thermal analysis of gearbox housing

4. TESTING ON PROOF-STAND

Testing on proof-stand is the final part of the process of production each gear unit. Testing of high power gearbox is implemented in several stages. After making gear unit is tested on stand without and under partial load (around 200 kW, which is about 20% of the installed motor power). The load is increased gradually, usually in 2-3 steps. For single testing (with or without a fan) is used alternately right (clockwise) and left (counter clockwise) turning direction of the input shaft. Testing paired gearboxes under load is applied only in one direction of rotation of the input shaft, so that each of the gear unit has a proper fan cooling.

Fig.4. Gearboxes with fan on proof-stand

For testing without load can be tested only one reducer, first without and then with a fan and finally with assembled deflection hood, and for testing under partial load shall be tested two gear units, connected between the flanged shafts through the cardan shaft. This is so-called "back to back" principle of load. Proof stand is with capacity of max. 300 kW and the rotation speed max. 1800 rpm. For practical purposes is used to load up to 250 kW, with a speed range of 600-1200 rpm. In the concrete case of testing parameters are: load 200-220 kW and speed 1000 rpm (short-time max. 1200 rpm).
Testing layout of paired gearbox under load on proof stand is shown in Figure 6.

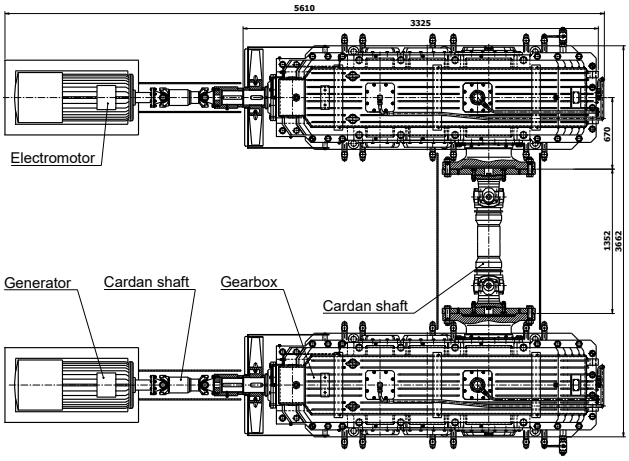

Fig. 5 Testing layout of paired gearbox under load

Testing procedure of gear units on proof-stand is presented in the Tables 3. to 5.

Table 3. Full testing procedure of gearbox on proof-stand

Case	Gearbox No.	Fan	Load	Time (min)	Input shaft direction
1.	1	-	-	min.120	CW / CCW
2.	1	+	-	min.120	CW
3.	2	-	-	min.120	CW / CCW
4.	2	+	-	min.120	CCW
5.	1 + 2	+	+	min.240	CW + CCW

Table 4. Short testing procedure of gearbox on proof stand

Case	Gearbox No.	Fan	Load	Time (min)	Input shaft direction
1.	1	-	-	min.180	CW / CCW
2.	2	-	-	min.180	CW / CCW
3.	1 + 2	+	+	min.240	CW + CCW

Table 5. Testing regimes of meshed gearboxes under load

Step	1.	2.	3.	4.
Load	-	5%	10%	20%
Time (min)	30 +30	30	30	120

Each gearbox testing must last until reaching a stable (holding) temperature of max.2K for 30 minutes for each measuring point (MM).

5. PARAMETERS MEASURING OF GEARBOXES

5.1. Equipment for monitoring of gearbox

The high power gear unit is equipped with following ("monitoring") equipment for measuring, condition monitoring and control of temperature, vibration and oil:

- resistance thermometers for temperature measuring of input shaft bearings,
- resistance thermometer for temperature measuring of oil sump,
- sensors for vibration measuring of the housing in the zone of the input shaft, with accessories
- connections for vibration casing measurements above others bearings, can be measured and shown by mobile device / equipment on site,
- oil level indicators - visually (numbered window) and an electronic device in a protective tube,
- oil heaters, for winter conditions.

The "monitoring" equipment of gearbox is shown in Figure 7.

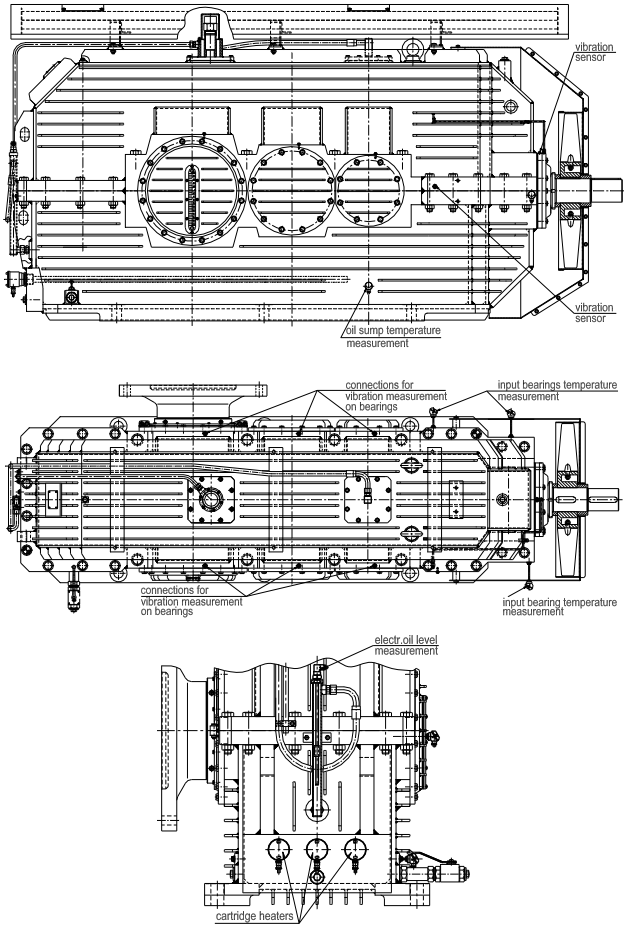

Fig.6. "Monitoring" equipment of gearbox

During the testing on each gear unit measures the temperature of all bearings and the vibrations of the housing near all bearings. Temperatures of bearings on the input shaft and oil sump are measured with resistance thermometers. Vibrations are measured on the housing near each bearing in 3 directions (vertical, horizontal and axial) with mobile device.

Example of results for temperature measurement of input shaft bearings (MM1 to MM3) and oil temperature (MM4) is shown in Figure 8.

Measuring point MM1 is bearing close to the fan, MM2 is the inner bearing from paired, MM3 is the bearing near to the gearing on the input shaft and MM4 is the oil sump. Ambient temperature (in the hall) was 27 ºC.

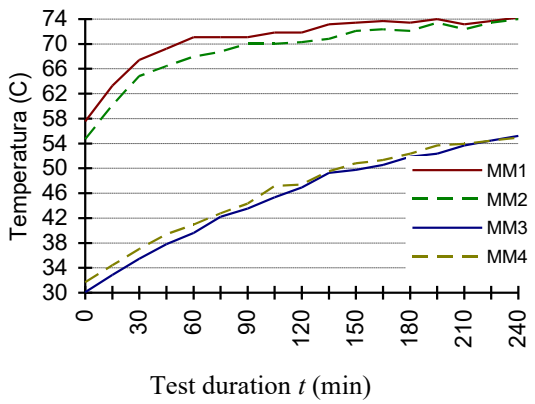

Fig.7. Bearings- and oil temperatures (example)

Display of vibration- velocity measuring on gearbox is shown in the figures 9.

Fig.8. Vibration velocity measuring (examples)

Scheme of measuring points in vibration velocity measuring of gearbox housing is given in the figure 10.

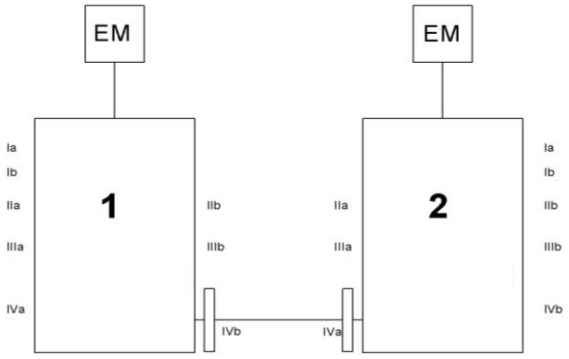

Fig.9. Vibration measuring points on gearboxes

Examples of results of vibration velocity measuring on gearbox housing are given in Tables 6. and 7.
The measured values are within the limits of zone B (terms "satisfactory", "acceptable" or "permissible") for machine group G (class IV), acc. VDI 2056 and DIN ISO 10816. The limit value is 3,5 mm/s for the criterion "rigid (strong)", i.e. 4,5 mm/s, for the criterion " flexible (soft)".

Table 6. Vibrations of gearbox 1 at measuring points (mm/s)

Measur. point	Ia	Ib	IIa	IIb	IIIa	IIIb	IVa	IVb
1. Vert.	0,97	1,23	0,66	0,69	0,8	0,72	0,57	1,04
2. Horiz.	-	0,79	0,71	0,76	0,9	0,66	0,71	0,52
3. Axial	-	-	1,29	1,87	1,72	1,85	1,88	1,64

Table 7. Vibrations of gearbox 2 at measuring points (mm/s)

Measur. point	Ia	Ib	IIa	IIb	IIIa	IIIb	IVa	IVb
1. Vert.	1,24	1,26	0,61	0,58	0,72	0,61	1,02	0,98
2. Horiz.	-	0,7	0,63	0,59	0,85	0,72	0,83	0,67
3. Axial	-	-	1,34	1,74	1,69	1,75	1,73	1,89

Also is measured the noise of gearbox, which does not exceed the value defined in customer requirements. If not specified, as authoritative maximum value for noise sound power level, acc. VDI 2159, is taken next value:

$$P_A = 0{,}8 \cdot (71{,}7 + 15.9 \cdot \log(P/\text{kW})) \quad [\text{dB}] \quad (4)$$

6. CONCLUSIONS

Modern approaches to thermal analysis of gearboxes combine numerical simulations, design optimization, and advanced modeling techniques with the aim of improving cooling efficiency and system reliability. This paper presents the development of a high-power gearbox for belt conveyors in open-pit mining, with a special focus on thermal stability. Finite Element Analysis (FEA) was used to optimize the housing design, and the gearbox was validated through experimental testing on a proof stand. The result of this approach in the development of high specific power gear transmissions is improved cooling efficiency, optimized gearbox housing design, and increased reliability.

REFERENCES

[1] Bauer, B., Hambrecht, R., Kube, A., Becka, S.: Thermal Analysis and Optimization of Gearboxes by Simulation, *Power Transmission Engineering*, Vol.6 (Dec), pp. 64-69, ISSN, 2018

[2] Lince, J.R.: Effective Application of Solid Lubricants in Spacecraft Mechanisms, *Lubricants 2020*, 8(7), 74

[3] Hildebrand, L., Dangl, F., Paschold, C., Lohner, T., Stahl, K.: CFD Analysis on the Heat Dissipation of a Dry-Lubricated Gear Stage, *Applied Sciences*, Vol.12, No.20: 10386. https://doi.org/10.3390/app122010386, 2022.

[4] Larson, R.: Thermal & Efficiency Analysis for a High-Speed Gearbox, Honors Theses 3525, 2022 https://scholarworks.wmich.edu/honors_theses/3525

[5] Nojner, V.: Thermal Analysis of a Crossed Helical Gearbox Using FEM, *The 3rd International Conference "Mechanical Engineering in XXI Century"*, September 17-18, Niš, pp. , ISSN, 2015.

[6] Miltenović, A., Banić, M.: Thermal Analysis of a Crossed Helical Gearbox Using FEM, *TRANSACTIONS OF FAMENA XLIV-1*, pp. 67-77, ISSN 1333-1124, 2020.

[7] Miltenović, A., Tica, M., Banić, M., Miltenović, Đ.: Prediction of temperature distribution in the worm gear meshing, *FACTA UNIVERSITATIS Series: Mechanical Engineering Vol. 18, No 2*, pp. 329 – 339, ISSN 0354-2025, 2020,

[8] Niemann, G., Winter, H.: *Machine Elements, vol. 2: "Gear units generally, Gearboxes - Fundamentals, Spur gears"* (in German), Springer-Verlag, Berlin Heidelberg, pp.218-229, ISSN, 2003

[9] GOŠA FOM Workshop documentation.

11th International Scientific Conference
IRMES 2025
Research and Development of
Mechanical Elements and Systems
June19 – 21, 2025;Vrnjačka Banja, Serbia

Original scientific paper DOI: 10.46793/IRMES25.033T

OPPORTUNITIES FOR THE APPLICATION OF A PLANETARY GEARBOX AS A REVERSING UNIT

SanjinTROHA[1]
Jelena STEFANOVIĆ MARINOVIĆ[2]
ŽeljkoVRCAN[3]
KristinaMARKOVIĆ[4]
MarkoPERIĆ[5]

[1]University of Rijeka, Faculty of Engineering, Rijeka, Croatia, HR-51000; sanjin.troha@riteh.uniri.hr;
ORCID iD: 0000-0003-2086-372X
[2]University of Niš, Faculty of Mechanical Engineering, Niš, Serbia, RS-18000; jelena.stefanovic@masfak.ni.ac.rs;
ORCID iD: 0000-0001-8823-5362
[3]University of Rijeka, Faculty of Engineering, Rijeka, Croatia, HR-51000; zeljko.vrcan@riteh.uniri.hr;
ORCID iD: 0000-0002-7005-4130
[4]University of Rijeka, Faculty of Engineering, Rijeka, Croatia, HR-51000; kristina.markovic@riteh.uniri.hr;
ORCID iD: 0000-0003-1569-7464
[5]University of Niš, Faculty of Mechanical Engineering, Niš, Serbia, RS-18000; marko.peric@masfak.ni.ac.rs;
ORCID iD: 0000-0001-9350-0351

Abstract:*gearbox. The gearbox has been designed as a two-carrier unit with two brakes, and it has been depicted using the Wolf-Arnaudov symbols. The ideal torque ratios for six pairs of reversing gear ratios have been determined and the relationship between the ideal torque ratios of both planetary gear setsrequired for obtaining reversible transmission ratios was determined. The efficiencies were determined for all considered cases. It was determined that the gearbox has relatively high parasitic power in all cases of operation with the brake Br2 active, and the parasitic power function and its intensity were determined. The procedure was performedassuming two constant component gear train efficiencies, namely $\eta_0 = 0.98$ and 0.95.*

Keywords:*planetary gearbox, reversing gearbox, parasitic power, two-carrier planetary gear train*

1. INTRODUCTION

1.1. Planetary gear trains

Planetary gear trains (PGTs) have many advantages over conventional gearboxes, the most important of which is the significant reduction in weight and dimensionsfor the same power rating. This key advantage has enabled the wide and rapid application of PGTs in many branches of engineering, such as automotive, aerospace, industrial automation, defense, shipbuilding, as well as renewable energy systems, i.e. wind turbines, solar power plants, and hydropower plants. Small overall dimensions, compact design, high efficiency in power transmission and the ability to transfer heavy loads make them particularly suitable for applications with limited space and weight, combined with requirements for long-term, reliable and uninterrupted operation.Furthermore, PGTs enable easier integration with modern automation and control systems, as they enable precise control of torque and rotational speed, which further increases their value in modern technological solutions. Overall, planetary gearboxes, and especially complex multi-carrier PGT systems, encompass a very wide, technically demanding and complex area of expertise [1,2]. The main advantage of multi-carrier systems is the possibility of simultaneous power transmission through several mechanical paths, resulting in greater load capacity, overload resistance and increased energy efficiency. This distribution of power allows the load to be carried more evenly by the gears, reducing local stress and extending the service life of individual components. By combining and interconnecting the shafts of different component gear train units, it is possible to build very complex, multi-stage, connected multi-carrier PGT systems, enabling various functionalities such as multiple gear ratios, changes in the direction of rotation, automatic changes between operating modes, as well as the ability to operate in different modes, for example full load mode, energy-saving mode or in reversible mode. Such systems often include additional control components such as clutches, brakes, actuators and sensor systems to monitor and optimize operation. The complexity of such systems requires the application of advanced methods of calculation, optimization, and simulation, including numerical methods such as finite element analysis (FEA)

to verify stresses and strains, and system dynamics to model and analyze behavior under different operating conditions. Proper design of multi-carrier PGT systems is essential to achieve high efficiency, long service life and optimal performance in actual operation conditions, with minimal maintenance costs and maximum operational availability.

1.2. Two-carrier planetary gear trains with two connecting shafts, four external shafts and two brakes

A particularly interesting direction of multi-carrier planetary gearbox development is two-speed transmissions. In such systems, the internal components of the gearbox are arranged to change the transmission ratio without interrupting the flow of power, that is, without stopping the drive system. This capability is extremely valuable in applications that require constant adjustment of operating conditions, such as automotive transmissions, industrial machinery, as well as in wind power systems where the optimal rotational speed must be continuously maintained for maximum efficiency. A key element that enables this functionality is the application of brakes on the single shafts of the planetary gearbox, as the strategic placementof brakes on selected shafts of the gear train makes it possible to change the flow of power inside the transmission. By applying one brake to block the rotation of a specific gear element (e.g. a planet carrier or ring gear), a single gear ratio is achieved. By deactivating that brake and activating the other, the power flow is diverted through another mechanical path, thus achieving a second gear ratio. This gear ratio change system is characterized by high shifting speed, reliability, and minimal mechanical losses, which makes them particularly suitable for demanding technical applications. In addition, due to the use of brakes instead of classic synchronization systems or clutches, the complexity of the mechanism is reduced, the overall reliability of the system increased, and maintenance costs reduced. The design variants of these two-speed planetary gearboxes can vary significantly depending on the specific application and technical requirements. Some systems use simple passive brakes with manual actuation, while more advanced systems might use electromagnetic, hydraulic or pneumatic actuator systems to control the brakes, allowing automatic gear changing depending on the operating conditions. The analysis of the kinetic characteristics of two-speed PGT systems with brakes shows that a properly selected combination of speeds, torque and power flows can significantly improve the overall efficiency and performance of the drive system. In this context, the design of the optimal gearbox involves not only the mechanical design of the transmission elements, but also the optimization of the control system that coordinates the operation of the brakes and manages the switching of gear ratios. After considering all these advantages, it can be concluded that two-speed planetary gearboxes with brakes on individual shafts represent an important area of contemporary development of mechanical transmission systems and open wide possibilities of application in the industry, transport and energy sectors.

1.3. Reversible two-carrier planetary gear trains

Reversible two-speed planetary gear trains represent an advancement in this technology, as they also allow the direction of rotation of the output shaft to be changed, while the rotational speeds remain stable or very similar in both operating modes. This functionality allows the power flow to be dynamically directed through the system, thus achieving high flexibility in applications that require a change in the direction of rotation with minimal changes in speed. Alternating actuation of the control brakes on different component planetary gear trains allows switching between different directions of rotation. Such gearboxes provide high controldynamics, which is crucial in applications such asindustrial robotics and autonomous systems, where the requirements for accuracy and adaptability are extremely high.

1.4. The selected two-carrier planetary gear train

The considered reversible two-speed planetary gearbox (Figure 1) is based on an innovative design that allows the active use of only one planetary gearset in the first gear (Br1), while in the second gear (Br2) it includes both planetary gearsets. This strategy allows the direction of rotation of the output shaft to be dynamically changed without the need for additional complex mechanical systems.

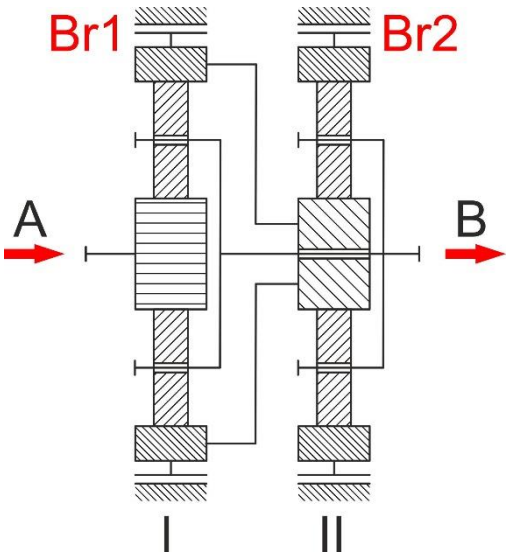

Figure 1. Design conceptof the selected reversing PGT

With brake Br1 activated, the gearbox operates in a simple PGT mode, where the power from the source is transferred to the output shaft through only one planetary assembly. This mode of operation is characterized by high efficiency because the power is transmitted through a smaller number of components, thus reducingfriction and mechanical losses. On the other hand, with brake Br2 activated, when both planetary gearsets are working, more complex power interactions occur within the gearbox, leading to parasitic power losses. These losses occur due to the circulation of power through the internal components of the transmission, resulting in a decrease in overall efficiency. Parasitic power causes some of the energy not to be

efficiently transferred to the output shaft but lost in the form of heat, becoming an issue at higher system loads in speed Br2. The reduction of these parasitic losses is crucial in the optimizationof the design of reversible planetary gearboxes, and can be achieved by carefully selecting gear materials, reducing friction between components, and optimizing transmission geometry. The investigation of these parameters is crucial for increasing energy efficiency and reducing system operating costs.

2. GEAR TRAIN ANALYSIS

2.1. Torque method analysis

The Wolf-Arnaudov symbol may be used to illustrate the structure of the selected reversible planetary gearbox, so that a better insight into the structure and topology of the system may be gained. The absolute and relative power flows through the gear train in both speeds were determined and the functions of the ideal and real specific torques on the gearbox shafts were determined by applying the torque method in accordance with the lever rule for planetary gearboxes of the 2k-h variant A. Figure 2 shows the flow of power through the gearbox when brake Br1 is activated and brake Br2 is deactivated.

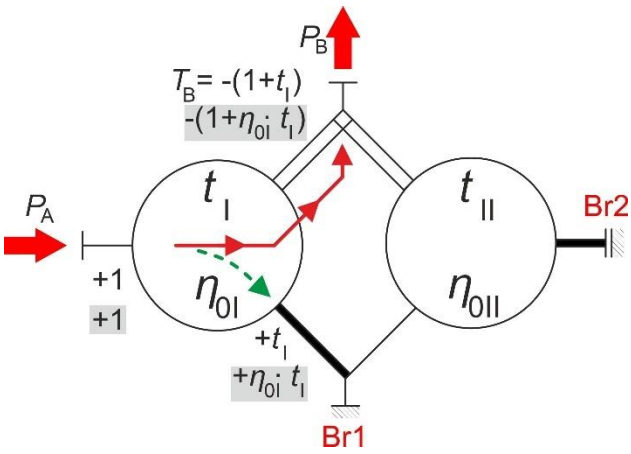

Figure 2. PGT operation with brake Br1 on

Based on the expression from [3], it is possible to obtain a kinematic gear ratio function where the arguments of the function are ideal torque ratios (the ratio of the number of teeth of the ring gear and the number of teeth of the sun gear) (1):

$$i_{\mathrm{Br1}} = -\frac{T_B}{T_A} = +1+t_{\mathrm{I}} \tag{1}$$

It is possible to obtain a function (2) of the efficiency based on the expression from [3], where the arguments of the function are the ideal torque ratio and the efficiency of the first planetary gear train[3].

$$\eta_{\mathrm{Br1}} = \frac{\left(-\frac{T_B}{T_A}\right)_{\text{losses}}}{\left(-\frac{T_B}{T_A}\right)_{\text{no losses}}} = \frac{1+\eta_{0I}t_I}{1+t_I} \tag{2}$$

In a similar way, using the torque method, the active and relative power flows on the planetary rows are obtained forthe case when the gearbox operates with brake Br2 on and brake Br1 off (Figure 3). The specific functions of gear ratio and torque on shafts have been calculated, and in this case, there are two ideal torque ratios and two relative efficiencies.

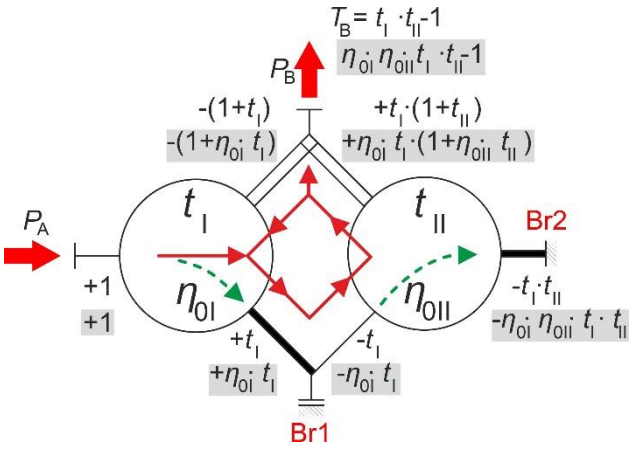

Figure 3. PGT operation with brake Br2 on

Based on the expression from [3], a kinematic gear ratio function can be obtained, where the function arguments are ideal torque ratios (3):

$$i_{\mathrm{Br2}} = -\frac{T_B}{T_A} = -\left(t_{\mathrm{I}}t_{\mathrm{II}} - 1\right) \tag{3}$$

The efficiency function(4) is also obtained by analogy (4):

$$\eta_{\mathrm{Br2}} = \frac{\left(-\frac{T_B}{T_A}\right)_{\text{losses}}}{\left(-\frac{T_B}{T_A}\right)_{\text{no losses}}} = \frac{\eta_{0I}\eta_{0II}t_I t_{\mathrm{II}}-1}{t_I t_{\mathrm{II}}-1} \tag{4}$$

The gearbox under consideration can operate as a reversing gearbox within a certain interval of gear ratios. In this paper, six reversible gearbox operating modes will be determined.

To obtain an equation that allows the determination of ideal torque ratios for these operating modes, we will start with the functions of transmission ratios, namely equations (1) and (3). Assuming that (1) is equal to the negative value of (3), the following (5) is obtained:

$$i_{\mathrm{Br1}} = -\,i_{\mathrm{Br2}} \tag{5}$$

By transferring over to the right-hand sides of (1) and (3), (6) is obtained:

$$1+t_{\mathrm{I}} = t_{\mathrm{I}}t_{\mathrm{II}} - 1 \tag{6}$$

This equation describes the condition for the reversible operation of the selected two-speed gearbox. Changing over to an explicit form provides (7), which is graphed in Figure 4:

$$t_{\mathrm{II}} = 1+\frac{2}{t_{\mathrm{I}}} \tag{7}$$

The red curve in Figure 4 represents the geometric location of the points (t_I, t_{II}) that ensure the reversing operation of the selected gearbox. Six characteristic points have been marked on the red curve and for these points the reversing ratio and the efficiencies based on the expressions (2) and (4) were determined.

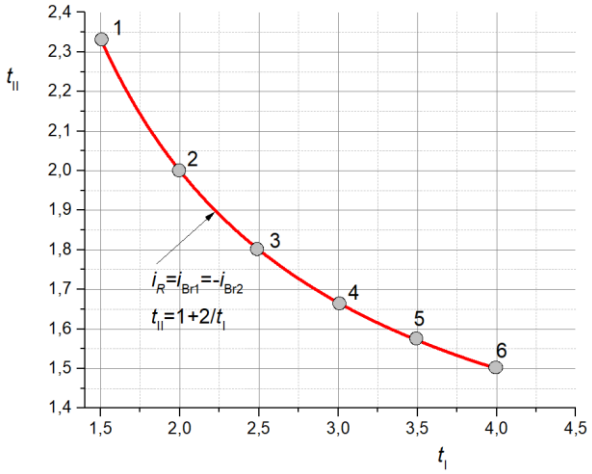

Figure 4. Reversing operation curve for the selected two-carrier PGT

Provided that each of the planetary gearsets has an internal efficiency degree equal to 0,98, which is the value that can be found in literature [4], the resulting efficiencies are provided in Table 1, which also lists the transmission ratios at characteristic points and the intensities of parasitic power with the gearbox working with brake Br2 on.

Table 1. Characteristic values for reversible operation of the selected PGT ($\eta_{0I} = \eta_{0II} = 0{,}98$)

	1	**2**	**3**	**4**	**5**	**6**
i_R	± 2,5	± 3	± 3,5	± 3,7	± 4,5	± 5
t_I	1,5	2	2,5	3	3,5	4
t_{II}	2,333	2	1,8	1,666	1,571	1,5
η_{Br1}	0,988	0,987	0,986	0,985	0,984	0,984
η_{Br2}	0,945	0,947	0,949	0,950	0,952	0,952
P_{par}	0,988	0,987	0,986	0,985	0,985	0,984

Analysis of the table datashows that the reverse gear ratios provided by this gearbox are in the ± 2,5 to ± 5 range. This can be achieved with certain ideal torque ratios in the 1,5 to 4 range. These reversing ratios may be required in practice in various cases where forward and reverse drive are required, such as industrial transport equipment. The transmission ratio interval may be further extended by using ideal torque ratios lower than 1,5. From Table 1 it can be concludedthat operation with brake Br1 on and brake Br2 offprovides a higher overall efficiency, as only onegear train is actively working.With brake Br2 on, both planetary gear trains are actively working, loaded with additional parasitic power which significantly reduces the gearbox efficiency. Interestingly, in all six cases there is almost the same parasitic power, which is equal to the power at the output. Figure 5 shows a trend of change in the efficiency for both speeds, assuming that the internal efficiency of both planetary gear trains is the same and amounts to 0,98. The efficiency curve with brake Br1 on (black curve) shows a degressive decline as the transmission ratio increases, and its value always remains above the internal efficiency rate of the planetary gear train. The efficiency curve with brake Br2 on (red curve) shows a degressive increase with an increase in the transmission gear ratio, but the efficiency even at its best value for $i = \pm 5$ is still significantly lower than the internal gear train efficiency ratio. Due to the above, it is very important to configure the gearbox in such a manner that the speed with brake Br1 on is most frequently used,as this speed exhibits greater efficiency. So, if, for example, such a gearbox were used for a boat, it should be installed for bow direction with brake Br1 on, and astern direction with brake Br2 on as it is less frequent.

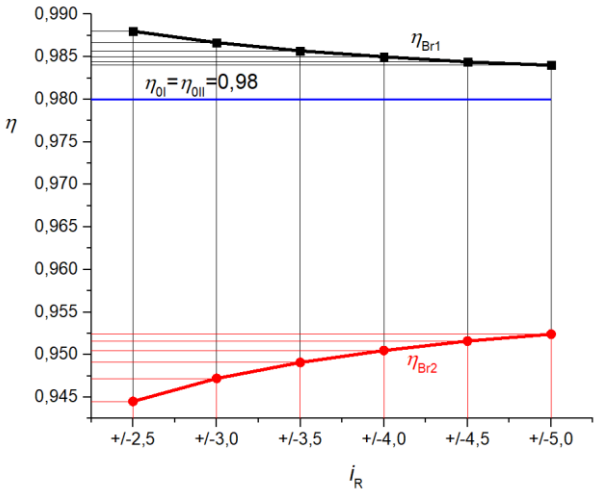

Figure 5.Efficiency curves of the selected reversing two-carrier planetary gear train

Since the arguments of the efficiency function are the ideal torque ratios and the internal efficiencies of the component gear trains, it is possible to influence the overall efficiency of the planetary gearbox. Given that it is not possible to adjust the ideal torque ratios for a certain overall gear ratio because there is only one combination of ideal torque ratios for one particular gear ratio, it is possible to influence the efficiency only by improving the internal efficiencies of the component gear trains. The internal efficiencies depend on several factors, such as the number of teeth of gearsin the component gear train, the gear manufacturing quality and the surface roughness of the tooth flanks, lubrication conditions, i.e. lubrication losses, sealing losses, bearing losses, ventilation losses, etc. Some of these factors can be managed as they do not have the same degree of influence. For example, if a planetary gear train with the same ideal torque ratio has more teeth, the sliding losses on the flanks of the teeth will be lower, resulting in a higher internal efficiency. Another way to control the internal efficiency is to use more precisely machined gears. Therefore, in the design process, great care must be taken to ensure that the efficiency rate reaches the optimum value. In [5] there is a graph (Figure 6) showing how theefficiency, if only meshing losses are considered, is affected by the number of teeth of the sun gear and the ideal torque ratio.

It is possible to estimate from the graph that with smaller ideal torque ratios and sun gear tooth number z_1=18 a slightly lower internal efficiency can be expected, therefore a new efficiency calculation for gear trains with medium-quality gearing (Q=7) has been made.

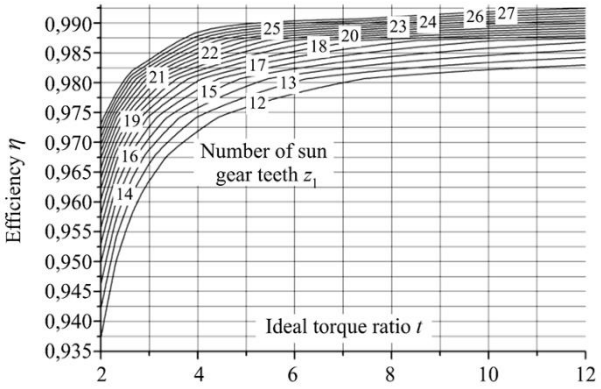

Figure 6. Determination of the internal efficiency of component gear trains

Data for this case with internal efficiencies equal to 0,95 has been provided in Table 2.

Table2. Characteristic values for reversible operation of the selected PGT ($\eta_{0I} = \eta_{0II} = 0{,}95$)

	1	2	3	4	5	6
i_R	± 2,5	± 3	± 3,5	± 3,7	± 4,5	± 5
t_I	1,5	2	2,5	3	3,5	4
t_{II}	2,333	2	1,8	1,666	1,571	1,5
η_{Br1}	0,970	0,967	0,964	0,963	0,961	0,960
η_{Br2}	0,863	0,870	0,875	0,878	0,881	0,883
P_{par}	0,970	0,967	0,964	0,963	0,961	0,960

2.2. Parasite power

The ideal parasitic power (the excess internal power in addition to the ideal power at the gearbox output) for this gearbox is calculated using the torque method analysis as shown in Figure 2 and calculated according to the expression (8):

$$P_{PAR}(\%) = 100\frac{P_{PAR}}{P_A} = 100\frac{1+t_I}{t_I t_{II} - 1} \quad (8)$$

Parasitic power of this magnitude can also reduce the basic gearbox efficiency as well as further reduce the efficiency in both speeds. This gearbox should be used with caution due to its high parasitic power, which, in addition to reducing the efficiency with brake Br2 on, places an increased load on the gearbox internals. If the gearbox is expected to seldom operate with brake Br2 on, then it can be considered as an acceptable solution due to its relatively low impact on efficiency.

2.3. Shifting capabilities of the selected gear train

The diagrams of the shifting capabilities given in the following figures below were obtained using data based on the developed 2-SPEED software system, the algorithm of which is described in [5,6]. Figure 7 shows a set of combinations of gear ratios that a gearbox can achieve if the ideal torque ratios change to an interval of 1,5 to 8. The color indicates the approximate calculatedefficiencyfor operation with brake Br1 on.

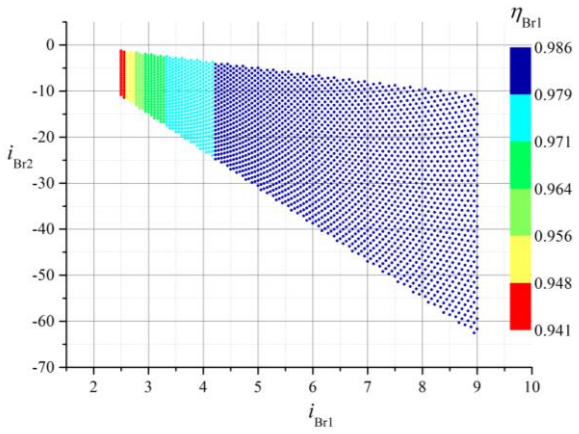

Figure 7. Possible transmission ratios with approximate values of $\eta_{Br1}$for t_I, t_{II} = 1,5…8

Figure 8 is provided for operation with brake Br2 on while all other data remains equal.

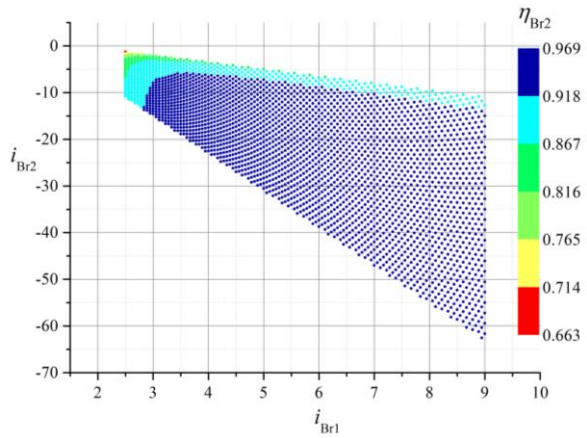

Figure 8. Possible transmission ratios with approximate values of η_{Br2} for t_I, t_{II} = 1,5…8

If the ideal torque ratios are restricted to the interval from 1,5 to 4, the shifting capabilities and the efficiencies are more easily visible in Figures 9 and 10.In this case, due to the reducedrange of the ideal torque ratios, the shifting capabilities are smaller.

The following expressions (9,10) allow the determination of ideal torque ratios that will provide the required ideal kinematic gear ratios.

$$t_I = i_{Br1} - 1 \quad (9)$$

$$t_{II} = \frac{1 - i_{Br2}}{i_{Br2} - 1} \tag{10}$$

These form the basis for determining the tooth numbers of the component PGTs of the considered gearbox [5-7].

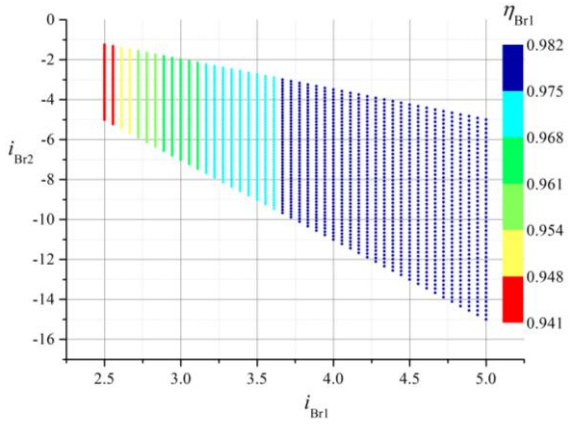

Figure 9. Possible transmission ratios with approximate values of η_{Br1} for t_I, t_{II} = 1,5…4

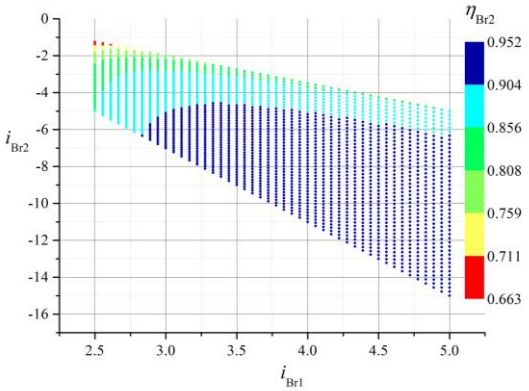

Figure 10. Possible transmission ratios with approximate values of η_{Br2} for t_I, t_{II} = 1,5…4

3. CONCLUSION

An analysis of the distribution of torques on the shafts of the planetary gearbox was performedusing the Wolf-Arnaudov symbol and the torque method. This analysis was used to obtain the transmission ratio functions, as well as the efficiency ratio functions, enabling a deeper understanding and quantitative evaluation of the gearbox performance. The results of the analysis have shown that the researched reversing gearbox can operate in the range of ± 2.5 to ±5, with ideal torque ratios ranging from 1.5 to 4. Such a broad operating range indicates the flexibility and applicability of the gearbox in different operating modes. The analysis has further shown that only one component planetary gear train is operating with brake Br1 on. This gear train operates in single mode, while achieving a relatively high efficiency ratio, confirming the efficiency of this operating mode. On the other hand, with brake Br2on, both planetary gear trains are engaged, resulting in significant power circulation. This reactive power, which can reach up to 100% in relation to the output powerin the observed interval, significantly reduces the efficiency of the gearbox, thus confirming that this mode should not be used during standard operation. It is then concluded that the gearbox operates optimallywith brake Br1 on, and that operation with brake Br2 on should be reduced to a minimum, in accordance with the functional requirements of the gearbox. The 2-SPEED software system was used to explore all possible combinations of transmission ratios.The corresponding efficiency ratios for each individual operating mode and speed were generated, enablingeasier optimization in the design stage. Finally, numerical expressions for the kinematic synthesis of gearboxes are defined, which enable designers to take an analytical approach when searching for the desired combination of gear ratios within technically achievable limits. This has confirmed that the researched gear train can be rationally designed and efficiently applied in various technical scenarios, with clearly defined optimal operating conditions.

ACKNOWLEDGMENT

This research was financially supported by the University of Rijeka, projects number uniri-iskusni-tehnic-23-298 and uniri-iskusni-tehnic-23-168.
This research was financially supported by the Ministry of Science, Technological Development and Innovation of the Republic of Serbia (Contract No. 415-03-137/2025-03/200109)

REFERENCES

[1] Yang, W., Xiao, X. Design and Analysis of Mechanisms of 7-, 8- and 9-Speed Automatic Transmissions for Vehicle Powertrains. *Energies,* Vol. 16 No. 21, 7402,1996-1073, 2023.
[2] Wang, J. Yang, S., Liu, Y., Mo, R.: Analysis of Load-Sharing Behavior of the Multistage Planetary Gear Train Used in Wind Generators: Effects of Random Wind Load. *Applied Sciences*. Vol 9, 5501, 2076-3417, 2019.
[3] Arnaudov, K., Karaivanov, D.P.: *Planetary Gear Trains*, CRC Press: Boca Raton, FL, USA, 978-0-429-45852-1, 2019.
[4] Opalić, M.: *Prijenosnici snage i gibanja*, Hrvatsko društvo za elemente strojeva i konstrukcije, Zagreb, Croatia, 953-97575-0-9, 1998.
[5] Troha, S.; Milutinović, M.; Vrcan, Ž.: *Characteristics and Capabilities of Two-Speed, Two-Carrier Planetary Gearboxes*: University of Rijeka, Faculty of Engineering: Rijeka, Croatia, 978-953-8246-02-9, 2024.
[6] Troha, S.:*Analysis of a Planetary Change Gear Train's Variants,*(Ph.D. Thesis), University of Rijeka—Faculty of Engineering, Rijeka, Croatia, 2011.
[7] Tica, M., Vrcan, Ž., Troha, S., Marinković, D.: Reversible Planetary Gearsets Controlled by Two Brakes, for Internal Combustion Railway Vehicle Transmission Applications. *Acta Polytechnica Hungarica*, Vol. 20 No. 1, pp. 95-108. 1785-8860, 2023.

11th International Scientific Conference
IRMES 2025
Research and Development of
Mechanical Elements and Systems
June 19 – 21, 2025; Vrnjačka Banja, Serbia

Original scientific paper DOI: 10.46793/IRMES25.039M

MECHANICAL PROPERTIES OF BONDED JOINTS MADE OF SLM ADDITIVE MANUFACTURED ADHEREND

Natalija MRATINKOVIĆ[1]
Miodrag MILČIĆ[2]
Nataša ZDRAVKOVIĆ[3]
Dragan MILČIĆ [4]
Marko PERIĆ[5]

[1]Faculty of Mechanical Engineering, University of Niš, 18000 Nis, Serbia, RS; natalija.mratinkovic@gmail.com;
ORCID iD: 0009-0009-2906-4642
[2]Faculty of Mechanical Engineering, University of Niš, 18000 Nis, Serbia, RS; miodrag.milcic@masfak.ni.ac.rs;
ORCID iD: 0000-0002-1089-8390
[3]Faculty of Mechanical Engineering, University of Niš, 18000 Nis, Serbia, RS; natasa.zdravkovic@masfak.ni.ac.rs;
ORCID iD: 0000-0001-6085-7522
[4]Faculty of Mechanical Engineering, University of Niš, 18000 Nis, Serbia, RS; dragan.milcic@masfak.ni.ac.rs;
ORCID iD: 0000-0002-3936-7462
[5]Faculty of Mechanical Engineering, University of Niš, 18000 Nis, Serbia, RS; marko.peric@masfak.ni.ac.rs;
ORCID iD: 0000-0001-9350-0351

Abstract: *This paper investigates the mechanical properties of bonded joints made of components manufactured using Selective Laser Melting (SLM), an additive manufacturing (AM) technique that enables the production of complex metal parts with high precision. In multi-part assemblies, adhesive bonding is often employed, placing demands on the strength and durability of the joints. In this study, maraging steel samples fabricated by SLM were joined using two types of epoxy adhesives. The mechanical performance of the joints was evaluated through double-lap shear tests in accordance with ASTM D3528. The aim of the research was to determine the influence of the additively manufactured structure, surface condition, and adhesive type on the strength of the bonded joints.*

Keywords: *additive manufacturing; Selective Laser Melting (SLM); bonded joint; maraging steel; mechanical properties*

1. INTRODUCTION

Additive manufacturing (AM), commonly referred to as 3D printing, is a fabrication technique that creates three-dimensional components with high levels of accuracy and complexity by sequentially adding material layer by layer. This approach contrasts with traditional subtractive or formative manufacturing processes [1]. Recognized as a transformative force in modern industry, AM has undergone significant advancements over the past decade. The procedure begins with the development of a 3D model using computer-aided design (CAD) software. This digital model is then divided into multiple horizontal layers, which are successively printed by the AM machine to construct the final part in physical form, corresponding exactly to the CAD representation [2]. Additive manufacturing (AM) has revolutionized the production of complex geometries, particularly in aerospace, biomedical, and automotive industries. However, instead of printing the entire product, 3D printing can be used to produce only the most complex parts, which can be furthercombined with simple, non-printed parts from other materials to make the final product [3]. Among various AM techniques, Selective Laser Melting (SLM) has emerged as a leading method for fabricating high-performance metal components with intricate structures and excellent dimensional accuracy. However, despite the advantages of SLM in manufacturing individual parts, the assembly of multiple components into functional systems remains a challenge.

Adhesive bonding is gaining increased attention as a viable joining technique for SLM components due to its ability to distribute loads evenly, preserve component integrity, and enable the joining of dissimilar materials. Nevertheless, the mechanical performance of bonded joints is highly dependent on factors such as the surface condition of the adherends, the properties of the adhesive, and the internal structure of the printed material. Unlike conventionally manufactured parts, SLM components may exhibit surface roughness and porosity that can significantly affect bonding quality.

Study [4] focused on evaluating the adhesion of resin cement to metal surfaces fabricated using the Selective Laser Melting (SLM) process, with the aim of enhancing the bond strength at the interface between biocomposites and metal substrates. The SLM-fabricated substrates were made from pure titanium (Ti), Ti_6Al_7Nb alloy, and cobalt-chromium (CoCr) alloy. Five different biocomposites were applied to the metal surfaces, including two commercially available resin-modified glass-ionomer cements (GC Fuji Plus and KETAC CEM) and three custom-developed materials. The mechanical properties of these biocomposites were assessed through compression and bending tests.

Studies [5–7] have shown that the bond strength of adhesively joined joints between two aluminum alloys or two stainless steel sheets varies depending on the surface preparation method and the adhesive used. This indicates that the use of the same adhesive and the same material, combined with different surface preparation techniques, can lead to significant differences in bond strength. Therefore, selecting an appropriate surface preparation method suited to the specific components and their surface roughness is crucial for increasing the strength of bonded joints.

As part of the research conducted in [8], an experimental investigation was carried out to examine the influence of static and cyclic loading on two characteristic types of adhesive joints in lightweight metal structures: a façade joint between trapezoidal sheet metal and a connecting T-profile, and a double-lap joint. The adherends in both types of joints were made of galvanized sheets. Various types of adhesives were used in layers with a thickness of 1 mm. Based on the results of the conducted tests, models and methods were formulated to describe and predict their behavior under static and cyclic loading.

This paper investigates the mechanical properties of double-lap adhesive joints made of SLM-produced maraging steel components. Two different epoxy adhesives were used, and joints were tested under shear load according to ASTM D3528. The study aims to evaluate the influence of the surface condition of SLM parts and adhesive type on joint strength, providing insight into the structural performance of bonded joints in additive manufacturing applications.

2. MATERIALS AND METHODS

The materials chosen for this investigation, encompassing maraging steel for samples and the two epoxy resins (LOCTITE EA 3450 and LOCTITE EA 9466), were chosen based on their compatibility with the selective laser sintering (SLM) manufacturing process and their applicability to the assessment of bonded connections. The mechanical performance of joints was experimentally evaluated under tensile-shear loading conditions.

2.1. Materials

Maraging steel (Material for SLM Adherents) [9]**:** a low-carbon, high-strength alloy, was used as the material for the adherents in this study. This steel is highly prized for its outstanding mechanical properties, including a high tensile strength and flexibility, which make it particularly suited for high-performance uses. Maraging steel's composition encompasses substantial percentages of nickel (17-19%), cobalt (8.5 – 9.5%), molybdenum (4.5 – 5.2%), and titanium (0.6 – 0.8%), resulting in its outstanding mechanical characteristics [8]. Maraging steel is well-suited for additive manufacturing techniques such as selective laser melting (SLM), which require high accuracy and material density for intricate shapes.

Epoxy Adhesive LOCTITE EA 3450™ [10]**:** a two-part epoxy adhesive widely recognized for its strong bond strength and durability. It is particularly effective for bonding metal substrates and is used extensively in aerospace and automotive industries. Key properties of LOCTITE EA 3450™ include high tensile strength, resistance to various chemicals, and temperature stability in the range of -55°C to +120°C. This adhesive was selected for its ability to provide reliable bonding for metal-to-metal applications in the SLM process.

Epoxy Adhesive LOCTITE EA 9466™ [11]**:** another two-part epoxy adhesive chosen for its excellent resistance to impact, high-strength performance, and durability in harsh environments. This adhesive excels in dynamic load applications and is frequently used in heavy-duty industries such as aerospace and automotive. LOCTITE EA 9466™ is resistant to both high temperatures and chemicals, ensuring its reliability in demanding environments. It was used in this study to bond the maraging steel adherents in comparison with LOCTITE EA 3450™.

2.2. Methods

Selective Laser Melting (SLM) is an additive manufacturing technique that uses a high-powered laser to selectively melt and fuse metallic powder particles layer by layer, following a predefined CAD model. In this study, the SLM process was employed to fabricate maraging steel specimens due to its ability to produce complex geometries with high dimensional accuracy and material density. The process parameters, such as laser power, scanning speed, and hatch spacing, were optimized to achieve consistent microstructure and mechanical integrity. 3D printing was performed at the Military Technical Institute using the EP-M450 Metal 3D Printer from Eplus3D. This printer features a build chamber size of 450 x 450 x 550 mm and supports various metal powders, including titanium, aluminum, nickel alloys, and stainless steel. It is designed for the production of large parts with high precision and performance, making it suitable for a wide range of industrial and military applications.

The resulting parts exhibited a rough surface finish typical for SLM-produced components, which was taken into account in the bonding process**.** For the purposes of this study, the surfaces of maraging steel parts produced by the SLM process were treated only with a cleaning agent.

2.3 Testing of adhesive joints according to ASTM D 3528 standard

The bonding procedure was conducted in accordance with the ASTM D3528 standard [12], which specifies the preparation and testing of double lap shear joints under

tensile loading. This standard is widely used in the aerospace, automotive, and structural industries for evaluating the mechanical strength and reliability of adhesively bonded joints.

In this configuration, the specimen consists of two outer adherends and one central adherend, forming two adhesive interfaces. The central adherend is subjected to direct tensile loading, while the adhesive layers are exposed to shear stress. This geometry enables a more uniform stress distribution and reduces peel effects, offering reliable measurement of adhesive performance under shear.

The specimen dimensions followed the proportions defined by ASTM D3528, as illustrated in Fig.1, Due to potential distortion during additive manufacturing, exact standard thicknesses could not be maintained. However, to meet the required dimensional ratio (1:8), the thickness was adapted to t_1 = 5 mm. The adhesive bond line thickness was maintained at 0.3 mm, controlled using calibrated spacers.

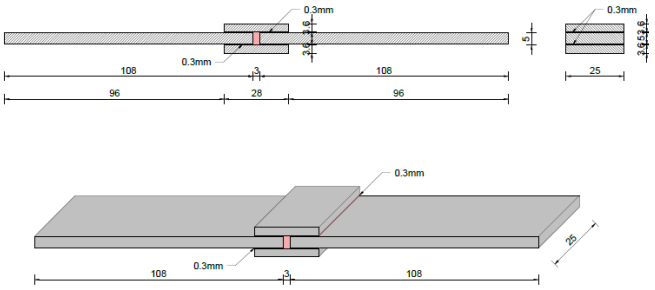

Fig.1. Double lap joint

3. EXPERIMENTAL TESTING AND RESULTS

It is crucial to take into account the surface roughness of parts produced via the Selective Laser Melting (SLM) technique prior to the bonding process, as this characteristic can considerably impact mechanical performance, friction, adhesion, and the overall efficacy of the joint. Surface roughness parameters may vary depending on production conditions; however, SLM parts typically exhibit Ra values (arithmetical mean roughness) in the range of 5 to 20 µm. The surface roughness measurements of the fabricated specimens are presented in Table 1.

Table 1. Surface roughness

No.	Measured Value	Specimen	Reinforcement
1.	Ra – Arithmetic mean roughness	6.22 µm	6.14 µm
2.	Ry – Maximum profile peak height	34.91 µm	38.19 µm
3.	Rz – Maximum roughness height	23.98 µm	24.54 µm
4.	Rq – Root mean square roughness	7.94 µm	7.90 µm

Since the surface roughness values were found to be satisfactory, no additional surface treatment was required on the bonding areas.

3.1. Experimental testing

Prior to the application of adhesive, the specimens were sorted into two classifications according to the type of adhesive employed, as depicted in Table 2. Specimens D 1.1 and D 2.1 were bonded using LOCTITE EA 3450™, while specimens D 2.1 and D 2.2 were bonded using LOCTITE EA 9466™. All specimens were labelled using a permanent marker to ensure identification during testing Fig.2.

Table 2. Specimen labelling

Type of adhesive	Specimen labels	
LOCTITE EA 3450™	D 1.1	D 1.2
LOCTITE EA 9466™	D 2.1	D 2.2

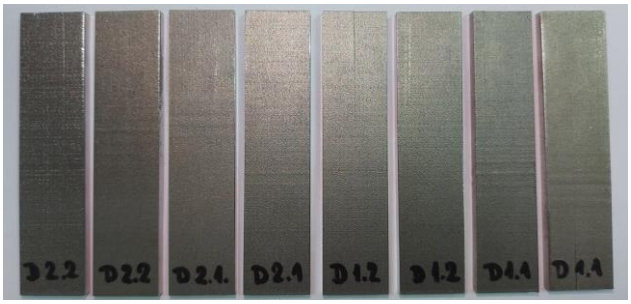

Fig.2. Specimen labelling

The procedure began with surface preparation, which included cleaning of all bonding surfaces. A solvent-based, non-CFC cleaner, LOCTITE SF 7063™, was used to remove any dust or grease [5-8, 13]. After wiping, the specimens were left to dry at room temperature.

Following surface preparation, the adhesive was applied within 4 to 7 minutes. For specimens bonded with LOCTITE EA 9466™, the adhesive was dispensed using a cartridge gun with a static mixer, ensuring uniform distribution. For LOCTITE EA 3450™, the adhesive was applied manually using a spatula, which offered slightly less precision.

The adhesive layer on the reinforcement was applied in a rectangular area of 28 × 25 mm, with a 3 mm gap between the bonded steel specimens. The adhesive layer thickness between the steel specimen and reinforcement was maintained at 0.3 mm. To achieve consistent spacing and alignment, a custom-made positioning fixture was designed and 3D printed.

The bonding process involved sequential assembly: first, the lower reinforcement was positioned in the fixture and coated with adhesive; next, the two steel specimens were placed and bonded; finally, the upper reinforcement was mounted using the fixture's cover Fig.3.

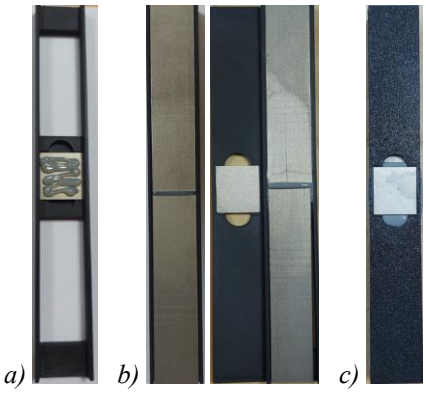

Fig.3. Gluing of samples a) gluing of the lower reinforcement; b) positioning of the specimen; c) gluing of the upper reinforcement

This procedure was repeated for both adhesive types, producing two specimens per adhesive. After assembly, the specimens were weighted and left to cure at room temperature for 7 days, as recommended by the manufacturer. Upon completion of the curing period, the specimens were removed from the fixture and prepared for testing.

The experimental testing of the bonded joints was conducted at the Laboratory for Mechanical Testing of Materials at the Faculty of Mechanical Engineering, University of Niš. The double lap joint specimens were tested in accordance with the ASTM D3528 standard, which defines the procedure for determining the shear strength of adhesives using double lap joints. The tests were performed on a universal testing machine until complete failure of the adhesive joint. The specimens were aligned vertically in the grips to ensure axial loading and prevent bending moments. Load and displacement data were continuously recorded using the machine's data acquisition system. All tests were conducted at room temperature, under controlled laboratory conditions.

3.2. Results

The tensile-shear tests were conducted in accordance with the ASTM D3528 standard. Each specimen was loaded in a way that induced tensile stress in the adherends and shear stress across the adhesive joint. The shear strength of the bonded joints was calculated by dividing the maximum load by the bonded area.

For the specimens bonded with LOCTITE EA 3450™, specimen D 1.1 Fig.4, exhibited the lowest failure load of all tested joints, with a maximum load of 4.86 kN and a corresponding shear strength of 38.86 N/mm². On the other hand, specimen D 1.2 Fig.5, demonstrated a significantly higher load-bearing capacity, reaching a failure load of 7.97 kN and a shear strength of 63.74 N/mm². The average failure load for this adhesive group was 6.415 kN.

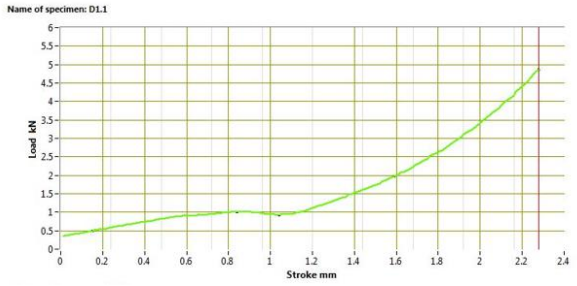

Fig.4. Load force diagram at a certain displacement – sample D 1.1

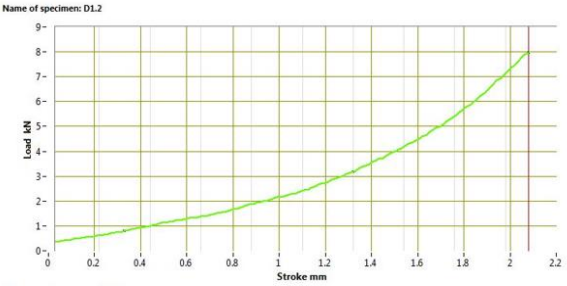

Fig.5. Load force diagram at a certain displacement – sample D 1.2

For the specimens bonded with LOCTITE EA 9466™, specimen D 2.1 Fig.6, showed a lower failure load of 4.96 kN and a shear strength of 39.71 N/mm², while specimen D 2.2 Fig.7, achieved the highest failure load of all tested joints, at 8.45 kN, with a shear strength of 67.62 N/mm². The average failure load for this adhesive was slightly higher, at 6.705 kN.

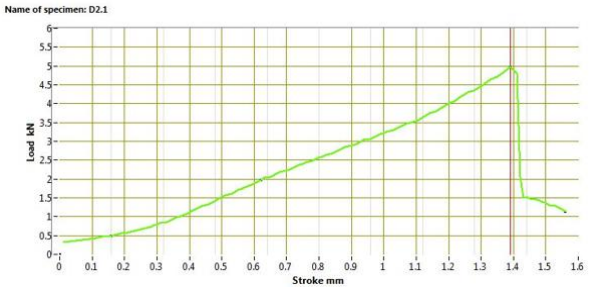

Fig.6. Load force diagram at a certain displacement – sample D 2.1

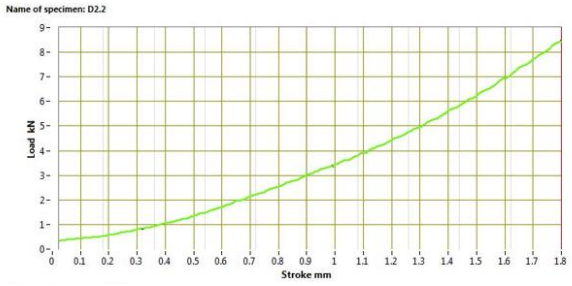

Fig.7. Load force diagram at a certain displacement – sample D 2.2

Despite the relatively small sample size, both adhesives demonstrated consistent bonding performance. In both

adhesive groups, one specimen failed at approximately double the load of the other, indicating variability possibly related to surface preparation or adhesive thickness.

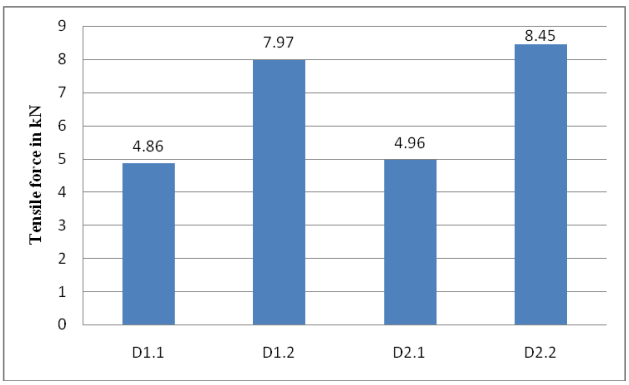

Fig.8. Tensile force per sample expressed

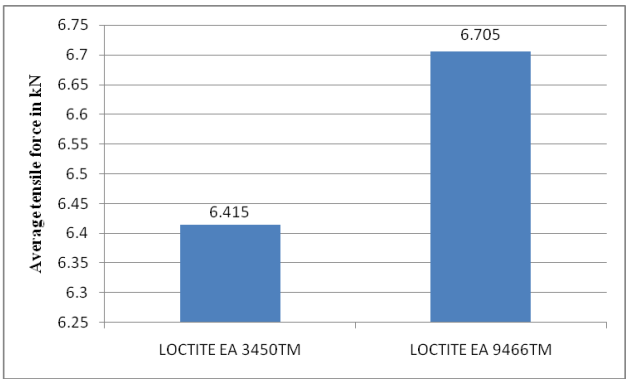

Fig.9. Average tear force of samples according to the adhesive used

Analysis revealed different failure modes. For specimens bonded with LOCTITE EA 3450™, a combination of adhesive and cohesive failure was observed. Some portions of the adhesive separated completely from the metal substrate, while others remained attached to both adherends, indicating partial adhesion loss and internal failure of the adhesive Fig.8.

In contrast, specimens bonded with LOCTITE EA 9466™ predominantly exhibited cohesive failure Fig.9. The adhesive layer remained intact on both substrate surfaces after fracture, suggesting strong adhesion between the adhesive and the substrate and failure occurring within the adhesive itself. This indicates effective surface preparation and good bonding quality for this adhesive type.

Overall, both adhesives provided satisfactory mechanical performance, with LOCTITE EA 9466™ showing slightly higher average strength and more consistent cohesive failure behavior.

4. CONCLUSION

Additive manufacturing technologies, particularly Selective Laser Melting (SLM), are rapidly advancing and play a critical role in modern industrial production within the framework of Industry 4.0. Bonded joints of SLM-manufactured parts present both challenges and opportunities, especially for assembling components with complex geometries and dissimilar materials. Adhesive bonding offers several advantages, such as reduced weight compared to welding, but also raises issues regarding surface quality and long-term joint performance.

This study investigated the mechanical performance of double-lap joints made from SLM-manufactured maraging steel, bonded with two types of two-component epoxy adhesives. The surface preparation involved only chemical cleaning, as the as-built surface roughness was considered adequate. Tensile-shear tests were performed according to ASTM D3528, and results showed comparable average failure loads for both adhesives, though somewhat lower than expected.

The inherent surface characteristics of SLM parts - such as roughness and potential porosity - may negatively impact adhesive bonding. Insufficient contact between the adhesive and substrate can lead to weak adhesion, resulting in premature joint failure. While one adhesive demonstrated more consistent cohesive failure, indicating better bonding performance, the variability between samples suggests that additional surface treatment - such as blasting, polishing, or surface coating - may be necessary to enhance adhesion and ensure joint reliability.

In conclusion, while adhesive bonding of SLM parts is a promising joining method, further optimization of surface preparation and adhesive selection is required to fully exploit the mechanical potential of such joints in demanding engineering applications.

ACKNOWLEDGMENT

This research was supported by the Faculty of Mechanical Engineering, University of Niš, whose facilities and resources made this work possible. The author also gratefully acknowledges the Military Technical Institute in Belgrade for their valuable technical assistance and cooperation.

REFERENCES

[1]*** ASTM Standard F2792, Standard terminology for additive manufacturing technologies, vol. 2012, ASTM International, West Conshohocken, Pa, USA (2012).

[2] Harris, M., Potgieter, J., Archer, R., Arif, K. M.: Effect of Material and Process Specific Factors on the Strength of Printed Parts in Fused Filament Fabrication: A Review of Recent Developments. *Materials*, Vol.12, No.10, 1664, 2019. https://doi.org/10.3390/ma12101664

[3] Singh, S., Ramakrishna, S., Singh, R.: Material issues in additive manufacturing: A review, *Journal of Manufacturing Processes* Vol. 25, pp. 185-200, 2017.

[4] Cuc, S, Burde, A., Cosma, C., Leordean, D., Rusu, M., Balc, N., Prodan, D., Moldovan, M., Ene, R.: Adhesion between Biocomposites and Different Metallic Structures Additive Manufactured. *Coatings*. Vol.11, No.4, :483. 2021. https://doi.org/10.3390/coatings11040483

[5] Zdravković, N., Klobčar, D., Milčić, D., Zupančič, M., Žužek, B., Milčić, M., Đurić, A.: Influence of Surface

Preparation of Aluminum Alloy AW-5754 and Stainless Steel X5CRNI18-10 on the Properties of Bonded Joints. *Materials*. Vol.17, No.11, 2561, 2024. https://doi.org/10.3390/ma17112561

[6] Zdravković, N., Milčić, D., Klobčar, D., Korunović, N., Milčić, M.: EFFECT OF SURFACE PREPARATION ON THE SHEAR STRENGTH OF ALUMINIUM ALLOY ADHESIVE SINGLE-LAP JOINTS, *Innovative Mechanical Engineering*, Vol. 3 No. 1, pp. 48-57, 2024. http://ime.masfak.ni.ac.rs/index.php/IME/article/view/86

[7] Zdravković, N., Klobčar, D., Milčić, D., Milčić, M., Pavlović, V., Đurić, A.: EFFECTS OF DIFFERENT SURFACE PREPARATIONS ON BONDING PROPERTIES OF ALUMINIUM ALLOY EN AW-5754, 11th International Scientific Conference on Defensive Technologies - OTEX 2024, Materials and technologies - MT, pp. 572-577. https://scindeks-zbornici.ceon.rs/Article.aspx?artid=proc-00182400572Z

[8] Stojković, N.: Investigation of the Behavior of Bonded Joints in Metal Structures under Static and Cyclic Loading, *Doctoral Dissertation*, Faculty of Civil Engineering and Architecture, University of Niš, 2017. http://eteze.ni.ac.rs/application/showtheses?thesesId=5803

[9] EOS Maraging Steel MS1 Material data sheet. https://www.eos.info/var/assets/05-datasheet-images/Assets_MDS_Metal/EOS_MargingSteel_MS1/Material_DataSheet_EOS_MaragingSteel_MS1_en.pdf?v=6

[10] LOCTITE EA 3450™. Technical Data Sheet 2019, Henkel AG & Co. https://www.henkel-adhesives.com/rs/sr/product/structural-adhesives/loctite_ea_3450.html

[11] Loctite® EA 9466 TM. Technical Data Sheet 2019, Henkel AG & Co. https://www.henkel-adhesives.com/rs/sr/product/structural-adhesives/loctite_ea_94661.html

[12] ASTM D 3528 – 96 (Reapproved 2002), Strength Properties of Double Lap Shear Adhesive Joints by Tension Loading

[13] Bujanić, B., Magdalenić, Bujanić, J.: Mehanizmi stvaranja lijepljenog spoja, *Tehnički glasnik* 5, pp. 89 – 93, 2011. http://hrcak.srce.hr/83838, 28.8.2017.

11th International Scientific Conference
IRMES 2025
Research and Development of
Mechanical Elements and Systems
June 19 – 21, 2025; Vrnjačka Banja, Serbia

Original scientific paper DOI: 10.46793/IRMES25.045P

GEAR MATERIAL SELECTION BY USING MCDM SOLVER

Dušan PETKOVIĆ[1]
Miloš MADIĆ[2]

[1] Faculty of Mechanical Engineering University of Niš, Serbia, SRB, dusan.petkovic@masfak.ni.ac.rs;
ORCID iD: 0000-0002-1871-7144
[2] Faculty of Mechanical Engineering University of Niš, Serbia, SRB, milos.madic@masfak.ni.ac.rs;
ORCID iD: 0000-0002-2310-2590

Abstract: *Material selection is a complex multi-criteria decision-making problem, which requires a lot of knowledge and experience for successful solving. This process is significant in product development, as it represents one of the factors on whose success the success of the product itself depends. Material selection process is influenced by several factors such as thermal, mechanical, electrical, chemical, physical and technological properties as well as their price and availability. Improper material selection frequently causes both unwanted costs and premature product failure. Gear material selection problem by using MCDM approach was considered in this paper. A decision support system named MCDM Solver was used to help decision makers to solve this complex task. MCDM Solver was used in decision-making process to rank materials for gear manufacturing with respect to several criteria. Based on the results the best ranked material is carburized steel, while nitride steel and surface hardened alloy steel was the second and third best choice respectively for gear design. The ranking results are also compared with those of past researchers.*

Keywords: *Material selection; Gear, MCDM Solver; Decision support system.*

1. INTRODUCTION

Engineering design is significantly dependent on objectives of performance, cost and environmental sensitivity, which are often limited by materials. To optimize product design, it is necessary to select the materials which best meet the needs of the design, maximizing its performance and minimizing its cost.
Material selection is the process of choosing the best material for a particular design. In mechanical design, this process enters at every stage of the design process. In total design model, material selection is rated as one of the fundamental parameters along with market investigation, product design specification, component design, design analysis, manufacture and assembly [1].
The basic principle of material selection is thus to carefully identify the application requirements, then define the foremost selection criteria and finally, alternative material choices are narrowed down by the method of elimination (screening) and amalgamation of the contradictory criteria [2]. The objectives and criteria in the material selection process are often in conflicts which usually involve certain trade-offs amongst decisive factors. Therefore, only with a systematic and structured mathematical approach, the best alternative for a specific engineering product can be selected [3]. The material selection problems with multiple non-commensurable and conflicting criteria can be efficiently solved using multi-criteria decision making (MCDM) methods. The MCDM methods have the capabilities to generate decision rules while considering the relative significance of considered criteria upon which the complete ranking of alternatives is determined [4].
Decision support system (DSS) is a special class of information system oriented to the decision-making process and aims to support, mainly business decision-doing processes. DSS is a symbiosis of information systems, application of functional knowledge and ongoing decision-making process. Their main goal, as the goal of other information systems, is to improve the efficiency and effectiveness of an organization [5].
In this paper the application of DSS named MCDM Solver is focused on gear material selection. A real time case study was solved by using MCDM Solver with obtained complete rankings. Moreover, ranking results are compared with results obtained by past researchers that were used different MCDM methods.

2. MCDM SOLVER

MCDM Solver is an “on-line” DSS which was developed within the doctoral dissertation of Dušan Petković [6]. The developed DSS is located on the “Virtuode”

Company web site (https://virtuodeportalapp.azurewebsites.net/WebTools/Home) and it is available to everyone who registers by creating an account (Figure 1). This DSS offers the possibility of working with maximization, minimization and target criteria [7].

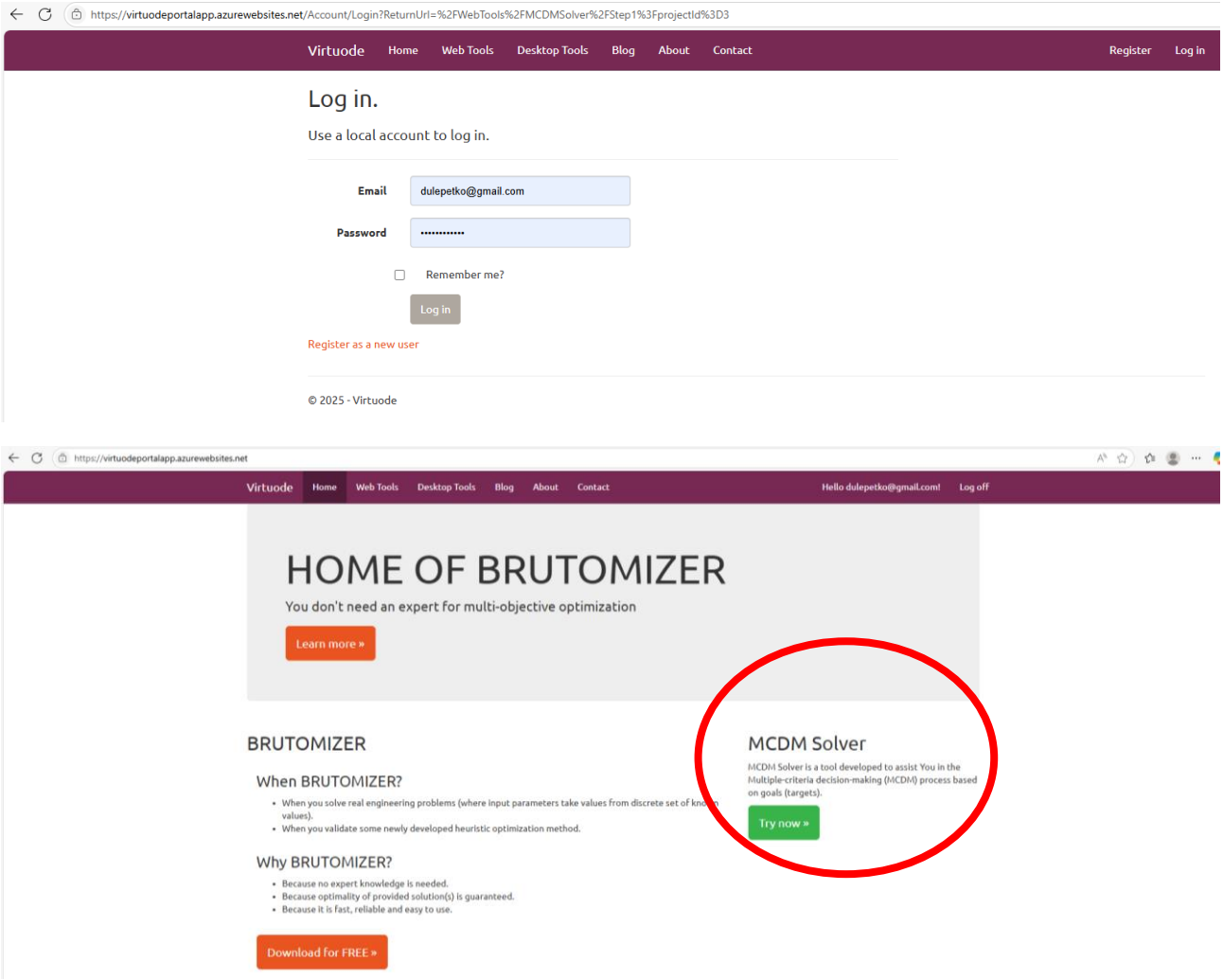

Fig.1. MCDM Solver – initial layout

The input data for MCDM Solver:

- Initial matrix of decision-making with target value of criteria (Step 1);
- η - Confidence level of decision maker in significance of the selected criteria (where η=1 corresponds to 100% confidence level, while η=0 corresponds to a confidence level of 0);
- Pairwise significance evaluation of the selected criteria.

Based on the input data, MCDM Solver can determine the values of the criteria weights (Step 2) and ranking alternatives (Step 3) with the corresponding values by means of Extended TOPSIS [8], Comprehensive VIKOR [9] and Comprehensive WASPAS [6, 10] methods.

Developed DSS architecture is flexible and easy to upgrade, so it enables the inclusion of new models that will come in future. MCDM Solver has a user-friendly interface, which enables a simple and efficient way of entering the necessary data not strictly related to material selection process [11]. The use of MCDM Solver simplifies the solution of the MCDM problems because it does not require expert knowledge (decision making theory) from the user.

3. GEAR MATERIAL SELECTION

This example of gear material selection is taken from Milani et al. [12] where nine alternative materials, i.e. cast iron (M1), ductile iron (M2), SG iron (M3), cast alloy steel (M4), through hardened alloy steel (M5), surface hardened alloy steel (M6), carburized steel (M7), nitride steel (M8) and through hardened carbon steel (M9) were considered. The mechanical properties of those nine material alternatives were measured with respect to five selection criteria, i.e. surface hardness (SH) (in HB), core hardness (CH) (in HB values), surface fatigue limit (SFL) (in N/mm^2), bending fatigue limit (BFL) (in N/mm^2) and ultimate tensile strength (UTS) (in N/mm^2). Among those five criteria, SH, SFL, BFL and UTS are beneficial in

nature where higher values are preferred, while the lower value of CH is usually desired as it is a non-beneficial criterion [13]. The problem, which consists of nine alternative materials and five material selection criteria, expressed as initial decision matrix, is shown in Table 1.

Table 1. Initial decision matrix for gear material selection

Gear material alternatives	SH	CH	SFL	BFL	UTS
M1 - cast iron	200	200	330	100	380
M2 - ductile iron	220	220	460	360	880
M3 - SG iron	240	240	550	340	845
M4 - cast alloy steel	270	270	630	435	590
M5 - through hardened alloy steel	270	270	670	540	1190
M6 - surface hardened alloy steel	585	240	1160	680	1580
M7 - carburized steel	700	315	1500	920	2300
M8 - nitride steel	750	315	1250	760	1250
M9 - through hardened carbon steel	185	185	500	430	635
Target value	750	185	1500	920	2300

4. RESULTS AND DISCUSSION

In this paper two scenarios are presented to test MCDM Solver and to analyze results sensitivity to the change in weight of criteria.

Scenario 1: significance of the criteria (criteria weights) is evaluated by the authors of this paper by means of MCDM Solver (Fig. 2) which has MDL (modified digital logic) as background [6]. The authors of this article also mean that surface fatigue limit (SFL) is the most significant criterion, followed by bending fatigue limit (BFL), surface hardness (SH), ultimate tensile strength (UTS) and core hardness (CH), respectively. By using MCDM Solver obtained weights of the considered criteria as follows: w_{SH} = 0.200, w_{CH} = 0.100, w_{SFL} = 0.300, w_{BFL} = 0.250 and w_{UTS} = 0.150.

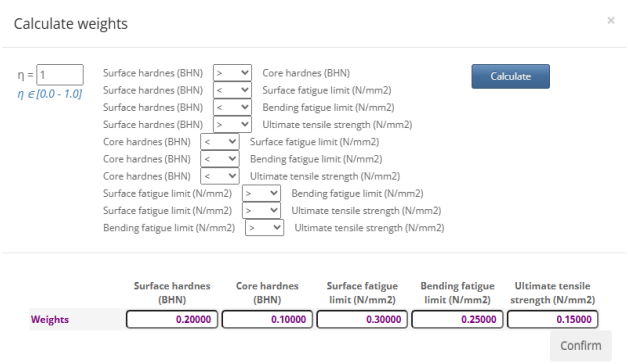

Fig.2. Pairwise significance evaluation of the criteria using MCDM Solver

Scenario 2: criteria weights are taken from previous study, where weights of the considered criteria were determined by applying entropy method as follows: w_{SH} = 0.172, w_{CH} = 0.005, w_{SFL} = 0.426, w_{BFL} = 0.292 and w_{UTS} = 0.102 [9, 14]. In this scenario the most significant criterion is also surface fatigue limit and the least significant is core hardness, while bending fatigue limit, surface hardness and ultimate tensile strength are considered as second, third and fourth significant criterion.

4.1. Scenario 1

Ranking results for Scenario 1 are given in Table 2 and graphically shown in Fig. 3.

Table 2. Ranking results - Scenario 1

Material	TOPSIS		WASPAS		VIKOR	
	C(i)	Rank	Q(i)	Rank	P(i)	Rank
M1	0.161	9	0.238	9	1.000	9
M2	0.238	8	0.380	8	0.895	8
M3	0.239	7	0.391	6	0.858	7
M4	0.281	6	0.416	5	0.814	5
M5	0.361	4	0.494	4	0.748	4
M6	**0.693**	**3**	**0.753**	**3**	**0.241**	**3**
M7	**0.818**	**1**	**0.940**	**1**	**0.000**	**1**
M8	**0.711**	**2**	**0.789**	**2**	**0.149**	**2**
M9	0.282	5	0.389	7	0.852	6

Based on the ranking results, three best ranked materials/alternatives are: M7 - carburized steel, M8 - nitride steel, M6 - surface hardened alloy steel respectively. In the above order of the ideal solutions, carburized steel is the best alternative without any doubt while nitride steel and surface hardened alloy steel are the second and third promising candidates respectively.

4.2. Scenario 2

Ranking results for Scenario 2 are given in Table 3.

Table 3. Ranking results - Scenario 2

Material	TOPSIS		WASPAS		VIKOR	
	C(i)	Rank	Q(i)	Rank	P(i)	Rank
M1	0.114	9	0.187	9	1.000	9
M2	0.189	8	0.338	8	0.905	8
M3	0.216	7	0.361	6	0.868	6
M4	0.291	5	0.407	5	0.819	5
M5	0.360	4	0.478	4	0.768	4
M6	**0.706**	**3**	**0.755**	**3**	**0.380**	**3**
M7	**0.972**	**1**	**0.985**	**1**	**0.000**	**1**
M8	**0.787**	**2**	**0.823**	**2**	**0.266**	**2**
M9	0.230	6	0.350	7	0.885	7

As could be seen, the ranking of materials for gear design is obtained as: M7-M8-M6. Same as the previous

scenario, carburized steel is observed to be the most appropriate for this application, without any doubt. Moreover, nitride steel and surface hardened alloy steel was the second and third best choice respectively for this design.

	TOPSIS	WASPAS	VIKOR
M1	9	9	9
M2	8	8	8
M3	7	6	7
M4	6	5	5
M5	4	4	4
M6	3	3	3
M7	1	1	1
M8	2	2	2
M9	5	7	6

	Surface hardnes (BHN)	Core hardnes (BHN)	Surface fatigue limit (N/mm2)	Bending fatigue limit (N/mm2)	Ultimate tensile strength (N/mm2)	C	TOPSIS
M1	200	200	330	100	380	0.16108	9
M2	220	220	460	360	880	0.23755	8
M3	240	240	550	340	845	0.23874	7
M4	270	270	630	435	590	0.28096	6
M5	270	270	670	540	1190	0.36095	4
M6	585	240	1160	680	1580	0.69309	3
M7	700	315	1500	920	2300	0.81796	1
M8	750	315	1250	760	1250	0.71117	2
M9	185	185	500	430	635	0.28225	5
Targets	750	185	1500	920	2300		
Weights	0.20000	0.10000	0.30000	0.25000	0.15000		

	Surface hardnes (BHN)	Core hardnes (BHN)	Surface fatigue limit (N/mm2)	Bending fatigue limit (N/mm2)	Ultimate tensile strength (N/mm2)	Q	WASPAS
M1	200	200	330	100	380	0.23789	9
M2	220	220	460	360	880	0.37968	8
M3	240	240	550	340	845	0.39190	6
M4	270	270	630	435	590	0.41617	5
M5	270	270	670	540	1190	0.49379	4
M6	585	240	1160	680	1580	0.75256	3
M7	700	315	1500	920	2300	0.94029	1
M8	750	315	1250	760	1250	0.78890	2
M9	185	185	500	430	635	0.38908	7
Targets	750	185	1500	920	2300		
Weights	0.20000	0.10000	0.30000	0.25000	0.15000		

	Surface hardnes (BHN)	Core hardnes (BHN)	Surface fatigue limit (N/mm2)	Bending fatigue limit (N/mm2)	Ultimate tensile strength (N/mm2)	P	VIKOR
M1	200	200	330	100	380	1.00000	9
M2	220	220	460	360	880	0.89474	8
M3	240	240	550	340	845	0.85830	7
M4	270	270	630	435	590	0.81424	5
M5	270	270	670	540	1190	0.74796	4
M6	585	240	1160	680	1580	0.24110	3
M7	700	315	1500	920	2300	0.00000	1
M8	750	315	1250	760	1250	0.14897	2
M9	185	185	500	430	635	0.85179	6
Targets	750	185	1500	920	2300		
Weights	0.20000	0.10000	0.30000	0.25000	0.15000		

Fig. 3. Ranking result – Scenario 1

4.3. Comparison of results

In this section the comparison of the obtained complete rankings is presented. The afore-stated gear material selection MCDM problem was solved by past researchers [14] using TOPSIS, COPRAS and ARAS methods (Table 4).

Table 4. Ranking results - Scenario 2 with past research results

Mat.	TOPSIS [14]	WASPAS	VIKOR	COPRAS [14]	ARAS [14]
M1	**9**	**9**	**9**	**9**	**9**
M2	**8**	**8**	**8**	**8**	**8**
M3	**7**	**6**	**6**	**6**	**6**
M4	**5**	**5**	**5**	**5**	**5**
M5	**4**	**4**	**4**	**4**	**4**
M6	**3**	**3**	**3**	**3**	**3**
M7	**1**	**1**	**1**	**1**	**1**
M8	**2**	**2**	**2**	**2**	**2**
M9	**6**	**7**	**7**	**7**	**7**

In Scenario 2, MCDM Solver was used to solve both the same problem with same weights of criteria as was done by Chatterjee and Chakraborty [14]. The ranking results graphically presented in Fig. 4.

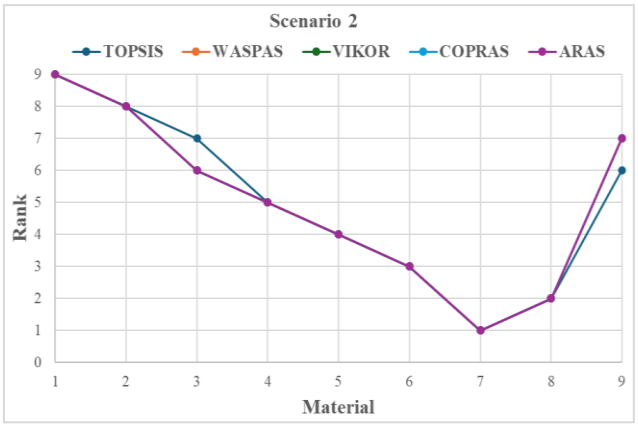

Fig. 4. Ranking results – Scenario 2 with past research results

This study shows absolute match results between the first five ranked materials for all used methods. The WASPAS, VIKOR, COPRAS and ARAS methods have completely matched results in this case. The only deviation occurs with the TOPSIS method, where the 6th and 7th ranked materials have switched in relation to all other methods. In such circumstances, deciding to select the most suitable material is very simple and unambiguous, so the best material for this purpose would be M7 - carburized steel. On the other hand, based on the presented results, the validity of the MCDM Solver for material selection can be confirmed with large certainty. However, since the criteria weights were taken from a previous study, the methodology validity for their determination, by using the MCDM Solver, cannot be confirmed. Therefore, the problem of significance of criteria determination for this design application was solved independently of past studies - Scenario 1.

Within Scenario 1, criteria weights were determined by pairwise significance evaluation of the criteria. In this way, Ones were obtained the criteria weights values were that are numerically significantly different, but the importance priority remained unchanged. On the other hand, it should be noted that use of different criteria weights may significantly affect final rankings.

Taking all the above into account, the results of material ranking using the MCDM Solver were obtained, which are shown in Fig. 5. Based on the results, an absolute match can be established for ranks 1, 2, 3, 4, 8 and 9. Differences occur in the ranking of the 5th, 6th and 7th materials. This clearly shows that changing the weight of criteria affects the ranking of materials. However, in this case their change does not affect the final choice of gear material, as it is confirmed that the top 4 highest ranked materials remain the same. Also, the 2 worst ranked materials did not change their status. Based on these results (Scenario 1), the validity and reliability of the MCDM Solver for material selection was confirmed, which was the main intention of its development.

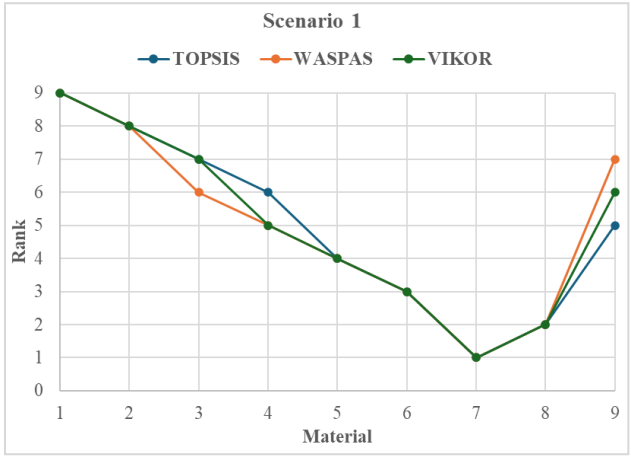

Fig. 5. Ranking results – Scenario 1

5. CONCLUSION

In this paper MCDM Solver was proposed for gear design material selection. The detailed procedure use of MCDM Solver was demonstrated while solving the material selection problem in two scenarios. The conclusions can be summarized as follows:

- MCDM Solver has been used directly for selecting gear material and can also be extended to cover other machine members, such as axle, shaft, pulley and so on.
- This study is turned out that carburized steel is the best ranked material for gear design without any doubt.
- Second ranked material for gear design is nitride steel.

- The obtained ranking results have excellent correlation with those derived by past researchers using different criterion weights and MCDM methods.
- In both scenarios, it is observed that the first four top-ranked materials exactly match with those derived by past researchers.
- WASPAS method is most robust for changing of criteria weight.
- Computational procedures are relatively simple and can be easily followed by the decision maker.
- Solving different MCDM problems by using MCDM Solver doesn't require the use of specialized software packages since the method can be easily implemented.

ACKNOWLEDGMENT

This research was financially supported by the Ministry of Science, Technological Development and Innovation of the Republic of Serbia (Contract No. 451-03-137/2025-03/200109).

REFERENCES

[1] Charles, J.A., Crane, F.A.A., Furness, J.A.E.: *Selection and use of engineering materials*, 3rd ed. Oxford, UK: Butterworth-Heinemann, 1997

[2] Ljungberg, L. Y.: Materials selection and design for development of sustainable products, *Materials & Design*, Vol. 28, No. 2, pp. 466-479, 2007

[3] Petković, D., Madić, M., Radenković G., Živković P.: An example of MCDM Solver application for material selection problems, *Proceedings of DEMI 2019,* Banja Luka, May 24-25, pp 65-70, 2019

[4] Chatterjee, P., Chakraborty, S.: Material selection using preferential ranking methods, *Materials and Design*, Vol. 35, pp. 384-393, 2012

[5] Čupić, M., Tummala, R., Suknović, M.: *Odlučivanje - formalni pristup*, Fakultet organizacionih nauka, Beograd, 2001

[6] Petković, D.: *Selection of biomaterials - Multi-criteria decision analysis and development of decision support system*, PhD dissertation, University of Niš, Faculty of Mechanical Engineering, Niš, 2017

[7] Petković. D., Madić. M., Radenković. G.: Knee Prosthesis Biomaterial Selection by Using MCDM Solver, *Advanced Technologies & Materials*, Vol. 46(2), pp. 37-41, 2021

[8] Petković, D., Madić, M.: Non-conventional machining processes selection using MCDM Solver, *Innovative Mechanical Engineering*, Vol. 1, No. 2, pp. 48 – 57, 2022

[9] Jahan, A., Bahraminasab, M., Edwards, K.L., A target-based normalization technique for materials selection, Materials and Design, Vol. 35, pp. 647-654, 2012

[10] Jahan, A., Mustapha, F., Ismail, M.Y., Sapuan, S.M., Bahraminasab, M., A comprehensive VIKOR method for material selection, Materials and Design, Vol. 32, pp. 1215-1221, 2011

[11] Petković D., Madić M., Radenković G., Ranking of Biomedical Materials by Using Comprehensive WASPAS Method, *Proceedings, MASING 2015*, Faculty of Mechanical Engineering Niš, September 17-18, pp. 339-344, 2015

[12] Milani, A.S., et al., The effect of normalization norms in multiple attribute decision making models: a case study in gear material selection, *Struct. Multidisciplinary Optim.* Vol. 29, pp. 312–318, 2005

[13] Petković, D., Madić, M., Radenković, G., Gear material selection using WASPAS method, *Proceedings, SMAT 2014,* Craiova, Romania, October 23-25, pp. 45-48, 2014

[14] Chatterjee, P., Chakraborty, S.: Gear Material Selection using Complex Proportional Assessment and Additive Ratio Assessment-based Approaches: A Comparative Study. *International Journal of Materials Science and Engineering,* Vol. 1, No. 2, pp. 104-111, ISSN 2047-6841, 2013

Product Development Process

11th International Scientific Conference
IRMES 2025
Research and Development of
Mechanical Elements and Systems
June 19 – 21, 2025; Vrnjačka Banja, Serbia

Original scientific paper DOI: 10.46793/IRMES25.051M

TOWARDS SMART ENGINEERING PRODUCTS

Radivoje MITROVIC [1]
Zarko MISKOVIC [2]
Vidosav D. MAJSTOROVIĆ [3]

[1] Faculty of Mechanical Engineering at the University of Belgrade, Belgrade, Serbia, 11000; rmitrovic@mas.bg.ac.rs ; ORCID iD: 0000-0003-0513-6540
[2] Faculty of Mechanical Engineering at the University of Belgrade, Belgrade, Serbia, 11000; zmiskovic@mas.bg.ac.rs ; ORCID iD 0000-0002-8320-7191
[3] Faculty of Mechanical Engineering at the University of Belgrade, Belgrade, Serbia, 11000; vmajstorovic@mas.bg.ac.rs ; ORCID iD 0000-0001-9534-8461

Abstract: *The evolution of traditional engineering products is moving towards the development of smart products, which are characterized by intelligence, networking and adaptability to the user. Using the elements of Industry 4.0, such as artificial intelligence (AI), Internet of Things (IoT), digital twins (DT) and data analytics (BDA), their design, manufacturing and life cycle management are carried out on a new basis. That is why smart engineering products are characterized by self-monitoring, autonomous decision-making and optimization of their work in real time. All this leads to greater satisfaction of their users, due to improved efficiency, reliability and a better user experience. Also, smart products include issues of cyber security, data privacy, interoperability and sustainability, which must be considered in order to fully realize the potential of smart engineering solutions in them. This paper provides an analysis and synthesis of smart engineering products (SEP) from the aspect of their development, characteristics, application examples and future research in this area.*

Keywords: *Smart engineering products; Industry 4.0 / 5.0; Research; Development; Case studies.*

1. INTRODUCTION

The rapid development of digital technologies and intelligent systems has led to the emergence of smart engineering products (SEPs), which represent innovative solutions based on the integration of big data analytics (BDA), artificial intelligence (AI) and interconnected systems (IoT), which have improved their performance, efficiency and adaptability. These products are designed to dynamically respond to environmental conditions, user needs and operational requirements, creating a seamless interaction between the physical and digital domains [1,2]. They use the key technologies of Industry 4.0: Internet of Things (IoT), Machine Learning (ML/DML) and Cyber-Physical Systems (CPS), to enable real-time monitoring, predictive maintenance and autonomous decision-making. As industries transition to Industry 4.0, these intelligent solutions become essential in sectors such as manufacturing, transportation, healthcare, energy, and others. This transformation is driven by the need for increased efficiency, sustainability and adaptability. Companies are moving from traditional static products to adaptive and connected systems that optimize the use of resources and improve the user experience. However, the itegration of smart technologies also presents challenges, including cybersecurity risks, high implementation costs, and the need for trained professionals.

SEPs are advanced engineered systems, machines, or devices that integrate computational intelligence, connectivity, sensors, and adaptive control to improve functionality, efficiency, and user interaction. Their main characteristics are [2,3,4]: (i) embedded intelligence - microprocessors, AI based machine learning for decision-making, (ii) connectivity and IoT integration - communication via wireless (Wi-Fi, Bluetooth, 5G) or wired networks, (iii) sensors and data collection - use sensors for noise, vibration, temperature, movement, pressure, etc., to monitor conditions, (iv) adaptive and autonomous operation - self-adjustment based on data in real-time or predictive analytics, (v) user-centered interaction – supporting interfaces such as voice control, touch screens or mobile applications, and (vi) cloud & edge computing – processing data locally or in the cloud for improved functionality of these products and real-time operation. Smart engineering products are no longer optional, but necessary for companies that want to thrive in the digital age. By using cutting-edge technologies, improving sustainability and enabling intelligent automation, they are shaping the future of modern industries, driving innovation, efficiency and long-term growth.

Their importance and relevance in modern industry is improvement of operational efficiency, because SEPs enable real-time monitoring, predictive maintenance and automated decision-making, reducing downtime and optimizing the use of resources. In industries such as manufacturing, smart machine tools and robots dynamically adjust operations to improve production efficiency and reduce scrap; (b) data-driven decision making, using IoT, AI and BDA, they collect and analyze vast amounts of data, providing actionable insights. This data-driven approach helps businesses optimize supply chains, improve product quality and increase customer satisfaction; (c) driving innovation and customization, as modern consumers demand personalized and customizable products. SEPs enable mass customization through the use of digital twins and cyber-physical systems for simulation, testing and detailed pre-production design, reducing development time and costs; (d) improving sustainability and environmental impact, as the concept of SEPs supports green initiatives by optimizing energy efficiency, reducing material waste and enabling circular economy practices; (e) strengthening competitiveness in Industry 4.0, as industries adopting based on the following facts [5,6,7,8]: (a) SEPs gain a competitive advantage by embracing automation, robotics and digital business transformation. For example in the automotive industry and healthcare, smart products such as autonomous vehicles and AI-assisted medical devices have revolutionized these fields; (g) increasing safety and reliability, as these products improve workplace safety through real-time risk assessment, failure prediction and automatic hazard prevention. This is particularly important in sectors such as construction, process industry, aerospace and mining, where safety and reliability are top priorities. An overview of the relevance of smart products for different industries is shown in Table 1.

This paper aims to provide a comprehensive concept of SEPs, highlighting their potential to drive industrial transformation. By presenting and analyzing technologies, applications, challenges and future development directions, the paper seeks to offer useful insights for researchers, engineers and industry leaders in adopting smart engineering solutions for SEPs. This paper also has partial objectives related to various aspects of smart products, primarily SEPs, which are given in Table 2.

Table 1. Analysis of the relevance of intelligent products for different industries

Industry	Application	Influence
Production	Smart factories, cobots, digital twins	Greater productivity, layoffs and scrap
Healthcare	Personal monitors, robotic surgery, smart implants	Improved patient care, remote diagnostics
Traffic	Autonomous vehicles, smart traffic systems	Safer, more efficient mobility
Energy sector	Smart grids, predictive maintenance of turbines and generators	Reduced downtime, optimized energy consumption
Agriculture	Precision agriculture, irrigation (fertilizing, watering) based on IoT	Higher yields, conservation of resources
Retail and logistics	Automated warehouses, smart inventory tracking	Faster deliveries, reduced inventory

Table 2. Overview of different aspects of analysis and synthesis of smart products

Analysis aspect	Focus areas of research and analysis
Technological	AI/ML integration, IoT connectivity, sensor fusion, cloud/edge computing
Industrial	Smart production, healthcare robotics, autonomous logistics
Economic	ROI for SEPs, cost benefit analysis, market growth trends
Social	Retraining of the workforce, cooperation between humans and machines, user trust in AI
Ecological	Energy efficiency, circular economy SEPs recycling, e-waste)
Secure and private	Cyber security risks, data encryption, blockchain for SEPs integrity

The analyzes and syntheses presented in this paper should contribute to new academic knowledge, industrial innovations and practices, as well as the creation of industrial policy, which should ensure that SEPs are developed as safe, efficient and sustainable solutions for the contemporary challenges of the digital revolution.

2. EVOLUTION OF SMART ENGINEERING PRODUCTS

The development of SEPs has been shaped by technological progress and industrial transformations. From traditional mechanical systems to intelligent, interconnected solutions, SEPs have evolved through various industrial revolutions and breakthroughs in digitization, automation and AI. The evolution of SEPs reflects the progress from purely mechanical devices to highly intelligent, self-learning and interconnected systems. As industries move towards Industry 5.0, SEPs will continue to redefine engineering by merging human creativity with digital intelligence, providing smarter, safer and more efficient solutions. The evolution of SEPs has ranged from basic automation to cognitive systems, and it can be divided into five key phases, each of which marks a significant leap in capabilities and applications, Table 3 [2,3,9-11].

Table 3. Stages of SEP development

Stage of development of intelligent products	Characteristics	Examples	Influence
Mechanical and electromechanical era (before 1990)	- Basic automated systems with limited programming - Reliance on mechanical controls and analog electronics - No linking or decision making based on data	✔ Early industrial robots (Unimate, 1961) ✔ Programmable logic controllers (PLC) in factories ✔ Thermostats with simple timer-based controls	Limitations: ➔ Robust, pre-programmed operations ➔ No real-time customization or customization
Digital & Embedded Systems (1990s - early 2000s)	- Introduction of microprocessors and digital controls - Digital & Embedded Systems - Basic sensor (temperature, pressure, movement)	✔ CNC machines with digital precision (an order of magnitude higher than the previous generation) ✔ Early Automotive ECU (Engine Control Units) ✔ Smart appliances (microwave ovens with preset programs)	Progress: ➔ Greater precision and repeatability ➔ Limited data logging, but no cloud connectivity
Connected and IoT-enabled systems (2000 - 2010)	- The emergence of IoT (Internet of Things) and wireless communication - Remote monitoring and control via cloud platforms - Data collection for basic analytics	✔ Smart home devices (Nest Thermostat, 2011) ✔ Industrial IoT (IIoT) for predictive maintenance ✔ Wearable fitness trackers (Fitbit, 2009)	Key developments: ➔ Real-time data transfer ➔ Early stage machine learning for pattern recognition
AI and autonomous systems (2010 -2020)	- Integration of AI, machine learning and big data analytics - Self-learning and adaptive decision-making - Edge computing for faster local processing	✔ Autonomous vehicles (Tesla Autopilot) ✔ Medical diagnostics with AI (IBM Watson) ✔ Collaborative robots (cobots) in production	Transformations: ➔ Transition from a rule-based system to a predictive and prescriptive system ➔ Improvements in human-machine interaction (voice, vision, motion controls)
Cognitive & Self-evolving SEPs (2020 -)	- Digital twins for real-time simulation and optimization - Self-healing systems that detect and repair faults autonomously - Quantum computing enabling ultra-fast decision-making - Swarm intelligence (multiple SEPs collaborating like a hive mind)	Future applications: ✔ Fully autonomous smart cities with AI-managed infrastructure ✔ Brain-computer interface (BCI) controlled prosthetics and devices ✔ Self-reconfiguring factories with zero human intervention	

The evolution of SEPs has come a long way, from simple mechanization to intelligent, self-sufficient systems. The next frontier involves cognitive, self-evolving products that blur the line between engineered machines and autonomous entities [1,4,7]. As AI, IoT, and quantum computing advance, SEPs will redefine industries, making them more efficient, sustainable, and human-centric. The key drivers of the development of SEPs are systematized in Table 4.

Already today, we have a whole range of examples of the application of smart products, including SEPs [4,6,12,13]: (i) health and medical technology, where these products enable early disease detection, precise surgical interventions, online monitoring of the patient's condition, using the following smart technologies: AI diagnostics (IBM Watson Health, Google DeepMind), wearable health monitors (Apple Watch ECG, continuous glucose monitors), telemedicine and remote monitoring of patients, smart surgical robots (Da Vinci Surgical

System); (ii) production (Industry 4.0), where stoppages and scrap are reduced by up to 80% and, accordingly, production costs, supply chains are effectively managed and energy-efficient production is ensured; (iii) automotive industry and transport, where accidents are eliminated, emissions are reduced and fleet monitoring is carried out in real time, all thanks to: autonomous vehicles (Tesla, Waymo), connected car ecosystems (OTA updates, V2X communication), AI-powered traffic management (smart cities), and electric vehicle (EV) smart charging; (iv) retail & e-commerce, where hyper-personalized shopping, reduced theft & stockouts, and seamless checkout experiences were achieved.

Table 4. Drivers of the development of SEPs

Era	Key Enablers	Impact
Mechanical	Gears, motors, analog circuits	Basic automation
Digital	Microprocessors, PLCs	Programmable control
Connected	IoT, cloud computing	Remote access & data analytics
AI-Driven	Machine learning, 5G	Predictive & adaptive systems
Cognitive	Quantum AI, digital twins	Self-optimizing ecosystems

All this was achieved with the support of smart technologies: AI recommendation engines (Amazon, Netflix), cashier-less stores (Amazon Go, AI-powered checkout), smart inventory management (RFID, drones), and AR/VR shopping experiences (virtual try-ons); (v) energy & utilities, where energy savings of up to 50% were achieved, reduced blackouts and better integration of renewables. SEPs for this area are: smart grids & meters (real-time energy monitoring), AI for renewable energy optimization (solar/wind forecasting), and predictive maintenance for power plants; (vi) agriculture (AgTech) is an area where these technologies can optimize irrigation up to 50%, increase crop yield and reduce the use of pesticides, using the following smart technologies: precision farming drones & IoT sensors (soil, moisture, crop health), AI-powered pest/disease detection, automated smart irrigation, and robotic harvesters; (vii) smart cities & infrastructure, in practice provide: reduced traffic jams, lower energy consumption, and improved emergency response, and this is realized by means of: intelligent traffic lights & congestion management, smart waste management (sensor-based trash collection), AI surveillance & public safety, and connected street lighting; (viii) logistics & supply chain, according to the SEP model, provide: faster, cheaper deliveries, real-time shipment tracking, and reduced human error. This is achieved by using: AI route optimization (UPS, FedEx), autonomous delivery drones/robots, blockchain for supply chain transparency, and warehouse automation (Amazon Robotics); (ix) banking & FinTech, where the following features are achieved: reduced fraud losses, 24/7 customer service, and faster loan approvals, all thanks to the following technologies: AI fraud detection, Chatbots & virtual assistants (Bank of America's Erica), blockchain-based smart contracts, and biometric authentication (facial recognition payments); and (x) aerospace & defense, by applying smart products will have: safer flights, lower maintenance costs, and enhanced military surveillance, and they will be used for: AI for predictive aircraft maintenance, autonomous drones & UAVs, smart materials (self-healing coatings), and AI-powered threat detection. In the future, SEPs will provide: in healthcare: AI drug discovery and nanorobotics, in manufacturing, production facilities without humans, in retail, metaverse-powered virtual stores, and energy, smart nuclear fusion monitoring. Smart technologies (products) will reshape today's industries, improving efficiency, reducing costs and improving user experience, making businesses more competitive and future-ready.

3. CORE TECHNOLOGIES ENABLING SMART PRODUCTS

The Internet of Things (IoT) is a key enabler of SEP, providing them with seamless connectivity, real-time data exchange, and intelligent automation [4, 11, 14-16]. By integrating IoT technologies, engineering products become smarter, self-controlling and more efficient, transforming industries such as manufacturing, healthcare, automotive and energy. The role of IoT in smart engineering products is to ensure: connecting physical devices to the digital world through sensors, networks and cloud platforms; enabling real-time monitoring of product performance and operational status; enabling remote control and automation for improved efficiency and security; and predictive maintenance support to prevent failures and reduce downtime. The key IoT components in SEP are: (a) smart sensors and actuators, where sensors collect real-time data (eg temperature, pressure, vibration, humidity), and actuators, which enable automated responses (adjust machine speed, trigger alerts). For example IoT-enabled smart turbines adjust blade angles based on wind conditions; (b) connectivity and communication protocols, where IoT devices communicate via Wi-Fi, 5G, Bluetooth, LPWAN and MQTT, thus enabling seamless machine-to-machine (M2M) communication. We have this, for example, with the smart machine tool, which shares operational data to optimize production scheduling; (c) cloud and edge computing, where cloud computing is used to generate and analyze IoT data for centralized decision-making, and edge computing systems perform local data processing, which are used for quick responses in real time. For example, autonomous vehicles use edge computing for instant processing of sensor data; (d) IoT platforms and data analytics, are the next dimension of this technology, and platforms such as AWS IoT, Microsoft Azure IoT and Google Cloud IoT are used, with which devices and data are managed, and at the same time AI-driven analytics are performed, where efficiency is optimized, anomalies are detected and failures are predicted. An example here is smart grids, which use AI to balance energy loads and

prevent interruptions in electricity supply. An analysis of the application of IoT for SEP in different industrial sectors is presented in Table 5. Thus, IoT serves as the central nervous system of SEPs, enabling real-time intelligence and autonomous functionality through comprehensive connectivity of various entities.

Table 5. IoT in support of SEPs

Industry	IoT-Enabled Smart Product	Benefits
Manufacturing	Smart factory machines with predictive maintenance	Reduced downtime, improved efficiency and quality
Automotive	Connected vehicles with real-time diagnostics	Enhanced safety, optimized fuel consumption
Healthcare	Smart medical devices (wearables, AI diagnostics)	Remote monitoring, early disease detection
Energy	Smart grids and intelligent power meters	Optimized energy distribution, cost savings
Construction	IoT-enabled smart buildings and HVAC systems	Energy efficiency, real-time monitoring

Artificial intelligence (AI) and machine learning (ML) are transforming SEP to enable autonomous decision-making, real-time optimization, and self-learning capabilities. These technologies enable SEP to analyze data, predict outcomes and adapt to changing conditions, making them more intelligent, efficient and reliable. The role of AI and ML in SEP is to improve its features by: automating complex tasks that traditionally require human intelligence, improving the efficiency and accuracy of decision-making using data, enabling the application of predictive maintenance, by detecting anomalies before failure occurs, optimizing operations in real time, based on sensor data and historical trends, and improving product adaptability, through continuous learning and self-improvement. The key AI and ML technologies in SEP are [17-20]: (a) machine learning algorithms, where the following models are used: supervised learning, where we have trained on labeled data to predict outcomes (fault detection in machines); unsupervised learning, where we use identifies hidden patterns in data (quality control analysis); and reinforcement learning, where the learning model is developed as learns through trial and error to optimize performance (robotics automation); (b) deep learning & neural networks, where we mimic human brain functions to recognize patterns, process images, and make decisions, such as AI powered medical imaging systems detect diseases with high accuracy; (c) natural language processing (NLP), where it should enable SEPs to understand and process human language for voice commands and automated responses. For example, AI-driven voice assistants in industrial machinery provide hands-free operation; (d) computer vision, where image processing and AI are used to detect defects, guide robotic systems, and enhance safety, so AI-based quality inspection in manufacturing identifies defects in real-time; (e) predictive analytics & decision support systems, where AI models are used for analysis of historical data to predict failures, optimize resource usage, and enhance performance, such as AI-driven predictive maintenance prevents unexpected machine breakdowns. Core AI/ML capabilities in SEPs are shown in Table 6.

Table 6. Analysis of AI/ML in SEPs

Function	Techniques	Implementation
Predictive Analytics	LSTM, Prophet	Equipment failure forecasting
Computer Vision	CNN, Vision Transformers	Quality inspection in manufacturing
Natural Language Processing	BERT, Whisper	Voice-controlled industrial systems
Reinforcement Learning	Q-Learning, PPO	Autonomous robot path optimization
Anomaly Detection	Autoencoders, Isolation Forest	Cybersecurity threat identification

Autonomous Decision Architectures are defined over five levels: level 1 - rule-based automation (if-then logic), level 2 - ML-assisted decisions (human oversight), level 3 - context-aware autonomy (multi-input analysis), level 4 - self-optimizing systems (reinforcement learning), and level 5 - cognitive adaptation (neuromorphic computing). AI and ML are the driving forces behind SEPs, enabling automation, intelligence, and self-optimization.

Digital Twins (DT) and simulation are key technologies enabling SEP to optimize performance, predict failures, and improve efficiency. A DT is a virtual replica of a physical product, system, or process that reflects its real-time status, behavior, and characteristics. Through simulation, these digital counterparts can be tested, optimized, and monitored before any physical prototype is created, and even after deployment to ensure continuous improvement. Simulation capabilities in the context of SEPs are shown in table 7 [15-17,21].

Table 7. Overview of simulation models for SEPs

Type	Technology	Application
Physics-Based	FEM, CFD, MBD	Structural analysis
Data-Driven	LSTM, GANs	Performance prediction
Hybrid	Physics-informed ML	Battery degradation
Real-Time	Reduced-order models	Control optimization

DT provides a real-time digital representation of a smart engineering product's lifecycle, allowing continuous monitoring and simulation of its behavior under various conditions. This enables products to: monitor real-time performance and collect data from sensors to continuously update the virtual model; predict and optimize product behavior and performance without physical testing; simulate scenarios to predict outcomes under different working conditions; improve product development and decision-making by providing a better understanding of System behavior; and enable continuous improvement, allowing the virtual model to evolve with new data and insights. The most important components of DT and simulation in SEP are: (a) real-time data collection, performed by sensors and IoT devices, collect data from physical products or systems (temperature, pressure, wear and others). This data is then transmitted to the DT to update the physical product state in real time; (b) virtual model creation, is done by creating DT using CAD models and simulations based on physics or mathematical representations of product components and systems. Also included here are hardware attributes (shape, size, material properties, etc.) and operational characteristics (response to external forces, wear over time, etc.); (c) simulation allows engineers to test scenarios and optimize design or manufacturing operations, virtually before applying them in the real world, and predictive analytics in DT can identify patterns and anomalies that can lead to unwanted phenomena (failure, scrap); (d) integration with AI and machine learning. AI and ML enhance DT by providing self-learning and predictive capabilities, enabling autonomous decision-making based on historical and real-time data. For example DT of a jet engine can use AI to predict when certain components need maintenance or when the engine might fail. DTs represent a transformative leap in SEP, creating dynamic virtual replicas that mirror physical products throughout their lifecycle. This technology enables unprecedented levels of optimization, prediction and control.

Big Data Analytics (BDA) , plays a key role in enabling SEP to operate at optimal levels by using massive amounts of data to drive real-time insights, optimize operations, improve product performance and predict future trends. These data-driven technologies use information from various sources such as IoT sensors, user interactions, machine performance data and environmental factors to ensure that SEPs are efficient, reliable and adaptable to changing conditions. BDA allows SEPs to extract valuable insights from massive datasets and use these insights for decision-making, optimization, and automation. Through the use of advanced data analytics tools, SEPs can: process vast amounts of real-time data for immediate decision-making and optimization; analyze historical data to identify patterns and predict future performance; enhance product lifecycle management, from design to manufacturing to maintenance; support predictive maintenance, to prevent equipment failures and reduce downtime; and enable continuous improvement by continuously monitoring and adapting product performance based on data-driven insights. Key BDA capabilities analysis is presented in Table 8.

Table 8. Overview of BDA models for SEPs

Analytics Type	Techniques	SEP Applications
Descriptive	SQL, OLAP	Operational dashboards
Diagnostics	Root cause analysis	Failure investigation
Predictive	XGBoost, LSTM	Remaining useful life
Prescriptive	Linear programming	Process optimization
Cognitive	Deep reinforcement learning	Autonomous control

Key components of BDA in SEP are [4,22]: (a) data collection & integration, by IoT sensors which provide continuous data on product health, environmental conditions, and user behavior. Second part is machine-generated data - includes information from automated systems, robots, and connected machinery. Part three is human interaction data, which collected from user interfaces and feedback loops, last not least are external data, where we have weather conditions, traffic patterns, and other external factors that influence product performance; (b) data storage & management including cloud / edge computing for storage solutions for managing vast amounts of data, also data lakes which used to store raw, unstructured data before analysis, and databases and data warehouses, by organizing and optimizing data for efficient querying and reporting. BDA serves as the central nervous system for SEPs, transforming raw sensor data into actionable intelligence that drives autonomous optimization and continuous improvement; (c) data analytics & processing tools has four approaches: descriptive analytics - provides insights into past performance, identifying trends and patterns (performance over time), predictive analytics - uses historical data to forecast future behavior, including predicting potential failures and optimizing maintenance schedules, prescriptive analytics - provides actionable recommendations on how to optimize product performance and operations, and real-time analytics - processes data as it is collected to enable immediate decision-making; and (d) AI & ML, where we have: AI models - use algorithms to analyze complex data patterns and make decisions autonomously, and also ML algorithms - learn from historical data and improve predictions over time. For example AI-driven algorithms predict the optimal settings for machines, reducing energy consumption while maintaining performance.

Edge computing and Cloud computing (ECC) are complementary technologies that form the backbone of modern SEP by facilitating the processing, storage, and analysis of data generated by connected devices, sensors, and systems. These technologies enable real-time

decision-making, enhance data accessibility, and improve scalability, ensuring that SEPs are efficient, responsive, and optimized for various industrial applications. Edge and Cloud computing provide the necessary infrastructure for data storage, processing, and analysis, enabling SEPs to perform at their best. They work together to: Edge computing - process data closer to the source (ie, at the device or local network level) for real-time decision-making and immediate responses. Cloud computing handles large-scale data storage, more complex data analytics, and long-term data management by leveraging centralized resources. Together, they allow SEPs to balance the needs for local real-time processing and global data analysis, delivering optimal performance and insights. The analysis of technology stack components is shown in table 9.

Table 9. Technology stack components SEPs

Layer	Computer	Storage	Networking
Virgo	MCU/FPGA	Embedded flash	BLE/Zigbee
Edge	SoC/GPU	NVMe SSD	Wi-Fi 6/5G
Fog	Server cluster	US	Ethernet/TSN
Cloud	Virtual machines	Object storage	Fiber/Satellite

Key components of Edge and Cloud computing in SEP are [9,18]: (a) Edge computing, where we have: local data processing - edge devices (eg, sensors, machines, gateways) process data locally, reducing latency and allowing immediate responses without needing to send data to the cloud; Real-time decision-making - Edge computing enables fast responses based on data gathered from SEPs, such as adjusting machine settings, detecting anomalies, or triggering alerts, and resource constraints - Edge devices typically have limited computational power and storage but are designed for rapid, localized decision-making and data pre-processing. For example, a smart thermostat uses edge computing to adjust temperature settings in real-time based on sensor data, without relying on cloud servers; (b) Cloud computing, also we have: Data storage and scalability - cloud computing offers centralized storage for large volumes of data generated by SEPs. This ensures scalability and long-term data retention for analysis and future use, advanced analytics - Cloud platforms support complex data analytics, machine learning, and AI algorithms, providing deeper insights that cannot be processed locally at the edge, and Data sharing and collaboration - Cloud computing enables seamless data sharing, access across devices, and collaborative decision-making, providing a single platform for all stakeholders. For example, cloud-based analytics platforms monitor multiple industrial machines across different facilities, analyzing performance trends and predicting maintenance schedules. Edge and Cloud computing (ECC) form the computing backbone of SEP, enabling real-time responsiveness while maintaining powerful analytical capabilities. This hybrid architecture provides the perfect balance between latency-sensitive processing and scalable data management.

4. DESIGN AND DEVELOPMENT OF SMART ENGINEERING PRODUCTS

Design and development of SEPs requires a multidisciplinary approach that integrates traditional engineering principles with cutting-edge digital technologies. The systematic methodology for SEP development includes: smart product development lifecycle includes the following stages [3,23]: phase 1 - smart requirement engineering there are the following steps - identify intelligence requirements (autonomy level, connectivity needs), define data strategy (collection points, processing hierarchy), and establish cyber-security and privacy parameters; phase 2 - cyber-physical co-design, consisting mechanical/electrical architecture with embedded intelligence, hardware-software interface definition, and DT integration planning; phase 3 - intelligent system integration includes sensor fusion implementation, edge-cloud workload partitioning, and AI/ML model deployment strategy; phase 4 - validation & certification, also contains, functional safety verification (ISO 26262, IEC 61508), AI model robustness testing, and connectivity stress testing; and the last phase 5 - lifecycle management, consisting of over-the-air (OTA) update infrastructure, continuous learning mechanisms, and predictive maintenance integration. The analysis of critical development technologies for SEPs is shown in table 10.

Table 10. Overview of critical development technologies for SEPs

Domain	Tools & Platforms	Application
Mechanical	Generative design (nTopology)	Lightweight smart structures
Electrical	Altium with IoT modules	Embedded system design
Software	ROS 2, Embedded Linux	Real-time control
AI/ML	TensorFlow Lite Micro	On-device learning
Connectivity	AWS IoT Greengrass	Edge-cloud integration

Key design methodologies for SEP are: (a) model-based systems engineering (MBSE), which has SysML for system architecture, simulation-driven development, and requirements traceability matrices, (b) agile-DevOps hybrid, which is implemented in several stages, CI/CD for embedded software, containerized AI model deployment, and A/B testing for algorithm evolution, and (c) biomimetic design using the following approaches, nature-inspired intelligence patterns, swarm behavior algorithms, and organic sensor architectures.

Key design considerations for SEPs require balancing traditional engineering principles with emerging digital capabilities. Here are the critical considerations [1,24-26]: (a) intelligence architecture, by autonomy level definition (L1-L5) including: edge vs. cloud processing split, AI model selection (accuracy vs. resource needs), and fail-safe mechanisms for AI decisions; (b) connectivity framework, has next steps: protocol selection matrix (bandwidth vs. power), multi-radio coexistence management, offline operation capabilities, and over-the-air (OTA) update infrastructure; (c) sensing strategy is implemented through stages - sensor fusion architecture, redundancy planning, environmental hardening, and self-calibration routines; (d) power management defines the following aspects: energy budget allocation, harvesting potential assessment, low-power states design, and battery health monitoring; (f) security implementation, means that the following should be determined: hardware root of trust, zero-trust architecture, secure boot sequence, and encrypted data pipelines; (g) human interaction, means that the following should be done: multimodal interface design, adaptive user experiences, explainable AI outputs, and accessibility compliance; (h) mechanical integration, means that the following should be done: thermal management solutions, vibration/shock protection, IP rating requirements, and modular serviceability; (i) data strategy, means that the following should be defined: collection frequency optimization, edge preprocessing requirements, retention policies, and privacy-by-design implementation; (j) verification & validation, means that the following should be done: digital twin testing environment, corner case simulation, AI model robustness testing, and field validation planning; and (k) lifecycle management, it is necessary to define: upgrade path planning, component obsolescence strategy, circular economy provisions, and decommissioning protocols. Defining the aforementioned design framework for SEPs, we can also define emerging design paradigms, namely: self-healing designs - materials and systems, evolutionary architectures - field-reconfigurable hardware, bio-inspired intelligence - neuromorphic approaches, and quantum-resistant security - future-proof cryptography. These considerations ensure SEPs deliver intelligent functionality while maintaining reliability, security, and usability across their operational lifespan. The design process must remain agile to incorporate advancing technologies while meeting stringent industry requirements.

The integration of sensors, software and hardware is a fundamental stage in the development of SEPs. During the design phase, this integration must be seamless and well coordinated to ensure that the product functions efficiently and meets its performance goals. This process involves collaboration across multiple engineering domains, including electrical engineering, software engineering, and mechanical engineering. This activity is carried out in the following steps: (a) defining the functional requirements, means that before the integration of sensors, software and hardware, the functional requirements of the SEP should be defined, which includes [2,17,27]: (i) what data should be collected, which determines the types of sensors needed (e.g. temperature, pressure, humidity, movement, etc.), (ii) what actions need to be triggered? – define how sensors will communicate with hardware and software, (iii) what performance is required? – means speed, accuracy, response times and power consumption should be considered, (iv) connectivity requirements, meaning determine how the SEP will communicate (eg, IoT protocols such as Wi-Fi, Bluetooth, Zigbee, etc.). These functional requirements will guide decisions about the types of sensors, computing hardware (eg microcontrollers or edge devices) and software platform to be used; (b) selection of sensors for data collection, which should enable the SEP to function intelligently. The choice of sensors depends on the specific use case and the requirements of the SEP, so the criteria for the selection of sensors are as follows: (i) sensor type, means to choose sensors based on environmental parameters for measurement (eg, temperature, pressure, motion, accelerometers, gyroscopes, gas sensors, etc.), (ii) accuracy and sensitivity, means that you should ensure that the sensors have sufficient accuracy and sensitivity for the intended application, (iii) energy consumption, means that you should take into account the power requirements of the sensors, especially for battery powered devices. Low-power sensors should be used when energy efficiency is essential, (iv) size and form factor, compact, lightweight sensors should be chosen that fit within the physical constraints of the SEP, and (v) integration compatibility, meaning that sensors should be ensured to be compatible with selected hardware platforms (eg, microcontrollers, IoT gateways); (c) integration of sensors into hardware, means designing the printed circuit board (PCB) to incorporate the sensors, ensuring proper power management and signal routing. Also, connectivity ensures that the sensors are connected to a suitable interface on the hardware, such as I2C, SPI, or analog-digital converters (ADC) for data transmission to the main processing unit. (d) hardware design and integration, meaning that the hardware of SEPs includes both the physical components (sensors, actuators, microcontrollers) and the communication infrastructure (eg, wireless communication modules, edge devices). Key hardware components are: (i) microcontrollers/processors - choose the appropriate processing unit (eg, MCUs, FPGAs, or Raspberry Pi for more complex computations). The processor must be capable of handling sensor inputs and controlling actuators in real-time, (ii) actuators - depending on the application, include motors, valves, or other actuators that respond to sensor data (eg, activating a cooling system when a temperature sensor detects heat), (iii) wireless modules - select wireless communication components (eg, Wi-Fi, Bluetooth, Zigbee) for connectivity and data transmission. In some cases, use edge devices to process data locally and reduce the dependency on cloud connectivity, (iv) power management systems - ensure efficient power management to support sensors and hardware components, especially if the product needs to run on battery power. Finally, hardware-sensor integration should be performed, which means sensor interfacing - integrate sensors with the microcontroller/processor via

digital or analog input channels. Proper signal conditioning may be needed to scale the data from sensors to usable values, and real-time processing - ensure that the hardware is capable of performing real-time processing of sensor data and actuating responses without significant delay. Software development and integration defines the software necessary to process sensor data, implement algorithms, and enable decision-making or automation within the SEP. Therefore, it is necessary to have the following software components: (i) firmware for hardware control: Develop the firmware that will run on the microcontroller to handle tasks such as reading sensor data, controlling actuators, and managing communication protocols, (ii) edge computing. In cases where edge processing is necessary, deploy software on local edge devices to perform data analytics, filtering, and decision-making close to the source of data, (iii) cloud connectivity and remote monitoring. For cloud-connected SEPs, develop software for data transmission and remote monitoring, ensuring that sensor data can be uploaded to a cloud platform for further analysis and insights, (iv) machine learning/AI. Implement machine learning algorithms on the software layer to enable the SEP to learn from the data and make autonomous decisions based on historical patterns, and (v) user interfaces - develop software for user interfaces, such as mobile apps or dash-boards, that allow users to interact with the SEP, view sensor data, and receive notifications. Software-sensor integration is implemented in several stages: (i) data processing and filtering. Process sensor data to remove noise, apply data smoothing techniques, and convert raw sensor signals into meaningful information (eg, calculating the average temperature from multiple readings), (ii) data storage. Ensure data from sensors is properly stored, either locally (eg, on SD cards or flash memory) or remotely in the cloud, and (iii) communication protocols. Implement the necessary communication protocols in software to send data from the hardware (via sensors) to the cloud or other devices, ensuring that the data is properly packaged for transmission. Once the hardware and software are integrated, sensor calibration is essential to ensure the accuracy and reliability of sensor readings, and is implemented in two stages: (i) calibration procedures. Calibrate sensors to ensure that data readings are accurate and consistent. For example, temperature sensors may need calibration against a reference thermometer, and (ii) testing and validation. Test the integration of sensors with hardware and software under real-world conditions to ensure proper operation, including edge cases and environmental variability. One of the most critical aspects of SEP design is ensuring that data flows seamlessly from the sensors through the hardware, then to the software, and ultimately to the user or cloud platform, by the following steps: (a) data collection and communication in three steps: (i) sensor data acquisition. Sensors collect data, which is passed to the microcontroller/processor for preliminary processing, (ii) edge processing - if applicable, edge devices or microcontrollers perform initial analysis and filtering of data to reduce the load on cloud servers, and (iii) communication interface - ensure that processed data can be sent to the cloud, user interface, or other connected devices via wireless communication protocols. Use MQTT, HTTP, or WebSocket protocols for communication depending on the requirements. Feedback and Control Loop includes: (i) actuator response, based on sensor data analysis, the software triggers actuators to perform specific actions (eg, turning on a cooling fan if temperature exceeds a threshold), and (ii) continuous monitoring - maintain a feedback loop to continuously monitor sensor data and adjust the SEP's operations accordingly. Power consumption and optimization are critical in SEPs, especially for battery-powered devices. Effective power management should be considered during the integration phase. Low-power sensors - choose sensors with low power consumption when possible, particularly for continuous monitoring applications , energy-efficient hardware - opt for low-power microcontrollers and processors that support sleep modes or power scaling to minimize energy usage, and power management - use efficient power management systems to extend battery life, including techniques like energy harvesting (eg, solar panels) and dynamic voltage and frequency scaling (DVFS). The integration of sensors, hardware, and software in the design phase of SEPs is a complex yet crucial process. By ensuring seamless communication between sensors and hardware, and efficient data processing via software, engineers can create SEPs that are not only functional but also intelligent, adaptive, and energy-efficient. Each component plays a vital role in ensuring that the SEP performs optimally, meets user requirements, and delivers value throughout its lifecycle. Effective integration also helps address challenges such as real-time performance, interoperability, scalability, and security, which are critical for the success of modern smart products.

Human-centered design (HCD) and user experience (UX) are essential principles for creating SEPs that are intuitive, efficient, and effective [24]. These approaches ensure that the product aligns with the needs, preferences, and behaviors of the users while also optimizing its functionality, usability, and overall satisfaction. Given that SEPs often involve advanced technologies such as IoT, AI, and sensors, it is critical to focus on the end-user experience to ensure the product is accessible, useful, and sustainable.

Human-Centered Design is a design methodology that emphasizes understanding the users' needs, challenges, and contexts to create products that offer meaningful solutions. In the context of SEPs, HCD involves several key principles: (a) empathy with users. Understanding the user's pain points, goals, and expectations is at the core of human-centered design. For SEPs, this means: user research - conducting interviews, surveys, and observations to gather insights about how users interact with existing products, what challenges they face, and what improvements they seek, and contextual understanding - considering the specific environment in which the SEP will be used, whether it's an industrial setting, healthcare environment, or home application; (b) iterative design process. HCD follows an iterative process

where design is continuously refined based on user feedback and testing. The stages typically include: prototyping - developing low-fidelity prototypes of the SEP to test basic concepts and interactions before finalizing the design, user testing - involving real users in the testing of the prototypes, gathering feedback on usability, and adjusting the design accordingly, and refinement - repeating the design and testing cycles to continuously improve the SEP's usability and overall experience; (c) collaborative design - incorporating input from multiple stakeholders throughout the design process ensures that all perspectives (eg, users, designers, engineers, and manufacturers) are considered. This collaborative approach helps in aligning user needs with technical constraints.

User Experience (UX) refers to the overall experience of a user when interacting with a product or system. For SEPs, delivering a high-quality UX is crucial for the product's adoption, satisfaction, and long-term success. A well-designed SEP should not only function effectively but also provide a seamless, enjoyable, and intuitive experience for the user. Key UX Elements in SEPs are: (i) usability - ease of use. The SEP should be easy to learn and operate. Users should be able to interact with the product without extensive training or technical knowledge, (ii) intuitive interface - whether it's a physical interface (eg, buttons, touchscreens) or digital (eg, app or dashboard), the interaction should be **intuitive** and require minimal effort from the user, and consistency - consistent design elements and interactions across the product help users feel comfortable and avoid confusion. Responsiveness - SEPs must provide quick and responsive feedback to user actions. Whether it's an immediate visual update on a screen, haptic feedback on a device, or a physical response from an actuator, real-time responsiveness is critical for maintaining trust and engagement. Accessibility - Inclusive Design. SEPs should be designed for a wide range of users, including those with disabilities. This includes considerations such as voice control, text-to-speech functionality, easy-to-read interfaces, and adaptability for varying user abilities. Multilingual Support. In global markets, ensuring that the interface supports multiple languages can improve the experience for non-native speakers. SEPs should offer customization options that allow users to tailor the product to their specific needs and preferences. For example, in a smart factory, users may want to adjust settings, receive notifications, or set alarms based on their role or the task at hand. User profiles. Allow users to create profiles that personalize their experience, such as saving configurations, preferences, or settings for repetitive tasks. Aesthetics and visual appeal. The visual design of SEPs should not only look attractive but also enhance usability. Clear iconography, appropriate color schemes, and a clean layout make it easier for users to interact with the product. Simplicity - avoid clutter and ensure that the design focuses on key actions and information. This is particularly important for users working in high-pressure environments like factories or hospitals where quick decision-making is crucial. SEPs often collect large amounts of data, and it's essential to present this data in a way that users can easily interpret and act upon: dashboards - use interactive dashboards to display real-time data, trends, and system status in a way that's easy for users to understand at a glance, and analytics and insights - incorporate predictive analytics to provide insights or recommendations based on historical data. For example, a smart maintenance system could suggest optimal times for equipment servicing based on usage patterns. SEPs may need to interact across different devices (eg, a mobile app, desktop dashboard, or wearable). Design the UX to ensure consistent interaction across these devices, enabling users to manage or control the SEP from different touch points. Responsive design - ensure that the interface scales properly across different devices and screen sizes, and synchronization - ensure that data and settings are synchronized across all devices, so users can access up-to-date information regardless of their location. Different industries and applications of SEPs require tailored human-centered design approaches. For example: industrial applications (eg, Smart Factories) - efficiency and speed. In high-paced environments, UX design should focus on quick access to critical information and minimal interaction time to avoid disrupting workflows. Wearables - SEPs for factory workers might involve wearable devices (eg, smart gloves or helmets) that provide hands-free control and real-time data, ensuring that workers can interact with the system without compromising safety.

5. APPLICATIONS AND CASE STUDIES

Autonomous vehicles (AVs) and mobility solutions are cutting-edge examples of SEPs that leverage a combination of advanced technologies to redefine transportation, improve safety, increase efficiency, and create more sustainable solutions for personal and commercial travel [6,28,29]. These products not only rely on smart engineering principles but also incorporate innovations in areas like AI, ML, IoT, sensors, and cloud computing to operate autonomously and efficiently. AV is a self-driving car or other vehicle capable of navigating and operating without human intervention. AVs use a variety of sensors, including lidar, radar, cameras, and ultrasonic sensors, along with advanced algorithms to perceive their environment, make decisions, and execute driving tasks. Key characteristics of AVs are: self-driving - the vehicle can drive itself by interpreting data from its sensors and making decisions using AI, connected - AVs are often equipped with connectivity features for real-time data sharing, remote monitoring, and over-the-air updates, and safe and efficient - by relying on precise sensors and advanced algorithms, AVs can reduce human error, avoid accidents, and optimize driving for fuel efficiency. Mobility solutions encompass a broad range of transportation systems that enhance the movement of people and goods. Smart mobility ecosystem integration is carried out through V2X communication layers, the analysis of which is shown in table 11.

In the context of smart engineering, these solutions often integrate autonomous vehicles, electric vehicles (EVs), ride-sharing platforms, and smart infrastructure to offer more efficient, sustainable, and user-friendly

transportation options. AVs represent a convergence of various advanced technologies, each contributing to making the vehicle smart, self-aware, and self-sufficient. The following features make AVs stand out as SEPs.

Table 11. Overview of models for smart mobility integration for SEPs

Layer	Protocol	Application
V2V	DSRC/C-V2X	Platooning coordination
V2I	LTE-V2X	Traffic signal optimization
V2N	5G NR	Fleet management
V2P	BLE/Wi-Fi	Pedestrian safety

Stamping tools , when designed and integrated as smart engineering products, can offer a lot of innovative advantages [7,30]. By incorporating sensors, automation, and connectivity, these tools can be enhanced for better performance, monitoring, and optimization. Here are some ways stamping tools can become smart: (a) sensor integration for real-time monitoring. Force sensors, monitor the pressure applied during stamping to ensure uniformity and prevent tool wear. Temperature sensors detect overheating or abnormal temperature conditions in the stamping die, reducing the risk of tool failure. Vibration sensors, measure vibrations to monitor tool alignment and detect irregularities that could lead to faults, (b) predictive maintenance, by analyzing data from sensors, machine learning algorithms can predict when maintenance is needed, preventing downtime and improving tool life. Real-time data can alert operators of potential failures, allowing for proactive rather than reactive maintenance, (c) automation and adaptability. Adjustable settings, use smart controllers to automatically adjust stamping force, speed, and other variables based on material thickness or part design, and smart dies - implement dies that can change shape or configuration automatically based on the product being stamped, allowing flexibility in production, (d) quality control - smart stamping tools can be integrated with cameras or image recognition systems to inspect the stamped part for defects immediately after it's made, and data from these inspections can be fed back into the system, enabling it to adjust parameters for optimal quality, (f) data connectivity and analysis - IoT integration, connect stamping tools to a cloud-based system to collect and analyze data over time, remote monitoring - engineers can remotely monitor the performance of stamping tools and access historical performance data for analysis and decision-making, and real-time performance tracking - integrate dashboards to show the health, performance, and output quality of the tools in real time, (g) energy efficiency - by monitoring the energy consumed during the stamping process, adjustments can be made to reduce unnecessary energy usage, contributing to cost savings and sustainability goals, (h) DT technology - a DT of the stamping tool can be created to simulate its performance, identify inefficiencies, and optimize tool designs or manufacturing processes before physical production, and (i) smart tool wear tracking - using real-time monitoring, the system can track tool wear and automatically adjust parameters to compensate for wear, thus maintaining consistent quality throughout the life of the tool. By transforming traditional stamping tools into smart engineering products, manufacturers can improve efficiency, reduce downtime, lower costs, and enhance the quality of their products.

6. CHALLENGES AND FUTURE DIRECTIONS FOR SMART ENGINEERING PRODUCTS

Today's **challenges** [1,4,30], which are set before the development and faster application of SEPs can be defined as: (a) high development costs - designing, testing, and deploying smart engineering products require substantial investment in R&D, hardware, and software development. Costly sensors, microcontrollers, and connectivity modules can increase production expenses, (b) data security and privacy concerns - smart products collect and transmit sensitive data, making them vulnerable to cyber threats. Ensuring robust encryption, authentication, and compliance with regulations like GDPR is critical, (c) integration with existing systems - legacy infrastructure may not be compatible with smart technologies. Upgrading traditional systems to support AI, IoT, and automation can be complex and expensive, (d) reliability and maintenance - smart products rely on software, sensors, and connectivity, which require regular updates and maintenance. Hardware failures or software bugs can disrupt operations and lead to downtime, (f) scalability issues - adapting smart solutions for large-scale deployment can be challenging due to variations in requirements and environments. Network bandwidth limitations and latency can impact performance in industrial applications. (g) regulatory and compliance hurdles - different regions have varying standards for smart technologies, making global deployment complex. Safety, environmental impact, and ethical considerations add layers of compliance, (h) user adoption and skill gaps - many industries face resistance to adopting smart technologies due to lack of expertise and fear of job displacement. Workforce training and upskilling are required to ensure effective implementation. On the other hand, **the future directions of the development of SEPs** [6,14,17,29] can be defined as: (a) AI-driven automation and decision-making - advanced AI and machine learning models will enhance real-time analytics, predictive maintenance, and autonomous operations, (b) edge computing for faster processing - moving computation closer to devices will reduce latency, improve efficiency, and enable real-time decision-making in smart products, (c) sustainable and energy-efficient designs - future smart engineering products will prioritize energy-efficient hardware, recyclable materials, and eco-friendly manufacturing processes, (d) blockchain for enhanced security - decentralized and tamper-proof data management can improve trust, authentication, and traceability in smart systems, (f) standardization and interoperability - industry-wide frameworks and protocols

will enable seamless integration between different smart products and platforms, (g) human-centric design and collaboration - smart products will focus on enhancing human-machine interaction, with intuitive user interfaces and augmented reality (AR) support, (h) 5G and beyond enhanced connectivity - high-speed, low-latency networks will enable real-time remote control, automation, and enhanced IoT applications, and (i) self-healing and adaptive systems - smart engineering products will incorporate self-repairing capabilities using AI, nanotechnology, and bio-inspired materials. A summary of the future directions of the development of SEPs is shown in table 12.

Table 12. Overview of future trends in the development of SEPs

Domain	Emerging Trends
Cybersecurity	Autonomous AI defense, quantum-resistant crypto
Interoperability	AI-driven self-configuring networks, semantic IoT
Sustainability	Solid-state batteries, ambient backscatter tech
Ethics	Global AI ethics treaties, ethics-by-design

7. CONCLUSION

SEPs and smart services are interdependent components of modern technological ecosystems, driving innovation in industries such as manufacturing, transportation, energy, healthcare, etc. Research into AI, cybersecurity, sustainability, interoperability and autonomous systems will drive the next generation of intelligent, ethical and energy-efficient engineering products. As industries move towards Industry 5.0, collaboration between academia, industry and policymakers will be essential for responsible and effective innovation in this area. The next frontier of SEPs lies at the intersection of AI, sustainability and human-centered design. Prioritizing research in these areas can unlock transformative applications that will address new societal challenges. The next frontier for smart engineering lies at the intersection of AI, sustainability, and human-centric design. Prioritizing research in these areas can unlock transformative applications while addressing pressing societal challenges. Early-stage work in biohybrid systems, self-healing AI, and quantum IoT appears particularly promising for groundbreaking advances for the next generation of SEPs. And ultimately - the question is not whether smart technology will advance, but whether it will advance with humanity's best interests at heart.

REFERENCES

[1] Tetsuo Tomiyama, Eric Lutters, Rainer Stark, Michael Abramovici, Development capabilities for smart products, CIRP Annals, Volume 68, Issue 2, 2019, Pages 727-750, https://doi.org/10.1016/j.cirp.2019.05.010.

[2] Abramovici, M. (2015). Smart Products. In: The International Academy for Production Engineering, Laperrière, L., Reinhart, G. (eds) CIRP Encyclopedia of Production Engineering. Springer, Berlin, Heidelberg. https://doi.org/10.1007/978-3-642-35950-7_16785-1 .

[3] Anderl, Reiner & Picard, André & Albrecht, Katharina. (2013). Smart Engineering for Smart Products. 10.1007/978-3-642-30817-8_1.

[4] Stefan Raff , Daniel Wentzel , Nikolaus Obwegeser , Smart Products: Conceptual Review, Synthesis, and Research Directions, Journal of Product Innovation Management: Volume 37, Issue 5 , Pages: 373-471 , September 2020, https://doi.org/10.1111/jpim.12544

[5] Pereira Pessoa MV. Smart design engineering: leveraging product design and development to exploit the benefits from the 4th industrial revolution. Design Science. 2020; 6: e25. 10.1017/dsj.2020.24.

[6] Michael Abramovici, Rainer Stark, editors, Smart Product Engineering, Proceedings of the 23rd CIRP Design Conference, Bochum, Germany, March 11th - 13th, 2013, Springer Berlin, Heidelberg, https://doi.org/10.1007/978-3-642-30817-8 .

[7] Sreedhara CJ, Industrie 4.0 - Advanced Engineering of Smart Products and Smart Production, International Journal of Science and Research (IJSR), Volume 9, Issue 3, March 2020, 10.21275/SR20309125010.

[8] Pai Zheng, Zuoxu Wang, Chun-Hsien Chen, Li Pheng Khoo, A survey of smart product-service systems: Key aspects, challenges and future perspectives, Advanced Engineering Informatics, Volume 42, 2019, 100973, ISSN 1474-0346, https://doi.org/10.1016/j.aei.2019.100973 .

[9] Anderl, Reiner & Picard, André & Albrecht, Katharina. (2013). Smart Engineering for Smart Products. 10.1007/978-3-642-30817-8_1.

[10] Zheng, Pai & Liu, Yang & Tao, Fei & Wang, Zuoxu & Chen, Chun-Hsien. (2019). Smart Product-Service Systems Solution Design via Hybrid Crowd Sensing Approach. IEEE Access. 10.1109/ACCESS.2019.2939828.

[11] Michael E. Porter and James E. Heppelmann, How Smart, Connected Products Are Transforming Competition, Harvard Business Review November 2014. https://eclass.aegean.gr/modules/document/file.php/TNEY202/HBR_How-Smart-Connected-Products-Are-Transforming-Competition%20copy.pdf

[12] https://softec.ris.uni-due.de/en/research/research-area-smart-products/design-and-development-of-smart-products/.

[13] Forte, Sven & Göbel, Jens & Dickopf, Thomas. (2021). System of systems lifecycle engineering approach integrating smart product and service ecosystems. Proceedings of the Design Society. 1. 2911-2920. 10.1017/pds.2021.552.

[14] Gubbi, Jayavardhana & Buyya, Rajkumar & Marusic, Slaven & Palaniswami, Marimuthu. (2012). Internet of Things (IoT): A Vision, Architectural Elements, and Future, Directions. Future Generation Computer Systems. 29. 10.1016/j.future.2013.01.010.

[15] Viola, Jairo & Chen, YangQuan. (2020). Digital Twin Enabled Smart Control Engineering as an Industrial AI: A New Framework and Case Study. 1-6. 10.1109/IAI50351.2020.9262203.

[16] https://hyperthings.in/product-engineering/

[17] Horváth, László. (2019). Smart Engineering Modeling for Smart Industrial Products. Acta Polytechnica Hungarica. 16. 11-30. 10.12700/APH.16.10.2019.10.2.

[18] Regenwetter, Lyle & Nobari, Amin & Ahmed, Faez. (2021). Deep Generative Models in Engineering Design: A Review. 10.48550/arXiv.2110.10863.

[19] Schiller, Barbara ; Brogt, Tobias ; Schuler, J. Peter M. ; Strobel, Gero : Can Self-Tracking Solutions Help with Understanding Quality of Smart, Connected Products?. In: Ais (Ed.): Proceedings of the 26th European Conference on Information Systems (ECIS). Portsmouth 2018.

[20] Russell S., Norvig, P., Artificial intelligence - a modern approach, Prentice Hall, 2020. https://people.engr.tamu.edu/guni/csce625/slides/AI.pdf

[21] Qinglin Qi, Fei Tao, Tianliang Hu, Nabil Anwer, Ang Liu, Yongli Wei, Lihui Wang, AYC Nee, Enabling technologies and tools for digital twin, Journal of Manufacturing Systems, Volume 58, Part B, 2021, Pages 3-21, https://doi.org/10.1016/j.jmsy.2019.10.001.

[22] Brogt, Tobias ; Eicker, Stefan : Einsatz von Servicesystemen zur Utsetzung von Innovationen im Kontext der Digitalisierung. In: Kollmann, Tobias (Ed.): Handbuch Digitale Wirtschaft. Springer Gabler, Wiesbaden 2019. 10.1007/978-3-658-17345-6_82-1 .

[23] Pereira P., Jauregui, M., Becker, M. Smart design engineering: a literature review of the impact of the 4th industrial revolution on product design and development. Res Eng Design 31 , 175–195 (2020). https://doi.org/10.1007/s00163-020-00330.

[24] Yin, Yuanyuan & Qin, Sheng-feng. (2019). A smart performance measurement approach for collaborative design in Industry 4.0. Advances in Mechanical Engineering. 11. 10.1177/1687814018822570.

[25] Norman Don, *The Design of Everyday Things,* Published by Basic Books, 2013. https://dl.icdst.org/pdfs/files4/4bb8d08a9b309df7d86e62ec4056ceef.pdf .

[26] Circular by design - Products in the circular economy, European Environment Agency, Brussels, 2017, 10.2800/860754.

[27] Holler, M., Dremel, C., van Giffen, B., Vogt, H. (2022). From Smart Connected Products to Systems of Systems: Case Studies and Archetypes. In: Canciglieri Junior, O., Noël, F., Rivest, L., Bouras, A. (eds) Product Lifecycle Management. Green and Blue Technologies to Support Smart and Sustainable Organizations. PLM 2021. IFIP Advances in Information and Communication Technology, vol 640. Springer, Cham. https://doi.org/10.1007/978-3-030-94399-8_1

[28] Arioli, V., Ruggeri, G., Sala, R., Pirola, F., & Pezzotta, G. (2023). A Methodology for the Design and Engineering of Smart Product Service Systems: An Application in the Manufacturing Sector. *Sustainability* , *15* (1), 64. https://doi.org/10.3390/su15010064 .

[29] Kuznietsov, Anton & Gyevnar, Balint & Wang, Cheng & Peters, Steven & Albrecht, Stefano. (2024). Explainable AI for Safe and Trustworthy Autonomous Driving: A Systematic Review. 10.48550/arXiv.2402.10086.

[30] https://www.uni-due.de/iw/en/research/psp3.php

11th International Scientific Conference
IRMES 2025
Research and Development of
Mechanical Elements and Systems
June 19 – 21, 2025; Vrnjačka Banja, Serbia

Original scientific paper DOI: 10.46793/IRMES25.065M

SELECTING OF SOLUTIONS IN DEVELOPING THE BOBCAT E62 EXCAVATOR CONTROL HANDLE

Biljana MARKOVIĆ[1]
Vidak ČAJEVIĆ[2]
Aleksija ĐURIĆ[3]
Srđan SAMARDZIĆ[4]

[1]Biljana Markovic, East Sarajevo, Bosnia and Herzegovina, 71123; biljana.markovic@ues.rs.ba ;
ORCID iD: 0000-0001-8915-4791
[2]Vidak Čajević, Sokolac, Bosnia and Herzegovina, V&D Čajević d.o.o. Sokolac, cajevic.v@gmail.com
[3]Aleksija Djuric, East Sarajevo, Bosnia and Herzegovina, 71123; aleksija.djuric@ues.rs.ba ;
ORCID iD: 0000-0002-0251-6364
[4]Srdjan Samardzic, East Sarajevo, Bosnia and Herzegovina, 71123; srdjan.samardzic@ues.rs.ba ;
ORCID iD: 0009-0003-4096-7523

***ABSTRACT**: The paper presents the method of using the solution selection method in developing a new concept of the BOBCAT E62 excavator control handle, with the aim of implementing a lightweight design. The lightweight design concept is used in various industries, including the design, i.e. construction of construction machinery, where the use of modern materials and design methods can lead to an optimal solution, while maintaining load-bearing capacity and functionality. The modified handle design solution aims to reduce weight, without major changes to other parts of the assembly of which it is a component. Two methods were used to assess the concept selection, as an integral part of the product development process, i.e. the solution selection phase. The selected concept solution should contribute to improvements in terms of durability, compactness and reduced energy consumption.*

***Keywords:** product development, lightweight design, concept selection, solution evaluation methods*

1. INTRODUCTION

The concept of lightweight design, with the aim of using materials and designing parts with reduced weight has become a key concept in the integral development of almost all industries, from the automotive to the aerospace industry. In this field, engineers are faced with the challenge of achieving the optimum between reducing weight and preserving the strength, safety and long-term performance of the system. Why is this important? In modern manufacturing and engineering, weight is a key factor in optimizing the performance of mechanical systems. In the global world and the challenges we face, this trend is becoming increasingly important due to the reduction of energy consumption, increasing efficiency and preserving resources [1].

As a fundamental influencing factor in achieving the aforementioned goal, the choice of materials is imposed, and this includes materials with low density and high strength. Materials such as aluminum, titanium, magnesium and carbon fiber reinforced composites (CFRP) are widely used due to their exceptional mechanical properties, including high strength-to-weight ratio, corrosion resistance and the ability to withstand significant stresses, while reducing the overall weight of the product [2].

In contemporary literature, the aircraft and automotive industries are mentioned as two branches of industry in which the concept of lightweight design is most prevalent. However, the mining and construction machinery sector has not bypassed this method of design. Engineers in this field have realized that by reducing the weight of parts and simplifying the design solution, they can reduce the possibility of product failure or damage, or achieve simpler maintenance. A major challenge in the field of mining and construction machinery is the occurrence of vibrations that occur during product exploitation. For this reason, significant material resources and intellectual capacities are sometimes used to modify some seemingly not so important element, thereby saving weight. One such example was given by the company LIEBHERR on the latest generation of excavators, when they changed the design of the keel of the part located at the junction of the first and second arms (Figure 1). With this move, they saved up to 60 kg, depending on the excavator model, while at the same time increasing the load capacity. As LIEBHERR is also known as a leader in innovation in the excavator segment, it was the first to use covers made of resin and glass fiber reinforced composite materials. This has also encouraged competitors to find innovative solutions, breaking the long-standing practice of using the same design solution for decades. Companies around the

world are now investing in new technologies that not only improve performance, but also reduce the negative impact on the environment, thus enabling sustainable development in this industry [3].

Analogous to the aforementioned practical examples, this paper explores the possibility of applying methods for developing a new solution for the control handle of the BOBCAT E62 backhoe loader, with the aim of reducing its weight by using modern materials and construction methods, while preserving the load-bearing capacity, functionality and extending the service life of the entire assembly.

Fig 1. Left - previous solution of the connection of the first and second hand, right - the new solution [3]

2. PROBLEM CLARIFICATION PHASE

This paper considers the control handles mounted on a mini excavator of the "BOBCAT" brand, model "E62". The purpose of the control handles is to, by moving the handle forward or backward, move one of the tracks in the direction in which the control handle is moved, thus giving the operator complete control over the movement of the excavator, allowing him to move precisely in all directions. This control handles come in pairs, one for each track, which allows for synchronized control. This system allows the operator to easily and efficiently control the excavator, even in challenging conditions or in confined spaces.

During the exploitation of this type of construction machine, operators can achieve up to 10,000 operating hours. During this period, the control handles are activated countless times.

The problem that occurs during exploitation is that, due to the length of the lever and extreme operating conditions, abrasion occurs at the connection with the pedal and the hydraulic valve to which the handle is attached with screws. Over time, due to continuous friction and load, excessive wear occurs between the parts (Figure 2), which causes the connection to become loose. Due to the resulting play, the connection becomes unstable, which can lead to serious problems in operation. As a result, the precision when using the control handles is significantly compromised, which can have major consequences, including possible accidents or damage to the machine.

This problem can cause not only a decrease in work efficiency and productivity, but also an increase in the risk of accidents, which makes regular maintenance and replacement of damaged parts necessary to ensure operator safety and long-term reliability of the machine.

Fig. 2. Consequences of exploitation

The current control handles (Figure 3.) are made of a hollow profile with a round cross-section of 17 mm diameter and 2 mm wall thickness (position no. 2). The construction material is structural steel S275JR. At a distance from the lowest point, the profile is bent at an angle of 25°, at a height of 125 mm (II). At the top there is a full square profile of dimensions 11 mm x 11 mm (Section A-A) and height 40 mm, on which there is an opening with an M6 thread, at a height of 20 mm, to which a handle made of plastic is attached with an M6 screw (position no.1). This part is connected to the other part by welding (Section A-A). At the bottom there is a square full profile (Section B-B) (position no. 3.), dimensions 30 mm x 30 mm and height 55 mm, on which there are two openings with M10 thread at a height of 13.5 mm and 41.5 mm, thread depth 15 mm, through which the attachment for the rest of the assembly (2) is made. Also, this part is also attached to the other part by welding. The weight of the existing variant is about 890 g.

In order to solve the aforementioned problem, a redesign process was initiated, as a shortened part development process, using lightweight materials, which will extend the life of this assembly so that it is consistent with the life of the entire excavator.

In addition, the goal is to achieve improvements in terms of their shape and dimensions, without negatively affecting other parts of the assembly.

Therefore, using known methods of the product development process, it is necessary to achieve greater efficiency, reduce wear and improve precision in operation, which will significantly increase the longevity and safety of the entire system.

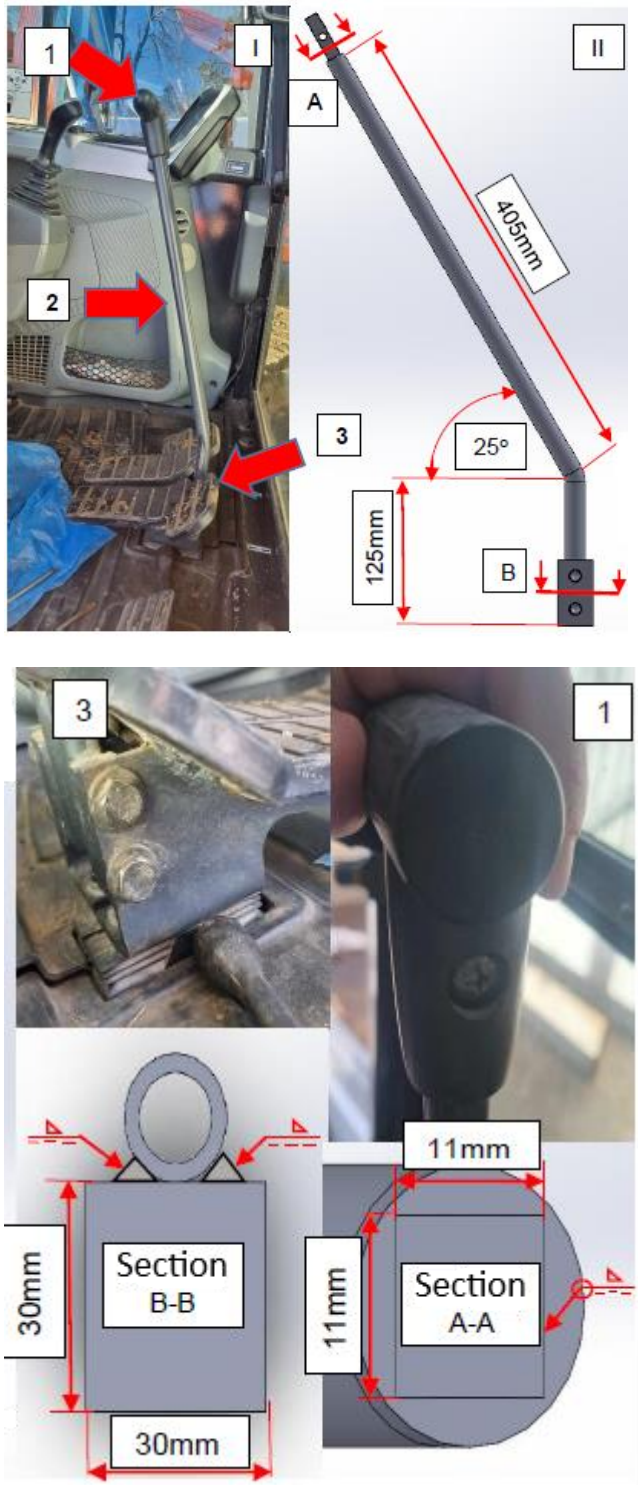

Fig. 3. Current construction solution

3. ELABORATION OF CONCEPTUAL VARIANTAS – NEXT PHASE

The proposal and development of conceptual variants was made using existing knowledge, experience, and professional literature.

3.1. Variant 1

A representation of the first variant is given in Figure 4. Here a rectangular hollow profile is used. This profile is not of a standard shape. The profile is made of anodized aluminum2. The external dimensions of the profile are 20 mm x 20 mm (position no. 1). Due to the specific shape of the profile, it is not necessary to weld other profiles for mounting the handrail and mounting the control handle to the rest of the assembly. However, it is necessary to redesign the plastic handles on the top and adapt them to the system defined by the manufacturer. The parts are attached to this profile by placing pins in the hole in the profile. There is a threaded hole in the pin (position no. 2). The advantage of this system is the ability to place the part at any height, as well as easy movement. The disadvantages are the need to adapt all parts to this system, as well as the inability to bend the profile (position no. 3). This variant weighs 410g.

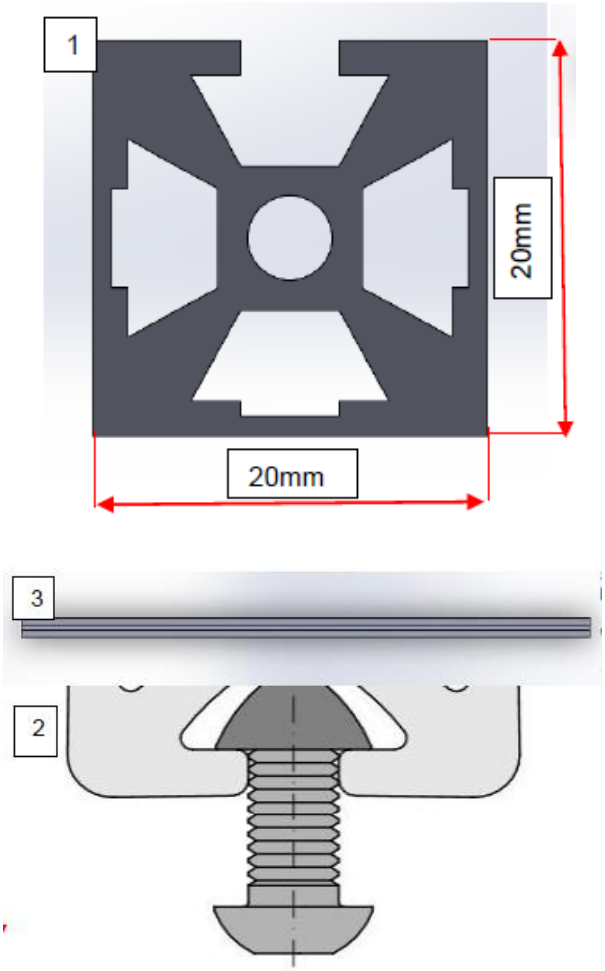

Fig .4. Variant solution 1 [5]

3.2. Variant 2

The presentation of solution 2 is given in Figure 5. In this construction solution, no significant changes were made to the shape of the part, but the emphasis was placed on the use of a combination of two light materials. The control handle is made of hollow aluminum profile (Al-6061) with a round cross-section of 17 mm diameter and 2 mm wall thickness (1). At the top there is a square

profile with a full section, with the same purpose as the original version, and the same dimensions. A similar case is on the lower side, where there is a square profile of full section, with small changes compared to the original version (Section A-A). The changes refer to the dimensions of the profile by which the handle is attached to the rest of the assembly. Instead of butt-welding the elements, here first a recess is cut on the rectangular profile into which the round-section rod fits. This was done in order to make the weld line as long as possible, and to distribute the load evenly over a larger area, so that bending does not occur. The interior of the hollow profile with a round section is filled with polyester resin and fiberglass fibers (light materials), which should provide the entire structure with additional resistance to twisting, bending and twisting. The variant has a weight of 450 g.

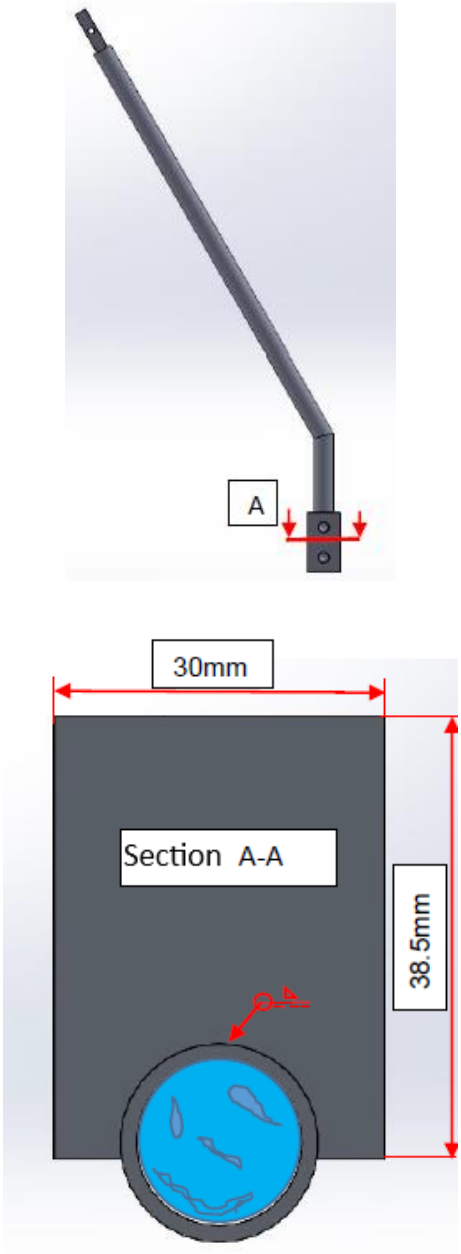

Fig. 5. Variant solution 2

3.3. Variant 3

A representation of variant 3 is given in Figure 6. This solution was made using a 3D printer, and the shape does not differ from the original variant. However, in this case there is no welding. All profiles are filled with filler with a filling of 70%. The filler used is PA6 CF, which contains carbon fibers for reinforcement. This material provides greater strength and lower weight, which further contributes to improving the mechanical properties of the final product. Also, the handle is made as a single part together with the control handle (position 1). In addition, the use of 3D printing in this solution allows for greater precision in manufacturing and faster production, while at the same time reducing the need for complex assemblies and welding. The 3D printing process is today very often used in rapid prototyping, in order to shorten product development time, it allows greater freedom in design, so manufacturers can easily adjust the dimensions or shape according to user needs. This variant has a weight of 360g, which represents a significant advantage compared to the previous variants, but the disadvantage in terms of carrying capacity cannot be ignored, which is significantly lower compared to the other variant

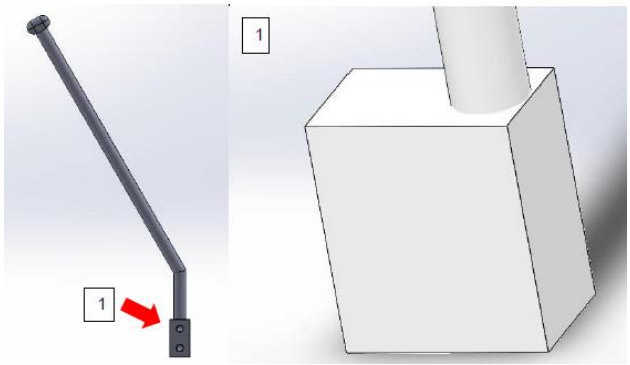

Fig. 6. Variant solution 3

After 3 variant solutions have been developed and presented, it is necessary to choose the optimal variant.

4. METHODES FOR CONCEPTUAL SOLUTIONS SELECTION (THREE VARIANTS)

In the product development process, before making a final decision, which implies the use of decision-making methods and techniques, it is necessary to use different methods for selecting solutions. Evaluation methods are applied throughout the entire process of creating a new or innovated product, and are of great importance in the evaluation of new conceptual solutions, the so-called "design is making decisions“[6]. Their task is to enable quick and correct decision-making, especially in conditions of intense market circumstances, when quick decision-making is necessary. A prerequisite for the successful evaluation of alternative solutions is that the degree of their concretization, expressed through the available information about the product, is aimed at

reducing complexity. Therefore, one should concentrate on the decisive criteria by correctly selecting the parameters that need to be evaluated. As is known from the literature, there are simple and complex selection methods, often used in practice, which are used depending on the type of problem and the need for a quick selection of solutions. In this case, two methods were used, namely techno-economic analysis and weighted analysis.

4.1. Techno-economic analysis

Technical-economic analysis is a widely used and well-known method of evaluating solutions in various industrial sectors during the product development process [6]. This method considers and evaluates the most important economic and technical aspects for a specific product. The method is repeatable and does not depend on the individual using it. The greatest attention should be paid to the selection of parameters to be evaluated, through both of the aforementioned aspects.

These economic and technical parameters need to be displayed in the X, Y coordinate system. A line is drawn from zero at an angle of 45°, which represents a perfect balance between technical and economic criteria. Both axes have a maximum value of 1. The optimal solution is the one that is farthest from zero and closest to the line at an angle. As mentioned previously, the most important step in the method is the correct selection of the parameters for the criterion. The following parameters were chosen:

Economic: the price of the base material, the price of additional processing and compatibility with the rest of the assembly;

Technical: mass, bending resistance and resistance to external influences.

Economical criteria:

The price of the base material in the original version, on 12.01.2025, is 7.75 KM [4] per meter long for a 17 mm diameter pipe. The price of variant 1 is 15.25 KM / m [5], variant 2 is 7.95 KM/m [4], and for the filler material about 0.90 KM, which is a total of 8.85 KM. For variant 3, the price of the filament (PA6 CF) with a filling of 70% is about 11.16 KM.

When considering additional processing in the original variant, there is welding. For steel profiles, welding is used, the price of which per meter is from 15.00 KM to 25.00 KM. In variant 1, there is no additional processing, because these profiles can be purchased in the required dimensions and with the given characteristics. Variant 2, it is made of aluminum, which also uses MIG welding, but with other gases, and due to the complexity of the process itself, the price of welding per meter is slightly higher, from 10.00 KM to 30.00 KM. For the Variant 3 is not necessary to perform additional processing in the form of welding, but additional surface treatment after printing should be taken into account.

The third criterion is compatibility with other parts of the assembly. The reason why this item is important from an economic point of view is that the more parts fit into the existing assembly, the fewer engineer hours are needed to adapt the existing parts to the new control lever. Therefore, it is necessary to consider the fixed price of the entire assembly, so that as many existing parts as possible are used.

All variants have the same dimensions and attachment points as the original variant, except variant 1 which has a square cross-section instead of a round one. The connection points with the rest of the assembly are also a problem, as different solutions are needed to match the redesigned profile section.

Technical criteria:

In terms of mass, the original variant weighs about 0.89 kg. The first variant weighs 0.41 kg. The second variant weighs 0.31 kg without filler, while the filler weighs about 0.14 kg, which is a total of 0.45 kg. The third variant would weigh 0.36 kg.

In order to set the same conditions for everyone, the calculation was made in such a way that the force arm was determined so that the force acts on the middle of a 1m long rod. The force that needs to be applied to the profile in order to cause permanent deformation is sought. For the original variant, a force of 445.5 N is required, for variant 1, a force of 500 N is required [5], a force of 415 N is required for variant 2, while a force of 157 N is required for variant 3, in order to avoid permanent deformation.

The third point takes into account resistance to external influences. Since this type of machine often operates in difficult operating conditions, it is necessary for the part to be resistant to various weather conditions. For example, these control handles often come into contact with water. Therefore, for the original version, the steel from which the part is made needs to be adequately protected against corrosion. This is easy on the outside, while the inside is unprotected, which provides fertile ground for corrosion. The other three variants have similar corrosion resistance, because they are made of stainless materials. The parts are often in contact with lubricants and oils, which causes dust to stick to that part. The original version has an opening on the bottom through which various impurities can enter, just like variant 1, while variants 2 and 3 do not have this problem, since they have a full cross-section. Tables 1 and table 2 show the scoring method for the selected parameters, within the framework of economic and technical criteria.

Table 1. Economical criteria

Criteria/ Variant	O V	V 1	V 2	V3	Max Scor
Price of basic material	4	2	3.5	2.5	4
Price of additional processing	2.5	4	2.5	2	4
Compatibility with the rest of the assembly	4	2.5	4	4	4
Total points	10.5	8.5	10	8.5	12
∑ points/ Max points	0.87	0.71	0.83	0.71	1

Table 2. Technical criteria

Criteria/Variant	OV	V1	V 2	V3	Max Scor
Mass	2	3	3.5	4	4
Bending resistance	3.5	4	3	1	4
Resistance to external influence	2	2.5	4	3.5	4
Total points	7.5	9.5	10.5	8.5	12
∑ points/Max p.	0.62	0.79	0.87	0.71	1

Fig. 7 shows the method of entering the numerical values of the selected parameters, within the criteria of the techno-economic analysis. It is clear that variant 2 is the optimal choice of the three versions offered.

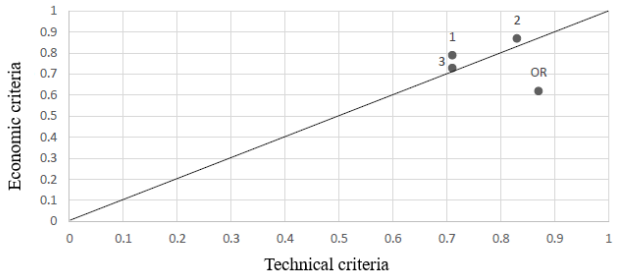

Fig 7. Variant ratings

4.2. Value analysis

Value analysis is a type of differential evaluation, in the form of a tabular evaluation for representing relations, networks, actions and causal dependencies. The method allows for a hierarchical structure of evaluation criteria, linked to their value. It is particularly suitable for complex systems with a large number of evaluation criteria.

In this case, value analysis method has been used in the selection of variant solutions, which implies that each selected criterion is assigned weight values, where the sum of these values must be equal to 1. After that, each variant is assigned points ranging from 5 to 10. After distributing the points, they are multiplied by the coefficient assigned to each criterion. Then, all the obtained values are added up for each variant separately. The maximum value that a variant can receive is 10. Finally, a ranking is performed. For this method, four parameters were chosen as dominant for the selection of solutions, namely: mass, bending resistance, material price and compatibility.

Table 3. Value analysis

Ranking and evaluation of alternative solutions								
Criteria	Mass		Bending resistance		The price of material		Compatibility	
∑wi=1	0.4		0,3		0.2		0.1	
OR	0.89kg		445		7.75		Excellent	
V1	0.41kg		500		15.25		Bad	
V2	0.45kg		415		8.85		Excellent	
V3	0.36kg		157		11.16		Excellent	
	Pi	Pi· wi	Pi	Pi· wi	Pi	Pi· wi	Pi	Pi· wi
OR	5	2	9	2.7	10	2	10	1
V1	9	3.6	10	3	5	1	5	0.5
V2	8	3.2	8	2.4	9	1.8	10	1
V3	10	4	5	1.5	6	1.2	10	1
	$\sum_{i=1}^{n}(P_i) \cdot (w_i)$							Rang
OR	7.7							4
V1	8.1							2
V2	8.4							1
V3	7.7							3

From Table 3 it is clearly visible that Variant 2 in total won the highest number of points, according to the selected parameters that were evaluated, and it is imposed as the optimal one.

5. CONCLUSION

The paper presents the product development process, using the example of redesigning the control handle for the BOBCAT E62 mini excavator. Existing knowledge, experience and professional literature for the given field were used. Dominantly, the construction solutions are based on the design for lightweight structures, where an adequate selection of lightweight materials is imposed as primary. Also, the 3D printing process was used, as one of the modern processes often used today in rapid prototyping. Three construction solutions were proposed, through three different variants, and then the choice of solutions was presented. In the solution selection phase, two well-known selection methods were used, namely techno-economic analysis and value analysis. Both methods showed that variant 2 is the optimal choice, from the point of view of the selected parameters that were evaluated. The goal of the handlebar redesign, which was to reduce the weight of the part, was successfully met. The weight of the part was reduced by almost 50%, which represents a significant success in realizing the initially detected problem, which was solved through the product development process.

REFERENCES

[1] Müller, H.: Materials for Lightweight Construction, 2017.
[2] William, D.: Callister Materials Science and Engineering: An Introduction, 2018.
[3] https://www.liebherr.com/deint/erdbewegung/erdbewegung-5376941, Accessed on: 2025-02-02
[4] https://www.hornbach.de/c/eisenwaren/profile-bleche/rohre/, Accessed on 2025-01-12
[5] https://www.item24.com/de-de/, Accessed on: 2024-24-12
[6] Miltenović V., Razvoj proizvoda-strategije, metode, primjena, University in Niš, Mechanical faculty, 2003.
[7] Miltenović, A., Marković, B., Banić, M.: Inovacioni menadžment i obrazovanje u razvoju proizvoda, University in Niš, Mechanical faculty, 2013.
[8] Pérez-Cardona, J.,Deng. S.,, Sutherlend, J.: Optimization of a parametric product design using techno-economic assessment and environmental characteristics with application to an electric traction motor, Elsevier, Resources, Conservation, Recycling, 2024.

11th International Scientific Conference
IRMES 2025
Research and Development of
Mechanical Elements and Systems
June 19 – 21, 2025; Vrnjačka Banja, Serbia

Original scientific paper DOI: 10.46793/IRMES25.071S

APPLICATION OF FIXTURES PRODUCED WITH FDM TECHNOLOGY IN THE ADHESIVE BONDING OF PARTS IN THE RAILROAD INDUSTRY

Srdjan SAMARDZIC[1]
Damjan KLOBCAR[2]
Aleksija DJURIC[3]
Biljana MARKOVIC[4]

[1]Srdjan Samardzic, East Sarajevo, Bosnia and Herzegovina, 71123; srdjan.samardzic@ues.rs.ba ; ORCID iD: 0009-0003-4096-7523
[2]Damjan Klobcar, Ljubljana, Slovenia, 1000; damjan.klobcar@fs.uni-lj.si ; ORCID iD: 0000-0002-6130-0328
[3]Aleksija Djuric, East Sarajevo, Bosnia and Herzegovina, 71123; aleksija.djuric@ues.rs.ba ; ORCID iD: 0000-0002-0251-6364
[4]Biljana Markovic, East Sarajevo, Bosnia and Herzegovina, 71123; biljana.markovic@ues.rs.ba ; ORCID iD: 0000-0001-8915-4791

Abstract: *Additive manufacturing enables the production of parts with complex geometries that would be difficult or impossible to produce with conventional manufacturing technologies - and with minimal waste. A more massive use of additive technologies makes it possible to shorten supply chains and reduce the need to store parts.*
Fixtures are essential production aids that position, hold and support workpieces, ensuring positioning accuracy, repeatability and operator safety during assembly and bonding. This paper presents how the Fused Deposition Modeling (FDM) process can provide such fixtures for the adhesive bonding of metal parts in rail vehicle composite structures. By adapting geometry, surface properties and ergonomics to the bonding task at hand, FDM fixtures improve alignment accuracy and simplify handling.

Keywords: *FDM; fixtures; adhesive bonding; railroad industry.*

1. INTRODUCTION

The railroad industry is experiencing a transition to lightweight composite vehicle structures [1,2] joined with high performance structural adhesives [2]. The increasing use of composites underlines their crucial role in modern engineering practice and the continuous pursuit of innovative design solutions [3,4]. Example of composite tram's cabin is presented at Figure 1.

Fig.1. Tram's cabin preparing for transport after production

Adhesive bonding represents a challenging and rapidly evolving area of research that has already gained significant attention from industry [5-7], and adhesive-bonded joints have become an excellent alternative to conventional joining methods [8]. The expansion of adhesive bonding in industry has been closely associated with the broader application of composite materials and the increasing demand for joining of dissimilar materials [9].
Additive manufacturing enables the production of parts with complex geometries that would be difficult or impossible to produce with conventional manufacturing technologies - and with minimal waste [10,11]. A more massive use of additive technologies makes it possible to shorten supply chains and reduce the need to store parts [11].
Fixtures play a critical role in manufacturing: they accurately position, support and secure the parts to be assembled, and this function can account for up to 29% of the total capital cost of a project [12].
Beyond their basic purpose, fixtures offer a variety of benefits, including the following [13]:

- Increased production: they reduce set-up times and streamline workflows, increasing overall production rates.

- Dimensional accuracy: Accurate control of part location minimizes variation and ensures consistent product quality.
- Lower costs: Faster cycles, fewer rejects and longer tool life reduce manufacturing costs.
- Reliable interchangeability: Precise, repeatable positioning guarantees that the parts fit together exactly in subsequent assemblies.
- Less testing: Consistent accuracy reduces the need for extensive in-process testing and quality control work.
- Reduced skill requirements: Even semi-skilled operators can safely operate the machines, reducing labor costs while maintaining quality.

Research [14] give experimental investigation on the effect of adhesive distribution on strength of bonded joints. High quality bonded joints require the use of equipment (fixture) that is essential for proper curing and uniform thickness. Improper adhesive application and fastening (method of fixturing) can cause irregularities in the distribution of the adhesive along the overlap, which can affect the strength of the joint. This is especially critical for aerospace components, as replacing parts can be costly and time consuming.

Research [15] presents design of hybrid welding jigs with additive manufactured (AM) functional elements for pre-series automotive body shops. In order to select the most suitable AM material, the AM materials with the highest cost-specific stiffness are analysed. The tests prove that the AM elements are stiff enough to withstand the process forces and securely fix the positions of the welded parts.

Günther Schuh et al [16] highlight high potential of Topology optimisation (TO) and Laser Powder Bed Fusion (LPBF) for the manufacturing of welding jigs used in automotive body shops. The results confirm that components optimized by Topology Optimization (TO) and manufactured with Laser Powder Bed Fusion (LPBF) have better physical and structural properties compared to the original designs. These elements not only achieve a significant reduction in volume and mass - between approximately 30% and over 65% - but also show improved performance under mechanical loading. These results highlight the considerable potential of metal additive manufacturing (AM) technologies, especially in combination with TO, for lightweight design in applications exposed to high loads.

Previous studies have clearly shown the importance of fixtures, as they can lead to a significant reduction in production costs. In addition, the use of fixtures leads to an increase in productivity, interchangeability and a reduction in the necessary quality controls. High quality adhesive joints depend largely on fixtures that ensure positioning of the parts, proper distribution and curing of the adhesive and prevent the occurrence of irregularities.

Additive manufacturing of fixtures has a wide range of applications, mainly due to the proven mechanical properties of the materials used and the possibility of reducing the weight of the fixture itself. Lightweight fixtures are much easier to handle in production, which confirms the perspective of using additive technologies in the production of fixtures.

This paper presents the application of fixtures produced with FDM technology in the adhesive bonding of parts in the railroad industry.

2. DESIGN OF FIXTURES PRODUCED BY FDM FOR ADHESIVE BONDING

At the outset, it is important to point out that a certain amount of information and photos are censored due to data protection obligations and to protect end customers.

Knowledge of the technologies used to manufacture composite structures, their basic phases and limitations is crucial for the design of a fixture for positioning metal parts when bonding them to composite structures. Some of the widely used manufacturing technologies are: open molding, closed molding, infusion (Figure 2), etc. Technologies for the production of composite parts enable the production of not only lightweight but also geometrically complex objects, especially through the use of molds. The molds are elements that are obtained directly from the 3D model and represent its negative. After cleaning, the surface of the mold is coated with gelcoat. The main purpose of this surface coating is to ensure a smooth and shiny surface and protection against UV radiation and water, but also to make the finished product easier to separate from the mold after curing. In the next phase, layers of fiber reinforcements are laid and the resin is applied.

Fig.2. Appearance of the composite after the infusion process

After curing and removal from the mold, the surface of the composite part on the side of the mold is of better quality and serves as a reference for positioning.

The repeatable positioning and alignment of a metal workpiece is achieved by interlocking degrees of freedom (DOF). Rigid bodies generally have six degrees of freedom in space, namely three translational degrees of freedom along the axes of the cartographic coordinate system and three rotational degrees of freedom around the corresponding axes.

The Figure 3 represent part of technical drawing that define adhesive bonding of metal plates (positions 2 and 3) to composite cover (position 1). Visible side (reference) for positioning is also indicated. The starting point for the design of fixtures is the analysis of the visible (reference) surfaces as well as the analysis of the degrees of freedom that need to be locked. By attaching a

metal plate 3 to the back of the composite (Figure 4), one translation (along the W axis) and two rotations (around the U and V axes) were locked. It is necessary to lock three more degrees of freedom, two translations (along the U and V-axis) and one rotation (around the W-axis).

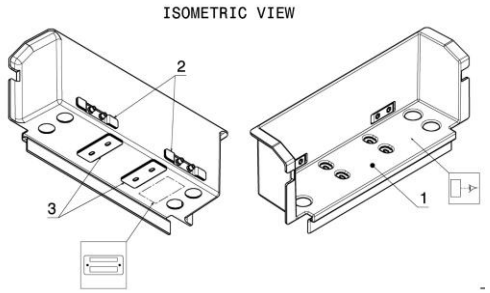

Fig.3. Part of technical drawing

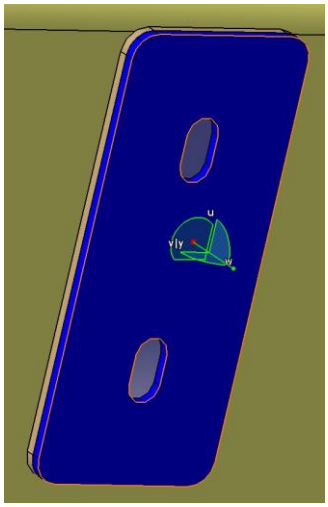

Fig.4. Metal plate attached to the back side of composite part

Figure 5 shows the final appearance of the fixture with the marked features. Feature 1 of the slot-shaped form is sufficient to lock all three required degrees of freedom. Features 2 of the cylindrical shape serve to prevent the rotation of the fixture itself around the W-axis. Surface 3 is the contact surface between the device and the composite.

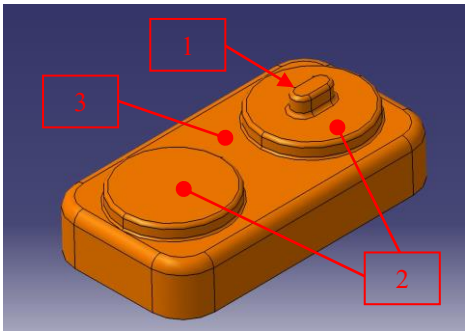

Fig.5. Final appearance of the fixture

The following example (positioning of plate 2) shows a combination of additively manufactured fixture with standard elements (bolts). Two standard bolts are used for the positioning of plate 3, which are connected to threaded rivets attached to the plate. The reference contact surfaces of the fixture are marked in blue, while the axes of the through-holes are shown in white (Figure 6).

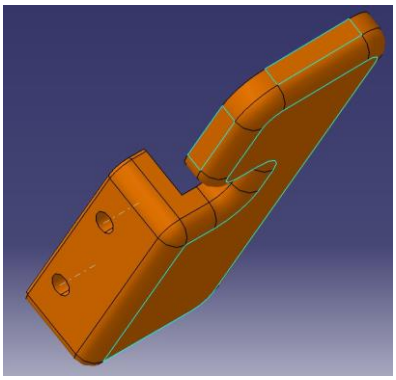

Fig.6. Fixture for positioning plate 2

The final appearance of the fixture with bolts is shown in Figure 7.

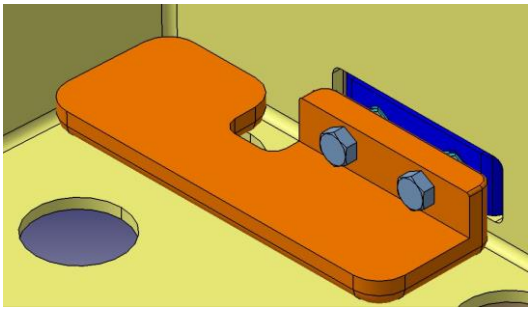

Fig.7. Fixture for positioning plate 2 with standard bolts

The previous examples are relatively simple and serve only to understand the basic design principles of fixtures for adhesive bonding parts and composites. Figure 8 shows a fixture with much more complex geometry used to position headlights for the front fairing of the train.
Figure 9 shows fixtures made from sheet metal together with additively manufactured fixtures on a transportation tool in the workshop.

Fig.8. Fixture for positioning headlights for the front fairing of the train

Fig.9. Sheet metal and additively manufactured fixtures

3. CONCLUSION

The article presents examples of the design of fixtures for positioning parts for adhesive bonding in the railroad industry. The design of fixtures requires knowledge of the manufacture of the composites themselves, general knowledge of fixtures and knowledge of the principle of interlocking degrees of freedom. The current state of the art in this field clearly shows the importance of fixtures in mass production and the possibilities of using additive technologies to manufacture these elements. The further development of AM and optimization methods such as topological optimization will certainly lead to an even greater spread of additively manufactured tools in the industry.

ACKNOWLEDGMENT

This paper is the result of activities carried out in the framework of the bilateral project no. 19/6-020/966-6-1/23.

REFERENCES

[1] de Souza, M. C., Moroz, I., Cesarino, I., Leão, A. L., Jawaid, M., & Dias, O. A. T. (2022). A review of natural fibers reinforced composites for railroad applications. Applied Science and Engineering Progress, 15(2), 5800-5800.

[2] Robinson, M., Matsika, E., & Peng, Q. (2017, August). Application of composites in rail vehicles. In ICCM Int. Conf. Compos. Mater (Vol. 2017, No. August, pp. 20-25).

[3] Rajak, D. K., Wagh, P. H., & Linul, E. (2021). Manufacturing technologies of carbon/glass fiber-reinforced polymer composites and their properties: A review. *Polymers*, 13(21), 3721,

[4] Bhong, M., Khan, T. K., Devade, K., Krishna, B. V., Sura, S., Eftikhaar, H. K., ... & Gupta, N. (2023). Review of composite materials and applications. *Materials Today: Proceedings*,

[5] Cavezza, F., Boehm, M., Terryn, H., & Hauffman, T. (2020). A review on adhesively bonded aluminium joints in the automotive industry. *Metals*, 10(6), 730,

[6] Hart-Smith, J. (2021). Aerospace industry applications of adhesive bonding. In Adhesive bonding (pp. 763-800). Woodhead Publishing,

[7] Delzendehrooy, F., Akhavan-Safar, A., Barbosa, A. Q., Beygi, R., Cardoso, D., Carbas, R. J. C., ... & Da Silva, L. F. M. (2022). A comprehensive review on structural joining techniques in the marine industry. *Composite Structures*, 289, 115490,

[8] Budzik, M. K., Wolfahrt, M., Reis, P., Kozłowski, M., Sena-Cruz, J., Papadakis, L., ... & Vassilopoulos, A. P. (2022). Testing mechanical performance of adhesively bonded composite joints in engineering applications: an overview. *The Journal of Adhesion*, 98(14), 2133-2209,

[9] Borges, C. S., Akhavan-Safar, A., Tsokanas, P., Carbas, R. J., Marques, E. A., & da Silva, L. F. (2023). From fundamental concepts to recent developments in the adhesive bonding technology: a general view. *Discover Mechanical Engineering*, 2(1), 8,

[10] Zhou, L., Miller, J., Vezza, J., Mayster, M., Raffay, M., Justice, Q., ... & Bernat, J. (2024). Additive Manufacturing: A Comprehensive Review. Sensors, 24(9), 2668,

[11] Vafadar, A., Guzzomi, F., Rassau, A., & Hayward, K. (2021). Advances in metal additive manufacturing: a review of common processes, industrial applications, and current challenges. Applied Sciences, 11(3), 1213,

[12] Fiedler, F., Ehrenstein, J., Höltgen, C., Blondrath, A., Schäper, L., Göppert, A., & Schmitt, R. (2024). Jigs and fixtures in production: A systematic literature review. Journal of Manufacturing Systems, 72, 373-405.

[13] Okpala, C. C., & Okechukwu, E. (2015). The design and need for jigs and fixtures in manufacturing. Science Research, 3(4), 213-219.

[14] Pisharody, A. P., Blandford, B., Smith, D. E., & Jack, D. A. (2019). An experimental investigation on the effect of adhesive distribution on strength of bonded joints. Applied Adhesion Science, 7, 1-12.

[15] Schuh, G., Bergweiler, G., Fiedler, F., Lichtenthäler, K., & Leimbrink, S. (2019, December). Hybrid welding jigs with additive manufactured functional elements. In 2019 IEEE International Conference on Industrial Engineering and Engineering Management (IEEM) (pp. 484-488). IEEE.

[16] Schuh, G., Bergweiler, G., Lichtenthäler, K., Fiedler, F., & de la Puente Rebollo, S. (2020). Topology optimisation and metal based additive manufacturing of welding jig elements. Procedia CIRP, 93, 62-67.

11th International Scientific Conference
IRMES 2025
Research and Development of
Mechanical Elements and Systems
June 19 – 21, 2025; Vrnjačka Banja, Serbia

Original scientific paper DOI: 10.46793/IRMES25.075T

ANALYSIS OF PROGRESS IN THE DEVELOPMENT OF HYDRAULIC ACTUATOR-BASED ABOVE-KNEE PROSTHESIS AND FUTURE GUIDELINES

Aleksandar TOMOVIC[1]
Remzo DEDIC[2]
Adisa VUCINA[2]
Nebojsa RASOVIC[2]
Radoslav TOMOVIC[1]
Milanko DAMJANOVIC[1]

[1]Faculty of Mechanical Engineering, University of Montenegro, Podgorica, Montenegro, 81000; aleksandart@ucg.ac.me; milanko@ucg.ac.me; radoslav@ucg.ac.me;
[2]Faculty of Mechanical Engineering, Computing and Electrical Engineering, University of Mostar, Mostar, Bosnia and Herzegovina, 88000; remzo.dedic@fsre.sum.ba; adisa.vucina@fsre.sum.ba; nebojsa.rasovic@fsre.sum.ba;

Abstract: *This paper analyzes the development of an above-knee prosthesis based on hydraulic actuators, which was initiated at the Faculty of Mechanical Engineering, Computing and Electrical Engineering at the University of Mostar, and has continued since 2023 in collaboration with the Faculty of Mechanical Engineering of the University of Montenegro. The evolutionary trajectory of the prosthetic design is presented, from the initial models with a single hydraulic cylinder in the knee joint, through the integration of an additional actuator in the ankle joint and modifications to the prosthetic foot, to modern solutions featuring double-acting cylinders and separate hydraulic power units. Experimental testing has confirmed significant improvements in user stability, functionality, and natural gait, especially when ascending stairs. The paper also emphasizes future development directions, including the implementation of servo valves in the hydraulic system to achieve more precise fluid control, smoother movements, and automatic adaptation of the prosthesis to varying walking conditions. The research results indicate that hydraulic systems represent a significant technological advancement in modern prosthetics, enabling transfemoral amputees greater independence, comfort, and quality of life.*

Keywords: *above-knee prosthesis; knee ankle; joint ankle; hydraulic cylinder.*

1. INTRODUCTION

Biomechatronics, as an interdisciplinary field that combines knowledge related to biological and mechatronic systems, first emerged in the 20th century. During that period, the development of biomechatronics was primarily associated with the field of prosthetic devices [1], where innovations such as powered prostheses and the integration of new materials (plastics, batteries, motors) enabled advancements in the functionality and comfort of these devices.

One of the earliest recorded medical issues among ancient human populations was amputation, as evidenced by findings at numerous archaeological sites [2]. Throughout history, numerous wars led to frequent injuries and limb loss, both upper and lower, which posed significant challenges for survivors. Faced with such losses, people attempted to compensate for missing limbs by using objects from their surroundings to ease daily functioning. Limb loss not only had physical consequences but also deeply affected the psychological and social well-being of the individual.

Prostheses, as one of the key groups of prosthetic devices, represent effective and useful replacements for missing human limbs such as the hand, arm, foot, or leg. Their primary function is to replace lost body parts and enable individuals with amputations to resume performing everyday activities, thereby significantly improving their independence and quality of life.

With the advancement of engineering and technology, new opportunities have emerged for innovation and improvements in the mobility of individuals with upper and lower limb amputations. Modern prostheses used around the world today can be categorized into three main groups based on their functionality:

- Passive prostheses have no power source, do not allow active movement or adaptation to usage conditions, and primarily serve as aesthetic or simple functional replacements for the missing limb.

- Semi-active prostheses allow a certain degree of movement adaptation, most commonly through the adjustment of damping or stiffness, which is achieved by modifying the prosthetic joints.
- Active prostheses, powered by an energy source, enable active movement, environmental responsiveness, and provide feedback to the user, significantly improving control and the sensation of natural motion.

2. DEVELOPMENT PROCESS OF A HYDRAULIC ACTUATOR-BASED ABOVE-KNEE PROSTHESIS

This paper analyzes the development of an above-knee prosthesis based on hydraulic actuators, which has been under development for several years at the Faculty of Mechanical Engineering, Computing and Electrical Engineering, University of Mostar. Research on the development of the hydraulically powered above-knee prosthesis began under the leadership of Professor Dedic, PhD. Professor Dedic [3], through his innovative approach and enthusiasm, initiated this project with the goal of improving the quality of life for individuals with amputations, particularly by addressing the challenge of stair climbing—one of the most significant difficulties faced by above-knee prosthesis users.

For the construction of the physical model of the above-knee prosthesis, the standard Endolite SFEUK (Stanceflex Uniaxial Knee Chassis) prosthesis [4] was selected due to its market availability and affordable price at the time. This prosthesis was subsequently modified by replacing the existing damper in the knee joint with a hydraulic cylinder, which significantly improved the functional characteristics of the device. The integration of the hydraulic cylinder enabled controlled movement and adaptation to different phases of gait, as well as enhanced stability and safety when overcoming obstacles such as stairs.

Fig.1. The first prototype of a hydraulic actuator-based above-knee prosthesis [4]

In the first phase of the research [5], the focus was on determining the required forces and moments necessary for successfully performing the stair-climbing process. Through an analysis of the biomechanical demands of knee joint movement, the research team calculated the driving force that a single-acting hydraulic actuator in the prosthetic knee joint must generate to lift the user during ascent. To accurately determine these parameters, an analysis was conducted on five standard male groups, taking into account different ranges of height and body mass. Based on the collected data, optimal technical requirements for the hydraulic cylinder were defined, including the required force, piston stroke, and operating pressure, in order for the prosthesis to effectively and safely support the user while climbing stairs. These results served as a foundation for further development and optimization of the prosthesis design, with the aim of achieving more natural and stable movement, as well as increased functionality and comfort for the end user.

The research on the development of the hydraulically powered above-knee prosthesis was extended through the doctoral dissertation of Vucina [6], which focused on establishing the kinematic model of the forces and moments generated during stair climbing. In line with the previous research, the fourth group of the male population (average height 176.9 cm, weight 81 kg) was selected as the target group for further studies, as this group has the highest frequency of transfemoral amputations. This selection allowed for a focus on the most representative parameters for prosthesis design and optimization. Experimental studies showed that:

- In addition to the knee joint, the critical point in the design of the prosthesis, which bears the highest loads during stair climbing, requires a robust construction of the hydraulic actuator that can withstand dynamic forces and bending moments.
- The ground reaction forces on the rigid foot of the prosthesis create significant moments at the ankle joint, which directly affect the stability and control of movement. The lack of adaptability in the ankle joint leads to an uneven distribution of loads, resulting in a loss of balance, unstable gait, and even falls.

Vucina concluded that the introduction of an additional actuator in the ankle joint would significantly contribute to the stability and functionality of the prosthesis, and thereby improve the comfort and stability of the user.

The third phase of the research was carried out through the master's thesis by Ziga [7], which continued in accordance with the conclusions and recommendations from Vucina's previous work. The main goal was to improve the stability and functionality of the prosthesis during stair climbing, particularly addressing issues related to the ankle joint. The integration of a second hydraulic cylinder in the ankle joint enabled better control over foot movements, damping of impact loads, and dynamic adaptation during ground contact. This directly addressed the previously identified problems with the rigid foot and uneven load distribution. Both hydraulic cylinders were powered by a single hydraulic unit. The

introduction of the additional actuator in the ankle joint showed improved results compared to the previous version and confirmed the conclusions set by Vucina.
Rupar [8] improves the previous model of the above-knee prosthesis by modifying the prosthetic foot, introducing a prototype with a passive joint connection at the front, thus simulating the natural joint connection between the foot and toes. This innovation allows for greater flexibility and adaptation of the foot during walking, particularly in the push-off phase (toe-off), contributing to a more natural gait pattern and better force distribution across the prosthesis.

Fig.2. Improved above-knee prosthesis with an additional hydraulic cylinder in the ankle joint [7]

The introduction of a passive joint at the front of the foot allows for better imitation of biomechanical characteristics, reduces the load on the limb residuum, and can increase the comfort and functionality of the user during stair climbing. Experimental testing compared all three previous variants of the above-knee prosthesis:

1. Above-knee prosthesis with actively powered knee and ankle joints, and a foot with passive bending at the front,
2. Above-knee prosthesis with actively powered knee and ankle joints, and a rigid foot,
3. Above-knee prosthesis with an actively powered knee joint, and a rigid ankle connection with a rigid foot.

Experimental analysis showed that the integration of the passive foot prototype with a joint connection at the front significantly improves the naturalness of movement compared to previous models. The passive joint allows for foot rotation in the sagittal plane, i.e., dorsiflexion of the foot.

Fig.3. Prototype prosthetic foot [8]

However, the research showed that a single hydraulic unit is insufficient to operate both hydraulic cylinders positioned in the knee and ankle joints, as it limits the synchronization of movement. It was concluded that the prosthesis should be modified by installing double-acting cylinders instead of the existing single-acting ones.
The fifth phase of the research was carried out through the doctoral dissertation of Jelacic [9]. Based on the conclusions and guidelines established by previous research, Jelacic improved the prosthesis by separating the drive into two separate hydraulic units and introducing double-acting cylinders instead of the existing single-acting ones.

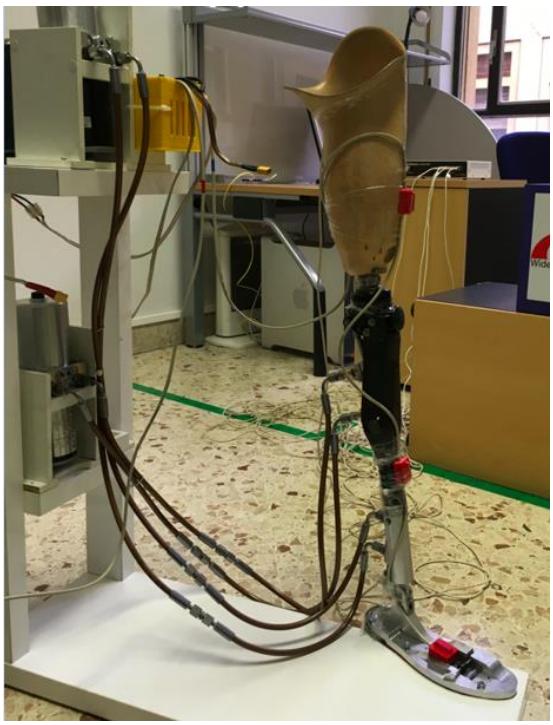

Fig.4. Above-knee prosthesis with separate hydraulic units and double-acting cylinders [9]

Jelacic also conducted experimental testing comparing the new enhanced model with the previous above-knee prosthesis models. The results of the testing showed improvements over previous models in terms of achieving a more adequate naturalness of gait.

3. FUTURE GUIDELINES FOR CONTINUED RESEARCH

Through the previous research, the development and progress of the above-knee prosthesis based on hydraulic actuators, which began at the University of Mostar, is clearly evident. All the authors and researchers involved in the development project have contributed to its improvement, as confirmed by numerous master's and doctoral dissertations, as well as many scientific papers on the subject.

The continuation of the research on the prosthesis development project will focus on the implementation of servo-valves in the hydraulic system to achieve more adequate and precise fluid regulation throughout the prosthetic system, which would contribute to generating more accurate forces in the hydraulic cylinders. As a result of achieving precise forces, the prosthesis would exhibit smoother movements, improving user comfort, precision in operation, and thus achieving a more natural gait. The integration of servo-valves would pave the way toward the concept of a "smart prosthesis" capable of automatic adaptation to different types of terrain and movement dynamics.

4. CONCLUSION

Hydraulic systems in active above-knee prostheses represent a significant step toward more natural mobility for users, thanks to their ability to dynamically adapt to changes in walking patterns. The ability to generate large forces at low speeds in these systems provides users with stability during the stance phase on the prosthesis, while simultaneously allowing smooth knee flexion during the transition between steps. The main advantage of the hydraulic system is its ability to dampen impact loads when the foot makes contact with the ground, reducing the transmission of vibrations to the remaining limb and spine. This is particularly important for active users who spend several hours a day in motion.

A significant benefit of an above-knee prosthesis based on hydraulic actuators is its assistance during stair climbing. The hydraulic system of the prosthesis provides sufficient force to lift the body, while simultaneously reducing the load on the ankle joint to maintain balance. For users with amputations, this technology means increased independence in daily activities, with reduced physical fatigue and pain in the remaining joints.

The main drawback of these systems is the use of oil as a hydraulic fluid, which can be mitigated with proper sealing and regular servicing of the prosthesis. Additionally, the bulkiness and slightly higher weight compared to other systems are considered disadvantages of hydraulic systems, but with advancements in technology and miniaturization of components, these barriers can be overcome.

REFERENCES

[1] Popovic, M. B.: *Biomechatronics*, Academic Press, Elsevier, ISBN: 978-0-12-812939-5, 2019.

[2] Kumar, A., Kumar, P.: *Endoskeletal prosthesis: a new era for amputee*, Med J Armed Forces India, 57(2):93-4. doi: 10.1016/S0377-1237(01)80121-0, Epub 2011 Jul 21., 2001.

[3] Dedic, R.: One possibility of getting up from a chair by modified above – knee prosthesis, *Proceedings of 13th International Research/Expert Conference "Trends in the Development of Machinery and Associated Technology"*, TMT 2009, Hammamet, Tunisia, 16-21 October, 2009.

[4] Dedic, R., Vucina, A., Ziga, A., Dedic, S., Jaramaz, B.: An experimental study of the kinematics of a modified above-knee prosthesis, *Proceedings of 10th International Research/Expert Conference "Trends in the Development of Machinery and Associated Technology"* TMT 2006, Barcelona-Lloret de Mar, Spain, 11-15 September, 2006.

[5] Huđec, M.: *Prilog analizi hidrauličkih komponenti za natkoljenične proteze,* (In Bosnian), MSc thesis, Mašinski fakultet, Univerzitet Džemal Bijedić, Mostar, 2001.

[6] Vučina, A.: *Prilog istraživanju kinematike sila u natkoljeničnoj protezi pri gibanju na stepenicama,* (In Bosnian), PhD thesis, Fakultet strojarstva i računarstva, Sveučilište u Mostaru, 2002.

[7] Žiga, A.: *Dizajn stopala natkoljenične proteze sa ugrađenim hidrauličkim pokretačima u članku i koljenu*, (In Bosnian), MSc thesis, Mašinski Fakultet, Univerzitet u Zenici, 2006.

[8] Rupar, M.: *Doprinos istraživanju natkoljenične proteze s aktivnim hidraulično pogonjenim zglobovima koljena i gležnja i protetskog stopala s pasivnim zglobnim savijanjem u prednjem dijelu*, (In Bosnian), PhD thesis, Fakultet strojarstva i računarstva, Sveučilište u Mostaru, 2017.

[9] Jelačić, Z.: *Doprinos dinamičkom modeliranju i upravljanju rehabilitacionih robota kroz razvoj aktivne hidraulične natkoljenične proteze,* (In Bosnian), PhD thesis, Univerzitet u Sarajevu, Mašinski fakultet, 2018.

11th International Scientific Conference
IRMES 2025
Research and Development of
Mechanical Elements and Systems
June 19 – 21, 2025; Vrnjačka Banja, Serbia

Original scientific paper DOI: 10.46793/IRMES25.079T

DEVELOPMENT OF THE CRNOJEVIC PRINTING MACHINE REPLICA

Radoslav TOMOVIĆ[1]
Aleksandar TOMOVIĆ[2]

[1] University of Montenegro, Faculty of Mechanical Engineering, Montenegro; radoslav@ucg.ac.me; ORCID iD: 0000-0002-4779-8019
[2] University of Montenegro, Faculty of Mechanical Engineering, Montenegro; aleksandart@ucg.ac.me;

Abstract: *The Crnojević printing machine is the first printing machine in the Balkans. It was installed in Cetinje in 1492, just 40 years after the first printing machine in the world – Gutenberg's printing press. It operated within the Crnojević Printing Press, the first state printing press in the world and the first printing press in the language of the South Slavic peoples and in the Cyrillic script. The Crnojević Printing Press is the first printing press in the Balkans where books are printed serially, so many associate the appearance of this machine with the beginning of techniques and technology and serial production in this region..*
This paper presents a project to create a replica of the Crnojević printing press, which was designed and created by a team from the Faculty of Mechanical Engineering in Podgorica, commissioned by the Ministry of Economic Development and Culture of Montenegro. The Project aimed to design the printing machine and define its functionality and operating principle. The replica is exhibited in the State Museum of Montenegro – Biljarda in Cetinje and is fully functional for printing, according to the methodology used in the fifteenth century.

Keywords: *Replica, Crnojevića Printing Press, Movable Type Technique, Gutenberg Printing Press.*

1. INTRODUCTION

Culture and history are integral parts of Montenegro's identity. Montenegrins value and take pride in their culture and history even more than in their natural beauty. The most significant milestone in the history of Montenegrin culture is, without a doubt, the start of printing. By the end of the fifteenth century, Montenegro, thanks to the Montenegrin Crnojevic dynasty—namely Ivan, the founder of Cetinje, and his son Djuradj—obtained a printing press, the first in the Balkans, only a few decades after Gutenberg's press, specifically only 40 years after the first printed book in the world. Two years later, the first printed book in Serbian, "Oktoih prvoglasnik," was produced by the Crnojevic Printing House in 1494. In that same year, two more books, "Oktoih petoglasnik" and "Psaltir sa posljedovanjem," were printed at the Crnojević Printing House [1].
The Crnojevic Printing House is the first South Slavic Cyrillic and the first state printing house in the world, representing a unique phenomenon of European significance in the medieval history of Montenegro. It was founded in 1492 by Djuradj Crnojevic, the eldest son of Ivan Crnojevic, the founder of Cetinje, thus permanently placing Montenegro on the cultural map of the enlightened nations of medieval Europe [2].
On the other hand, if we look closely, it can be concluded that the Crnojevic printing press machine is one of the first and oldest machines used in the Balkans, which in itself is a true curiosity. Although not manufactured in Montenegro, it was certainly assembled and used there, making the Crnojevic Printing House, in a way, a pioneer of technology and serial production in this region[3] .
On the occasion of a significant anniversary—530 years since the appearance of the first printed book in Serbian, "Oktoih prvoglasnik"—the Montenegrin Ministry of Economic Development and Tourism requested that the Faculty of Mechanical Engineering in Podgorica design, construct, and later produce a replica of the first printing press machine in the Balkans, the Crnojevic Printing Press machine.
According to the technical requirements, the printing press machine project should provide a detailed description of the primary design and construction of the press, including its components, their shape and arrangement, and the authentic materials from which the parts should be made. It should also describe the assembly process of the machine's components, as well as a description of the mechanism of pressure creating of the plate over the plate, the method of making and fitting movable clichés and the methodology of imprinting with the letterpress technique. In addition to the design of the printing machine, the goal of the Project was to define the functioning and operating principle of the printing machine [4].

After its construction and assembly, the printing press was installed in Njegos Museum – Biljarda in Cetinje and is available for visitors to view.
This paper briefly presents the basic results of this project's development.

2. GUTENBERG'S INVENTION OF PRINTING WITH MOVEABLE LETTERS TECHNIQUE

Of all the inventions and patents that humanity has conceived and created, none has influenced the development of civilization as profoundly as Gutenberg's printing press and his invention of serial book printing (Fig. 1.) [5].

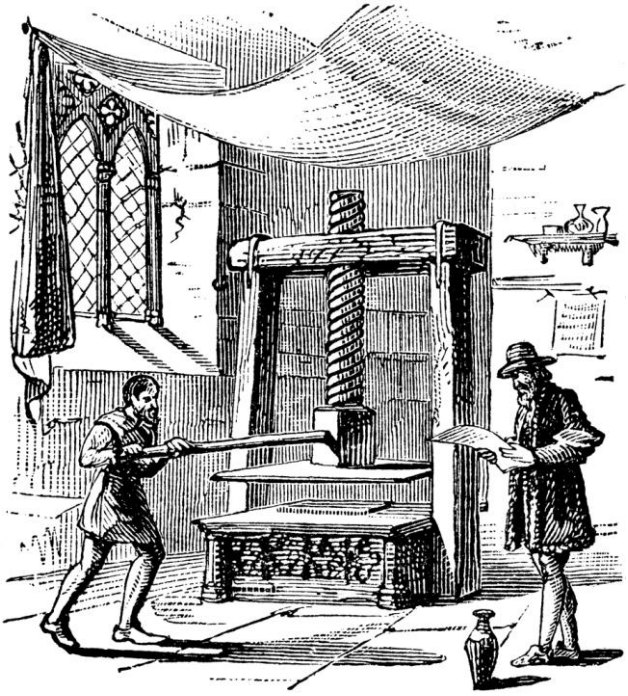

Fig.1. Gutenberg's printing press machine [6]

Johannes Gutenberg (Fig. 2) was a German inventor and craftsman who developed the technique of movable letters-type printing—a revolutionary method of text reproduction that enabled the mass production of books. Before Gutenberg's invention, books were mainly reproduced by copying (through scriptorium schools), a lengthy and arduous process. As a result, books were extremely expensive, considered small treasures, and owned only by the wealthiest individuals, rulers, and certain monasteries. Gutenberg's innovation allowed for faster and cheaper book production, significantly increasing the availability of written materials. This first wave of mass book printing opened the door to widespread education and information sharing, leading to a rise in literacy and the formation of public opinion. Shortly after Gutenberg, printing houses spread across Europe, making books more accessible to a wider population. This sparked a printing revolution in Europe, marking a turning point of the second millennium and the beginning of the modern era in human history. That played a crucial role in the development of the Renaissance, Reformation, Enlightenment, and scientific expansion, laying the foundation for a knowledge-based modern economy and the spread of learning among the general public.

Fig.2. Johannes Gutenberg (1394-1468) [7]

3. BASIC INFORMATION ABOUT THE PROJECT ASSIGNMENT

The project's aim is to provide a comprehensive project for the printing press machine, utilizing available historical sources, literature, and studies, to ensure the creation of a replica of the first printing press machine in the Balkans. The project team is tasked with reconstructing the technical aspects of this historical machine through the analysis of available historical sources, literature, and artistic works from the Renaissance and early modern centuries. During this time, printing was not merely a technical activity; it was an art form in the truest sense of the word. This serves as the inspiration for designing a replica that is not only functional but also visually appealing. In this process, the project team had to consider various aspects—from the materials to be used to the printing techniques to be applied [4].
A significant challenge in implementing the project was the absence of historical sources detailing how the Crnojevic printing press machine looked. It is known only that it was made of wood and modeled after Gutenberg's original press machine. Consequently, the project designer is expected to take into account the available information regarding Gutenberg's printing press in Mainz, whose invention spurred the formation of similarly styled printing presses in other European centers. Additionally, historical facts should be considered to understand how the Crnojevic printing press differed from its predecessors. Notably, the Crnojevic

printing press was unique for its use of movable metal (lead) Cyrillic letters of original typography, in two-color printing, combined with woodcuts that graphically shaped decorative initials, flags, and illustrations [2, 8, 9].

The project designer is also expected to execute this project in all aspects in accordance with the existing regulations of Montenegro. During the design process, it is essential to consider the applicable regulations, rules, and standards for this type of project, as well as the conceptual solutions outlined in the feasibility study prepared by the Ministry of Economic Development for the project's implementation. For defining specific project elements for which technical standards are not prescribed in Montenegrin regulations or the conditions specified in the project task, it is recommended to use technical requirements and standards from foreign regulations, with prior approval from the Client.

As a result of the project, it is necessary to produce complete constructional and technical documentation, which should include all the essential elements for the fabrication of the printing press machine.

4. TECHNICAL SOLUTION AND CONSTRUCTIONAL-TECHNICAL DOCUMENTATION

The complete appearance, shape, dimensions, and arrangement of the components of the replica of Djuradj Crnojevic printing press machine are defined in the constructional and technical documentation. Fig. 3. shows the 3D drawing and Fig. 4. rendered illustration of the replica.

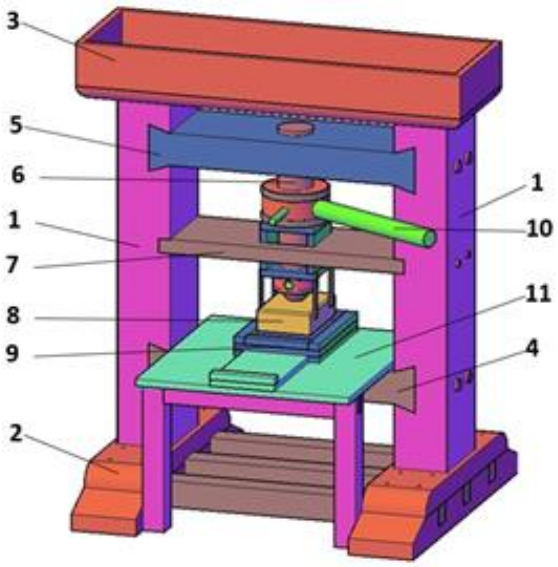

Fig.3. 3D drawing of the Crnojevic printing press replica

The construction of the replica of Djuradj Crnojevic printing press machine features a massive frame structure made of oak, weighing approximately 780 kg. The base of the frame consists of two solid vertical pillars (1), which connect two bases: the lower base (2) and the upper base (3). The lower base also serves as the machine's support, while the upper base contains a box for storing maintenance tools and spare parts. Between the pillars, there are two additional beam supports that further strengthen the structure. The first beam support is the support beam (4), which receives the working force and transmits it to the pillars and the base. The second support is a threaded beam (5), which carries the threaded spindle (6). Additionally, there is a guide beam (7) positioned between the pillars, ensuring the translational movement of the stamp (8) without simultaneous rotation. The stamp is used to transfer pressure onto the working plates of the drawer with movable clichés (9).

Fig.4. Rendered illustration of replica

The basis of the mechanism for generating pressure force is the threaded spindle (6). The pressure force is applied through the rotation of the handle (10) connected to the threaded spindle. The force is then transferred through the stamp to the working plates of the drawer with movable clichés, creating an impression on the paper.

Another important element of the construction is the drawer with movable clichés (9), which is capable of sliding along the guide of the worktable (11). The most critical positions of the drawer are the front and rear end positions. In the front position, the clichés are arranged in the drawer, and the paper for the impression is set. Pushing the drawer to the rear position brings the clichés directly under the stamp, ready for printing. After printing, the drawer is moved back to the front position, the paper is changed, and printing continues.

Fig. 5. shows the assembly drawing of the Crnojević printing machine replica.

Fig. 6. shows the completed printing press machine installed in Njegos Museum Biljarda in Cetinje, along with the first imprint produced by the press—the Coat of Arms of the Crnojevic dynasty (Fig 7.).

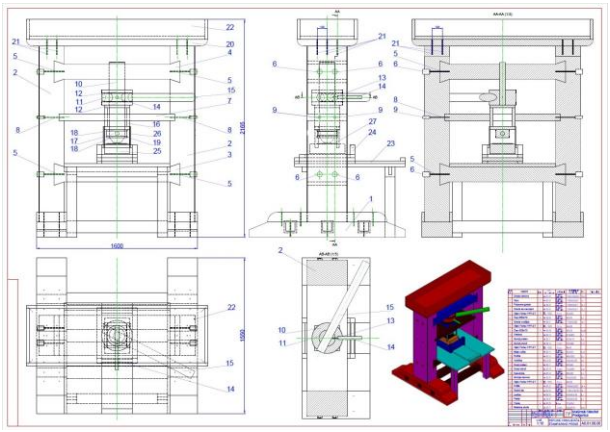

Fig.5. Assembly drawing of the Crnojevic printing pressreplica

Fig.6. The printing press machine replica installed in the Njegos Museum in Cetinje

Fig.7. The first imprint printed by the press—the Coat of Arms of the Crnojevic dynasty

5. CONCLUSION

The replica of the Crnojevic printing press machine visualizes an important aspect of our history and culture. The combination of historical heritage with modern technical knowledge creates a unique blend that can inspire and ensure that key ideas and innovations from the past are passed on to future generations. This replica will not only serve as a museum exhibit but also as a dynamic educational platform that will inspire art, technology, and culture enthusiasts to understand and appreciate the evolution of one of the most significant inventions in human history. In this way, the project continues to play a key role in preserving and promoting the rich cultural heritage of Montenegro, as well as in laying the foundation for future development and research in this field.

REFERENCES

[1] Tomović R., 530 godina od štampanja prve knjige na srpskom jeziku - Oktoiha prvoglasnika – Prvi dio, Svetigora, Pravoslavna Mitropolija Crnogorsko-Primorska, br. 325., (2024).
[2] Studija izvodljivosti za potrebe definisanja prostora i izrade replike prve Štamparije na Balkanu – Štamparije Crnojevića, (2019), Ministarstvo održivog razvoja i turizma Crne Gore.
[3] [1] Tomović R., 530 godina od štampanja prve knjige na srpskom jeziku - Oktoiha prvoglasnika – drugi dio, Svetigora, Pravoslavna Mitropolija Crnogorsko-Primorska, br. 326., (2024).
[4] Tomović, R., Jovanović, J., Tomović A., (2022). Glavni projekat za izradu Replike prve štamparske prese na Balkanu - Crnojevića štamparije, Univerzitet Crne Gore, Mašinski fakultet u Podgorici.
[5] Evgenij Ljvovič Nemirovski, (1999), Počeci štamparstva u Crnoj Gori (1492-1496), CNB „Đurđe Crnojević“, Cetinje.
[6] https://etc.usf.edu/clipart/56100/56142/56142_printpress.htm.
[7] https://en.wikipedia.org/wiki/Johannes_Gutenberg
[8] https://rtcg.me/tv/emisije/dokumentarni/istorijskialbum/170370/gutembergova-galaksija-stamparija-crnojevica.html.
[9] https://www.youtube.com/watch?v=DLctAw4JZXE&t=2s.

11th International Scientific Conference
IRMES 2025
Research and Development of
Mechanical Elements and Systems
June 19 – 21, 2025; Vrnjačka Banja, Serbia

Original scientific paper DOI: 10.46793/IRMES25.083K

ASSESSING ACHIEVED SAVINGS USING OPTIMIZED TRUSSES WITH CARDINALITY CONSTRAINTS

Nenad KOSTIĆ[1]
Nenad PETROVIĆ[2]
Vesna MARJANOVIĆ[3*]
Nenad MARJANOVIĆ[4]

[1]University of Kragujevac, Faculty of Engineering, Kragujevac, Serbia, 34000; nkostic@kg.ac.rs;
ORCID iD: 0000-0002-0157-7501
[2]University of Kragujevac, Faculty of Engineering, Kragujevac, Serbia, 34000; npetrovic@kg.ac.rs;
ORCID iD: 0000-0002-7563-9883
[3]University of Kragujevac, Faculty of Engineering, Kragujevac, Serbia, 34000; vmarjanovic@kg.ac.rs;
ORCID iD: 0000-0001-6266-5540
[4]University of Kragujevac, Faculty of Engineering, Kragujevac, Serbia, 34000; nesam@kg.ac.rs;
ORCID iD: 0000-0002-8441-4328

Abstract: *This research presents the additional benefits gained when using cardinality constraints in just sizing and combined sizing and shape optimization to find solutions with minimal weight while using a set number of different cross-sections allowed in the design. When limiting the number of cross-sections, an optimal solution can result in a structure with a reasonable number of different types of stock needed, unlike an approach which is unconstrained in this regard. This creates a more practical solution, which reduces the complexity of the solution and more resembles an experience-driven design, but with a lower overall weight than analytical solutions due to the optimization methods' ability to explore practically the entire search space for a minimal weight solution. This limitation has adverse effects on the design. The downside is that the weight of the resulting structure is higher than the global optimum (one which disregards the number of different types or sizes of cross-sections used). However, it means that there are fewer different bar stock dimensions to be ordered, and less waste is created once the necessary pieces are cut from standard bar stock. The example used for these purposes is a typical optimization problem of a 17-bar truss with various numbers of different cross-sections used. The optimal solutions for this example were made using original software developed by the authors for the purposes of previously published research. Standard, available, bar stock dimensions were used in the optimization process in order to best resemble a real-world application. The results illustrate the added benefits of including fewer different bar stock types and the accompanying savings, which are indirectly created using this method.*

Keywords: *truss; optimization; sizing; shape; cardinality constraint.*

1. INTRODUCTION

Recent advancements in structural optimization have been largely driven by improvements in algorithmic speed and capability. This trend is particularly evident in the field of structural truss optimization, where researchers have extensively applied both new and modified algorithms to standard benchmark problems. While such problems are valuable for comparing performance metrics, they often fall short in addressing the practical applicability of the solutions in real-world scenarios. The introduction of heuristic methods initially brought significant improvements, but since then, progress has been more gradual, focused mainly on enhancing convergence speed and fine-tuning specific algorithm parameters.

Researchers in [1] proposed an enhanced version of the Grey Wolf Optimization algorithm (EGWO) to address its limitations in exploration and susceptibility to local optima. They improved the algorithm using gamma, z-position, and the golden ratio, then evaluated its performance on benchmark functions and two real-world engineering problems, demonstrating superior results compared to several other metaheuristic algorithms. [2] proposed several optimization models for both continuous and discrete truss design problems, incorporating constraints such as Euler buckling, Hooke's law, and limits on stress and displacement. Their approach significantly outperforms traditional MILO solvers in both speed and solution quality, achieving up to 66%

weight reduction and solving previously intractable large-scale truss design problems. Serdar Avcı et al. applied the Improved Stochastic Ranking Evolution Strategy (ISRES) algorithm in [3] to the sizing and layout optimization of various truss benchmark structures, aiming to minimize weight while satisfying stress and displacement constraints. They tested the algorithm on multiple configurations, validated the optimized designs using finite element analysis, and compared its performance with other methods. The results showed that ISRES is both efficient and robust, making it a practical and reliable tool for complex structural optimization problems in engineering applications.

Building on this trend, more recent studies have shifted their focus toward handling increasingly realistic constraints, such as those arising from buckling behaviour, which greatly influence the structural integrity and practicality of optimized designs. Dynamic buckling constraints have become increasingly common in truss optimization due to their significant impact on problem complexity, introducing nonlinear and non-convex solution spaces. Evolutionary algorithms have enabled researchers to tackle these challenges effectively by avoiding local optima. However, many studies, such as [4], continue to use fixed values for buckling constraints, which do not guarantee minimal weight or practical applicability. A comparison in [5] demonstrated a substantial increase in optimal weight when Euler buckling constraints were applied, due to the need for larger cross-sections in compression members. In [6], the authors used dynamic buckling constraints to achieve better weight minimization, showing improvement over the results presented in [7] for various benchmark examples. The PO (Political Optimization) algorithm introduced in [8] successfully addressed standard test problems with buckling constraints, though it relied on continuous sizing variables, limiting its real-world applicability. More recently, researchers in [9] developed an iterative algorithm for truss size optimization that incorporates stress, displacement, and local buckling constraints, particularly addressing the added complexity introduced by dynamic buckling conditions.

In parallel with these developments, efforts have also been made to incorporate additional constraints aimed at enhancing practical applicability—particularly those related to limiting the number of distinct cross-sections used in optimized trusses. Researchers in [10] explored the practical implications of introducing a constraint on the number of different cross-sections used in truss sizing optimization. By applying this constraint to four benchmark problems, under dynamic Euler buckling conditions and discrete cross-section sets, the study analyses how limiting cross-section variety affects solution quality. The paper [11] investigates the impact of applying cardinality constraints to limit the number of distinct cross-sections in simultaneous sizing and shape optimization of truss structures. Standard benchmark examples are used to compare solutions with varying cardinality limits against both unconstrained optimal solutions and single cross-section cases. The results are also compared to earlier research focused solely on sizing optimization under the same constraints.

This paper investigates the additional savings that can be achieved by imposing cardinality constraints on truss sizing and combined sizing and shape optimization, focusing on how limiting the number of different cross-sections can offset the weight savings typically achieved through other optimization methods. By examining a typical 17-bar truss, the research demonstrates that while the optimal weight solutions with fewer cross-sections may not match the global optimum, they offer significant practical advantages, such as reduced material waste and simplified construction. The results reveal that limiting cross-section types can lead to lower material requirements when considering both weight reduction and the reduction of offcuts, offering a more practical solution for real-world applications.

2. THE 17-BAR TRUSS

The 17-bar truss example is made from construction steel with a Young modulus of 21000 MPa and a density of 7400 kg/m^3 [10, 11]. A load of F =444.82 kN is applied to node (9) as is shown in Fig.1. The chosen set of cross-sections comprises 49 distinct diameters, ranging from 3 mm to 125 mm, as follows: 6, 8, 12, 12, 14, 15, 16, 17, 18, 20, 22, 24, 25, 28, 30, 32, 35, 36, 38, 40, 45, 50, 55, 56, 60, 63, 65, 70, 75, 80, 85, 90, 95, 100, 105, 110, 115, 120, 125, 130, 140, 150, 160, 170, 180, 190, 200, 220, and 250 mm. Displacement is constrained to ±0.0508m for all nodes in both directions, and Euler buckling constraints are used for all compressed bars.

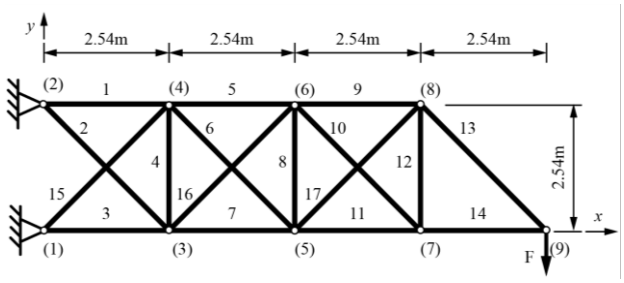

Fig.1. The 17-bar truss layout [11]

Coordinates for nodes (3-8) can take any position from 0 to 10.16 m in the x and from -2.54 to 5.08 m in the y-direction with from their initial configuration. The y-component of the node (9) coordinates is the only one that can vary from 0 to 2.54 m from its initial configuration.

The resulting weights for sizing optimization (S) and sizing and shape (S+S) optimization, as per [10] and [11], respectively, are presented in Table 1. In this table, results for each optimization type are shown with cardinality values from one to three, as well as the global optimum with the corresponding number of different cross-sections used when cardinality constraints are not applied.

Table 1. Optimal weights of solutions from literature.

Solution	Weight [kg]	Solution	Weight [kg]
S 1	3181.777	S+S 1	2720.745
S 2	2047.368	S+S 2	1647.07
S 3	1836.005	S+S 3	1471.678
S 8	1571.875	S+S 6	1355.876

Fig. 2 shows the difference from the solution with a single cross-section for the given solution type. Table 2 shows the coordinates of nodes in the optimal configurations for the sizing and shape-optimized solutions from [10, 11].

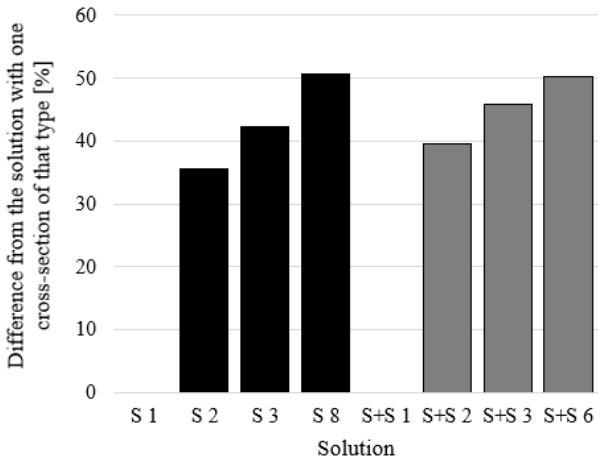

Fig.2. difference from the solution with a single cross-section for the given solution type.

Table 2. Optimal coordinates of points according to the number of different cross-sections used for the 17-bar truss example [11].

Coordinate [m]	S+S1	S+S2	S+S3	S+S6
x_3	2.652	2.722	2.741	2.651
y_3	0.123	-0.247	-0.269	-0.303
x_4	3.12	1.524	1.532	1.604
y_4	2.125	2.498	2.436	2.411
x_5	5.192	5.676	4.99	5.45
y_5	0.373	-0.136	-0.285	-0.272
x_6	5.184	3.993	4.029	4.068
y_6	1.881	1.833	2.194	2.356
x_7	6.665	6.949	7.699	8.16
y_7	0.296	-0.144	-0.445	-0.205
x_8	6.649	6.385	7.085	7.766
y_8	1.917	1.338	1.927	1.909
y_9	0.828	0.343	0.718	0.584

3. ANALYSIS OF RESULTS

The optimal results taken from literature, which were presented in the previous heading, have been compared according to various criteria. The first step was to determine which cross-sections were used for which bar and to group the same profiles in each of the eight analysed trusses. For easier visual tracking of results, a color-coding system was implemented, which is the same for all trusses, in the sense that from largest to smallest, the colours are in the same order, but the colours do not necessarily correspond to the same cross-section diameter across all trusses. This color-coding system is the same for all subsequent figures and corresponds to the colour scheme shown in Table 3.

This table shows the bar cross-section diameter and corresponding colour for each of the eight solutions. Table 4 presents the lengths of each of the bars for all of the solutions. Since the sizing-optimized solutions all have the same initial layout, the lengths of bars for all those solutions are the same.

Table 3. Bar cross-section diameter according to solution

	Bar cross-section diameter for given solution [mm]							
Bar no.	S 1	S 2	S 3	S 8	S+S 1	S+S 2	S+S 3	S+S 6
1	105	75	75	75	105	105	85	85
2	105	75	75	55	105	22	45	50
3	105	105	105	105	105	105	105	105
4	105	75	75	8	105	22	45	50
5	105	75	75	85	105	105	85	85
6	105	75	75	55	105	22	45	50
7	105	105	105	105	105	105	105	100
8	105	75	75	6	105	22	45	25
9	105	105	75	70	105	105	85	75
10	105	75	75	70	105	22	45	25
11	105	105	85	85	105	105	85	85
12	105	75	75	70	105	22	45	25
13	105	75	75	70	105	105	45	50
14	105	75	75	75	105	105	85	75
15	105	75	75	80	105	105	85	75
16	105	75	75	85	105	22	85	75
17	105	105	85	80	105	105	85	85

Corresponding to the colours of the cells in Table 3, Figures 3 and 4 give a visual representation of the locations of each cross-section on the optimal structures for sizing-optimized solutions in Fig. 3 and sizing and shape-optimized solutions in Fig 4.

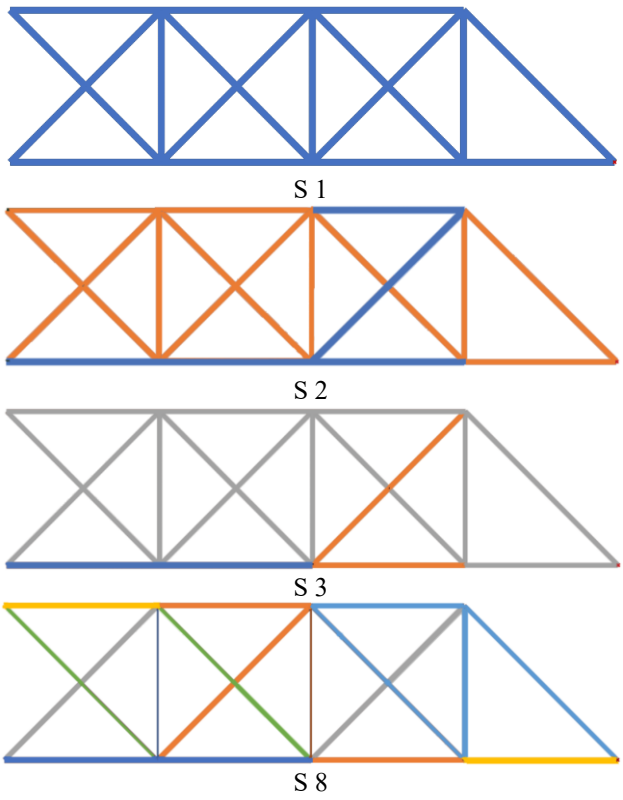

Fig.3. Cross-section configuration layout corresponding to Table 3 for sizing optimization

Table 4. Bar lengths for each of the observed solutions

	Bar lengths for given solution [m]				
Bar no.	**S 1, S 2, S 3 and S 8**	**S+S 1**	**S+S 2**	**S+S 3**	**S+S 6**
1	2.540	3.147	1.525	1.536	1.609
2	3.592	3.588	3.896	3.925	3.887
3	2.540	2.655	2.733	2.754	2.668
4	2.540	2.056	2.995	2.963	2.909
5	2.540	2.078	2.557	2.509	2.465
6	3.592	2.713	4.917	4.400	4.689
7	2.540	2.552	2.956	2.249	2.799
8	2.540	1.508	2.590	2.659	2.969
9	2.540	1.465	2.443	3.068	3.725
10	3.592	2.169	3.556	4.520	4.827
11	2.540	1.475	1.273	2.714	2.711
12	2.540	1.621	1.586	2.450	2.150
13	3.592	3.676	3.904	3.304	2.736
14	2.540	3.535	3.248	2.722	2.150
15	3.592	3.775	2.926	2.878	2.896
16	3.592	3.082	2.438	2.779	3.013
17	3.592	2.123	1.636	3.047	3.181

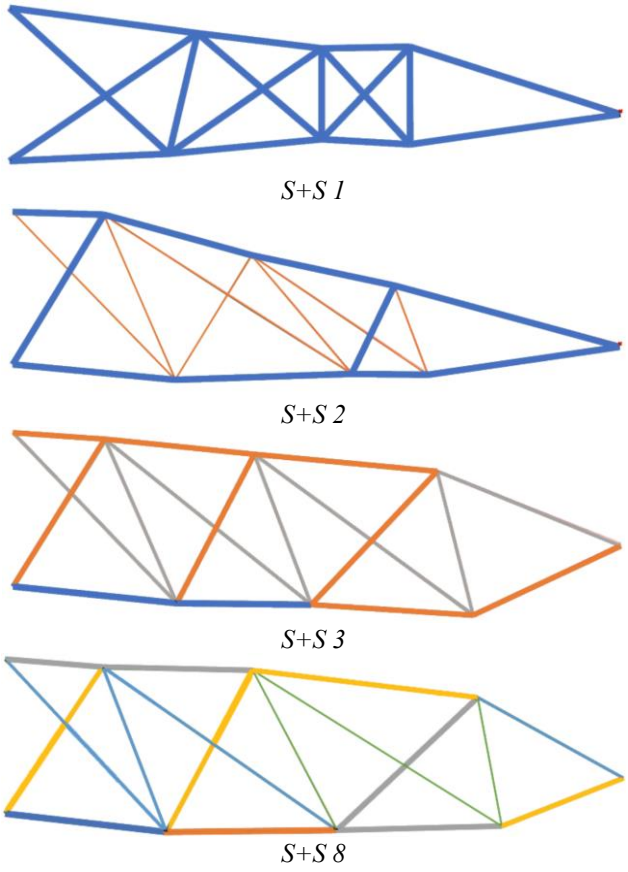

Fig.4. Cross-section configuration layout corresponding to Table 3 for sizing and shape optimization

Fig. 5 shows the distribution of the lengths of each of the cross-sections for all of the optimal solutions following the same colour-coding scheme as Table 3.

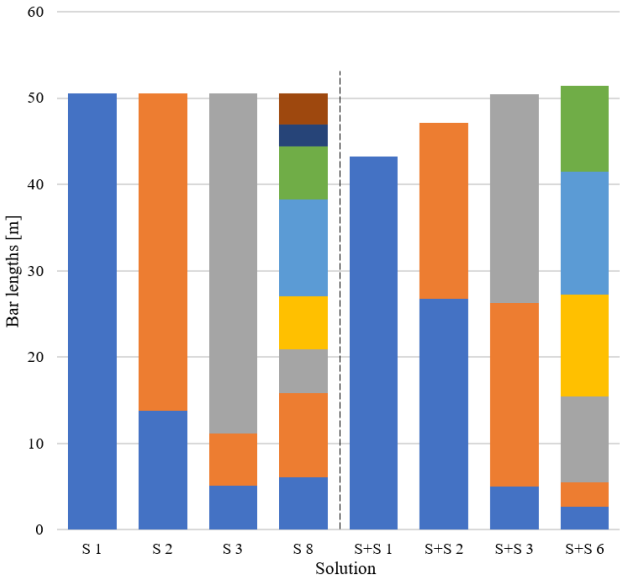

Fig.5. Lengths of bars by cross-section for each of the solutions.

Figure 6 shows the number of pieces of 6m bar stocks which need to be acquired for each of the different cross-sections used in each of the solutions. These numbers are calculated by dividing the total length of each type of bar needed, and then those values are rounded up to obtain whole numbers of bar stocks. This is done as a rough estimate of the necessary material needed since, for these types of structures, bars are most commonly extended by welding to minimize waste.

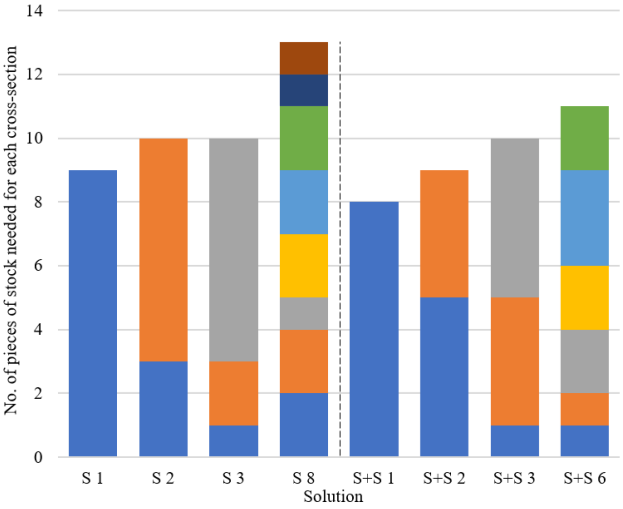

Fig.6. Number of pieces of 6m bar stocks needed of each of the different cross-sections used in each of the solutions.

Since the total length of acquired material needs to be cut to size, there will inevitabely be wasted material after cutting, which results in off-cuts which are scrapped. The length of these off-cuts is calculated by taking the total length of the number of each cross-section stock (shown in Fig. 5) and subtracting the total used length (shown in Fig. 6) for that cross-section (shown in Fig.7).

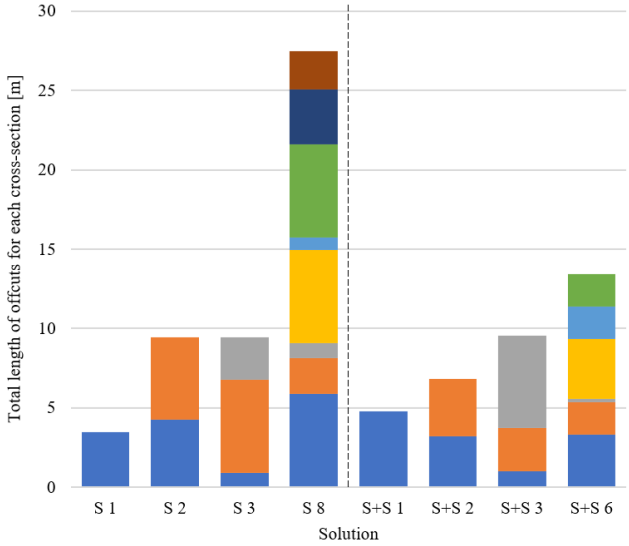

Fig.7. Total lengths of offcuts for each cross-section of each of the solutions.

Fig. 8 shows the overall weight used for each of the solutions.

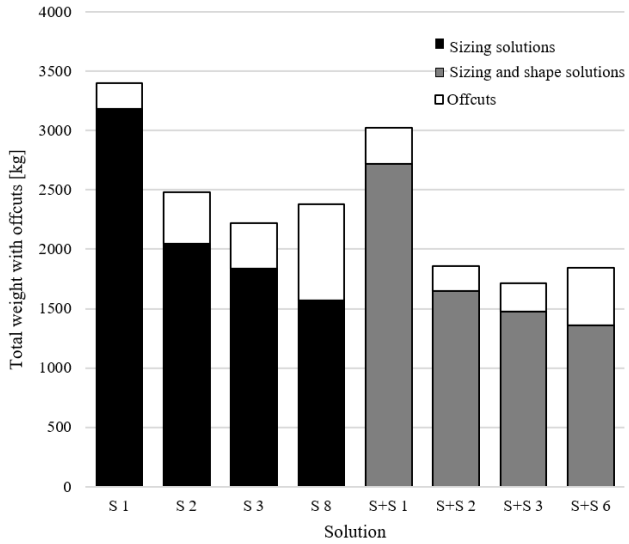

Fig.8. Overall weight of material used.

4. CONCLUSION

This research considered possible added benefits of using optimal solutions limited by cardinality constraints in order to further demonstrate the benefits of using such limits in optimization. These limitations are more in line with actual trusses found in practice and present a more feasible solution to those that do not take into account the total number of different cross-section types that need to be used to achieve the optimal, minimal weight.

In order to have the results comparable to other solutions found in literature, a typical 17-bar truss example was examined. Results from papers where the cardinality constraint was implemented were used in order to analyse the benefits of using such solutions, compared to those which do not consider this constraint. Sizing (S) and combined sizing and shape (S+S) optimization results were considered. The analysed parameters were the total lengths of each of the cross-section diameters, the number of whole pieces of 6m bar stock needed to cut and extend in order to achieve all those lengths, and the lengths of offcuts for each type of stock.

Since the sizing-optimized solutions do not vary the locations of the connection nodes, the total length of the total numbers of bars for each solution is the same. The decrease in weight compared to the single-cross-section solution (S 1) for the two and three different cross-sections solutions are 35.653% and 42.296%, respectively. Compared to the global optimum, which doesn't include the cardinality constraint in sizing optimization (S 8), which is ~50% of the weight of the S 1 solution, the S 3 solution is the better choice since the total weight with offcuts is lower than the S 8 solution.

It should be noted that solutions S 1 and S+S 1 use the same cross-section, and from the graph, it is obvious that the main savings in weight that can be made when using only one cross-section, in this case, is basically just shape optimization. This decrease in length of ~7m correlates directly with a reduction of ~461kg, or ~14.5% of both length and weight.

The sizing and shape optimized solutions (S+S) show a similar trend to the sizing solutions. Though out of the four observed S+S solutions, S+S 2 has the least amount of discarded material, the S+S 3 solution, with only ~30kg more of waste, has a lower overall weight compared to the S+S 2 solution by ~145kg.

It is evident from the presented analysis that when considering wasted material from bar stock, the minimal construction weight solution is not the minimal total material required solution. It should also be considered that the offcut material isn't necessarily directly wasted as it can be used in other, subsequent structures and that the number of repetitions of the same construction would influence the amount of wasted material. Still, for this research, only a single construction was considered. If multiple constructions of the same design are needed, then this analysis could be used as a basis for selecting the optimal solution in that case as well, just with the added consideration of multiplying the number of element lengths used by the number of construction instances. Cutting plans can be further optimized or included in a new multi-objective optimization process as an additional way to ensure savings.

ACKNOWLEDGMENT

This paper results from research conducted under the author's contract No. 451-03-137/2025-03/200107, dated February 4, 2025.

REFERENCES

[1] Mohammed, H., Abdul, Z. and Hamad, Z.: Enhancement of GWO for solving numerical functions and engineering problems. *Neural Computing and Applications*, Vol.36, No.7, pp. 3405-3413, ISSN 0941-0643, 2023

[2] Shahabsafa, M., Mohammad-Nezhad, A., Terlaky, T., Zuluaga, L., He, S., Hwang, J. T. and Martins, J. R. R. A.: A novel approach to discrete truss design

problems using mixed integer neighborhood search. *Structural and Multidisciplinary Optimization*, Vol.58, No.6, pp. 2411-2429, ISSN 1615-1488, 2018

[3] Avcı, M. S., Yavuz, D., Ercan, E. and Nuhoğlu, A.: Efficient Sizing and Layout Optimization of Truss Benchmark Structures Using ISRES Algorithm. *Applied Sciences*, Vol.14, No.8, pp. 3324, ISSN 2076-3417, 2024

[4] Pham, H.-A. and Tran, T.-D.: Optimal truss sizing by modified Rao algorithm combined with feasible boundary search method. *Expert Systems with Applications*, Vol.191, pp. 116337, ISSN 09574174, 2022

[5] Petrović, N., Kostić, N., Marjanović, N. and Marjanović, V.: Influence of Using Discrete Cross-Section Variables for All Types of Truss Structural Optimization with Dynamic Constraints for Buckling. *Applied Engineering Letters*, Vol.3, No.2, pp. 78-83, ISSN 2466-4677, 2018

[6] Artar, M. and Carbas, S.: Discrete sizing design of steel truss bridges through teaching-learning-based and biogeography-based optimization algorithms involving dynamic constraints. *Structures*, Vol.34, pp. 3533-3547, ISSN 23520124, 2021

[7] Hasançebi, O., Çarbaş, S., Doğan, E., Erdal, F. and Saka, M. P.: Performance evaluation of metaheuristic search techniques in the optimum design of real size pin jointed structures. *Computers & Structures*, Vol.87, No.5-6, pp. 284-302, ISSN 00457949, 2009

[8] Awad, R.: Sizing optimization of truss structures using the political optimizer (PO) algorithm. *Structures*, Vol.33, pp. 4871-4894, ISSN 23520124, 2021

[9] Bich Quyen, V. T., Khanh, C. Q., Thuy Van, T. T., Khoa, D. N. and Truc, T. P.: A New Algorithm for Size Optimization of the Truss Structures with Buckling Constraint using Finite Element Method. *IOP Conference Series: Materials Science and Engineering*, Vol.661, pp. 012041, ISSN 1757-899X, 2019

[10] Petrović, N., Marjanović, V., Kostić, N., Marjanović, N. and Viorel Dragoi, M.: Means and Effects of Constraining the Number of Used Cross-Sections in Truss Sizing Optimization. *Transactions of FAMENA*, Vol.44, No.3, pp. ISSN 13331124, 2020

[11] Kostic, N., Petrovic, N., Marjanovic, V., Nikolic, R. R., Szmidla, J., Marjanovic, N. and Ulewicz, R.: Effects of Limiting the Number of Different Cross-Sections Used in Statically Loaded Truss Sizing and Shape Optimization. *Materials (Basel)*, Vol.17, No.6, pp. ISSN 1996-1944, 2024

11th International Scientific Conference
IRMES 2025
Research and Development of
Mechanical Elements and Systems
June 19 – 21, 2025; Vrnjačka Banja, Serbia

Original scientific paper DOI: 10.46793/IRMES25.089J

MEASUREMENT OF THE KINEMATIC CHARACTERISTICS OF ZIPLINE PASSENGERS

Tanasije JOJIĆ[1]
Jovan VLADIĆ[2]
Radomir ĐOKIĆ[3]
Nikola ILANKOVIĆ[4]
Mirko KATONA[5]

[1]Faculty of Technical Sciences, Novi Sad, Serbia, 21000; tanasijejojic@uns.ac.rs; ORCID iD: 0000-0002-2174-3394
[2]Faculty of Technical Sciences, Novi Sad, Serbia, 21000; vladicj@gmail.com; ORCID iD: 0000-0003-1518-1935
[3]Faculty of Technical Sciences, Novi Sad, Serbia, 21000; djokic@uns.ac.rs; ORCID iD: 0000-0002-1578-0543
[4]Faculty of Technical Sciences, Novi Sad, Serbia, 21000; ilankovic@uns.ac.rs; ORCID iD: 0000-0002-9110-4926
[5]Faculty of Technical Sciences, Novi Sad, Serbia, 21000; katona.m@uns.ac.rs; ORCID iD: 0000-0002-2365-7975

Abstract: *The paper provides a detailed description of the procedure for measuring the kinematic characteristics of passengers on a zipline. This paper outlines the preliminary steps preceding the measurement itself, provides a list of necessary measuring equipment, and explains its arrangement and connection. There are two specific challenges in measuring the kinematic characteristics of zipline passengers. First, in addition to measuring the passengers' characteristics, it is also necessary to monitor the change of the force in the carrying rope. This force must be measured at the ends of the zipline route, which can span distances greater than one kilometer. The second challenge lies in measuring the travel speed, where both the absolute velocity relative to the rope and the relative velocity concerning the surrounding air must be determined. The latter is crucial, as it directly affects aerodynamic drag values. Finally, observations from a specific measurement session are presented, along with recommendations for future work.*

Keywords: *zipline; measurement; kinematic characteristics; measuring equipment.*

1. INTRODUCTION

This paper presents the methodology for measuring the kinematic characteristics of zipline passengers, with a detailed description of the preparatory steps, selection and arrangement of measuring equipment, as well as the procedure for its connection and application in real conditions. Special attention is paid to the analysis of two key specificities that characterize this process. The first refers to the need to measure, in addition to measuring the kinematic characteristics of the trolley itself, the change in force in the supporting rope [1], and this is possible only at its ends, i.e. at the beginning and end of the route. This means that the sensors are located at distances greater than 1 km. The second specificity refers to the fact that it is not enough to know only the absolute value of the trolley's speed, but it is also necessary to know its relative value measured in relation to the surrounding air in order to include the influence of the wind.

2. MEASURING EQUIPMENT

Within this point a list of the measuring equipment will be given, as well as its layout, that was used during the experimental verification of the zipline mathematical model [2]. Subsequent parts of this section will also describe attempts to utilize alternative equipment, along with the reasons why such approaches proved to be unfeasible. Fig 1 shows following measuring equipment:

- Universal measuring amplifier *QuantumX*, (*MX410B*, *MX440B* and *MX840B*), pos. 1, pos. 9 and pos. 17,
- Software for acquisition and processing of measuring signals *HBM catmanEasy-AP*,
- A computer for storing the measuring signals (*Dell Latitude E7240*), pos. 10,
- Accelerometer *HBM B12*, pos. 19 and pos. 20,
- Inclinometer *Vigor Technology SST20*, pos. 23,
- Antennas for the wireless transfer of the measuring signal *Mirkotik SXT Lite 5*, pos. 6, pos. 7, pos. 14 and pos. 15,
- Rope tension meter *TRC PRO HMU*, pos. 5 and pos. 12,

- Inductive displacement transducers *HBM WA100*, pos. 4 and pos. 13,
- Anemometer for air flow measurement, i.e. differential pressure sensor *NXP Semiconductors MPXV7002* which is connected to a Pitot tube, pos. 22,
- Optical measuring device for the number of revolutions *Monarch Instrument SPSR-115/230*, pos. 21,
- UPS device *nJoy Horus 800*, pos. 18.

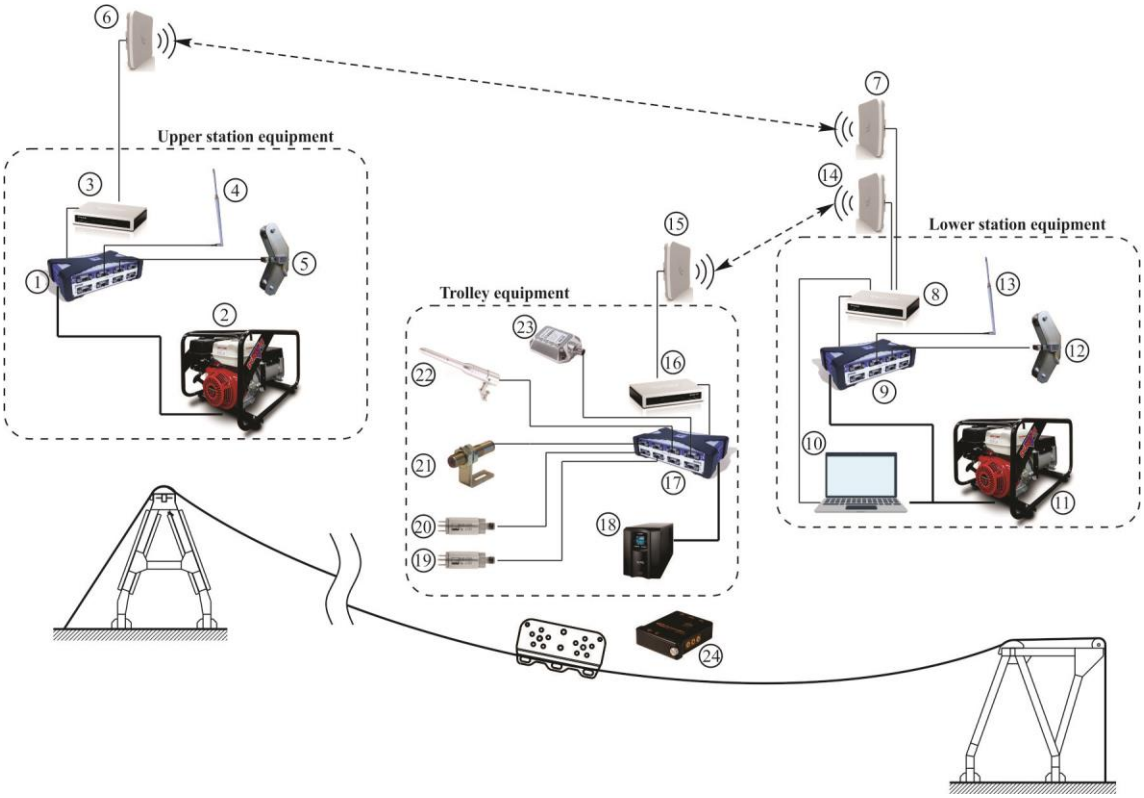

Fig.1. Measuring equipment layout

A more detailed view of the used measuring equipment components can be seen in the Fig. 2.

Fig.2. Detailed view of some measuring equipment

An inductive displacement transducer for measuring rope deflection in the vertical direction (pos. 4) at the upper station is attached to the rope at a distance of 950 mm from the support. A rope tension meter (pos. 5) is attached next to it and moved towards the field. Both devices are connected to the universal measuring amplifier *QuantumX MX440B* (pos. 1) which sends a signal by *SXT Lite 5* antenna (pos. 6) via radio connection to the *SXT Lite 5* antenna (pos. 7) which is connected to the universal measuring amplifier *QuantumX MX410B* (pos. 9) located at the lower station, which is connected to the computer (pos. 10) on which the measured values are monitored and stored.

Fig.3. Rope tension meter

A rope tension meter (pos. 12), as well as an inductive displacement transducer for measuring the deflection of the rope in the vertical direction (pos. 13), are also

installed at the lower station, at a distance of 900 mm from the support. The way in which the rope tension meters and the inductive displacement transducers are attached to the rope are shown in Fig. 3 and Fig. 4.

Fig.4. Inductive displacement transducer

The universal measuring amplifier located at the lower station (pos. 9) also receives, besides from the above-mentioned amplifier (pos. 1), a signal via radio connection from the universal measuring amplifier *QuantumX MX840B* (pos. 17) which collects data from two accelerometers (pos. 19 and pos. 20) located on the trolley, one of which measures "horizontal" accelerations (pos. 20), and the other in the "vertical" (pos. 19) direction of the trolley, as well as one inclinometer (pos. 23) that provides information about the inclination angle of the trolley.

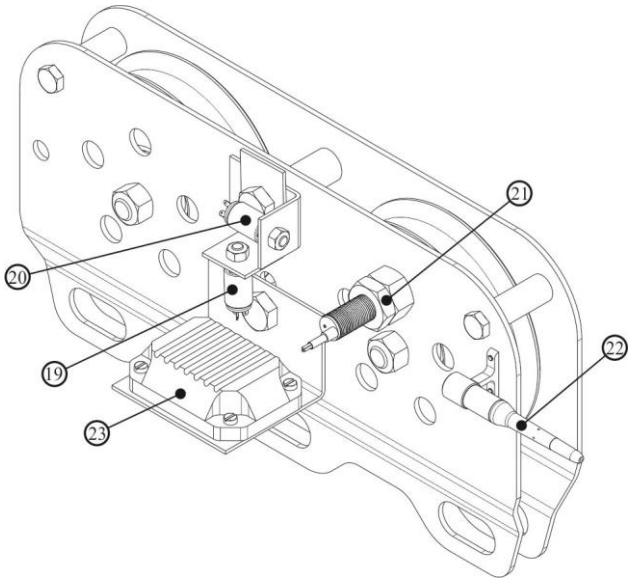

Fig.5. Detailed measuring equipment layout on the trolley

In addition, the aforementioned measuring amplifier also collects the data provided by the optical measuring device for the number of revolutions (pos. 21), i.e. it records the number of revolutions of the wheel on the basis of which the traveled distance can be monitored, as well as the data provided by the differential pressure sensor attached to the Pitot tube (pos. 22), on the basis of which the velocity at which the trolley moves in relation to the surrounding air can be determined.

To track the traveled distance and calculate the speed of movement by monitoring the number of wheel revolutions, a division of 36 black-and-white fields was made on the wheel in order to generate a signal every 10 degrees, as shown in Fig. 6. The figure shows both the divisions printed on paper and those cut from a special reflective foil, since the printed version experienced "skipping" issues due to insufficient reflection under reduced ambient lighting conditions.

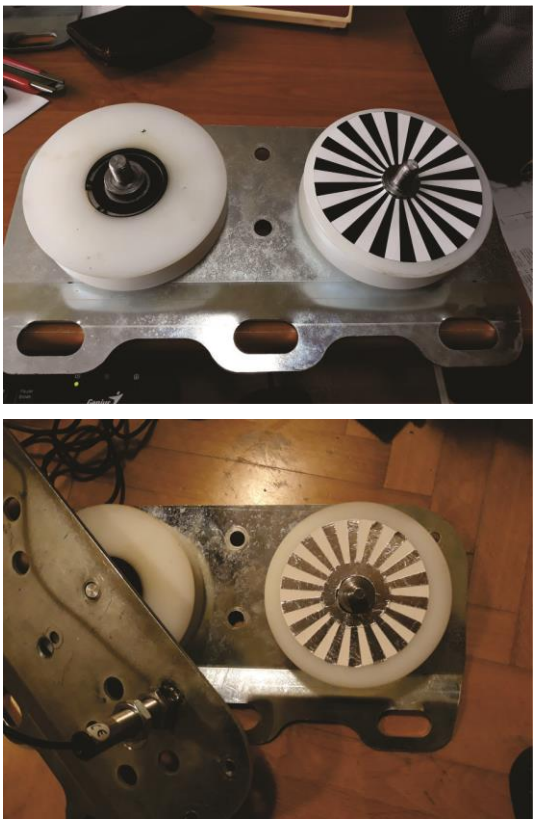

Fig.6. Trolley wheel

The devices at the upper and lower stations were powered using two portable petrol generators (pos. 2 and 11), while the devices on the trolley were powered using a UPS device (pos. 18).

Fig.7. Performance Box Sport GPS device

As an additional verification method, a GPS device of the type *Performance Box Sport* by *Racelogic* was also mounted on the trolley (pos. 24).
The aforementioned device is completely independent from the other equipment and devices. Measurement data is recorded onto a memory card, and power is supplied via a separate battery. Since the device is primarily intended for use in automobiles and is equipped with a 12 V plug, an improvised socket was created, as shown in Fig. 7.
As mentioned earlier, it is not enough to just know the absolute trolley velocity, it is also necessary to have information about the relative velocity in relation to the surrounding air.
To determine the air flow speed, it was initially planned to use a Hot-Wire Thermo-Anemometer model *405i* by *Testo*, shown in Fig. 8. This device does not support connection to the *QuantumX* measuring amplifier and instead connects via Bluetooth to a mobile phone.

Fig.8. Thermal anemometer, [3]

However, the inability to connect to the *QuantumX* did not represent the biggest problem. According to the catalog specifications, the mentioned device is capable of measuring speeds up to 30 m/s, which, considering the maximum expected speed of approximately 85 km/h (23.6 m/s) on the zipline, should have been sufficient. However, the device began displaying errors at speeds significantly lower than the mentioned value. Therefore, an airspeed meter with a Pitot tube and a differential pressure gauge, shown in Fig. 9, was procured.

Fig.9. Pitot tube

For the displayed Pitot tube, several different differential pressure gauges are produced depending on the microcontroller to which the sensor is planned to be connected. However, there is no sensor designed for connection to the universal *QuantumX* measuring amplifier. Therefore, it was necessary to calibrate the sensor, which was carried out under laboratory conditions, as shown in the Fig. 10.

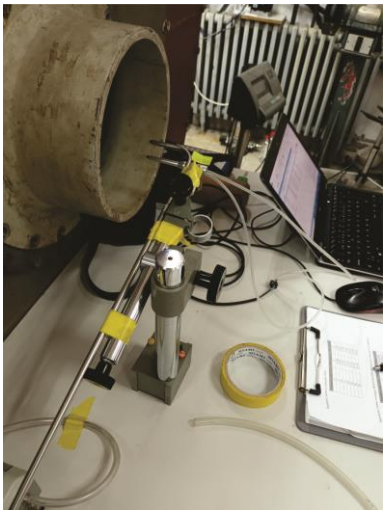

Fig.10. Pitot tube calibration under laboratory conditions

To determine the wind speed and direction at the stations, a mini-meteorological station with an anemometer, shown in Fig. 11, was used. The station is independent from the rest of the measurement equipment.

Fig.11. Mini weather station

Given the exceptionally large distance between the terminal stations (approximately 1.5 km), and considering the movement of the trolley between them, data exchange was carried out using two pairs of *SXT Lite 5* antennas, which are shown in Fig. 12.

Fig.12. Two different types of antennas

The antennas were initially paired so that the measuring amplifier at the upper station sends the collected data to the measuring amplifier on the trolley, which then sends the data measured on the trolley itself to the measuring amplifier at the lower station. However, with this antenna arrangement, a problem arose after the trolley passed the lowest point of catenary, as the signal between the trolley and the upper station was lost in that case.

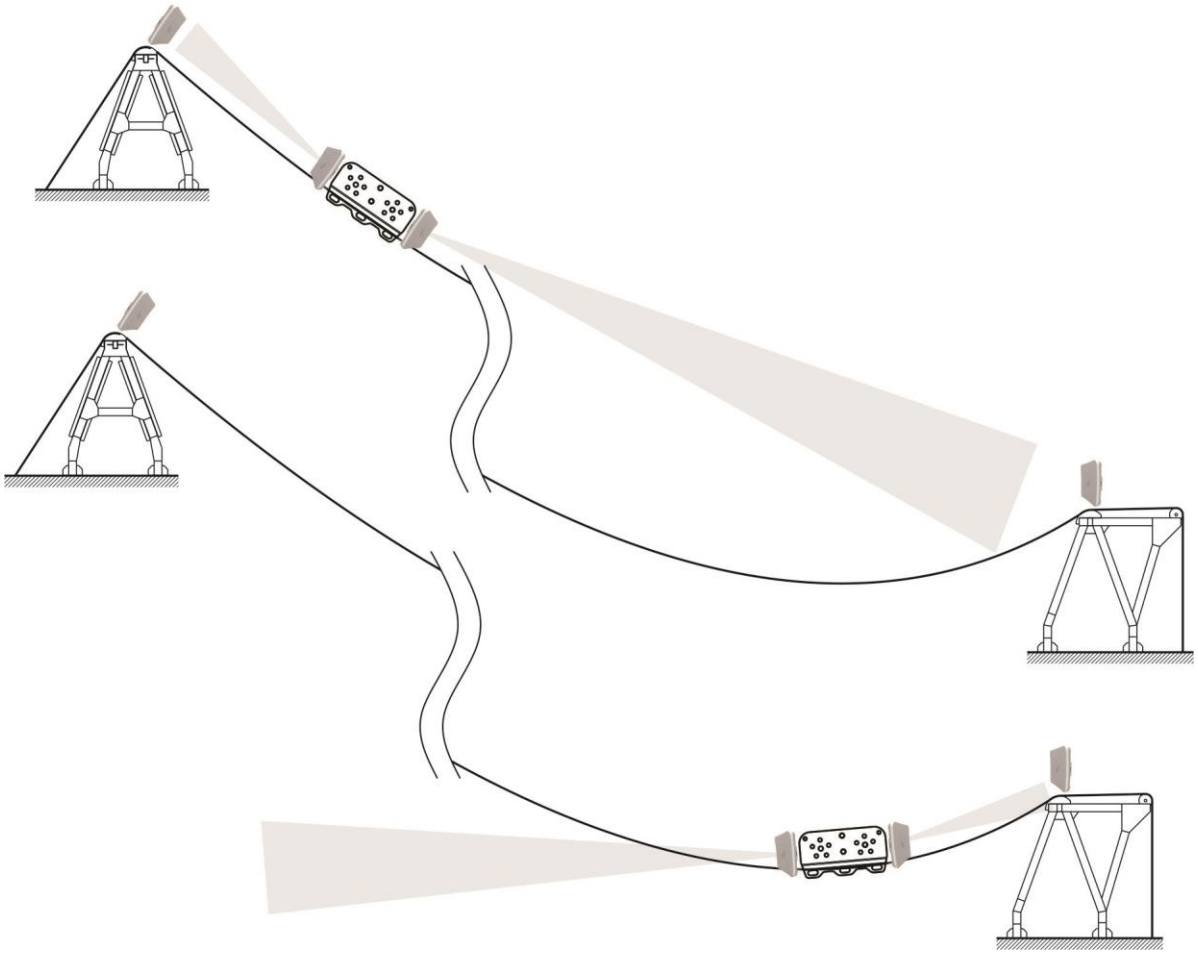

Fig.13. One of the antenna layouts

Since during the movement there is a significantly smaller angle change between the trolley and the lower station compared to the angle change between the trolley and the upper station, in the second variant, the upper and lower stations were paired using one pair of antennas, and the trolley and the lower station were paired using a second pair of antennas (configuration shown in Fig. 1).

3. MEASURING PROCEDURE

The measurement process can be divided into two phases: preparatory activities and the main measurement. Given the relatively large number of sensors used - some of which are positioned at significant distances from one another, and some functioning independently - it was necessary to carefully plan the preparation for the experimental measurements. The participants would first go to the upper station, where they would install the displacement sensor (pos. 4) and the rope tension meter (pos. 5). Since the displacement sensor is mounted to the station's steel structure using a magnetic base, it is crucial to ensure that the sensor is positioned in a strictly vertical orientation. Additionally, after installation, it is necessary to measure the exact distance between the point at which deflection is recorded and the point where the rope rests on the station structure.

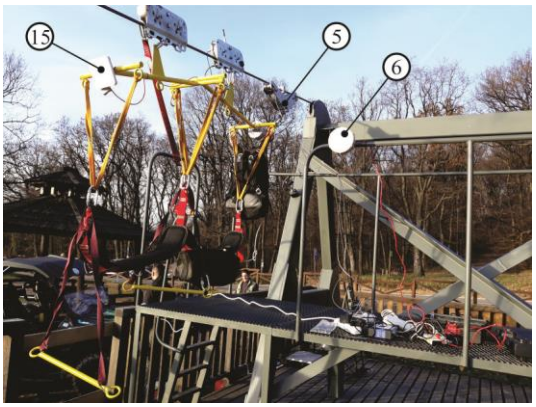

Fig.14. Sensor layout at the upper station

Next, a group of participants proceeds to the lower station, where the procedure is repeated by installing the displacement sensor (pos. 13) and the device for measuring the rope force (pos. 12). Following this, the sensors are connected to the measurement amplifiers

(pos. 1) and (pos. 9), and then the antennas (pos. 6) and (pos. 7) are connected. The antennas are then adjusted to identify positions at each station where the signal strength is maximized, after which they are fixed in place.

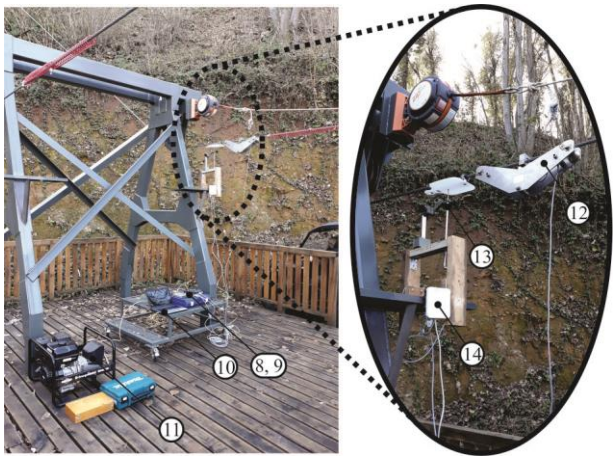

Fig.15. Sensor layout at the lower station

The main measurement phase can also be divided into two phases. The first phase involves measuring the static parameters of the unloaded rope, and the second encompasses the recording of all other quantities. In the first segment, a connection is established between the measuring amplifier (pos. 1) located at the upper station and the amplifier (pos. 9) at the lower station. During this phase, the rope tension values measured by the rope tension meters at the upper (pos. 5) and lower (pos. 12) station are recorded, along with the instantaneous readings of the displacement sensors at the upper (pos. 4) and lower (pos. 13) stations. The displacement sensor values may be zeroed, as only the change in deflection during the descent is required for validation, rather than their absolute values.

Afterwards, the trolley and passengers are placed on the rope. Since the passengers carry a GPS device on the trolley, which operates independently from the rest of the measurement system, the device is activated first, followed by a verification to ensure that all sensors are functioning and recording data properly.

The release of the trolley with passengers must be carried out under completely steady conditions. To ensure a "tangential" release and thereby avoid the effects of vertical "drop", the passengers are positioned for descent, while two operators at the upper station hold the trolley. The passengers lift their legs off the platform and remain suspended in their harnesses. Once any swinging motion has fully subsided, the trolley is released without any additional pushing force.

4. CONCLUSION

As noted in the introduction, this paper provides a detailed description of the measurement equipment, its layout, as well as the procedure for measuring the kinematic characteristics of passengers descending along the zipline. Theoretical foundations that motivated the measurements presented in this study can be found not only in [2] but also in [4] and [5]. The measurements described herein were used to validate a mathematical model that enables rapid and straightforward determination of the kinematic parameters of zipline passengers. This model can serve as a basis for the design of zipline systems, as well as for the selection of appropriate braking devices [6].

REFERENCES

[1] Jojić, T., Vladić, J., Đokić, R.: Anchorage type and tension rope force impact on zipline's kinematic characteristics. *Machine Design*, Vol. 11, No. 4, pp. 149-154, 2019.

[2] Jojić, T., Vladić, J., Đokić, R.: Zipline mathematical model forming, experimental verification and analysis of influential parameters. *Archive of Applied Mechanics,* Vol. 93, No. 11, pp. 4157-4180, ISSN 1432-0681, 2023.

[3] https://www.testo.com/en/testo-405i/p/0560-1405, accesed on 08.05.2025.

[4] Vladić, J., Đokić, R., Jojić, T.: Teorijska analiza i određivanje parametara kretanja kod ZIPLINE-a. *Tehnika*, Vol. 68, No. 3, pp. 405-412, 2019.

[5] Jojić, T., Vladić, J., Đokić, R.: Zipline Design Issues and Analysis of the Influencing Parameters on Passenger's Velocity. *Proceedings of the fifth international conference "Mechanical engineering in XXI century – MASING 2020"*, 09-10 December 2020, Niš, Serbia, pp. 129-132.

[6] Jojić, T., Vladić, J., Đokić, R.: Determination of zipline braking distance. *Proceedings of KOD 2021 "Machine and Industrial Design in Mechanical Engineering"*, 10-12 June 2021, Novi Sad, Serbia, pp. 707-712.

Advanced Technologies in Mechanical Engineering

11th International Scientific Conference
IRMES 2025
Research and Development of
Mechanical Elements and Systems
June 19 – 21, 2025; Vrnjačka Banja, Serbia

Original scientific paper DOI: 10.46793/IRMES25.095S

NUMERICAL ANALYSIS OF FOUR TYPES OF ARC STAR SHAPED AUXETIC STRUCTURES

Vladimir SINĐELIĆ[1]
Snežana ĆIRIČ-KOSTIĆ[2]
Aleksandar NIKOLIĆ[3]
Nebojša BOGOJEVIĆ[4]

[1] University of Kragujevac, Faculty of Mechanical and Civil Engineering in Kraljevo, Kraljevo, Serbia, 36000
sindjelic.v@mfkv.kg.ac.rs; ORCID iD: 0000-0001-5728-8218
[2] University of Kragujevac, Faculty of Mechanical and Civil Engineering in Kraljevo, Kraljevo, Serbia, 36000;
cirickostic.s@mfkv.kg.ac.rs; ORCID iD: 0000-0002-9684-0850
[3] University of Kragujevac, Faculty of Mechanical and Civil Engineering in Kraljevo, Kraljevo, Serbia, 36000;
nikolic.a@mfkv.kg.ac.rs; ORCID iD: 0000-0003-2548-4083
[4] University of Kragujevac, Faculty of Mechanical and Civil Engineering in Kraljevo, Kraljevo, Serbia, 36000;
bogojevic.n@mfkv.kg.ac.rs; ORCID iD: 0000-0003-3951-3519

Abstract: *This paper presents a numerical investigation of four types of auxetic star-shaped structures: the conventional 2D Arc Star-Shaped (2D-AS), the Improved 2D Arc Star-Shaped (i2D-AS), the newly proposed Tangent 2D Arc Star-Shaped (t2D-AS), and the standard 2D Star-Shaped (2D-SS) structure. By modifying the geometry of the original 2D-AS structure, the t2D-AS variant was developed and analyzed for the first time. All structures were designed to maintain the same geometric parameters, allowing for a consistent comparison of their mechanical properties. Numerical simulations were performed using the finite element method in ANSYS Workbench under periodic boundary conditions, with a focus on evaluating Poisson's ratio and Young's modulus. The i2D-AS structure exhibited the highest stiffness due to the use of circular arches, while the t2D-AS structure demonstrated the lowest relative density, making it a promising candidate for lightweight applications. Although its mechanical properties are slightly lower than those of the 2D-SS, the t2D-AS offers a favorable balance between structural efficiency and weight reduction. Future research will focus on the analytical modeling and energy absorption capabilities of the newly proposed structure.*

Keywords: *Auxetic structure, Negative Poisson's ratio, FEM, Young's modulus, Lightweight design.*

1. INTRODUCTION

Auxetic structures are artificially designed structures aimed at reducing weight and adding new mechanical properties, such as high impact resistance [1-5]. The term auxetic is of Greek origin and means increase [1-3]. Thanks to their design, auxetic structures contract under loading which allows them to absorb energy efficiently upon impact, unlike conventional materials (Fig.1).

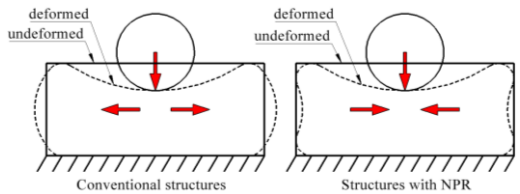

Fig.1. The difference between conventional structures and structures with NPR [1]

A new mechanical property that auxetic structures impart to materials is a negative value of the Poisson's ratio (NPR in the further). These structures have found wide application across various industries such as aerospace, automotive, defense, space, construction, medicine, textile industry, and more [1-5].

In this paper, we present a new design of a 2D auxetic structure, based on the previously developed 2D Arc Star-Shaped structure (2D-AS in the further) [4]. The mechanical properties of the newly designed structure, named the 2D Tangent Arc Star-Shaped structure (t2D-AS in the further) due to its unique geometry, were investigated numerically. The obtained results were compared with those of the Improved 2D Arc Star-Shaped structure (i2D-AS in the further) [5] and the conventional star-shaped structure (2D-SS in the further). The mechanical properties of the structures were compared using a numerical method.

2. DESIGN OF THE 2D STAR STRUCTURE

In Fig.2(a-d), four representative volume elements (RVE in the further) are shown. Based on the 2D-AS structure [4] (Fig.2(a)), three structures (Fig.2(b-d)) were designed, which retain the geometric parameters of the basic RVE 2D-AS structure. The modification of *i*2D-AS, shown in Fig.2(b), is explained in reference [5]. RVE *t*2D-AS shown in Fig.2(c) was obtained by removing the straight parts and part of the arc of the 2D-AS structure marked by red line. From the intersection of the straight roads, two roads were drawn marked by the purple line that tangents the arc of 2D-AS structure. The method by which it was obtained gives it the prefix name tangent, or *t*2D-AS. The classical star structure, 2D-SS, in order to retain the geometric parameters RVE of the 2D-AS structure, was obtained in the same manner as *t*2D-AS structure, except that the roads tangential to the arc of the 2D-AS were extended until they intersected the vertical and horizontal rods, marked in green shown in Fig.2(d).

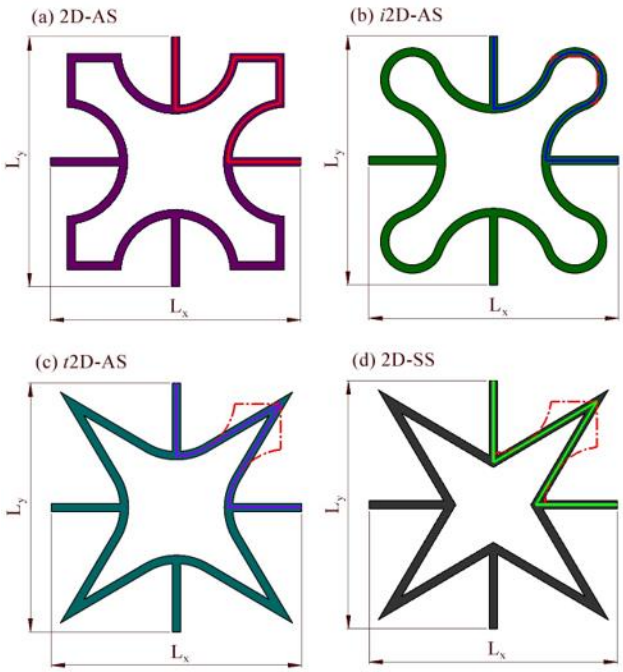

Fig.2. RVE: (a) 2D-AS [4]; (b) i2D-AS [5]; (c) t2D-AS; (c) 2D-SS

2.1. Geometric parameters of structures

All four structures have the same geometric parameters defined by the 2D-AS structure, which are: the total length of the structure in the horizontal and vertical direction L_x and L_y, respectively, (see Fig.2(a-d)), the half length L, the hight h, depth d, the thickness t, the arc radius r, the arc angle θ, as shown Fig.3(a-d). And the design coefficients a and b must satisfy the condition $0<a<1$ and $0<b<1$ [1-5].

By the relationship between the geometric parameters ah and bh, the parameters θ and r can be determined, as defined in reference [4], as follows:

$$\theta = 2\arctan\frac{bh}{ah}, \tag{1}$$

$$r = \frac{ah}{\sin\theta}. \tag{2}$$

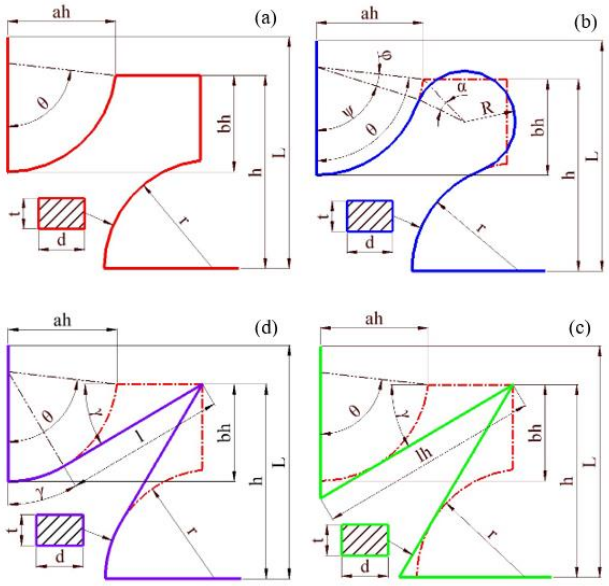

Fig.3. Geometric parameters: (a) 2D-AS [4]; (b) i2D-AS [5]; (c) t2D-AS; (c) 2D-SS

According to reference [4] and reference [5] relative density for 2D-AS and *i*2D-AS can be written:

$$\rho_{r2D-AS} = \frac{t\pi\theta(ah)^2}{180l^2\sin^2\theta} + \frac{2t(l+bh-ah)}{l^2}, \tag{3}$$

$$\rho_{ri2D-AS} = \left(L-h+bh+(\pi+2\alpha)R+2r\psi\right)\frac{t}{L^2}. \tag{4}$$

where, the angle ψ and the angle φ explained in reference [5].

The geometric description of *t*2D-AS structure requires the introduction of two new geometric parameters to describe it as a function of the geometric parameters of the 2D-AS structure. These geometric parameters are the length of the rod l, which tangents part of the arc of radius r, and the angle γ, which represents the angle between the rod l and the removed vertical and horizontal rods of the 2D-AS structure, as shown in Fig.3(c).

For calculating the length of the rod l and the angle γ as a function of the geometric parameters ah and bh, the following two equations are used, respectively:

$$l = \frac{h}{\cos\gamma} - r\tan\gamma, \tag{5}$$

$$\frac{\left(r-h\sin\gamma\right)}{\cos\gamma}=r\cos\theta\,. \tag{6}$$

Then the relative density of the RVE of the *t*2D-AS can be represented as:

$$\rho_{rt2D-AS}=\left(2r\gamma+2\frac{h-r\sin\gamma}{\cos\gamma}+L-h+bh\right)\frac{t}{L^2} \tag{7}$$

The of RVE the of 2D-SS structure has one new geometric parameter *lh* which is the length of the rod than tangents the removed arc *r* of the 2D-AS and intersects the horizontal and vertical rods, and take the angle γ from the *t*2D-AS (see Fig.3(d)). For calculating the parameter *lh* as a function of *ah* and *bh*, as follows:

$$lh=\frac{h}{\cos\gamma} \tag{8}$$

Then the relative density of the RVE of the 2D-SS can be represented as:

$$\rho_{r2D-SS}=\left(2\frac{h}{\cos\gamma}+L-h+h\tan\gamma\right)\frac{t}{L^2} \tag{9}$$

2.2. The values of the geometric parameters and the comparison of the relative densities of the structures

For the analysis of four types of structures, one set was applied. Value of *ah* varies from *10mm* to *18mm* with step of *2mm*, while *bh* is constant [4-5]. The other geometric parameter values is *h=25mm, L=30mm, bh=12.5mm, t=2mm, d=3mm*.

The values for the relative density of all four types of structures are shown in in Fig.4.

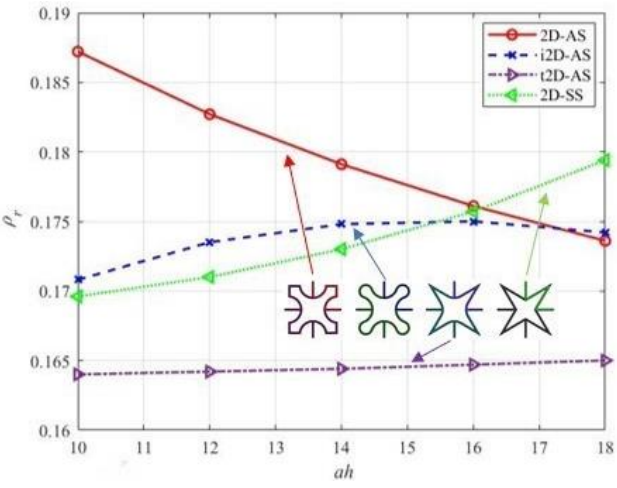

Fig.4. The change in relative density with variation parameter ah

3. NUMERICAL MODEL

All four types of metamaterials, with varying geometric parameters, were designed in SolidWorks. For the numerical analysis of the influence of Poisson's ratio and Young's modulus on the metamaterial, we used ANSYS Workbench module Static Structural. The material used in numerical analysis is isotropic, and its characteristics are: Young's modulus E_m*=1740 MPa*, Poisson's ratio v_m*=0.4* and a density ρ_m*=1150 kg/m*^{3} [4]. In all analysed models, the Hex Dominant method was applied, the element order is Use Global Setting, and free face mesh type is Quad/Tri. This approach ensures that the numerical model includes the Solid186 element, which is a higher order 3D element, defined by 20 nodes, each with three degrees of freedom. Element size is *0.25mm*. In Fig.5. is shown an example of a generated mesh on the *i*2D-AS structure.

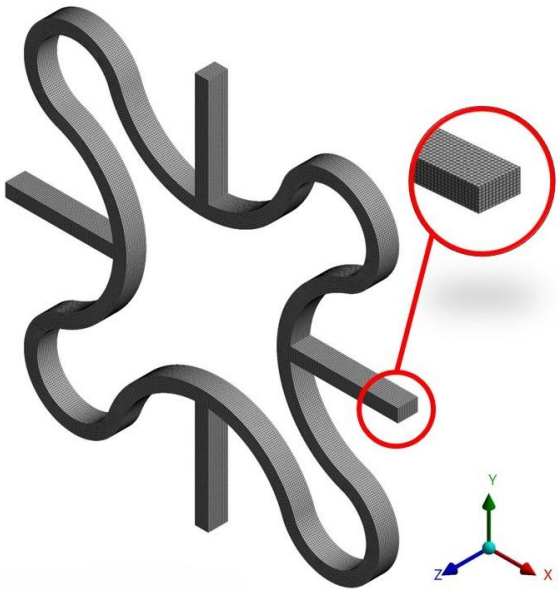

Fig.5. The generated mesh on the i2D-AS structure

To simulate periodic boundary conditions (PBC in the further) on as structure, boundary conditions applied at the ends of the metamaterials, as shown for example in the Fig.6. At the ends of rods A, B and C, remote displacement is applied, while end D is free. At end A od rod, only horizontal displacement along the *x*-axis is free. At end B, vertical displacement along the *y*-axis is free. At end C, a fixed displacement of *-3 mm* in the vertical direction is given, while displacement in the horizontal direction is free. The output result from the software is the reaction force in the vertical direction at point C, necessary for calculating the Young's modulus, and the horizontal displacement of point D, necessary for calculating the Poisson's ratio of the metamaterial.

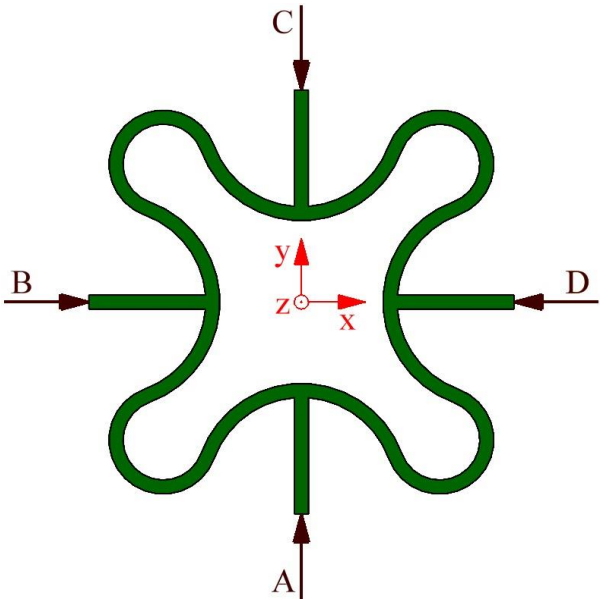

Fig.6. Example PBC on the i2D-AS structure

The values for NPR and Young's modulus are calculated using the following equations [1-5]:

$$\nu = -\frac{\varepsilon_x}{\varepsilon_y} = -\frac{\delta_x \cdot L_y}{\delta_y \cdot L_x}, \tag{10}$$

$$E_y = \frac{\sigma_y}{\varepsilon_y} = \frac{F_y / A}{\delta_y / L_y} = \frac{F_y \cdot L_y}{\delta_y \cdot t \cdot L_x}. \tag{11}$$

where, ε_x and ε_y strain in horizontal and vertical direction, δ_x and δ_y displacement in horizontal and vertical direction, σ_y normal stress in vertical direction, F_y reaction force in vertical direction and $A=tL_x$ cross-sectional area occupied by the structure in space.

3.1. Results of the numerical analysis

Under the influence of vertical loading in the vertical direction, all four structures exhibit high stress concentration at the points where the vertical and horizontal beams connect with the arches (2D-AS, *i*2D-AS and *t*2D-AS), or at the intersection of three beams, as is the case with the 2D-SS. In the 2D-AS, *t*2D-AS and 2D-SS structures, stress concentration also occurs at the points where other beams in the structure intersect at certain angles. This phenomenon is avoided in the *i*2D-AS structure because such beams are replaced by a circular arch. Fig.7 shows the Von-Mises stress nephograms for all four types of structures for the values *ah14*. Fig.8 presents the results for Poisson's ratio and Young's modulus for the variation of parameter *ah*.

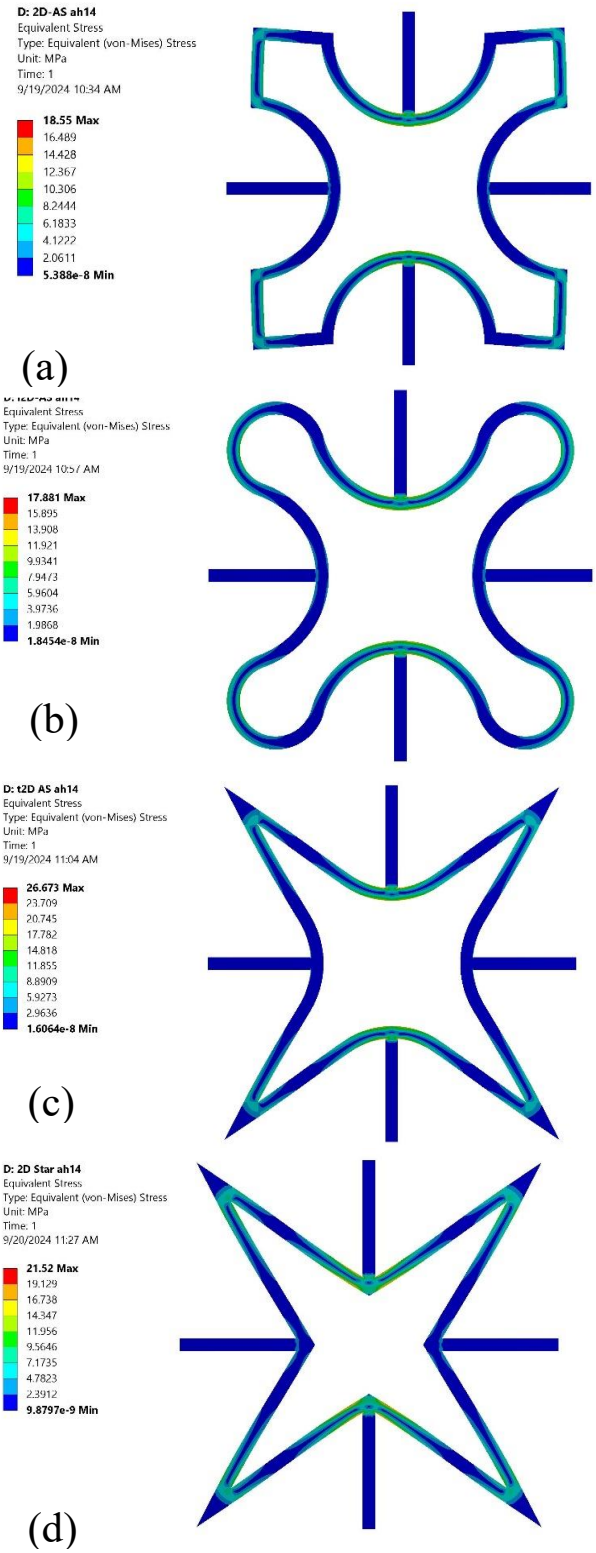

Fig.7. Von-Mises stress nephograms for ah14

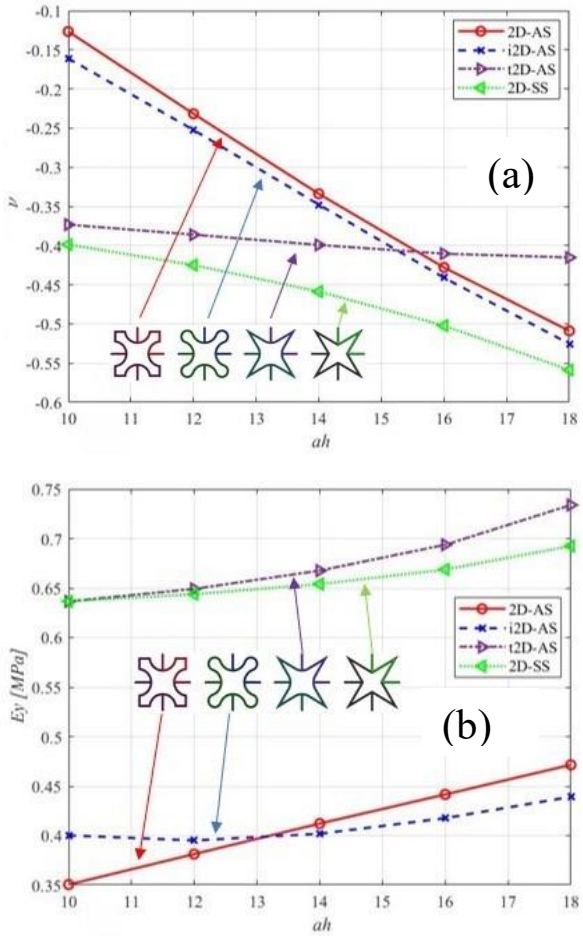

Fig.8. The change in NPR (a) and Young's modulus (b) with variation parameter ah

CONCLUSION

The aim of this paper is to numerically determine and compare the mechanical properties of four types of star-shaped structures. Additionally, by manipulating the geometry of the 2D-AS, a new structure, *t*2D-AS, was obtained, which proved to be the lightest structure compared to the remaining three. Considering its weight advantage, the NPR and Young's modulus values for *t*2D-AS, although lower compared to the traditional 2D-SS, are still very close to those of the 2D-SS for the given geometric parameters. Thanks to its arches, *i*2D-AS has shown that for most variations of geometric parameters *ah* it has the best Young's modulus values. In future work, it will be necessary to analytically and numerically examine the new *t*2D-AS structure, and it would also be very interesting to investigate and compare energy absorption values for all four structures.

ACKNOWLEDGMENT

This paper is a result of the research conducted within the project grant number 451-03-137/2025-03/200108 supported by the Ministry of Science, Technology and Innovation of the Republic of Serbia and the CEEPUS project grant "Building Knowledge and Experience Exchange in CFD - RS-1012-10-2425" supported by the Central European Exchange Program for University Studies.

REFERENCES

[1] Sinđelić V., Nikolić A., Bogojević N., Ćirić Kostić S., Minak G.: Analytical and numerical analysis of the modified 2D arc-star-shaped structure with negative Poisson's ratio. *Engineering TODAY,* Vol. 3, No. 1, pp. 55-62, ISSN 2812-9474, 2024

[2] Sinđelić V., Nikolić A., Bogojevič N., Erić Cekić O., Ćirić Kostić S.: Modified 2D arc-star-shaped structure with negative Poisson's ratio. *In: XI International Triennial Conference on Heavy Machinery-HM 2023*, pp. E.21–E.26. Faculty of Mechanical and Civil Engineering in Kraljevo, Vrnjačka Banja, 2023

[3] Sinđelić V., Ćirić Kostić S., Bogojevič N., Nikolić A.: Numerical Analysis of the Modified 3D Arc-Star-Shaped Auxetic structure. *In: KOD 2024*, pp. 695–705. 12th Int'l Conference on Machine and Industrial Design in Mechanical Engineering, Balaton, 2024

[4] Zhang, Z.Y., Li, J., Liu, H.T., Wang, Y.B.: Novel 2D arc-star-shaped structure with tunable Poisson's ratio and its 3D configurations, *Materials Today Communication*, Vol. 30, pp. 1–13, ISSN 2352-4928, 2022

[5] Sinđelić V., Nikolić A., Minak G., Bogojevič N., Ćirić Kostić S.: An improved 2D arc-star-shaped structure with negative Poisson's ratio: In-plane analysis. *Materials Today Communication*, Vol. 37, pp. 1–12, ISSN 2352-4928, 2023

11th International Scientific Conference
IRMES 2025
Research and Development of
Mechanical Elements and Systems
June 19 – 21, 2025; Vrnjačka Banja, Serbia

Original scientific paper DOI: 10.46793/IRMES25.101D

COMPARISON OF CONVENTIONAL AND IMACHINING STRATEGIES USING THE SOLIDCAM SOFTWARE

Eleonora DESNICA[1]
Ivan PALINKAŠ[2]
Dejan LANDUP[3]
Mića ĐURĐEV[4]
Borivoj NOVAKOVIĆ[5]
Luka ĐORĐEVIĆ[6]

[1]University of Novi Sad, Technical Faculty "Mihajlo Pupin", Zrenjanin, Serbia, 23000, eleonora.desnica@tfzr.rs; ORCID iD: 0000-0002-4724-5764
[2]University of Novi Sad, Technical Faculty "Mihajlo Pupin", Zrenjanin, Serbia, 23000, ivan.palinkas@uns.ac.rs, ORCID iD: 0000-0001-9253-1375
[3]University of Novi Sad, Technical Faculty "Mihajlo Pupin", Zrenjanin, Serbia, 23000, dejan.landup@tfzr.rs, ORCID iD: 0009-0009-3836-2182
[4]University of Novi Sad, Technical Faculty "Mihajlo Pupin", Zrenjanin, Serbia, 23000, mica.djurdjev@tfzr.rs, ORCID iD: 0000-0002-1825-2754
[5]University of Novi Sad, Technical Faculty "Mihajlo Pupin", Zrenjanin, Serbia, 23000, borivoj.novakovic@tfzr.rs, ORCID iD: 0000-0003-2816-3584
[6]University of Novi Sad, Technical Faculty "Mihajlo Pupin", Zrenjanin, Serbia, 23000, luka.djordjevic@uns.ac.rs, ORCID iD: 0000-0003-4578-9060

Abstract – *Material processing by chip removal is one of the crucial manufacturing processes, accounting for approximately 70% of all manufacturing processes in the global market. Given the machining industry's economic significance, both in Europe and worldwide, optimizing this process is essential. The modern market demands high-quality products in the shortest time and at the lowest cost, pushing companies to enhance efficiency and remain competitive. In machining technology, efforts focus on minimizing both auxiliary and machining times while reducing production costs. Advancements in software development have enabled high-speed and high-productivity machining. Various CAM (Computer-Aided Manufacturing) systems, such as SolidCAM, Catia, NX, and MasterCAM, support CNC programming. This study analyzes SolidCAM, one of the most widely used CAM software due to its extensive tools and capabilities. The paper compares two machining strategies within SolidCAM—the conventional method and the iMachining module—evaluating their advantages and disadvantages. The objective is to develop a control program using SolidCAM and, through comparative analysis, determine the suitable and efficient programming approach.*

Keywords – machining; SolidCAM; iMachining; machining time.

1. INTRODUCTION

When it comes to CNC (Computer Numerical Control) machines, today's production processes cannot be imagined without CAD (Computer Aided Design) and CAM (Computer Aided Manufacturing) programs, which significantly facilitate the entire production process, from designing to the final product [1]. CAD software, as the name only speaks, serve as a constructor in the design of the desired element, allowing faster and more precise performance than it would be possible in manual design [1-3]. On the other hand, CAM software is used to generate programs that CNC machine recognizes and uses to process an element according to the correct defined specifications [4]. When talking about production processes on CNC machines, turning, milling and cutting is most often thought. CAM tools play a key role in automating these processes, because they allow a wide range of options for efficient and precise production [5]. Although there are several different CAM software, all of them have the same purpose - generating programs for CNC machine, while the methodology of arrival to goal can be significantly different [6]. Some of the most

famous CAM software include SolidCam, MasterCam, Fusion 360, Hypermill, Catia, Edgecam, NX. The key role of these software is in reducing the time required for production, which leads to reducing total costs, extending tools life, faster adaptability in processing, as well as better fulfillment of market requirements [6]. In this paper, it will be discussed in more detail about SolidCam, including its functions, operations, advantages and disadvantages, with a special accent to iMachining module in this software. For further analysis the examples of milling machining operations will be used to show the functioning of conventional milling and iMachining modules.

2. CAM MACHINING PROCESS AND SOLIDCAM SOFTWARE

Machining process that uses CAM software is shown of Fig. 1.

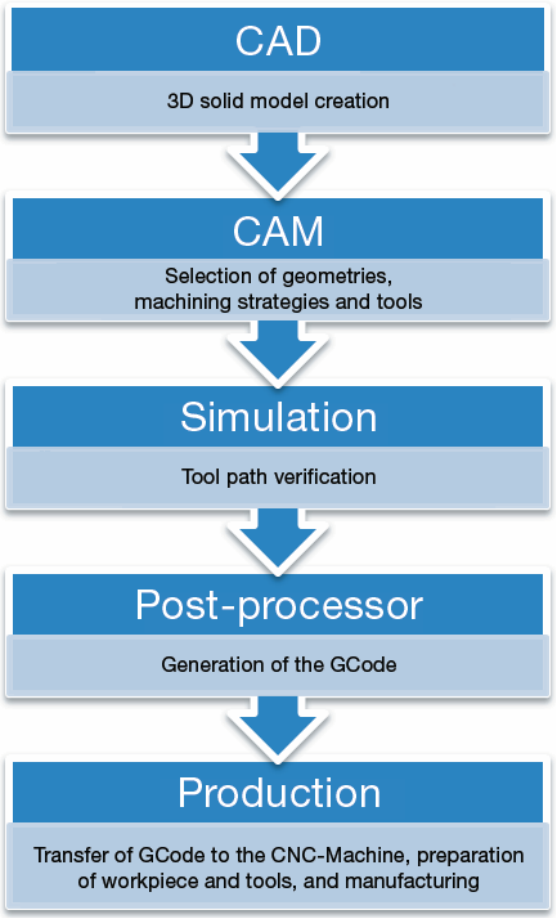

Fig. 1. Part machining procedure with usage of CAM [7]

Part production as shown on fig. 1 have stages. In the first stage (CAD) part is designed as 3D model in CAD software. In this stage the part can be redesigned, analyzed and verified without the need to manufacture physical part [8-10]. In second stage the design is imported in CAM software, and all the geometries, machining strategies and tools are defined for part production. In third stage the simulation of machining process is conducted for the purpose of tool path verification. In this stage, if there are any errors made in second stage, it can be determined and necessary correction can be made. For the generation of the GCode (stage 4) the CAM software uses post-processor that is needed to generate adequate GCode for the CNC machine Controller that is used in production. Without post-processor GCode can not be exported to the machine, and also, the whole machining operation is defined with machine that will be used in production. The fifth stage is production of part on CNC machine. GCode is transferred to the machine, and workpiece and tools are prepared for production.

For the serial production, the stages 1 – 4 are only needed for the first part.

SolidCam is software primarily used to program machining on CNC machines. The most common types of machining that are performed include turning and milling, but also there are other while other machining process such as drilling, engraving, cutting, etc. This program offers many benefits in production planning. In SolidCAM, except that all machining processes are defined (containing all machining parameters and which CNC machine can recognizes and perform), the possibility of inspecting all parameters related to machining is extremely important). These parameters can be adapted to needs, but should pay attention to certain boundaries, such as: drilling / cutting depth, tool movement, path tools, path of tool support, etc. In addition to the parameters optimization for more efficient and productive production, extremely useful functionality is also a SolidCAM simulation of operations. The simulation enables the visualization of tool movements in accordance with the generated G-code, ie in accordance with previously defined parameters such as tool selection, tool movement, order of operations. If any irregularity or deviation is determined, such as: poorly defined parts, wrong order or any improper machining parameter, error must be immediately corrected and generate a new GCode created for the machining process on the CNC machine. The most compatible CAD program with SolidCAM is SolidWorks, especially in terms of transfer and understanding of 3D models. Since both software has been developed by the same company, it is possible to open SolidCAM within SolidWorks. One of the biggest advantages of their integration is automatically updating all changes to the 3D model in SolidCam.

2.1. SolidCAM machining operations

SolidCAM SolidCAM consists of different operating modules (submodules) that are used for machining the desired part. These sub-modules have been developed to meet the requirements of both small- and large-scale production. SolidCAM consists of four main modules:

- Milling,
- Turning,
- Mill-Turn (combination of milling and turning),
- Wire Cut.

Given that the paper is based on the comparative analysis of conventional and iMachining operations during milling, some of the operations that can be performed are: Face Milling, Profile Milling, Pocket Milling, Drilling, Thread Milling, Slot Milling, T-Slot Milling.

Face Milling is usually the first operation used to smooth the top surface of the workpiece. Large-diameter face milling cutters are most often used, as they enable the machining of large surfaces in the shortest possible time.
Profile Milling is one of the most common operations in conventional machining, along with Pocket Milling. This operation removes the material around the desired outer contour in order to obtain the desired geometric shape of the part.
Pocket Milling is the most commonly used operation in SolidCAM in conventional machining. This operation is the opposite of the profile milling operation and is usually applied immediately after profile milling. When the desired external shape of the contour of the element is achieved by Profile Milling, Pocket Milling is used for the internal machining of the part. Also, there is a special case of "open pocket" milling, which can be done faster and more efficiently because the outer contour is already open. This method can only be applied if it is not harmful to the tool or the workpiece, which can be checked by comparing the defined and allowed parameters or by running a machining simulation.
Drilling operations can be carried out in different ways, depending on the type of opening or hole that is required. The parameters of this operation can be verified, and drilling simulation allows precise control. Some of the operations available are: Drilling, F_Drill, Peck, Tapping, Boring, F_Boring.
Slot Milling is a characteristic operation in which the geometry of the groove is defined, with the possibility of making two types of grooves. The first type of groove has a constant depth, while the second type can have a conical shape or a variable depth of milling. If the depth of the groove is constant, this operation is very similar to the profile milling operation.

2.2. SolidCAM iMachining

iMachining is a module in the SolidCAM program that focuses on increasing the load on the cutting tool, thereby increasing the efficiency of material removal and reducing machining time. Reduction of machining time can be achieved in several ways. One of the key factors is the reduction of idle time, which significantly affects the total machining time. The goal is for the tool to be constantly engaged, which enables continuous removal of material. If idle runs are necessary, it is important that the tool is not returned to the "zero" position, but that the repositioning maneuver is performed on a new safety plane that accommodates the material already removed.
An increase in axial depth and width of cut results in an increase in the volume of chips to be removed, which can also contribute to a reduction in machining time. However, it is important to pay attention to the durability and service life of the tool. Regardless of the methods to reduce machining time, if tool degradation occurs during the machining, it can cause a serious problem. One of the main factors that negatively affect tool life is vibration, which increases cutting forces and tool load. Vibrations are related to thermal loads, but when using the iMachining module, it was found that almost 95% of the heat produced during machining is dissipated by the chips, which means that only a small percentage of the heat affects the machining tool.
In addition to vibration and temperature, it is important to pay attention to the surface of the cutting layer, as well as to ensure that the volume of material to be removed is in accordance with the chip removal conditions that are allowed. By using the iMachining module, it is possible to increase the life of the tool, with regular periodic checks of the condition of the tool.
The procedure of iMachining process is shown on Fig. 2.

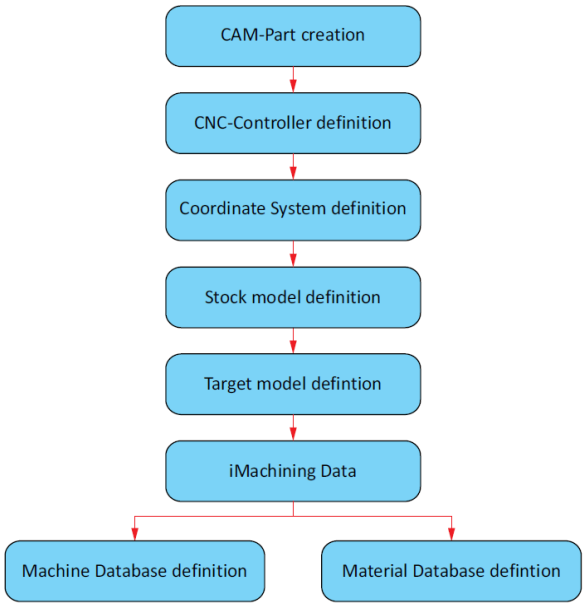

Fig. 2. iMachining Process [11]

As shown on fig. 2. there are the following stages: [11]
CAM-Part creation. At this stage, CAM-Part name and location needs to be defined.
CNC-Controller definition. The choice of CNC-Controller is a necessary step. That choice influences the Coordinate System definition and the Geometry definition.
Coordinate System definition. The origin for all machining operations of the CAM-Part must be defined.
Stock model definition. In this stage SolidCAM enables user to define the stock model, as initial state of workpiece.
Target model definition. SolidCAM enables user to define the model of the part in its final state after the machining.
iMachining Data. User have to define the machine and work material parameters. The Technology Wizard requires this data to automatically determine the optimal Cutting conditions for an iMachining operation [12].

3. COMPARATIVE ANALYSIS OF MILLING AND IMACHINING OPERATIONS

Conventional toolpath strategies do not use to full extent the possibilities of modern CNC machines. The biggest problem is the uneven load on the cutting tool, even if the depth of cut is constant. Not only is the load not uniform, in critical places there are much higher forces than in

other places. During rough machining, there are more critical places, where higher loads occur, which can lead to tool breakage.

CAM software manufacturers have been trying for years to develop new tool path strategies that ensure even loading of cutting tools. Which makes it possible to use a depth of cut several times greater than the diameter of the tool.

The characteristic of these new strategies is that the path of the tool does not have to follow the contour of the piece, but when defining it, the software tries to keep some parameters (grip width, grip angle, revolutions, displacement) at constant values, or change them if necessary. These corrections give a more even load on the cutting tool.

iMachining module provides constant load on the cutting tool. As mentioned the, reduction of the machining time can be achieved if there is an increase in cutting efficiency by:

- reduction of time of tool repositioning and returning to the safety plane, the goal is for the tool to always be in the grip, which ensures the consistency of material removal, and therefore less main machining time,
- an intelligent software solution that, if it is not necessary, the tool is not returned to the safety plane, but that the repositioning of the tool is done on a new safety plane that is generated in relation to the already removed material,
- by increasing the chip removal volume, which increases by increasing the axial cutting depth, cutting width and chip length.

For the comparative analysis of conventional machining (milling) and iMachnining operation two parts are used [13]. One of the distinctive characteristics between this two technologies is creation of toolpath. The purpose is to show if there will be the difference in machining time of the workpiece. The manufacturing parameters for milling operations are shown in Table 1. The tool depth a is defined in order to mill part in one pass. On Fig. 3 and Fig 4, the 3D model of parts is shown (Part 1 and Part 2).

On Fig. 5 and Fig. 7, the toolpath for milling operation can be seen, and on Fig. 6 and Fig 8 the toolpath for iMachining operation is shown. Comparing the toolpath it can be determined that the algorithms for both machining procedures work differently and give different results regarding machining time.

Table 1. Machining parameters for milling operation

	Part 1	**Part 2**
Stock size [mm]	140x140x40	250x180x50
Tool dimension [mm]	8x50 (40)	8x50 (40)
Tool speed n [rpm]	1200	1200
Feed rate v_s [mm/min]	60	60
Tool depth a [mm]	10	15

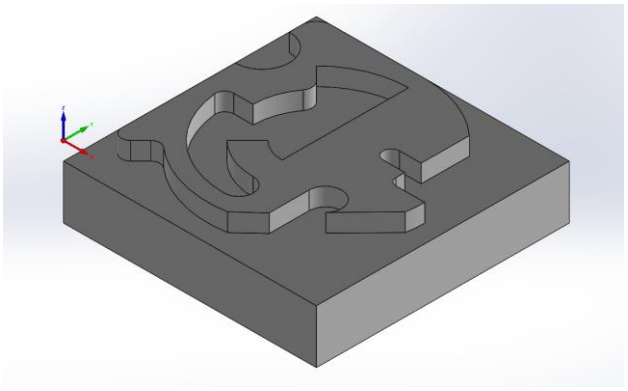

Fig. 3. 3D model of Part 1

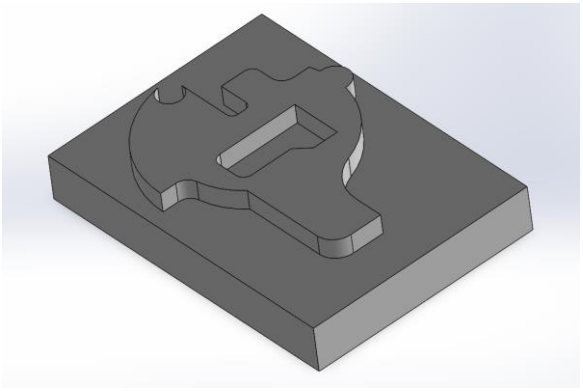

Fig. 4. 3D model of Part 2

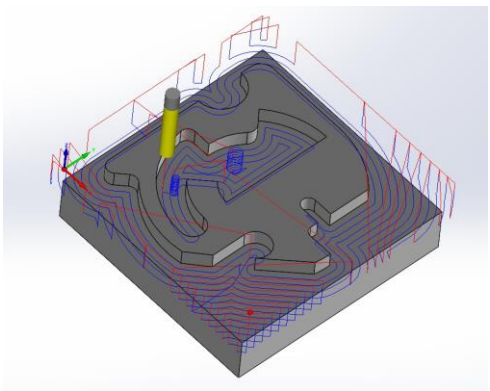

Fig. 5. Milling operation toolpath (Part 1)

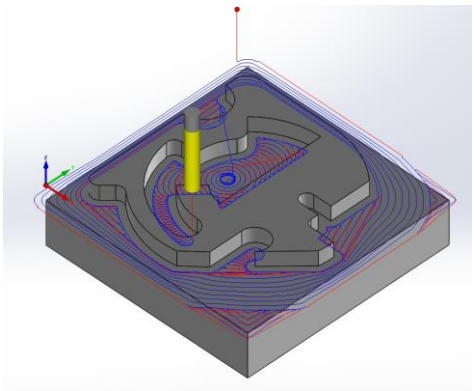

Fig. 6. iMachining operation toolpath (Part 1)

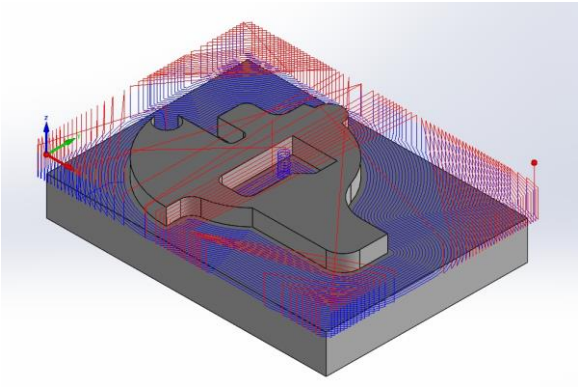

Fig. 7. Milling operation toolpath (Part 2)

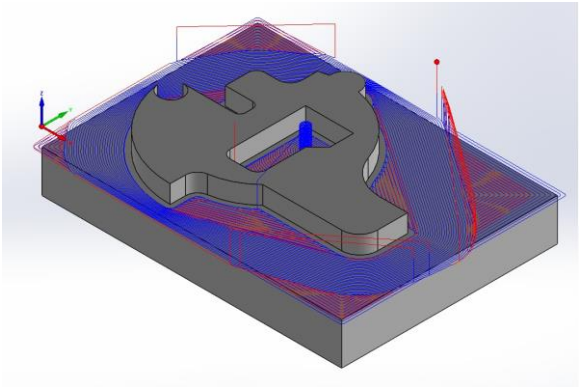

Fig. 8. iMachining operation toolpath (Part 2)

After the machining simulation in SolidCAM software the manufacturing time for both procedures is obtained (Table 2.). As viewed by data in Table 2. the time in iMachining is lesser then in conventional milling operation.

Table 2. Machining times of individual parts using different technologies

	Milling time	**iMachining**
Part 1	6 min 45 sec	6 min 26 sec
Part 2	27 min 36 sec	21 min 27 sec

For this two examples only one milling operation was conducted – the Pocket Milling, and all the other parameters were defined so the time of the machining can be compared based on the toolpath for this operations.

4. CONCLUSION

CAD/CAM softwares had become the necessary tools in modern machining production. The software provides environment for designing and virtualy manufacturing the product for analysis without the cost of production of physical prototype. Also the softwares provides the basis for product development and technology analysis in the early stages of manufacturing.

The purpose of this paper was the compare the capabilities of SolidCAM software, especially the iMachining module that represents innovative approach in machining with CNC machines. The comparison was conducted between conventional milling operation and iMachining operation on two different workpieces. On this two examples it has been shown that iMachining process provides the shorter machining time, on the basis of different toolpath.

But there are room for further investigations of iMachining process, and that is impact of different machining operations and parameters that provide the analysis of machining time as well as durability and service life of the tool.

ACKNOWLEDGMENT

The research was supported through the project "Creating laboratory conditions for research, development, and education in the field of the use of solar resources in the Internet of Things", at the Technical Faculty "Mihajlo Pupin" Zrenjanin, financed by the Provincial Secretariat for Higher Education and Scientific Research, Republic of Serbia, Autonomous Province of Vojvodina, Project number 003101190 2024 09418 003 000 000 001.

REFERENCES

[1] Bozic, D., Lukic, D., Milosevic, M., Spaic, O., Radovanovic, M.: Optimization of machining process planning – case study of a prismatic part, *Proceeding of MMA 2024 Flexible technologies, 15th International Scientific Conference,* 24-26.09.2024., Novi Sad, pp. 135-138, ISBN 978-86-6022-681-7, 2024.

[2] Gazić, T., Begović, E., Ekinović, S., Plancić, I.: SolidCAM iMachining technology positive effects on cutting tool life during machining AISIS 304 steel, *International Research Journal of Engineering and Technology,* Vol. 9., No. 5., pp. 2198-2202, ISSN 2395-0056, 2022.

[3] Markovič, F.: iMachining, *Diplomsko delo,* Univerza v Ljubljani, Fakulteta za strojništvo, 2018.

[4] Sultana, N., Quader, R., Rahman, J., Rahman, H.: SolidCAM iMachining (2D): A Simulation Study of a Spur Gear Machining and G-code Generation for CNC, *International Journal of Mechanical Engineering and Automation,* Vol. 3., No. 1., pp. 1-9, print ISSN 2333-9179, 2016.

[5] Peterka, J., Hipp, J.: Comparison of creating technological operations based on similarity in CAM software, *Proceedings of the 35th DAAAM International Symposium,* Vienna, 2024. DOI: 10.2507/35th.daaam.proceedings.xxx

[6] Varga, Č., Tabaković, S.: Analiza mogućnosti optimizacije putanje alata za pozicionu petoosnu obradu na CNC glodalicama, *Zbornik radova Fakulteta tehničkih nauka*, Vol. 36., No. 3., pp. 157-164, ISSN 050-428X, 2021.

[7] VDW Nachwuchsstiftung: *Design with SOLIDWORKS Manufacture with SolidCAM* ,VDW-Nachwuchsstiftung GmbH, Bielefeld/Frankfurt, ISBN 978-3-942817-28-8, 2019.

[8] Petrović, M., Desnica, E., Pekez, J., Palinkaš, I.: CAD Software in Teaching as a Tool for Education and Training of Future Engineers, *Journal of Engineering and Management,* Vol. 3, No. 1, pp. 1-9, ISSN 2831 – 1434, 2025, DOI 10.7251/JEM2501001P

[9] Palinkaš, Desnica E., Pekez, J., Dezso, G., Radovanović, Lj.: Comparative Study of Different Software for Design Optimization, In: Rackov M., Miltenović, A., Banić, M. (eds) Machine and Industrial Design in Mechanical Engineering - KOD 2024, *Mechanisms and Machine Science*, vol 174. Springer, Cham., pp. 655-664, ISBN 978-3-031-80511-0, 2025,

[10] Djurdjev, M., Desnica, E., Novaković, B., Đorđević, L., Palinkaš, I.: Analiza stanja i primene metaheurističkih algoritama za rešavanje problema inženjerske optimizacije, *International Scientific Conference – ETIKUM 2021*, December 2-4, Novi Sad, pp. 85-88, ISBN 978-86-6022-387-8, 2021.

[11] SolidCAM: *SolidCAM 2014 Interactive Training Course iMachining 2D & 3D*, 2014.

[12] Petrakov, Y. V., Myhovych, A. V.: IMachining technology analysis for contour milling, *Mechanics and Advanced Technologies,* Vol. 1., No. 89., pp. 114-120, ISSN 2521-1943, 2020. DOI: 10.20535/2521-1943.2020.89.202065

[13] Mladenović, G.: *CAD/CAM sistemi – Praktikum za Creo Parametric,* Univerzitet u Beogradu, Mašinski fakultet, Beograd, ISBN 978-86-6060-096-9, 2021.

11th International Scientific Conference
IRMES 2025
Research and Development of
Mechanical Elements and Systems
June 19 – 21, 2025; Vrnjačka Banja, Serbia

Original scientific paper DOI: 10.46793/IRMES25.107LJ

CAVITATION EROSION PARAMETERS OF LASER SINTERED MS1 STEEL TESTED ACCORDING TO ASTM G32 STANDARD

Pavle LJUBOJEVIĆ[1]
Tatjana LAZOVIĆ[2]
Marina DOJČINOVIĆ[3]

[1]Faculty of Mechanical Engineering, Belgrade, Serbia, 11120; pljubojevic@mas.bg.ac.rs; 0000-0002-5546-5046
[2]Faculty of Mechanical Engineering, Belgrade, Serbia, 11120; tlazovic@mas.bg.ac.rs; 0000-0001-8919-3336
[3]Faculty of Technology and Metallurgy, Belgrade, Serbia,11120; rina@tmf.bg.ac.rs; 0000-0002-8158-3468

Abstract: *The paper analyses data obtained from cavitation erosion testing of MS1 tool steel. The testing samples, cylindrical in shape with a height of 5 mm and a diameter of 10 mm, were fabricated using Direct Metal Laser Sintering (DMLS), a 3D printing technique. The samples were subjected to cavitation erosion testing in accordance with the ASTM G32 standard for a total duration of 4 hours. Mass loss measurements were recorded every 30 minutes. Based on the collected data, key parameters such as Cumulative Mass Loss, Cumulative Volume Loss, Mean Depth of Cavitation Erosion (MDE), and Mean Depth Erosion Rate (MDER) were determined and analyzed. Understanding material behaviour under cavitation conditions is crucial for its potential application in manufacturing mechanical components, particularly gears, bearings, and valves, where cavitation-induced damage is a common issue in operational environments. Given that the specimens were produced by metal powder-based 3D printing, it is especially relevant to assess the performance of such material under these conditions. This insight is particularly valuable for the geometric optimization of components to minimize erosion, where additive manufacturing offers significant advantages over conventional production technologies.*

Keywords: *Cavitation Erosion; MS1; ASTM G32; Mean Depth Erosion Rate (MDER); Additive Manufacturing*

1. INTRODUCTION

Cavitation can be defined as a non-stationary process of vapour or vapour-gas bubble formation in fluid flow and their implosion (condensation) near or directly on a solid surface [1]. This phenomenon occurs due to a pressure drop in the fluid below the critical pressure of cavitation nuclei (mainly bubbles of non-condensable gas), which become larger bubbles due to intense evaporation [2].

The first occurrences of cavitation were observed as early as the 18th century in turbomachinery, while term cavitation was first used in literature at the late 19th century, and reffered to hydrodynamic cavitation [3]. The increasing use of ultrasound in industrial processes in the late 1920s, mainly for cleaning, homogenisation, plastic welding, etc., led to the discovery of the physical impact (erosion) of ultrasonic waves on solid surfaces, which represents acoustic cavitation [4, 5]. There are two additional types of cavitation based on their source – optical cavitation (caused by an optical breakdown of a laser focused into a liquid) and particle cavitation (due to the electric discharge of elementary particles) [6, 7]. According to Lauterborn, these types of cavitation can occur through two mechanisms – tension in the liquid (hydrodynamic and acoustic cavitation) and local deposit of energy (optic and particle cavitation) [4]. In engineering systems, hydrodynamic and acoustic cavitation are the most common, causing not only the erosion of machine elements and components but also noise, vibrations, and overall system malfunction [8]. Hydrodynamic cavitation occurs in hydrodynamic flows when a change in geometry leads to an increase in velocity and a drop in pressure below the vapour pressure, which directly follows Bernoulli's equation [9, 10]. Acoustic cavitation refers to the formation and collapse of cavities induced by ultrasound [11, 12]. By conducting an experimental comparative analysis of these two types of cavitation on stainless steel X3CrNiMo13-4/S41500/ CA6NM QT780, it was concluded that acoustic cavitation causes smaller pits that appear more quickly, while hydrodynamic cavitation leads to larger pits that form somewhat more slowly. For the same exposure time, the percentage of the sample surface affected by pits was lower in acoustic cavitation. Subsequent SEM analysis of small areas affected by cavitation erosion revealed that acoustic cavitation causes damage more rapidly [13].

The machine elements that most commonly suffer from cavitation are gears, bearings, and valves as specific machine elements.

- *Gears*

Cavitation of gears most commonly occurs in gear pumps. In gear transmissions, cavitation occurs due to the specific geometry of the involute tooth profile. During the meshing of the teeth, at a certain moment, the fluid becomes trapped in a pocket between two teeth, causing a sudden pressure increase. As the teeth exit the meshing zone, this pocket opens, and the fluid transitions from a high-pressure zone to a low-pressure zone. At this point, the fluid velocity increases, resulting in a local pressure drop below the saturation pressure, leading to cavitation. This process repeats during each meshing cycle and has a frequency that is a function of the number of teeth and the angular velocity of the driving gear [14]. In external gear machines, cavitation also occurs in the lateral and radial lubricating gaps [15]. A group of authors studied the influence of vibrations on cavitation erosion in high-speed gears, also considering the thermal effect, as high-temperature fields develop in the meshing of such gears. Additionally, a CFD model was developed to predict cavitation in gear transmissions [16–19].

- *Bearings*

As mechanical elements where fluid is present between surfaces in relative motion, the occurrence of cavitation in bearings is a very common problem [20]. In the 1980s, research in the field of bearing cavitation experienced a sharp increase as a result of the design of bearings with higher rotational speeds [21]. Previous studies on cavitation have mainly focused on journal bearings, but cavitation is also present to a lesser extent in rolling bearings [22–25]. There are numerous negative consequences of cavitation erosion, such as a reduction in the coefficient of friction, power loss, and decreased bearing load capacity, etc. [20]. Due to the eccentric rotation of the shaft, journal bearings exhibit both convergent and divergent zones. The divergent zone is the area with the largest clearance between the shaft and the bearing. In the convergent zone, due to the reduction in cross-sectional area, the fluid pressure increases [26, 27]. Upon entering the divergent zone, the pressure at operating temperature drops below the saturation pressure, leading to the formation of vapour bubbles that cause bearing cavitation. With an increase in eccentricity, both the maximum pressure and temperature rise, which is why shaft deformation can significantly influence cavitation occurrence [25, 28]. Due to different geometries and kinematics in crankshaft bearings, there are several potential causes of cavitation In addition to the negative effects of cavitation itself, material particles generated by cavitation erosion can subsequently cause abrasive wear of the bearing [24].

The traditional method for modelling cavitation in bearings relies on the Reynolds equation derived from the Navier-Stokes equation and the continuity equation. However, this model has several limitations, particularly at high Reynolds numbers, with thin fluid films and surface roughness [29]. For this reason, CFD models are increasingly used to model and predict cavitation by solving the Navier-Stokes equation. Based on CFD modelling of cavitation in journal bearings, it has been concluded that the cavitation zone begins at 190º, while the maximum vapour fraction occurs at 340º angle of the bearing [28].

- *Valves*

As an essential part of all hydraulic systems, whose main function is fluid flow regulation, valves are often exposed to cavitation. It most commonly occurs in ball valves, control valves, globe valves, and spool valves, but also in mechanical heart valves, where it can lead to blood cell damage and thromboembolic complications, which can be life-threatening [30, 31]. In general, cavitation in hydraulic systems represents a significant problem. In addition to increased energy consumption, contamination, reduced physical properties of the fluid, and flow blockages, it often causes noise and vibrations, with valves being the most common source of noise and vibrations in such systems [32, 33]. Cavitation occurs, as previously described in hydrodynamic cavitation, due to a local pressure drop below the saturation pressure, leading to the formation of cavitation bubbles [32]. Cavitation modelling in valves for predictive purposes is performed using CFD models [34]. Many factors influence valve cavitation, primarily the valve geometry and the degree of openness, as well as the material, whose mechanical properties are crucial for cavitation erosion resistance. Research shows that cavitation erosion damage is most severe at small valve openings, where the pipeline can be damaged up to 20 diameters downstream of the valve [35]. From a valve design perspective, to prevent cavitation, it is important that the geometric parameters of the valve be as large as possible, with additional limitations on the maximum fluid velocity [32]. From the fluid perspective, the outlet pressure has the greatest impact on erosion, as reducing it decreases cavitation intensity, while operating temperature has a significantly smaller effect [36]. Interestingly, cavitation can also be a desirable phenomenon in treating organic wastewater, chemical reactions, sterilisation, etc. [35].

Since the geometry of components has a significant influence on cavitation, and additive manufacturing technologies offer a major advantage in this regard compared to conventional manufacturing methods, this study analyses the impact of acoustic (vibratory) cavitation on metal 3D-printed samples. Testing samples made from MS1 metal powder using the DMLS (Direct Metal Laser Sintering) technology were tested according to the ASTM G32 standard, and characteristic parameters of cavitation erosion were obtained.

2. MATERIAL AND TECHNOLOGY

2.1. Material properties

The tested specimens obtained by laser sintering of MS1 metal powder are cylinders with a diameter of 10 mm and a height of 5 mm. According to the manufacturer, the chemical composition of parts made from MS1 powder is given in Table 1. This chemical composition corresponds to the European classification 1.2709, the American 18% Ni Maraging 300, and the German X3NiCoMoTi 18-9-5. The grain size ranges from 15 to 65 μm and the density of the manufactured parts is 8 g/cm³ [37].

Table 1. Chemical composition of MS1 metal powder

Element	Percent (%)	Element	Percent (%)
Ni	17 - 19	Cu	0.5
Co	8.5 – 9.5	C	0.03
Mo	4.5 – 5.2	Mn	0.1
Ti	0.6 – 0.8	Si	0.1
Al	0.05 – 0.15	P	0.01
Cr	max. 0.5	S	0.01
Fe		Balance	

To improve mechanical properties and reduce porosity, manufactured parts are typically subjected to an ageing process for 6 hours at 490°C, which can increase hardness up to 50 HRC [37]. However, the test samples examined in this study were not subjected to the ageing process – *as-built* state samples. The test samples were subsequently polished to achieve a smoother surface and ensure more relevant results. The average hardness of testing samples measured before the experiment using the ZWICK ROELL device was 43.42 HRC, with a maximum deviation up to 5%.

2.2. DMLS technology

DMLS (Direct Metal Laser Sintering) technology is one of the additive manufacturing methods [38]. Additive manufacturing itself developed in the 1990s from rapid prototyping (RP) technologies, which are based on the direct layer-by-layer fabrication of models from a three-dimensional computer-aided design (CAD) model, developed in the 1980s. The idea of DMLS, which had been evolving since the 1970s, was finally realised and became commercial in 1995 by the company EOS GmbH of Munich, Germany [39–41]. According to the ISO/ASTM 52900 standard, this method belongs to powder bed fusion (PBF), which is based on the production of solid parts by selectively melting powder material using thermal energy [42]. This technology is quite similar to Selective Laser Melting (SLM). Both technologies belong to Laser Beam Melting (LBM) since the heat source is a fibre laser that emits beams in the infrared spectrum with a wavelength between 1060 and 1080 nm [38, 39, 43]. The difference is that in SLM technology, the powder is completely melted, while in DMLS, the powder fuses through thermal energy [44]. When it comes to precision and surface roughness, SLM has the advantage, whereas DMLS provides higher dimensional accuracy [45].

The DMLS process starts with a CAD model, which is converted into the stereolithography (STL) format, where the part is sliced into layers containing information for each layer, which is then opened in the machine software [39]. The working chamber of a DMLS machine consists of three platforms and a recoater. On the far right side is the dispenser platform, which contains the metal powder. The central area is occupied by the build plate, while the left side houses the collector platform, which collects excess powder. This powder can be reused in subsequent processes, which is one of the advantages of this technology. The recoater moves translationally from right to left, applying the powder in layers of the recommended thickness, typically between 20 and 100 µm. Then, the scanner head emits laser beams, which are selectively switched on and off to heat the powder according to the information contained in the STL file. Due to the absorption of laser energy, the metal powder solidifies. In the next pass, the dispenser platform rises to provide a sufficient amount of powder for the next layer, while the build plate lowers by the thickness of the layer. The process takes place in a nitrogen atmosphere, with nitrogen being supplied to the working environment from a nitrogen generator [38, 41, 43, 44].

Test samples analysed in this paper were cut from the wider part of the specimen for fatigue testing under rotating bending according to ISO 1143 standard [46]. The specimens were produced using the M280 DMLS machine. The laser power is 200W, and the wavelength of the emitted infrared light is 1064 nm. The build plate within the machine chamber has dimensions of 250x250mm, while the maximum height of the produced part is 325mm. The printing direction of the specimens is vertical with direct build on the plate without support structures, and the layer thickness is 40 µm. Before the process began, the build plate was preheated to 40ºC.

3. EXPERIMENTAL PROCEDURE

Sample testing was conducted according to the ASTM G32 standard. This standard includes two types of testing: one with a non-stationary sample (direct method) and one with a stationary sample (indirect method). In the method with a non-stationary sample, the sample is attached via threading to the tip of the mechanical vibration concentrator [47].

In this experiment, the stationary sample method was used, which eliminates possible mechanical stresses. The sample was fixed in a water bath just below the mechanical vibration concentrator - horn. The device is powered by a generator which produces an electrical energy frequency of 20 to 50 Hz. Using a piezoelectric element, electrical energy is converted into mechanical vibrations, which are transmitted to the fluid film between the horn and the test sample, causing pressure fluctuations and inducing cavitation. The prescribed experimental conditions were as follows [1]:

- The water temperature in the bath was 25±1 ºC
- The gap between the sample and the horn was 0.5 mm
- The vibration amplitude of the horn was 50 µm
- The vibration frequency was 20±0.2 kHz

At 30-minute intervals, the mass of the samples was measured using an analytical scale AS 120.R2, RADWAG with an accuracy of 0.01 mg, over a total duration of 4 hours. Mass losses were calculated for each interval, and a Cumulative Mass Loss function as a function of time was formed and presented in the paper [48]. In addition to the tabular representation of mass losses (Table 2), this study determines the Mean Depth of Erosion (*MDE*) based on the available data on material density and the geometric characteristics of the tested samples, according to Equation 1 [49]. MDE can also be found in the literature as *MDP* (Mean Depth of Penetration), but according to the standard, it is more precise to use the designation *MDE* [50].

$$MDE_{\sum_i} = \sum_{i=0}^{n=8} \Delta MDE_i \sum_{i=0}^{n=8} \frac{4\Delta m_i}{\rho \pi d^2} 10^3 [\mu m] \quad (1)$$

where:
i is the testing period
ΔMDE_i – Mean depth erosion for i period
Δm_i is a mass loss for i period in milligrams
ρ is the density of the material (8 g/cm^3)
d is the diameter of the testing samples (10 mm)

Subsequently, the erosion rate MDER (Mean Depth Erosion Rate) was determined using the following equation (Mitelea):

$$MDER_i = \Delta MDE_i / \Delta t_i \left[\frac{\mu m}{min}\right] \quad (2)$$

where Δt_i is the duration of the testing period i.

Based on MDE, the Cumulative Erosion Rate (CER) can be calculated, which, unlike MDER, takes previous intervals into account and is simpler to plot, can be determined using the following equation [51]:

$$CER_i = \frac{\sum_i MDE_i}{\sum_i t_i} \left[\frac{\mu m}{min}\right], \quad i = 0, 1, 2, \ldots, 8 \quad (3)$$

4. RESULTS AND DISCUSSION

Cumulative mass losses as a function of time are given in Table 2.

Table 2 Cumulative mass loss (mg) vs. exposure time (min)

Δm	0.14	0.38	0.48	0.84	0.95	1.11	1.22	1.51
Δt	30	60	90	120	150	180	210	240

Fig. 1 shows MDE as a function of time. Experimental data points are mostly approximated using linear regression, which typically employs a simpler version of the least squares method called ordinary least squares (OLS) to obtain parameters [52,53]. Since *MDE* (Mass Loss Due to Erosion) directly follows from mass losses, the same methods used for approximating mass loss will be applied for its approximation as well.

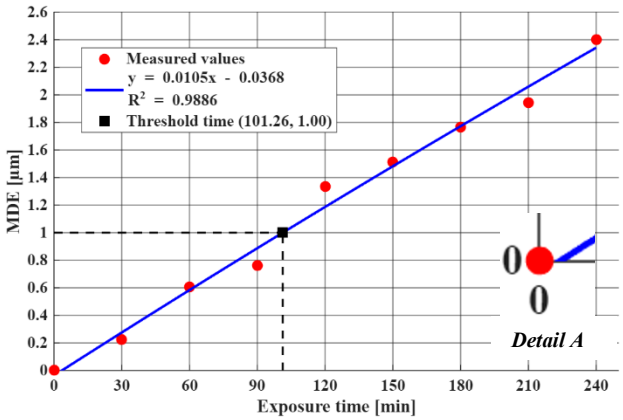

Fig. 1 MDE vs Exposure time

The approximation of experimentally obtained points using the least squares method, with a coefficient of determination R^2 = 0.9886, indicates a very small error, meaning that the dependence of *MDE* on exposure time is approximately linear. According to the standard, erosion threshold time (*ETT*) is the time required for the mean depth of erosion to reach 1 µm, which is the smallest accurately measurable value, and for tested samples, this time is 101.26 min. However, this approximation model does not provide an exact solution for the initial boundary condition that there is no cavitation erosion at time t = 0 (Fig. 1, detail A). To avoid this, some authors propose an approximation for cumulative mass loss using the following equation (Bordeau):

$$\Delta m\,(t) = A_1(at - bte^{-ct}) \quad (4)$$

If the tabular representation of mass losses is approximated using the given function, a very high coefficient of determination R^2=0.9779 is obtained, indicating a high approximation accuracy. In this case, the coefficient A_1 is pre-fixed to a value of 1, while the values of the coefficients a, b, and c are, respectively, 0.00601, 0.00319, and 0.01406. However, suppose the same function is applied to approximate *MDE*. In that case, significant numerical instability occurs around zero, where the function exhibits a sudden drop and an extremum in the negative part of the y-axis, which is unacceptable due to the nature of the problem. Therefore, in this study, Equations 1 and 4 were utilised, leading to a numerically stable equation for approximating *MDE* as a function of time:

$$MDE\,(t) = A_1(a_1 t - b_1 te^{-ct}) \quad (5)$$

where parameters a_1 and b_1 are: $a_1 = 4000\,a/\rho\pi d^2$, $b_1 = 4000\,b/\rho\pi d^2$. The calculated values of these parameters are respectively, 0.00957 and 0.00507. In Fig. 2, the modified approximation is shown.

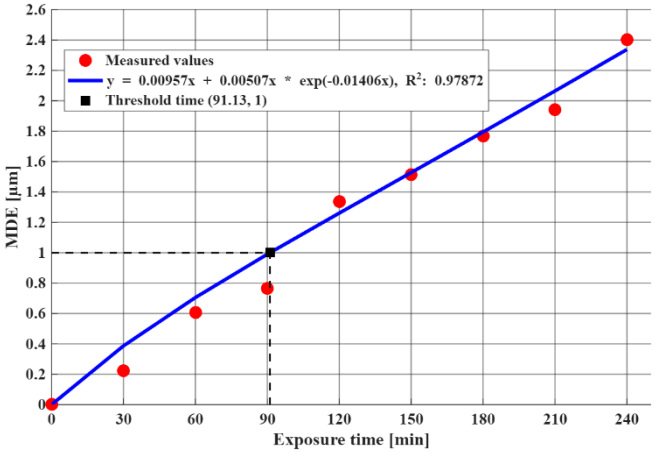

Figure 2 Exponential function of MDE vs. Exposure time

The new approximation yields an *ETT* = 91.13, which significantly differs from the previous one. The coefficient of determination is R^2 = 0.97872, indicating that the approximation is somewhat less accurate compared to the least squares method. This function, like the function for approximating mass losses according to Equation 4, is

concave, meaning it differs in shape from the function proposed by the author Bordeau in Equation 4 [56]. This is because, in our case, the coefficient *b* is less than zero. If a condition were imposed in the Matlab code that *b* should not be less than 0 to obtain a convex function, the program would output a value of b equal to 0, which would produce a straight line with no intercept on the y-axis, with the slope coefficient $a_1 = 0.006304$. However, if the condition that b must be greater than 0 is imposed, the program outputs a value for b very close to zero, which brings us back to almost linear approximating with a line close to the previous. This case of the concave function could be the subject of one of the following papers.

In Fig. 3, the MDER obtained according to Equation 2 is shown as a function of time. A spline function was used to connect the points, as frequent jumps in calculations make using another type of approximation function unsuitable.

Fig. 4 shows the dependence of CER on time according to Equation 3, where the points are connected using a spline function for the same reason as in the previous case, although the jumps are smaller.

MDER can be interpreted as the instantaneous erosion rate, and its maximum value is used to determine the Cavitation Erosion Resistance as its reciprocal, which is related to the mechanical properties of the material.

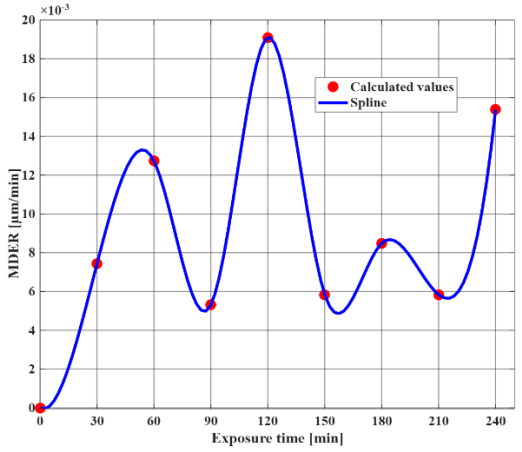

Fig. 3 MDER vs. Exposure Time

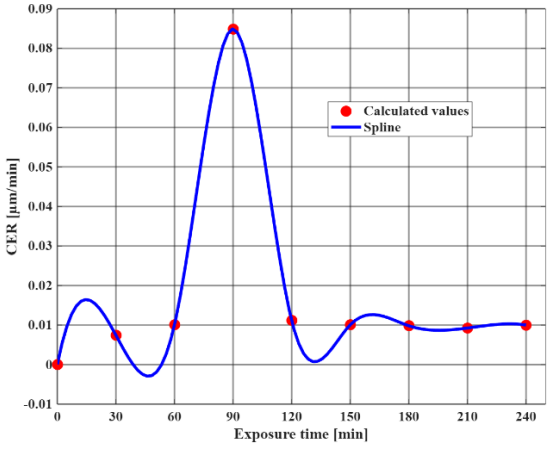

Fig. 4 CER vs. Exposure time

5. CONCLUSIONS

Cavitation is a common problem in systems where fluid serves as the working medium or as a lubricant for contact surfaces to reduce friction and energy losses through the release of heat, noise, and vibrations. Machine elements most frequently exposed to cavitation include gears, bearings, and valves. Due to their complex geometry, manufacturing technology and achieved accuracy, as well as material selection, play a crucial role in mitigating damage caused by cavitation erosion. To overcome the challenges of manufacturing complex geometries, additive technologies offer advantages over conventional methods. This study examines MS1 steel produced by the DMLS technology without mechanical and thermal post-processing. The mass loss due to erosion (MDE) was analyzed using two types of approximation, leading to the conclusion that this type of tool steel exhibits good mechanical properties and resistance to cavitation erosion.

ACKNOWLEDGMENT

This work was supported by the Ministry of Science, Technological Development and Innovations of the Republic of Serbia (Contracts: 451-03-137/2025-03/ 200105 and 451-03-136/2025-03/200135) and CA23155 - A pan-European network of Ocean Tribology (OTC).

REFERENCES

[1] Dojčinović, M.: *Razaranje materijala pod dejstvom kavitacije*, Monogr. Teh.-Met. Fak. Beogr., 978-86-7401-305-2, 2013

[2] Adama Maiga, M. et al.: Analysis of the critical pressure of cavitation bubbles, *Meccanica*, 53., 4–5., pp. 787–801, 1572-9648, 2018

[3] Young, F.R.: *Cavitation*. World Scientific, 978-1-78326-186-4, 1999

[4] Lauterborn, W.: Cavitation and Inhomogeneities in Underwater Acoustics, *Proceedings of the First International Conference,* July 9–11, 1979, Göttingen, Fed. Rep. of Germany, Springer Science & Business Media, 978-3-642-51070-0, 2012

[5] Laborde, J.-L. et al.: Acoustic cavitation field prediction at low and high frequency ultrasounds, *Ultrasonics*, 36., 1–5., pp. 581–587, 0041624X,1998

[6] Padilla-Martinez, J.P. et al.: Optic cavitation with CW lasers: A review, *Phys. Fluids*, 26., 12., pp. 122007,1089-7666, 2014

[7] Kurz, T. et al.: Optic cavitation in an ultrasonic field. *Phys. Rev. E*, 74., 6., pp. 066307, 1550-2376, 2006

[8] A. Ferrari: Fluid dynamics of acoustic and hydrodynamic cavitation in hydraulic power systems, *Proceedings of the Royal Society A: Mathematical, Physical and Engineering Sciences,* 20160345, 2017

[9] Caupin, F., Herbert, E.: Cavitation in water: a review, *Comptes Rendus Phys.*, 7., 9–10., pp. 1000–1017, 1878-1535, 2006

[10] Gogate, P.R., Pandit, A.B.: A review and assessment of hydrodynamic cavitation as a technology for the future, *Ultrason. Sonochem.*, 12., 1–2., pp. 21-27, 13504177, 2005

[11] Neppiras, E.A.: Acoustic cavitation series: part one, *Ultrasonics*, 22., 1., pp. 25–28, 0041624X, 1984

[12] Smirnov, I.V. et al.: Analysis of Dependences of Threshold Parameters for Acoustic Cavitation Onset in a

Liquid on an Ultrasonic Frequency, Hydrostatic Pressure, and Temperature, *Tech. Phys.*, 67., 2., pp. 161-170, 1090-6525, 2022
[13] Hofmann, J. et al.: Comparison of acoustic and hydrodynamic cavitation: Material point of view, *Phys. Fluids*, 35., 1, pp. 017112, 1070-6631, 2023
[14] Battarra, M., Mucchi, E.: Incipient cavitation detection in external gear pumps by means of vibro-acoustic measurements, *Measurement*, 129., pp. 51-61, 0263-2241, 2018
[15] Thiagarajan, D., Vacca, A.: Modelling of the Lateral Lubricating Interfaces in External Gear Machines Considering the Effects of Cavitation, *BATH/ASME 2018 Symposium on Fluid Power and Motion Control,* Bath, UK: American Society of Mechanical Engineers, 978-0-7918-5196-8, 2018
[16] Ouyang, T. et al.: Vibration and cavitation in high-speed gears caused by faults, *Int. J. Mech. Sci.*, 250., pp. 108322, 0020-7403, 2023,.
[17] Ouyang, T. et al.: Numerical investigation of vibration-induced cavitation for gears considering thermal effect, *Int. J. Mech. Sci.*, 233., p. 107679, 0020-7403, 2022
[18] Ouyang, T. et al.: CFD-vibration coupled model for predicting cavitation in gear transmissions, *Int. J. Mech. Sci.*, 225., pp. 107377, 0020-7403, 2022
[19] Ouyang, T. et al.: Cavitation mechanism of high-speed helical gears induced by vibration, *Tribol. Int.*, 193., pp. 109440, 0301-679X, 2024
[20] Brewe, D.E.: Theoretical Modeling of the Vapor Cavitation in Dynamically Loaded Journal Bearings, *J. Tribol.*, 108., 4., pp. 628-637, 1528-8897, 1986
[21] Garner, D.R. et al.: Cavitation Erosion Damage in Engine Bearings: Theory and Practice, *J. Eng. Power*, 102., 4., pp. 847-857,0022-0825, 1980
[22] Dowson, D., Taylor, C.M.: Cavitation in Bearings, *Annu. Rev. Fluid Mech.*, 11., 1., pp. 35-65, 1545-4479, 1979
[23] Ausas, R. et al.: The Impact of the Cavitation Model in the Analysis of Microtextured Lubricated Journal Bearings, *J. Tribol.*, 129., 4., pp. 868-875, 1528-8897, 2007
[24] Chen, Y.-M., Mongis, J.: Cavitation wear in plain bearing: Case study, *Mech. Ind.*, 6., 2., pp. 195-201, 2257-7750, 2005
[25] He, T. et al.: Influence of Cavitation and Shaft Deformation in the Analysis of Lubrication of the Stern Bearing, *Appl. Sci.*, 13., 15, pp. 9033, 2076-3417, 2023
[26] Rasep, Z.: A study of cavitation effect in a journal bearing using CFD: A case study of engine oil, palm oil and water, *Jurnal Tribologi, 28., pp. 48-62,* 2021.
[27] Dhande, D.Y., Pande, D.W.: Multiphase flow analysis of hydrodynamic journal bearing using CFD coupled Fluid Structure Interaction considering cavitation, *J. King Saud Univ. - Eng. Sci.*, 30., 4., pp. 345-354, 10183639, 2018
[28] Cai, L. et al.: The Numerical Simulation of Pure-Oil Lubrication Journal Bearing, *Adv. Mater. Res.*, 143–144., pp. 609-613, 1662-8985, 2010
[29] Meng, F., Yang, T.: Preliminary study on mechanism of cavitation in lubricant of textured sliding bearing, *Proc. Inst. Mech. Eng. Part J J. Eng. Tribol.*, 227., 7., pp 695-708, 2041-305X, 2013
[30] Qian, J. et al.: A comprehensive review of cavitation in valves: mechanical heart valves and control valves, *Bio-Des. Manuf.*, 2., 2., pp. 119-136, 2522-8552, 2019
[31] Martin, C.S. et al.: Cavitation Inception in Spool Valves, *J. Fluids Eng.*, 103., 4., pp. 564-575, 1528-901X, 1981
[32] Jin, Z. et al.: A Parametric Study of Hydrodynamic Cavitation Inside Globe Valves, *J. Fluids Eng.*, 140., 3., pp. 031208, 1528-901X, 2018
[33] Gao, H. et al.: Investigation of Cavitation Near the Orifice of Hydraulic Valves, *Proc. Inst. Mech. Eng. Part G J. Aerosp. Eng.*, 220., 4, pp. 253-265, 2041-3025, 2006
[34] Ferrari, J., Leutwyler, Z.: Fluid Flow Force Measurement Under Various Cavitation State on a Globe Valve Model, *Volume 4: Fluid-Structure Interaction ASME 2008 Pressure Vessels and Piping Conference*, pp. 157-168, ASMEDC, Chicago, Illinois, USA, 978-0-7918-4827-2, 2008
[35] Jazi, A.M., Rahimzadeh, H.: Waveform analysis of cavitation in a globe valve, *Ultrasonics*, 49., 6–7., pp. 577-582, 0041624X, 2009
[36] Li, J. et al.: Numerical Investigation of Methodologies for Cavitation Suppression Inside Globe Valves, *Appl. Sci.*, 10., 16., pp. 5541, 2076-3417, 2020
[37] *http://eos.org* - EOS
[38] Herzog, D. et al.: Additive manufacturing of metals, *Acta Mater.*, 117., pp. 371-392, 13596454, 2016
[39] Wong, K.V., Hernandez, A.: A Review of Additive Manufacturing, *Int. Sch. Res. Not.*, 2012., 1., pp. 208760, 2356-7872, 2012
[40] Shellabear, M., Nyrhilä, O.: DMLS – DEVELOPMENT HISTORY AND STATE OF THE ART, *Laser assisted netshape engineering 4, proceedings of the 4th LANE,* pp. 21-24, 2004
[41] Bineli, A.R.R. et al.: DIRECT METAL LASER SINTERING (DMLS): TECHNOLOGY FOR DESIGN AND CONSTRUCTION OF MICROREACTORS, *6º Congress Obrasileiro De Engenharia De Fabrica Ção,*11., 2011
[42] Bochnia, J. et al.: The Mechanical Properties of Direct Metal Laser Sintered Thin-Walled Maraging Steel (MS1) Elements, *Materials*, 16., 13., pp. 4699, 1996-1944, 2023
[43] Dev Singh, D. et al.: Powder bed fusion process: A brief review, *Mater. Today Proc.*, 46., pp. 350-355, 22147853, 2021
[44] Croccolo, D. et al.: Fatigue Response of As-Built DMLS Maraging Steel and Effects of Aging, Machining, and Peening Treatments, *Metals*, 8., 7., pp. 505, 2075-4701 2018
[45] Ghani, S.A.C. et al.: Dimensional accuracy of internal cooling channel made by selective laser melting (SLM) And direct metal laser sintering (DMLS) processes in fabrication of internally cooled cutting tools. *MATEC Web Conf.*, 90., pp. 01058, 2017
[46] *ISO-1143-2021*, Metallic materials — Rotating bar bending fatigue testing
[47] ASTM G32-16, *Test Method for Cavitation Erosion Using Vibratory Apparatus*
[48] Ljubojević, P.M. et al.: Cavitation Resistance of Laser-Sintered MS1 Steel. *Sci. Sinter.*, 2024, *on-line first*
[49] Mitelea, I. et al.: Cavitation Erosion Characteristics of the EN AW-6082 Aluminum Alloy by TIG Surface Remelting, *Materials*, 16., 7., pp. 2563, 1996-1944, 2023
[50] Kwok, C.T. et al.: Cavitation erosion and damage mechanisms of alloys with duplex structures, *Mater. Sci. Eng. A*, 242., 1–2., pp. 108-120, 09215093, 1998
[51] Steller, J.: International Cavitation Erosion Test and quantitative assessment of material resistance to cavitation, *Wear*, 233–235., pp. 51-64, 0043-1648, 1999
[52] Abdi, H.: *The Method od Least Squares*, *Encyclopedia of measurement and statistics* 1, pp. 530-532, 2007
[53] Mohammadizadeh, S. et al.: Experimental Analysis of Cavitation Erosion: Parameter Sensitivity and Testing Protocols, *Coatings*, 14., 10., pp. 1288, 2079-6412, 2024
[54] Patrăşcoiu, C., et al.:New contributions to cavitation erosion curves modeling, *FME Transactions,* 34., pp. 39-43, 2006

11th International Scientific Conference
IRMES 2025
Research and Development of
Mechanical Elements and Systems
June 19 – 21, 2025; Vrnjačka Banja, Serbia

Original scientific paper DOI: 10.46793/IRMES25.113P

VAT PHOTOPOLYMERIZATION RISK ASSESSMENT USING THE KINNEY METHOD

Danilo PEJČIĆ[1]
Žarko MIŠKOVIĆ[2]
Jovana ANTIĆ[3]
Radivoje MITROVIĆ[4]
Lubos MAGDOLEN[5]
Tomas MILESICH[6]
Jan DANKO[7]

[1]Faculty of Mechanical Engineering, University of Belgrade, Belgrade, Serbia, 11000; dpejcic@mas.bg.ac.rs; ORCID iD: 0009-0007-1661-2924
[2]Faculty of Mechanical Engineering, University of Belgrade, Belgrade, Serbia, 11000; zmiskovic@mas.bg.ac.rs; ORCID iD: 0000-0002-8320-7191
[3]Faculty of Mechanical Engineering, University of Belgrade, Belgrade, Serbia, 11000; jrantic@mas.bg.ac.rs; ORCID iD: 0009-0002-6452-0294
[4]Faculty of Mechanical Engineering at the University of Belgrade, Belgrade, Serbia, 11000; rmitrovic@mas.bg.ac.rs; ORCID iD: 0000-0003-0513-6540
[5] Faculty of Mechanical Engineering at the Slovak University of Technology in Bratislava, Bratislava, Slovakia, 81231; lubos.magdolen@stuba.sk; ORCID iD: 0000-0002-0507-3378
[6] Faculty of Mechanical Engineering at the Slovak University of Technology in Bratislava, Bratislava, Slovakia, 81231; tomas.milesich@stuba.sk; ORCID iD: 0000-0002-1294-5429
[7] Faculty of Mechanical Engineering at the Slovak University of Technology in Bratislava, Bratislava, Slovakia, 81231; jan.danko@stuba.sk; ORCID iD: 0000-0002-7193-7728

Abstract: *Additive manufacturing technologies are becoming increasingly prevalent across industries, educational institutions, and even households. Their primary application lies in the production of prototypes and components with intricate geometries. However, despite their widespread adoption, the potential risks these technologies pose to occupational safety and human health remain insufficiently explored. This paper presents a risk assessment of one of the most widely used additive manufacturing processes—Vat Photopolymerization. The evaluation was conducted using the Kinney risk assessment method to identify potential hazards associated with the technology. Based on the findings, appropriate safety measures were proposed to mitigate risks and enhance workplace safety.*

Keywords: *Additive manufacturing technologies; Vat Photopolymerization; Risk assessment; The Kinney method; Safety measures.*

1. ADDITIVE MANUFACTURING TECHNOLOGIES

Additive manufacturing technologies involve the layer-by-layer construction of a product or component, in contrast to traditional manufacturing methods that rely on material removal or plastic deformation [1]. By adding material instead of subtracting it, these processes significantly reduce material waste.

One of the key advantages of additive manufacturing is its ability to streamline the production of complex geometries, which would be challenging or costly to achieve using conventional methods. Unlike traditional techniques that require extensive material removal and specialized tooling, additive manufacturing enables a more flexible and innovative approach to part fabrication.

According to the ISO/ASTM 52900-21 standard, Additive Manufacturing — General Principles — Fundamentals and Vocabulary, seven main categories of additive manufacturing processes are defined:

- Vat Photopolymerization
- Material Jetting
- Binder Jetting
- Powder Bed Fusion
- Material Extrusion
- Sheet Lamination
- Directed Energy Deposition

1.1. Vat photopolymerization

Vat photopolymerization is an additive manufacturing process in which a liquid photopolymer stored in a vat is selectively solidified through light-activated polymerization [1].

The base materials used in this process are photopolymers, which solidify upon exposure to specific wavelengths of light, bonding together to form a solid structure.

Most 3D printers utilizing vat photopolymerization store the liquid photopolymer in a vat. The process begins with the build platform partially submerging into the vat. A light source, guided by data from a CAD file, then selectively cures the photopolymer to create a solidified layer of the part. The build platform subsequently lowers again into the vat, repeating the process layer by layer until the final part is fully formed [2].

The two most widely used vat photopolymerization processes are:

- Stereolithography (SLA): Utilizes a laser to precisely cure and solidify layers of the part.
- Digital Light Processing (DLP): Uses a Digital Micromirror Device (DMD) to project light, selectively curing the photopolymer.

Depending on the composition and manufacturer, photopolymers may contain hazardous or harmful substances. Table 1 provides an overview of some potentially hazardous compounds commonly found in photopolymer formulations.

Table 1. Hazardous and harmful substances in photopolymers

Substances	Hazards and harmful factors
Methacrylate Monomer(s), Urethane dimethacrylate, Ethyl phenyl (2,4,6-trimethylbenzoyl) phosphinate [3]	Causes skin irritation, Causes serious eye irritation, May cause an allergic skin reaction [3]
2,4,6-trioxo-1,3,5-triazine-1,3,5(2H,4H,6H)-triyl, tri-2,1-ethanediyl triacrylate, Acrylate Monomer(s), Urethane Dimethacrylate [4]	Causes serious eye damage, May cause respiratory irritation, Specific target organ toxicity - single exposure, Causes skin irritation, May cause an allergic skin reaction [4]
Methyl acetoacetate, N, N'- 2,2- dimethylpropylidene, hexamethylenediamine, Hexamethylene diacrylate, hexane-1,6-diol diacrylate, Diphenyl (2,4,6-trimethylbenzoyl) phosphine oxide [5]	Causes skin irritation, Causes serious eye irritation, May cause an allergic skin reaction, Suspected of damaging fertility [5]
Acrylate oligomer, Acrylate monomer, Photoinitiator [6]	Causes skin irritation, May cause an allergic skin reaction, Causes serious eye irritation, Suspected of damaging fertility, May cause damage to organs through prolonged or repeated exposure [6]
2-Propen-1-one,1-(4-morpholinyl), Acrylate derivative, Phenyl acrylate, Diphenyl (2,4,6-trimethylbenzoyl) phosphine oxide, Proprietary compound [7]	Causes serious eye damage, Causes skin irritation, Harmful if swallowed, May cause an allergic skin reaction, May cause damage to organs through prolonged or repeated exposure, Suspected of damaging fertility, Suspected of damaging the unborn child [7]
Urethane Acrylate Oligomer, Pentaerythritol tetraacrylate, (5-ethyl-1,3-dioxan-5-yl) methyl acrylate, Exo-1,7,7-trimethylbicyclo [2.2.1] hept-2-yl methacrylate, Diphenyl(2,4,6-trimethylbenzoyl) phosphine oxide, 2,2-bis (acryloyloxymethyl) butyl acrylate, Diisodecyl phenyl phosphite, Toluene, Phenol [8]	Causes skin irritation, May cause an allergic skin reaction. Toxic if swallowed, in contact with skin or if inhaled. May be fatal if swallowed and enters airways. Causes serious eye irritation. Highly flammable liquid and vapour. Suspected of causing genetic defects. Suspected of damaging the unborn child. Suspected of damaging fertility. Causes severe skin burns and eye damage. May cause an allergic skin reaction. May cause damage to organs through prolonged or repeated exposure. May cause respiratory irritation. May cause drowsiness or dizziness [8]

2. RISK ASSESSMENT

Ensuring employee safety and health is one of the primary objectives of any enterprise. According to Article 4 (Definition of Terms) of the Occupational Safety and Health Act ("Official Gazette of the Republic of Serbia," No. 35/2023), the following key terms are defined concerning risk assessment:

- **Hazard:** A circumstance or condition that may endanger an employee's health or cause injury.
- Harmfulness: A property or characteristic that may pose a threat to an employee's health.
- **Risk:** The probability of injury, illness, or health impairment occurring due to exposure to hazards or harmful factors.
- **Risk assessment:** The systematic identification and evaluation of all hazards and harmful factors present in the work process, workplace, and working environment that may lead to work-related injuries, illnesses, or health impairments, along with determining the possible methods for preventing, eliminating, or reducing risks to the lowest achievable level.

Various risk assessment methods are employed across industries, including the Singapore Model (3x3), Fault Tree Analysis (FTA), Failure Mode and Effects Analysis (FMEA), and Failure Mode, Effect, and Criticality Analysis (FMECA). However, applying these methods to additive manufacturing technologies presents challenges due to the diversity of processes (e.g., different material types) and the complexity of additive manufacturing systems [9].

In this study, the Kinney method was selected for risk assessment of the vat photopolymerization process within additive manufacturing technologies, providing a structured approach to evaluating potential hazards and determining appropriate safety measures.

2.1. The Kinney risk assessment method

The Kinney risk assessment method evaluates risk based on the occurrence of hazards and harmful factors. Systematic identification of these potential threats determines the associated risks to occupational safety. The risk value is calculated using Equation (1), with the corresponding factor values presented in Table 2 [10] [11].

$$\mathbf{R}(\text{Risk}) = \mathbf{F}\ (\text{Frequency}) \times \mathbf{P}\ (\text{Probability}) \times \mathbf{C}\ (\text{Consequence}) \quad (1)$$

Based on the numerical risk value (R), the risk can be classified into five categories, as shown in Table 3 [11].

Table 3. Classification based on risk level

Risk level (R)	Classification	Description of the classification
R<20	Acceptable risk	No measure required
20 - 70	Possible risk	Monitoring
71 - 200	Substantial risk	Measuring is required
201 - 400	High risk	Improvements
R>400	Very high risk	Activity cessation

2.2. Checklists for Hazards and Harmful Factors during the vat photopolymerization

The checklists provided in Table 4 are used to identify hazards and harmful factors in the workplace during the vat photopolymerization process. These checklists are based on the ISO 12100:2010 standard – Safety of Machinery – General Principles for Design – Risk Assessment and Risk Reduction [12]. Table 4 includes the completed checklists, filled with data specific to the vat photopolymerization process.

Table 2. Description of the criteria for assessing the probability

F	Criteria for frequency	P	Criteria for assessing the probability	C	Criteria for assessing the consequences
1	Rare (yearly)	0.1	Virtually impossible	1	Disease, injury that requires first aid, and any other treatment
2	Monthly	0.2	Practically impossible	2	Medical treatment by a doctor
3	Occasional (weekly)	0.5	Plausible, but unlikely	3	Serious – disability, serious violation with individual hospitalization and lost days
6	Regular (daily)	1	Improbable, but possible at boundary conditions	6	Very serious – individual accidents with lethal outcome
10	Permanent	3	Unusual, but possible	10	Catastrophic – with multiple lethal outcomes
		6	Possible		
		10	Predictable		

Table 4. Analysis of potential hazards and harms

Hazard/Harm group	Code	Hazard / Harm subgroup	Hazard/Harm Yes/No
Mechanical hazards that arise from using work equipment, such as:	(1)	Insufficient safety due to rotating or moving parts	No
	(2)	Free movement of parts or materials that can cause harm to employees	No
	(3)	Internal transport and movement of working machines or vehicles	No
	(4)	The use of dangerous work equipment that can cause explosions and fires	Yes
	(5)	The inability or limited ability to timely remove oneself from the workplace, exposure to closure, mechanical impact, etc.	No
	(6)	Other factors that may appear as mechanical sources of danger	No
Hazards that arise in relation to the characteristics of the workplace, such as:	(7)	Hazardous surfaces (floors and all types of walking surfaces, surfaces that employees come into contact with those that have sharp edges, spikes, groups of surfaces, etc.)	Yes
	(8)	Working at height or in-depth, in terms of occupational health and safety regulations	No
	(9)	Working in a cramped, limited, or dangerous space (between two or more fixed parts, between moving parts or vehicles, etc.)	No
	(10)	Possibility of slipping and tripping	No
	(11)	Physical instability of the workplace	No
	(12)	Possible consequences or disruptions due to the mandatory use of personal protective equipment at work	No
	(13)	Effects due to the performance of work processes using inappropriate or unsuitable methods of work	No
	(14)	Other hazards that may arise in connection with the characteristics of the workplace and the method of work	No
Hazards that arise from the use of electrical energy, such as:	(15)	Hazards from direct contact with live electrical installations and equipment	Yes
	(16)	Hazard from direct contact	No
	(17)	Hazard from thermal effects caused by electrical equipment and installations (overheating, fire, explosion, electric arc or sparking, etc.)	No
	(18)	Hazards resulting from lightning strikes and atmospheric discharge	No
	(19)	Hazard from harmful effects of electrostatic charging	No
	(20)	Other hazards that may arise from the use of electrical energy	No
Harmful effects that arise or occur during work processes, such as:	(21)	Chemical hazards, dust and fumes (inhalation, suffocation, introduction into the body, penetration into the body through the skin, etc.)	Yes
	(22)	Physical harm (noise and vibration)	No
	(23)	Biological damage (infections, exposure to microorganisms and allergens)	No
	(24)	Harmful effects of microclimate (high or low temperature, humidity and air flow speed)	No
	(25)	Inadequate brightness	No
	(26)	Harmful effects of radiation	Yes
	(27)	Harmful climate impacts (work on open)	No
	(28)	Harms caused by the use of dangerous substances in production, transport, packaging, storage or destruction	Yes
	(29)	Other harms that appear in the work process, and which can be the cause of an employee's injury at work	No
Harmful effects arising from mental and psychophysical efforts that are causally related to the workplace and jobs that employees perform, such as:	(30)	Efforts or physical exertion	No
	(31)	Non-physiological position of the body (long-term standing, sitting, crouching, kneeling, etc.)	No
	(32)	Efforts in the performance of certain jobs that cause psychological stress (stress, monotony, etc.)	No
	(33)	Responsibility in receiving and transmitting information, use of appropriate knowledge and abilities, responsibility in rules of conduct, responsibility for rapid changes in work procedures, etc.	No
Harmful effects related to work organization, such as:	(34)	Work longer than full time, work in shifts, reduced working hours, night work, preparedness in case of interventions	Yes
Other harmful effects that occur in the workplace, such as:	(35)	Damage caused by other persons (violence towards persons working at counters, etc.)	No
	(36)	Working with animals	No
	(37)	Work in an atmosphere with high or low-pressure	No
	(38)	Working near water or underwater surface	No

3. RESULTS OF THE RISK ASSESSMENT AND RECOMMENDED SAFETY MEASURES

Based on the completed checklists identifying hazards and harmful factors, the Kinney risk assessment method was applied. Table 5 presents the evaluated risk levels for all potential hazards and harmful factors associated with the vat photopolymerization process.

Safety measures are crucial for minimizing risks during vat photopolymerization process because this technology involves several hazards that can pose significant threats to the health and safety of operators. These risks include exposure to harmful materials, such as toxic fumes released during the rapid prototyping process, as well as potential radiation hazards from certain printing methods (e.g., UV radiation). Additionally, there is the risk of electrical accidents, burns from heated surfaces, and physical injuries from moving parts or the handling of equipment. Implementing safety measures, such as proper ventilation, personal protective equipment (PPE), and safety protocols, helps to mitigate these risks. These measures ensure that workers are shielded from potential hazards like chemical exposure, thermal injuries, and radiation. Moreover, safety guidelines help create a safer work environment, which is vital for reducing workplace accidents, improving employee well-being, and ensuring compliance with occupational health and safety regulations. By proactively addressing these risks, companies can not only safeguard their workforce but also enhance productivity and ensure the quality and consistency of their vat photopolymerization process operations. Ultimately, establishing safety measures contributes to the long-term success and sustainability.

The proposed safety measures, outlined in detail, are discussed in the following chapters.

3.1 Storage Guidelines for Photopolymers

To ensure safe storage, photopolymers should be:

- Kept in a cool, dry, and well-ventilated area, away from direct sunlight.
- Stored separately from food and beverages.
- Protected from freezing and physical damage.
- Kept away from heat sources, open flames, and other ignition sources.
- Stored in tightly sealed containers.
- Separated from incompatible materials.

3.2 Protective Equipment for Photopolymers Handling

When working with photopolymerization processes, the following personal protective equipment (PPE) should be used consistently, with its usage monitored by authorized personnel:

- Safety goggles to protect against splashes and harmful radiation.
- Chemical-resistant, waterproof gloves to prevent skin contact.
- A protective lab coat to minimize exposure to hazardous materials.
- A respiratory mask to reduce inhalation of harmful fumes.

Table 5. Risk levels

Hazard/Harm	Description of Hazard/Harm	Consequences	F	P	C	Risk Level
The use of dangerous work equipment that can cause explosions and fires	Certain photopolymers are highly flammable	Potential fire outbreak and burn injuries	3	3	6	54
Hazardous surfaces	Removal of supports using sharp tools (scissors, scalpels, etc.)	Possible cuts and lacerations	6	1	6	36
Hazards from direct contact with live electrical installations and equipment	Device powered by electrical supply	Electric shock, burns, injury due to explosion	0.5	6	1	3
Chemical hazards, dust and fumes (inhalation, suffocation, introduction into the body, penetration into the body through the skin, etc.)	Use of photopolymers	Possible skin and eye irritation, acute/chronic organ damage, nausea, headache	10	3	10	300
Harmful effects of radiation	UV radiation, laser radiation	Skin and eye damage	6	3	10	180
Harms caused by the use of dangerous substances in production, transport, packaging, storage or destruction	Use of photopolymers in part manufacturing	Possible skin and eye irritation, acute/chronic organ damage, nausea, headache	10	3	10	300
Work longer than full time, work in shifts, reduced working hours, night work, preparedness in case of interventions	Extended working hours, night shifts, potential emergency interventions	Physical and psychological fatigue	10	1	10	100

3.3 Reducing Exposure to Harmful Radiation and Vapors

Exposure to harmful radiation, such as UV or laser radiation, can be minimized by using protective machine components. If it becomes necessary to remove a protective component while the machine is operating, specialized safety goggles designed for the specific type of radiation emitted by the machine must be worn.
During operation, machines utilizing photopolymers may release harmful vapors and gases. Therefore, it is essential to do the following:

- Place the machine in an enclosed room.
- Ensure the area is equipped with a properly functioning ventilation system.

3.4 Electrical Safety Measures

Before each use, the machine's power supply should be inspected, as it operates on electric power.

3.5 Workload Management and Employee Well-being

Extended working hours, night shifts, and on-call duties can contribute to stress and fatigue, increasing the risk of workplace accidents. It is recommended to:

- Distribute work tasks evenly among employees.
- Provide adequate rest periods between shifts.

3.6 Risk Reduction Strategies

Organizations and individuals can further minimize risks by following measures:

- Implementing standardized operating procedures.
- Providing ongoing professional development opportunities.
- Conducting regular training sessions to keep employees updated on advancements in additive manufacturing technologies, ensuring a safer working environment.

4. CONCLUSION

Additive manufacturing technologies are increasingly applied across various industrial sectors and other areas of human activity. As these technologies become more widespread, it is essential to assess and address the risks associated with their use. This paper focuses on one of the most commonly utilized processes - vat photopolymerization - which is widely used for model creation where aesthetics and intricate details are crucial.
The primary risk identified in this process is exposure to chemical hazards, leading to safety measures primarily focused on the handling and storage of photopolymers. Enhancing safety in vat photopolymerization can be achieved through the establishment of new standards that define risk assessment procedures and offer clear guidelines for safety measures. Additionally, providing users with comprehensive information and training on the correct use of machines and materials, as well as awareness of potential risks, is vital to improving overall safety.

ACKNOWLEDGMENT

The authors sincerely appreciate the support of the relevant ministries of the Republic of Serbia and the Slovak Republic in facilitating this research. The study was conducted as part of the bilateral project No. 337-00-3/2024-5/08, within the 2024-2025 bilateral cooperation cycle between Serbia and Slovakia, and also by the Slovak Research and Development Agency as part of the bilateral project No. SK-SRB-23-0024 and project no. APVV-20-042.

REFERENCES

[1] ISO/ASTM52900-21: Additive manufacturing — General principles — Fundamentals and Vocabulary
[2] L., Yang et al.: *Additive Manufacturing of Metals: The Technology, Materials, Design and Production*, Springer, ISBN 978-3-319-55127-2, 2017.
[3] https://media.formlabs.com/m/646358214a67cc1e/original/-ENEU-Safety-Data-Sheet-White-V5-Resin.pdf - FormLabs, Accessed on: 2025-02-15
[4] https://formlabs-media.formlabs.com/datasheets/2001047-SDS-ENEU-0.pdf - FormLabs, Accessed on: 2025-02-15
[5] https://www.matterhackers.com/r/lVtkfe - MatterHackers, Zortrax Inkspire Beige Photopolymer Resin – DENTAL (Zortrax Resin Dental SDS), Accessed on: 2025-02-15
[6] https://www.matterhackers.com/r/UYvcI9 - MatterHackers, PhotoCentric 3D UV DLP Firm Resin, Accessed on: 2025-02-15
[7] https://www.matterhackers.com/r/3uOCOc - MatterHackers, Nexa3D XiP Black xFlex475 Resin, Accessed on: 2025-02-15
[8] https://www.matterhackers.com/r/eK6GC8 - MatterHackers, Liqcreate Resin for SLA & DLP 3D Printers - Flexible-X, Accessed on: 2025-02-15
[9] Pejčić, D., Mišković, Ž., Popović, M., Pjević, M., Mitrović, R., Magdolen, L., Danko, J.: *PROCENA RIZIKA ADITIVNIH PROIZVODNIH TEHNOLOGIJA PRIMENOM KINIJEVE METODE*, 2024., 44. JUPITER KONFERENCIJA - ZBORNIK RADOVA, Univerzitet u Beogradu - Mašinski fakultet., 2.52-2.57.
[10] Stanković M., Stanković V.: *Comparative analysis of methods for risk assessment – "KINNEY" and "AUVA"*, Safety Engineering 3, 2013, 129–136.
[11] Mitrović R., Mišković Ž., Stamenić Z., Marković B., Tica M.: *Osnove tehničkih propisa*, Univerzitet u Beogradu – Mašinski fakultet, Beograd, ISBN 978-86-7083-861-1, 2015.
[12] ISO 12100-2010: Safety of machinery — General principles for design — Risk assessment and risk reduction

11th International Scientific Conference
IRMES 2025
Research and Development of
Mechanical Elements and Systems
June 19 – 21, 2025; Vrnjačka Banja, Serbia

Review paper DOI: 10.46793/IRMES25.119DJ

APPLICATIONS AND ANALYSIS OF NANOSTRUCTURED ADHESIVES: A REVIEW

Aleksija ĐURIĆ[1]
Biljana MARKOVIĆ[2]
Srđan SAMARDŽIĆ[3]
Dragan MILČIĆ[4]
Damjan KLOBČAR[5]
Miodrag MILČIĆĆ[6]

[1] University of East Sarajevo, Faculty of Mechanical Engineering, East Sarajevo, RS, Bosnia and Herzegovina, 77123
aleksija.djuric@ues.rs.ba, ORCID iD 0000-0002-0251-6364
[2] University of East Sarajevo, Faculty of Mechanical Engineering, East Sarajevo, RS, Bosnia and Herzegovina, 77123
biljana.markovic@ues.rs.ba, ORCID iD 0000-0001-8915-4791
[3] University of East Sarajevo, Faculty of Mechanical Engineering, East Sarajevo, RS, Bosnia and Herzegovina, 77123
srdjan.samradzic@ues.rs.ba, ORCID iD 0009-0003-4096-7523
[4] University of Niš, Faculty of Mechanical Engineering, Aleksandra Medvedeva 14, Niš, Serbia, 18211,
dragan.milcic@masfak.ni.ac.rs, ORCID iD 0000-0002-3936-7462
[4] University of Ljubljana, Faculty of Mechanical Engineering, Aškerčeva cesta 6, Ljubljana, Slovenia, 1000,
damjan.klobcar@fs.uni-lj.si, ORCID iD 0000-0002-6130-0328
[6] University of Niš, Faculty of Mechanical Engineering, Aleksandra Medvedeva 14, Niš, Serbia, 18211,
miodrag.milcic@masfak.ni.ac.rs, ORCID iD 0000-0002-1089-8390

Abstract: *Nanostructured adhesives represent a paradigm shift in bonding technology, leveraging the unique physicochemical properties of nanoscale materials to enhance adhesive performance. This review examines the fundamental principles underlying nanostructured adhesive design, focusing on the role of nanoparticles, nanofillers, and nanocrystals in improving mechanical properties. Furthermore, this paper will explore the diverse applications of nanostructured adhesives across industries, including aerospace, automotive, electronics, and biomedicine, highlighting the potential for tailored adhesive solutions.*

Keywords: *Nanostructured adhesives; nanoparticles; nanomaterials*

1. STRUCTURAL EPOXY ADHESIVE

The increasing demand for lightweight, high-performance materials across various engineering sectors has positioned structural epoxy adhesives at the forefront of advanced joining technologies [1-3]. Unlike traditional mechanical fasteners, epoxy adhesives offer advantages such as improved stress distribution and the ability to bond dissimilar materials. These superior performance attributes have significantly contributed to innovations in product design and manufacturing efficiency [4].

The effective bonding of structural epoxy adhesives is a critical aspect of their performance, relying on a combination of fundamental theories of adhesion. Below are some of the key adhesive theories important to understanding epoxy structural adhesives [5-6]:

- **Mechanical Interlocking Theory:** The adhesion occurs when the liquid adhesive flows into the microscopic pores, crevices, and irregularities on the substrate surface. Upon curing, the solidified adhesive creates a strong mechanical interlock with the surface topography. For epoxies, surface preparation that creates a rough, yet clean, surface (like grit blasting or sanding) often enhances this mechanical interlocking, leading to better bond strength.
- **Adsorption and Wetting Theory:** This theory suggests that adhesion arises from the intimate molecular contact between the adhesive and the substrate. For this to happen, the adhesive must effectively "wet" the substrate surface. Wetting refers to the ability of a liquid to spread over a solid surface, displacing air and maximizing contact. Good wetting is crucial for strong adhesion because it allows the adhesive molecules to get close enough to the substrate molecules for intermolecular forces to act.
- **Diffusion Theory:** While more prominent in the adhesion of polymers to other polymers (where molecular chains can intertwine), the diffusion theory also plays a role in some epoxy applications, particularly with certain plastic substrates. It suggests that adhesion can be

enhanced by the diffusion of polymer chains across the interface between the adhesive and the substrate. This intermingling of molecular segments creates a "gradient" interface rather than a sharp boundary, leading to a stronger, more cohesive bond.

- **Electrostatic Theory:** This theory, while less commonly cited for general epoxy adhesion, suggests that adhesion can be influenced by the formation of electrostatic forces across the interface due to differences in electron distribution between the adhesive and the substrate. This can lead to attraction between oppositely charged regions, contributing to the overall bond strength.
- **Chemical Bonding Theory:** This is arguably the strongest form of adhesion and often the most desirable for structural epoxies. It proposes that adhesion results from the formation of primary chemical bonds (covalent, ionic, or metallic) between the adhesive and the substrate. While many epoxy bonds are dominated by secondary forces (like van der Waals forces or hydrogen bonding), specific surface treatments or primers can facilitate the formation of chemical bonds, significantly increasing bond strength and durability, especially in harsh environments. For instance, some silane coupling agents used with epoxies are designed to react with both the substrate and the epoxy, forming chemical bridges.

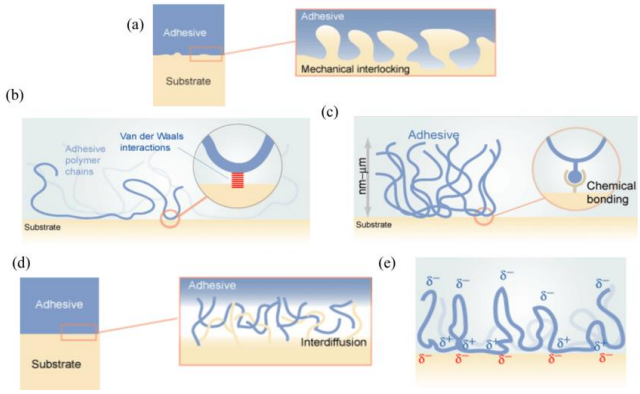

Fig.1. Five types of adhesion: mechanical interlocking (a), adsorption (b), chemical (c), adhesion by diffusion (d) and electrostatic adhesion (e) [7].

The adhesion of structural epoxy adhesives is rarely due to a single mechanism. Instead, it's typically a combination of these theories acting synergistically. The specific contribution of each theory depends on factors such as the type of epoxy, the substrate material, surface preparation, and curing conditions. Engineers and material scientists continually work to optimize these factors to achieve maximum bond strength and long-term durability in critical applications.

Structural epoxy adhesives are typically two-component systems consisting of an epoxy resin and a hardener (curing agent). The type of epoxy resin and the type of hardener dictate the curing mechanism and the final properties of the cured adhesive. Filler, toughener, plasticizer and other additives, such as colorant, can be formulated as needed [8]. Epoxy resins' chemical structure is characterized by the presence of at least two epoxide (oxirane) rings per molecule, allowing for cross-linking reactions that result in highly durable, strong, and chemically resistant thermoset networks. Some of the types of epoxy resin used for structural adhesives are: Glycidyl ether of Bisphenol A; Glycidyl ether of Bisphenol F, Glycidyl ether of Novalac, Cycloaliphatic [9].

Bisphenol A diglycidyl ether, often called as bisphenol A type epoxy resin, is the first commercialized and still most widely used epoxy resin. In volume base, it is estimated that over 75% of epoxy resin used in industry is this type. Figure 2 illustrates synthesis of DGEBA and chemical structure and key features of various functional groups for bisphenol A diglycidyl ether [8,10].

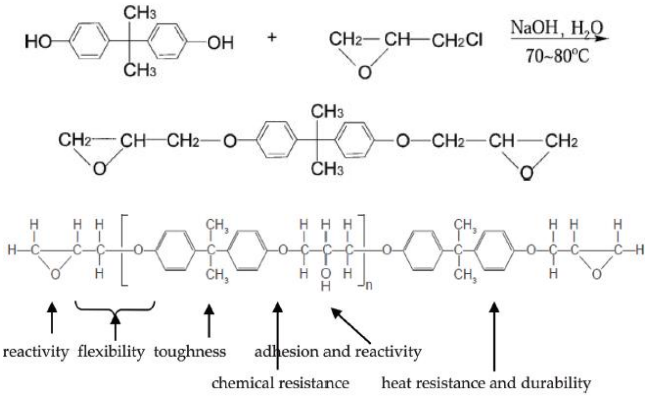

Fig.2. Synthesis of DGEBA and chemical structure and key features of various functional groups for bisphenol A diglycidyl ether [8].

2. NANOSTRUCTURED EPOXY ADHESIVE

Structural epoxy adhesives must withstand demanding conditions, including high service temperatures, thermal cycling, fatigue and vibration loading. Consequently, ongoing research focuses on enhancing their properties. A promising approach involves creating epoxy by incorporating reinforcing fillers. Recently, the trend has shifted from micro-scale to nano-scale fillers, leading to epoxy-based nanocomposite adhesives that demonstrate significantly improved multifunctional properties compared to traditional neat epoxies or those with conventional micro-particles [11,12].

Nanoparticles, owing to their dimensions below 100 nm, exhibit a unique combination of mechanical and physical properties. The introduction of even low concentrations of these nanomaterials into an epoxy adhesive matrix has been demonstrated to profoundly enhance the processing characteristics during application and, crucially, the multifunctional performance of the adhesively bonded assemblies [13, 14].

Zahed Ahmadi [11], in their review paper, show that the nanoparticles significantly increase lap shear strength of epoxy adhesive.

The author also states that the following nanoparticles are most commonly used for structural adhesives:

- Carbon-based nanoparticles: Nano-diamond, Carbon nanotubes, Carbon nanofibers, Graphene nanosheets, Graphene oxide nanoplatelets;
- Mineral nanoparticles: Clay nanosheets, Halloysite nanotubes;
- Metal-based nanoparticles: Au nanoparticles; Ag nanoparticles; Al_2O_3, ZrO_2, Fe_3O_4, SiO_2, TiO_2;
- Silica nanoparticles;
- Rubber nanoparticles.

Xiaoqian Ma et all [15] in their study concluded that the results from mechanical tests showed that the inclusion of ZrO2 nanoparticles in proper percentage contents (~3 wt%) into the epoxy resin could significantly enhance the tensile strength, modulus, fracture toughness and hardness of the composite through different mechanisms such as crack path deflection, crack pinning, plastic deformation and plastic void growth so on. Undoubtedly, these mechanical properties strongly depended on many factors, such as ZrO2 nanoparticle content, particle size, particle/matrix interface adhesion, and so on. Moreover, results of thermal analysis revealed that the char yield of the composites was significantly improved due to the incorporation of nanoparticles and additional crosslinkage between nanoparticles and matrix.

In this study of authors Iclal Avinc Akpinar et al. [14] investigated the effects of nanocomposite adhesives obtained by adding Graphene-COOH, CNT-COOH and Fullerene to the rigid, flexible and toughened adhesives at three different ratios (0.25%, 0.5%, 1%, 2% and 3%) on tensile failure load in single lap-joint geometry was investigated. Thay concluded that adding 1% Graphene-COOH to the rigid adhesive increases the failure load of the joint by 109%, adding 2% Graphene-COOH increases the failure load of the joint by 276%. However, adding Fullerene to a rigid adhesive does not cause a significant increase or decrease in the failure load of the joint.

Kübra Demir et al [16] investigated the static four-point bending loads of adhesively bonded joints after fully reversed four-point bend fatigue loading where nanoadhesives – obtained by adding carbon nanostructures into aerospace grade structural adhesive – were used to bond the joints. Single lap joint specimens were produced using a nanocomposite adhesive obtained by adding 1 wt % graphene, 1 wt % carbon nanotubes COOH and 1 wt % fullerene C60 nanostructures to a DP460 structural adhesive. AA2024-T3 aluminum alloy and carbon fiber-reinforced composites (CFRCs) with a plain weave fabric (0/90◦) were used as adherend materials. The results of the experiment show that adding nanostructures into the adhesive based on the chemical properties of the adhesive, increases the failure load up to 62% in joints subjected to dynamic (fatigue) loading at certain levels of static bending loads.

This paper of authors Jiejie Longet al [17] proposes epoxy adhesives modified by different active groups of SiO2 nanoparticles. With the introduction of SiO2-0, SiO2-NH2, and SiO2-C4H8 nanoparticles into epoxy adhesives at a mass fraction of 0.05%, the improvement in mechanical properties reached its maximum. When added to modify the epoxy adhesives, the SiO2-C4H8 nanoparticles showed the most significant improvement in mechanical properties, while the SiO2-0 nanoparticles showed the least improvement.

In addition to nanoparticles, nanofillers also have a significant impact on the properties of adhesive. Silica, alumina, carbon black, carbon nanotubes, graphene, lime, metal particles and nanoclay are some fillers that can be included in adhesives for construction, automotive and aerospace applications. Type, size and properties of the filler are important parameters for improving mechanical properties of adhesive.

To minimize the effect of moisture absorption, carbon nanofillers such as carbon nanotubes (CNTs), carbon nanohorns (CNHs), graphene nanoplatelets (GNPs) are added to reinforce epoxy adhesives. The resulting adhesive can be employed in forming adhesive joints. The results of lap shear test of adhesives without or with different carbon nano-fillers before and after hygrothermal ageing are given in Table 1 [18].

Table 1. shear strength of adhesives without or with different carbon nano-fillers before and after hygrothermal ageing [18].

Adhesive joint type	**Lap shear strength of adhesive joint prior to ageing (MPa)**	**Lap shear strength of adhesive joint after 12 weeks hygrothermal ageing (MPa)**
Pure epoxy adhesive	14 ± 0.6	6.2 ± 0.4
Epoxy adhesive with 0.5 wt% CNTs	19.7 ± 0.5	13.8 ± 0.7
Epoxy adhesive with 0.5 wt% GNPs	20.7 ± 0.8	15.1 ± 1.5
Epoxy adhesive with 0.5 wt% CNHs	20.3 ± 0.9	11.5 ± 1

In this study of authors Nergizhan Anaç and Zekeriya Doğan [19], waste mussel, olive pomace, and walnut shells were added to an adhesive material in different ratios (5%, 15%, and 30% by weight) and in different sizes (38 and 45 μm) after being recycled. Then, they were used as an adhesive in single-lap joints for the experimental investigation of joint strength. Finally, the tensile test was applied to examine the joint strength and the effects of the additives on the joints were interpreted. DX51D+Z galvanized steel material and Araldite 2015 Huntsman were used for producing specimens. The results shows that the bond strength decreased when the amount of the powder (in 38 μm size) added to adhesive was more than 5%. The the lowest strength value was obtained in joints where 38 μm olive pomace was added in the ratio of 30% by weight, and the highest strength value was obtained in joints where 45 μm olive pomace was added in the ratio of 30% by weight.

Nanostructural adhesives are used in the following branches of industry: Dental, Wood, Electrical,

Automotive, Aerospace, Construction, Pressure-sensitive, and Thermal industries.

Nano-based adhesives are extensively used in the aerospace industry due to their superior tensile characteristics, such as fatigue resistance and enhanced mechanical properties. Recently, carbon fibers incorporated within adhesive epoxy matrices have created lightweight, specialized structural materials optimized for modern spacecraft. Incorporating nanoparticles with different geometries, such as planar, tubular, and spherical, to adhesives is an innovative approach to enhancing the properties of adhesive joints in modern aircraft [20].

3. CONCLUSION

This review paper has underscored the transformative potential of nanostructured adhesives, demonstrating how the deliberate integration of nanoscale materials fundamentally redefines adhesive capabilities. The paper shows the core principles that enable nanoparticles and nanofillers to significantly bolster mechanical properties, moving beyond the limitations of conventional adhesive systems. The broad spectrum of applications, from critical aerospace components and advanced automotive designs to sophisticated electronics and innovative biomedical devices, highlights the unprecedented opportunity for developing highly customized and superior bonding solutions across diverse industries. While challenges in manufacturing, dispersion uniformity, and long-term performance validation remain, the insights gained from this review affirm that continued research and development in nanostructured adhesives will unlock new frontiers in material science, leading to adhesives with unparalleled strength, durability, and multifunctionality for future engineering demands.

ACKNOWLEDGMENT

This article/publication is based upon work from COST Action MecaNano, supported by COST (European Cooperation in Science and Technology).

REFERENCES

[1] Đurić, A., Milčić, D., Klobčar, D., Marković, B., & Milčić, M.: Tehnologije spajanja limova od čelika i legura aluminija–pregled stanja - Joining technology of steel and alluminum alloy sheets–state of the art. *Zavarivanje i zavarene konstrukcije*, pp. 107-116, 2023

[2] Sandeep, R., Natarajan, A.: Advances in joining technologies for the innovation of 21st century lightweight aluminium-CFRP hybrid structures. *Proceedings of the Institution of Mechanical Engineers, Part E: Journal of Process Mechanical Engineering*, 236(3), pp. 1239-1255, 2022.

[3] Mallick, P. K.: Joining for lightweight vehicles. In *Materials, design and manufacturing for lightweight vehicles*, pp. 321-371, Woodhead Publishing, 2021.

[4] Zdravković, N., Klobčar, D., Milčić, D., Zupančič, M., Žužek, B., Milčić, M., & Đurić, A.: Influence of surface preparation of aluminum alloy AW-5754 and stainless steel X5CRNI18-10 on the properties of bonded joints. *Materials*, 17(11), 2561, 2024.

[5] Comyn, J.: Adhesion Science 2nd Edition, Royal Society of Chemistry, 2021.

[6] Gardner, D. J.: Theories and mechanisms of adhesion. In *Handbook of adhesive technology*, pp. 3-18, CRC Press, 2017.

[7] Maia, B. S.: Study on the effect of surface energy of polypropylene/Polyamide12 polymer hybrid matrix reinforced with virgin and recycled carbon fiber. University of Toronto (Canada), 2017.

[8] Chen, C., Li, B., Kanari, M., Lu, D.: Epoxy adhesives. adhesives and adhesive joints in industry applications, IntechOpen, 2019

[9] Jin, F. L., Li, X., Park, S. J.: Synthesis and application of epoxy resins: A review. *Journal of industrial and engineering chemistry*, 29, pp. 1-11, 2015.

[10] Pethrick, R. A: Design and ageing of adhesives for structural adhesive bonding–a review. *Proceedings of the Institution of Mechanical Engineers, Part L: Journal of Materials: design and applications*, 229(5), pp. 349-379. 2015.

[11] Ahmadi, Z.: Nanostructured epoxy adhesives: A review. *Progress in Organic Coatings*, 135, pp. 449-453, 2019

[12] Khoee, S., Hassani, N.: Adhesion strength improvement of epoxy resin reinforced with nanoelastomeric copolymer. *Materials Science and Engineering: A*, 527(24-25), pp. 6562-6567, 2010.

[13] Dorigato, A., Pegoretti, A., Bondioli, F., Messori, M: Improving epoxy adhesives with zirconia nanoparticles. *Composite Interfaces*, 17(9), pp. 873-892, 2010.

[14] Akpinar, I. A., Gültekin, K., Akpinar, S., Akbulut, H., Ozel, A.: Experimental analysis on the single-lap joints bonded by a nanocomposite adhesives which obtained by adding nanostructures. *Composites Part B: Engineering*, 110, pp. 420-428, 2017.

[15] Ma, X., Peng, C., Zhou, D., Wu, Z., Li, S., Wang, J., Sun, N.: Synthesis and mechanical properties of the epoxy resin composites filled with sol− gel derived ZrO 2 nanoparticles. Journal of Sol-Gel Science and Technology, 88, pp. 442-453, 2018.

[16] Demir, K., Gavgali, E., Yetim, A. F., Akpinar, S.: The effects of nanostructure additive on fracture strength in adhesively bonded joints subjected to fully reversed four-point bending fatigue load. *International Journal of Adhesion and Adhesives*, 110, 102943, 2021.

[17] Long, J., Li, C., & Li, Y.: Enhancement of mechanical and bond properties of epoxy adhesives modified by SiO2 nanoparticles with active groups. *Polymers*, 14(10), 2052, 2022.

[18] Sanghvi, M. R., Tambare, O. H., More, A. P: Performance of various fillers in adhesives applications: A review. Polymer Bulletin, 79(12), pp. 10491-10553, 2022

[19] Anaç, N., & Doğan, Z.: The effect of organic fillers on the mechanical strength of the joint in the adhesive bonding. Processes, 11(2), 406, 2023

[20] https://www.azonano.com, Accessed on: 2025-05-05

11th International Scientific Conference
IRMES 2025
Research and Development of
Mechanical Elements and Systems
June 19 – 21, 2025; Vrnjačka Banja, Serbia

Original scientific paper DOI: 10.46793/IRMES25.123P

EXPERIMENT PREPARATION FOR LASER-CUT SPUR GEARS EFFICIENCY TESTING

Andjela PEROVIĆ[1]
Mirko BLAGOJECIĆ[2,*]
Miloš MATEJIĆ[3]
Lozica IVANOVIĆ[4]
Ivan MILETIĆ[5]

[1]University of Kragujevac, Faculty of Engineering, Kragujevac, Serbia, 34000; andjela.perovic@kg.ac.rs; ORCID iD: 0009-0005-5637-9827
[2,*] University of Kragujevac, Faculty of Engineering, Kragujevac, Serbia, 34000; mirkob@kg.ac.rs; ORCID iD: 0000-0002-0209-5010 (corresponding author)
[3]University of Kragujevac, Faculty of Engineering, Kragujevac, Serbia, 34000; mmatejic@kg.ac.rs; ORCID iD: 0000-0003-0488-0992
[4]University of Kragujevac, Faculty of Engineering, Kragujevac, Serbia, 34000; lozica@kg.ac.rs; ORCID iD: 0000-0002-9503-593X
[5]University of Kragujevac, Faculty of Engineering, Kragujevac, Serbia, 34000; imiletic@kg.ac.rs; ORCID iD: 0000-0002-1935-5771

Abstract: *Cylindrical spur gears remain widely used in mechanical systems due to their simplicity and effectiveness, despite being a long-established component in engineering. While many aspects of spur gear design, analysis, and application have been thoroughly studied during decades, recent research trends have shifted toward optimizing manufacturing efficiency and reducing production costs. This paper presents the preparation of laser-cut spur gears for the purpose of evaluating their power transmission efficiency. The gears were produced using laser cutting technology, which offers potential advantages in terms of production speed and cost-effectiveness compared to conventional manufacturing methods. The experimental evaluation is planned to be conducted using the GUNT AT200 test rig, where the gears will be mounted on test gearboxes. Multiple gear pairs with identical center distances will be examined under controlled conditions to assess their mechanical efficiency. The primary objective is to determine whether laser-cut gears, despite potential limitations in precision and surface finish, can achieve acceptable performance for practical applications, particularly in prototyping and low-load scenarios.*

Keywords: *spur gears; efficiency testing, test rig, laser-cut gears.*

1. INTRODUCTION

Gears are fundamental components in mechanical engineering, designed to transfer motion and torque efficiently between rotating shafts. A gear typically consists of a central body and a toothed rim, where the teeth are geometrically distributed to ensure smooth meshing and load transmission. The field of gear geometry focuses on defining the shape and dimensional characteristics of these teeth, which directly affect performance parameters such as efficiency, wear, and operational lifespan. Among various profile types, involute and cycloidal gears are the most prevalent, with involute gears widely favored due to their consistent transmission ratio and manufacturability. In this paper, the gears are produced from flat steel plate by laser cutting method.

Conventional gear manufacturing involves methods such as hobbing, shaping, and milling. While these techniques offer high precision, they also require significant time and cost, especially in small-batch or prototype production. In response, modern manufacturing seeks alternatives that enable faster and more economical fabrication. Laser cutting has emerged as one such method, offering speed, flexibility, and reduced tooling complexity. However, existing literature on laser-cut gears is largely limited to small-scale gears (outer diameters below 9.04 mm), typically made from stainless steel and intended for lightweight applications [1–4].

The present study extends this research by investigating the production and dimensional quality of laser-cut spur gears of varying sizes and materials. A streamlined fabrication approach was adopted to minimize time and cost while ensuring sufficient geometric accuracy. Post-processing measurements were conducted using precision

metrology tools to evaluate the resulting gear dimensions and profile conformity. Multiple gear samples were analyzed, and their geometric properties compared to assess the influence of cutting parameters, material selection, and gear size on manufacturing quality [5–6].
Previous papers such as [7] explored laser beam machining of miniature gears with emphasis on surface integrity and burr formation, while [8] focused on the operational efficiency of non-metallic meshing elements in gear reducers. Building on these directions, this paper investigates not only the manufacturing outcomes but also the functional evaluation of laser-cut gears under load.
As part of this research, six gear pairs with identical center distances were designed and fabricated using laser cutting. These gear sets have been mounted onto dedicated test gearboxes, and preparation has been completed for efficiency testing using the GUNT AT200 apparatus. Each gear pair will undergo individual testing under controlled conditions, enabling the quantification of mechanical efficiency and performance. This experimental phase aims to validate the viability of laser-cut gears for use in functional, low-load transmission systems and provide comparative insight into the suitability of different gear configurations.

2. DESIGN PARAMETERS OF THE SPUR GEARS FOR EFFICIENCY TESTING

In preparation for this research, six gear pairs (twelve individual gears) were designed, all with a fixed center distance of 80 mm, but with different transmission ratios. The gear geometries were modelled using Autodesk Inventor 2019, where each pair was designed to ensure accurate meshing under experimental conditions.
To ensure the highest fidelity of the tooth profile, the "Export Tooth Shape" function within the software was used (Figure 1). This tool exports the true involute geometry of gear teeth and avoids approximations inherent in generic CAD features. Without this export function, the resulting tooth profiles would deviate from the theoretical involute, which could lead to meshing issues or incorrect load distribution during testing.

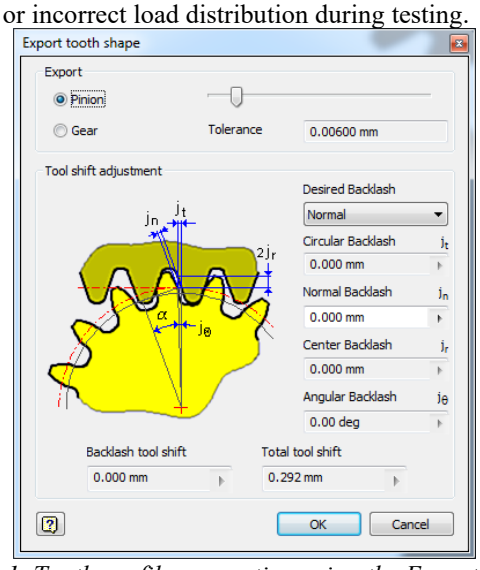

Fig. 1. Tooth profile generation using the Export Toot Shape function in Autodesk Inventor

The gear pairs were carefully selected to provide a range of transmission ratios, enabling an evaluation of performance under different kinematic conditions, while maintaining a constant center distance. Each gear pair consists of a driving gear and a driven gear, designed with a consistent module but varying tooth count.
Table 1 presents the fundamental geometric parameters of each gear pair: module m, number of teeth z, pitch diameter d, addendum diameter d_a, dedendum diameter d_f, and gear ratio u. The gear pairs are denoted as 1–6 (driving) and 1′–6′ (driven), corresponding to each test configuration.

Table 1. Basic parameters of the gear pairs

$a_{1,2}$ = 80 mm (const.)							
No.	**Gear**	***m***	***z***	***d* (mm)**	***d*$_a$ (mm)**	***d*$_f$ (mm)**	***u*$_{1,2}$**
1	1	3	26	78	83.977	70.5	
2	1'	3	27	81	88	74.523	1.04
3	2	2.75	26	71.5	76.994	64.625	
4	2'	2.75	32	88	94	81.631	1.23
5	3	2.75	24	66	71.494	59.125	
6	3'	2.75	34	93.5	99.5	87.131	1.42
7	4	2.5	25	62.5	67.5	56.25	
8	4'	2.5	39	97.5	102.5	91.25	1.56
9	5	2.5	23	57.5	62.5	51.25	
10	5'	2.5	41	102.5	107.5	96.25	1.78
11	6	2.25	24	54	58.499	48.375	
12	6'	2.25	47	105.75	110.5	100.376	1.96

The gear sets were designed with the intention of gradually increasing the transmission ratio in increments of approximately 0.2 between each test configuration. This incremental approach allows for a systematic analysis of efficiency variation as a function of transmission ratio. While exact steps of 0.2 were the target, slight deviations occurred due to the discrete nature of gear tooth counts and the requirement to maintain a constant center distance. Nevertheless, the selected configurations closely approximate the intended progression and provide a reliable basis for comparative evaluation.

3. LASER-CUT GEAR PREPARATION

The gears used in this study were manufactured using a high-precision laser cutting process, which is particularly suitable for creating complex profiles like involute teeth. The machine used was a BODOR C6 laser cutter, equipped with a fiber laser source optimized for cutting carbon steel plates with high accuracy.
The gear blanks were cut from S355 structural steel, a commonly used material in mechanical components due to its good balance of strength, machinability, and cost. The material thickness was 10 mm, and all laser-cutting operations were performed using the following parameters, given in Table 2.

Table 2. Laser-cut parameters

/	Laser cut parameters	Value
1	Thickness	10 mm
2	Speed	2.2 m/min
3	Power	7200 W
4	Frequency	5000 Hz
5	Duty cycle	100%
6	Cut height	1 mm
7	Nozzle	D-1.2 mm
8	Cut focus	8 mm
9	Gas pressure	0.9 bar
10	Gas type	Oxygen

These parameters were chosen to achieve the best possible quality for gear contours, ensuring sharp edges and minimal thermal distortion. The cutting focus and cut height were carefully calibrated to maintain consistent kerf width and avoid excessive burr formation.

The tolerances expected from this laser cutting setup are within ±0.1 mm for overall dimensions and ±0.05 mm for the tooth profiles. While laser cutting offers a high degree of precision, small deviations may still occur due to material warping, laser beam divergence, or uneven heat distribution. These deviations are particularly relevant in gear production, where even minor geometric inaccuracies can affect meshing behavior and efficiency.

Previous research [7,8] has demonstrated the feasibility of using laser cutting for producing both miniature and full-scale gears. These studies examined surface roughness, thermal effects, and tooth engagement behavior, confirming that laser-cut gears can be functionally comparable to traditionally machined ones—especially for low- to medium-load applications.

Figure 2 shows the laser-cut gear pairs fabricated for the experimental evaluation.

Fig. 2. Laser-cut produced spur gear pairs

After the laser cutting process, the gear blanks were manually de-burred using a belt sander to remove any residual slag or burrs that may have formed along the tooth edges. This post-processing step was essential to ensure smooth meshing between gear pairs and to minimize premature wear during efficiency testing. The use of the belt sander provided a quick and effective surface cleanup, especially along the root and flank areas of the teeth, without compromising the geometric accuracy of the profile.

4. PREPARATION OF TEST ASSEMBLIES FOR THE GUNT AT200

In order to evaluate the mechanical efficiency of laser-cut spur gears, a series of experimental tests was prepared using the GUNT AT200 apparatus (Figure 3).

Fig. 3. GUNT AT 200 Determination of gear efficiency

The GUNT AT200 is a didactic test rig designed for analyzing gear efficiency under controlled conditions. It allows precise measurements of input and output torque, rotational speeds, and mechanical losses across the gear stage.

4.1 Gear Assembly and Installation

Each of the six laser-cut gear pairs was mounted in a dedicated test gearbox module supplied with the GUNT system. The gearboxes were disassembled to allow precise shaft alignment and secure gear placement. Spur gears were mounted on standardized steel shafts with press-fit tolerances, ensuring minimal backlash and consistent meshing.

To preserve the integrity of the setup, all shafts were lubricated with light machine oil, and axial alignment was checked using digital calipers and alignment gauges. Proper tooth engagement was verified by rotating the shafts manually before reassembling the gear housing.

Figure 4 shows the 3D model of the dedicated test module in which the gear pair with a transmission ratio of 1.04 is installed. The model represents a simple and functional configuration designed specifically for laboratory testing. In addition to the gears, the main components of this assembly include a housing made from a standard box profile, which serves as the structural support for all other parts.

The gears are mounted on steel shafts, connected using key joints to ensure reliable torque transmission without slippage. The shafts are supported by bearings designated as UCLF 202 and UCLF 204, which are fitted into the side walls of the housing and allow stable rotation with minimal friction. This configuration enables accurate simulation of real working conditions and reliable

measurement of the mechanical efficiency of the gear assembly.

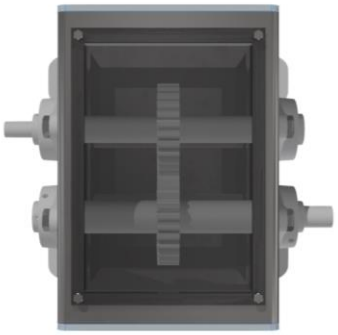

Fig. 4. 3D model of the dedicated gearbox module with a gear ratio of 1.04 – top view

Figure 5 shows the side view of the same test module, where the feet on which the entire structure is mounted are also visible. These feet provide elevation and structural stability to the gearbox housing, ensuring secure placement and proper alignment within the testing setup.

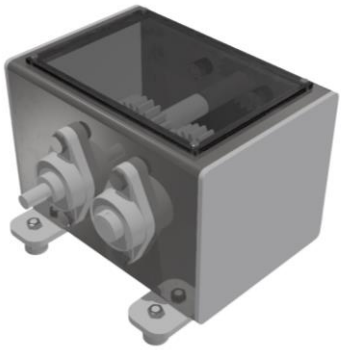

Fig. 5. 3D model of the dedicated gearbox module with a gear ratio of 1.04 – side view

This configuration follows the same structural concept as previously described, with laser-cut spur gears mounted onto precision-aligned shafts using key connections. The module maintains the standardized housing design and provides the same mounting interface for repeatable and comparable testing under identical boundary conditions (Figure 6).

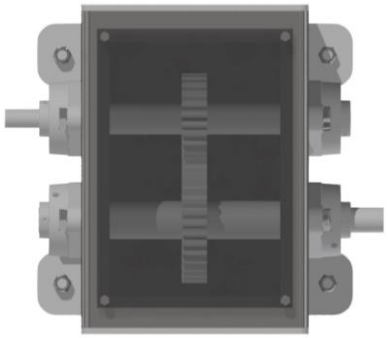

Fig. 6. 3D model of the dedicated gearbox module with a gear ratio of 1.23 – top view

In variation shown in Figure 7, the gear pair features a larger driven gear, increasing the transmission ratio while preserving the center distance. The spatial arrangement within the box-profile housing remains unchanged, ensuring that all gear pairs are tested under geometrically consistent setups. Lubrication and alignment procedures were carried out identically for all modules.

Fig. 7. 3D model of the dedicated gearbox module with a gear ratio of 1.23 – side view

Top view of the test module containing the gear pair with a transmission ratio of 1.42. This model demonstrates the effect of increased transmission ratio on gear size and tooth count while maintaining the same 80 mm center distance. All dimensional adjustments were made exclusively through the gear geometry, without altering the housing or shaft positions (Figure 8).

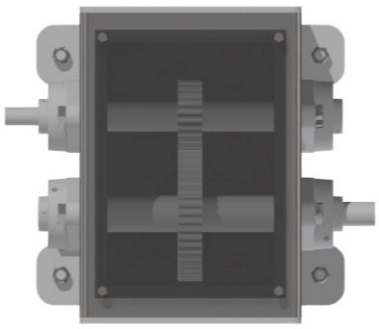

Fig. 8. 3D model of the dedicated gearbox module with a gear ratio of 1.42 – top view

Side view of the test module with the gear pair of ratio 1.42, mounted on structural feet. As in previous configurations, the module rests on robust steel feet, providing a stable base during testing. This side perspective highlights the spatial distribution of components within the housing and confirms the compact, modular design intended for rapid assembly and disassembly during experimental procedures (Figure 9).

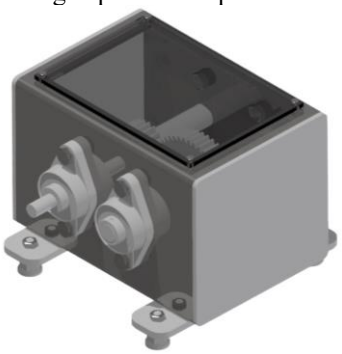

Fig. 9. 3D model of the dedicated gearbox module with a gear ratio of 1.42 – side view

Figure 10 shows the technical drawing of the assembled test model. The top part of the image presents the front

view of the housing with the visible shaft positions and mounting elements.
Below, the sectional view A–A clearly displays the internal configuration, including the placement of shafts, gears, and the housing walls. This drawing was provided to illustrate the internal structure of the gearbox and ensure dimensional accuracy during assembly. It also serves as a reference for verifying alignment, spacing, and mechanical compatibility between components.

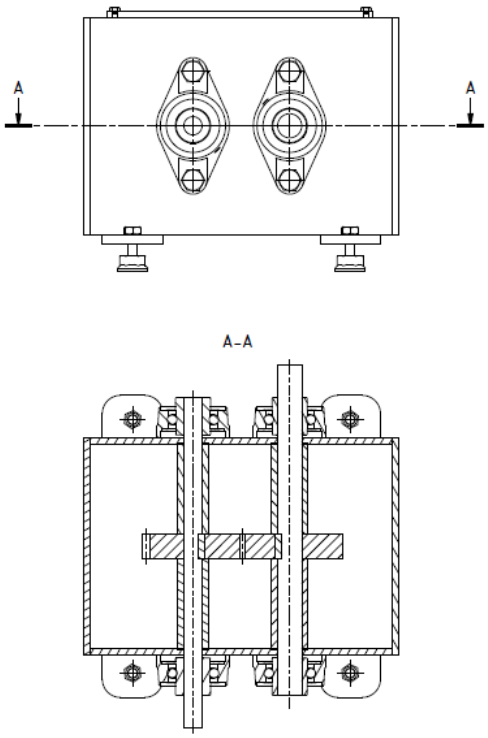

Fig. 10. Technical drawing of the test gearbox – front view and section A–A.

4.2 Test Environment and Measurement Setup

The GUNT AT200 system is equipped with an electromagnetic brake and a precision torque sensor to enable controlled loading of the gearbox. The test rig records input torque, output torque, and angular speed of both shafts. These parameters allow for direct calculation of mechanical efficiency:

$$\eta = \frac{T_{out} \cdot \omega_{out}}{T_{in} \cdot \omega_{in}} \times 100\% \quad (1)$$

where T represents torque and ω angular velocity:

- T_{in} - is the input torque,
- T_{out} - is the output torque,
- ω_{in} - is the angular velocity of the input shaft,
- ω_{out} - is the angular velocity of the output shaft

The GUNT AT200 test rig is equipped with an electromagnetic brake and high-precision torque sensors, enabling accurate measurement of input and output torque, as well as rotational speed. These values are continuously recorded throughout testing to enable real-time efficiency calculations.
Prior to each test sequence, the system was calibrated to ensure reliable data acquisition. Environmental parameters such as ambient temperature and humidity were also monitored, as they may influence frictional losses and sensor stability. All tests were conducted under comparable environmental conditions to ensure consistency and data validity across gear pairs.
Before the experiments, the apparatus was calibrated to ensure accurate measurements. Temperature and ambient humidity were logged, as they can influence friction and measurement stability. Each gearbox was tested under similar environmental conditions to ensure comparability of the results.

4.3 Experimental Plan

The experimental campaign consists of six gear pairs, all having an identical center distance of 80 mm, but varying transmission ratios from 1.00 to 1.96, as presented in Chapter 2. The test plan is structured as follows:

- Each gear pair is tested individually.
- Measurements are taken under three different load conditions to evaluate the load-dependence of efficiency.
- For each load condition, the test is repeated three times to ensure result consistency and reduce statistical deviation.
- The sequence of tests follows increasing gear ratios to observe efficiency trends with higher transmission ratios.

Data from the torque sensors is recorded using the GUNT software interface and exported for further analysis. All results will be compared to evaluate the effect of gear size, module, and ratio on overall system efficiency.

5. CONCLUSION

This study presented the preparation and initial methodology for testing the efficiency of laser-cut spur gears using the GUNT AT200 apparatus. Spur gears remain a widely used mechanical component, and this research aims to contribute to the cost-effective and rapid production of gears using modern laser-cutting techniques.

A total of six gear pairs were designed with varying transmission ratios, yet all maintained a constant center distance of 80 mm. CAD modeling was carried out using Autodesk Inventor 2019, employing the *Export Tooth Shape* function to ensure accurate involute profiles. The gear blanks were produced via laser cutting on a BODOR C6-12kW machine, with carefully selected cutting parameters and post-processing procedures to ensure surface quality and dimensional accuracy.

Test assemblies were prepared in accordance with the GUNT AT200 configuration, which allows precise measurement of torque and speed to evaluate mechanical efficiency. The experimental setup includes consistent measurement conditions, repeated load scenarios, and a structured testing plan to ensure result reliability.
Future work will involve conducting all planned tests and analyzing the efficiency trends in relation to gear geometry and transmission ratio.
The final goal is to determine whether laser-cut gears, prepared using simplified manufacturing processes, can offer acceptable performance levels in practical

applications—especially for prototyping, educational use, or light-duty mechanical systems.

This study lays a solid foundation for further investigation into the mechanical performance and application scope of laser-cut gears.

ACKNOWLEDGMENT

This research was supported through the collaboration with two companies that contributed by providing laser-cut gear samples used in the experimental phase. The authors would like to express their sincere gratitude to **Zastava TERVO** and **Limes Processing** for their technical support and material contributions, which were essential for the successful realization of this work.

REFERENCES

[1] Anghel, C., Gupta, K., Jen, T.C.: *Analysis and optimization of surface quality of stainless steel miniature gears manufactured by CO_2 laser cutting*, Optik, Vol. 203, ISSN 0030-4026, 2020.

[2] Anghel, C., Gupta, K., Jen, T.C.: *Optimization of Laser Machining Parameters and Surface Integrity Analysis of the Fabricated Miniature Gears*, Procedia Manufacturing, Vol. 51, pp. 878–884, ISSN 2351-9789, 2020.

[3] Elmanov, A., Kengboev, S., Nematov, S.: *Mathematical Model of Cutting Gears from Steel with Laser Beams*, Universum: Технические науки, Vol. 2(119), pp. 19–25, ISSN 2308-8079, 2024.

[4] Du, X.Y., Liu, S.W., Guan, J.: *Design and Performance Analysis of an Electromagnetic Railgun*, Journal of Physics: Conference Series, Vol. 2378(1), pp. 115–125, ISSN 1742-6588, 2022.

[5] Belarhzal, S., Daoudi, K., Boudi, E.M., Bachir, A., Elmoumen, S.: *A Multiobjective Optimization Analysis of Spur Gear Pair: The Profile Shift Factor Effect on Structure Design and Efficiency*, Mathematical Problems in Engineering, Vol. 2021, Article ID 123456, ISSN 1024-123X, 2021.

[6] Li, T., An, X., Deng, X., Li, J., Li, Y.: *A new tooth profile modification method of cycloidal gears in precision reducers for robots*, Applied Sciences, Vol. 10(4), ISSN 2076-3417, 2020.

[7] Popa, C., Gupta, K., Mashamba, A., Jen, T.C.: *Investigation on laser beam machining of miniature gears*, Proceedings of Conference on Manufacturing, pp. 1–7, 2020.

[8] Matejić, M., Matejić, M., Miletić, I., Marić, D., Milojević, S., Stojanović, B.: *Efficiency Calculation of Cycloid Reducer with Plastic Meshing Elements*, Tehnički vjesnik, Vol. 32(2), pp. 748–755, ISSN 1330-3651, 2025.

11th International Scientific Conference
IRMES 2025
Research and Development of
Mechanical Elements and Systems
June 19 – 21, 2025; Vrnjačka Banja, Serbia

Original scientific paper DOI: 10.46793/IRMES25.129M

ANALYSING NETWORK INFRASTRUCTURE IMPACT ON INFORMATION - COMMUNICATION TECHNOLOGY (ICT) DEVELOPMENT

Miloš MILOVANČEVIĆ[1]
Srđan STOJIČIĆ[2]
Mirjana MILJANOVIĆ[3]
Nikola SIMONOVIĆ[4]
Dragana TRNAVAC[5]

[1]University of Niš, Faculty of Mechanical Engineering, 18000, Serbia;
milos.milovancevic@masfak.ni.ac.rs; ORCID iD: 0000-0002-7891-1010
[2]University of Niš, Faculty of Mechanical Engineering, 18000, Serbia;
srdjan.stojicic@masfak.ni.ac.rs; ORCID iD: 0000-0002-6743-2196
[3]University of East Sarajevo, Faculty of Production and Management Trebinje
ORCID iD: 0000-0002-7394-8703
[4]University MB, Faculty of Business and Law, 11000 Belgrade, Serbia;
[5]University MB, Faculty of Business and Law, 11000 Belgrade, Serbia;
ORCID iD: 0000-0003-1571-4500

Abstract: *An investigation on the impact that network infrastructure has on the growth of information and communication technology (ICT) would be carried out as part of this project. Because of the difficulty of the problem from a statistical standpoint, the neuro-fuzzy technique is used for analysis. The nature of information and communications technology, which is characterized by fast change and diversity, adds an additional layer of complexity to the challenge of evaluating impacts in any subject. This research has shown that there is a complicated web of relationships between the individual influence and background variables such as the education level of a nation and the regulations that are imposed by the government. The network infrastructure is the primary metric for information and communication technology development in this research. The findings have shown that the percentage of homes who have access to a computer has a favorable effect on the IDI score. Therefore, the percentage of houses that have a computer has a considerable impact on the IDI index. This is especially true when the percentage of households that have a computer is paired with the number of fixed telephone lines per 100 people.*

Keywords: *ICT; ICT development index (IDI); network infrastructure; neuro-fuzzy.*

1. INTRODUCTION

Communication infrastructure and networks have globally influenced economic and social growth, as well as the development of information and communication technology (ICT) [1], [2]. The interconnection between these factors has been extensively studied, highlighting the role of network infrastructure as a cornerstone of modern development. Policymakers have increasingly acknowledged the importance of expanding and enhancing communication networks, given their direct impact on productivity, physical capital, and overall economic growth. There exists a wealth of technical evidence supporting the idea that improved quality and accessibility of network infrastructure can significantly elevate human productivity and stimulate economic advancement. This paper specifically aims to explore the quantity and types of network infrastructure, their output levels over time, and their growth trajectories in developing and transition economies. These aspects remain insufficiently examined in existing literature, despite their critical importance in understanding global ICT dynamics [3-5]. ICT has revolutionized how people live and work worldwide, transforming businesses, government functions, individual quality of life, interpersonal interactions, and the natural and built environment.

The advancement of ICT has led to the development of internationally comparable statistics, enabling governments to design, implement, monitor, and evaluate ICT policies more effectively. The remarkable progress in measuring ICT infrastructure and its usage has provided valuable insights, although it also presents certain statistical challenges. These challenges arise from the complex nature of quantifying the impact of network infrastructure on ICT development [6]. Understanding a nation's ICT achievement is vital for assessing its socio-economic transformation, as ICT acts as a key driver of innovation, productivity, and competitiveness. A valid

national evaluation of ICT development status is, therefore, indispensable. Research by [7] has delved into this domain, proposing future directions for examining the micro- and macro-level impacts of ICT on national development, with a specific focus on Africa.

In Kenya, for instance, challenges related to network infrastructure, such as network service control, coverage, growth, and resource allocation, have significantly influenced the ability of mobile service providers to share open ICT infrastructure [8]. These challenges underscore the critical need for improved network infrastructure to facilitate ICT development. ICT progress is often measured by the ICT Development Index (IDI) developed by the International Telecommunication Union (ITU). IDI serves as a composite measurement tool, combining national scores derived from 11 weighted indicators. These indicators reflect various dimensions of ICT access, use, and skills, providing a comprehensive assessment of a nation's telecommunication sector [9]. By benchmarking IDI scores, countries can identify their strengths and weaknesses in ICT development compared to other nations [10].

The primary objective of this research is to evaluate the effect of network infrastructure on IDI. Specifically, it investigates the impacts of fixed telephone lines per 100 inhabitants, mobile phone subscriptions, and the proportion of households with computers and Internet access at home on a nation's IDI score. This analysis offers a nuanced understanding of how specific elements of network infrastructure contribute to ICT development.

Methodologically, the study utilizes data spanning from 2007 to 2014 across 155 countries, providing a robust dataset for analysis. Given the statistical complexity of assessing the relationship between network infrastructure and IDI, a neuro-fuzzy approach is employed. This method integrates neural networks and fuzzy logic to handle nonlinear relationships and imprecise data, enabling a more accurate evaluation of the underlying dynamics [11]. By leveraging this advanced analytical technique, the study seeks to shed light on the intricate interactions between network infrastructure and ICT development, offering valuable insights for policymakers and stakeholders aiming to enhance ICT-related outcomes globally.

2. METHODOLOGY

2.1. ICT Development Index (IDI)

The ICT Development Index (IDI) is a crucial indicator published by the International Telecommunication Union (ITU) in the United States, developed through an international agreement to standardize the measurement of information and communication technologies (ICT) [10]. This index serves as a key benchmarking tool, enabling comprehensive assessments of ICT progress within and across nations. Governments, development agencies, telecommunications operators, and researchers widely use the IDI to make informed comparisons and formulate policies aimed at advancing ICT development. Its structure reflects three core dimensions: access, usage, and skills, encapsulated in 11 distinct indices that provide a multidimensional view of ICT growth.

The IDI's access sub-index, which is particularly relevant to this study, evaluates the availability of ICT infrastructure and connectivity. Indicators include the prevalence of fixed telephone lines per 100 inhabitants, which ranges from 0.2 to 61.1, and mobile cellular telephone subscriptions, varying between 6.4 and 322.6. The proportion of households with a computer, spanning from 2.2% to 98.1%, illustrates disparities in access to personal computing technology, while the proportion of households with Internet access at home, ranging from 1.5% to 98.5%, highlights variations in digital connectivity. These indicators collectively offer a detailed picture of the foundational elements supporting ICT development.

For this research, data from 2007 to 2014 across 155 countries was analyzed, providing a rich dataset for understanding global trends in ICT infrastructure and its impact on IDI. The statistical complexity of assessing relationships between network infrastructure and IDI necessitated the use of advanced analytical techniques. To address this, a neuro-fuzzy approach was employed, blending the predictive capabilities of neural networks with the flexibility of fuzzy logic to handle nonlinear and uncertain data relationships. This methodology allows for a nuanced understanding of how network infrastructure contributes to the broader goals of ICT development.

In addition to the neuro-fuzzy approach, the analysis incorporated key statistical metrics to evaluate model performance and reliability. The coefficient of determination (R^2) was used to quantify how effectively the model explains variations in IDI, while the root mean square error (RMSE) provided a measure of the average prediction error. Together, these metrics ensure the robustness of the findings, offering a precise and reliable depiction of the influence of network infrastructure on ICT development.

This study underscores the critical role of network infrastructure as a driver of ICT development, as reflected in the IDI. By providing a standardized framework for measuring ICT progress, the IDI enables stakeholders to identify strengths, address weaknesses, and craft policies tailored to their unique socio-economic contexts. The findings highlight the need for continued investment in ICT infrastructure and provide valuable insights for future research and policymaking efforts aimed at bridging digital divides and fostering sustainable technological growth worldwide..

3. RESULTS

IDI prediction errors based on each input are separately shown (Fig. 1). Thus, the input with the smallest training prediction error has the largest effect on IDI indicator. Noting that the Proportion of households with a computer has the smallest training error (0.6478) with the highest effect on IDI index. Also, mobile cellular telephone has the highest training error (1.5708) with the smallest effect on IDI index.

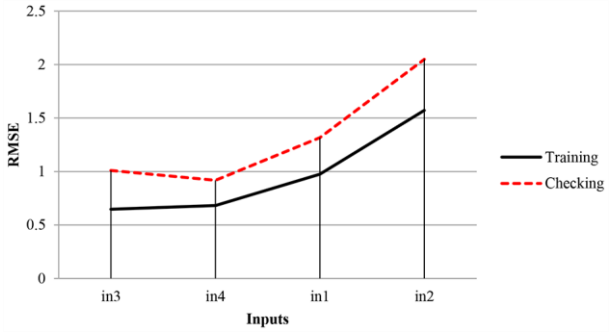

Fig. 1. Inputs influence on IDI prediction

The combination of two inputs affects the IDI prediction (Fig. 2). Based on the results, the combinations of fixed telephone lines per 100 inhabitants and proportion of households with a computer is the optimal combination with the largest impact on IDI index because the training error is the smallest one for this combination (0.4883). on the other hand, the combination of fixed telephone lines per 100 inhabitants and mobile cellular telephone has the smallest effect on IDI indicator because of the highest training error (0.6742).

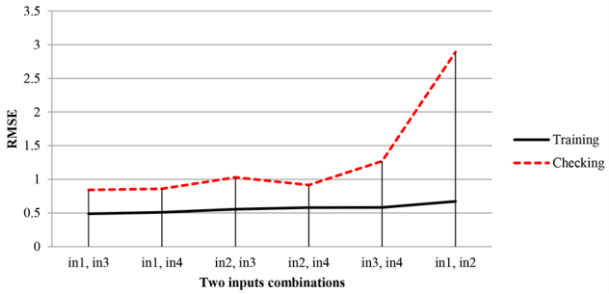

Fig. 2. Two inputs combinations influence on IDI prediction

Thus, the selected influential inputs have been separately extracted and analyzed. Fig. 3 has shown the neuro-fuzzy prediction of IDI indicator based on the proportion of households with a computer. Fig. 4 has shown the neuro-fuzzy prediction of IDI indicator based on the combination of fixed telephone lines per 100 inhabitants and proportion of households with a computer. Based on the scatter plots, IDI prediction for two inputs has the most prediction accuracy, accordingly, Neuro-fuzzy models with six bell-shapes membership functions and 300 epochs are also used.

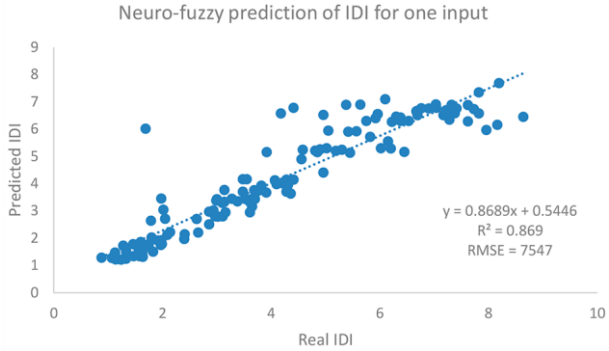

Fig. 3. Neuro-fuzzy prediction of IDI indicator based on the proportion of households with a computer

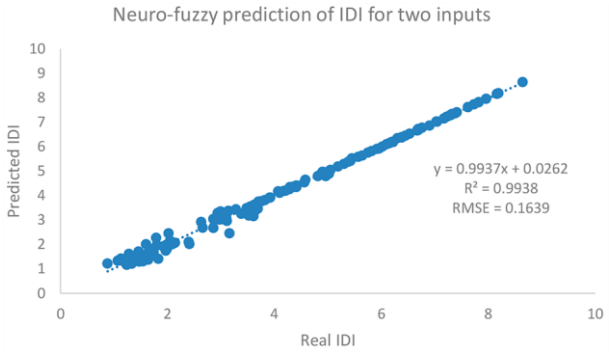

Fig. 4. Neuro-fuzzy prediction of IDI indicator based on combination of fixed telephone lines per 100 inhabitants and the proportion of households with a computer

Thus, the selected influential inputs have been separately extracted and analyzed. Fig. 3 has shown the neuro-fuzzy prediction of IDI indicator based on the proportion of households with a computer. Fig. 4 has shown the neuro-fuzzy prediction of IDI indicator based on the combination of fixed telephone lines per 100 inhabitants and proportion of households with a computer. Based on the scatter plots, IDI prediction for two inputs has the most prediction accuracy, accordingly, Neuro-fuzzy models with six bell-shapes membership functions and 300 epochs are also used.

4. CONCLUSION

The impact of network infrastructure on the development of information and communication technology (ICT) has been thoroughly analyzed, revealing its significant influence on economic and social growth as well as ICT advancement in any country. Network and communication infrastructure play a pivotal role in driving technological progress and fostering broader development. ICT development is often assessed using the ICT Development Index (IDI), which provides a standardized measure of a nation's progress in this field. However, measuring the effects of network infrastructure on ICT development poses unique challenges due to the rapidly evolving and highly diverse nature of ICT. The dynamic and multifaceted nature of these technologies makes it particularly difficult to establish clear causal relationships and quantify their impact across different contexts.

To address these complexities, a neuro-fuzzy analytical approach was employed in this study. This advanced methodology combines the adaptive learning capabilities of neural networks with the interpretative power of fuzzy logic, making it well-suited for analyzing nonlinear and uncertain relationships. Through this approach, it was observed that the proportion of households with a computer exerts a positive and significant effect on the IDI. The presence of computers in households contributes not only to improved access to ICT tools but also to broader engagement with digital platforms, ultimately enhancing a country's overall ICT development as captured by the IDI. This finding highlights the critical role that household-level access to technology plays in driving national ICT progress.

Moreover, the study uncovered that the effect of household computer access on the IDI is amplified when combined with other infrastructure elements, particularly fixed telephone lines per 100 inhabitants. This synergistic relationship suggests that the integration of traditional and modern communication technologies creates a more robust and interconnected network infrastructure, which further facilitates ICT development. Fixed telephone lines, while often considered outdated in the context of mobile and broadband technologies, still provide foundational connectivity that can complement the use of computers in households. The interplay between these two indicators underscores the importance of a holistic approach to infrastructure development, where investments in diverse forms of connectivity work together to maximize their collective impact.

These findings reinforce the idea that ICT development is a multifaceted process requiring coordinated efforts across multiple dimensions of infrastructure. The positive effects of network infrastructure on the IDI, as demonstrated in this study, underscore the importance of prioritizing investments in both modern digital technologies and traditional communication systems. Such an approach not only enhances the accessibility and functionality of ICT but also supports broader socio-economic growth by bridging digital divides and fostering inclusive development. By leveraging advanced analytical methods like the neuro-fuzzy approach, researchers and policymakers can gain deeper insights into the complex interactions between network infrastructure and ICT development, ultimately guiding more effective strategies for technological advancement.

REFERENCES

[1] Czamanski, D. and D. Broitman, *Information and communication technology and the spatial evolution of mature cities.* Socio-Economic Planning Sciences, 2017. **58**: p. 30-38.

[2] Peeraer, J. and P. Van Petegem, Integration or transformation? Looking in the future of Information and Communication Technology in education in Vietnam. Evaluation and Program Planning, 2015. **48**: p. 47-56.

[3] Mitra, A., C. Sharma, and M.-A. Véganzonès-Varoudakis, Infrastructure, information & communication technology and firms' productive performance of the Indian manufacturing. Journal of Policy Modeling, 2016. **38**(2): p. 353-371.

[4] Kobos, M., et al., Information Inference in Scholarly Communication Infrastructures: The OpenAIREplus Project Experience. Procedia Computer Science, 2014. **38**: p. 92-99.

[5] Cepolina, S. and H. Ghiara, *New trends in port strategies. Emerging role for ICT infrastructures.* Research in Transportation Business & Management, 2013. **8**: p. 195-205.

[6] Zou, P.X., et al., Cloud-based safety information and communication system in infrastructure construction. Safety science, 2017. **98**: p. 50-69.

[7] Bankole Dr, F. and L. Mimbi, *ICT infrastructure and it's impact on national development: a research direction for Africa.* The African Journal of Information Systems, 2017. **9**(2): p. 1.

[8] Namisiko, P., M. Sakwa, and M. Waweru, Effects of Network Infrastructure sharing Challenges on Open Information Communication Technology Infrastructure Sharing among Mobile Service Providers in Kenya. International Journal of Information Engineering and Electronic Business, 2015. **7**(3): p. 11.

[9] Gerpott, T.J. and N. Ahmadi, Composite indices for the evaluation of a country's information technology development level: Extensions of the IDI of the ITU. Technological Forecasting and Social Change, 2015. **98**: p. 174-185.

[10] James, J., *The ICT Development Index and the digital divide: How are they related?* Technological Forecasting and Social Change, 2012. **79**(3): p. 587-594.

[11] Jang, J.-S., *ANFIS: adaptive-network-based fuzzy inference system.* IEEE transactions on systems, man, and cybernetics, 1993. **23**(3): p. 665-685.

11th International Scientific Conference
IRMES 2025
Research and Development of
Mechanical Elements and Systems
June 19 – 21, 2025; Vrnjačka Banja, Serbia

Original scientific paper
DOI: 10.46793/IRMES25.133K

OPTIMIZATION OF PREDICTIVE MODELS FOR THE THERMAL BEHAVIOR OF LEADING AND THREADED SPINDLES AND THEIR CORRESPONDING ROLLING BEARINGS USING AI AND BIG DATA

Vladislav KRSTIC[1]
Dragan MILCIC[2]
Miodrag MILCIC[3]

[1] [1]Pedagogical Faculty in Vranje - University of Nis,Vranje, Republic of Serbia, 17500; vladanis73@gmail.com; 0000-0002-4372-7977
[2] Faculty of Mechanical Engineering -- University of Nis, Nis, Republic of Serbia, 18000; dragan.milcic@masfak.ni.ac.rs; 0000-0002-3936-7462
[3] Faculty of Mechanical Engineering -- University of Nis, Nis, Republic of Serbia, 18000 ; miodrag.milcic@masfak.ni.ac.rse; 0000-0002-1089-8390

Abstract: *The thermal behavior of mechanical components has a critical impact on the accuracy and reliability of machine tools, especially for components such as leading spindles, threaded spindles, and their rolling bearings. During intensive operation, heat is generated due to friction, internal losses in lubrication, and external influences, leading to thermal deformations, increased clearance, and loss of positioning.*
Managing and predicting the thermal behavior of these components is crucial for ensuring machining accuracy, particularly in high-precision and CNC machine tools. The development of numerical methods such as thermal FEM simulations and the application of deep learning models and artificial intelligence have enabled a deeper understanding and better prediction of thermal effects. Additionally, a large number of new algorithms allow for the optimization of models, particularly in the domain of boundary conditions in thermal models.
The aim of this research is to present methods for optimizing models for predicting the thermal behavior of leading and threaded spindles and their bearings under real operating conditions, based on collected temperature data, operating parameters, and experimental validation.

Keywords: *boundary conditions; AI; Big Data; product optimization; Fourth industrial revolution*

1. INTRODUCTION

The cornerstone and main characteristic of the Fourth Industrial Revolution is the Cyber-Physical System (CPS). The simplest definition of a CPS can be formulated as: "A CPS is a system that represents an intelligent integration of the physical and digital worlds." The physical interpretation of this definition actually represents a physical system composed of machines, various tools, and devices that are enhanced and upgraded with sensors, actuators, and installed software that enable data processing and autonomous communication. From this definition, it can be concluded that all devices and machines that are elements of a CPS have the capability for fully autonomous operation as well as communication with other devices with which they are networked. For this reason, especially the process modules of the CPS must have very good operational performance. Therefore, great importance is placed on the design phase, which should deliver an optimized product that can guarantee a high level of accuracy and reliability through its construction.

Fig.1 CPS sistem [1]

At the beginning, it is necessary to define the process module. The process module is responsible for performing specific actions on products—workpieces. These are essentially machine tools that have now been structurally reduced to a process module that can be easily mounted, for example, on a mobile robot that moves completely autonomously. Of course, the machine tool as

a specific part of the module possesses all necessary devices and elements required for its proper operation, and in addition, the tool itself is equipped with essential sensors and communication and networking devices. Examples of process modules include drilling, grinding, milling modules, and special assembly cells, etc.

Process models related to material removal (drilling, turning, milling, etc.) are particularly interesting. These are machine tools that have a wide application in material processing technology. Since we are primarily discussing fully automated machine tools here, the well-known conditions related to the level of quality and speed of workpiece processing are present. In many cases, these machine tools operate at high rotational speeds, requiring exceptionally high processing quality. Given these facts and considering the nature of the technological processes for which these tools are intended, it can be concluded that they will be exposed to increased thermal loads arising partly from resistance during material processing and partly from friction in the rolling bearings of leading/threaded spindles. Therefore, it is crucial to properly optimize all parts of the machine tool to ensure the required level of product quality, reliability, and the designed operational lifespan of the machine.

In the era of sophisticated technologies such as Artificial Intelligence (AI), Big Data (BD), Cloud Computing (CC), Virtual and Augmented Reality (VR and AR), simulations, etc., great opportunities have been offered in terms of optimization and better insights into relevant phenomena closely tied to the optimization of future process modules. This paper will present examples of the use of various tools that have proven to be very effective for predicting, estimating, optimizing, and describing the thermal behavior of leading and threaded spindles and their associated rolling bearings.

There is a significant number of scientific papers related to the simulation and optimization of various machine systems. Research on thermal processes in complex machine systems, such as leading/threaded spindles and their associated bearings, is particularly interesting. In [2], a three-dimensional finite element model was established along with the mechanisms of heat transfer boundary conditions. The temperature distribution and the thermal displacement field of the spindle under thermal load were simulated. According to the simulation results, it was determined that the total temperature is radially distributed from the center of the spindle core to the environment after the temperature reaches dynamic equilibrium, while the thermal displacement in the axial (z-direction) is maximized, which is the main cause that affects processing accuracy. To reduce the temperature difference, a Peltier material was applied to the spindle housing, and using carbon fiber material with a negative coefficient of thermal expansion, a reduction in thermal deformation was achieved. By combining the addition of the Peltier material and the carbon fiber material, the temperature distribution throughout the spindle was improved, while thermal deformations were reduced from 31.4 μm to 24.1 μm, resulting in a total reduction in deformations of 23.2%. Neglecting the interaction of the thermal structure in high-speed spindle systems can lead to errors in modeling thermal characteristics. To improve modeling accuracy, [3] analyzed the mechanism of interaction of the thermal structure (finite element mesh) and proposed a method for iterative modeling of thermal characteristics in a closed loop to modify heat sources and thermal boundary conditions of the spindle system at each sub-step. The amount of generated heat in the bearings and the built-in motor, as well as convective coefficients and thermal contact resistances of bearing contact surfaces, were calculated.

The generated heat from the bearings was calculated using SKF's thermal model, and the obtained results were compared with results obtained through the integral method. The determination of the generated amount of heat from the bearings was modified, taking into account the combined effect of variations in the viscosity of the lubricant and the thermally induced preloading of the bearings. Furthermore, a new geometric-mechanical model was proposed for calculating thermal contact resistances of bearing connections, utilizing the characterization of the rough surface morphology and establishing the mechanics of “multi-scale contact” of the contacting surfaces. The verification of the proposed model was carried out through experiments on a spindle system subjected to different rotational frequencies. The results showed that the errors in modeling the temperature field and thermal deformations were significantly reduced and that the proposed model has the capability to compensate for thermal errors. The performance of high-speed machine tools depends not only on speed, power, torque, dynamic and static stiffness, but also on the thermal behavior of the spindle. These parameters directly impact productivity and the quality of machining operations.

In [4], a 3D thermal finite element model was presented based on the thermomechanical model of the bearing and a numerical model of the spindle. Based on the thermomechanical analysis of bearings with angular contact, the generated heat and thermal contact resistance were determined for each position of the ball. To ensure the most accurate possible analysis in determining the thermal contact resistance, the bearings were divided into several zones based on the geometry of their cross-section. The aforementioned constraints were applied to the 3D FEM model (Finite Element Method), which enabled the establishment of the temperature field distribution and thermal equilibrium of the spindle. To demonstrate the effectiveness of the proposed model, experimental measurements of spindle and bearing temperatures were conducted using thermocouples and thermography.

Thermal deformations caused by temperature rise affect the dynamic performance of the spindle. Additionally, changes in dynamic performance will influence the temperature rise and thermal deformation of the system. The latter case has rarely been the focus of previous research. Therefore, in [5], the thermal network model of the spindle was improved by considering the effects of thermomechanical coupling (the simultaneous influence of mechanical and thermal loads) and an iterative method for solving coupled equations was presented. The model was verified by measuring spindle temperature. The relative error between the predicted and experimental

results at two measurement points was reduced by 9.56% and 3.44% after accounting for thermomechanical coupling effects. Comparison with experimental results shows that the proposed model, which takes into account thermomechanical coupling, provides a more accurate temperature field than previous models.

The thermal characteristics of the spindle have a significant impact on the quality of the workpiece. In [6], a new approach to modeling the thermal characteristics of spindles in real-time was proposed, based on a bond graph method with a simplified thermal structure and a brief assessment and calibration of thermal parameters. First, the thermal characteristics of the spindle were analyzed and then divided into different thermal components. A network of thermal capacitances and thermal resistances was established based on the analysis of heat generation and transfer mechanisms, leading to the development of a thermal characteristics model using the bond graph method. The parameters of the spindle's thermal conditions were briefly assessed using theoretical analysis and empirical formulas. An experiment was conducted to calibrate the thermal parameters of the model, followed by experiments aimed at verifying accuracy and robustness, with results showing stable prediction performance with a maximum error of 0.7355°C and an average error of 0.1989°C. Finally, this model was applied in a quantitative investigation of the effects of operating conditions on the thermal characteristics of the spindle and in real-time prediction of spindle thermal deformation with a maximum error of 5.26 μm and an average error of 1.45 μm. The results indicate that this approach has significant advantages in predicting spindle thermal behavior in real-time and can be utilized in industrial applications.

2. THEORETICAL FOUNDATIONS

Throughout engineering and scientific practice, temperature has been taken as a relevant and reliable parameter for describing and monitoring various processes. Temperature has conditionally become one of the leading parameter upon which complex analyses and assessments of both processes and the state of machine systems are based. It carries multiple essential pieces of information that, when placed in the proper context, can aid in understanding and describing various phenomena. It is important to note that temperature, as a physical quantity, can be easily measured, which is significant when choosing relevant parameters. Its measurement can be conducted using various sensors that are relatively inexpensive, sufficiently precise, and of simple construction, making them easy to position at measurement points. As such, temperature becomes one of the standard parameters that is increasingly utilized (ranging from the simplest measurements to its use as an auxiliary variable in, for example, vibration diagnostics).

The focus of this paper is on the thermal behavior of leading and threaded spindles. The leading spindle (the spindle of the tool head) is one of the very important elements of any machine tool. It serves to hold the tool and transfer motion from the machine drive to the workpiece. The tool's movement realizes the function of the machine tool, meaning that material processing is carried out. During machining, the tool, along with its holder (leading spindle), endures additional resistances that arise as a result of the machining process. All these resistances, for the context of this work, are converted into thermal energy, which generates a specific temperature field that now becomes an additional load factor for the machine tool. The most affected components are the tool itself and the leading spindle, as well as the rolling bearing through which the leading spindle is supported. The temperature field that forms induces thermal loads manifested through elastic deformations of the tool, the leading spindle, and the rolling bearing. If the operating temperature during machine operation remains within the prescribed limits, the resulting deformations of the aforementioned machine elements will be within the elastic deformation zone, which is not dangerous for the machine itself. However, if for some reason the operating temperature increases and remains elevated for a certain period, the elastic deformations of these machine elements transition into plastic deformations, resulting in permanent deformations of the elements. Following the plastic deformation of the machine elements, there is a loss of product quality due to the use of a tool that no longer maintains its designed processing accuracy. In addition to the heat generated due to resistance during machining, the leading spindle also experiences additional thermal loads stemming from friction in the rolling bearing. The situation with threaded spindles is similar to that of leading spindles, with the added thermal load induced by the corresponding nut of the threaded spindle on one side and friction in the rolling bearings through which the threaded spindle is supported. Plastic deformations of threaded spindles are undesirable as they directly affect the accuracy of guidance, e.g., the machine's working table.

To conduct a proper analysis of the thermal behavior of the elements (leading/threaded spindle and associated rolling bearings), it is essential to create the most accurate digital model possible, on which appropriate tools will be applied to provide the most truthful representation of the temperature field occurring under pre-established machining conditions. For this purpose, advanced tools and technologies brought by the Fourth Industrial Revolution can be utilized, such as digital twins (Digital Twin – DT), digital shadows (Digital Shadow – DS), and AI.

The task can be reduced to analyzing thermal processes that can be stationary or more frequently non-stationary. For this purpose, it is best to use the Law of Conservation of Energy for the general transport quantity Φ, which has the form [7]:

$$\frac{\partial(\rho\Phi)}{\partial\tau} + div\left(\rho\vec{W}\Phi\right) = div(\Gamma_{\Phi} grad\Phi) + S_{\Phi} \quad (1)$$

Γ_{Φ} - diffusion coefficient,

S_{Φ} - the term of the equation relating to the source

The left side of differential equation (1) consists of the unsteady and convective terms, while the right side contains the diffusive and source terms. According to the index notation "Φ," it is concluded that the diffusion

coefficient and the source term relate to the transport quantity. In many cases, the analysis of the thermal behavior of a system is carried out by considering the source term in the unsteady three-dimensional diffusion problem of heat conduction through homogeneous isotropic bodies with constant physical parameters (ρ = const, Γ_Φ = const). The differential equation that describes the unsteady three-dimensional problem of heat conduction through homogeneous isotropic bodies takes the following form:

$$\rho c \frac{\partial T}{\partial \tau} = \lambda \left(\frac{\partial^2 T}{\partial x^2} + \frac{\partial^2 T}{\partial y^2} + \frac{\partial^2 T}{\partial z^2} \right) + S \qquad (2)$$

In this case, the transport quantity is a function of the spatial coordinates x, y, z, and time τ, or in mathematical form [7]:

$$T=T(x, y, z, \tau) \qquad (3)$$

Equation 2 is a second-order differential equation that describes unsteady heat conduction in a solid body. In a physical sense, it establishes a relationship between temperature, time, and spatial coordinates.

From this formulation of Equation 2, it can be concluded that the set of solutions satisfying the equation is large. In order to narrow it down to the examined problem, it is necessary to define what are known as the conditions of uniqueness, which are [8]:

- Geometric conditions (dimensions and shape of the body in which the process occurs);
- Conditions (thermo-physical properties of the substance from which the body is made, such as thermal conductivity coefficient λ, specific heat c, density ρ, etc.);
- Intensity of internal sources (or sinks) of heat in space and time;
- Initial conditions (temperature distribution in the body at the initial moment in time);
- Boundary conditions - conditions of heat exchange on the external surfaces of the body.

Considering the theoretical principles of the Law of Conservation of Energy, one can move on to the selection of technology and tools that should provide the most accurate digital model of the system whose thermal behavior is being analyzed. For this purpose, DT, DS, and BD, as well as AI with their available tools for analyzing large data sets, can be utilized. Of course, software for simulations (numerical analysis) [9] such as MATLAB, COMSOL Multiphysics, LabVIEW, Dymola, etc., are also included.

For a quality analysis of the thermal behavior of a system, the use of DT and BD is very effective. DT is essentially a digital twin (copy) of a physical object in the virtual world, but not just any copy; it is a "living" one. What does "living" mean in the virtual world, and what gives the DT its "life"? The answer lies in the intelligent devices installed on the real physical model that continuously measure relevant parameters during the operation of the system so that they can be visualized in real-time and used for analysis. All this data, along with any data generated as a product of the analysis (e.g., intermediate results of certain calculations), is considered part of a large data set. Since all this data is generated by smart devices connected to cloud software and has the capability for mutual communication and information exchange, BD technology is needed for processing, consolidating, and storing the data. All data from the large data set is very important and contributes to the increase in the quality of the analysis by providing data that, when grouped (set), becomes an input for the tools that will conduct the thermal analysis of the spindle and corresponding rolling bearings. This data finds its application in both simulations and in the design of predictive models that have the ability to forecast the thermal behavior of the system. Additionally, it is very effectively used as input for algorithms that can optimize specific parameters important for the thermal analysis of a system. There is a significant amount of scientific literature that presents a range of different algorithms and tools for optimizing certain parameters.

3. OPTIMIZATION OF THE MODEL

An increasing number of studies on the thermal behavior of leading/threaded spindles and their corresponding rolling bearings combine multiple tools to enhance the analysis as much as possible, thereby achieving more accurate results. Since the rolling bearings used for supporting leading/threaded spindles are special bearings that qualitatively and structurally differ from standard rolling bearings, modeling and creating a digital model, as well as the thermal analysis of these models, is quite complex. The situation is somewhat simpler for leading spindle systems, while systems with threaded spindles are significantly more complex due to the much more complicated support structure.

Taking into account Equations 1 and 2 when analyzing the thermal behavior of leading/threaded spindles and their corresponding rolling bearings, attention must be paid to the existing heat transfer mechanisms and the reference surface over which heat transfer occurs. In this segment, one of the specific parameters is identified, which itself becomes an independent task: the contact surfaces, that is, the contact resistances and boundary thermal conditions. The existing software designed for numerical analyses offers a range of standard types of finite elements that can be used to create a mesh for conducting thermal analysis of the observed system. However, using them allows for only partial modeling of the contact surface between two elements in a system, and hence those surfaces, i.e., the boundary conditions, require some additional method to optimize them, which would provide a more accurate description of the behavior of the analyzed system, thereby further improving the overall thermal model in the context of predicting and evaluating thermal behavior.

In [10-12], a numerical analysis of the temperature field in the support of a threaded spindle conducted using the ABACUS program is presented. Supporting threaded spindles is one of the most demanding tasks in engineering, and accordingly, the thermal model of the support is quite complex. Two details are crucial for analyzing the thermal behavior of this system: the reference surface over which heat is transferred and the overall heat transfer coefficient. The reference surface is

clearly defined from the outset by the geometry and size of all structural elements that comprise it, while determining the overall heat transfer coefficient through the system is a special challenge in the entire analysis. This arises from Equations 1 and 2 and the conditions that define the set of solutions for the observed system in [10-12]. Specifically, the reference surface, among other things, is formed by the contact surfaces that constitute two or more elements that are in mutual contact.

For the precise determination of thermal behavior, a complete understanding, or a full description of the boundary conditions, which currently represent an unknown, is required. Several factors affect the boundary conditions, such as preload, quality of the processed surfaces, or surface roughness, etc. Therefore, the analysis presented in [10-12] goes beyond the boundary conditions by using special thermal diffusion axisymmetric finite elements, with the main assumption that it describes the boundary conditions using an elastic model, with air as the medium of the contact surface. By combining the mentioned finite elements, a temperature field has been obtained that successfully describes the thermal behavior of the support structure.

The thermal analysis of the tool head spindle - leading spindle is presented in [13]. As with the previously mentioned analyses, determining the boundary conditions is a significant challenge here as well. In order to obtain the most accurate thermal model of the leading spindle, two methods were utilized: numerical analysis using finite elements that has been further optimized and enhanced with one of the bio-inspired algorithms. The optimization of the boundary conditions of the analyzed system employed the artificial bee colony algorithm. This algorithm is a well-known method that is based on the natural behavior of bees in a colony, where bees "share" their tasks to optimize the entire colony's work in the context of food collection and colony preservation. Accordingly, this algorithm was used to solve the mixed-variable optimization problem of the response surface model. This significantly optimizes the thermal behavior of the boundary surfaces as well as the boundary conditions. The ultimate result was a thermal model that provided significantly more accurate simulation results due to the optimization of the boundary conditions.

Since elevated operating temperatures affect the elastic deformations of the spindle, it is essential to maintain operating temperatures within permissible limits to prevent plastic deformations that can impact tool machining accuracy. In this regard, [14] presents a combination of two methods to optimize accuracy and robustness in predicting thermal displacement of the spindle. The elbow method and the Long Short-Term Memory (LSTM) deep learning method were used for optimization.

Similar algorithms can also be used for optimizing technological processes, as demonstrated in [1]. Here, the problem of material flow and the technological process in the BMW company was optimized using an ant colony algorithm (artificial ant colony algorithm).

AI, with its methods and tools, is also very prominent in the analysis and prediction of the thermal behavior of leading/threaded spindles. The most commonly used are Artificial Neural Networks (ANN), which are often optimized using one of the existing methods, depending on the ultimate goal of the ANN. For instance, the thermal behavior of an axial angular contact ball bearing intended for supporting a threaded spindle can be predicted using an ANN as shown in [15], while [16] presents a model for predicting the friction coefficient in a sliding bearing. AI methods are popular in predicting and analyzing various processes, not just thermal ones, because they correlate multiple parameters that are physically difficult or nearly impossible to interrelate. AI is also effective in cases where the correlations of relevant parameters are highly nonlinear or stochastic, which is the case for the boundary conditions of leading/threaded spindles and their associated rolling bearings. In some cases, if the system is simpler, standard ANN can be designed relatively easily; however, systems with more specific boundary conditions need to be modeled by combining various AI methods and tools.

For example, in a system involving the leading/threaded spindle and their corresponding bearings, which are often of specific designs and predict additional coupled elements such as preload nuts, bolt connections, etc., it is essential to consider the thermo-mechanical coupling for designing a predictive model of such a system. This involves the simultaneous influence of temperature on mechanical characteristics (dilatation, deformation, pre-stress, etc.). This is particularly pronounced in models for predicting thermal errors of the spindle (here referring to the error or accuracy of spindle guidance). In this case, it is advisable to combine multiple methods and tools to optimize the boundary conditions, which have a significant share in the final outcome.

Therefore, [17] presents a model for predicting thermal spindle errors based on the improved particle swarm optimization neural network and back propagation (IPSO-BP). IPSO was used to optimize the parameters of the BP neural network, such as initial weights and thresholds. In comparison with the prediction model of the genetic algorithm (Genetic Algorithm - GA) combined with back propagation (GA-BP), the IPSO-BP neural networks demonstrated superiority regarding modeling efficiency, robustness, and accuracy compared to the GA-BP model.

4. CONCLUSION

From the presented paper, it can be concluded that the massive data set that is increasingly expanding day by day in the era of IoT is highly useful for analyzing and improving existing products as well as for designing new ones. Most products on the market today are "smart" products that contain essential elements (sensors, wireless communication devices, microcontrollers, etc.) that enable continuous recording and measurement of relevant parameters, which can later be transformed into knowledge through Big Data technology, and that knowledge can lead to innovation, profit, and a leadership position in the global market.

Raw data by itself means nothing, but when placed in the right context, at the right time, and with the right user, it becomes significant value. This is why AI and Big Data technology are actively expanding their resources and

tools that will, on one hand, be easy to use, and on the other hand, be able to process massive data sets very quickly and in real-time.

This paper focuses on the use of massive data sets for the purpose of product optimization and development, particularly in the context of the Fourth Industrial Revolution. The emphasis is placed on methods and the use of massive data sets aimed at optimizing boundary conditions in the thermal behavior of leading/threaded spindles and their corresponding rolling bearings. Since these are highly responsive systems intended for Cyber-Physical Systems (CPS), it is necessary for all relevant parameters affecting the efficiency and operability of CPS to be as optimized as possible, which will be achieved through the use of IoT and the appropriate tools offered by AI and Big Data.
It should be noted that Big Data can be very successfully used in the domain of predictive maintenance and monitoring of machine systems. As a result, an increasing number of machine elements are receiving new designs and additional elements that now make them intelligent. As intelligent, these machine elements (rolling bearings, leading/threaded spindles, etc.) become generators of massive data sets that help improve and optimize all processes as well as the designs of machine systems and elements, thus achieving better quality, energy efficiency, and increased reliability and availability of machine systems.

REFERENCES

[1] G., Reinhart.: *Handbuch Industrie 4.0-Geschäftsmodelle, Prozesse, Technik,* Carl Hanser Verlag, ISBN: 978-3-446-44642-7, 2017

[2] Bin, C., Xin, G., Decheng, C., Haolin, L: Simulation on thermal characteristics of high-speed motorized spindle. *Case Studies in Thermal Engineering*, Volume 35, 102144, ISSN 2214-157X, 2022 https://doi.org/10.1016/j.csite.2022.102144

[3] Jialan, L., Chi, M., Shilong, W., Sibao, W., Bo, Y., Hu, S.: Thermal-structure interaction characteristics of a high-speed spindle-bearing system. *International Journal of Machine Tools and Manufacture*, Volume 137, ISSN 0890-6955, 2019 https://doi.org/10.1016/j.ijmachtools.2018.10.004.

[4] Živković, A. M., Zeljković, M. V., Mlađenović, C. D., Tabaković, S. T., Milojević, Z. L., Hadžistević, M. J.: A study of thermal behavior of the machine tool spindle, *Thermal Science*, 23(3 Part B), 2117-2130. 2019 https://doi.org/10.2298/TSCI180129118Z

[5] Zhou, C., Qu, Z., Hu, B., & Li, S.: Thermal network model and experimental validation for a motorized spindle including thermal–mechanical coupling effect, *The International Journal of Advanced Manufacturing Technology*, 115(1), pp. 487-501. 2021 https://doi.org/10.21203/rs.3.rs-159145/v1

[6]]Yang, Y., Du, Z., Feng, X., & Yang, J.: Real-time thermal modelling approach of a machine tool spindle based on bond graph method, *The international journal of advanced manufacturing technology*, 113(1), pp. 99-115. 2021 https://doi.org/10.1007/s00170-021-06611-8

[7]] Ilić, G., Vukić, M., Radojković, N., Živković, P., Stojanović. I.: *Termodinamika II – Osnove prostiranja toplote i materije,* Mašinski fakultet Univerziteta u Nišu, ISBN 978-86-6055-056-1, 2014

[8] Krstić., V.: Istraživanje konstrukciono-triboloških parametera kugličnih ležaja sa kosim dodirom tipa ZKLF sa aspekta optimalne osnovne funkcije - doktorska disertacija, Mašinski fakultet Univerziteta u Nišu 2018

[9] https://automatika.elfak.ni.ac.rs/files/Nastavni_materijal/Softver%20za%20simulaciju/Skripta_Softver%20za%20simulaciju%20dinamickih%20sistema.pdf, Accessed on: 2025-04-15

[10] Krstić, V., Milčić, D., Milčić, M.: Thermal Analysis of the Threaded Spindle Bearing Assembly in Numerically Controlled Machine Tools, *Facta Universitatis, Series: Mechanical Engineering,* ISSN 0354-2025. Vol. 16, 2, pp. 261-261. 2018, DOI: 10.22190/fume170512022k

[11] Krstić, V. Milčić, D.: Numerical Analysis of the Thermal Load of the Bearing Assembly of Threaded Spindle Realized Using the ZKLN- and ZKLF-Type Bearing, *Proceedings of The 3rd International Conference Mechanical Engineering in XXI Century*, ISBN: 978-86-6055-072-1, 2015

[12] Krstić, V., Milčić, D.: The Research of Heat Balance of Bearing Mounting Realized by Axial Ball Bearings with Angular Contact Intended For the Threaded Spindles, *17th Symposium on Thermal Science and Engineering of Serbia, Sokobanja*., ISBN: 978-86-6055-076-9 , 2015

[13] Zhang, L., Xuan, J., Shi, T.: Obtaining More Accurate Thermal Boundary Conditions of Machine Tool Spindle Using Response Surface Model Hybrid Artificial Bee Colony Algorithm, *Symmetry*, 12(3), 361, 2020, https://doi.org/10.3390/sym12030361

[14]] Liu, Y., C., Li, K..Y., Tsai, Y.C.: Spindle Thermal Error Prediction Based on LSTM Deep Learning for a CNC Machine Tool, *Applied Sciences*, 11(12), 5444. 2021 https://doi.org/10.3390/app11125444

[15] Krstić, V., Milčić, D., Madić, M., Milčić, M., Milovančević, M.: Prediction of Friction Torque and Temperature on Axial Angular Contact Ball Bearings for Threaded Spindle Using Artificial Neural Network, *Journal of Vibration Engineering & Technologies,* ISSN: 2523-3920. Vol. 10, 4 pp 1473-1480. 2022, DOI: 10.1007/s42417-022-00461-8

[16] Milčić D., Alsammarraie, A., Madić, M., Krstić, V., Milčić, M.: Predictions of Friction Coefficient in Hydrodynamic Journal Bearing Using Artificial Neural Networks, *Strojniški vestnik – Journal of Mechanical Engineering.* ISSN: 0039-2480. Vol. 67, 9 pp. 411-420, 202, DOI: 10.5545/sv-jme.2021.7230

[17] Li, B., Tian, X., Zhang, M.: Thermal error modeling of machine tool spindle based on the improved algorithm optimized BP neural network,).. *Int J Adv Manuf Technol*, 105, pp. 1497–1505, 2019, https://doi.org/10.1007/s00170-019-04375-w

11th International Scientific Conference
IRMES 2025
Research and Development of
Mechanical Elements and Systems
June 19 – 21, 2025; Vrnjačka Banja, Serbia

Original scientific paper
DOI: 10.46793/IRMES25.139G

EFFICIENCY OPTIMIZATION OF A WORM GEAR TRANSMISSION USING THE CCD METHOD AND ANOVA

Sandra GAJEVIĆ[1]
Aleksandar SKULIĆ[2]
Anđela ŽIVKOVIĆ[3]
Slavica MILADINOVIĆ[4]
Stefan ČUKIĆ[5]
Milan BUKVIĆ[6]
Blaža STOJANOVIĆ[7]

[1]University of Kragujevac, Faculty of Engineering, Kragujevac, Serbia, 34000; sandrav@kg.ac.rs; ORCID iD: 0000-0002-7169-8907
[2]Kosovo and Metohija Academy of Applied Studies, Leposavić, Serbia; 43500; aleksandarskulic@gmail.com ; ORCID iD: 0000-0002-5332-3087
[3]University of Kragujevac, Faculty of Engineering, Kragujevac, Serbia, 34000; andjela.zivkovici123@gmail.com;
[4]University of Kragujevac, Faculty of Engineering, Kragujevac, Serbia, 34000; slavicam@kg.ac.rs; ORCID iD: 0000-0002-4408-0634
[5]University of Kragujevac, Faculty of Engineering, Kragujevac, Serbia, 34000; stefan.cukic@kg.ac.rs; ORCID iD: 0009-0002-5765-1712
[6]University of Kragujevac, Faculty of Engineering, Kragujevac, Serbia, 34000; milanbukvic76@gmail.com; ORCID iD: 0000-0003-2892-0389
[7]University of Kragujevac, Faculty of Engineering, Kragujevac, Serbia, 34000; blaza@kg.ac.rs; ORCID iD: 0000-0003-4790-2856

Abstract: *This study investigates the application of experimental design methods in optimizing the efficiency of a single-stage worm gearbox, with the CCD method being used to achieve maximum efficiency. The experiments were conducted on the AT200 device, considering rotational speed, lubricant type (VG220) and experiment duration as key factors. The optimization of efficiency was performed using the CCD method, and the results were analyzed through ANOVA. The findings indicate that rotational speed is a more influential factor compared to operating time, with the highest efficiency values recorded at the maximum rotational speed (≈1603.5 min⁻¹) and an operating time of 10 minutes. Mathematical models were developed with a 95% confidence level, enabling the prediction of efficiency based on the examined factors.*

Keywords: *worm gearbox, efficiency, optimization, CCD method, ANOVA.*

1. INTRODUCTION

Worm gear transmissions are key components in many machine systems where high-speed reductions, compact structure and quiet operation are essential. These transmissions are widely used in industry, including the automotive, tool, construction, and mining industries [1, 2]. Their ability to achieve a high transmission ratio in a small space, with characteristic sliding contact between the worm and worm gear, makes them suitable for many engineering applications. However, this contact leads to efficiency challenges as sliding friction causes significant energy losses, heat generation and accelerated component wear. Despite numerous advantages, their efficiency can be significantly reduced due to high energy dissipation due to friction and heating, which poses challenges regarding the long-term working life and maintenance of these systems [1-4].

Compared to classic cylindrical and bevel gears, worm gears often have a lower efficiency, which negatively affects performance and economy of operation. The effectiveness of these systems depends on several factors, including teeth geometry, gear material, machining quality, lubrication method, as well as the operating conditions.

Optimization of these parameters can significantly improve transmission performance, reduce energy losses and increase system reliability. Advanced optimization methods, such as the Response Surface Methodology (RSM) in combination with the Central Composite Design (CCD), enable a systematic analysis of the influence of key parameters and their optimization [5-7]. The application of the CCD method enables a detailed

investigation of the interactions between various factors and the identification of optimal combinations that improve the efficiency of the worm gear transmission. After the conducted experimental tests, the Analysis of Variance (ANOVA) is used to evaluate the statistical significance of individual parameters and their mutual interactions [8]. Miladinović et al. [9] applied the Taguchi-Grey method for optimization of the worm gear transmission efficiency. The experiments involved varying the rotational speed, the viscosity of the lubricant and the current intensity of the control unit, using a Taguchi L27 orthogonal matrix. The results showed that the current intensity (72.1%) has the greatest influence on the efficiency, while the viscosity of the lubricant has a negligible effect. The optimization made it possible to reduce energy losses and increase output power. ANOVA confirmed that increasing the rotational speed and current intensity provides the highest efficiency. Stojanović et. al. [10] investigated the influence of materials on the efficiency of the worm gear transmission. Experiments have shown that the best combination of materials to increase efficiency include bronze for the worm gear and steel for the worm, which reduces friction and wear, thus extending the service life of the system. Skuilić et al. [11] analyzed the factors that influence the power losses and the efficiency of the worm gear transmission, such as gear materials, geometry of the worm pair, type and viscosity of the lubricant, rotational speed, shape of the worm, amperage and temperature. Experiments were carried out with lubricants of different viscosities to study their effect on the efficiency.

Additionally, research has shown that worm gear efficiency can be increased by analysis the power losses and thermal characteristics of the system. Friction losses and temperature distribution on the tooth contact surface were analyzed using finite element methods (FEM) [12]. Also, the application of neural networks (ANN) enables the modeling of power losses based on the input and output parameters of the transmission [13]. These models showed that changing parameters, such as the contact pattern of the teeth, can significantly affect the thermal behavior and efficiency of the transmission. More effective control of the contact pattern can reduce heat losses and increase the load capacity of worm gears, which has been confirmed through experimental analyzes and simulations [14].

The aim of this paper is to optimize the efficiency of the worm gear transmission using the CCD method and statistical analysis of the results. It is expected that the research results will contribute to the development of more efficient, reliable and economical machine systems based on worm gears.

2. DESIGN OF THE EXPERIMENT

Design of the experiment is an extremely important tool in the scientific and engineering world for improving the process of product manufacture. Key components of these activities are found in the design and development of new manufacturing processes as well as in process management [6]. The application of experimental design techniques in the early stages of process development can bring the following results [3]: improved process yield, reduced variability and better compliance with nominal or target requirements, reduced development time, reduced overall costs.

Design of the experiment methods are also of crucial importance in engineering design where new products are developed and existing ones are improved. The use of experimental design in product manufacture can result in products that are easier to manufacture, that have improved performance and reliability in the field, lower production costs, and shorter product design and development time.

2.1. CCD Methodology

The CCD method of experimental design allows a comprehensive analysis of interactions between multiple factors at different levels. This method is based on three basic types of points: factorial design points, axial points and central points. Factorial points define the basic experimental structure, axial points allow for examination of response curvature and central points serve to assess the reliability of the model. By combining these points, the CCD method provides a systematic approach to the investigation of complex systems and process optimization [15, 16].

There are three types of CCD designs, where the value of the parameter α is determined depending on how high the accuracy is required and how feasible its calculation is. The position of the star points, which depends on the value of α, directly affects the quality of the experimental design and the accuracy of the results. The number of experiments performed at the central point of space significantly contributes to increasing the accuracy of the estimation of the obtained data.

A "quality of design" approach is important for estimating the variability of the coefficients and system responses. One of the most important characteristics of a CCD is its rotatability, which means that the prediction error is the same for all points that are equidistant from the central point. This property allows for uniform accuracy throughout the experimental space [16-18]. Based on these characteristics, CCD designs are classified into three main types [17]: Central Composite Circumscribed (CCC), Central Composite Inscribed (CCI) and Central Composite Face Centered (CCF).

2.2. Experimental research plan using CCD

Experimental research was conducted on a single-stage worm gear, mounted on the AT200 device at the Center for Testing of Mechanical Gears of the Faculty of Engineering in Kragujevac. A description of the device and components is available in the literature [19]. The efficiency was calculated according to the model given in the AT200 device catalog and literature [16, 20]. Lubrication of the worm gear pair transmission was performed by the immersion method for uniform distribution of the lubricant. The basic characteristics of the lubricant, such as viscosity index, flash point, freezing point and density, are listed in the literature [19]. The efficiency of the worm gear transmission was tested on the AT200 device at different operating modes, using oil with a viscosity of 220 mm²/s and a fixed current intensity

value of 0.125 A. The experimental research plan was based on the CCC method, as a variant of the CCD.

This research varied the rotational speed (three levels), the duration of the experiment (three levels) and one load level. Based on the defined factors and a certain value of α (according to the equations presented in the literature [16]), an experimental matrix was formed, which was used to conduct the experiments.

3. APPLICATION OF CCD METHOD IN OPTIMIZATION OF THE EFFICIENCY OF A WORM GEAR

The experimental design consists of 13 experimental points and variables whose influence on the efficiency is observed. The significance of the effects of the independent variables and their influence on the dependent variables is checked by analysis of variance (ANOVA). ANOVA was performed to determine the individual linear, quadratic and interaction regression coefficients. Table 1 shows the values obtained based on the calculation of the uncoded value of α.

Table 1. The uncoded value of α

Factor level	Input rotational speed, min^{-1}	Duration of experiment, min
-α	896.5	2.93
-1	1000	5
0	1250	10
+1	1500	15
+α	1603.5	17.07

Table 2 shows the experimental matrix generated by the CCD method, with variation in the rotational speed (factor A) and the duration of the experiment (factor B). The factors were analyzed at five levels, including the central and axial points, to ensure even coverage of the experimental space and to allow accurate modeling of nonlinear effects.

Table 2. Experimental results

No	A	B	Efficiency
1.	-1.00000	-1.00000	0.504754
2.	1.00000	-1.00000	0.523200
3.	-1.00000	1.00000	0.509785
4.	1.00000	1.00000	0.524980
5.	-1.414	0.00000	0.501979
6.	1.414	0.00000	0.531811
7.	0.00000	-1.414	0.510229
8.	0.00000	1.414	0.516234
9.	0.00000	0.00000	0.512648
10.	0.00000	0.00000	0.512102
11.	0.00000	0.00000	0.512880
12.	0.00000	0.00000	0.513073
13.	0.00000	0.00000	0.511906

Nonlinear factors occur when a change in one factor does not lead to a proportional change in the output factor, in this case the efficiency. If an increase in the rotational speed initially increases the efficiency, but after a certain rotational speed the efficiency begins to decrease, this is a nonlinear effect. The axial points allow capturing these curvatures because they are located at the boundaries of the experimental space, where nonlinearity is usually most pronounced. If nonlinear effects are not taken into account, the model could mispredict the results, especially for values outside the central points. Adding axial points allows a more precise description of such relationships and more valid conclusions.

Based on the experimental results in Table 2, it is observed that the efficiency ranges from ≈0.502 to ≈0.532. The central points provide values close to the mean, confirming the stability and reproducibility of the experiment, and also serve to estimate the experimental error and model stability. The factor points represent combinations of the minimum and maximum values of factors A and B, which allows for the assessment of their main effects and interactions. The axial points extend the experimental space to the extreme values of the factors, allowing for the assessment of quadratic effects and the identification of nonlinear relationships.

Table 3 shows the regression analysis for the efficiency.

Table 3. Regression analysis for efficiency

Term	Coef	SE Coef	T-Value	*VIF*
Constant	0.512522	0.000567	904.00	
A	0.013405	0.000634	21.15	1.00
B	0.002705	0.000634	4.27	1.00
*A*A*	0.004681	0.000961	4.87	1.02
*B*B*	0.001018	0.000961	1.06	1.02
*A*B*	-0.00163	0.00127	-1.28	1.00

The results of the regression analysis obtained in the Minitab 20 software indicate a significant influence of factors A and B. The model constant is 0.512522, while the coefficients of factors A (0.013405) and B (0.002705) are positive and statistically significant with P-values of 0.000 and 0.004, indicating that an increase in these factors contributes to an increase in the efficiency. The square of factor A (A*A) also shows a significant influence (P = 0.002), suggesting the existence of a nonlinear effect, while the square of factor B (B*B) is not statistically significant (P = 0.325), indicating a weaker nonlinear effect of this factor.

The interaction effect of factors A and B (A*B) is not significant (P = 0.241), indicating that their mutual interaction does not significantly affect the efficiency. High T-values for factors A and A*A confirm their dominant influence, while low VIF (<1.02) indicate the absence of multicollinearity. These results suggest that the optimization of the transfer should be focused primarily on factor A, considering its quadratic effects, while the interaction effects and nonlinear influence of factor B do not play a key role.

Table 4. ANOVA analysis

Source	DF	Adj SS	Adj MS	F-Value	P-Value
Model	5	0.000789	0.000158	98.20	0.000
Linear	2	0.00748	0.000374	232.72	0.000
A	1	0.00719	0.000719	447.23	0.000
B	1	0.000029	0.000029	18.21	0.004
Square	2	0.000038	0.000019	11.95	0.006
A*A	1	0.000038	0.000038	23.72	0.002
B*B	1	0.000002	0.000002	1.12	0.325
2-Way Interaction	1	0.000003	0.000003	1.64	0.241
A*B	1	0.000003	0.000003	1.64	0.241
Error	7	0.000011	0.000002		
Lack-of-Fit	3	0.000010	0.000003	13.61	0.014
Pure Error	4	0.000001	0.000000		
Total	12	0.000800			
R-sq (98.59%)*; R-sq(adj)* (97.59%); *R-sq(pred)* (90.70%)					

The high value of R-sq (98.59%) indicates that the model successfully explains almost all the variability in the data. This value is characteristic of well-designed experiments and shows that the selected factors are crucial for the studied process. The high value of the coefficient of determination R-sq(adj) of 97.599% means that the model accurately describes the variations in the data, without being too complex. The predictive coefficient of determination R-sq(pred) of 90.709%, although slightly lower than R-sq, shows that the model has a good ability to predict new data. The difference between R-sq and R-sq(pred) suggests the possibility of improving the model, potentially by including additional factors.

Based on Table 4, it can be seen that the overall model is statistically significant ($P < 0.05$), with an F – value of 98.20. This confirms that the selected factors are adequate for describing variations in the efficiency. Factor A (rotational speed) has the most dominant effect ($F = 447.23$, $P< 0.005$). This indicates that increasing the rotational speed significantly affects the efficiency. While factor B (experimental duration) is also significant ($F = 18.21$, $P< 0.005$), but its effect is significantly smaller compared to factor A. A model with a low P– value and a higher F – value indicates that the model is significant. If P– values are higher than 0.1000, they indicate that the terms in the model are not significant.

The regression equation for the efficiency is given in the equation:

$$\eta=0.512522 + 0.009479*A + 0.001913*B + 0.002341*A*A + 0.000509*B*B - 0.000813*A*B \quad (1)$$

The Normal plot of residuals, Figure 1, is a graphical method for identifying any deviations from normality, including any outliers, skewness and the need for change. The plot shows that there are minimal deviations from normality.

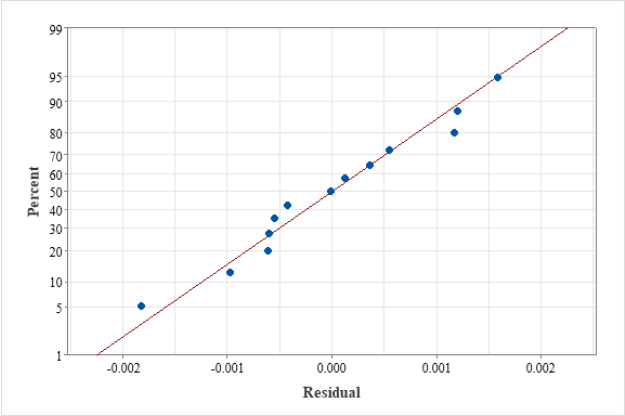

Fig.1. Normal Plot of Residuals

The contour plot in Figure 2 shows the dependence of the efficiency as a function of factors A and B, with different colors indicating the level of efficiency. Dark blue areas indicate the lowest values of the efficiency, while lighter shades of green indicate higher values, which allows the identification of regions with optimal experimental conditions.

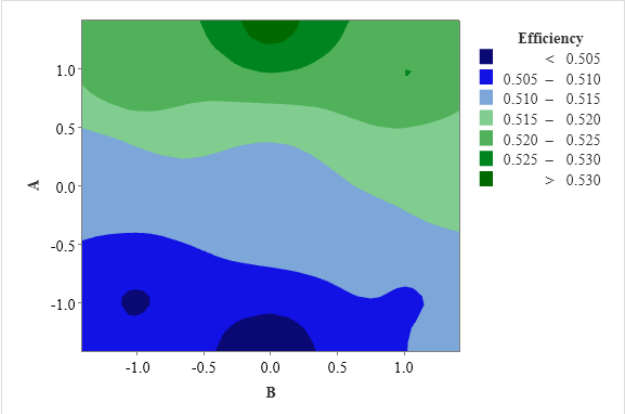

Fig.2. The contour plot of efficiency

After plot analysis (Figure 2), it can be observed that the maximum values of the efficiency are located in the upper right part of the plot, which suggests that increasing factors A and B contributes to improving the efficiency. Conversely, the minimum values are concentrated in the lower left corner, indicating the unfavorable impact of low factor values on the objective function.

This plot allows a visual analysis of the interaction of factors and identification of areas where the optimal system response is achieved. Further optimization can be directed towards precisely determining the experimental conditions that allow for achieving the maximum efficiency, thereby improving the overall efficiency of the system. The three-dimensional (3D) diagram shown, Figure 3, represents the dependence of the efficiency on two factors labeled A and B. This type of graphical representation allows for a more detailed analysis of the impact of variations in these factors on the value of the objective function, i.e. the efficiency.

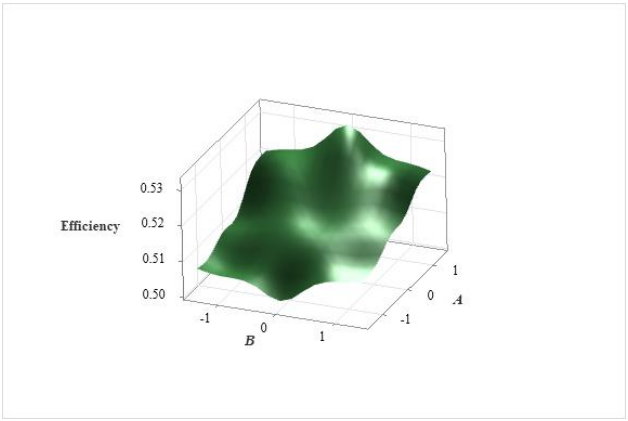

Fig.3. 3D plot of efficiency

The surface of the plot (Figure 3) is uneven, with gentle and abrupt transitions, which indicates the complex nature of the interdependence of factors A and B. Areas with local maximum and minimum are visible, indicating the existence of specific combinations of factors that lead to an increase or decrease in the efficiency.

From the plot shown, Figure 3, it can be concluded that the highest values of the efficiency are located in the upper central part of the plot, where the surface reaches its highest points. This indicates that certain values of the factors A and B lead to maximum utilization. Conversely, lower levels of the utilization rate can be observed in the lower left part of the graph, which indicates less favorable experimental conditions.

The slope of the surface in different regions of the plot indicates that there is an interaction between factors A and B. In some areas, changing one factor has a higher impact on the efficiency, while in other areas the impact is not as pronounced. This is an important aspect to consider when optimizing parameters.

3.1. Discussion of the results

It is evident that the literature and scientific research in the field of gear pair optimization is extensive, and therefore it is important to systematically select and summarize relevant information depending on the specific research problem. In the context of gear pair optimization, various aspects can be considered such as reducing the volume of the gear pair, minimizing power losses, the influence of transmission error and noise, as well as optimizing macro- and micro-geometry. In addition, the choice of materials and other design parameters also plays a key role in achieving optimal performance, and it is necessary to take all these factors into account when defining optimization objectives.

In [21], the authors performed the optimization of gear pairs, focusing on improving efficiency and reducing transmission error. They used a multi-criteria optimization with a genetic algorithm (Non-Dominated Sorting Genetic Algorithm II - NSGAII), taking into account the macro and micro geometry of the teeth. Their goal was to find an optimal design that minimizes power losses (friction and total losses) and transmission ratio error. They concluded that different optimization approaches (different objective functions) lead to different optimal solutions, and that the inclusion of micro-geometry of the teeth is key to significantly improving efficiency. The optimization showed that the best results are achieved when both macro and micro geometric parameters are optimized simultaneously. Similarly, research [22] has shown that optimizing gear pairs achieves a significant reduction in power, volume and vibration losses, which directly contributes to improving dynamic performance, reducing energy consumption and minimizing volume in gear transmissions.

Another study using multi-criteria optimization of spur gears with application of genetic algorithm (GA) in the aim of reduction of volume and power loss in transmission was recorded in the Belarhzal et al. investigation [23]. The optimization included correction factors of the driving and driven gear profiles, modulus, gear width and number of gear teeth, while the objective functions were volume, axial distance and efficiency. The results showed that higher values of the profile correction factor reduce volume and increase axial distance, but increase power losses at high correction values. A smaller modulus increases losses due to the increase in normal load, while an increase in the number of teeth and a decrease in gear width allow for a more compact design while maintaining efficiency. It was concluded that the optimal combination of parameters is achieved with a moderate profile correction factor, a larger number of teeth, and a smaller gear width, thus ensuring a compact and efficient design compared to standard gears.

Based on the available multi-criteria studies, achieving higher efficiency requires increasing the gear volume and vice versa [24]. Therefore, it is necessary to find a compromise depending on the requirements of the specific application and there is a large range of intervals of influencing factors considered in order to reduce power losses depending on the observed system. Some researchers have concluded that the combination of a higher number of teeth and a lower modulus leads to a reduction in power losses.

The influence of individual factors on the characteristics of worm gears is presented in the study [25]. The focus of this study was on the efficiency, contact pressure and service life of worm gears. The authors proposed methods for improving these parameters, including a new method of manufacturing the worm and worm gears, as well as the use of a special anti-friction hard coating based on nickel and carbon nanotubes. The goal was to reduce the contact pressure and friction coefficient, thereby increasing the efficiency (up to 75-80%), load capacity and service life of worm gears.

Analyzing previous research in the field of optimization of gear transmissions, it was noted that the application of the CCD method is rarely applied. Therefore, a significant contribution of this paper lies in the implementation of this method, which has proven to be effective in the analysis and interpretation of experimental results.

In this study, the selection of materials, lubricant viscosity and current intensity is based on previous studies and the specific objectives of this study. The material CuSn12 (bronze) was selected as a suitable material for the worm gear, which is in accordance with the findings of the study [10] that showed good performance of this material combination. The selection of lubricant viscosity was

based on the recommendations of the study [9]. Although the optimal value of the current intensity is 0.20 A according to the study [9], in this study a lower value of 0.125 A was selected in order to optimize the efficiency. The highest values of the efficiency of the worm gear using the oil with viscosity VG220 were recorded at the highest speed, which is 1603.5 min^{-1} and the operating time of the worm gear was about 10 min.

By applying the CCD method and analyzing the created diagrams, it was observed that the areas of maximum and minimum values of the worm gear efficiency are located in similar positions, but depending on the speed. Specifically, the areas of maximum efficiency were observed at higher speeds, while the areas of minimum efficiency occurred at lower speeds.

4. CONCLUSION

By using experimental design and optimization methods, it is possible to significantly increase the accuracy of measurements during the experiments. Also, the time required to perform the experiment, as well as the amount of resources necessary for its implementation, can be reduced. Experimental design provides an advantage in designing complex systems, as well as in investigating the influence of various factors on samples and their other properties.

CCD is a comprehensive and flexible tool for planning simulation experiments. This approach has proven useful in research in various fields where it is necessary to solve complex problems with multiple factors. Due to its ability to efficiently and reliably create second-order regression models, CCD allows researchers to better understand and interpret the obtained data.

By applying the CCD optimization method and analyzing the results using ANOVA analysis, it was concluded that the more influential factor is the rotational speed in relation to the operating time of the worm gear. It was found that the highest values of the worm gear efficiency rate using VG220 viscosity oil are achieved at the highest speed, which is about 1603.5 min^{-1}, and the worm gear operating time is about 10 min.

A mathematical model has been developed that allows prediction of efficiency depending on the influencing factors. Based on the conducted statistical analysis, it was found that the developed mathematical models are at a reliability level of 95%.

Future research should include expanding the experimental analysis by increasing the number of factors considered, such as oil temperature, load, tooth surface roughness and material influence. Applying multi-criteria optimization would allow simultaneous evaluation of multiple objectives, including maximum efficiency, minimum wear, and reduced noise and vibration, leading to more specific and practically applicable conclusions. Additionally, comparing the obtained results with those derived from other optimization methods is recommended to better assess the robustness and reliability of the proposed solution.

REFERENCES

[1] Skulić, A., Milojević, S., Marić, D., Ivanović, L., Krstić, B., Radojković, M., Stojanović, B.: The impact of lubricant viscosity and materials on power losses and efficiency of worm gearbox. *Tehnički vjesnik*, Vol. 29, No. 6, pp. 1853-1860, ISSN 1330-3651, https://doi.org/10.17559/TV-20220207092015, 2022.

[2] Nikolić, V.: *Mašinski elementi – teorija, proračun primeri*, Mašinski fakultet u Kragujevcu, CIPMES, Kragujevac, 2004.

[3] Montgomeri, D. C.: *Design and Analysis of Experiments*, John Wiley & Sons, Hoboken, ISBN 978-1118-14692-7, 2013.

[4] Skulić, A., Bukvić, M., Gajević, S., Miladinovic, S., Stojanovic, B.: The influence of worm gear material and lubricant on the efficiency and coefficient of friction, *Tribology and Materials*, Vol. 3, No. 1, pp. 15-23, ISSN2812-9717, https://doi.org/10.46793/tribomat.2024.001, 2024.

[5] B. Stojanović, S. Gajević, N. Kostić, S. Miladinović, A. Vencl: Optimization of parameters that affect wear of A356/Al2O3 nanocomposites using RSM, ANN, GA and PSO methods, *Industrial Lubrication and Tribology*, Vol.74, No.3, pp. 350-359, ISSN 0036-8792, https://doi.org/10.1108/ILT-07-2021-0262, 2022.

[6] Barshikar, R. R., Baviskar, P. R.: Experimental Investigation for Fault Diagnosis of a Single Stage Worm Gearbox Using Response Surface Methodology, *Nigerian Journal of Technological development*, Vol. 20 No. 2, pp. 11-22, ISSN 0189-9546, http://dx.doi.org/10.4314/njtd.v18i4.1259, 2023.

[7] Kah Yung, Y., Chua, H.S., Bashir, M. J. K., Albert, F.Y.C.,Govinda, S.: Central Composite Design (CCD) for Parameters Optimization of Maximum Power Point Tracking (MPPT) by Response Surface Methodology (RSM), Journal Of Mechanics Of Continua And Mathematical Sciences, Special Issue No. – 1, pp. 259-270, ISSN 0973-8975, https://doi.org/10.26782/jmcms.2019.03.00025, 2019.

[8] Gajević, S., Miladinović, S., Güler, O., Özkaya, S., Stojanović B.: Optimization of dry sliding wear in hot-pressed Al/B4C metal matrix composites using Taguchi method and ANN, *Materials*, Vol.17, No.16, pp. 4056, ISSN 1996-1944, https://doi.org/10.3390/ma17164056, 2024.

[9] Miladinović, S., Radosavljević, S., Veličković, S., Atyat, R., Skulić, A., Šljivić, V., Optimization of efficiency of worm gear reducer by using taguchi-grey method, *Applied Engineering Letters*, Vol.2, No.2, pp. 69-75, ISSN 2466-4677, 2017.

[10] Stojanović, B., Vencl, A., Skulić, A., Miladinović, S., Gajević, S.: Influence of materials on the degree of efficiency of worm gear transmission, Proceedings of *6th International scientific conference, COMETa 2022*, 17th – 19th November, East Sarajevo – Jahorina, B&H, RS, pp. 402-409, ISBN 978-99976-947-6-8, 2022.

[11] Skulić, A., Stojanović, B., Radosavljević, S., Veličković, S., Experimental determination of worm gearing efficiency, *Applied Engineering Letters*, Vol.4, No.4, pp. 115-119, ISSN 2466-4847, 2019.

[12] Miltenović, A., Banić, M., Vitković, N., Simonović, M., Perić, M., & Rangelov, D.: Investigation of the Influence of Contact Patterns of Worm-Gear Sets on Friction Heat Generation during Meshing. *Applied Sciences*, Vol.14, No.2, Article No. 738, ISSN: 2076-3417 https://doi.org/10.3390/app14020738, 2024.

[13] Desai, M., Bhat, J., Bhapkar, U.: Experimental investigation of effect of tribological parameters on worm gear pair under lubricating conditions. *Materials Today: Proceedings*, Vol.50, No. 5, pp. 1666-1670, ISSN: 2214-7853, https://doi.org/10.1016/j.matpr.2021.09.147, 2022.

[14] Karabacak, Y. E., Baş, H.: Experimental investigation of efficiency of worm gears and modeling of power loss through artificial neural networks, *Measurement*, Vol. 202, Article No. 111756, ISSN 0263-2241, https://doi.org/10.1016/j.measurement.2022.111756, 2022.

[15] Gregor, M., Grznar, P., Mozol, S., Mozolova, L.: *Design of simulation experiments using Central Composite Design*, *Acta Simulatio-International Scientific Journal about Simulation*, Vol. 9, No. 2, pp. 21-25, ISSN 1339-9640, https://doi.org/10.22306/asim.v9i2.99, 2023.

[16] Živković, A.: *Optimizacija parametara pužnog zupčastog prenosnika*, Master rad, Fakultet inženjerskih nauka Univerziteta u Kragujevcu, Kragujevac, 2025.

[17] Web page, https://www.itl.nist.gov/div898/handbook/pri/section3/pri3361.htm, Accesed: December 2024.

[18] Bhattacharya, S.: Central Composite Design for Response Surface Methodology and Its Application in Pharmacy, In: *Response Surface Methodology in Engineering Science*, IntechOpen, (ed.) Palanikumar K., ISBN 978-1-83968-918-5, http://dx.doi.org/10.5772/intechopen.95835, 2021.

[19] Skulić, A.*: Identifikacija optimalnih vrednosti stepena iskorišćenja pužnih zupčastih prenosnika*, Doktorska disertacija, Fakultet inženjerskih nauka Univerziteta u Kragujevcu, Kragujevac, 2022.

[20] GUNT. (2011). *Experiment Instructions*, AT200 Apparatus for Determination of Gear Efficiency.

[21] Younes, E. B., Changenet, C., Bruyère, J., Rigaud, E., Perret-Liaudet, J. Multi-objective optimization of gear unit design to improve efficiency and transmission error. *Mechanism and Machine Theory*, Vol.167, Article. No. 104499, https://doi.org/10.1016/j.mechmachtheory.2021.104499, ISSN: 0094-114X, 2022.

[22] Wang, C.: Study on dynamic performance and optimal design for differential gear train in wind turbine gearbox. *Renewable Energy*, Vol. 221(C), Article No. 119776, ISSN 0960-1481 http://dx.doi.org/10.1016/j.renene.2023.119776, 2024.

[23] Belarhzal, S., Daoudi, K., Boudi, E. M., Bachir, A., Elmoumen, S.: A multiobjective optimization analysis of spur gear pair: The profile shift factor effect on structure design and efficiency, *Mathematical Problems in Engineering*, Vol. 2021, No. 1, Article No. 8873769, ISSN1563-5147, http://dx.doi.org/10.1155/2021/8873769, 2021.

[24] Miler, D., Hoić, M.: Optimisation of cylindrical gear pairs: A review, *Mechanism and Machine Theory*, Vol. 156, Article No. 104156, ISSN 0094-114X, https://doi.org/10.1016/j.mechmachtheory.2020.104156, 2021.

[25] Sukhanova, O., Spirina, D., Nikitina, L., Sobol, K., Trifanov, I.: *Increasing the operational parameters of worm gears.* In E3S Web of Conferences- XIV International Conference on Transport Infrastructure: Territory Development and Sustainability, Vol. 471, Article No. 04010, eISSN: 2267-1242, https://doi.org/10.1051/e3sconf/202447104010, 2024.

11th International Scientific Conference
IRMES 2025
Research and Development of
Mechanical Elements and Systems
June 19 – 21, 2025; Vrnjačka Banja, Serbia

Original scientific paper
DOI: 10.46793/IRMES25.147Z

EXPERIMENTAL AND NUMERICAL ANALYSIS OF SINGLE LAP ALUMINIUM JOINTS BONDED WITH DIFFERENT EPOXY ADHESIVES

Nataša ZDRAVKOVIĆ[1]
Milan BANIĆ[2]
Damjan KLOBČAR[3]
Miodrag MILČIĆ[4]
Szabolcs FISCHER[5]

[1] University of Niš, Faculty of Mechanical Engineering, Niš, Serbia, 18000; natasa.zdravkovic@masfak.ni.ac.rs; ORCID iD: 0000-0001-6085-7522
[2] University of Niš, Faculty of Mechanical Engineering, Niš, Serbia, 18000; milan.banic@masfak.ni.ac.rs; ORCID iD: 0000-0001-8684-042X
[3] University of Ljubljana, Faculty of Mechanical Engineering, Ljubljana, Slovenia, 1000; damjan.klobcar@fs.uni-lj.si; ORCID iD: 0000-0002-6130-0328
[4] University of Niš, Faculty of Mechanical Engineering, Niš, Serbia, 18000; miodrag.milcic@masfak.ni.ac.rs; ORCID iD: 0000-0002-1089-8390
[5]Széchenyi István University, Faculty of Architecture, Civil- and Transport Engineering, Győr, Hungary, H-9026; fischersz@sze.hu; ORCID iD: 0000-0001-7298-9960

Abstract: *Experimental and numerical analysis was conducted on single lap adhesively bonded aluminium joints. Static tensile lap-shear tests were carried out using three different epoxy adhesives to evaluate the maximum forces and displacements. Following the experimental phase, results were compared with those obtained through finite element analysis (FEA), providing validation and deeper understanding of the joint performance under loading. The comparison confirmed good agreement between experimental data and numerical predictions, highlighting the reliability of the FEA approach in assessing the performance of adhesive joints.*

Keywords: *adhesive bonding; aluminium joints; epoxy adhesives; single lap; FEA.*

1. INTRODUCTION

Adhesive bonding is one of the most important joining methods in modern industry, particularly in applications where weight reduction, uniform stress distribution, and ease of fabrication are required [1,2]. Among the various joint configurations, the single lap joint (SLJ) is one of the most used due to its simple geometry and wide application in the automotive, aerospace, and construction industries [3,4]. Despite the numerous advantages of adhesively bonded joints, their mechanical performance and joint strength are highly dependent on the choice of adhesive, the properties of the substrates, and the loading conditions [5-7]. Therefore, accurate prediction of bonded joint performance is essential for effective design.

Numerous studies have focused on comparing experimental and numerical results for single lap joints [8-10]. For instance, Ghahramanzadeh Asl et al. [11] performed experimental tests and finite element analysis (FEA) simulations on SLJs made of aluminium and steel, bonded with epoxy adhesives of different thicknesses and surface roughness. The results showed good agreement between the experimental data and numerical predictions, confirming the validity of the employed models.

Similarly, Gültekin et al. [12] investigated the mechanical properties of various SLJ configurations with different adherend widths under tensile loading, using both experimental tests and numerical simulations. The study revealed that increasing the adherend width had a more significant effect on joint strength than increasing the overlap length. Furthermore, the results of the finite element analysis showed good agreement with the experimental data, confirming the accuracy of the numerical model.

In a study conducted by Goudarzi and Khedmati [13], the failure and fracture behavior of two shear-resistant joint types, SLJs and double lap joints (DBLJs), was investigated using both experimental methods and finite element simulations under static tensile loading. The joints consisted of aluminium and GFRP adherends bonded with a ductile adhesive. Contrary to some previous research suggesting that DBLJs provide higher strength when aluminium adherends are used, this study found that SLJ configurations bonded with aluminium-GFRP adherends exhibited, on average, 33% higher tensile strength than DBLJs. However, the finite element

analysis based on a cohesive zone model (CZM) tended to overestimate both the failure load and the joint stiffness compared to the experimental results.

Previous research has demonstrated that combining experimental testing with numerical simulations is an effective approach for understanding the mechanical properties of SLJs. The type of adhesive, joint geometry, and substrate materials significantly influence joint strength and overall joint performance. Finite element analysis (FEA) can offer valuable insights for optimizing joint design. However, it is essential to validate numerical models against experimental data.

This study presents the results of experimental testing on aluminium alloy EN AW-5754 SLJ specimens bonded with three different types of industrial adhesives, with the objective of determining the maximum force and displacement. Following the experimental testing, a finite element analysis was conducted using ANSYS software to compare the force and displacement values obtained through simulation with those measured experimentally. The comparison was based on the joint geometry and the mechanical properties of both the substrate and the adhesive. This approach enables more accurate validation of the numerical model, a better understanding of the behavior of different adhesives, and provides a solid foundation for optimizing material selection and joint design in future applications. Additionally, it allows for the prediction of joint strength as a function of the adhesive and substrate material properties, as well as the joint geometry.

2. EXPERIMENTAL INVESTIGATIONS

Cold-rolled aluminium alloy 5754 sheets, 2.0 mm thick and in the H22 temper condition, were prepared and cut into 100 mm × 25 mm specimens in accordance with the EN 1465 [14] standard (Fig. 1). These specimens were used to prepare adhesive single lap joints with an overlap length of 12.5 mm. Three types of epoxy adhesives (SikaPower®-880, SikaPower®-492G and SikaFast®-580) were selected for this study. During bonding, the adhesive layer thickness was kept constant at 0.3 mm. The joints were then subjected to static shear testing.

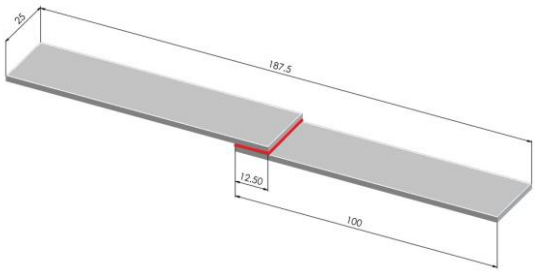

Fig.1. Specimen geometry for the single lap-shear test

Prior to bonding, the specimens were cleaned and degreased using SIKA Remover-208. For each adhesive type, three samples were bonded. In accordance with the manufacturer's recommendations, the epoxy adhesive was applied to the cleaned surfaces and then cured in a drying and heating chamber. Following bonding, the specimens were cured at room temperature for 24 hours prior to testing.

The tests were performed at room temperature using an INSTRON 8802 250 kN (Norwood, MA, USA) testing machine under displacement control at 1 mm/min speed. The elastic properties of the adherends and adhesives, based on the manufacturer's specifications, are presented in Table 1.

Table 1. The elastic properties of bonded materials

Materials	E (MPa)	v (-)
EN AW-5754	70000	0.33
SikaPower®-880	1900	0.34
SikaPower®-492G	1600	0.38
SikaFast®-580	900	0.3

3. NUMERICAL ANALYSIS OF BONDED JOINTS

Numerical simulations of the adhesive single lap joints were performed using FEA in ANSYS WORKBENCH software. The static structural analysis was defined, fully replicating the experimental tensile lap-shear tests. The analysis incorporated the exact joint geometry (Figure 2), material properties of the aluminum substrate and adhesives.

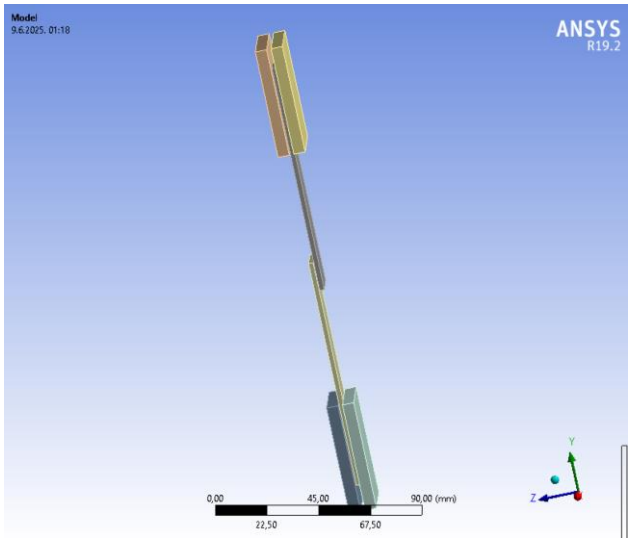

Fig.2. 3D model of tensile lap-shear tests

For generating the finite element mesh the elements of a higher order or SOLID 186 are used. The mesh is generated with 13116 nodes which form 2042 elements, as shown in Figure 3. Mesh quality parameters and convergence of results were monitored to obtain valid finite element analysis results.

The contacts in analysis were treated as bonded, as per ANSYS WORKBENCH definition, between the specimen and the griping mechanism, as well as between bonding agent and aluminium sheets. The contact

stiffness was updated in every step of numerical calculation.

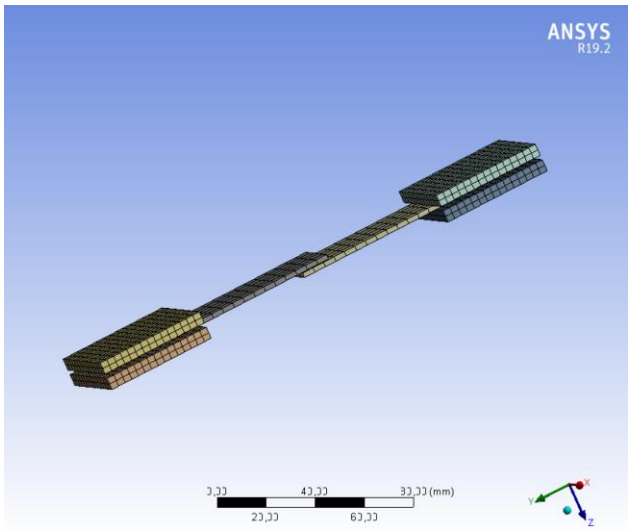

Fig.3. Generated finite element mesh of the tensile lap-shear tests

Loads and boundary conditions for the analysis setup are shown in Figure 4. The lower griping plates were fixed, while the upper ones displaced to simulate the realistic conditions during the tensile lap-shear tests. A force probe was attached to the fixed support to obtain the reaction force coused be specimen displacement. The gravity farce acting on the system was also taken into account.

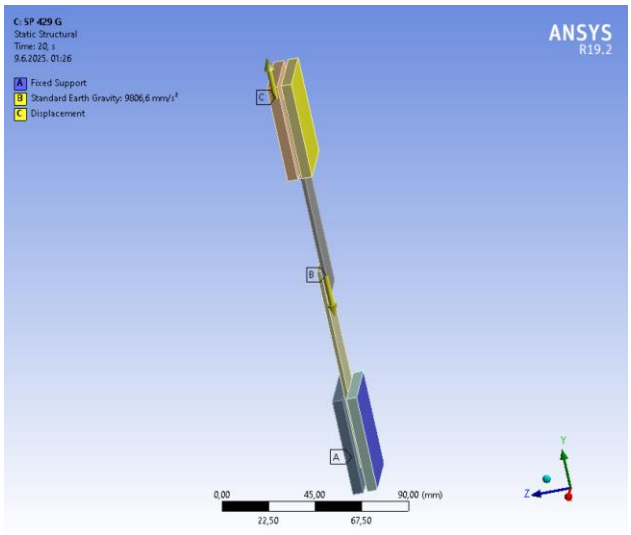

Fig. 4. Loads and boundary conditions for tensile lap-shear tests

4. RESULTS AND DISCUSSION

4.1. Experimental Results

The experimental testing was conducted on three types of epoxy adhesives applied to aluminium SLJ specimens. The measured maximum forces and corresponding displacements are presented in Table 2. The results demonstrate clear differences in joint performance depending on the adhesive type.

Table 2. Experimental results

Materials	Displacement (mm)	Average maximum force (N)
SikaPower®-880	0.2335	5705
SikaPower®-492G	0.3094	6637
SikaFast®-580	0.2485	4905

The average values of the maximum force range from 4905 N to 6637 N, with the highest value recorded for SikaPower®-492G, and the lowest for SikaFast®-580. The associated displacements varied accordingly, reflecting the stiffness characteristics of each adhesive. These results confirm that adhesive selection significantly influences joint strength and deformation behavior.

4.2. Numerical Analysis and Results

The displacements and corresponding forces obtained from the FEA simulations are presented in Table 3 and Figure 5.

Table 3. Numerical results

Materials	Displacement (mm)	Force (N)
SikaPower®-880	0.2333	5032
SikaPower®-492G	0.3083	7567
SikaFast®-580	0.2499	4741

The comparison between experimental and numerical results for all three adhesives shows deviations ranging from approximately 3.3% to 14.0%. Specifically, for SikaFast®-580, the numerical force (4741 N) was about 3.3% lower than the experimental value (4905 N). For SikaPower®-880, the deviation increased to approximately 11.8%, with the numerical force (5032 N) being lower than the experimental force (5705 N). Finally, for SikaPower®-492G, the numerical force (7567 N) exceeded the experimental force (6637 N) by about 14.0%. These differences can be attributed to simplifications and assumptions made in the numerical model, such as idealized bonding conditions and material homogeneity.

Nonetheless, the FEA model demonstrates a good correlation with the experimental results, with deviations not exceeding 14% for any of the three adhesives. This level of accuracy is consistent with observations reported

in previous studies [15, 16], thereby confirming the validity of the developed numerical model.

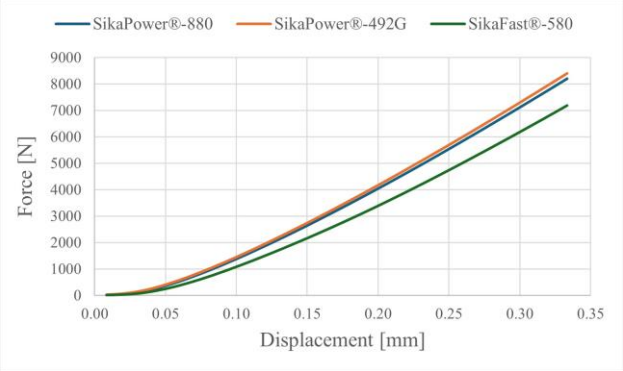

Fig.5. Force-displacement curves

5. CONCLUSION

This study successfully developed and validated a finite element analysis model of aluminium single lap joints bonded with three different epoxy adhesives. Experimental tensile lap-shear tests were performed to obtain maximum loads and displacements, which served as a basis for validating the numerical model.

The FEA results showed good correlation with the experimental data, with deviations ranging from approximately 3% to 14%. These discrepancies are attributed to idealized assumptions in the numerical model, such as perfect bonding and material homogeneity. Despite this, the model effectively predicted the force-displacement behavior for all adhesives tested.

Among the adhesives, differences in maximum force and displacement were clearly observed, highlighting the significant influence of adhesive selection on joint performance. The developed numerical model provides a reliable tool for predicting adhesive joint strength and can be used for further optimization and design of bonded structures.

The results obtained align well with findings from previous studies, confirming the validity of the applied approach. Future work could focus on incorporating more complex material behaviors and failure mechanisms to improve prediction accuracy.

ACKNOWLEDGMENT

This research was financially supported by the Ministry of Science, Technological Development and Innovation of the Republic of Serbia (Contract No. 451-03-137/2025-03/200109).

REFERENCES

[1] Pizzi, A., Mittal, K.L.: *Handbook of Adhesive Technology*, CRC Press: Boca Raton, FL, USA, 2017

[2] Ebnesajjad, S.: *Adhesives Technology Handbook*, 2nd ed., pp. 1-17, William Andrew Inc.: Norwich, NY, USA, 2008

[3] Brockmann, W., Gei, P.L., Klingen, J., Schrder, B., Mikhail, B.: *Adhesive Bonding: Materials, Applications and Technology*, Wiley: Hoboken, NY, USA, 2009

[4] Hosseinabadi, O.F., Khedmati, M.R.: A review on ultimate strength of aluminium structural elements and systems for marine applications, *Ocean Eng.* 232: 109153, 2021

[5] Zdravković, N.; Klobčar, D.; Milčić, D.; Zupančič, M.; Žužek, B.; Milčić, M.; Đurić, A. Influence of Surface Preparation of Aluminum Alloy AW-5754 and Stainless Steel X5CRNI18-10 on the Properties of Bonded Joints. *Materials*, *17*, 2561. https://doi.org/10.3390/ma17112561, 2024

[6] Silva, J.M, Ferreira, F., Abreu, S.M., Matos, J.E., Durao, L.M.P.: Correlation of drilling damage with mechanical strength: A geometrical approach. *Compos. Struct.*, 181, 306-314, 2017

[7] Petrie, E.M.: *Handbook of adhesives and sealants*, pp. 1-48, McGraw-Hill Companies: NY, USA, 2000

[8] Negru, R., Marsavina, L., Hluscu, M.: Experimental and numerical investigations on adhesively bonded joints, *IOP Conf. Series: Materials Science and Engineering,* 123, 012012, doi:10.1088/1757-899X/123/1/012012, 2016

[9] Ferreira, C.L., Campilho, R.D.S.G., Moreira, R.D.F.: Experimental and numerical analysis of dual-adhesive stepped-lap aluminum joints, *Proc IMechE Part E: J Process Mechanical Engineering,* Vol. 234(5) 454-464, 2020

[10] Raos, P., Matejiček, F., Lucić, M.: Experimental and numerical analysis of single lap adhesively bonded joints*, Polimeri* 24, 2-4:79-83, 2003

[11] Ghahramanzadeh Asl, H., Çam, S., Orhan, O., Özel, A.: Experimental and Numerical Analysis of Epoxy Based Adhesive Failure on Mono- and Bi-Material Single Lap Joints Under Different Displacement Rates. *Fracture and Structural Integrity*, *14*(52), 9–24. https://doi.org/10.3221/IGF-ESIS.52.0, 2020)

[12] Gültekin, K., Akpinar, S., Özel, A.: The effect of the adherend width on the strength of adhesively bonded single-lap joint: Experimental and numerical analysis, *Composites Part B: Engineering*, Vol. 60, pp. 736-745, ISSN 1359-8368, 2014

[13] Goudarzi, R. H., Khedmati, M. R.: An experimental and numerical investigation of adhesive bond strength in Al-GFRP single lap and double butt lap joints due to applied longitudinal loads, *Ships and Offshore Structures,* 15(4):1-14, doi: 10.1080/17445302.2019.1659879, 2019

[14] EN 1465 (2009), Adhesives—Determination of Tensile Lap-Shear Strength of Bonded Assemblies

[15] Alami, A. H., Bilal, H.: Modelling and verification of an acrylic adhesive as a hyperelastic material, *Advances in Materials and Processing Technologies*, http://dx.doi.org/10.1080/2374068X.2015.1095028, 2015

[16] Eskenati A. R., Mahboob, A., Bernat-Maso, E., Gil, L.: Experimental and Numerical Study of Adhesively and Bolted Connections of Pultruded GFRP I-Shape Profiles, *Polymers*, 14(5), 894, https://doi.org/10.3390/polym14050894, 2022

11th International Scientific Conference
IRMES 2025
Research and Development of
Mechanical Elements and Systems
June 19 – 21, 2025; Vrnjačka Banja, Serbia

Original scientific paper DOI: 10.46793/IRMES25.151P

FINITE ELEMENT ANALYSIS OF THREE-STAGE PLANETARY GEAR TRAIN FOR ROAD VEHICLE WINCH

Marko PERIĆ[1]
Aleksandar MILTENOVIĆ[1]
Jelena STEFANOVIĆ-MARINOVIĆ[1]
Damjan RANGELOV[1]
Lazar STOJANOVIĆ[2]
Saša PAVLOVIĆ[1]
Daniela ALIC[3]

[1] University of Niš, Faculty of Mechanical Engineering, Niš, Serbia, 18000; marko.peric@masfak.ni.ac.rs;
ORCID iD: 0000-0001-9350-0351
[1] University of Niš, Faculty of Mechanical Engineering, Niš, Serbia, 18000; aleksandar.miltenovic@masfak.ni.ac.rs;
ORCID iD: 0000-0002-1453-2548
[1] University of Niš, Faculty of Mechanical Engineering, Niš, Serbia, 18000; jelena.stefanovic@masfak.ni.ac.rs;
ORCID iD: 0000-0001-8823-5362
[1] University of Niš, Faculty of Mechanical Engineering, Niš, Serbia, 18000; damjan.rangelov@masfak.ni.ac.rs;
ORCID iD: 0000-0003-3071-893X
[2] Coming Computer Engineering, Belgrade, Serbia, 11000, lazar.stojanovic@coming.rs;
ORCID iD: 0000-0001-5120-8889
[1] University of Niš, Faculty of Mechanical Engineering, Niš, Serbia, 18000; sasa.pavlovic@masfak.ni.ac.rs;
ORCID iD: 0000-0001-8806-6693
[3] Polytechnic University of Timişoara, Faculty of Engineering Hunedoara, 331128 Romania; daniela.alic@fih.upt.ro;
ORCID iD: 0009-0007-5773-5058

Abstract: *In the winch system of an off-road vehicle, the planetary gear train (PGT) is very significant for the mechanical transmission which connects the electric drive motor to the winch drum. It's primary function to provide the necessary torque and speed required to efficiently transfer power from the high-speed, low-torque electric motor to the low-speed, high-torque drum. The compact design, high load capacity, and efficiency of the planetary gear make it an ideal choice for this application, ensuring reliable operation in demanding conditions where traction forces are significant. For these reasons, it is necessary to perform an analysis of a three-stage planetary gear using the finite element method. The planetary gear is composed of three stages which is all of them type 1AI connected in series. During the design of the gear, to enable the functionality and reliability of the gear, it is necessary to consider the stress-strain state of the gears. FEM tooth root stress analysis was performed for sun and planetary gears, as one of the most critical elements of the transmission. It was demonstrated that the stresses at the gear contact points are within acceptable limits, with no risk of failure.*

Keywords: *Tooth root stress; Deformation; Strain; Modeling; Planetary gear.*

1. INTRODUCTION

Planetary gears are among the most widely used mechanical components used in a wide range of industrial systems. Due to their high efficiency, high torque, ability to achieve high transmission ratios, compact design, low mass and high load capacity, planetary gears are in many mechanical devices. Their applications include automatic transmissions in vehicles, bicycle hubs, as well as road vehicle winch, which are the subject of analysis in this paper [1].

To verify the basic performance, reliability, and service life of a planetary gearbox, it is necessary to analyse the gearbox itself using the finite element method. High stresses, deformations, and strains can be the main causes of planetary gearbox failure [2,3]. Stresses can be caused by misalignments resulting from tolerances in the centre distance between gears, as well as tolerances on individual components [4]. In some software, as Ansys workbench, in addition to static analysis, it is also possible to perform dynamic analysis, specifically modal analysis, with the aim of determining the natural frequency of the gearbox. This allows for comparison with the operating frequency to predict the occurrence of

resonance within the gearbox [5]. Through the analysis of a three-stage planetary gearbox model and the application of CAD-CAE tools, it has been shown that average efficiency can be achieved even with a smaller number of gear ratios [6].

In the following work, the geometry of the three-stage planetary gear, the method and materials used to analyse the planetary gear and the results obtained are given.

2. CAD MODEL

The transmission system consists of three stages connected in series, each based planetary gear train (PGT) configuration type 1AI. The output of the first stage is the input to the second stage, and the output of the second stage is the input the third stage. The stages are interconnected as follows: the carrier of the first stage drives the sun gear of the second stage, while the carrier of the second stage drives the sun gear of the third stage. The overall input to the transmission is the sun gear of the first stage, and the final output is taken from the carrier of the third stage. The complete structure of the three-stage planetary gear train is presented in Figure 1.

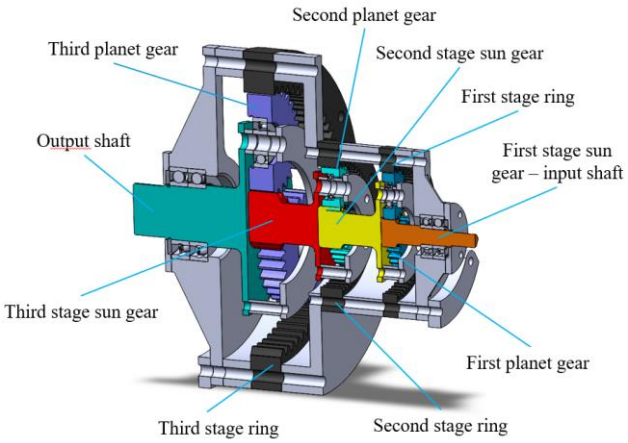

Fig. 1. 3D model (cross section) of three-stage Planetary Gear Train

3. METHOD AND MATERIALS

The method used to test Tooth Root Stress of the sun and planet gears was structural static analysis by the finite element method. The analysis was performed in KISSsoft software package [7]. Tooth Root Stress was used to calculate the effects of static loading of the tooth root of Sun and planet gear for each stage in transmission. Testing the structural integrity of three-stage planetary gear train using the finite element numerical method aimed to critical elements as sun and planet gear during design. Boundary conditions of the gear segment in simulation are lateral at the gear segment fixed (Fig. 2)

Fig. 2. Lateral at the gear segment fixed

Materials which are used in design of planetary gear are shown in Table 1 and Table 2.

Table 1. Material properties of the sun and planets gear 16MnCr5 [7]

Properties	Values
Density (kg/m3)	7800
Young's modulus (N/mm²)	206000
Poisson´s ratio	0.3
Tensile strength (N/mm²)	1000
Yield point (N/mm²)	695
Surface hardness (HRC)	59

Table 2. Material properties of the ring gear 42CrMo4 [7]

Properties	Values
Density (kg/m3)	7800
Young's modulus (N/mm²)	206000
Poisson´s ratio	0.3
Tensile strength (N/mm²)	1000
Yield point (N/mm²)	900
Surface hardness (HRC)	56

4. GEOMETRICAL DESIGN

The input values used to generate the CAD model of three-stage planetary gear, for each stage are shown in Tables 3, 4, and 5.

Table 3. Technical specification of first stage

Items	Sun gear	Planetary gear	Ring gear
Number of teeth	12	23	-60
Module (mm)	2.25		
Helix angle at reference circle β (°)	0		
Face width(mm)	14		
Number of planets	3		
Normal pressure angle (°)	20		

Table 4. Technical specification of second stage

Items	Sun gear	Planetary gear	Ring gear
Number of teeth	12	19	-51
Module (mm)	2.75		
Helix angle at reference circle β (°)	0		
Face width(mm)	30		
Number of planets	3		
Normal pressure angle (°)	20		

Table 5. Technical specification of third stage

Items	Sun gear	Planetary gear	Ring gear
Number of teeth	12	23	-50
Module (mm)	4.5		
Helix angle at reference circle β (°)	0		
Face width(mm)	40		
Number of planets	3		
Normal pressure angle (°)	20		

5. RESULTS AND DISCUSSION

The required input parameters for the three-stage planetary gear transmission are defined for each stage. For the first stage, the input data are: transmission ratio i = 6.03, input speed $n_{(in)}$ = 1500 min^{-1}, input power P = 4.5 kW, input torque $T_{(in)}$ = 28.6 Nm, service life L = 2000 h, application factor K_a = 1.25, and manufacturing tolerance grade IT7. The second stage uses the following parameters: i = 5.38, $n_{(in)}$ = 250 min^{-1}, $T_{(in)}$ = 171.882 Nm, L = 2000 h, K_a = 1.25. The third stage is defined by: i = 4.95, $n_{(in)}$ = 47.619 min^{-1}, $T_{(in)}$ = 902.38 Nm, L = 2000 h, K_a = 1.25, with manufacturing tolerance IT7.

Fig. 3, 5 and 7 represents the equivalent Von Misses stress profile while Fig. 4, 6 and 8 is a representation of the deformation distribution components resulting from the dynamics of the planetary gear during rotation. In the simulation, the ring gear was considered as statically constrained member because it is practically fixed to the gearbox housing while the dynamics of the planet gear, planet carrier and the sun pinion were considered as rotating members about an axis.

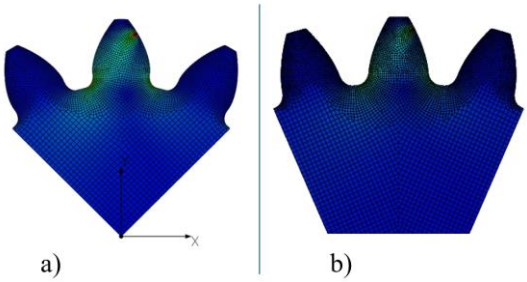

Fig.3. Von Mises stress distribution of (a) sun gear and (b) planet gears in the first stage

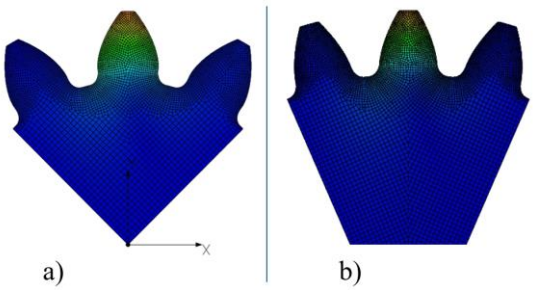

Fig.4. Deformation distribution of (a) the sun and (b) the planet gears in the first stage

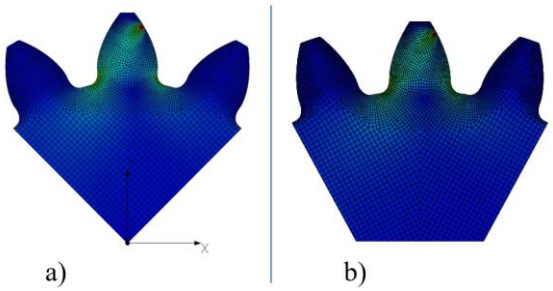

Fig.5. Von Mises stress distribution of (a) the sun gear and (b) the planet gears in the second stage

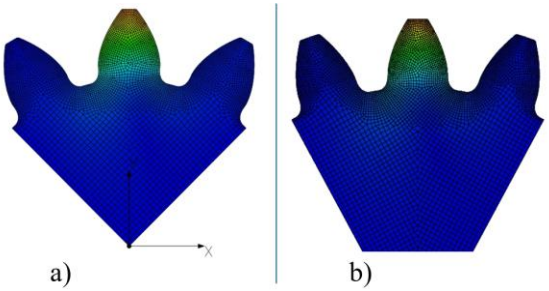

Fig.6. Deformation distribution of (a) the sun gear and (b) the planet gears in the second stage

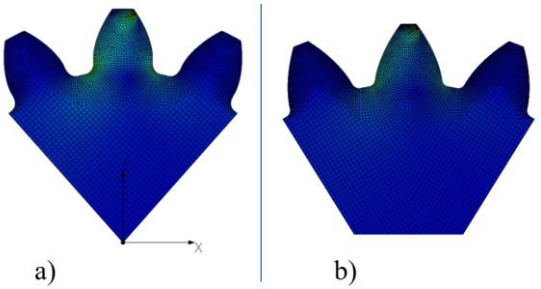

Fig.7. Von Mises stress distribution of (a) the sun gear and (b) the planet gears in the third stage

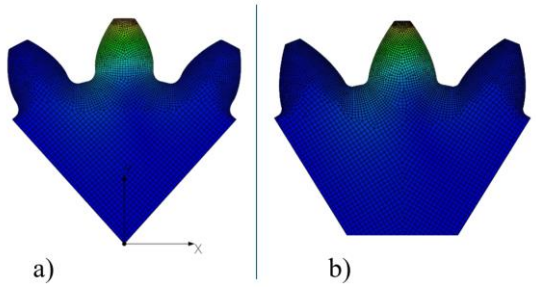

Fig.8. Deformation distribution of (a) sun gear and (b) the planet gears in third stage

Von Mises stress and deformation for all gears in each stage of three-stage planetary gear are shown in table 10 and 11.

In Table 10, values Von Mises stress on sun gear has increased depending on input torque in each stage, which is expected to grow. Also, it's the same situation with deformation. Generated stresses on components are under maximum allowable stress, the maximum values of Von Mises stress and deformation are on sun gear in third stage which is 359.7413 N/mm2 which is under maximum allowable stress limit for given material (Yield

strength for given material is 695 N/mm2) so we can conclude that the Von Mises stress value in the third gear is within the permissible limits, which indicates that the safety level of components is 1.93.

Tab. 10. Results of numerical simulation of sun gear

First planet stage	*Max. value*
Equivalent Stress [N/mm2]	113.6497
Deformation Magnitude [μm]	2.9312
Second planet stage	*Max. value*
Equivalent Stress [N/mm2]	227.7301
Deformation Magnitude [μm]	6.8164
Third planet stage	*Max. value*
Equivalent Stress [N/mm2]	359.7413
Deformation Magnitude [μm]	16.6144

In Table 11, values Von Mises stress on planet gear are also increased depending on input torque in each stage and transmission ration, which is also expected to grow. It's the same situation with deformation. Generated stresses on components are under maximum allowable stress, the maximum values of Von Mises stress and deformation are on planet gear in third stage, which is 421.3347 N/mm2 which is under maximum allowable stress limit for given material (Yield strength for given material is 695 N/mm2) so we can conclude that the Von Mises stress value in the third gear is within the permissible limits, which indicates that the safety level of components is 1.64.

Tab. 11. Results of numerical simulation of planet gears

First planet stage	*Max. value*
Equivalent Stress [N/mm2]	140.9397
Deformation Magnitude [μm]	3.0159
Second planet stage	*Max. value*
Equivalent Stress [N/mm2]	213.6696
Deformation Magnitude [μm]	7.289
Third planet stage	*Max. value*
Equivalent Stress [N/mm2]	421.3347
Deformation Magnitude [μm]	14.2754

6. CONCLUSION

In this study, a three-stage planetary gear train applicable to road vehicle winch has been successfully modelled and analysed to determine its in-service performance.

The results obtained from the finite element analysis, additionally, a stress-strain analysis, focusing on the meshing of the central gear with the planetary gear, identified as the most critical source of stress and deformation. Based on the obtained results, it can be concluded that the material 16MnCr5 for sun and planet gears mechanical properties satisfy meet the requirements all load in transmission. Von Mises stresses are lower than the yield strength of the material used for design three-stage planetary gear, which indicates an optimal design. Future research should focus on further mass reduction and design optimization, as well as investigating the gear train's performance under dynamic loads, thermal effects, and fatigue conditions to ensure long-term durability in real-world applications.

ACKNOWLEDGMENT

This research was financially supported by the Ministry of Science, Technological Development and Innovation of the Republic of Serbia (Contract No. 415-03-137/2025-03/200109).

REFERENCES

[1] Filiz, İ. H., Olguner, S., Evyapan, E. A study on optimization of planetary gear trains. *Acta physica polonica, A*., 2017, 132(3).

[2] A. E. IkpeSpotts, E. M. Etuk, A. U. Adoh, Modelling and analysis of 2-stage planetary gear train for modular horizontal wind turbine application, *Journal of Applied Research on Industrial Engineering*, 2019, Vol. 6, No. 4, pp. 268–282.

[3] A. Nigam, S. JainCohen, Modelling and Structural Analysis of Planetary Geared Winch, *International Journal of Science and Research*, 2015, Vol. 4, pp. 330-333, ISSN (Online): 2319-7064.

[4] A. Narayankutty, A Review of Design and Analysis of A 3-Stage Planetary Gearbox, *International Journal of Advance Research and Innovative Ideas in Education,* 2016, Vol. 2, No.3, pp. 395-399, IJARIIE-ISSN(O)-2395-4396.

[5] M. Sarıtaş, Ö. Gölbol, P. Yayla, Finite element stress analysis of three-stage gearbox, *Niğde Ömer Halisdemir University Journal of Engineering Sciences*, 2021, doi: 10.28948/ngmuh.794874.

[6] S. Tamada, M. Chandra, P. Patra, S. Mandol, D. Bhattacharjee, P. K. Dan, Modeling for Design Simplification and Power-Flow Efficiency Improvement in an Automotive Planetary Gearbox: A CaseExample, *FME Transactions (2020)* Vol. 48, pp. 707-715.

[7] KISSsoft Release 2024, Product Description.

11th International Scientific Conference
IRMES 2025
Research and Development of
Mechanical Elements and Systems
June 19 – 21, 2025; Vrnjačka Banja, Serbia

Original scientific paper DOI: 10.46793/IRMES25.155R

AN EXPERIMENTAL STUDY ON LAYER ADHESION IN FDM 3D PRINTING: COMPARING CONVENTIONAL AND BRICK-LAYER DEPOSITION PATTERNS

Damjan RANGELOV [1]
Lazar STOJANOVIĆ[2]
Aleksandar MILTENOVIĆ[3]
Jovan ARANĐELOVIĆ[5]
Marko PERIĆ[5]

[1]University of Niš, Faculty of Mechanical Engineering, Niš, Serbia, 18000; damjan.rangelov@masfak.ni.ac.rs;
ORCID iD: 0000-0003-3071-893X
[2]University of Niš, Faculty of Mechanical Engineering, Niš, Serbia, 18000; lazar.stojanovic@masfak.ni.ac.rs;
ORCID iD: 0000-0001-5120-8889
[3]University of Niš, Faculty of Mechanical Engineering, Niš, Serbia, 18000; aleksandar.miltenovic@masfak.ni.ac.rs;
ORCID iD: 0000-0002-1453-2548
[4]University of Niš, Faculty of Mechanical Engineering, Niš, Serbia, 18000; jovan.arandjelovic@masfak.ni.ac.rs;
ORCID iD: 0000-0001-9653-4119
[5]University of Niš, Faculty of Mechanical Engineering, Niš, Serbia, 18000; marko.peric@masfak.ni.ac.rs;
ORCID iD: 0000-0001-9350-0351

Abstract: *This study explores the potential benefits of the brick-layer deposition pattern in FDM 3D printing, focusing on its influence on inter-layer adhesion. Standard tensile test specimens conforming to the ISO 527-2/1B geometry were printed using a Bambu Lab X1 Carbon 3D printer with PLA filament. All printing parameters—such as layer height, speed, and temperature—were kept constant, with the only variables being the deposition pattern (conventional vs. brick-layer) and extrusion flow rate (default, +5%, and +10%). A total of six sets of specimens (five per set) were printed vertically to emphasize layer adhesion characteristics. Mechanical testing was conducted via uniaxial tensile testing to failure on universal testing machine. Preliminary results indicate improved performance in specimens printed using the brick-layer method, particularly when combined with increased flow rates. These findings suggest that the brick-layer strategy, though currently underutilized, holds promise for enhancing part strength in FDM printing—warranting further investigation.*

Keywords: *FDM 3D printing, layer adhesion, brick-layer pattern, tensile testing.*

1. INTRODUCTION

Additive manufacturing (AM), and particularly *Fused Deposition Modeling* (FDM), has evolved from a prototyping tool into a viable method for functional part production across industries such as aerospace, automotive, and biomedical engineering. Its appeal lies in low-cost material usage, reduced tooling requirements, and unparalleled design flexibility. The proliferation of consumer-grade 3D printers (often found in small workshops, classrooms, and even households) has democratized access to this technology, enabling on-demand fabrication of complex geometries.

FDM outlines the extrusion-based layer-by-layer deposition of thermoplastic material. In this method, polymer is extruded through a heated nozzle and deposited along a programmed toolpath, gradually building a part from the bottom up. While conceptually elegant and industrially scalable, this process introduces a well-known challenge: interlayer adhesion. The nature of FDM deposition creates interfaces between layers that are susceptible to poor polymer diffusion, void formation, and weak bonding, especially in the Z-axis direction. [1,2,3]

The consequence of this inherent anisotropy is a significant reduction in mechanical strength, particularly under tensile or bending loads applied perpendicular to the build direction. Studies have shown that porosity, surface roughness, and weak filament fusion contribute to premature failure in load-bearing applications. [4,5] These issues are exacerbated when using commonly employed materials like PLA (Polylactic Acid), which (despite being easy to print) has limited thermal and mechanical resilience.

Efforts to mitigate these problems have focused on modifying key process parameters such as extrusion temperature, layer height, and extrusion flow rate [5,6]. A

widely discussed approach is to increase extrusion flow, which can improve layer fusion by increasing filament overlap and reducing internal voids. However, excessive flow can lead to dimensional inaccuracies, material overbuild, and nozzle clogging, posing a trade-off between mechanical strength and geometric precision [3,7].

In this context, alternative deposition strategies have gained attention as a structural solution to improve interlayer adhesion. One such method is the brick-layer deposition pattern, inspired by masonry techniques, in which each new layer is offset from the previous one. This pattern has the potential to disrupt continuous void channels and enhance mechanical interlocking between layers, which could positively influence failure propagation and overall tensile strength.

This study aims to compare the interlayer bonding strength between conventional and brick-layer deposition patterns in FDM-printed PLA parts. The experiments use Creality PLA as the print material, chosen for its commercial relevance and widespread use. Tensile test specimens were fabricated according to the ISO 527-2/1B standard.

Six distinct groups were analysed: three using standard deposition and three using brick-layer deposition. Within each group, the extrusion flow rate was systematically varied at 100% (baseline), 105%, and 110%, with all other parameters held constant. The goal was to isolate the effects of flow rate and pattern on bonding strength.

Mechanical testing was performed using a universal testing machine (UTM) under unidirectional tensile loading perpendicular to the layer planes, ensuring that failure occurs primarily due to delamination or weak interlayer bonding. This testing configuration allows for direct assessment of the structural integrity introduced by each deposition strategy.

By systematically quantifying the influence of deposition architecture and flow adjustment, this study provides insights into process optimizations that enhance layer cohesion, a key factor in advancing FDM from prototyping to functional manufacturing.

2. TESTING

This chapter is divided into three sections to provide greater clarity for each segment. The first part is focused on preparation of the specimens. This part is followed by the section that explains the properties of the material used in this research. At the end of the chapter, the testing procedure is described, encompassing the testing machines's technical details and tensile test conditions (i.e., loading speed, test temperature, etc.).

2.1. Specimen Preparation

Specimens were prepared according to ISO 527-2 standard for tensile testing of plastic materials, the chosen specimen geometry 1B. Dimensions of used 1B specimen are given in Figure 1 and Table 1.

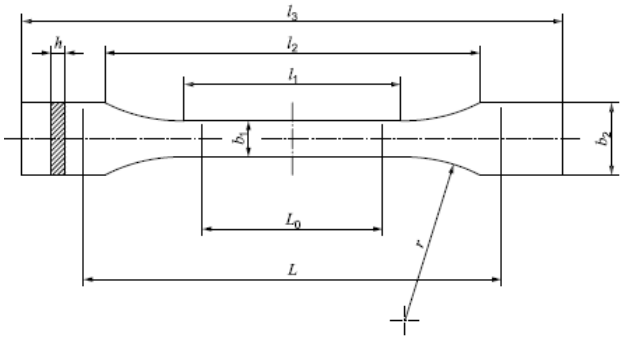

Fig.1. Type 1B test specimen [8]

Table 1. Dimensions of type 1B test specimens [8]

Dimensions in milimetres

	Specimen type	**1B**
l_3	Overall length	≥150
l_1	Length of narrow parallel-sided portion	60,0 ± 0,5
r	Radius	60 ± 0,5
l_2	Distance between broad parallel-sided portions	108 ± 1,6
b_2	Width at ends	20,0 ± 0,2
b_1	Width at the narrow portion	10,0 ± 0,2
h	Thickness	4,0 ± 0,2
L_0	Gauge length	50,0 ± 0,5
L	The initial distance between grips	115 ± 1

Six distinct batches of specimens were produced, with five specimens in each batch. As per ISO 527-1:2012, Clause 7, minimum of five test specimens shall be tested for each of the required directions of testing. The number of measurements may be more than five if greater precision of the mean value is required. The batches differ in deposition pattern and corresponding flow rate. The specimens are categorized into two main groups based on the deposition pattern: Conventional and Brick-layer. Each group is further subdivided based on the applied flow rate, which includes the default value as well as two increased values: +5% and +10%.

Specimens were printed vertically using a Bambu Lab X1 Carbon 3D printer (see Fig. 2). Slicing and G-code generation were performed in Bambu Lab Studio using the "0.28 mm Extra Draft @ BBL X1C" profile, with adjustments made according to recommendations for using the brick-layer deposition pattern script [9].

The following parameters were modified:

- The ***wall generator*** option was set to Classic, as it performs better than Arachne with the brick-layer script.
- The ***wall printing order*** was set to inner/outer to achieve better results with the brick-layer deposition pattern.
- ***Arc fitting*** was disabled because the script does not account for this parameter.
- The ***number of walls*** was increased to six (default is two) to focus on inter-wall layer adhesion, thereby emphasizing the influence of the brick-layer deposition pattern.

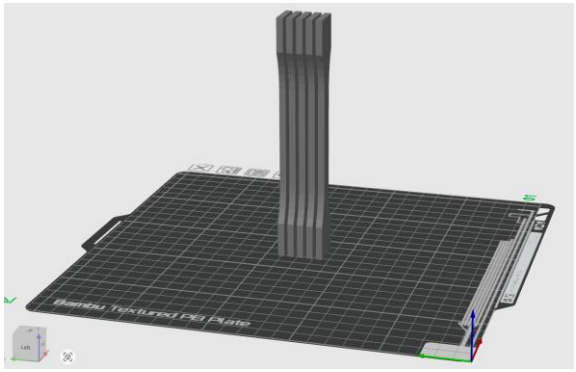

Fig.2. Batch of specimens for printing

2.2. Material

The specimens for this research were printed with PLA (Polylactic Acid) is one of the most commonly used materials in desktop FDM 3D printing. It is favored for its ease of use, low warping, odorless printing, and ability to print without a heated bed. Additionally, PLA is more environmentally friendly than many other plastics, as it is derived from renewable resources like corn starch and requires less energy to produce. [10] The parameters used for printing the specimens were primarily the default slicing settings defined by the slicing software. Other secondary parameters were left at their default values unless otherwise specified.

2.3. Testing procedures

The batches of specimens were differentiated by variations in deposition patterns and flow rates, which is explained in more detail in section 2.1. Important dimension for finding the cross-section of specimens is width at narrow portion (b_1) and thickness (h) from Fig. 1. Nominal values of these dimensions are b_1=10 mm, h=4 mm. The final dimensions of the cross-section were measured and used for calculating stress σ (Eq. 2). The width at the narrow portion (b_1) and thickness (h) of the specimens were measured three times and the mean results were utilized for tests and were within tolerance limits. Although the specimens were prepared in accordance with the ISO 525-2 standard, the initial distance between grips (L) was reduced from 115 mm to 110 mm to improve clamping stability and prevent slippage in the testing machine jaws. This adjustment is not expected to affect the test results, as the specimens are gripped at the wider ends outside the gauge length.

The testing procedure of the specimens is done according to ISO 527-1 standard. [8] To perform a tensile test Shimadzu AGS-X (Figure 3) universal testing machine was used, with a load cell capacity of 10kN. The machine is capable of performing tensile, compressive, and bending tests with different adaptors for each required test. Highly accurate measurements are possible due to the high precision of this device which is within ±0.5% of the indicated test force. The machine is capable of reproducing speeds from 0.001 to 1000 mm/min (stepless) [11].

The tensile test was carried out at a speed of 10 mm/min according to the ISO 527-1 standard. Software Trapezium-X (Shimadzu Corp., Kyoto, Japan) was used to acquire results of the tensile tests, provided by the manufacturer of the universal testing machine Shimadzu. For this testing, the sampling rate of 100 Hz was used, to precisely capture the moment of failure when it happens in fraction of a second.

Fig.3. Shimadzu AGS-X Universal Testing Machine with a specimen

3. RESULTS

Tensile tests were done following ISO 527 standard. All of 30 specimens were tested until the breaking point. Results measured from the tests are strain ε and stress σ which were calculated using equations from ISO 527-1, shown in Eq. (1) and (2) respectively.

$$\varepsilon = \frac{\Delta L}{L_0} \tag{1}$$

where

ε is the strain value in question, expressed as a dimensionless ratio, or as a percentage.

L_0 is the gauge length of the test specimen [mm];

ΔL is the increase of the specimen length between the gauge marks [mm].

$$\sigma = \frac{F}{A} \tag{2}$$

where

σ is the stress value in question [MPa];

F is the measured force concerned [N];

A is the initial cross-sectional area of the specimen [mm^2].

In this testing extensometer was not used, priority was to determine ultimate tensile strength of the specimens and compare it between groups. Strain values are used as a comparison between groups, and not to have absolute values of the material. The engineering stress was used in this research.

Using Equations 1 and 2 from standard ISO 527-1, mechanical properties, strain (ε), and stress (σ), can be calculated for all tested specimens and are shown in Table 2 with the following graph (see Fig. 4).

Table 2. Mechanical properties of the tested specimens

Orientation	Specimen	Mean value	Min value	Max value
BRICK 1.00	Tensile strength [MPa]	23.199	22.345	23.557
	Strain [%]	1.331	1.270	1.491
BRICK 1.05	Tensile strength [MPa]	25.291	24.531	26.112
	Strain [%]	1.396	1.307	1.496
BRICK 1.10	Tensile strength [MPa]	26.665	26.222	27.244
	Strain [%]	1.444	1.362	1.557
CONV 1.00	Tensile strength [MPa]	22.136	22.017	22.314
	Strain [%]	1.224	1.182	1.289
CONV 1.05	Tensile strength [MPa]	24.348	23.896	24.907
	Strain [%]	1.382	1.343	1.404
CONV 1.10	Tensile strength [MPa]	25.448	25.130	25.593
	Strain [%]	1.404	1.346	1.455

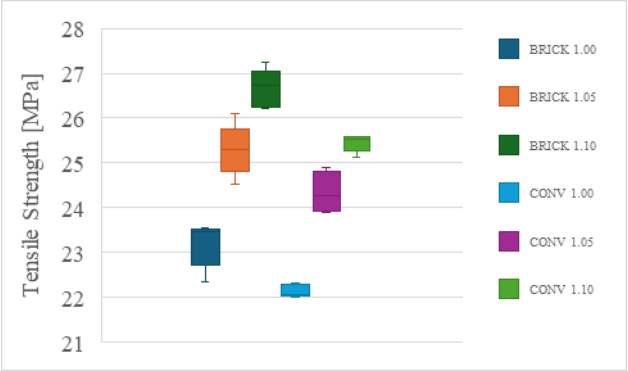

Fig.4. Tensile strength of the specimens

CONCLUSION

This study evaluated the effect of deposition pattern and extrusion flow rate on the interlayer adhesion strength of FDM 3D printed PLA specimens. Two printing strategies (conventional and brick-layer deposition) were compared.
The experimental results demonstrate that the brick-layer deposition pattern significantly improves both tensile stress and strain, compared to the conventional deposition pattern at all flow rates. The highest mean tensile strength (26.665 MPa) and strain (1.44%) were achieved by the brick-layer group at 110% flow, outperforming the best-performing reference group (25.45 MPa, 1.40%). These improvements are attributed to enhanced mechanical interlocking and filament overlap introduced by the staggered brick-like geometry.
Furthermore, increasing the extrusion flow rate positively influenced interlayer cohesion in both strategies. However, the combined effect of brick-layering and flow adjustment produced the most robust and consistent bonding, as evidenced by lower standard deviations and higher mean values.
These findings highlight that strategic control of deposition geometry and flow rate can be an effective and low-cost means to mitigate the anisotropic weaknesses of FDM-printed parts. The brick-layer pattern, inspired by traditional masonry, emerges as a practical solution for improving the structural performance of FDM components, especially where interlayer adhesion is critical.
Brick-layer deposition shows potential for improving layer adhesion in FDM printing. Further investigation of other non-conventional deposition patterns could reveal additional performance benefits for 3D printed parts.

ACKNOWLEDGMENT

This research was financially supported by the Ministry of Science, Technological Development and Innovation of the Republic of Serbia (Contract No. 451-03-136/2025-3/200109).

REFERENCES

[1] Y. Lyu, Y. Chen, L. Lin, A. K. Schlarb, Y. Li, and X. Shi, “Architecture of covalent bonds between filament layers to enhance performance of 3D printing biodegradable polymer blends,” Polymer Testing, vol. 106, p. 107456, 2022
[2] Thumsorn, S.; Prasong, W.; Kurose, T.; Ishigami, A.; Kobayashi, Y.; Ito, H.: Rheological Behavior and Dynamic Mechanical Properties for Interpretation of Layer Adhesion in FDM 3D Printing. *Polymers*, *14*, 2721, 2022
[3] Török, J., Törökova, M., Duplakova, D., Murcinkova, Z., Duplak, J., Kascak, J., & Karkova, M.: Advanced Configuration Parameters of Post Processor Influencing Tensile Testing PLA and Add-Mixtures in Polymer Matrix in the Process of FDM Technology. *Applied Sciences*, *11*(13), 6212, 2021
[4] Pezer, D., Vukas, F., Butir, M.: Experimental Study of Tensile Strength for 3D Printed Specimens of HI-PLA Polymer Material on In-house Tensile Test Machine. *Technium* Vol. 4, No.10 pp.197-206, ISSN: 2668-778X, 2022
[5] Prasong, W., Ishigami, A., Thumsorn, S., Kurose, T., & Ito, H.: Improvement of Interlayer Adhesion and Heat Resistance of Biodegradable Ternary Blend Composite 3D Printing. *Polymers*, *13*(5), 740, 2021
[6] Liparoti, S., Sofia, D., Romano, A., Marra, F., & Pantani, R.: Fused Filament Deposition of PLA: The Role of Interlayer Adhesion in the Mechanical Performances. *Polymers*, *13*(3), 399, 2021
[7] Saleh, A. M, Jaber, A. S., Jabbar, M. S.: Layer adhesion investigation of three dimension printed parts by controlling the environment temperature. *Advances in Science and Technology Research Journal,* 19(3), 74–83, ISSN 2299-8624, 2025
[8] ISO 527–2012: Plastics - Determination of tensile properties.
[9] https://github.com/GeekDetour/BrickLayers – GeekDetour. (2025). BrickLayers (Version 0.2.1) [Source code]. GitHub.
[10] https://www.matterhackers.com/3d-printer-filament-compare – MatterHackers. (n.d.). *3D Printer Filament Comparison Guide*. MatterHackers.
[11] https://www.shimadzu.com/an/products/materials-testing/uni-ttm/autograph-ags-x-series/spec.html – Shimadzu Corporation. (n.d.). *Autograph AGS-X Series – Specifications*. Shimadzu.

11th International Scientific Conference
IRMES 2025
Research and Development of
Mechanical Elements and Systems
June 19 – 21, 2025; Vrnjačka Banja, Serbia

Review paper DOI: 10.46793/IRMES25.159A

PREDICTION OF TRIBOLOGICAL PROPERTIES OF ALUMINUM WELDED BY FRICTION STIR WELDING (FSW), A REVIEW

Amir ALSAMMARRAIE[1]
Abdul SALAM Y. OBAID[2]

[1]Tikrit University, Baghdad, Iraq, email amircraft@tu.edu.iq; ORCID iD: 0000-0001-7934-1454
[2] Engineering Affairs Department, University of Fallujah, email dr.eng.abdulsalam@uofallujah.edu.iq; ORCID iD: 0000-0002-0152-7069

Abstract: *Friction Stir Welding (FSW) is a solid-state welding method innovatived in 1991 by Wayne Thomas at the Welding Institute (TWI) of the UK. In the beginning, It was considered a laboratory curiosity, but it soon came to provide many benefits in the aviation, railway, and shipbuilding industries, especially in the manufacture of aluminum alloys as a major bonding process. The FSW method has many advantages, including environmental friendliness and energy saving. This technique is designed to join high-strength aluminum alloys and metal materials that are difficult to be joined using the traditional processes. This research reviews a set of research on friction stir welding of aluminum alloys.*

Keywords: *Friction stir welding, Aluminum alloy. Dissimilar Al alloy, Tilt angle.*

1. INTRODUCTION

FSW is a novel form of solid-state welding in which the two components are joined by solder joints rather than melting the metal to be welded. Because of its superior strength-to-weight ratio, exceptional ductility, corrosion resistance, and resistance to cracking in harsh environments, 6061 aluminum alloy has been more and more in demand in aerospace, aviation, and automotive applications in recent years. However, welding these alloys is still difficult. Hot cracking in the weld may be a significant issue in addition to softening the heat-affected zone and the weld seam . The authors sought to compare changes in mechanical properties with fatherly metal, as well as examine the effect of welding parameters on the joint's tensile characteristics, microstructure, weld metal toughness, and heat zone[1] .

The process of friction stir welding is an innovative manufacturing scientific discovery that is in considerable employed in numerous sectors.It operates in all directions, is simple to use, and doesn't harm the environment . Using polycarbonate and alloy sheet materials as a base, and looked at the factors that affect the process parameters and understood the links of alloys of aluminum to different metals. High tensile strength, and microhardness due to enhanced plastic deformation are investigated and examined various modeling approaches to enhance the factors and reactions. These included the Taguchi method, creating experiments that serve as strong and trustworthy instruments[2].

Modern friction stir welding (FSW) has surpassed more traditional methods of combining aluminum alloys, such as laser welding, resistance welding, metal inert gas, and tungsten inert gas. For aluminum alloy 6082 it has varying amounts of Al_2O_3 reinforcing. Further, studies on MMCs subjected to friction stir welding are being carried out by researchers worldwide to deduce how various welding parameters influence flow behavior as well as mechanical and metallurgical characteristi [3].

The quality of welded connections is affected by several operational parameters, such as welding velocity, rotation velocity, shoulder diameter, tilt angle, and so on. When it comes to the production of joint strength, every process parameter is crucial .The researchers kept all other process parameters constant while they changed one process parameter and if affected the properties of the microstructure and tensile strength of the aluminum alloy AA2014-T6. Furthermore, the junction was made with a tilt angle of 1.5∘[4].

The friction stir welding, may provide lightweight, inexpensive, and waste-free solder junctions of excellent quality. The researchers used samples of 5 mm 6061-T6 aluminum alloy sheet and were able to improve the process parameters by combining the tool profile, rotational speed, and tangential speed. Rotation and traverse speeds were identified as critical factors with a 99% confidence interval, and a combined efficiency of 91.3% was attained [5].

The friction welding (FSW) is, a novel solid-state welding method, to produce strong connections. Scientists were used friction stir welding to effectively combine two aluminum alloys, AA 7075-O, and AA 5052-O. They

examined how changes in tool rotation speed and tool pin profile affected mechanical parameters including microhardness and tensile strength. TAGUCHI procedures were taken into consideration. After that, they used Minitab to compile tabular data from the experiments, TAGUCHI analysis, and ANOVA. The results from the experiments and the statistics are quite consistent with one another; the margin of error is less than 5% of the average difference value [6] .

Researchers attempted to fuse AA7075 alloy employing the frictional stir welding technique . A TAGUCHI L18 orthogonal matrix was utilized to develop experimental procedures. Joings were done by varying the inclination angle, tool rotation speed, tool feed speed, and axial load. According to studies. Tilting the tool makes the welds softer, they found. To try to FSW alloy AA7075, researchers varied input factors such as inclination angle, velocity, feed, and axial load, and then used these loads to manipulate mechanical and microstructural behavior [7] .

A sophisticated welding technology that may combine materials and alloys that are similar or different is friction stir welding (FSW). Researchers fused two different aluminum alloys, AA6063 and AA7075, and then evaluated the resulting joint's properties. Researchers made of different alloys by changing the welding speed and the tool's spinning speed . SEM and data on the mechanical characteristics were investigated by changing the input parameters [8] .

Many different types of businesses employ friction stir welding (FSW), a solid-state method. By combining the two different aluminum alloys, AA2014 and AA6063, researchers were able to increase the microhardness, ultimate tensile strength, and yield strength. They used four input parameters: tool pin shape, rotating speed, axial force, and traverse speed. Weld micrographs reveal enhanced bonding and mechanical strength due to grain refinement and correct material fusion. All of the outputs are substantially affected by the input characteristics .There are no holes, oxides, or fractures visible in the micrographs taken from the heat-affected zone (HAZ) area[9] .

There is complicated interaction between plastic deformation, heat history, and residual stress. The team used the Coupled Eulerian-Lagrangian (CEL) technique to create a cutting-edge finite element model. Aluminum alloy AA 6082-T6 FSW processed and a combination of optical macrography, neutron diffraction residual stress measurement and monitored cross-weld temperature history was used .The speed of tool rotation controls the temperature development. Various welding processes were influenced by the rotation speed, including plastic deformation, material flow, and stirred volume[10] .

The friction stir welding of AA 5052 and AA 6061alloys, reaved that the cylindrical tool pin was effectively stirred while maintaining a reduced feed rate, resulting in optimum mixing. Additionally, grain size varied between zones, which affected mechanical capabilities.The hardness,ductility and tensile were tested [11].

Taguchi method was used to conduct a specific number of experiments with dissimilar aluminum alloys AA2024-T3 and AA7075-T73 plates to identify the most important parameters and the percentage contribution of each parameter to the tensile strength and joint efficiency of the FS welded joint. The variables were tool tilt angle 2, pin profiles, welding rates (20, 45, and 69 mm/min), and rotation speeds (898, 1200, and 1710). The optimized parameters, determined via S\N ratio analysis, include a threaded cylindrical pin profile with a junction efficiency of 76%, a welding speed of 45 mm/min, and a rotation speed of 898 rpm. The welding speed stood was the most relevant process parameter, accounting for 66.05% of the total. The L9 Taguchi orthogonal array is used to find the best welding process parameters. Additionally, the significance of each parameter to the process is determined using ANOVA [12].

FSW on 6-mm-thick aluminum alloy sheets (AA2024 T351) was performed . Welding settings used were rotational speed of (73, 116, and 150 mm/min), with a constant tool rotation speed of 750 rpm. The weld joint's Vickers hardness was measured in a plane perpendicular to the welding direction. The EN 910 standard was used for the bend testing. Joints under stress on both the face and root sides were used .Examining how different factors affect the mechanical and structural properties of FSW welded joints[13] .

The AA 2014-T6 finds extensive use in the construction of aircraft and vehicle bodies. Due to its low weldability, the alloy cannot be welded using gas welding procedures. Arc and resistance welding this aluminum alloy requires specialized procedures, which may be rather expensive. AA 2014-T6 alloy joints generated by friction stir welding with the process parameters as a traverse speed of 40 mm/min, a tool rotating speed of 900 rpm, and a taper cylindrical tool pin shape were all used. The microstructure and mechanical properties of friction stir welded AA 2014-T6 have been studied [14].

AA 7075-T73 welded joints and the mechanical characteristics are affected by ultrasonic peening. The rotating speed was set at 710 rpm and the travel speed at 35 mm/min. The tensile tests revealed that the welding efficiency for the welded samples was around 60%. The welded samples revealed microhardness variations along the welding centerline.The mechanical qualities enhanced by using the ultrasonic peening process, which produces compressive stresses [15].

Various process parameters have been used to friction stir weld AA6061 and AA7075 alloy. Throughout the nugget zone, grain refining was seen. During tensile testing cracks were produced in the HAZ . This line where the lowest values found in microhardness profiles. It was discovered that when heat input decreases, the tensile strength joint improves. The temperature history profiles were also monitored using thermocouples and modeled using a three-dimensional computer model to help with interpretation [16].

Friction stir welding of AA 6061-T6 and AA 8011-h14alloys is studied relative to the alloy location and tool offset, with all other welding parameters held constant (1070 rpm tool rotation speed, 50 mm/min tool traverse speed and 2° tool tilt angle). Visual examination is carried out. Subsurface defects were understood with radiography tests. The tensile strength was 77.88 MPa and an elongation was 21.96% at tool offset 1 mm on the advancing side, the tensile tests showed superior ductlitly

at the welded joints . The hardness levels do not change as a function of the experimental variables. The asymmetrical profile shows that the advancing side has a greater temperature [17].

FSW of two different alloys, AA 6061-T6 and AA 8011-h14 was performed . In order to find surface flaws , tensile and hardness tests are also used to determine mechaical qualities. The impact of tool tilt angle on friction stir welding (FSW) heat production, temperature field, and material flow behavior is also examined in both experimental and numerical simulations. Welding speeds and tool rotation rates both contribute to a bigger crescent-shaped uncontacted region. A greater peak temperature and more intense material flow are seen at the lagging advancing side. The updated model accurately predicts the thermomechanically impacted zone and the peak temperature at the tool/workpiece interface are the tool tilt angle and pin thread [18].

Examination of the microstructural changes, mechanical characteristics, and residual stress distribution of 7075-T651 Al alloy connected by friction stir welding were studied. The welding speeds were 20, 40, and 60 mm/min, while the rev/min was 900, 1250, and 1600. Also, the hole drilling approach found out how the joints' residual stresses were distributed. The resulting welded joints were subjected to tensile and hardness testing as well as metallographic analyses [19].

The fatigue behavior of friction stir welded joints of 7075-T6 and 5052-H34 alloys were tested. With the help of an MTS-5 axis friction stir welder, a 4.826mm thick plate underwent FSW. With a forge load of 9KN , a travel speed of 187 mm/min, and a rotating speed of 400 rpm . The stress ratio R=0.1 and testing frequency of 7 Hz were used in the tension-tension fatigue tests. [20].

2. EXPERIMENTAL WORK

Accurately measuring 300mm × 150 mm and thickness of 6 mm sheets of AA6061 aluminum alloy. The high-carbon steel spinning tool that was used. Dimensions: 6 mm for the probe, 18 mm for the shoulder, and 5.5 mm for the pin. RV machine was used for the process. The fixtures are set up for constructing FSW joints with aluminum plates in them, and mechanical clamps are used to keep the plates from coming loose when welding [1].

The joining of AA7075-T651 and AA6082-T651 alloys with a 6 thickness and measures 100 mm × 50 mm. Aluminum AA7075-T651 are placed on the advancing side of the fixtures. The specimens that have been welded with a square tool are put on the retreating side, together with aluminum alloys AA 6082 T-651. The experimental parameter are: Turning and welding speeds, as well as the degree of tilt [2].

Composite material that consisted of an Al_2O_3 were employed as a reinforcement matrix to an Al Alloy 6082 to be mixed with varying concentrations (5% to 15%.) of Aluminum Oxide. The fixture is engineered to endure the axial force. It all started with taking two identically sized specimens of Aluminum Oxide and FSW joining them into one solid piece.. Tensile testing, hardness testing, and microstructure analysis were all performed mechanically [3].

Researchers used a 2 mm thick AA2014-T6 aluminum alloy sheet with dimensions 300x150 mm. Keller's reagent was used to etch alumina suspension onto the surfaces. The tensile specimens were set according to the ASTM-E8-M04 standard. A tensile test was performed with a crosshead velocity of 1.5 mm/min. Applying a continuous load of 50 N and a dwell duration of 15 seconds. Using scanning electron microscopy (SEM), The shape of the fractures in the joints was investigated. The elemental content in the weld area determined by using energy-dispersive spectroscopy (EDS) [4].

An abutt joint design was used utilizing 606-T6 aluminum alloy. The welding sheet in dimensions of (101 mm × 20 mm ×5 mm). Experiments was performed using a powerful XHS7145 vertical CNC machine. The tool made of H13 tool steel with different pin profiles . The quality of FSW was determined by using a securely fastened fixture constructed to prevent any undesired oscillations [5].

Annealed AA7075 and AA5052 are subjected to FSW. The workpieces are with dimensions of 170×60×5 mm. Four pin profiles (circular, cylindrical taper, square, and triangular) are considered in this investigation. A10 T type horizontal FSW machine manufactured by ETA is used.The process parameters are: rotational speeds of 800,1000,1200, and 1400 rpm and the tool offset -0.5 mm, 0mm, 0.5mm, and 1mm. The tensile tests are conducted following the ASTM E8 standards, whereas the micro-hardness tests adhere to the ASTM E-92 requirements [6].

Scientists employed FSW of AA 7075 aluminum alloy. Measurements of 18 mm for the shoulder distance and 6 mm for the pin were taken. The specimens were first sheared perpendicular to the weld line and then treated with Keller's reagent. The study of microstructure with the Trinocular metallurgical microscope. The researchers estimated the hardness throughout the crossover or middle part of the weld. With a 0.5 kg load and a dwell length of 10 seconds using a Vickers' hardness analyzer at a depth of 1.5mm below the weld area, with a spacing of 1mm between each measurement [7].

Researchers welded together 70 mm x 75 mm aluminum combinations AA6063-T6 and AA 7075-T5 with a thickness of 6 mm. The apparatus rotational speed was selected to be 800 - 1200 rpm, the rotational speed was further narrowed down to 100-200 mm/min, and an axial force 0f 8 KN was used in this study. The cylindrical pin profile was chosen because of its straightness. [8].

Both AA2014 and AA6063 were used in FSW joining process using LMW-KODI 40 model vertical machine. The center has a table size of 900×410mm, a traversal movement of 560×410×460mm, a rapid feed rate of 20/12 mm/min, a spindle rotation speed range of 150 - 4000 rpm. Aluminum alloy plates with dimensions of 75×50×6 mm. Joints are created .The tools have a 2° tilt angle on the advancing side. When welding, a 5 mm plunge depth is taken into account. For 8 seconds, the tool is heated first to provide the required friction at a down feed rate of 10 mm/min. The mechanical behavior of the welded. Work pieces includes the tensile test and micro-Vickers hardness assessments are based on the ASTM E92 standard, whereas ultimate and yield strengths and

percentage elongation are determined by the ASTM E8 standards [9].

Friction stir welded rolled sheets of aluminum alloy AA6082-T6 measuring 150×60×4 mm while in the solution heat-treated condition T6. The welding tool constructed from chromium hot work tool steel AISIH13, had a concave and smooth shape with a 16 mm shoulder diameter. The pin is threaded with 6 mm in diameter and 3.3 mm in height, a 0.2 mm plunge depth was employed and the tool's rotating axis was angled 2˚ off the sheet normal. A continuous welding speed of 200 mm/min was used in conjunction with tool rotating speeds of 800 and 1100 rpm to create the joints. The welding temperature fluctuation significantly decreased after 20 mm of lateral displacement from the weld center. This investigation used a high friction coefficient of 0.8 [10].

A conventional milling machine is used to butt welds of alloys AA 5052 and AA 6061. The specimens with dimensions of 100 mm x 50 mm and clamping device used to hold them in place at all angles. The cylindrical AISI H13 tool steel with two threads was used . The parameters used: 710 rpm at 28mm/min and 710 rpm at 20mm/min. The samples were immersed in a solution of 150 ml water, 3 ml nitric acid, and 6 ml hydrochloric and hydrofluoric acid, optical microscopy investigations were performed. The INSTRON 8801 UTM was used to perform the tensile testing. The Matsuzawa MMT-X Vickers hardness tester was used. For a weld length of 30mm, indentations were formed every 0.5mm with a 100gf stress [11].

The FSW has been chosen to combine aluminum alloy plates AA2024-T3 and AA7075-T73with dimensions of (150×70×3) mm. A spectrometer analytical tool was used to determine the chemical composition of these alloys .A tool steel type X12M was used to conduct the FSW . The experimental variables were the pin's shape, welding speed, and rotational speed (rpm).At each welding parameter, the tensile characteristics of FSW joints were estimated using transverse tensile testing. The samples were examined using an optical microscope. The Vickers hardness test was carried out using a digital microhardness tester of the Layree type, namely the HVS-1000 mode [12].

Aluminium alloy EN AW 2024-T351 welded plates had dimensions of 500 mm × 65 mm × 6 mm. A 6 mm thickness is machined with a backing plate made of austenitic metal is positioned underneath the welding plates. The experimental parameters that were used including the tool rotation speed and the welding speed . Radiological control of samples and visual inspection of the weld face and seam root were used. Tensile specimens, impact specimens with V-notches at various FSW joint sites, and fracture mechanics parameter specimens were all created from FSW welded samples [13].

The AA 2014-T6 plates were subjected to a single pass FSW. Wire cut is used to achieve the specimens with dimensions (240mm × 60 mm × 5mm). By clamping for joint arrangement was achieved. The welding direction is perpendicular to the rolling direction.The pin has a diameter of 6 mm and a length of 4.8 mm, while the tool shoulder has a diameter of 18 mm.The yield strength, tensile strength, and elongation of the joints were evaluated using smooth tensile specimens that were produced according to ASTM standard [14].

FSW joining, 3 mm thick aluminum alloy plates of AA7075-T73 were used. Plates with dimensions of 150×75×3 mm were cut. Spectrometer was used to get the chemical analysis of this alloy. A milling machine of the GmbH Knuth Werkzeug machine type from Germany. With a tool shoulder has a diameter of 15 mm, the base pin of 5 mm, and the top pin of 3 mm. The height of the pin is 2.85 mm, were employed in this study. Welding parameters, such as 35, 45, and 60 mm/min travel speed, 500, 710, and 900 rpm rotating speed, 2° tilt angle, and 30 sec dwelling time were applied. An HC-S-1 ultrasonic peening equipment is used to enhance the mechanical qualities of welded joints. The tensile tests and the Vickers hardness test was performed [15].

Al alloys of AA6061 and AA7075 in T6 temper state are joined with FSW . The plates was 300x 50 mm degreased with acetone, then air dried. The longitudinal butt joints created by use of a FSW robot, with downward force of 12 kN. The threaded conical probe has three flats and a base diameter of 5 mm; the shoulder is 15 mm in diameter. Three different welding/travel speeds of 2,3,5 mm/sec while keeping the tool rotation speed constant at 1200 rpm were emplyed. In situ, K-type thermocouples with a 0.25 mm diameter wire were used to monitor the temperature profiles in the heat-affected zones (HAZ). Utilizing the commercial finite element program ANSYS, a transient thermal study was conducted. The specimen was subjected to tensile testing at a rate of 1 mm/min-1 in accordance with the ASTM E8-04 standard [16].

The aluminum alloys AA 6061-T6 and AA 8011-h14cut with specimen dimension of 100 mm × 50 mm × 3 mm and prepared by polishing them with silicon carbide paper and cleaning them with acetone to execute FSW. The tools were tapered pin tools made of high-carbon, high-chromium tool steel. The plates were secured tightly to the apparatus. The welding temperature profile was accomplished with the use of 1.5 mm sheath diameter K-type thermocouples allowing for continuous recording of temperatures on both the advancing and receding sides. The following parameters were maintained: tool traverse speed of 50 mm/s, tool rotational speed of 1070 rpm, and tool tilt angle of 2°. The radiography testing, optical microscopy, tensile, hardness testing, and time-temperature plots were investigated [17].

Aluminum alloy (AA6061-T6) butt-welded using specimens of a dimension of 6 x 200x 75 mm . The tool had a 15 mm shoulder diameter and a 2(k) concave shape. While the conical pin's diameter declined from 7.0 mm to 5.2 mm, the threaded pin's length was 5.75 mm. Tool slanted at an angle of 0° and 2.5° was used, with a tool rotation speed ranging from 400 to 800 rpm and a welding speed of 50 to 150 mm/min, respectively. Temperature sensor is used at the interface between tools and workpieces. Through-holes of 0.8 mm in diameter were machined into the tool and a pair of type K thermocouples are set up at the holes' exteriors. Both the temperature at the tool/workpiece contact and the tool torque were monitored .The numerical work completed

by using the ANSYS Fluent 14.5 Computational Fluid Dynamics (CFD) program [18].

7075-T651 Al alloy sheets with dimensions of 6×125×300 mm were joint by FSW. Tools were made using X210Cr12 steel and the pin was given a conical shape with height 5.8 mm, and shoulder diameter was 20 mm. A FIRST MCV 300 CNC milling machine, executed the FSW . The following welding speeds and rotational velocities were used: 900, 1250, and 1600 rev/min, and 20, 40, and 60 mm/min, respectively. The welded joints were subjected to tensile and hardness tests as well as metallographic analyses. The Dino-Lite Pro digital microscope was used to examine the specimens' macrostructure .A scanning electron microscope (SEM) from Japan, the JEOL JSM-6060LV, was used to study the microvoids and large grain band zones [19].

Two types of aluminum alloys, one with a thickness of 4.826 mm and the other of 7075-T6 (Al-Zn-Cu-Mg). specimens were cut with a dimension of 203x 19.8mm perpendicular to the weld line.The pin tool constructed from H13 tool steel. The I-stir 10 Multi Axis friction stir welding equipment was used for FSW process. The Instron universal test system, model 8800R, was used to conduct the tensile tests.The Buehler micromet II, a Vickers micro hardness tester, was used for the testing. We employed an immersion ultrasonic testing equipment (UNIDEX 11) to look for flaws in the FSW plate [20].

3. RESULT AND DISCUSSION

Visual inspection of all welded specimens reveals that the weldments are free of defects.Weld center hardness is lower than base metal hardness. This is because the tool action induces shear stress, which in turn generates an extremely tiny grain structure. The toughness of the welding is found to increase when the rotating speed rises over 1200 rpm. With a 16–31.5 mm/min traverse speed, the hardness decreases by 80-90% compared to the base metal. Additionally, an increment 90% of the strength compared to base material was recorded. Weldment specimen elongation approaches base metal elongation when the welding speed is lowered [1].

FSW heats up the stir zone, the angle of tilt affects the tensile strength. Rotational speed was inversely proportional to impact strength. The impact strength is affected by the welding speed. The impact strength is affected by the tilt angle. As the degree of tilt lowers, the impact strength rises. The rotational speed is directly proportional to elongation %. The amount of heat applied has significantly affected the elongation %. The square tool pin influences the elongation % as a function of tilt angle [2].

A combination of FSW and butting two sheets of aluminum alloy AA6082 reinforced with 5%,10%, or 15% Al_2O_3 produced the desired result. The ultimate tensile strength is significantly affected by changes in the tool's rotating speed. Reduced tool rotational rates resulted in reduced heat input. Poor plastic flow of the metal was the result of this. The weld zone has a far higher hardness value than the underlying metal. [3].

The welding speed has a substantial impact on the rate of heat production throughout the thermal cycle during FSW. The FSW method dissolves and distributes the Cu eutectic components uniformly throughout the aluminum matrix of the AA2014-T6 aluminum alloy. This solute is kept in the FSW's aluminum matrix according to the thermal cycle's rate of heat dissipation. The transfer of material is accomplished by rotating the tool's shoulders [4].

The tensile strength of comparable FS welded Al-alloys was tested three times (6061). Findings show that rotating speed has a direct correlation with hardness and tensile strength, whereas tool traverse speed has an inverse relationship. Under optimal parameter conditions, with a rotational speed of 1400 rpm and a traverse speed of 37.5 mm/min, the higher hardness value of 71.6 HR was achieved. The temperature grows as the rotating speed increases whereas the traverse speed decreases the temperature [5].

TAGUCHI methodologies is a scientifically rigorous approach to test and optimize process parameters and the overall percentage of error between experimental trial results and statistically proven approaches is below 5%. The most important thing to tune here is the rotating speed, then the tool pin profile, feed, and tool offset. The tensile strength is at its highest at rotational speeds ranging from 1100 to 1300 rpm, feed rates from 100 to 130 mm/min, and tool offsets from -0.50 mm to 0 mm, 0.25 mm to 0.75 mm [6].

In the microstructure, the base metal showed signs of precipitation solidification after being treated with a solution. The hardness values of the welded joints were lower when the tool angles were 1.50^0, Research shows that a tilt angle helps with material replenishment and mixing at the weld joint [7].

Rotational velocities of 800, 1000, and 1200 rpm, as well as spindle feed rates of 1.66 and 2.5 mm/sec, were used to determine the tensile strength for similar aluminum alloys used in FSW weldments. The weld is fine-grained, revealing that the welded region is defect-free. The presence of beta precipitates in the secondary phase is the primary cause of the stir zone hardening [8].

A triangular pin profile, a tool traverse speed of 25 mm/min, a tool speed of 1010 rpm, and an axial force of 7 KN are the optimal settings here. The specimens' weld zones show no signs of defects, fractures, or voids, and the mechanical strength of the aluminum alloy joint is improved due to the smaller grain sizes. On the way to the nugget zone, the hardness of the base metal AA2014 increases little compared to what is farther out. The hardnesses however, are much lower when compared to weld plate AA6063 [9].

FSW joint of AA6082-T6 aluminum alloys. As the plunge depth is increased, the generated temperature in the center of the weld region increases. The region right next to the tool shoulder has the highest level of heat effect. The region around the tool pin on the side that was receding generated more heat compared to the side that was being advanced. Weld II's nugget zone has a considerably higher limit of high plastic strain compared to Weld I, Faster rotational speed of the welding tool produces a greater stirring effect [10].

It has also been observed that a micro void becomes apparent at 28 mm/min. This might be because the weld nugget does not include frictional heat. Both fractures

occurred in the TMAZ on the AA6061 side, proving that the weld is stronger than the parent metals. The hardness values exhibit a declining trend from the welding's advancing side (AA 5052) to its retreating side (AA 6061), before gradually rising again. The TMAZ hardness values on the retreating side are somewhat lower than on the weld nugget side. The hardness values in the weld nugget are lower than in the two base metals. This might be because the grain coarsening effect is at work [11].

In the analysis of variance (ANOVA) for the tensile result, the welding speed is the most important parameter with a percentage of 66.05%, followed by the pin geometry with 15.68% and the rotation speed with 5.21%. All the tested joints of 2024 and 7075 had less tensile strengths than the basic alloys. The tensile strength increases in direct proportion to welding speed. The tensile strength grows as the tool rotation speed rises up to 898 rpm, beyond which it steadily declines. The tensile characteristics are improved due to a reduction in the thickness of the TMAZ and the heat input needed for joining is reduced when the welding speed is increased and the tool rotation speed is decreased. The welded joint hardness is reduced in HAZ [12].

Using the welding settings 750/73 rpm/(mm/min), it is evident that the mixing zone produces the most amount of heat. High-speed welding causes the material to be well mixed, which in turn increases the creation of microvoids in the lower zone TMAZ. The hardness rises as the welding speed lowers, even while the grain size in the mixing zone is biggest at the lowest welding speed .This trend indicates that the massive hardening that occurs when the welding speed drops is dependent on the distribution and size of second-phase particles and precipitates rather than grain size. When tested under bending conditions, welded connections near the root exhibit somewhat improved deformation capabilities compared to those around the face [13].

Friction stir welded AA 2014 alloy joints were tested for transverse yield and tensile strengths as well as elongation and joint efficiency. The joint produced by using SS tool material and a taper cylindrical tool profile at 900 rpm had better tensile strength, yield strength, and percentage of elongation than the straight cylindrical joint. This could be because we generated just the right amount of heat to allow the plasticized material to flow freely and provide enough mechanical working [14].

Following a single line peening of FSW welded joint of AA 7075-T73, the tensile strength was lower than that of the base alloy. The welded parts with two lines peened have a greater tensile strength compared to those with one line peened (1UP), the hardness of welded joints rose to 234.7 HV in the stir zone SZ, whereas it peaked at 158.1 HV in the TMAZ and 196.6 HV in the HAZ. In the stir zone, the hardness of welded joints with one-line peening 1UP was 382.5 HV, while in the TMAZ and HAZ it was 260.3 and 182.1 HV, respectively and the base metal BM had a hardness value of 155 HV [15].

Local thermal hysteresis may have a significant impact on the distribution of precipitates, leading to their coarsening, dissolution, and re-precipitation, especially for heat treatable Al alloys. It is easily apparent that the total friction heat created during FSW is inversely related to the travel speed. Positioning AA7075 Al on the advancing side results in a slightly higher peak temperature in AA6061 at the same rotation and travel speed. Welds made of AA6061 and AA7075 alloys often show a reduction in microhardness relative to the base metals [16].

The tensile strength and quality of the welded connections of AA 6061 and AA 8011 are significantly affected by the tool offset when using FSW with dissimilar alloys. Because it is a tougher material, AA 6061 resists deformation and does not get pushed into the nugget zone, which causes a lack of penetration and inappropriate stirring of the material, leading to a lower value of tensile strength and poor weld quality . The improved tensile qualities are a result of the higher process temperature, which allows for more heat to be applied along the weld [17].

The friction heat rises at a tool tilt angle of 2.5◦ with downward axial force and the viscous dissipation heat density is greater at the shoulder and pin corners compared to 0◦ tool tilt angles .With a 2.5◦ tool tilt angle, the peak temperature is also greater than that of a 0◦ tool tilt angle. Joint quality improves when the material is heated to a point where it softens and flows more easily [18].

Hardness values were higher when the welding speed was raised while maintaining a constant rotating speed during FSW of 7075-T651. The maximum tensile strength was found to be 610.5 MPa and the breaking elongation to be 12%. All specimens showed reduced ductilities and tensile strengths when compared to the parent material, the tensile stress was 26-45% lower. While the highest % elongation and maximum tensile strength were achieved with a high welding speed at 900 rev/min rotating speed, the maximum tensile strengths were found to be greater at a medium speed of 40 mm/min at 1250 and 1600 rev/min. [19].

For both the age-hardening alloy (7075-T6) and the strain-hardening alloy (5052-H34), the microhardness values were strongly dependent on the distance from the weld line. FSW zone has a greater hardness value than the base alloy 5052-H34 side. Hardness rises with decreasing grain size. The precipitation of hardening phases and the fine particles of intermetallic compounds both contribute to the enhancement of hardness. The fatigue limit is lower for basic materials than the fatigue strength at 2×106 cycles [20].

4. CONCLUSION

All of the weldments seemed to have a level, sound, and well-joined surface at the weld root. improved the weld strength as a consequence linked to the dynamic recovery and recrystallization at the weld. The creation of small, evenly distributed strengthening precipitates and fine, equiaxed grains in the weld area causes FSW joints of 6061 aluminum to have superior tensile characteristics. As the welding speed was raised, the size of the weld nugget zone shrank. Welding at a minimum speed of 16 mm/min improves mechanical characteristics and increases weld nugget area compared to other speeds [1].

FSW of 7075T651 and AA6082T65 reveals that rotational speed is a key factor. Variable properties

influence the main responses to tensile strength, impact strength, and elongation [2].

Factors influencing the tensile strength of FSW Aluminum Alloy AA-6082 reinforced with different percentages of Al_2O_3 include the speed of rotation, the hardness of the nugget region, and the formation of defects. The ultimate tensile strength is highest at 1000 rpm and gradually drops. Heat input was minimal at lower tool rotating speeds . An increase in the strain rate, may result from very high rotating speeds. This leads to an increase in hardness as well as maximal tensile strength. Statistical methods like analysis of variance (ANOVA) and response surface methodology (RSM) were used to determine the empirical correlations in order to predict the ultimate tensile strength (UTS) of the FSW joints. [3].

The weld joint of AA2014-T6 was effectively created. The density distribution of the course second phase particle A12Cu has reduced, and the tensile properties have improved, caused by the increase in the number of sub-grains in the SZ due to optimal heat input. For UTS, the maximum efficiency is 83% and for % elongation, it is 5.8% [4].

FSW of 6061-T6 combining the Taguchi-based Grey relational analysis approach using 1400 rpm, with a traverse speed of 37.5 mm/min and a taper threaded pin produced a maximum hardness of 71.6 HR and a tensile strength of 283 MPa. Tensile strength decreased to 217 MPa and hardness to 54.23 HR when the speed was 47.5 mm/min and 900 rpm. An increase in the rotating speed causes the welding temperature to rise, which in turn achieves the maximum hardness and tensile strength [5].

Weld joints of AA7075 and AA5052 alloy produced by the FSW technique have greater microhardness and tensile strength, making them suitable for use in plate joining, high tool rotating speed provide superior results [6].

Tool tilt angle is the most crucial element affecting weld strength of AA7075 alloy .The weld strength decreases with increasing tool travel rates. The microhardness was reduced when the tool was tilted. Faster welding rates result in reduced pressure, which may affect the formation of flaws [7].

The FSW of AA6063-T6 and AA 7075-T5 with the tool turning at 1000 revolutions per minute, 2.5 millimeters per second, and 8.5 N the Vickers hardness at the welded zone reaches a maximum of 94.36 VHN, well exceeding any other hardness value [8].

FSW AA2014 and AA6063 reveal superior mechanical strength.High tool traverse rates increase plasticization, whereas high tool rotating speeds increase heat production. Increasing the traverse or rotational speed causes the axial force to grow. A larger axial increases the elongation and microhardness [9].

Spinning too quickly during welding of AA6082-T6 aluminum alloy will alter the stirring volume's plastic strain and thermal history. Superior weld quality is achieved as a result of the stirring zone's elevated temperature and enhanced plastic deformation [10].

Alloys AA 5052 and AA 6061 have shown great weldability and performance qualities using threaded pin. Sample B scored better in areas related to ductility, but Sample A showed approximately similar ultimate strength [11].

FSW of AA2024-T3 and AA7075-T73 such as traverse speed (898 mm/min), pin geometry (cylinder threaded), and rotating speed (898 rpm) produced ideal weldment .The welding speed, the rotation speed, and the pin shape each contributed 66.05%, 5.21%, and 15.68% to the final product. An increase in welding speed results in an increase in the tensile strength of the welded joints. SZ has a greater microhardness than TMAZ and HAZ [12].

A maximum of 750/73 rpm/(mm/min) and a minimum of 750/150 rpm/(mm/min) are the welding settings of AA2024 T351 that produce the least heat, respectively.The temperature and plastic deformation levels determine the microhardness distribution and allocation profile, which is greatest beneath the tool shoulder and around the pin [13].

FSW of AA 2014-T6 alloy using cylindrical pin incorporates both numerical and analytical .The material flow rate is proportional to the square of the diameter of the shoulder and the diameter of the rotatable pin. Additionally, and material flow velocity within the weldment can be improved by increasing the pin tip diameter [14].

The FSW technique of Al 7075-T73 improved the mechanical characteristics .The microhardness in the (SZ) was higher than in (HAZ)/(TMAZ), the tensile strength that was increased by one-line peening 1UP was 14%. The tensile strength was only 11% higher with two lines peening 2UP compared to the samples that were not welded [15].

As the welding speed is increased, the grain size in both AA6061 and AA7075 alloys falls substantially, indicating dynamic recrystallization.The microhardness as compared to base metals, decreases .The cracked surface of the joints, created by a reduction in heat input, showed shallower dimples [16].

Dissimilar AA 6061 and AA8011 alloys were fused and when using AA 8011 on the advancing side and a tool offset of 1 mm towards it, the maximum tensile strength is 77.88 MPa. Elongation percentages are consistently greater. There is a maximum elongation of 21.96% . The highest hardness value that was achieved is 89.4 HV. Tools should be offset by no more than 2 mm for improved tensile characteristics and less flaws [17].

The tool torque, traverse force, and axial force all rise when the tool tilt angle is 2.5° , and the peak temperature at the tool/workpiece contact is greater when the tool tilt angle is 0° by FSW of AA 6061-T6 and AA 8011-h14 alloys [18].

FSW joining of 7075-T651 Al alloy sheets developed tunnel flaws at their roots leading to fracture development. The distribution of hardness in the weld zone was greatly impacted by the rotational and welding rates. Welded joint tensile strengths were 26–45% lower than base alloy values. Specimens connected by rapid rotation had lower residual stresses [19].

An impressive 87% joint efficiency was achieved with FSW of 7075-T6 and 5052-H34 alloys .The microstructures revealed the mixed-alloy structures. The specimens' fracture surfaces after the fatigue test showed the creation of steps towards the conclusion of the

propagation stage. With a load of up to 65% of the tension fracture load, the joint may safely operate [20].

REFERENCES

[1] Leon Joseph Leon S, Vijayarangan J, Stephen Leon J, et al. Investigation of Mechanical Properties of Aluminium 6061 Alloy Friction Stir Welding [Internet]. Int. J. Students' Res. Technol. Manag. Available from: http://www.giapjournals.org/ijsrtm.html140.

[2] Shaik B, Harinath Gowd G, Durga Prasad B. Experimental and parametric studies with friction stir welding on aluminium alloys. Mater Today Proc. Elsevier Ltd; 2019. p. 372–379.

[3] Ahmed KE, Nagesh BM, Raju BS, et al. Studies on the effect of welding parameters for friction stir welded AA6082 reinforced with Aluminium Oxide. Mater Today Proc. Elsevier Ltd; 2020. p. 108–119.

[4] Rajendran C, Srinivasan K, Balasubramanian V, et al. Mechanical properties and microstructural characteristics of friction stir welded AA2014-T6 aluminium alloy joints. J Mech Behav Mater. 2020;28:169–185.

[5] Asmare A, Al-Sabur R, Messele E. Experimental investigation of friction stir welding on 6061-t6 aluminum alloy using taguchi-based gra. Metals (Basel). 2020;10:1–21.

[6] Ramesha K, Sudersanan PD, Santhosh N, et al. Design and optimization of the process parameters for friction stir welding of dissimilar aluminium alloys. Eng Appl Sci Res. 2021;48:257–267.

[7] Mahesha CR, Suprabha R, Kumar NM, et al. Effect of Friction Stir Welding on the Mechanical and Microstructural Behaviour of AA7075 Aluminium Alloy. Adv Mater Sci Eng. 2022;2022.

[8] Varunraj S, Ruban M. Investigation of the microstructure and mechanical properties of AA6063 and AA7075 dissimilar aluminium alloys by friction stir welding process. Mater Today Proc. 2022;68:1654–1657.

[9] Ramamurthy M, Balasubramanian P, Senthilkumar N, et al. Influence of process parameters on the microstructure and mechanical properties of friction stir welds of AA2014 and AA6063 aluminium alloys using response surface methodology. Mater Res Express. 2022;9.

[10] Salih OS, Ou H, Sun W. Heat generation, plastic deformation and residual stresses in friction stir welding of aluminium alloy. Int J Mech Sci. 2023;238.

[11] RajKumar V, VenkateshKannan M, Sadeesh P, et al. Studies on effect of tool design and welding parameters on the friction stir welding of dissimilar aluminium alloys AA 5052 - AA 6061. Procedia Eng [Internet]. 2014;75:93–97. Available from: http://dx.doi.org/10.1016/j.proeng.2013.11.019.

[12] Al-kubaisy MM. Optimization of Friction Stir Welding Process Parameters of Dissimilar AA2024-T3 T3 and AA7075-T73 Aluminum Alloys Alloy by Using Taguchi Method. Al-Khwarizmi Eng J. 2016;12:100–109.

[13] Miodrag Milčić 3) Igor Radisavljević 1) Zijah Burzić D Ljubica Radović) Tomaž Vuherer 2) Dragan Milčić 3) Nataša Zdravković 3) The Influence of Welding Speed on Mechanical Properties of Friction Stir Welded Joints of AA2024 T351 Aluminum Alloy, Scientific Technical Review, 2020, Vol.70, No.2,pp.53-57

[14] Ugender S, Kumar A, Reddy AS. Experimental Investigation of Tool Geometry on Mechanical Properties of Friction Stir Welding of AA 2014 Aluminium Alloy. Procedia Mater Sci. 2014;5:824–831.

[15] Jebur AA, Amin S, Mahmood I. The Influence of Ultrasonic Impact Peening on the Mechanical Properties of Similar Friction Stir Welded Joints of AA 7075-T73. Eng Technol J. 2021;39:1345–1351.

[16] Guo JF, Chen HC, Sun CN, et al. Friction stir welding of dissimilar materials between AA6061 and AA7075 Al alloys effects of process parameters. Mater Des. 2014;56:185–192.

[17] Khanna N, Sharma P, Bharati M, et al. Friction stir welding of dissimilar aluminium alloys AA 6061-T6 and AA 8011-h14: a novel study. J Brazilian Soc Mech Sci Eng [Internet]. 2020;42. Available from: https://doi.org/10.1007/s40430-019-2090-3.

[18] Zhai M, Wu CS, Su H. Influence of tool tilt angle on heat transfer and material flow in friction stir welding. J Manuf Process [Internet]. 2020;59:98–112. Available from: https://doi.org/10.1016/j.jmapro.2020.09.038.

[19] Çevik B, Ozçatalbaş Y, Gülenç B. Rührreibschweißen einer 7075-T651-Aluminiumlegierung. Prakt Metallogr Metallogr. 2016;53:6–23.

[20] Zainulabdeen, Ahmed A. Abbass, Muna K. Ataiwi, Ali H. Khanna, Sanjeev K. Jashti, Bharat Widener Investigation of Fatigue Behavior and Fractography of Dissimilar Friction Stir Welded Joints of Aluminum Alloys 7075-T6 and 5052-H34, International Journal of Materials Science and Engineering, 2014

Mechanical engineering education

11th International Scientific Conference
IRMES 2025
Research and Development of
Mechanical Elements and Systems
June 19 – 21, 2025; Vrnjačka Banja, Serbia

Original scientific paper DOI: 10.46793/IRMES25.167B

CORE COMPETENCIES FOR MECHANICAL ENGINEERS IN MACHINE DESIGN AND PRODUCT DEVELOPMENT OVER THE NEXT DECADE

Milan BANIĆ[1]
Aleksandar MILTENOVIĆ[2]
Dragan MILČIĆ[3]

[1]Faculty of Mechanical Engineering, University of Niš, 18000 Nis, Serbia, RS; milan.banic@masfak.ni.ac.rs;
ORCID iD: 0000-0001-8684-042X
[2]Faculty of Mechanical Engineering, University of Niš, 18000 Nis, Serbia, RS; aleksandar.miltenovic@masfak.ni.ac.rs;
ORCID iD: 0000-0002-1453-2548
[3]Faculty of Mechanical Engineering, University of Niš, 18000 Nis, Serbia, RS; dragan.milcic@masfak.ni.ac.rs;
ORCID iD: 0000-0002-3936-7462

Abstract: *Mechanical engineers in the field of machine design and product development are facing a rapidly changing environment. Over the next decade, emerging technologies such as artificial intelligence (AI), additive manufacturing, and the pursuit of sustainability will significantly influence the required skill sets. This paper outlines the technical, digital, and soft competencies that are considered essential for future mechanical engineers from both academic and industry perspectives.*

Keywords: *additive manufacturing; Selective Laser Melting (SLM); bonded joint; maraging steel; mechanical properties*

1. INTRODUCTION

Mechanical engineering is transforming, improving, and adapting to new knowledge, and history shows that it has been a driving force of change and transformation in every known industrial revolution. The core importance of mechanical engineering in Industry 4.0 lies in the fact that it serves as the design platform for various physical assets – such as robots, conveyor belts, actuators, mechanisms, devices, and machines – which form the foundation of production systems in factories and various companies. At the outset, we must ask ourselves: Do we have a sufficient supply of strong engineering skills needed for the next decade? Are we ready for the fourth industrial revolution, "Made Smarter"? Are we prepared to create new innovation jobs that will replace those being displaced? Recent strategic reports emphasize the urgency of reforming engineering education and talent pipelines to meet future industry needs ([1], [2]).

The field of machine design and product development is undergoing a profound transformation, driven by the accelerated pace of technological advancement and global challenges. Over the next decade, mechanical engineers will be expected to navigate an increasingly complex environment shaped by emerging technologies such as artificial intelligence (AI), additive manufacturing, and the growing imperative for sustainability. These shifts demand a redefinition of the skills and competencies required for success. This paper aims to identify the core competencies mechanical engineers should acquire between 2025 and 2035 to remain relevant and effective in their roles. It categorizes these competencies into three key areas: technical, digital, and soft skills. Drawing from academic literature and industry insights, the paper explores how engineering education and professional development must evolve to meet future demands. Emphasis is placed on integrating sustainability into design practices, leveraging digital tools for innovation, and fostering human-centric abilities such as collaboration and adaptability. In doing so, this work provides a comprehensive overview of the multidimensional skillset mechanical engineers will need to contribute meaningfully to the design and development of next-generation products and systems. As an example, the results of a student project carried out during the final years of study at the Faculty of Mechanical Engineering in Niš, in the study program Mechanical Constructions, Development, and Engineering, are presented. The project focused on the development of devices intended for industrial application.

2. MECHANICAL ENGINEERS EDUCATION

Mass customization is a new form of production in Industry 4.0 that involves designing production systems in such a way that they can be reconfigured in the face of changes in production volumes and product design. This

involves the design and development of specialized, flexible and reconfigurable machines. Mechanical Engineering has functional interactions with some of the disruptive technologies of Industry 4.0. Figure 1 shows the relationship of mechanics to just six of these disruptive technologies.

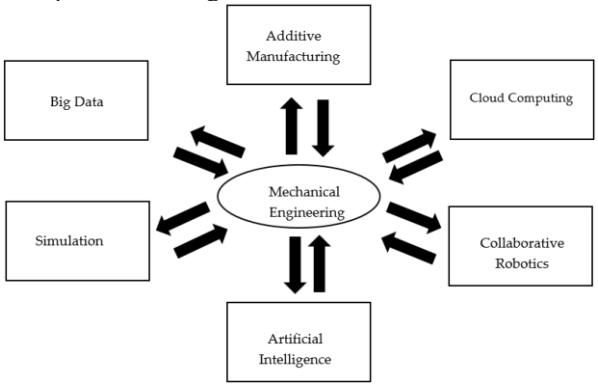

Fig. 1. Relations between Mechanical Engineering and the technologies of the new industrial revolution. Improved and adapted from [3].

As illustrated in Figure 1, the relationship between mechanical engineering and disruptive technologies is bidirectional. Mechanical engineering provides essential methods, machines, and systems that enable these technologies, while in return, it gains theoretical knowledge, experience, and technological support. For instance, artificial intelligence offers algorithms for solving complex multiphysics problems, while mechanics contributes to the development of hardware systems capable of running these algorithms. A similar exchange occurs with Cloud Computing, which supports design and manufacturing (CAD/CAM/CAE), while mechanics supplies the hardware infrastructure. Additive manufacturing benefits from mechanical engineering in testing mechanical properties of 3D-printed prototypes, just as collaborative robotics relies on mechanical models for movement and interaction analysis. Likewise, renewable energy technologies and materials science interact closely with mechanics to support innovation, development, and application in modern engineering systems.

Mechanical engineering plays a crucial role in Industry 4.0. It is interconnected with various disruptive technologies and other fields of knowledge such as computing and electronics, as well as numerous specialized application areas. Due to this strong connection between mechanical engineering and the Fourth Industrial Revolution, the education of mechanical engineers has become a priority.

Key aspects of modern mechanical engineers education include the introduction of innovative teaching methods, the automation of educational processes, the integration of Industry 4.0 technologies into instruction, and the development of engineering competencies.

Traditionally, mechanical engineers education has been teacher-centered, which has made it difficult to implement new didactic approaches. To overcome this, educators must shift toward student-centered learning. Competency -based education is one of the effective approaches - it emphasizes learning outcomes, promotes assessment methods focused on student progress, and encourages the application of knowledge as well as the development of interpersonal skills.

Technical, digital, and soft competencies are considered essential for future mechanical engineers from both academic and industry perspectives.

3. TECHNICAL SKILLS

Engineers must be proficient in designing products with sustainability in mind – considering energy efficiency, low-carbon technologies, recyclability, and whole life-cycle impact. Climate change and global initiatives (e.g. net-zero goals and UN Sustainable Development Goals) are driving the need to embed sustainable, low-carbon solutions into every aspect of engineering practice. This includes skills like life-cycle assessment, design for reuse/recycling, and knowledge of how engineering decisions impact ecological and social systems ([4], [5]). Overarching "green" competencies now encompass whole-lifecycle design thinking, regenerative design, and the ability to challenge unsustainable practices – all critical for engineers to deliver climate-resilient solutions ([6]).

Mastery of new materials (such as composites, smart materials, and nano-engineered materials) and modern manufacturing processes is increasingly important. In particular, additive manufacturing (AM) has become a pivotal technology for rapid prototyping and production. The rise of 3D printing requires engineers to learn Design for Additive Manufacturing (DfAM) principles. Recent studies note that the drive for faster prototyping "has necessitated the deployment of AM technologies," with 3D modeling, scanning, and printing enabling the design of functional components at industrial scale ([7-9]).

Mechanical design curricula are beginning to integrate AM: for example, courses on mechanical component design now include topics like 4D/5D printing and applications of smart materials. Future mechanical engineers should be capable of selecting appropriate advanced materials and leveraging additive processes to innovate new product designs.

The ability to approach engineering problems with a holistic systems perspective is a core technical competency for modern machine designers. As machines and products grow more complex and interdisciplinary, engineers must understand how components and subsystems interact within a larger system. This systems thinking skill – recognizing interconnections and the broader context of one's design – is increasingly critical in addressing both digital complexity and green transitions. Industry trends show strong demand for engineers who can extend product lifecycles, improve overall system efficiency, and anticipate future problems or opportunities. In practice, this means mechanical engineers need a firm grasp of multidisciplinary fundamentals (mechanical, electrical, control, etc.) and the capability to solve complex, open-ended problems. Analytical reasoning, engineering judgment, and critical thinking are all part of this competency, and they remain "core aspects of an engineer's role" even as routine technical tasks become automated.

Machine design engineers are increasingly expected to integrate mechanical designs with electronics, sensors, and control systems. Competence in mechatronics – combining mechanical engineering with electrical and computer engineering – is therefore vital. For instance, mechanical engineers often design the physical structure of robotic systems and must understand actuators, sensor integration, and control principles. They play a pivotal role in robotics development by designing hardware that works in concert with software (AI algorithms, control logic) and by maintaining these automated systems. Over the next decade, as industries embrace automation and Industry 4.0, mechanical engineers should be comfortable working with industrial robotics, autonomous machines, and advanced automation equipment. This includes understanding PLCs or microcontrollers, knowing how to design for manufacturability in automated production, and applying robotics and control theory in product development. In short, the traditional boundaries of machine design are widening – tomorrow's mechanical engineer will often act as a system integrator who can marry mechanical components with digital intelligence.

A strong grounding in classical mechanical engineering principles (mechanics, thermodynamics, fluid dynamics, etc.) remains essential. However, applying these fundamentals in innovative ways will set future engineers apart. For example, design skills now frequently intersect with emerging considerations like human-centered design, safety engineering, and even ethics and regulatory knowledge. Product development engineers will need to incorporate new knowledge areas – from human factors to circular economy principles – into the design process. They should be adept at design optimization (e.g. using topology optimization or lightweighting techniques) and comfortable iterating designs through rapid prototyping. Moreover, as new fields (biomedical devices, renewable energy systems, etc.) open up, mechanical engineers should be ready to extend their fundamental knowledge to novel applications. In summary, technical excellence in core engineering science, combined with creativity and an innovative mindset, will empower mechanical engineers to tackle the complex design challenges of the next decade.

4. DIGITAL SKILLS

Engineers in product development must cultivate literacy in artificial intelligence and machine learning tools. AI is increasingly used to automate routine tasks, optimize designs, and improve quality control in mechanical engineering. When applied correctly, AI can analyze large data sets (from simulations, sensors, or field performance) and suggest design improvements, allowing engineers to focus on more complex creative tasks. For example, generative design software uses AI algorithms to produce optimal component geometries under given constraints, and machine learning can predict equipment failures (predictive maintenance) from sensor data. While mechanical engineers need not become AI researchers, they should be comfortable working with data and leveraging AI-driven tools in their workflow. This means developing a basic understanding of data analytics, training models (or collaborating with data scientists), and validating AI recommendations with engineering judgment. As one industry expert noted, AI can "free engineers from menial work" and even open the door to engineering innovations like smart autonomous systems when used appropriately. Embracing data-driven decision making and AI-assisted design will be increasingly critical for competitiveness.

The next generation of mechanical engineers must be adept at using advanced simulation software and digital twins to design and test products virtually [10]. Simulation tools (FEA for stress analysis, CFD for fluid flow, multiphysics solvers, etc.) have long been part of the engineer's toolkit, but now high-fidelity modeling is taken further with digital twin technology. A digital twin is a data-driven virtual replica of a physical system, which enables engineers to simulate real-world performance and iteratively optimize designs in a risk-free environment. Mastery of such tools allows design teams to identify problems and refine solutions before building physical prototypes, dramatically reducing development time and cost. By 2030, it's expected that real-time data integration with digital models (e.g. feeding sensor data from products in the field back into simulations) will become standard, so mechanical engineers should understand how to set up, interpret, and iterate with these virtual models. This skill set aligns with lean and sustainable engineering goals, since virtual testing minimizes material waste and trial-and-error in the physical world. In practice, future mechanical designers will routinely use simulation-driven design and digital twins to validate performance, test durability, and ensure reliability of their machines under a variety of conditions.

Proficiency in the digital design and manufacturing "toolchain" is a fundamental requirement. This includes traditional Computer-Aided Design (CAD) for 3D modeling, Computer-Aided Engineering (CAE) for analysis, and Computer-Aided Manufacturing (CAM) for translating designs to fabrication – all increasingly integrated in modern workflows. Academic experts emphasize that mechanical engineering students must learn to handle a range of software tools (CAD, CAM, CAE, CAPP, CIM, etc.) and understand digital manufacturing processes. In coming years, CAD software augmented by AI (e.g. autonomous CAD assistants or physics-informed design recommendations) will help engineers explore more design options in less time. Likewise, CAM is evolving with additive manufacturing and robotics in mind, so engineers should grasp how to directly generate toolpaths for 3D printers or CNC machines from their designs. Generative design, which automatically produces optimized shapes based on input requirements, is another breakthrough digital skill – it pushes engineers to become curators and decision-makers, guiding the software and evaluating results. Ultimately, a mechanical engineer should be fluent in using modern digital platforms from concept through production. The ability to quickly learn new engineering software and adapt to updated digital workflows will remain crucial, given the continuous advancements in design technology.

As mechanical engineering becomes more digitized, the line between engineering and programming blurs.

Engineers who can script and program will have an edge in automating tasks, customizing simulations, or analyzing data. Core languages might include Python or MATLAB for data analysis, and knowledge of how to work with engineering APIs or mechatronic controllers (e.g. writing basic code for microcontrollers/PLC in automated systems). In academic literature, "digital and computational skills" are listed among the top competencies for the Engineer 4.0 era. Even if coding isn't a mechanical engineer's primary job, computational thinking – the ability to algorithmically break down problems and use computers to solve them – is increasingly important. For instance, writing a script to optimize a design parameter sweep, or developing a quick program to process sensor data from a prototype, can greatly enhance productivity and innovation. Moreover, basic familiarity with data structures and software logic helps engineers collaborate with software developers and AI specialists in interdisciplinary teams. In sum, future mechanical engineers should treat programming as a powerful tool in their arsenal, enabling them to extend what traditional CAD/CAE packages offer and engage with the "digital thread" of product development.

The ongoing digitalization of manufacturing and products means mechanical engineers need literacy in Industry 4.0 technologies and the Internet of Things (IoT). Smart factories and connected products produce vast amounts of data and rely on networks of sensors and devices. Competence in this area might include understanding industrial automation protocols, IoT sensor integration, and data security basics for connected equipment. For product development, an engineer should know how to design mechanical components that incorporate IoT sensors or connectivity (for example, designing a machine with embedded condition-monitoring sensors). They should also appreciate how their designs fit into a larger digital ecosystem – such as how maintenance data from a machine will be collected and analyzed, or how a device might interface with cloud services. From the academic perspective, virtual collaboration and working with cyber-physical systems are part of the Engineer 4.0 skill set. This implies engineers must be comfortable working in digitally connected environments (e.g. using collaborative CAD platforms, or remote monitoring tools). Additionally, knowledge of cyber-physical integration (where mechanical systems are tightly coupled with software/control networks) will be increasingly valuable. In practice, a mechanical engineer might be expected to collaborate with IT specialists to ensure that a new machine design is compatible with a factory's digital infrastructure. Embracing these digital domain skills ensures that mechanical engineers remain relevant and effective as the industry undergoes digital transformation.

5. SOFT SKILLS

Modern product development is a team sport, often involving diverse specialists (electrical engineers, software developers, materials scientists, business strategists, etc.). Mechanical engineers must excel at working in multidisciplinary teams and communicating across disciplines. This involves not only teamwork skills but the ability to appreciate other fields' perspectives – a competency often termed interdisciplinary aptitude. Research indicates these skills will become even more crucial as many breakthroughs occur at the boundaries between disciplines. Engineers are now expected to "widen their skillsets" beyond the traditional silo of mechanical engineering and understand how different technologies intersect. Practically, this means being able to collaborate with, say, AI experts or sustainability consultants on a project, and integrating their insights into the design. Strong interpersonal skills, respect for diverse expertise, and an openness to new ideas all contribute to effective collaboration. By developing these skills, mechanical engineers can better lead and contribute to complex projects where mechanical, electrical, and software components must work in harmony.

"The trend in science is toward more interdisciplinary work, and more and more the real innovation comes from people with different backgrounds working together" [11].

Collaboration across engineering domains boosts innovation and problem-solving. Multidisciplinary teams - those spanning mechanical, electrical, computer science, materials science, and beyond - tend to perform better and generate more impactful ideas than homogenous groups. Academic studies confirm that boundary-crossing collaborations, such as in mechatronics or aerospace projects, accelerate breakthroughs by combining diverse expertise. The practical impact is clear: mechanical engineers who are comfortable coordinating with specialists in software, sensors, business strategy, and ecology will be more effective in delivering integrated, cutting-edge solutions [12].

The ability to convey technical information clearly and to listen and adapt is a defining soft skill for engineers. Mechanical engineers in design roles often need to explain complex ideas to non-engineers (management, clients, or other stakeholders) and justify design decisions. Effective communication skills – both written and verbal – are therefore essential. This includes technical writing (for reports, specifications) and presentation skills. Moreover, with the rise of global and remote teams, engineers must navigate communication across cultural and language barriers. An ASME report observes that engineers today are expected to demonstrate emotional intelligence in virtual collaborations and to handle asynchronous communication adeptly. In practice, that could mean being aware of tone in emails or understanding team dynamics in a multicultural project meeting. Emotional intelligence also helps engineers empathize with end-users (informing better product design) and resolve conflicts within teams. By honing communication and EQ, mechanical engineers ensure their technical ideas gain traction and that they can rally support for innovative solutions.

Given the pace of technological change, a growth mindset and adaptability are indispensable. The most valuable engineers will be those who can continuously update their skills and quickly learn new tools or methods. Over the next decade, it's expected that many core engineering tasks and knowledge areas will evolve – for example, new AI-driven design techniques, new manufacturing processes, or new regulatory standards might emerge.

Mechanical engineers should cultivate the habit of lifelong learning, seeking ongoing education and training (something noted as crucial in the context of Continuing Engineering Education for a sustainable future). Adaptability also means being open to change and resilient in the face of unforeseen challenges. Projects may pivot due to market needs or global events, and engineers must adjust designs or strategies accordingly. Studies emphasize that an adaptive mindset is increasingly valued in engineering roles. From an academic viewpoint, this translates to instilling students with meta-skills like learning how to learn, critical reflection, and comfort with ambiguity. Employers, too, recognize this trait – many now prioritize hiring engineers who demonstrate agility and the capacity to acquire new competencies as needed. In summary, the ability to adapt, reskill, and stay curious will define an engineer's success in the 2025–2035 timeframe.

While engineering is grounded in analysis, the coming era puts a premium on creativity. Complex global challenges and rapidly changing markets require innovative solutions – and mechanical engineers are front-line problem solvers in this regard. Creative problem-solving combines imagination with technical knowledge to generate novel designs or improvements. It is cited as an "essential component of ideation" in engineering design. In academic literature, creativity is often linked with innovation and seen as a uniquely human skill that gains importance as AI handles more rote tasks. For mechanical engineers, this competence might involve using design thinking methodologies (empathize, define, ideate, prototype, test) to ensure products truly meet user needs in new ways. It also means being comfortable exploring unconventional ideas, tolerating failure in iterative design, and thinking outside the box of established solutions. Employers value engineers who can not only solve problems but find problems – identifying latent needs or inefficiencies that others overlooked. Fostering a creative mindset, alongside strong analytical abilities, helps mechanical engineers drive innovation in machine design (for instance, inventing a new mechanism or reinventing a product to be more eco-friendly and user-friendly than anything before). As routine design tasks become automated, the engineer's creative and integrative thinking becomes even more of a differentiator.

As mechanical engineers progress in their careers, many will take on roles leading projects or teams. Even for those in purely technical roles, project management skills are invaluable for delivering complex development projects on time and within budget. Key elements include planning and organizing work, risk management, and coordinating multidisciplinary efforts. Mechanical engineers should understand the principles of project management (e.g. scheduling, resource allocation, using tools like Gantt charts or Agile methods in development cycles). In the context of emerging challenges, leadership also means guiding teams through change – for instance, championing the adoption of a new sustainable design practice or a new digital tool in the organization. Studies in engineering education have called for greater emphasis on leadership, teamwork, and even entrepreneurial mindset as part of an engineer's training. Moreover, with industry transformations, mechanical engineers increasingly find themselves managing not just technical tasks but also people and processes. Strong leadership skills involve motivating team members, making informed decisions, and communicating a clear vision of the project goals. Soft-skill development in this area (often gained through experience in team projects or internships) can greatly enhance an engineer's effectiveness. As the Institution of Mechanical Engineers notes, pairing technical competencies with management and communication skills will ensure engineers are "fit-for-purpose" to tackle global challenges. Engineers who can lead cross-functional teams – while balancing technical details with big-picture objectives – will be critical in an era of fast-paced innovation and complex projects.

6. EXAMPLES OF STUDENT PROJECTS AT FACULTY OF MECHANICAL ENGINEERING NIŠ

During the later years of their studies at the Faculty of Mechanical Engineering in Niš, in the field of Mechanical Design, students had student projects under professor and assistants supervision on the development of devices intended for use in industry.

6.1 Non-contact laser wheel profile measuring device

For the needs of the railway industry, a device was developed to measure the qR parameter, which characterizes the level of wheel wear in railway vehicles. In Serbia, primitive measuring devices are currently used for this purpose. Similar devices do exist on the market, and students reviewed competing solutions whose prices range from €6,000 to €20,000. After analyzing the market, the students developed a concept based on which a suitable laser profilometer was selected, and they designed a setup that enables field measurement of railway wheels using this profilometer.

By laser scanning is obtained points that form a line. These data points are then processed to generate accurate measurements of critical parameters such as rim height, thickness, and sharpness. This method not only eliminates the risk of human error but also offers significantly higher accuracy and repeatability. By automating the process, laser devices can provide real-time data that allow for more efficient and reliable assessments of wheel condition, ensuring the safety and longevity of the vehicle. Developed device was tested in real life scenarios, wheel rim was scanned and wheel profile parameters were obtained with it (see Figure 2).

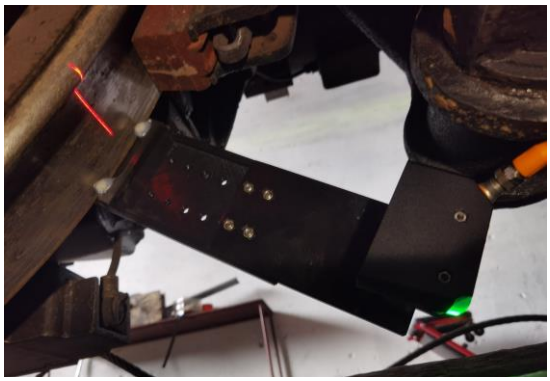

Fig. 2. Wheel rim profile scanning [13]

In order to complete this project, the students had to learn how the scanning process is performed and what the key parameters are for capturing the profiles of railway vehicle wheels. They designed a setup for the profilometer, including a stand and magnetic mounting, applying their knowledge of 3D printing and prototyping in the process. Based on the data obtained through scanning, the students had to develop a software environment to provide the user with a clear insight into the results, as shown in Figure 3. For this purpose, they needed knowledge in software engineering.

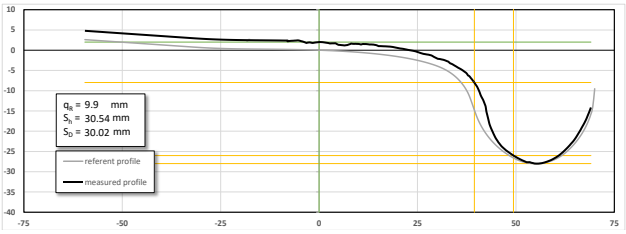

Fig. 3. Example of measured wheel profile [13]

Device can be used in remote locations and the students had to learn how to determine the required battery capacity. Additionally, since the device is IoT-based, they needed knowledge in this field to make laser scanning easy to use and to eliminate unnecessary cables.

Fig. 4. Laser measuring device housed in its portable suitcase for wheel rim inspection [13]

Also, in the end, they needed to design a case that would house the laser profilometer, battery, IoT device, screen, an additional stand and additional parts, and appropriate buttons and ports, making the device easy to transport and use, as shown in Figure 4. During the development process, the students frequently tested the device in both laboratory and real-world environments to confirm that their ideas were valid and that the device could be used effectively. On the end they created device with the price of basic components of around €2.000.

6.2. Autonomous robot for train undercarriage visual inspection

At the Faculty of Mechanical Engineering Niš was carried out project for design of autonomous robot for train undercarriage visual inspection. Such a device does not exist on the market, and researchers at the faculty have designed a completely new device that is quite complex and required knowledge of state-of-the-art technologies. Parts of the work within the project were assigned to students as part of several student projects, under the supervision of professors and teaching assistants. In this project were integrated subjects like CAD, lightweight design, DfMA, Internet of Things (IoT), cloud computing, artificial intelligence (AI), machine learning (ML).

The first step was the creation of hardware, which primarily involved the application of CAD knowledge according to the concept defined by the professors in collaboration with lead users from the railway industry. The concept definition was defined as a basic concept, such as the number of wheels, device mass, methods of device control, user needs, etc. According to basic concept and further project work, students under the supervision of professors and assistants made first CAD model and defined motor size, battery capacity and robot design. Based on their technical drawings, the first prototype was produced and students showed their knowledge in CAD and DfMA. Some parts were made on 3D printers where student show knowledge in additive materials. Students assembled first prototype as it is shown in Figure 5.

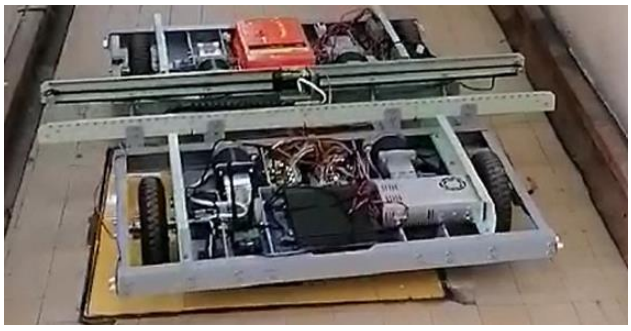

Fig. 5. ATUVIS prototype testing in Laboratory at the Faculty of Mechanical Engineering Niš [14]

Mass of the prototype device was 30% over the target mass defined on the beginning. Here students need to use knowledge in FEM and lightweight design to decrease the mass and the decrease mass for 20% which was still over the target mass.

Students made numerous experiments on the real track and found out conclusions for the changies in design. Additionally, they created a substantial dataset of images used in machine vision, which is crucial for producing the final product. Based on the dataset, a student project was

defined for labelling images of undercarriage components for dataset creation for AI defect recognition software. Students learned machine vision and create software architecture that is used for this device. During visual inspection, images are made of vehicle undercarriage, after this with use of cloud computing, this images were send to the cloud that is important for machine vision and gives to the final product new value.

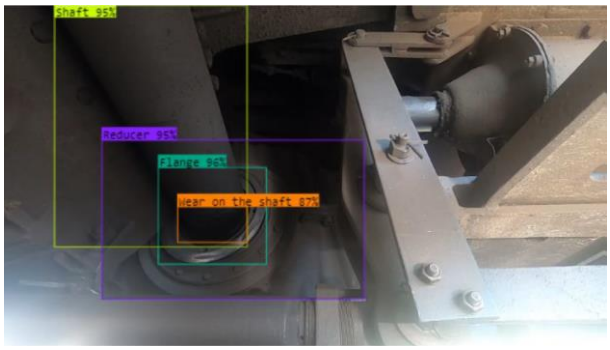

Fig. 6. Results of recognition based on machine vision used in ATUVIS

7. CONCLUSION

The essential competencies of mechanical engineers and the emerging trends in machine design and product development are derived from various academic and professional sources, including engineering education research, industry reports, and expert commentary. These sources highlight how the roles of mechanical engineers are evolving under the influence of artificial intelligence (AI), advanced manufacturing, sustainability, and Industry 4.0. Notably, initiatives by ASME and the academic Vision 2030 program emphasize the need to combine strong technical foundations with new digital skills and professional competencies.

Particular emphasis should be placed on the growing importance of systems thinking, global responsibility, and soft skills alongside technical expertise.

In the paper were given two examples of student projects were student show their knowledge and the needs of further knowledge.

A future-ready mechanical engineer in the field of design must be a versatile innovator-technically competent, digitally proficient, and equipped with human-centric skills necessary for collaboration, adaptability, and leadership in addressing the engineering challenges of the coming decade.

ACKNOWLEDGMENT

This research was financially supported by the Ministry of Science, Technological Development and Innovation of the Republic of Serbia (Contract No. 451-03-136/2025-03/200109)

REFERENCES

[1] The Royal Academy of Engineering. *Engineering Skills for the Future: The 2013 Perkins Review Revisited*. London, 2019. Available: https://www.raeng.org.uk/perkins2019

[2] ASME. *Vision 2030: Creating the Future of Mechanical Engineering Education*. Available: https://www.asme.org/asme-programs/students-and-faculty/engineering-education/strategy-vision-2030

[3] Zhang, C., Yang, J.: Summary of Mechanical Engineering in New Era. *A History of Mechanical Engineering*, 1st ed.; Springer: Singapore, pp. 351–387. 2020.

[4] Gallego-Schmid, A., Mendoza, J. M. F., Jeswani H. K., Azapagic, A.: *Life cycle environmental impacts of vacuum cleaners and the effects of European regulation.* Science of The Total Environment, 559, pp. 192–203. 2016. https://doi.org/10.1016/j.scitotenv.2016.03.149

[5] Navarro, I. J., Yepes, V., Martí, J. V.: *Life Cycle Cost Assessment of Preventive Strategies Applied to Prestressed Concrete Bridges Exposed to Chlorides*. Sustainability, 10(3), 845. 2018. https://doi.org/10.3390/su10030845

[6] Saidani, M., Yannou, B., Leroy, Y., Cluzel, F., Kendall, A.: *A taxonomy of circular economy indicators*. Journal of Cleaner Production, 2019, 207, pp.542-559. 2019. https://doi.org/10.1016/j.jclepro.2018.10.014

[7] Wiberg, A., Persson, J., Ölvander, J.: *Design for additive manufacturing – A review of available design methods and software*. Rapid Prototyping Journal, 25(6), 1080–1094. 2019. https://doi.org/10.1108/RPJ-10-2018-0262

[8] Gao, W., Zhang, Y., Ramanujan, D., Ramani, K., et al.: *The status, challenges, and future of additive manufacturing in engineering*. Computer-Aided Design, 69, pp. 65-89. 2015. https://doi.org/10.1016/j.cad.2015.04.001

[9] Tang, Y., Zhao, Y. F.: *A survey of the design methods for additive manufacturing to improve functional performance*. Rapid Prototyping Journal, 22(3), 569–590. 2016. https://doi.org/10.1108/RPJ-03-2014-0021

[10] Tao, F., Zhang, H., Liu, A., Nee, A. Y. C.: Digital Twin in Industry: State-of-the-Art. *IEEE Transactions on Industrial Informatics*, 15(4), pp. 2405–2415. 2018. https://doi.org/10.1109/TII.2018.2873186

[11] ASME: Training the Future Engineering Workforce. https://www.asme.org/topics-resources/content/training-the-future-engineering-workforce (accessed on 14 June 2025)

[12] https://www.wired.com/2002/09/engineers-meet-for-mass-mind-meld/ (accessed on 14 June 2025)

[13]Rangelov, D., Miltenović, A., Stamenković, D., Stojanović, L., Perić, M., *Preventive maintenance in railway vehicles using new technologies*, Railcon 2024, pp. 121-124

[14] Simonović, M., Banić, M., Miltenović, A., Stamenković, D., Rajić, M., Perić, M., Rangelov, D., Tomić, M., Pavlović, V., *Autonomous robot for train undercarriage visual inspection*, Railcon 2022, pp. XI-XVIII

INDEX OF AUTHORS

A

ALIC, Daniela 151
ALSAMMARRAIE, Amir 159
ANTIĆ, Jovana 1, 113
ARANĐELOVIĆ, Jovan 155

B

BANIĆ, Milan XXIII, 27, 147, 167
BLAGOJECIĆ, Mirko 123
BOGOJEVIĆ, Nebojša 95
BOJANIĆ ŠEJAT, Mirjana 5
BRAČUN, Drago XXXV
BUKVIĆ, Milan 139
BUŠIĆ, Matija XXXV

C

CONCLI, Franco XIII
CUPAR, Andrej III

Č

ČAJEVIĆ, Vidak 65
ČUKIĆ, Stefan 139

Ć

ĆIRIĆ-KOSTIĆ, Snežana 95

D

DAMJANOVIĆ, Milanko 75
DANKO, Jan 113
DEDIĆ, Remzo 75
DEMMLER, Matthias 1
DESNICA, Eleonora 101
DIX, Martin 1
DOJČINOVIĆ, Marina 107

Đ

ĐOKIĆ, Radomir 89
ĐORĐEVIĆ, Luka 101
ĐORĐEVIĆ, Zorica 13
ĐURĐEV, Mića 101
ĐURIĆ, Aleksija XXXV, 65, 71, 119

E

ERIĆ OBUĆINA, Jelena 17

F

FISCHER, Szabolcs 147

G

GAJEVIĆ, Sandra 139
GUBELJAK, Nenad XXXIII

H

HEIDRICH, Jürgen 1
HÖHN, Bernd-Robert I

I

ILANKOVIĆ, Nikola 89
IMŠIROVIĆ, Mirza XXXV
IVANOVIĆ, Lozica 123

J

JOJIĆ, Tanasije 89
JOVANOVIĆ, Saša 13

K

KALJUN, Jasmin III
KANOVIĆ, Željko 5
KARIĆ, Marina 17
KATONA, Mirko 89
KLOBČAR, Damjan XXXV, 71, 119, 147
KNEŽEVIĆ, Ivan 5
KONJATIĆ, Pejo XXXIII
KOPŠE KALJUN, Klavdija III
KOSTIĆ, Nenad 83
KOSTIĆ, Sonja 13
KOZAK, Dražan XXXIII
KRSTIĆ, Vladislav 133

L

LANDUP, Dejan 101
LAZOVIĆ, Tatjana 107

Lj

LJUBOJEVIĆ, Pavle 107

M

MACCIONI, Lorenzo XIII
MADIĆ, Miloš 45
MAGDOLEN, Lubos 113
MAJSTOROVIĆ, Vidosav D. 51
MARJANOVIĆ, Nenad 83
MARJANOVIĆ, Vesna 83
MARKOVIĆ, Biljana 65, 71, 119
MARKOVIĆ, Kristina 33
MATEJIĆ, Miloš 123
MIHAJLOVIĆ, Goran 17
MILADINOVIĆ, Slavica 139
MILČIĆ, Dragan 27, 39, 119, 133, 167
MILČIĆ, Miodrag XXXV, 39, 119, 133, 147
MILESICH, Tomas 113
MILETIĆ, Ivan 123
MILOVANČEVIĆ, Miloš 23, 129
MILOVANOVIĆ, Vladimir XLIX
MILTENOVIĆ, Aleksandar XXIII, 151, 155, 167
MILJANOVIĆ, Mirjana 23, 129
MISKOVIĆ, Žarko 51
MIŠKOVIĆ, Žarko 1, 113
MITROVIĆ, Radivoje 51, 113
MRATINKOVIĆ, Natalija 39

N

NIKOLIĆ, Aleksandar 95

NIKOLIĆ, Danijela	13
NOJNER, Vojkan	27
NOVAKOVIĆ, Borivoj	101
P	
PALINKAŠ, Ivan	101
PAVLOVIĆ, Saša	151
PAVLOVIĆ, Vukašin	XXIII
PEJČIĆ, Danilo	1, 113
PERIĆ, Marko	XXIII, 33, 39, 151, 155
PEROVIĆ, Anđela	123
PETKOVIĆ, Dušan	45
PETROVIĆ, Nenad	83
PETROVIĆ, Zvonko	17
PIERER, Alexander	1
POLANSKI, Marek	XXXV
R	
RACKOV, Milan	5
RANGELOV, Damjan	XXIII, 151, 155
RAŠOVIĆ, Nebojša	75
REZA GHAVI, Mohammad	XXXV
S	
SALAM Y. OBAID, Abdul	159
SAMARDZIĆ, Srđan	65, 71, 119
SAMARDŽIĆ, Ivan	XXXIII
SIMONOVIĆ, Miloš	XXIII
SIMONOVIĆ, Nikola	23, 129
SINĐELIĆ, Vladimir	95
SKULIĆ, Aleksandar	139
STAN, Sergiu-Dan	151
STEFANOVIĆ-MARINOVIĆ, Jelena	33, 151
STOJANOVIĆ, Blaža	139
STOJANOVIĆ, Lazar	XXIII, 151, 155
STOJIČIĆ, Srđan	23, 129
T	
TOMERLIN, Damir	XXXIII
TOMOVIĆ, Aleksandar	75, 79
TOMOVIĆ, Radoslav	75, 79
TRDAN, Uroš	XXXV
TRNAVAC, Dragana	23, 129
TROHA, Sanjin	33
V	
VLADIĆ, Jovan	89
VRCAN, Željko	33
VUČINA, Adisa	75
VUHERER, Tomaž	XXXV
Z	
ZDRAVKOVIĆ, Nataša	39, 147
Ž	
ŽIVKOVIĆ, Aleksandar	5
ŽIVKOVIĆ, Anđela	139

Vodeća firma u prodaji kotrljajućih ležajeva na području Jugoistočne Evrope

SKF
DB RAZVITAK
Ovlašćeni Distributer

Osnovni podaci:

- Godina osnivanja **1992.**
- **5.2% tržišnog učešća** u Srbiji
- Najveći lager u regionu sa preko **20 hiljada proizvoda** u prodajnom portfoliju
- Magacin površine **1300 m²**
- Bonitetna ocena **AAA** by dun&bradstreet
- ISO sertifikati **9001, 14001, 45001**
- 11 brendova renomiranih svetskih proizvođača u ponudi:

SKF FKL ZKL INA FAG NTN SNR BGL Sleeves for Bearings HFB ISB INDUSTRIES TIMKEN CORTECO thyssenkrupp

Sa više od **30 godina iskustva**, DB Razvitak je sinonim za kvalitet, pouzdanost i stručnost u oblasti ležajeva i srodnih proizvoda. Pažljiva selekcija i odabir pouzdanih visokokvalitetnih dobavljača sa kojima se gradi dugogodišnje partnerstvo, dovelo je do toga da firma danas snabdeva preko **500 zadovoljnih klijenata u 29 država.**

Fokus poslovanja je **na brzim isporukama sa visokom preciznošću, stručnoj tehničkoj podršci i kvalitetnom servisu.**

Dugogodišnje iskustvo rada rezultiralo je time da DB RAZVITAK postane **pouzdan dobavljač** firmama iz raznorodnih industrija, kao sto su: **elektroprivreda, čeličane, rudnici, železnice, poljoprivreda, prehrambena industrija, cementare, ciglane i druge.**

Kao što slogan kaže, DB Razvitak je najbolja opcija za korisnike koji traže **"sve na jednom mestu".**

Učešće grupa proizvoda u prodajnom asortimanu

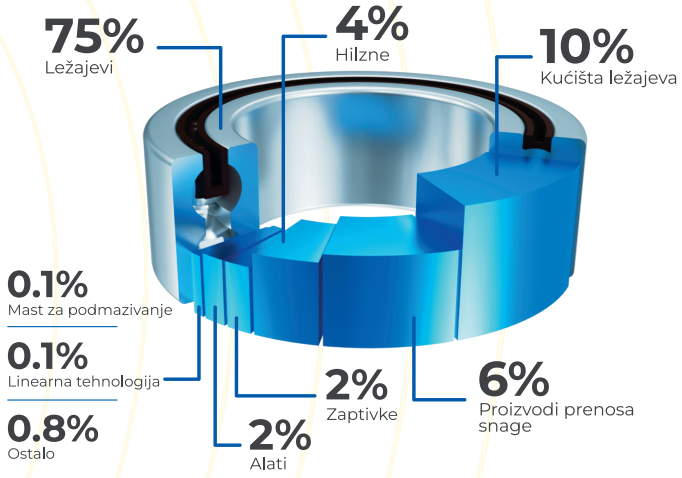

Kontakt podaci:

DB-RAZVITAK doo Veternik

Tri bagrema 2, 21203 Veternik, Srbija

+381 21 895 072

www.dbrazvitak.rs

DB RAZVITAK
Sve na jednom mestu!

Edicija 2025